Journal of Applied Mechanics

Published Bimonthly by ASME

VOLUME 72 • NUMBER 1 • JANUARY 2005

TECHNICAL PAPERS

BRIEF NOTES

(Contents continued on inside back cover)

This journal is printed on acid-free paper, which exceeds the ANSI Z39.48-1992 specification for permanence of paper and library materials. ∞™
♲ 85% recycled content, including 10% post-consumer fibers.

Editor
ROBERT M. McMEEKING
Assistant to the Editor
LIZ MONTANA

APPLIED MECHANICS DIVISION
Executive Committee
(Chair) **M. C. BOYCE**
W.-K. LIU
T. N. FARRIS
K. RAVI-CHANDAR
Associate Editors
E. ARRUDA (2007)
H. ESPINOSA (2007)
H. GAO (2006)
S. GOVINDJEE (2006)
D. A. KOURIS (2005)
K. M. LIECHTI (2006)
A. M. MANIATTY (2007)
I. MEZIC (2006)
M. P. MIGNOLET (2006)
S. MUKHERJEE (2006)
O. O'REILLY (2007)
K. RAVI-CHANDAR (2006)
N. SRI NAMACHCHIVAYA (2006)
Z. SUO (2006)
T. E. TEZDUYAR (2006)
N. TRIANTAFYLLIDIS (2006)
B. A. YOUNIS (2006)

PUBLICATIONS DIRECTORATE
Chair, **ARTHUR G. ERDMAN**

OFFICERS OF THE ASME
President, **HARRY ARMEN**
Executive Director, **V. R. CARTER**
Treasurer, **R. E. NICKELL**

PUBLISHING STAFF
Managing Director, Engineering
THOMAS G. LOUGHLIN
Director, Technical Publishing
PHILIP DI VIETRO
Production Coordinator
JUDITH SIERANT
Production Assistant
MARISOL ANDINO

Transactions of the ASME, Journal of Applied Mechanics (ISSN 0021-8936) is published bimonthly (Jan., Mar., May, July, Sept., Nov.) The American Society of Mechanical Engineers, Three Park Avenue, New York, NY 10016. Periodicals postage paid at New York, NY and additional mailing office. POSTMASTER: Send address changes to Transactions of the ASME, Journal of Applied Mechanics, c/o THE AMERICAN SOCIETY OF MECHANICAL ENGINEERS, 22 Law Drive, Box 2300, Fairfield, NJ 07007-2300. **CHANGES OF ADDRESS** must be received at Society headquarters seven weeks before they are to be effective. Please send old label and new address.

STATEMENT from By-Laws. The Society shall not be responsible for statements or opinions advanced in papers or . . . printed in its publications (B7.1, Para. 3).
COPYRIGHT © 2005 by The American Society of Mechanical Engineers. For authorization to photocopy material for internal or personal use under those circumstances not falling within the fair use provisions of the Copyright Act, contact the Copyright Clearance Center (CCC), 222 Rosewood Drive, Danvers, MA 01923, tel: 978-750-8400, www.copyright.com. Request for special permission or bulk copying should be addressed to Reprints/Permission Department.

INDEXED by Applied Mechanics Reviews and Engineering Information, Inc. Canadian Goods & Services Tax Registration #126148048. ded Piezoelectric Material Strip

(**Contents continued**)

Journal of Applied Mechanics **Volume 72, Number 1** **JANUARY 2005**

ANNOUNCEMENTS AND SPECIAL NOTES

The ASME Journal of Applied Mechanics is abstracted and indexed in the following:

Alloys Index, Aluminum Industry Abstracts, Applied Science & Technology Index, Ceramic Abstracts, Chemical Abstracts, Civil Engineering Abstracts, Compendex (The electronic equivalent of Engineering Index), Computer & Information Systems Abstracts, Corrosion Abstracts, Current Contents, EEA (Earthquake Engineering Abstracts Database), Electronics & Communications Abstracts Journal, Engineered Materials Abstracts, Engineering Index, Environmental Engineering Abstracts, Environmental Science and Pollution Management, Fluidex, Fuel & Energy Abstracts, GeoRef, Geotechnical Abstracts, INSPEC, International Aerospace Abstracts, Journal of Ferrocement, Materials Science Citation Index, Mechanical Engineering Abstracts, METADEX (The electronic equivalent of Metals Abstracts and Alloys Index), Metals Abstracts, Nonferrous Metals Alert, Polymers Ceramics Composites Alert, Referativnyi Zhurnal, Science Citation Index, SciSearch (Electronic equivalent of Science Citation Index), Shock and Vibration Digest, Solid State and Superconductivity Abstracts, Steels Alert, Zentralblatt MATH

O. G. McGee

J. W. Kim

Georgia Institute of Technology,
Atlanta, GA

A. W. Leissa
Ohio State University,
Columbus, OH

Sharp Corner Functions for Mindlin Plates

Transverse displacement and rotation eigenfunctions for the bending of moderately thick plates are derived for the Mindlin plate theory so as to satisfy exactly the differential equations of equilibrium and the boundary conditions along two intersecting straight edges. These eigenfunctions are in some ways similar to those derived by Max Williams for thin plates a half century ago. The eigenfunctions are called "corner functions," for they represent the state of stress currently in sharp corners, demonstrating the singularities that arise there for larger angles. The corner functions, together with others, may be used with energy approaches to obtain accurate results for global behavior of moderately thick plates, such as static deflections, free vibration frequencies, buckling loads, and mode shapes. Comparisons of Mindlin corner functions with those of thin-plate theory are made in this work, and remarkable differences are found. [DOI: 10.1115/1.1795221]

Introduction

The existence of stress singularities in sharp corners of loaded plates has been well known for more than a century. The nature of these singularities was carefully studied by Williams [1,2] for thin plates in bending, and for the plane stress and plane strain problems of two-dimensional elasticity, all of them relating to the biharmonic differential equation. Williams investigated all combinations of boundary conditions along the intersecting edges; for plate bending, these were for clamped, simply supported, and free edges. He derived the eigenfunctions that satisfied the biharmonic equation and the boundary conditions along the edges and, thus, at the sharp corner of intersection.

These eigenfunctions, which may be called ''corner functions,'' have been found to be very useful in solving problems involving the overall behavior of plates. For example, free vibrations of circular sectorial plates having reentrant corners or V-notches [3–5], of cantilevered skew plates [6,7], and of rhombic plates [8,9] have been studied using these functions. Transverse deflections of statically loaded plates, or bifurcation buckling of them, could equally well be analyzed with the functions; but to the authors' knowledge they have not yet been. Mathematically complete sets of other functions (trigonometric and algebraic) are added to the corner functions to effect accurate solutions by means of an energy approach—the Ritz method, in the case of the free vibration problems.

It is well known that at least shear deformation and rotary inertia effects need to be considered if the plate is moderately thick or if the higher free vibration frequencies of thin plates are needed (cf. Leissa, [10]). Thus, it is desirable to have corner functions that consider the shear deformation, as well as the bending deformation, inherently. These may be used when sharp corners containing bending and/or transverse shear stress singularities are present to solve not only free vibration problems, but also static deflection and buckling problems for moderately thick plates. Haggblad and Bathe [11] examined the stress singularities near a corner for the case of two intersecting simply supported edges, as a part of a more general study of boundary layer behavior of a Reissner/Mindlin plate theory in choosing proper mesh sizes near edges when using finite elements. The purpose of the present work is to derive the corner functions for all types of intersecting edge conditions that may be encountered or closely approached in physical situations and to compare them with those that have been used for the thin plate theory.

Governing Equations of the Mindlin Theory

The well-known Mindlin theory assumes displacement components in the form [12–14]

$$
\begin{aligned}
u_r(r,\theta,z)&=z\,\phi_r(r,\theta)\\
u_\theta(r,\theta,z)&=z\,\phi_\theta(r,\theta)\\
w(r,\theta,z)&=w(r,\theta)
\end{aligned}
\tag{1}
$$

in polar coordinates where u_r and u_θ are radial and circumferential components in the midplane, respectively, and w is transverse. Thus, ϕ_r and ϕ_θ are rotations of normals to the midplane due to bending. The transverse shear strains are implicitly present as the differences between the total slopes $[\partial w/\partial r,(1/r)\partial w/\partial\theta]$ of the deformed middle surface and the bending rotations.

The governing equations of equilibrium for a plate in polar coordinates are expressed in terms of moment resultants M_r, M_θ, and $M_{r\theta}$ and shear force resultants Q_r and Q_θ as

$$
\begin{aligned}
&\frac{\partial M_r}{\partial r}+\frac{1}{r}\frac{\partial M_{r\theta}}{\partial\theta}+\frac{M_r-M_\theta}{r}-Q_r=0\\
&\frac{\partial M_{r\theta}}{\partial r}+\frac{1}{r}\frac{\partial M_\theta}{\partial\theta}+\frac{2}{r}M_{r\theta}-Q_\theta=0\\
&\frac{\partial Q_r}{\partial r}+\frac{1}{r}\frac{\partial Q_\theta}{\partial\theta}+\frac{1}{r}Q_r=0
\end{aligned}
\tag{2}
$$

The resultants are related to the bending rotations and transverse displacement by

$$
\begin{aligned}
M_r&=D\left[\frac{\partial\phi_r}{\partial r}+\frac{\nu}{r}\left(\phi_r+\frac{\partial\phi_\theta}{\partial\theta}\right)\right]\\
M_\theta&=D\left[\frac{1}{r}\left(\phi_r+\frac{\partial\phi_\theta}{\partial\theta}\right)+\nu\frac{\partial\phi_r}{\partial r}\right]\\
M_{r\theta}&=\frac{(1-\nu)D}{2}\left[\frac{1}{r}\left(\frac{\partial\phi_r}{\partial\theta}-\phi_\theta\right)+\frac{\partial\phi_\theta}{\partial r}\right]\\
Q_r&=\kappa^2Gh\left(\phi_r+\frac{\partial w}{\partial r}\right)
\end{aligned}
\tag{3}
$$

Contributed by the Applied Mechanics Division of THE AMERICAN SOCIETY OF MECHANICAL ENGINEERS for publication in the ASME JOURNAL OF APPLIED MECHANICS. Manuscript received by the Applied Mechanics Division, June 5, 2002; final revision, January 8, 2004. Associate Editor: O. O'Reilly. Discussion on the paper should be addressed to the Editor, Prof. Robert M. McMeeking, Journal of Applied Mechanics, Department of Mechanical and Environmental Engineering, University of California—Santa Barbara, Santa Barbara, CA 93106-5070, and will be accepted until four months after final publication of the paper itself in the ASME JOURNAL OF APPLIED MECHANICS.

$$Q_\theta=\kappa^2Gh\left(\phi_\theta+\frac{1}{r}\frac{\partial w}{\partial\theta}\right)$$

In Eq. (3) $D=Eh^3/12(1-\nu^2)$ is the flexural rigidity, where E is Young's modulus, h is the plate thickness, and ν is the Poisson ratio. In addition, $G=E/2(1+\nu)$ is the shear modulus and $\kappa^2=\pi^2/12$ [12] is the shear correction factor. Substituting Eq. (3) into Eq. (2) yields

$$\frac{D}{2}\left[(1-\nu)\left(\frac{\partial^2\phi_r}{\partial r^2}+\frac{1}{r}\frac{\partial\phi_r}{\partial r}-\frac{\phi_r}{r^2}-\frac{2}{r^2}\frac{\partial\phi_\theta}{\partial\theta}+\frac{1}{r^2}\frac{\partial^2\phi_r}{\partial\theta^2}\right)+(1+\nu)\left(\frac{\partial^2\phi_r}{\partial r^2}+\frac{1}{r}\frac{\partial\phi_r}{\partial r}-\frac{\phi_r}{r^2}-\frac{1}{r^2}\frac{\partial\phi_\theta}{\partial\theta}+\frac{1}{r}\frac{\partial^2\phi_\theta}{\partial r\partial\theta}\right)\right]-\kappa^2Gh\left(\phi_r+\frac{\partial w}{\partial r}\right)=0$$

$$\frac{D}{2}\left[(1-\nu)\left(\frac{\partial^2\phi_\theta}{\partial r^2}+\frac{1}{r}\frac{\partial\phi_\theta}{\partial r}-\frac{\phi_\theta}{r^2}+\frac{1}{r^2}\frac{\partial^2\phi_\theta}{\partial\theta^2}+\frac{2}{r^2}\frac{\partial\phi_r}{\partial\theta}\right)+(1+\nu)\left(\frac{1}{r^2}\frac{\partial^2\phi_\theta}{\partial\theta^2}+\frac{1}{r}\frac{\partial^2\phi_r}{\partial r\partial\theta}+\frac{1}{r^2}\frac{\partial\phi_r}{\partial\theta}\right)\right]-\kappa^2Gh\left(\phi_\theta+\frac{1}{r}\frac{\partial w}{\partial\theta}\right)=0 \quad (4)$$

$$\kappa^2Gh\left(\frac{\partial\phi_r}{\partial r}+\frac{\phi_r}{r}+\frac{1}{r}\frac{\partial\phi_\theta}{\partial\theta}-\frac{\partial^2w}{\partial r^2}-\frac{1}{r}\frac{\partial w}{\partial r}-\frac{1}{r^2}\frac{\partial^2w}{\partial\theta^2}\right)=0$$

General Solutions and Boundary Conditions

To obtain solutions of Eq. (4), the bending rotations and transverse displacement of the Mindlin plate are assumed as

$$\begin{aligned}\phi_r(r,\theta)&=r^\lambda\Psi_r(\theta)\\ \phi_\theta(r,\theta)&=r^\lambda\Psi_\theta(\theta)\\ w(r,\theta)&=r^{\bar\lambda+1}F_z(\theta)\end{aligned}\quad (5)$$

where the eigenvalues λ and $\bar\lambda$ are generally complex numbers, and Ψ_r, Ψ_θ, and F_z are functions of θ only.

Consider now the explicit forms of Ψ_r, Ψ_θ, and F_z. Equation (5) is inserted into the equilibrium equations (4). This yields a system of three simultaneous ordinary differential equations in terms of three unknown functions Ψ_r, Ψ_θ, and F_z as follows:

$$D\{(1-\nu)[\Psi_r''+(\lambda^2-1)\Psi_r-2\Psi_\theta']+(1+\nu)[(\lambda^2-1)\Psi_r+(\lambda-1)\Psi_\theta']-2\kappa^2Gh[r^2\Psi_r+(\lambda+1)r^{\bar\lambda-\lambda+2}F_z]\}=0$$

$$D\{(1-\nu)[\Psi_\theta''+(\lambda^2-1)\Psi_\theta+2\Psi_r']+(1+\nu)[(\Psi_\theta''+(\lambda+1)\Psi_r']-2\kappa^2Gh(r^2\Psi_\theta+r^{\bar\lambda-\lambda+2}F_z')\}=0 \quad (6)$$

$$F_z''+(\bar\lambda+1)^2F_z-r^{\lambda-\bar\lambda}[(\lambda+1)\Psi_r+\Psi_\theta']=0$$

where the primes indicate derivatives with respect to θ. It should be pointed out that the variable r is still present since the shear terms involving r^2, $r^{\bar\lambda-\lambda+2}$, and $r^{\lambda-\bar\lambda}$ appear in Eq. (6). However, in the immediate neighborhood of the vertex (i.e., as $r\to 0$), these terms vanish when compared to other terms in Eq. (6), provided that $\lambda-2<\bar\lambda<\lambda$ and the displacements and slopes are bounded. This is a key point in this derivation. No attempt is being made here to obtain solutions of Eq. (6) that are valid for all values of r. Instead, corner functions are being derived that satisfy Eq. (6) and boundary conditions exactly only at the corner ($r=0$). As described earlier in the Introduction, the value of such functions is that they account for the stress singularities exactly in the corner when used with additional smooth functions to solve problems by an energy method, thereby accelerating considerably the convergence of the solutions (e.g., free vibration frequencies) toward the exact values as more terms are added. Thus, Eq. (6) reduces to

$$\begin{aligned}&(1-\nu)[\Psi_r''+(\lambda^2-1)\Psi_r-2\Psi_\theta']+(1+\nu)[(\lambda^2-1)\Psi_r\\&+(\lambda-1)\Psi_\theta']=0\end{aligned}\quad (7a)$$

$$(1-\nu)[\Psi_\theta''+(\lambda^2-1)\Psi_\theta+2\Psi_r']+(1+\nu)[\Psi_\theta''+(\lambda+1)\Psi_r']=0 \quad (7b)$$

$$F_z''+(\bar\lambda+1)^2F_z=0 \quad (7c)$$

Differentiating Eq. (7*a*) with respect to θ and rearranging the result, the following equation is obtained:

$$(1-\nu)\Psi_r'''+2(\lambda^2-1)\Psi_r'+[\lambda(1+\nu)-3+\nu]\Psi_\theta''=0 \quad (8)$$

From Eq. (7*b*),

$$\Psi_r'=-\frac{1}{\lambda(1+\nu)+3-\nu}[2\Psi_\theta''+(1-\nu)(\lambda^2-1)\Psi_\theta] \quad (9)$$

and substituting this into Eq. (8) yields

$$\Psi_\theta^{IV}+[(\lambda+1)^2+(\lambda-1)^2]\Psi_\theta''+(\lambda+1)^2(\lambda-1)^2\Psi_\theta=0 \quad (10)$$

The general solution of the above equation is found to be

$$\begin{aligned}\Psi_\theta(\theta)=&A\cos(\lambda+1)\theta+B\sin(\lambda+1)\theta+C\cos(\lambda-1)\theta\\&+D\sin(\lambda-1)\theta\end{aligned}\quad (11)$$

where A, B, C, and D are arbitrary constants. It should be noted that the above solution is not valid for $\lambda=0$ or $\lambda=\pm1$ because for such eigenvalues, the general solution of Eq. (10) is not in the form given by Eq. (11).

The function Ψ_r is determined by back substitution of Eq. (11) into (9) and integration of the resulting equation. That is,

$$\begin{aligned}\Psi_r(\theta)=&A\sin(\lambda+1)\theta-B\cos(\lambda+1)\theta+\gamma C\sin(\lambda-1)\theta\\&-\gamma D\cos(\lambda-1)\theta\end{aligned}\quad (12)$$

where

$$\gamma=\frac{\lambda(1+\nu)-3+\nu}{\lambda(1+\nu)+3-\nu} \quad (13)$$

The solution F_z of Eq. (7*c*) is

$$F_z(\theta)=G\sin(\bar{\lambda}+1)\theta+H\cos(\bar{\lambda}+1)\theta \tag{14}$$

where G and H are also arbitrary constants.

Consequently, by introducing Eqs. (11), (12), and (14) into Eq. (5), the following solutions for bending rotations and transverse displacement are obtained:

$$\phi_r(r,\theta)=r^{\lambda}[A\sin(\lambda+1)\theta-B\cos(\lambda+1)\theta+\gamma C\sin(\lambda-1)\theta - \gamma D\cos(\lambda-1)\theta] \tag{15a}$$

$$\phi_\theta(r,\theta)=r^{\lambda}[A\cos(\lambda+1)\theta+B\sin(\lambda+1)\theta+C\cos(\lambda-1)\theta + D\sin(\lambda-1)\theta] \tag{15b}$$

$$w(r,\theta)=r^{\bar{\lambda}+1}[G\sin(\bar{\lambda}+1)\theta+H\cos(\bar{\lambda}+1)\theta] \tag{15c}$$

where the characteristic values λ and $\bar{\lambda}$ are determined from the boundary conditions along the radial edges.

Since the circumferential edge condition away from the vertex of the sharp corner does not influence stress behavior within a sufficiently small neighborhood of the vertex, only support conditions along the radial edge are considered. Boundary conditions along the radial edge $\theta=\theta_0$ (a constant) are characterized as one of following four cases.

1. *Free radial edge*. In Mindlin plate theory, the bending moment, twisting moment, and shear force must all vanish so that

$$M_\theta(r,\theta_0)=M_{r\theta}(r,\theta_0)=Q_\theta(r,\theta_0)=0 \tag{16}$$

2. *Simply supported radial edge*. There are two possible ways of enforcing simply supported conditions in Mindlin plate theory:

   a. Condition S. For the first simply supported condition,

$$M_\theta(r,\theta_0)=\phi_r(r,\theta_0)=W(r,\theta_0)=0 \tag{17a}$$

   b. Conditions S*. For the second simply supported boundary condition,

$$M_\theta(r,\theta_0)=M_{r\theta}(r,\theta_0)=W(r,\theta_0)=0 \tag{17b}$$

3. *Clamped radial edge*. For this type of support condition,

$$\phi_r(r,\theta_0)=\phi_\theta(r,\theta_0)=w(r,\theta_0)=0 \tag{18}$$

Characteristic Equations and Corner Functions

In this section the procedure of deriving characteristic equations for λ and $\bar{\lambda}$ and the associated corner functions is demonstrated in the case where both radial edges are simply supported. Here, Mindlin simply supported conditions along the radial edges $\theta=\pm\alpha/2$ are defined such that the circumferential moment, tangential rotation, and transverse displacement all vanish (i.e., condition S). Because of the symmetry of the edge conditions with respect to $\theta=0$ the displacement components ϕ_r, ϕ_θ, and w may be divided into symmetric and antisymmetric parts.

For the symmetric case, when the even functions of θ in Eqs. (15*a*) and (15*c*) and the odd functions of θ in Eq. (15*b*), that is $A=C=G=0$, are inserted into the boundary conditions (Eqs. (17*a*)) a set of algebraic equations for B, D, and H are obtained,

$$\lambda(1-\nu)B\cos\frac{(\lambda+1)\alpha}{2}-\hat{\gamma}D\cos\frac{(\lambda-1)\alpha}{2}=0 \tag{19a}$$

$$-B\cos\frac{(\lambda+1)\alpha}{2}-\gamma D\cos\frac{(\lambda-1)\alpha}{2}=0 \tag{19b}$$

$$H\cos\frac{(\bar{\lambda}+1)\alpha}{2}=0 \tag{19c}$$

where $\hat{\gamma}=\gamma(\nu\lambda+1)-(\lambda-1)$. For a nontrivial solution, the determinant of the coefficients of Eqs. (19*a*)–(19*c*) must vanish. That is,

$$\begin{vmatrix} \lambda(1-\nu)\cos\frac{(\lambda+1)\alpha}{2} & -\hat{\gamma}\cos\frac{(\lambda-1)\alpha}{2} & 0 \\ -\cos\frac{(\lambda+1)\alpha}{2} & -\gamma\cos\frac{(\lambda-1)\alpha}{2} & 0 \\ 0 & 0 & \cos\frac{(\bar{\lambda}+1)\alpha}{2} \end{vmatrix}=0 \tag{20}$$

After expanding and simplifying Eq. (20) the resulting characteristic equations for λ and $\bar{\lambda}$ are, respectively,

$$\cos\alpha=-\cos\lambda\alpha, \qquad \cos\frac{(\bar{\lambda}+1)\alpha}{2}=0 \tag{21}$$

From Eq. (19*b*), the relationship between B and D is

$$\frac{B}{D}=-\frac{\gamma\cos\frac{(\lambda-1)\alpha}{2}}{\cos\frac{(\lambda+1)\alpha}{2}} \tag{22}$$

Similarly, for the antisymmetric case, when coefficients B, D, and H are set to zero in Eqs. (15*a*)–(15*c*), the characteristic equations for λ and $\bar{\lambda}$ are

$$\cos\alpha=\cos\lambda\alpha, \qquad \sin\frac{(\bar{\lambda}+1)\alpha}{2}=0 \tag{23}$$

and the A are related to C by

$$\frac{A}{C}=-\frac{\gamma\sin\frac{(\lambda-1)\alpha}{2}}{\sin\frac{(\lambda+1)\alpha}{2}} \tag{24}$$

As a result, upon combining Eqs. (21) and (23), the characteristic equations for Mindlin plates, which are simply supported (condition S) along both intersecting, radial edges are

$$\cos\alpha=\mp\cos\lambda\alpha \tag{25a}$$

$$\sin(\bar{\lambda}+1)\alpha=0 \tag{25b}$$

in which Eq. (25*a*) is exactly the same as the characteristic equations for thin sectorial plates with simply supported radial edges [1], and Eq. (25*b*) is additional for the transverse shear stress resultant. There are an infinite number of real roots, (i.e., eigenvalues, λ and $\bar{\lambda}$) of Eqs. (25). Corresponding to each λ and $\bar{\lambda}$, eigenfunctions ϕ_r, ϕ_θ, and w are the desired corner functions, obtained by substituting Eqs. (22) and (24) back into Eqs. (15*a*) and (15*b*).

Using the sets of boundary conditions given by Eqs. (16)–(18) and following the same procedure, characteristic equations for λ and $\bar{\lambda}$ and corner functions can be derived for Mindlin plate theory for arbitrary boundary conditions along the two intersecting edges. Table 1 summarizes the characteristic equations for all ten possible combinations of boundary conditions. It is found that the first of the two equations shown in Table 1 for both edges simply supported (S) is identical to that arising from thin plate theory, but all other cases yield equations that are significantly different. As described above, the second characteristic equation for transverse shear stress resultants in each case, which is accounting for the transverse shear stress, does not arise in thin plate theory. In the Appendix, the Mindlin corner functions for the different combinations of free, simply supported (S and S*), and clamped radial edge conditions are summarized.

Table 1 Characteristic equations of λ_k and $\bar{\lambda}_k$ for different boundary conditions based on Mindlin plate theory

Boundary Condition		Characteristic equation
$\theta=0$	$\theta=\alpha$	
Clamped	Clamped	$\sin\lambda_k\alpha=\pm\left(\frac{1+\nu}{3-\nu}\right)\lambda_k\sin\alpha,\quad \sin(\bar{\lambda}_k+1)\alpha=0$
Clamped	Simply supported (S)	$\sin 2\lambda_k\alpha=-\left(\frac{1+\nu}{3-\nu}\right)\lambda_k\sin 2\alpha,\quad \sin(\bar{\lambda}_k+1)\alpha=0$
Clamped	Simply supported (S*)	$\sin^2\lambda_k\alpha=\frac{4-(1+\nu)^2\lambda_k^2\sin^2\alpha}{(3-\nu)(1+\nu)},\quad \sin(\bar{\lambda}_k+1)\alpha=0$
Clamped	Free	$\sin^2\lambda_k\alpha=\frac{4-(1+\nu)^2\lambda_k^2\sin^2\alpha}{(3-\nu)(1+\nu)},\quad \cos(\bar{\lambda}_k+1)\alpha=0$
Simply supported (S)	Simply supported (S)	$\cos\lambda_k\alpha=\mp\cos\alpha,\ \sin(\bar{\lambda}_k+1)\alpha=0$
Simply supported (S)	Simply supported (S*)	$\sin 2\lambda_k\alpha=\lambda_k\sin 2\alpha,\ \sin(\underline{\lambda}_k+1)\alpha=0$
Simply supported (S)	Free	$\sin 2\lambda_k\alpha=\lambda_k\sin 2\alpha,\ \cos(\underline{\lambda}_k+1)\alpha=0$
Simply supported (S*)	Simply supported (S*)	$\sin\lambda_k\alpha=\mp\lambda_k\sin\alpha,\ \sin(\underline{\lambda}_k+1)\alpha=0$
Simply supported (S*)	Free	$\sin\lambda_k\alpha=\mp\lambda_k\sin\alpha,\ \cos(\underline{\lambda}_k+1)\alpha=0$
Free	Free	$\sin\lambda_k\alpha=\mp\lambda_k\sin\alpha,\ \sin(\lambda_k+1)\alpha=0$

Discussion of Stress Singularities at Reentrant Corners of Mindlin Plates

When the displacement functions given in Eq. (5) are substituted into Eq. (3), the bending and twisting moment resultants are written as

$$M_r=Dr^{\lambda-1}\left[(\lambda+\nu)\Psi_r+\nu\frac{\partial\Psi_\theta}{\partial\theta}\right]$$

$$M_\theta=Dr^{\lambda-1}\left[(\nu\lambda+1)\Psi_r+\frac{\partial\Psi_\theta}{\partial\theta}\right]\tag{26}$$

$$M_{r\theta}=\frac{(1-\nu)D}{2}r^{\lambda-1}\left[(\lambda-1)\Psi_\theta+\frac{\partial\Psi_r}{\partial\theta}\right]$$

and the transverse shear stress resultants become

$$Q_r=\kappa^2Ghr^{\bar{\lambda}}[\Psi_r+(\bar{\lambda}+1)F_z]$$

$$Q_\theta=\kappa^2Ghr^{\bar{\lambda}}\left(\Psi_\theta+\frac{\partial F_z}{\partial\theta}\right)\tag{27}$$

where the functions Ψ_r, Ψ_θ, and F_z are presented in Eqs. (11), (12), and (14). It can be recognized from Eq. (26) that the bending moments M_r, M_θ, and $M_{r\theta}$ at the vertex ($r=0$) of intersecting straight edges, according to the Mindlin theory, vary identically to those found for classical thin plate theory, namely, an $r^{\lambda-1}$-type singularity for $0<\lambda<1$. The transverse shear forces Q_r and Q_θ (Eqs. (27)) near $r=0$ of Mindlin theory vary as $r^{\bar{\lambda}}$ when $-1<\bar{\lambda}<0$. For $\lambda>1$ and $\bar{\lambda}>0$, no singular moments and shear forces exist at the vertex of intersecting edges according to the Mindlin theory. Characteristic values of $\lambda<0$ for the rotations ϕ_r and ϕ_θ and $\lambda<-1$ for transverse displacement w also exist, but are not used. For such values the displacement components [see Eqs. (15)] become infinite at $r=0$, which is not acceptable in the physical sense.

Figure 1 shows a plot of the minimum real parts of λ as function of α arising from the characteristic equations shown in Table 1. In constructing Fig. 1 the Poisson ratio ν has been set to 0.3. The cusps arise in the curves because only the minimum roots are shown. A study of Fig. 1 reveals that for vertex angles (α) between 180 and 360 deg, all the cases considered have the bending and twisting moment singularities; that is, Eq. (26) shows that this occurs when $\lambda<1$. On the other hand, regardless of the radial edge conditions of the Mindlin sectorial plates, there is no moment singularity if the vertex angle α is less than 63 deg. The moment singularities are present at $\alpha>90$ deg for simply supported (S)

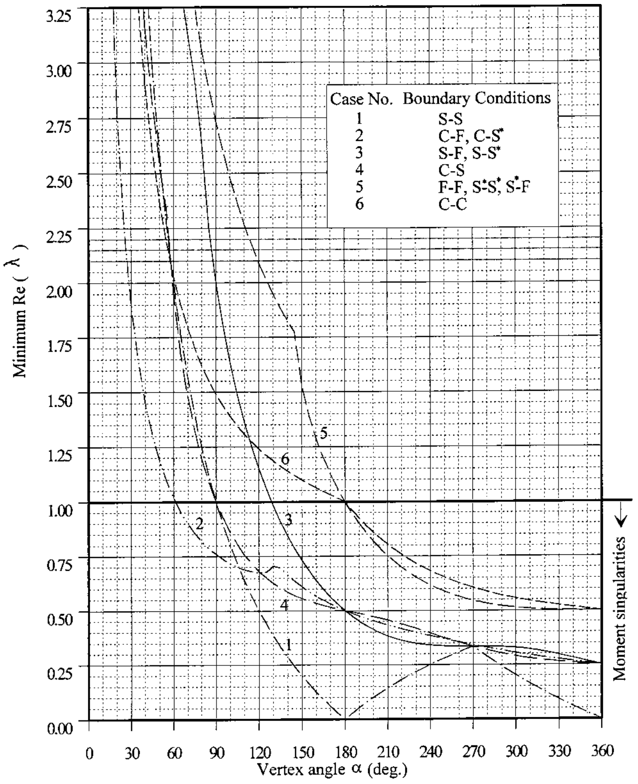

Fig. 1 Variation of minimum values of Re(λ) with vertex angle α based on Mindlin plate theory (ν=0.3)

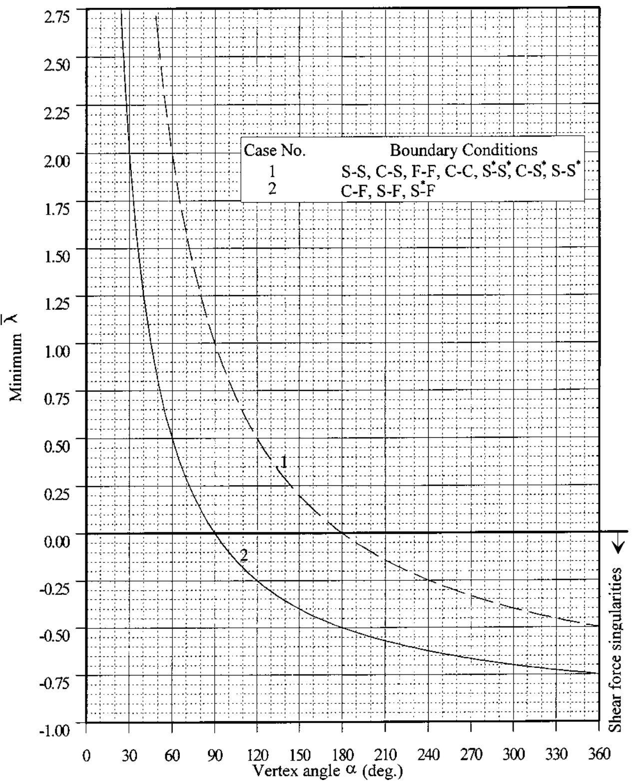

Fig. 2 Variation of minimum values of $\bar{\lambda}$ with vertex angle α based on Mindlin plate theory (all ν)

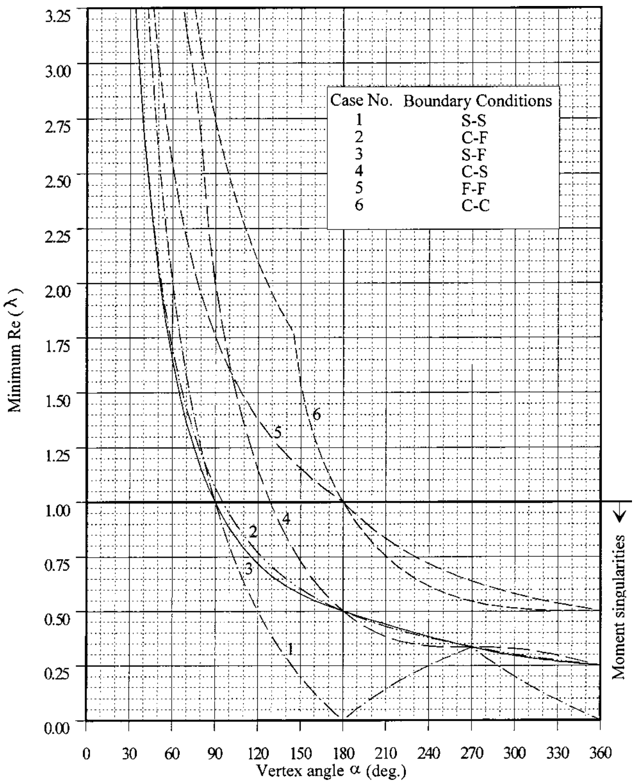

Fig. 3 Variation of minimum values of Re(λ_k) with vertex angle α based on classical plate theory (ν=0.3)

(Case 1) and clamped-simply supported (S) (Case 4) radial edges, whereas the singular moments exist at α>180 deg for free-free (Case 5) and clamped-clamped (Case 6) radial edges. For the clamped-free (Case 2) and simply supported (S)-free (Case 3) radial edges, the moment singularities exist at α>63 deg and α>128 deg, respectively. In all the cases except Case 1, the strength of the moment singularity at the vertex of the Mindlin sectorial plates increases with increasing α. When α=360 deg (i.e., radial line crack), the orders of the moment singularities at the tip of the crack are $r^{-1/2}$ for Cases 5 and 6, $r^{-3/4}$ for Cases 2–4, and r^{-1} for Case 1.

The minimum values of $\bar{\lambda}$ given in Table 1 are presented in Fig. 2 as a function of vertex angle α. Here, the values of $\bar{\lambda}$ are independent of the Poisson ratio ν. According to Eq. (27), transverse shear force singularities occur when $\bar{\lambda}<0$. Figure 2 shows clearly that the strength of this singularity at the vertex of the Mindlin sectorial plates increases monotonically with increasing α. The singular shear forces exist at α>180 deg for Case 1 (which includes simply supported (S), clamped-simply supported (S), free-free, and clamped-clamped radial edges). For Case 2 (which includes clamped-free and simply supported (S)-free radial edges) the singular shear forces arise at α>90 deg. When α=360 deg, the orders of the shear force singularities at the tip of the crack are $r^{-1/2}$ for Case 1, and $r^{-3/4}$ for Case 2. It appears, from Figs. 1 and 2, that for the vertex angles greater than 180 deg, all the cases, regardless of radial edge conditions, have singular moments and transverse shear forces. For clamped-free radial edges, both moment and transverse shear force singularities arise when α>90 deg, whereas those singularities on the simply supported (S)-free radial edges are introduced when α>128 deg.

In order to demonstrate the types of moment and transverse shear force singularities obtained from the foregoing analysis, calculations are made for characteristic values in the case where the radial edges are both simply supported (S). Here, the characteristic equations for λ and $\bar{\lambda}$ [see Eqs. (25)] have closed form, exact solutions. These are, for moments,

$$\begin{cases} \lambda_p=\dfrac{p\pi}{\alpha}-1, \quad (p=1,2,3,\ldots) & \text{for } 0 \text{ deg} \leqslant \alpha \leqslant 180 \text{ deg} \\ \lambda_q=\dfrac{q\pi}{\alpha}+1, \quad (q=-1,1,2,\ldots) & \text{for } 180 \text{ deg} \leqslant \alpha \leqslant 360 \text{ deg} \end{cases} \tag{28}$$

and for the transverse shear forces,

$$\bar{\lambda}_s=\frac{s\pi}{\alpha}-1, \quad (s=1,2,3,\ldots) \quad \text{for all } \alpha \tag{29}$$

It is clear from Eqs. (28) and (29) that the orders of bending and twisting moments are $r^{\pi/\alpha-2}$ for 0 deg $\leqslant\alpha\leqslant$180 deg and $r^{-\pi/\alpha}$ for 180 deg $\leqslant\alpha\leqslant$360 deg, while the order of transverse shear forces is $r^{\pi/\alpha-1}$ for all α.

Comparisons of Classical and Mindlin Plate Singularities

One would think that the results from a moderately thick plate theory, such as that of Mindlin, would be similar to those of the classical (thin) plate theory and would approach them as the thickness ratio becomes small. But such is not the case with the moment singularities considered above. Not only do the Mindlin characteristic equations (Table 1) not contain a thickness ratio, but, except for the plate having the intersecting edges both simply supported (S), the characteristic equations are significantly different. These equations for the thin plate theory are available in the paper by Leissa et al. [3].

To permit direct comparison with the eigenvalues (λ) shown in Fig. 1, the corresponding eigenvalues of thin plate theory are shown in Fig. 3, which are the roots of their characteristic equations. One sees, for example, that Case 1 (S-S) is the same curve in both figures, as it should be, arising from the same characteristic equation. But one sees also that Case 5 (F-F,S*-S*,S*-F) of Mindlin plate theory has the same curve as Case 6 (C-C) of classical plate theory. Remarkably, the characteristic equations (Table 1) for all three edge combinations are identical and do not contain ν. Interestingly, the C-C plate for the Mindlin theory (Case 6) has a curve in Fig. 1 similar to, but slightly different from the F-F classical plate (Case 5). The Poisson ratio appears in the characteristic equations for both theories, but for $\nu=0$ they would be identical.

Of particular interest is the relative strengths of the moment singularities between the theories. Comparing them for the C-C edges at, for example $\alpha=240$ deg, one sees $\lambda=0.68$ for Mindlin theory (Fig. 1) and $\lambda=0.74$ for classical plate theory (Fig. 3), indicating a slightly stronger singularity for the former. The higher roots of λ contribute less, if any, singularity. But if one compares Cases 2, 3, and 4 (C-F,S-F,C-S) of classical theory in Fig. 3 with those of Fig. 1, one sees large differences in λ. It is also interesting to observe in Fig. 1 that, according to the Mindlin theory, the C-F and C-S* combinations (Case 2) of intersecting edges generate moment singularities for external corners having acute angles greater than 63 deg; whereas in classical theory, they arise only for obtuse ($\alpha>90$ deg) and reflex ($\alpha>180$ deg) angles.

Concluding Remarks

In the above work the corner functions are derived for each of the ten possible combinations of radial edge conditions that may exist at a sharp corner, according to the Mindlin plate theory, accounting for transverse shear deformation as well as bending deformation. These functions are different from those of classical (thin) plate theory for bending, not only in the functional forms, but also in the eigenvalues (λ and $\bar{\lambda}$), which appear as arguments in the functions. The Mindlin plate corner functions may be used to obtain accurate results for the global behavior (static deflections, vibration frequencies, buckling loads, mode shapes) of moderately thick, isotropic, homogeneous plates, in the same manner that has been carried out for thin plates when sharp corners causing moment singularities are present.

It was also shown that the moment singularities arising in the Mindlin theory are, in some cases, significantly different from those arising in the thin plate theory. Why this should be the case is a topic worthy of further study.

Appendix: Mindlin Plate Corner Functions for Various Radial Edge Conditions

In this appendix the Mindlin plate corner functions are summarized for the possible combinations of clamped, simply supported (conditions S and S*), and free radial edge conditions that are examined in the present study. The corresponding characteristic equations for λ_k and $\bar{\lambda}_k$ are given in Table 1.

Clamped-Clamped Radial Edges

For Symmetric Modes.

$$\phi_r(r,\theta)=\sum_{k=1}^{\infty} D_k r^{\lambda_k}\left[\frac{\gamma_k\cos\frac{(\lambda_k-1)\alpha}{2}}{\cos\frac{(\lambda_k+1)\alpha}{2}}\cos(\lambda_k+1)\theta-\gamma_k\cos(\lambda_k-1)\theta\right] \tag{A1a}$$

$$\phi_\theta(r,\theta)=\sum_{k=1}^{\infty} D_k r^{\lambda_k}\left[-\frac{\sin\frac{(\lambda_k-1)\alpha}{2}}{\sin\frac{(\lambda_k+1)\alpha}{2}}\sin(\lambda_k+1)\theta+\sin(\lambda_k-1)\theta\right] \tag{A1b}$$

$$w(r,\theta)=\sum_{k=1}^{\infty} H_k r^{\bar{\lambda}_k+1}\cos(\bar{\lambda}_k+1)\theta \tag{A1c}$$

where γ is given by Eq. (13).

For Antisymmetric Modes.

$$\phi_r(r,\theta)=\sum_{k=1}^{\infty} C_k r^{\lambda_k}\left[-\frac{\gamma_k\sin\frac{(\lambda_k-1)\alpha}{2}}{\sin\frac{(\lambda_k+1)\alpha}{2}}\sin(\lambda_k+1)\theta+\gamma_k\sin(\lambda_k-1)\theta\right] \tag{A1d}$$

$$\phi_\theta(r,\theta)=\sum_{k=1}^{\infty} C_k r^{\lambda_k}\left[-\frac{\cos\frac{(\lambda_k-1)\alpha}{2}}{\cos\frac{(\lambda_k+1)\alpha}{2}}\cos(\lambda_k+1)\theta+\cos(\lambda_k-1)\theta\right] \tag{A1e}$$

$$w(r,\theta)=\sum_{k=1}^{\infty} G_k r^{\bar{\lambda}_k+1}\sin(\bar{\lambda}_k+1)\theta \tag{A1f}$$

Clamped-Simply Supported (S) Radial Edges

$$\phi_r(r,\theta)=\sum_{k=1}^{\infty} C_k r^{\lambda_k}[-\sin(\lambda_k+1)\theta+\gamma_k f_{1k}\cos(\lambda_k+1)\theta+\gamma_k\sin(\lambda_k-1)\theta-\gamma_k f_{1k}\cos(\lambda_k-1)\theta] \tag{A2a}$$

$$\phi_\theta(r,\theta)=\sum_{k=1}^{\infty} C_k r^{\lambda_k}[-\cos(\lambda_k+1)\theta-\gamma_k f_{1k}\sin(\lambda_k+1)\theta+\cos(\lambda_k-1)\theta-f_{1k}\sin(\lambda_k-1)\theta] \tag{A2b}$$

$$w(r,\theta)=\sum_{k=1}^{\infty} G_k r^{\bar{\lambda}_k+1}\sin(\bar{\lambda}_k+1)\theta \tag{A2c}$$

where

$$f_{1k}=\frac{\sin(\lambda_k+1)\alpha-\gamma_k\sin(\lambda_k-1)\alpha}{\gamma_k[\cos(\lambda_k+1)\alpha-\cos(\lambda_k-1)\alpha]} \tag{A2d}$$

Clamped-Simply Supported (S*) Radial Edges

$$\phi_r(r,\theta)=\sum_{k=1}^{\infty} C_k r^{\lambda_k}[-\sin(\lambda_k+1)\theta-\gamma_k f_{2k}\cos(\lambda_k+1)\theta+\gamma_k\sin(\lambda_k-1)\theta+\gamma_k f_{2k}\cos(\lambda_k-1)\theta] \tag{A3a}$$

$$\phi_\theta(r,\theta)=\sum_{k=1}^{\infty} C_k r^{\lambda_k}[-\cos(\lambda_k+1)\theta+\gamma_k f_{2k}\sin(\lambda_k+1)\theta+\cos(\lambda_k-1)\theta-f_{2k}\sin(\lambda_k-1)\theta] \tag{A3b}$$

$$w(r,\theta)=\sum_{k=1}^{\infty} G_k r^{\bar{\lambda}_k+1}\sin(\bar{\lambda}_k+1)\theta \tag{A3c}$$

where

$$f_{2k}=\frac{2\lambda_k\cos(\lambda_k+1)\alpha-(\gamma_k+1)(\lambda_k-1)\cos(\lambda_k-1)\alpha}{2\gamma_k\lambda_k\sin(\lambda_k+1)\alpha-(\gamma_k+1)(\lambda_k-1)\sin(\lambda_k-1)\alpha} \tag{A3d}$$

Clamped-Free Radial Edges

$$\phi_r(r,\theta)=\sum_{k=1}^{\infty} C_k r^{\lambda_k}[-\sin(\lambda_k+1)\theta+\gamma_k f_{3k}\cos(\lambda_k+1)\theta+\gamma_k\sin(\lambda_k-1)\theta-\gamma_k f_{3k}\cos(\lambda_k-1)\theta] \tag{A4a}$$

$$\phi_\theta(r,\theta)=\sum_{k=1}^{\infty} C_k r^{\lambda_k}[-\cos(\lambda_k+1)\theta-\gamma_k f_{3k}\sin(\lambda_k+1)\theta+\cos(\lambda_k-1)\theta+f_{3k}\sin(\lambda_k-1)\theta] \tag{A4b}$$

$$w(r,\theta)=\sum_{k=1}^{\infty} G_k r^{\bar{\lambda}_k+1}\sin(\bar{\lambda}_k+1)\theta \tag{A4c}$$

where

$$f_{3k}=\frac{\lambda_k(1-\nu)\sin(\lambda_k+1)\alpha+\hat{\gamma}_k\sin(\lambda_k-1)\alpha}{\gamma_k\lambda_k(1-\nu)\cos(\lambda_k+1)\alpha+\hat{\gamma}_k\cos(\lambda_k-1)\alpha} \tag{A4d}$$

and $\hat{\gamma}_k=\gamma_k(\nu\lambda_k+1)-(\lambda_k-1)$.

Simply Supported (S)-Simply Supported (S) Radial Edges

For Symmetric Modes.

$$\phi_r(r,\theta)=\sum_{k=1}^{\infty} r^{\lambda_k}D_k\left[\frac{\gamma_k\cos\dfrac{(\lambda_k-1)\alpha}{2}}{\cos\dfrac{(\lambda_k+1)\alpha}{2}}\cos(\lambda_k+1)\theta-\gamma_k\cos(\lambda_k-1)\theta\right] \tag{A5a}$$

$$\phi_\theta(r,\theta)=\sum_{k=1}^{\infty} r^{\lambda_k}D_k\left[-\frac{\gamma_k\cos\dfrac{(\lambda_k-1)\alpha}{2}}{\cos(\lambda_k+1)\dfrac{\alpha}{2}}\sin(\lambda_k+1)\theta+\sin(\lambda_k-1)\theta\right] \tag{A5b}$$

$$w(r,\theta)=\sum_{k=1}^{\infty} H_k r^{\bar{\lambda}_k+1}\cos(\bar{\lambda}_k+1)\theta \tag{A5c}$$

For Antisymmetric Modes.

$$\phi_r(r,\theta)=\sum_{k=1}^{\infty} r^{\lambda_k}C_k\left[-\frac{\gamma_k\sin(\lambda_k-1)\dfrac{\alpha}{2}}{\sin(\lambda_k+1)\dfrac{\alpha}{2}}\sin(\lambda_k+1)\theta+\gamma_k\sin(\lambda_k-1)\theta\right] \tag{A5d}$$

$$\phi_\theta(r,\theta)=\sum_{k=1}^{\infty} r^{\lambda_k}C_k\left[-\frac{\gamma_k\sin(\lambda_k-1)\dfrac{\alpha}{2}}{\sin(\lambda_k+1)\dfrac{\alpha}{2}}\cos(\lambda_k+1)\theta+\cos(\lambda_k-1)\theta\right] \tag{A5e}$$

$$w(r,\theta)=\sum_{k=1}^{\infty} G_k r^{\bar{\lambda}_k+1}\sin(\bar{\lambda}_k+1)\theta \tag{A5f}$$

Simply Supported (S)-Simply Supported (S*) Radial Edges

$$\phi_r(r,\theta)=\sum_{k=1}^{\infty} C_k r^{\lambda_k}[-\tilde{\gamma}_k\sin(\lambda_k+1)\theta+\hat{\gamma}_k f_{4k}\cos(\lambda_k+1)\theta+\gamma_k\sin(\lambda_k-1)\theta+\gamma_k\lambda_k(1-\nu)f_{4k}\cos(\lambda_k-1)\theta] \tag{A6a}$$

$$\phi_\theta(r,\theta)=\sum_{k=1}^{\infty} C_k r^{\lambda_k}[-\tilde{\gamma}_k\cos(\lambda_k+1)\theta-\hat{\gamma}_k f_{4k}\sin(\lambda_k+1)\theta+\cos(\lambda_k-1)\theta-\lambda_k(1-\nu)f_{4k}\sin(\lambda_k-1)\theta] \tag{A6b}$$

$$w(r,\theta)=\sum_{k=1}^{\infty} G_k r^{\bar{\lambda}_k+1}\sin(\bar{\lambda}_k+1)\theta \tag{A6c}$$

where

$$\tilde{\gamma}_k=\frac{(\gamma_k+1)(\lambda_k-1)}{2\lambda_k} \tag{A6d}$$

$$f_{4k}=\frac{(\gamma_k+1)(\lambda_k-1)\sin(\lambda_k+1)\alpha-2\gamma_k\lambda_k\sin(\lambda_k-1)\alpha}{2\lambda_k[\hat{\gamma}_k\cos(\lambda_k+1)\alpha+\gamma_k\lambda_k(1-\nu)\cos(\lambda_k-1)\alpha]} \tag{A6e}$$

Simply Supported (S)-Free Radial Edges

$$\phi_r(r,\theta)=\sum_{k=1}^{\infty} C_k r^{\lambda_k}[-\tilde{\gamma}_k\sin(\lambda_k+1)\theta+\hat{\gamma}_k f_{4k}\cos(\lambda_k+1)\theta \\ +\gamma_k\sin(\lambda_k-1)\theta+\gamma_k\lambda_k(1-\nu)f_{4k}\cos(\lambda_k-1)\theta] \tag{A7a}$$

$$\phi_\theta(r,\theta)=\sum_{k=1}^{\infty} C_k r^{\lambda_k}[-\tilde{\gamma}_k\cos(\lambda_k+1)\theta-\hat{\gamma}_k f_{4k}\sin(\lambda_k+1)\theta \\ +\cos(\lambda_k-1)\theta-\lambda_k(1-\nu)f_{4k}\sin(\lambda_k-1)\theta] \tag{A7b}$$

$$w(r,\theta)=\sum_{k=1}^{\infty} H_k r^{\bar{\lambda}_k+1}\cos(\bar{\lambda}_k+1)\theta \tag{A7c}$$

where f_{4k} is given in Eq. (*A*6*e*).

Simply Supported (S*)-Simply Supported (S*) Radial Edges

For Symmetric Modes.

$$\phi_r(r,\theta)=\sum_{k=1}^{\infty} D_k r^{\lambda_k}\left[\frac{\bar{\gamma}_k\sin(\lambda_k-1)\frac{\alpha}{2}}{2\lambda_k\sin(\lambda_k+1)\frac{\alpha}{2}}\cos(\lambda_k+1)\theta \right. \\ \left. -\gamma_k\cos(\lambda_k-1)\theta\right] \tag{A8a}$$

$$\phi_\theta(r,\theta)=\sum_{k=1}^{\infty} D_k r^{\lambda_k}\left[-\frac{\bar{\gamma}_k\sin(\lambda_k-1)\frac{\alpha}{2}}{2\lambda_k\sin(\lambda_k+1)\frac{\alpha}{2}}\sin(\lambda_k+1)\theta \right. \\ \left. +\sin(\lambda_k-1)\theta\right] \tag{A8b}$$

$$w(r,\theta)=\sum_{k=1}^{\infty} H_k r^{\bar{\lambda}_k+1}\cos(\bar{\lambda}_k+1)\theta \tag{A8c}$$

where $\bar{\gamma}_k=(\gamma_k+1)(\lambda_k-1)$.

For Antisymmetric Modes.

$$\phi_r(r,\theta)=\sum_{k=1}^{\infty} C_k r^{\lambda_k}\left[-\frac{\bar{\gamma}_k\cos(\lambda_k-1)\frac{\alpha}{2}}{2\lambda_k\cos(\lambda_k+1)\frac{\alpha}{2}}\sin(\lambda_k+1)\theta \right. \\ \left. +\gamma_k\sin(\lambda_k-1)\theta\right] \tag{A8d}$$

$$\phi_\theta(r,\theta)=\sum_{k=1}^{\infty} C_k r^{\lambda_k}\left[-\frac{\bar{\gamma}_k\cos(\lambda_k-1)\frac{\alpha}{2}}{2\lambda_k\cos(\lambda_k+1)\frac{\alpha}{2}}\cos(\lambda_k+1)\theta \right. \\ \left. +\cos(\lambda_k-1)\theta\right] \tag{A8e}$$

$$w(r,\theta)=\sum_{k=1}^{\infty} G_k r^{\bar{\lambda}_k+1}\sin(\bar{\lambda}_k+1)\theta \tag{A8f}$$

Simply Supported (S*)-Free Radial Edges

$$\phi_r(r,\theta)=\sum_{k=1}^{\infty} C_k r^{\lambda_k}[-\tilde{\gamma}_k\sin(\lambda_k+1)\theta-\hat{\gamma}_k f_{5k}\cos(\lambda_k+1)\theta \\ +\gamma_k\sin(\lambda_k-1)\theta-\gamma_k\lambda_k(1-\nu)f_{4k}\cos(\lambda_k-1)\theta] \tag{A9a}$$

$$\phi_\theta(r,\theta)=\sum_{k=1}^{\infty} C_k r^{\lambda_k}[-\tilde{\gamma}_k\cos(\lambda_k+1)\theta+\hat{\gamma}_k f_{5k}\sin(\lambda_k+1)\theta \\ +\cos(\lambda_k-1)\theta+\lambda_k(1-\nu)f_{5k}\sin(\lambda_k-1)\theta] \tag{A9b}$$

$$w(r,\theta)=\sum_{k=1}^{\infty} H_k r^{\bar{\lambda}_k+1}\sin(\bar{\lambda}_k+1)\theta \tag{A9c}$$

where

$$f_{5k}=\frac{\cos(\lambda_k+1)\alpha-\cos(\lambda_k-1)\alpha}{2\lambda_k\sin(\lambda_k+1)\alpha+\lambda_k(1-\nu)\sin(\lambda_k-1)\alpha}. \tag{A9d}$$

Free-Free Radial Edges

For Symmetric Modes.

$$\phi_r(r,\theta)=\sum_{k=1}^{\infty} D_k r^{\lambda_k}\left[\frac{\overline{\gamma_k}\sin(\lambda_k-1)\,\frac{\alpha}{2}}{2\lambda_k\sin(\lambda_k+1)\,\frac{\alpha}{2}}\cos(\lambda_k+1)\,\theta - \gamma_k\cos(\lambda_k-1)\,\theta\right] \tag{A10a}$$

$$\phi_\theta(r,\theta)=\sum_{k=1}^{\infty} D_k r^{\lambda_k}\left[-\frac{\overline{\gamma_k}\sin(\lambda_k-1)\,\frac{\alpha}{2}}{2\lambda_k\sin(\lambda_k+1)\,\frac{\alpha}{2}}\sin(\lambda_k+1)\,\theta + \sin(\lambda_k-1)\,\theta\right] \tag{A10b}$$

$$w(r,\theta)=\sum_{k=1}^{\infty} H_k r^{\overline{\lambda_k}+1}\cos(\overline{\lambda_k}+1)\,\theta \tag{A10c}$$

where $\overline{\gamma_k}=(\gamma_k+1)(\lambda_k-1)$

For Antisymmetric Modes.

$$\phi_r(r,\theta)=\sum_{k=1}^{\infty} C_k r^{\lambda_k}\left[-\frac{\overline{\gamma_k}\cos(\lambda_k-1)\,\frac{\alpha}{2}}{2\lambda_k\cos(\lambda_k+1)\,\frac{\alpha}{2}}\sin(\lambda_k+1)\,\theta + \gamma_k\sin(\lambda_k-1)\,\theta\right] \tag{A10d}$$

$$\phi_\theta(r,\theta)=\sum_{k=1}^{\infty} C_k r^{\lambda_k}\left[-\frac{\overline{\gamma_k}\cos(\lambda_k-1)\,\frac{\alpha}{2}}{2\lambda_k\cos(\lambda_k+1)\,\frac{\alpha}{2}}\cos(\lambda_k+1)\,\theta + \cos(\lambda_k-1)\,\theta\right] \tag{A10e}$$

$$w(r,\theta)=\sum_{k=1}^{\infty} G_k r^{\overline{\lambda_k}+1}\sin(\overline{\lambda_k}+1)\,\theta \tag{A10f}$$

References

[1] Williams, M. L., 1952, "Surface Stress Singularities Resulting From Various Boundary Conditions in Angular Plates Under Bending," *Proc. of First U.S. National Congress of Applied Mechanics*, ASME, New York, pp. 325–329.

[2] Williams, M. L., 1952, "Stress Singularities Resulting Form Various Boundary Conditions in Angular Corners of Plates in Extension," ASME J. Appl. Mech., **19**, pp. 526–528.

[3] Leissa, A. W., McGee, O. G., and Huang, C. S., 1993, "Vibrations of Sectorial Plates Having Corner Stress Singularities," ASME J. Appl. Mech., **60**(1), pp. 134–140.

[4] Leissa, A. W., McGee, O. G., and Huang, C. S., 1993, "Vibrations of Circular Plates Having V-Notches or Sharp Radial Cracks," J. Sound Vib., **161**(2), pp. 227–239.

[5] McGee, O. G., Leissa, A. W., Huang, C. S., and Kim, J. W., 1995, "Vibrations of Circular Plates With Clamped V-Notches or Rigidly Constrained Radial Cracks," J. Sound Vib., **181**(2), pp. 185–201.

[6] McGee, O. G., Leissa, A. W., and Huang, C. S., 1992, "Vibrations of Cantilevered Skewed Plates With Corner Stress Singularities," Int. J. Numer. Methods Eng., **35**, pp. 409–424.

[7] McGee, O. G., Leissa, A. W., and Huang, C. S., 1992, "Vibrations of Cantilevered Skewed Trapezoidal and Triangular Plates With Corner Stress Singularities," Int. J. Mech. Sci., **34**(1), pp. 63–84.

[8] Huang, C. S., McGee, O. G., Leissa, A. W., and Kim, J. W., 1995, "Accurate Vibration Analysis of Simply Supported Rhombic Plates by Considering Stress Singularities," ASME J. Vibr. Acoust., **117**, pp. 245–251.

[9] McGee, O. G., Kim, J. W., Kim, Y. S., and Leissa, A. W., 1996, "Corner Stress Singularity Effects on the Vibrations of Rhombic Plates With Combinations of Clamped and Simply Supported Edges," J. Sound Vib., **193(3)**, pp. 555–580.

[10] Leissa, A. W., 1969, *Vibration of Plates*, NASA SP-160, U.S. Government Printing Office, Washington, DC (reprinted 1993 by Acoustical Society of America).

[11] Haggeblad, B., and Bathe, K. J., 1990, "Specifications of Boundary Conditions for Reissner/Mindlin Plate Bending Finite Elements," Int. J. Numer. Methods Eng., **30**, pp. 981–1011.

[12] Mindlin, R. D., 1951, "Influence of Rotatory Inertia and Shear on Flexural Motions of Isotropic, Elastic Plates," ASME J. Appl. Mech., **18**, pp. 31–38.

[13] Mindlin, R. D., and Deresiewicz, H., 1954, "Thickness-Shear and Flexural Vibrations of a Circular Disk," J. Appl. Phys., **25**, pp. 1329–1332.

[14] Reismann, H., 1988, *Elastic Plates: Theory and Application*, Wiley, New York.

Terahertz Vibration of Short Carbon Nanotubes Modeled as Timoshenko Beams

J. Yoon

C. Q. Ru[1]
e-mail: c.ru@ulaberta.ca

A. Mioduchowski

Department of Mechanical Engineering,
University of Alberta,
Edmonton T6G 2G8, Canada

Short carbon nanotubes of smaller aspect ratio (say, between 10 and 50) are finding significant application in nanotechnology. This paper studies vibration of such short carbon nanotubes whose higher-order resonant frequencies fall within terahertz range. Because rotary inertia and shear deformation are significant for higher-order modes of shorter elastic beams, the carbon nanotubes studied here are modeled as Timoshenko beams instead of classical Euler beams. Detailed results are demonstrated for double-wall carbon nanotubes of aspect ratio 10, 20, or 50 based on the Timoshenko-beam model and the Euler-beam model, respectively. Comparisons between different single-beam or double-beam models indicate that rotary inertia and shear deformation, accounted for by the Timoshenko-beam model, have a substantial effect on higher-order resonant frequencies and modes of double-wall carbon nanotubes of small aspect ratio (between 10 and 20). In particular, Timoshenoko-beam effects are significant for both large-diameter and small-diameter double-wall carbon nanotubes, while double-beam effects characterized by noncoaxial deflections of the inner and outer tubes are more significant for small-diameter than large-diameter double-wall carbon nanotubes. This suggests that the Timoshenko-beam model, rather than the Euler-beam model, is relevant for terahertz vibration of short carbon nanotubes. [DOI: 10.1115/1.1795814]

1 Introduction

Because of novel electronic properties and superior mechanical strength, carbon nanotubes (CNTs) have become the most promising candidate materials for nanoelectronics, nanodevices, and nanocomposites [1–8]. Mechanical behavior of CNTs, including vibrational behavior, has been the subject of numerous recent studies. Since controlled experiments at nanoscale are difficult and molecular dynamics simulations remain expensive and formidable for large scale systems, continuum mechanics models, such as the classical Euler elastic-beam model, have been effectively used to study overall mechanical deformation of CNTs, such as static deflection, column buckling, resonant frequencies and modes, and sound-wave propagation [9,10]. In particular, the single elastic-beam model, which ignores intertube radial displacements and the related internal degrees of freedom, has been used to study static and dynamic behavior of multiwall nanotubes (MWNTs) [11–14]. As shown in [15] for column buckling of MWNTs and [16,17] for vibration of MWNTs, such a simplified model is adequate for MWNT of larger aspect ratio (length-to-diameter ratio).

Many proposed applications and designs of CNTs, however, are involved with short CNTs of aspect ratio down to 10, or periodically supported CNTs with finite spans. Such examples include suspended crossing CNTs with spans about 20 nm [1], CNTs as single-electron transistors of length down to 20 nm [2], MWNTs of aspect ratio around 20 (about 300 nm long and 10–20 nm diam) as electrometers [3] or building blocks in nanoelectronics [4], CNT-nanomechanical switches of aspect ratio around 10 [18], and CNTs of aspect ratio about 10–25 as AFM tip [19,20]. Owing to the hollow structure of CNTs, short CNTs are preferred in many cases to prevent undesirable kinking and buckling. Therefore, vibrational behavior of short CNTs, say, of aspect ratio between 10 and 50, is of practical significance. In this case, intertube radial displacements of MWNTs, which are ignored by the existing single elastic-beam model [11–14], could come to play a significant role. Recently, we have studied the role of interlayer radial displacements in transverse vibration of MWNTs [16,17] based on a simple linear model of multiple elastic beams. Our results show that noncoaxial intertube vibration of MWNTs will be excited at ultrahigh frequencies (above 1 THz) at which the characteristic wavelength of vibrational modes is just a few times the outermost diameter of MWNTs. For instance, for a shorter 1.4 nm dia double-wall carbon nanotube (DWNT) of aspect ratio between 10 and 20, the wavelength of the higher-order (say, third, fourth, or fifth) modes are just a few times the outermost diameter and the associated vibrational modes are substantially noncoaxial. In this case, the existing single-beam model of coaxial vibration fails, and a more relevant model that considers noncoaxial intertube radial displacements of MWNTs is required. These results, first predicted by a simple linear multiple-beam model [16,17], are found to agree well with more recent atomistic simulations [21,22] on noncoaxial vibration of MWNTs. Since noncoaxial distortion could significantly affect some important physical (such as electronic and optical) properties of MWNTs, the study of noncoaxial vibration is relevant to terahertz vibration of short MWNTs.

Another relevant issue to be clarified is the effect of rotary inertia and shear deformation in terahertz vibrations of short CNTs. It is well known that rotary inertia and shear deformation, which are ignored in the classical Euler-beam model, would become substantial for vibration of elastic beams when the characteristic wavelength is just a few times the diameter of their cross-section [23–26]. For this reason, the relevance of the classical Euler-beam model to short CNTs is questionable. To clarify this issue, vibration of short DWNTs is studied in this paper based on the double elastic-beam model developed in [15–17]. Unlike pre-

---

[1] To whom correspondence should be addressed.

Contributed by the Applied Mechanics Division of THE AMERICAN SOCIETY OF MECHANICAL ENGINEERS for publication in the ASME JOURNAL OF APPLIED MECHANICS. Manuscript received by the Applied Mechanics Division, April 16, 2003; final revision; May 15, 2004. Associate Editor: A. A. Ferri. Discussion on the paper should be addressed to the Editor, Prof. Robert M. McMeeking, Journal of Applied Mechanics, Department of Mechanical and Environmental Engineering, University of California—Santa Barbara, Santa Barbara, CA 93106-5070, and will be accepted until four months after final publication of the paper itself in the ASME JOURNAL OF APPLIED MECHANICS.

vious work [15–17], however, CNTs in the present paper are modeled as Timoshenko beams, instead of classical Euler beams. The major goal of this study is to identify the cases in which the Euler-beam model leads to substantial errors, and thus, the more relevant Timoshenko-beam model is required, and also to compare the Timoshenko-beam effects with the double-beam effects studied in [15–17]. To this end, detailed results are demonstrated based on the Timoshenko-beam model, as well as the Euler-beam model. As will be shown below, the results show that the rotary inertia and shear deformation have a substantial effect on higher-order resonant frequencies (within terahertz range) of DWNTs of smaller aspect ratio (between 10 and 20). Therefore, the Timoshenko-beam model, rather than the Euler-beam model, should be used for terahertz vibrations of short CNTs.

2 Double Timoshenko-Beam Model

Many prior studies showed that the classical Euler elastic beam offers a reliable model for overall mechanical deformation of CNTs when its characteristic wavelength is much larger than the diameter [10]. For example, static deflection of CNTs under point load is found to be well predicted by the beam model [11], and resonant frequencies and vibational modes of CNTs given by the cantilever-beam model are in good agreement with experimental data [13]. In particular, because elastic-beam models give simple general formulas in many important cases, such as critical stress for column buckling, resonant frequencies, and sound speeds, etc., which clearly indicate major factors affecting mechanical behavior of CNTs, they have the potential to identify key parameters and predict new physical phenomena.

So far, to our knowledge, all elastic-beam models used for CNTs are based on the classical Euler-beam model. The present paper studies vibration of short DWNTs [27–29], as shown in Fig. 1, based on the Timoshenko-beam model. In addition, unlike the single-beam model [11–14] which assumes that all originally concentric tubes of a MWNT remain exactly coaxial during vibration and thus can be described by a single deflection curve, the present analysis considers interlayer radial displacements within the MWNT and assumes that each individual tube of MWNTs has an individual deflection curve, which is not necessarily coincident with the deflection curves of other nested tubes of the MWNT. Thus, each of the inner and outer tubes of DWNTs is modeled as a Timoshenko-elastic beam. It is known that the total deflection $Y(x,t)$ of a Timoshenko beam, and the slope $\varphi(x,t)$ of the beam due to bending deformation alone are determined by the following two coupled equations [23–26]:

$$\begin{aligned} -kAG\left(\frac{\partial\varphi}{\partial x}-\frac{\partial^2 Y}{\partial x^2}\right)+p&=\rho A\frac{\partial^2 Y}{\partial t^2}\\ EI\frac{\partial^2\varphi}{\partial x^2}-kAG\left(\varphi-\frac{\partial Y}{\partial x}\right)&=\rho I\frac{\partial^2\varphi}{\partial x^2} \end{aligned} \tag{1}$$

where x is the axial coordinate, t is time, I and A are the moment of inertia and the area of the cross-section of the beam, p is the distributed pressure per unit axial length, E and G are Young's modulus and shear modulus, respectively, ρ is the mass density per unit volume, and k is the so-called shear coefficient which is about 0.6–0.7 for thin-walled circular cross-sections and 0.9 for solid circular cross-sections [25,26].

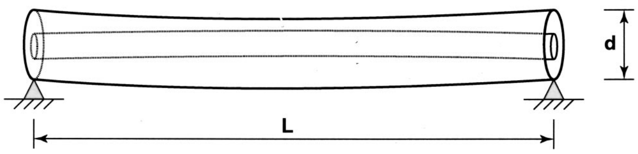

Fig. 1 Vibration of a short doublewall carbon nanotube

Let us apply Eq. (1) to each of the inner and outer tubes of a DWNT. Thus, transverse vibration of a DWNT, of length L and outer diameter d (Fig. 1), is described by the following four equations

$$\begin{aligned} -kA_1G\left(\frac{\partial\varphi_1}{\partial x}-\frac{\partial^2 Y_1}{\partial x^2}\right)+p&=\rho A_1\frac{\partial^2 Y_1}{\partial t^2}\\ EI_1\frac{\partial^2\varphi_1}{\partial x^2}-kA_1G\left(\varphi_1-\frac{\partial Y_1}{\partial x}\right)&=\rho I_1\frac{\partial^2\varphi_1}{\partial t^2}\\ -kA_2G\left(\frac{\partial\varphi_2}{\partial x}-\frac{\partial^2 Y_2}{\partial x^2}\right)-p&=\rho A_2\frac{\partial^2 Y_2}{\partial t^2}\\ EI_2\frac{\partial^2\varphi_1}{\partial x^2}-kA_2G\left(\varphi_2-\frac{\partial Y_2}{\partial x}\right)&=\rho I_2\frac{\partial^2\varphi_2}{\partial t^2} \end{aligned} \tag{2}$$

where $Y_j(x,t)$ and $\varphi_j(x,t)$ $(j=1,2)$ are the total deflection and the slope due to bending of the jth nanotube, I_j and A_j are the moment of inertia and the area of the cross-section of the jth tube, here the subscripts 1, 2 are used to denote the quantities of the inner and outer tubes, respectively, p is the van der Waals interaction pressure between the two tubes per unit axial length, and the two tubes have the same Young's modulus $E=1$ TPa and shear modulus $G=0.4$ Tpa (with Poisson ratio $\nu=0.25$), with the effective thickness of single-walled nanotubes, 0.35 nm. In addition, the dependence of the shear coefficient k on the radius is neglected for DWNTs, and we take $k=0.8$. Here, it should be mentioned that a mass density $\rho=1.3$ g/cm^3, based on a slightly different definition (p. 724 of [30]), has been used in our previous papers [16,17]. To be consistent with the definitions of the effective thickness and the Young's modulus listed above, the mass density of graphite is used in the present paper. Therefore, throughout this paper, we shall use the mass density $\rho=2.3$ g/cm^3 (for graphite).

It is noticed that the deflections of the two tubes are coupled through the van der Waals intertube interaction p. Since the inner and outer tubes of a DWNT are originally concentric and the van der Waals interaction is determined by the interlayer spacing between two tubes, the net van der Waals interaction pressure remains zero for each of the tubes if they vibrate coaxially and, thus, share the same deflection curve. Hence, the van der Waals interaction plays no role in the single-beam model for isolated DWNTs. For the double-beam model [15–17], however, the inner and outer tubes are described by two individual deflection curves, which are not necessarily coincident. Therefore, for small-amplitude non-coaxial linear vibration, the van der Waals interaction pressure at any position x between the two tubes depends linearly the difference of their deflection curves at that position, namely

$$p(x)=c[Y_2(x)-Y_1(x)] \tag{3}$$

where c is the intertube van der Waals interaction coefficient. In particular, the coefficients c can be estimated based on an effective interaction width $(2r)$ of the tubes (where r is the inner radius of DWNTs) as [15,17]

$$c=\frac{200\times(2r)\ \ \text{erg/cm}^2}{0.16D^2},\quad (\text{D}=0.142\ \ \text{nm}) \tag{4}$$

Thus, substitution of (3) into (2) leads to four coupled equations for four unknowns Y_j(x,t) and φ_j(x,t) $(j=1,2)$.

3 Resonant Frequencies of DWNT

Here, to isolate the effects of shear deformation and rotary inertia on resonant frequencies (rather than resonant modes), we consider the case in which the inner and outer tubes of the DWNT are simply supported. In this case, vibrational modes of the DWNT are of the form [21,22]

$$\begin{aligned} Y_j &= a_j e^{i\omega t}\sin\frac{n\pi x}{L} \\ \varphi_j &= b_j e^{i\omega t}\cos\frac{n\pi x}{L} \end{aligned} \qquad (j=1,2) \tag{5}$$

where a_1 and a_2 represent the amplitudes of deflections of the inner and the outer tubes, and b_1 and b_2 represent the amplitudes of the slopes of the inner and outer tubes due to bending deformation alone, respectively. In addition, integer n is the mode-number, and ω is the circular frequency. Substitution of (5) into (2) with (3), one has

$$\begin{bmatrix} \rho A_1\omega^2 - kA_1G\left(\frac{n\pi}{L}\right)^2 - c & kA_1G\left(\frac{n\pi}{L}\right) & c & 0 \\ kA_1G\left(\frac{n\pi}{L}\right) & \rho I_1\omega^2 - EI_1\left(\frac{n\pi}{L}\right)^2 - kA_1G & 0 & 0 \\ c & 0 & \rho A_2\omega^2 - kA_2G\left(\frac{n\pi}{L}\right)^2 - c & kA_2G\left(\frac{n\pi}{L}\right) \\ 0 & 0 & kA_2G\left(\frac{n\pi}{L}\right) & \rho I_2\omega^2 - EI_2\left(\frac{n\pi}{L}\right)^2 - kA_2G \end{bmatrix} \begin{bmatrix} a_1 \\ b_1 \\ a_2 \\ b_2 \end{bmatrix} = 0 \tag{6}$$

Thus, the resonant frequencies are determined by the eigenequation obtained by setting the determinant of the coefficient matrix of (6) to zero. It is readily seen that for given order number *n*, the present double-Timoshenko-beam model gives four *n*-order resonance frequencies, in contrast to two *n*-order resonant frequencies given by the single-Timoshenko-beam model [23], two *n*-order resonant frequencies given by the double Euler-beam model [16,17], and the single *n*-order resonance frequency given by the single Euler-beam model. In particular, the single *n*-order resonant frequency given by the single Euler-beam model is [10]

$$f_{n1} = \frac{\omega_{n1}}{2\pi}, \quad \omega_{n1}^2 = \frac{\lambda_n^4 EI}{(\rho A)}, \tag{7}$$

where $\lambda_n = (n\pi/L)$ for simply supported beams

where *I* and *A* are the total moment of inertia and the total cross-sectional area of MWNT. Thus, $I = I_1 + I_2$ and $A = A_1 + A_2$ for a DWNT.

In what follows, the resonant frequency $f = \omega/(2\pi)$ of simply supported DWNTs is calculated based on four different elastic beam models:

- DT: the double-Timoshenko beam (DT) model described by (2), which gives four *n*-order frequencies, $f_{n1} < f_{n2} < f_{n3} < f_{n4}$;
- DE: the double-Euler beam (DE) model described in [16,17] which treats each of the inner and outer tubes of the DWNT as a single Euler beam and gives two *n*-order frequencies, $f_{n1} < f_{n2}$;
- ST: the single-Timoshenko beam (ST) model that treats the DWNT as a single Timoshenko beam described by (1), with $I = I_1 + I_2$ and $A = A_1 + A_2$, and gives two *n*-order frequencies, $f_{n1} < f_{n2}$;
- SE: the single-Euler beam (SE) model that gives the single *n*-order frequency f_{n1} (7).

The *n*-order frequencies given by the different models are distinguished by DT1<DT2<DT3<DT4, DE1<DE2, ST1<ST2, or SE, when necessary. All nine *n*-order frequencies given by the four different models are shown in Figs. 2–7 for a DWNT of the inner diameter 0.7 nm or 7 nm and aspect ratio 10, 20, or 50, respectively. All frequencies are shown as a function of the mode number *n*, from $n = 1$ to $n = 10$, where L/d is the aspect ratio. It is found from Figs. 2–7 that:

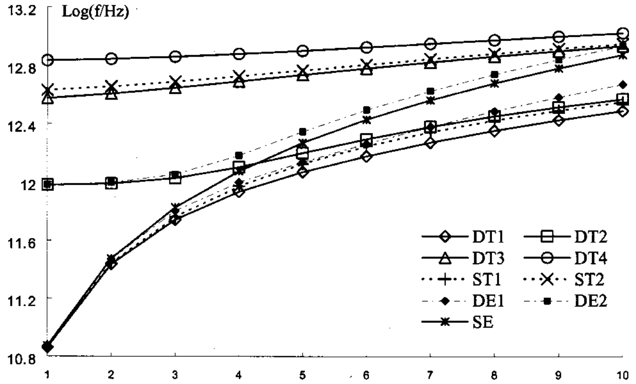

Fig. 2 DWNT frequencies for the inner radius 0.35 nm and $L/d = 10$

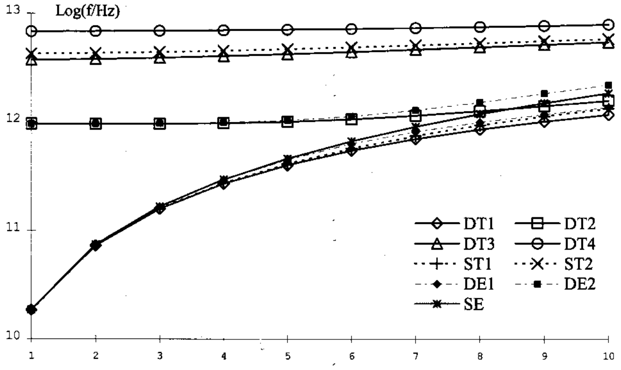

Fig. 3 DWNT frequencies for the inner radius 0.35 nm and $L/d = 20$

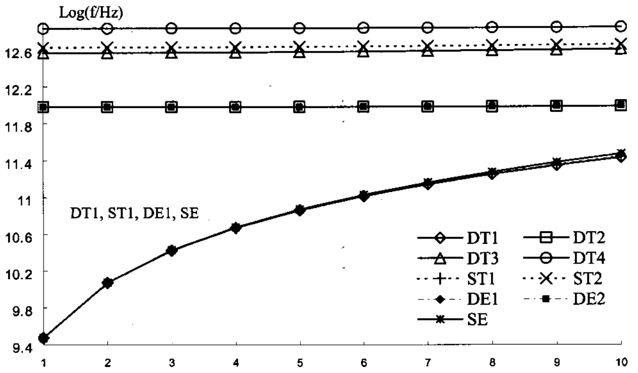

Fig. 4 DWNT frequencies for the inner radius 0.35 nm and $L/d=50$

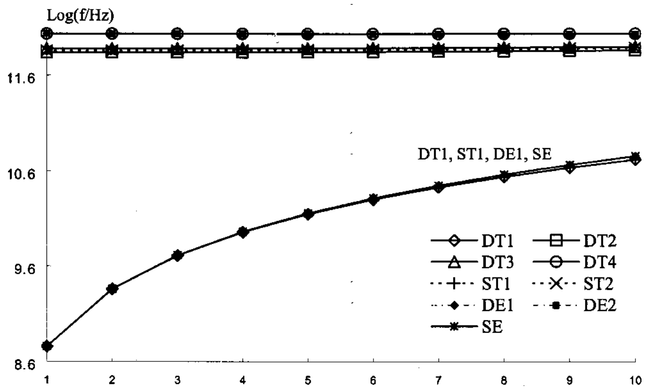

Fig. 7 DWNT frequencies for the inner radius 3.5 nm and $L/d=50$

1. The lowest n-order frequency f_{n1} increases quickly with increasing mode number n, while other higher n-order frequencies $f_{nk}\,(k>1)$ are not sensitive to the number n especially for n smaller than 3 or 4.
2. For all examples considered here, the four lowest first-order frequency f_{11} given by the four different models are very close to each other and almost indistinguishable. For example, for DWNT of inner-diameter 0.7 nm and aspect ratio 10, the lowest first-order frequency f_{11} given by the four models DT, DE, ST, and SE are 0.0728 THz, 0.0745 THz, 0.0731 THz, and 0.0746 THz, respectively. On the other hand, for DWNT of inner diameter 7 nm and aspect ratio 10, the lowest first-order frequency f_{11} given by the four models are 0.141 THz, 0.144 THz, 0.141 THz, and 0.144 THz, respectively. In addition, the small differences of the lowest first-order frequencies given by the four different models further diminish with increasing aspect ratio of DWNTs.

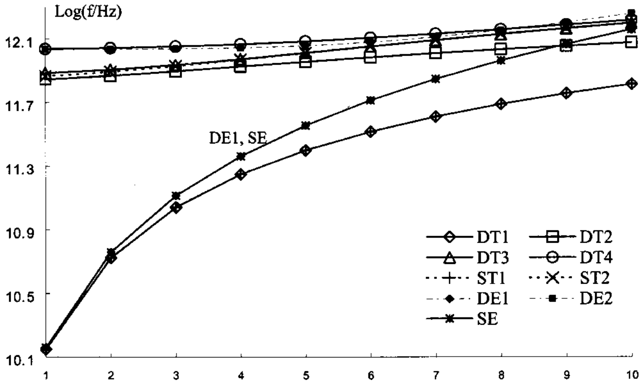

Fig. 5 DWNT frequencies for the inner radius 3.5 nm and $L/d=10$

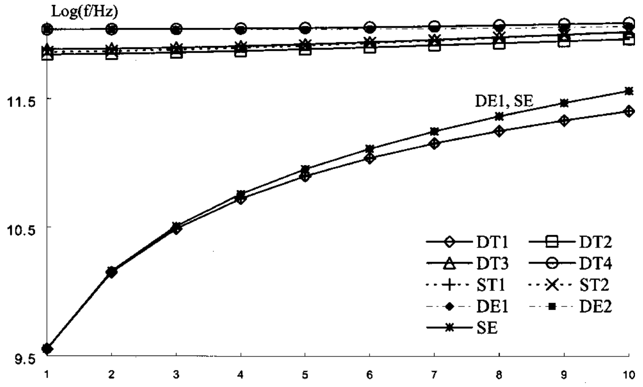

Fig. 6 DWNT frequencies for the inner radius 3.5 nm and $L/d=20$

3. For the mode-number $n=1$, beside the lowest first-order frequency, the DT model gives three higher frequencies, while the ST model and the DE model give another higher frequency, respectively. It is seen that the second first-order frequency f_{12} given by the DT model corresponds to the second first-order frequency given by the DE model for smaller radii (Figs. 2–4), and the third first-order frequency f_{13} given by the DT model is close to the second first-order frequency given by the ST model for larger radii (Figs. 5–7). These higher first-order frequencies $(n=1)$ are characterized by substantial shear deformation or noncoaxial deflections of the inner and outer tubes (as will be demonstrated below) and are at least one order of magnitude higher than the lowest first-order frequency. Hence, if only the single lowest resonant frequency f_{11} is concerned, the lowest first-order frequency given by the SE model (7) for $n=1$ is accurate enough, and any double-beam model or Timoshenko-beam model is not needed.
4. This conclusion remains qualitatively true even for the first few higher-order frequencies ($n=3$, 4, 5, or even higher) when the aspect ratio is larger (say, $\geqslant 50$). Indeed, when $L/d=50$, it is seen from Figs. 4 and 7 that the four lowest n-order frequencies given by the four different models for the mode-number n up to 10 are very close to each other. Hence, it is concluded that the lowest n-order frequency f_{n1} for n up to 10 can be estimated satisfactorily by the SE-model (7) provided that the aspect ratio of DWNTs is sufficiently large (say, $\geqslant 50$).
5. However, when the aspect ratio is relatively small, say between 10 and 20, it is seen from Figs. 2, 3, 5, and 6 that the lowest n-order (such as $n=3$, 4, or 5) frequencies f_{n1} given by the DT, ST, and DE models are substantially lower than that given by the SE model (7). For example, for DWNT of inner diameter 0.7 nm and aspect ratio 10, the lowest fourth-order frequency $(n=4)$ given by the four models DT, DE, ST, and SE are 0.861 THz, 1.00 THz, 0.940 THz, and 1.19 THz, respectively, and the lowest fifth-order frequency $(n=5)$ given by the four models DT, DE, ST, and SE are 1.18 THz, 1.37 THz, 1.34 THz, and 1.86 THz, respectively. In addition, for DWNT of inner diameter 7 nm and aspect ratio 10, the lowest fourth-order frequency $(n=4)$ given by the four models DT, DE, ST, and SE are 0.177 THz, 0.231 THz, 0.178 THz, and 0.231 THz, respectively, and the lowest fifth-order frequency (n=5) given by the four models (DT,DE,ST,SE) are 0.252 THz, 0.360 THz, 0.252 THz, and

0.361 THz, respectively. Therefore, the single Euler-beam (SE) model (7), used widely in the literature, leads to substantial errors for the lowest *n*-order resonant frequencies f_{n1} for $n>1$, (such as $n=3$, 4, or 5) of short DWNTs of aspect ratio below 20.

6. Finally, because both the Timoshenko-beam model [21–24] and the double-beam model [10,16,17] are significant only when the characteristic wavelength is just a few times the diameter of CNTs, it is interesting to compare the relative importance of the Timoshenko-beam effect and the double-beam effect. It is anticipated that the role of intertube displacements of MWNTs is more significant for small-diameter than large-diameter CNTs [16,17] (because the amplitude of the intertube radial displacements is of the order of magnitude of the intertube spacing, they are significant only compared to the deflections of small-diameter CNTs, but not to the deflections of large-diameter CNTs). Indeed, it is seen from Figs. 2 and 3 that the lowest *n*-order frequencies f_{n1} (for $n>1$) given by the double-beam models (DT and DE) for small-diameter DWNTs are significantly different from those given by the single-beam models (ST,SE). For larger-diameter DWNTs, however, it is seen from Figs. 5 and 6 that the double-beam models (DT) and (DE) give almost the same lowest *n*-order frequencies f_{n1} (for $n>1$) as those given by the single-beam models (ST,SE). On the other hand, the effects of the Timoshenko-beam are significant for all DWNTs of smaller aspect ratio (Figs. 2, 3, 5, and 6), regardless of their radii. Therefore, it is concluded that both the Timoshenko-beam effects and the double-beam effects are significant for CNTs of smaller aspect ratio (around or below 20), while the double-beam effects are further restricted to small-diameter DWNTs. Despite this, because the radii of DWNTs are usually small (with inner diameter 0.6–0.9 nm and outer diameter 1.3–1.6 nm, see [27–29]), the double-beam effects are significant for short DWNTs.

4 Shear Deformation and Noncoaxial Deflections

Let us now discuss the effects of the Timoshenko-beam model, as well as the double-beam model, on the deflection curves of DWNTs. The contribution of shear deformation to the total deflection slope is defined by

$$\theta=\varphi-\frac{dY}{dx}=\gamma e^{i\omega t}\cos\frac{n\pi x}{L} \tag{8}$$

where γ represents the amplitude of shear deformation. Obviously, for the single-Euler-beam (SE) model, the deflection curves of the inner and outer tubes are exactly the same and the shear deformation $\theta(x,t)$ is identically zero, thus $a_1=a_2$, $b_1=b_2=a_1(n\pi/L)$ and $\gamma_1=\gamma_2=0$. However, when the Timoshenko-beam model is adopted, shear deformation and rotary intertia are taken into account, which given rise to nonzero shear deformation γ. On the other hand, the double-beam model accounts for intertube radial displacement between the inner and outer tubes and thus can quantify the difference between two (noncoaxial) deflection curves $(a_1\neq a_2)$. Therefore, the effects of the Timoshenko beam and the double beam can be studied by examining the ratio a_1/a_2, which indicates the degree of the noncoincidence of the deflections of the two tubes, and the ratio γ_2/b_2, which indicates the relative amplitude of the shear deformation of the outer tube of DWNTs (the result for the inner tube is qualitatively similar and thus not included here). It follows from (2), (5), and (8) that the deflection amplitude ratio of the inner to the outer tubes and the ratio of the outer tube's shear deformation to its deflection slope due to bending deformation are given by

$$\left.\begin{aligned}\frac{a_1}{a_2}&=\frac{(kA_2G\beta)^2-(\rho A_2\omega^2-kA_2G\beta^2-c)(\rho I_2\omega^2-EI_2\beta^2-kA_2G)}{c(\rho I_2\omega^2-EI_2\beta^2-kA_2G)}\\ \frac{\gamma_2}{\varphi_2}&=\frac{I_2(\rho\omega^2-E\beta^2)}{kA_2G}\end{aligned}\right\},\quad(\beta=n\pi/L) \tag{9}$$

In what follows, the ratio a_1/a_2 given by the DT model and DE model for the lower two *n*-order frequencies are shown in Figs. 8 and 9 and Figs. 10 and 11, respectively, for the examples considered in Figs. 2–7. Here, because the second *n*-order frequency f_{n2} given by the DT model corresponds to the second *n*-order frequency given by DE model only for smaller radii (see Section 3), the results for the second *n*-order frequencies given by the DT model and the DE model are demonstrated only for small radius 0.35 nm (Figs. 9 and 11). Related data for the ratio γ_2/b_2 given by the DT model and the ST-model for all *n*-order frequencies are shown in Figs. 12–15 and Figs. 16 and 17, respectively. It is found from Figs. 8–17 that:

1. The amplitude ratio a_1/a_2 corresponding to the lowest (first-order) frequency f_{11}, as shown in Fig. 8 for the DT model and Fig. 10 for the DE model, are always very close to unity for all examples considered here. This indicates that the deflection curves of the inner and outer tubes for the lowest (first-order) frequency f_{11} are almost coincident and thus the vibration of the DWNT is almost coaxial at the lowest (first-order) frequency f_{11}.
2. For the lowest *n*-order frequencies f_{n1} with $n>3$, it is seen from Figs. 8 and 10 that the associated amplitude ratio a_1/a_2 is no longer close to unity for small-diameter DWNTs of aspect ratio 10 or 20, which indicates that the deflection curves of the inner and outer tubes are no longer coincident in these cases. However, for larger aspect ratio (50) or larger inner radius (3.5 nm), it is seen from Figs. 8 and 10 that the amplitude ratio a_1/a_2 for the lowest *n*-order frequencies f_{n1} with $n>3$ is still very close to unity and thus the deflection curves of the inner and outer tubes are still almost coinci-

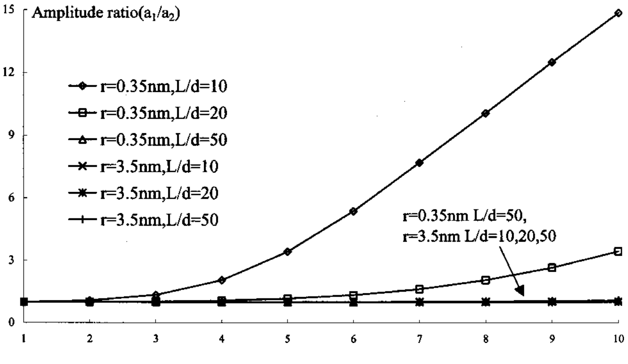

Fig. 8 DWNT amplitude ratio (a_1/a_2) for f_{n1} using a double-Timoshenko-beam model

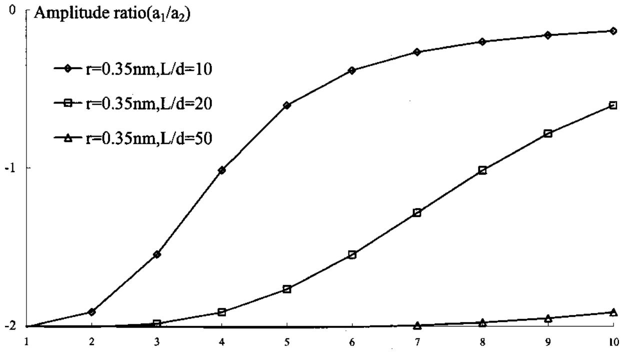

Fig. 9 DWNT amplitude ratio (a_1/a_2) for f_{n2} using a double-Timoshenko-beam model

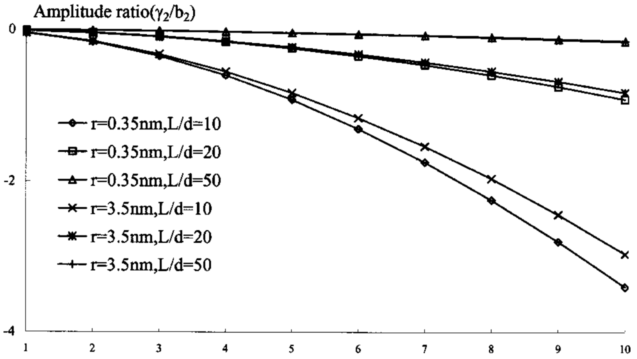

Fig. 12 DWNT amplitude ratio (γ_2/b_2) for f_{n1} using a double-Timoshenko-beam model

dent. Consistent with Section 3, these results also confirm that the effect of the double-beam model is significant only for small-diameter CNTs of smaller aspect ratio. Here it is noticed from Figs. 8 and 10 that the ratio a_1/a_2 for the lowest n-order frequency with $n>1$ of small-diameter DWNTs given by the DT model and the DE model are qualitatively similar, but quantitatively different.

3. On the other hand, the amplitude ratio a_1/a_2 of other higher n-order frequency (f_{nk} with $k>1$) is not close to unity. For example, for small-diameter DWNTs, it is seen from Figs. 9 and 11 that the amplitude ratio a_1/a_2 of the second n-order frequency f_{n2} is always negative, which indicates that the deflection of the inner tube is simply opposite to the deflection of the outer tube, and thus vibration of the DWNT is substantially noncoaxial. It is seen that from Figs. 2–7 that the second n-order frequency f_{n2} for all examples discussed here is always within terahertz range. Hence, this also indicates that the effects of the double-beam model are essential for terahertz vibration of MWNTs.
4. Now, let us discuss the relative amplitude of shear deformation. For the lowest n-order frequency f_{n1}, the ratio γ_2/b_2, which represents the relative amplitude of shear deformation of the outer tube, is negligible only for $n=1$, or for $n>1$ with larger aspect ratio 50. This indicates that the shear deformation is significant provided that the wavelength is sufficiently short, consistent with the common concepts of the Timoshenko beam [23,24]. For example, it is seen from Figs. 12 and 16 that the six curves can almost be classified by the wavelength, only slightly affected by the radius.

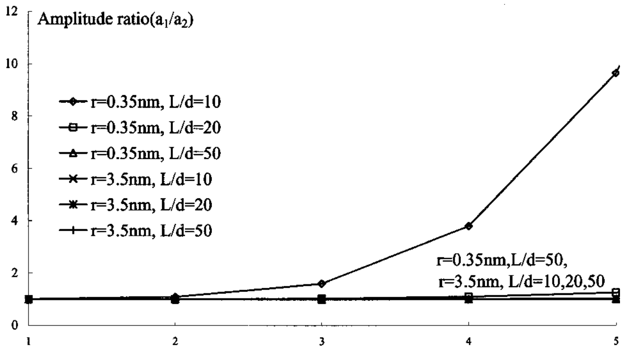

Fig. 10 DWNT amplitude ratio (a_1/a_2) for f_{n1} using a double-Euler-beam model

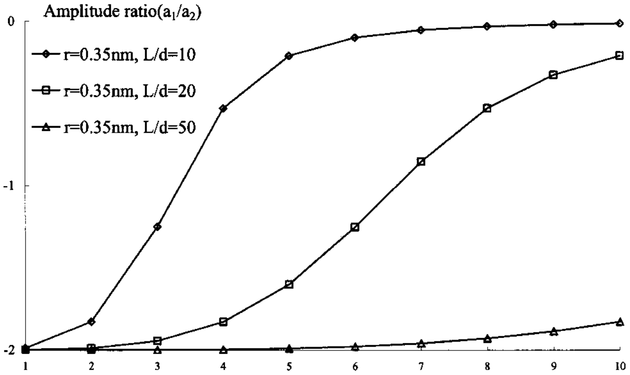

Fig. 11 DWNT amplitude ratio (a_1/a_2) for f_{n2} using a double-Euler-beam model

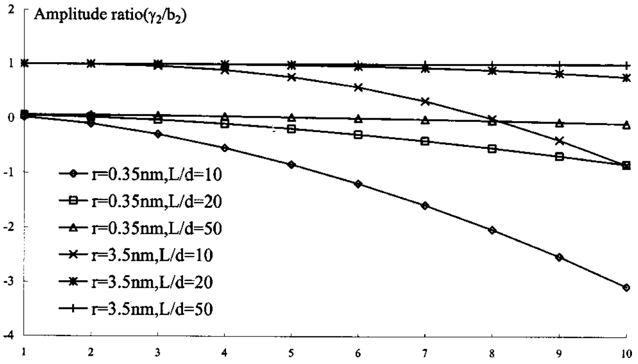

Fig. 13 DWNT amplitude ratio (γ_2/b_2) for f_{n2} using a double-Timoshenko-beam model

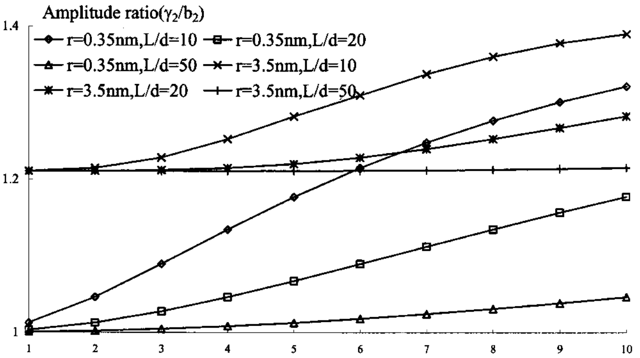

Fig. 14 DWNT amplitude ratio (γ_2/b_2) for f_{n3} using a double-Timoshenko-beam model

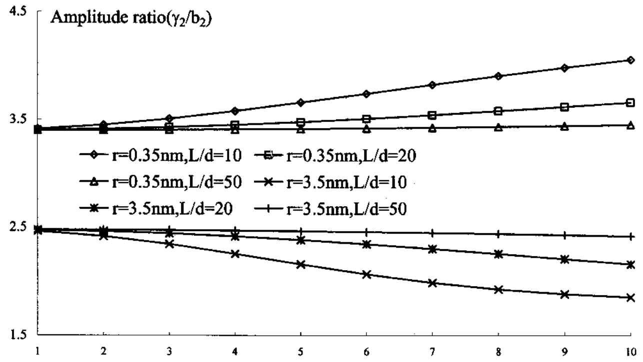

Fig. 15 DWNT amplitude ratio (γ_2/b_2) for f_{n4} using a double-Timoshenko-beam model

5. For small aspect ratio (10 and 20) and higher mode number $n>3$, it is seen from Figs. 12 and 16 that the shear deformation has a substantial effect on the deflections even for the lowest n-order frequency f_{n1}. For example, it is seen from Figs. 12 and 16 that the absolute value of the ratio γ_2/b_2 is larger than unity for small aspect ratio $L/d=10$, and is about 25% for moderate aspect ratio $L/d=20$, almost regardless of the radius. In these cases, the shear deformation, which is neglected by the classical Eulerbeam model, is significant and cannot be neglected.
6. It is seen from Figs. 13–15 and 17 that almost all higher n-order frequencies (f_{nk} with $k>1$) are characterized by substantial shear deformation, with the only exception described in Fig. 13 for the second n-order frequency f_{n2} given by the DT model for small diameter 0.35 nm and smaller order number n (up to $n=4$ or 5). In the latter case, as mentioned before, the second n-order frequency f_{n2} given by the DT model corresponds to the second n-order frequency f_{n2} given by the DE model in which shear deformation is neglected. This explains why the shear deformation is negligible in this case.
7. Except for the above case, all other cases described in Figs. 13–15 and 17 exhibit substantial shear deformation characterized by large absolute values of the ratio γ_2/b_2. In particular, it is seen from Figs. 13–15 and 17 that the six curves shown there can almost be classified by the radius, only moderately affected by the wavelength. This indicates that, unlike the vibration of the lowest n-order frequency f_{n1} which largely depends on the wavelength, the vibration of the higher n-order frequencies f_{nk} (with $k>1$) is not sensitive to the wavelength. This conclusion is consistent to similar results obtained in the analysis of resonant frequencies given in Section 3.

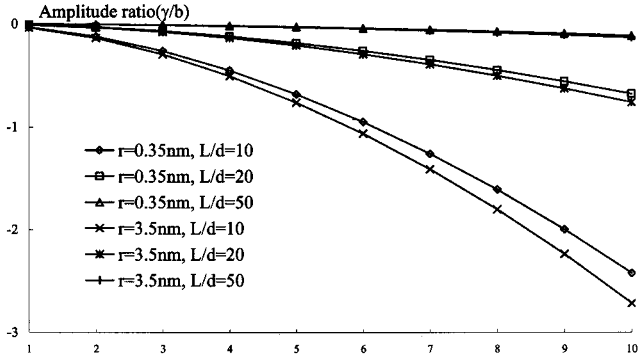

Fig. 16 DWNT amplitude ratio (γ/b) for f_{n1} using a single-Timoshenko-beam model

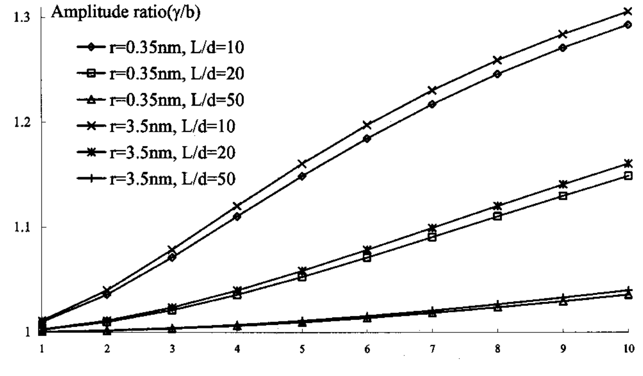

Fig. 17 DWNT amplitude ratio (γ/b) for f_{n2} using a single-Timoshenko-beam model

5 Conclusions

Free vibration of short DWNTs is studied using a double-Timoshenko-beam model, which considers intertube radial displacements between the inner and outer tubes and treats the inner and outer tubes as two individual Timoshenko beams. The results indicate that both the Timoshenko-beam effect and the double beam effect are significant when the wavelength of DWNTs is just a few times larger than the outer diameter of DWNTs. In particular, it is the case when the higher-order frequencies (within the terahertz range) of short DWNTs (of smaller aspect ratio around or below 20) are considered. Furthermore, the results show that the effects of the double beam are more significant for small-diameter than for large-diameter DWNTs, while the Timoshenko-beam effects are significant for both large-diameter and small-diameter DWNTs. This is attributed to the fact that the double-beam effects become significant only when the amplitude of interlayer radial displacements (which are of the order of the interlayer spacing) is comparable to the overall deflections of MWNTs (which are of the order of the radius). Because the radii of DWNTs are usually small, the double-beam effects play a significant role in free vibration of short DWNTs. Hence, the effects of the Timoshenko beam and the double beam are relevant for terahertz vibration of short MWNTs of aspect ratio below or around 20. On the other hand, if only the single lowest (first-order) resonant frequency is concerned, the classical single Euler-beam model is accurate enough, any double-beam or Timoshenko-beam model is not needed even for short MWNTs.

Here it should be stated that the present work is limited to small-amplitude linear free vibration of simply supported DWNTs. Although there is evidence (as stated in the present paper) that noncoaxial vibrational frequencies and modes first predicted by the simple linear double-beam model are found to agree well with more recent atomistic simulations, the nonlinearity of the intertube van der Waals interaction (which is not considered by the present linear model) would play a significant role in moderate or large amplitude noncoaxial vibration of MWNTs. In addition, further study is needed for the effects of the Timoshenko-beam model on the natural modes of MWNTs with other end conditions (such as clamped or cantilever MWNTs, or different end conditions for the inner and outer tubes), and forced vibrations of MWNTs, especially under impulsive loading. Finally, the role of internal damping in ultrahigh-frequency noncoaxial vibration of MWNTs is also of interest for future work.

Acknowledgments

The authors thank the three anonymous referees for their helpful comments. The financial support of the Natural Science and Engineering Research Council of Canada is gratefully acknowledged.

References

[1] Rueckers, T., Kim, K., Joselevich, E., Tseng, G. T., Cheung, C. L., and Lieber, C. M., 2000, ''Carbon Nanotube-Based Nonvolatile Random Access Memory for Molecular Computing,'' Science, **289**, 94–97.

[2] Postma, H. W. C., Teepen, T., Yao, Z., Grifoni, M., and Dekker, C., 2000, ''Carbon Nanotube Single-Electron Transistors at Room Temperature,'' Science, **293**, 76–79.

[3] Roschier, L., Tarkiainen, R., Ahlskog, M., Paalanen, M., and Hakonen, P., 2001, ''Multiwalled Carbon Nanotubes as Ultrasensitive Electrometers,'' Appl. Phys. Lett., **78**, 3295–3297.

[4] Ahlskog, M., Hakonen, P., Paalanen, M., Roschier, L., and Tarkiainen, R., 2001, ''Multiwalled Carbon Nanotubes as Building Blocks in Nanoelectronics,'' J. Low Temp. Phys., **124**, 335–352.

[5] Dai, H., Hafner, J. H., Rinzler, A. G., Colbert, D. T., and Smalley, R. E., 1996, ''Nanotubes as Nanoprobes in Scanning Probe Microscopy,'' Nature (London), **384**, 147–150.

[6] Kim, P., and Lieber, C. M., 1999, ''Nanotube Nanotweezers,'' Science, **286**, 2148–50.

[7] Cumings, J., and Zettel, A., 2000, ''Low-Friction Nanoscale Linear Bearing Realized From Multiwall Carbon Nanotubes,'' Science, **289**, 602–604.

[8] Thostenson, E. T., Ren, Z., and Chou, T. W., 2001, ''Advances in the Science and Technology of Carbon Nanotubes and Their Composites: A Review,'' Compos. Sci. Technol., **61**, 1899–1912.

[9] Qian, D., Wagner, G. J., Liu, W. K., Yu, M. F., and Ruoff, R. S., 2002, ''Mechanics of Carbon Nanotubes,'' Appl. Mech. Rev., **55**, 495–533.

[10] Ru, C. Q., 2004, ''Elastic Models For Carbon Nanotubes,'' *Encyclopedia of Nanoscience and Nanotechnology*, Vol. 2, H. S. Nalwa, ed., American Scientific Publishers, Stevenson Ranch, CA, pp. 731–744.

[11] Wong, E. W., Sheehan, P. E., and Lieber, C. M., 1997, ''Nanobeam Mechanics: Elasticity, Strength, and Toughness of Nanorods and Nanotubes,'' Science, **277**, 1971–75.

[12] Treacy, M. M. J., Ebbesen, T. W., and Gibson, J. M., 1996, ''Exceptonally High Young's Modulus Observed for Individual Carbon Nanotubes,'' Nature (London), **381**, 678–680.

[13] Poncharal, P., Wang, Z. L., Ugarte, D., and de Heer, W. A., 1999, ''Electrostatic Deflections and Electromechanical Resonances of Carbon Nanotubes,'' Science, **283**, 1513–16.

[14] Harik, V. M., 2001, ''Ranges of Applicability for the Continuum Beam Model in the Mechanics of Carbon Nanotubes and Nanorods,'' Solid State Commun., **120**, 331–335.

[15] Ru, C. Q., 2000, ''Column Buckling of Multiwalled Carbon Nanotubes With Interlayer Radial Displacements,'' Phys. Rev. B, **62**, 16962–67.

[16] Yoon, J., Ru, C. Q., and Mioduchowski, A., 2002, ''Non-Coaxial Resonance of an Isolated Multiwall Carbon Nanotube,'' Phys. Rev. B, **66**, 233–402.

[17] Yoon, J., Ru, C. Q., and Mioduchowski, A., 2003, ''Vibration of Embedded Multiwall Carbon Nanotubes,'' Compos. Sci. Technol., **63**, 1533–1542.

[18] Dequesnes, M., Rotkin, S. V., and Aluru, N. R., 2002, ''Calculation of Pull-In Voltages for Carbon-Nanotube-Based Nanoelectromechanical Switches,'' Nanotechnology, **13**, 120–131.

[19] Snow, E. S., Campbell, P. M., and Novak, J. P., 2002, ''Singlewall Carbon Nanotube Atomic Force Microscope Probes,'' Appl. Phys. Lett., **80**, 2002–4.

[20] Ishikawa, M., Yoshimura, M., and Ueda, K., 2002, ''A Study of Friction by Carbon Nanotube Tip,'' Appl. Surf. Sci., **188**, 456–459.

[21] Zhao, Y., Ma, C. C., Chen, G., and Jiang, Q., 2003, ''Energy Dissipation Mechanisms in Carbon Nanotube Oscillators,'' Phys. Rev. Lett., **91**, 175–504.

[22] Li, C., and Chou, T. W., 2004, ''Vibrational Behaviors of Multiwalled-Carbon-Nanotube-Based Nanomechanical Resonators,'' Appl. Phys. Lett., **84**, 121–123.

[23] Timoshenko, S., 1974, *Vibration Problems in Engineering*, Wiley, New York.

[24] Rao, S. S., 1974, ''Natural Vibrations of Systems of Elastically Connected Timoshenko Beams,'' J. Acoust. Soc. Am., **55**, 1232–1237.

[25] Cowper, G. R., 1996, ''The Shear Coefficient in Timoshenko's Beam Theory,'' ASME J. Appl. Mech., **33**, 335–340.

[26] Hutchinson, J. R., 2001, ''Shear Coefficients for Timoshenko Beam Theory,'' ASME J. Appl. Mech., **68**, 87–92.

[27] Smith, B. W., and Luzzi, D. E., 2000, ''Formation Mechanism of Fullerene Peapods and Coaxial Tubes: A Path for Large Scale Synthesis,'' Chem. Phys. Lett., **321**, 169–174.

[28] Saito, R., Matsuo, R., Kimura, T., Dresselhaus, G., and Dresselhaus, M. S., 2001, ''Anomalous Potential Barrier of Double-Wall Carbon Nanotube,'' Chem. Phys. Lett., **348**, 187–193.

[29] Bandow, S., Takizawa, M., Hirahara, K., Yudasaka, M., and Iijima, S., 2001, ''Raman Scattering Study of Double-Wall Carbon Nanotubes Derived From the Chains of Fullerenes in Single-Wall Carbon Nanotubes,'' Chem. Phys. Lett., **337**, 48–54.

[30] Dresselhaus, M. S., and Eklund, P. C., 2000. ''Phonons in Carbon Nanotubes,'' Adv. Phys., **49**, 705–814.

Sauvik Banerjee
Ph.D. Student,
Mechanical and Aerospace Engineering
Department,
University of California,
Los Angeles, CA 90095-1597
e-mail: sauvik@ucla.edu
Assoc. Mem. ASME

William Prosser
Nondestructive Evaluation Branch,
NASA Langley Research Center,
MS231,
Hampton, VA 23681-0001
e-mail: w.h.prosser@larc.nasa.gov

Ajit Mal[1]
Mechanical and Aerospace Engineering
Department,
University of California,
Los Angeles, CA 90095-1597
e-mail: ajit@ucla.edu
Fellow ASME

Calculation of the Response of a Composite Plate to Localized Dynamic Surface Loads Using a New Wave Number Integral Method

This study is motivated by the need for an efficient and accurate tool to analyze the wave field produced by localized dynamic sources on the surface or the interior of isotropic plates and anisotropic composite laminates. A semi-analytical method based on the wave number integral representation of the elastodynamic field is described that reduces the overall computational effort significantly over other available methods. This method is used to calculate the guided wave field produced in a thin unidirectional graphite/epoxy composite laminate by a dynamic surface point load. The results are compared with those obtained from a finite element analysis, showing excellent agreement, except for minor differences at higher frequencies. A recently discovered feature of the calculated surface motion, namely, a spatially periodic "phase reversal" of the main pulse with propagation distance, is observed in both cases. The present work is expected to be helpful in developing impact damage monitoring systems in defect-critical structural components through real time analysis of acoustic emission wave forms. [DOI: 10.1115/1.1828064]

1 Introduction

Elastic waves generated by foreign object impact and initiation or growth of fatigue cracks in aircraft, aerospace, and civil structures carry useful information about the nature of the damage associated with these events. A clear understanding of the quantitative relationship between the waves and their sources is essential in developing algorithms for detecting and characterizing the damage. Model-based analysis of the wave form signals recorded by surface mounted or embedded sensors located in the vicinity of the sources can lead to the development of an effective health monitoring system for a variety of structures.

The general features of elastic waves that can be transmitted in isotropic and anisotropic plates have been studied in great detail over the past several decades [1,2]. These studies were motivated, in part, by the need to understand the nature of ultrasonic waves that can be transmitted in structural components [3]. In contrast, the literature on the response of anisotropic plates to buried or surface sources that are representative of imapact or fatigue damage is relatively sparse [4–8]. Approximate thin-plate theories, such as classical plate theory (CPT, under Kirchoff-Love kinematic assumption) and shear deformation plate theory (SDPT) or Mindlin theory have been developed to obtain the analytical solution to a variety of problems involving the dynamic response of thin isotropic and anisotropic laminated plates [9,10]. A comprehensive review of recent research on guided waves in composite plates and their use in nondestructive material characterization can be found in [11]. An extensive review of published research on low velocity as well as ballistic impact on laminated composites can be found in [12].

The exact solution of three-dimensional problems consisting of multilayered, angle-ply laminates of finite thickness and large lateral dimensions subjected to various types of surface loads, has been given in [6–8]. In these papers, the response problem was formulated using triple integral transforms involving one in time and two in space, leading to an exact representation of the elastodynamic field in the transformed frequency–wave number domain. The inversion of the transforms required numerical evaluation of a double wave number integral followed by frequency inversion using the fast Fourier transform algorithm. The main computational effort in this approach involves the accurate evaluation of the double wave-number integral. The evaluation of this integral is extremely difficult due to the presence of singularities within the integration domain and the highly oscillatory nature of the integrands at higher frequencies and large distances between the field and source points.

Although several efficient and accurate methods are available to evaluate the single wave-number integrals which arise for two-dimensional problems, [13,14], no such algorithm is available to date to evaluate the double wave number integrals that appear in the corresponding three-dimensional problems. The conventional integration schemes (e.g., Simpson, Gaussian, Clenshaw-Curtis, etc.) require millions of function evaluations, resulting in extremely slow turnaround time. An ''adaptive surface-fitting scheme'' using material dissipation was used in [7,8] to evaluate the double integral for dissipative media. However, the computational effort is still quite large to achieve the desired degree of accuracy due to its two-dimensional nature and the presence of spikes near points where the integrand becomes singular in the absence of dissipation.

The finite element method (FEM) is also a versatile tool to analyze this class of problems and a dynamic finite element code has been developed by NIST for the calculation of acoustic emission wave forms in isotropic and anisotropic plates [15–17]. This code has been validated with both experimental measurements

---

[1] To whom correspondence should be addressed.

Contributed by the Applied Mechanics Division of THE AMERICAN SOCIETY OF MECHANICAL ENGINEERS for publication in the ASME JOURNAL OF APPLIED MECHANICS. Manuscript received by the Applied Mechanics Division, May 12, 2003; final revision, July 7, 2004. Editor: K. Ravi-Chandar. Discussion on the paper should be addressed to the Editor, Prof. Robert M. McMeeking, Journal of Applied Mechanics, Department of Mechanical and Environmental Engineering, University of California—Santa Barbara, Santa Barbara, CA 93106-5070, and will be accepted until four months after final publication in the paper itself in the ASME JOURNAL OF APPLIED MECHANICS.

and analytical predictions for a variety of source conditions and plate dimensions in isotropic materials. Although the FEM can handle complex geometries and has the capability to accommodate reflections from the lateral boundaries, it is computationally much more intensive than the analytical methods discussed above.

A method for relatively rapid calculation of the wave forms generated by localized dynamic sources in isotropic as well as anisotropic composite plates is presented in this paper. The method involves a new scheme, in which the double integral is transformed, using contour integration, into a single integral, which is then evaluated numerically using conventional integration schemes. This reduces the computational effort significantly. The method is used to calculate the surface motion in a unidirectional graphite/epoxy composite laminate due to a localized dynamic surface load. The results are compared with those obtained from FEM for their mutual verification.

2 Problem Formulation

A detailed formulation of the exact and approximate theories, SDPT and CPT, for wave field calculations in composite laminates can be found elsewhere [7,10], and will not be repeated here. The typical wave number integral representation of the surface displacement in three-dimensional problems can be expressed in the form

$$I=\frac{1}{4\pi^2}\int_{-\infty}^{\infty}\int_{-\infty}^{\infty}\frac{f(k_1,k_2,\omega)}{g(k_1,k_2,\omega)}e^{i(k_1x_1+k_2x_2)}dk_1dk_2 \qquad (1)$$

where k_1 and k_2 are the wave numbers in 1 and 2 directions, respectively, ω is the circular frequency, and x_1, x_2 are the coordinates of the field point. The functions f and g are obtained from the solution of a system of linear equations of order $6N$, where N is the number of layers. This integral must, in general, be evaluated numerically for a large number (>100) of frequency points. As indicated in the Introduction, the integrand undergoes highly irregular and rapid oscillations at higher frequencies and larger propagation distances, and its denominator vanishes at the "poles" on the integration path associated with the guided waves in the plate. In [7], the poles were removed from the path of integration through the introduction of dissipation in the medium, and the double integration was carried out using an adaptive quadrature scheme to reduce the number of function evaluations. Although the method produced accurate results, the computational effort is still quite high, especially for thicker laminates.

2.1 A New Integration Scheme. As an alternative to evaluate the double integral numerically, it is proposed that one integral in Eq. (1) be evaluated by contour integration analytically, using the residue theorem. For example, the k_2-integral in Eq. (1) can be evaluated by contour integration in the complex plane, keeping k_1 fixed, resulting in residue contributions at the roots $k_2(k_1)$ of $g(k_1,k_2)$. The remaining integral with respect to k_1 can then be integrated numerically. At a given frequency, $g(k_1,k_2)$ has a finite number of real roots, and an infinite number of complex roots. The real roots represent the propagating guided waves in the plate, while the complex roots represent nonpropagating modes that decay exponentially with propagation distance from the source. It has been shown [18] that the amplitude of the nonpropagating modes become negligible in comparison with the propagating modes at distances from the source larger than about only a few multiples of the plate thickness. Since this condition is satisfied in most nondestructive evaluation applications, the residue contributions from the complex roots can be ignored without significantly affecting the accuracy of the results.

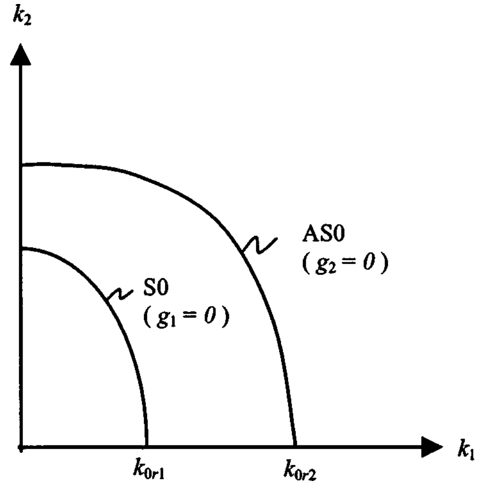

Fig. 1 The locus of the real roots, $k_2(k_1)$ of $g(k_1,k_2)$ in the k_1-k_2 plane

For a given frequency, the real roots, $k_{2r}(k_1)$, of $g(k_1,k_2,\omega)=0$ describe closed symmetric curves on the k_1-k_2 plane due to the fact that g is an even function of both k_1 and k_2. Each curve corresponds to a fixed propagating mode. In Fig. 1, the first symmetric and antisymmetric (AS0) modes are drawn in the positive quadrant for simplicity. It can be assumed, without loss of generality, that these curves are defined by $g_1(k_1,k_2)=0$ (symmetric), $g_2(k_1,k_2)=0$ (antisymmetric), where both g_1 and g_2 are even functions of k_1 and k_2, and are obtained from the decomposition of g in the form $g=g_1g_2$. Let us assume that the functions $g_1=0$ and $g_2=0$ cut the k_1 axis at the points $\pm k_{0r1}$ and $\pm k_{0r2}$ as shown in Fig. 1. For a given k_1, the roots $k_2(k_1)$ can be expressed in the form

$$k_2=\sqrt{k_{0rn}^2-\psi_n(k_1)}=k_{2r},$$

$$|k_1|<k_{0rn}=i\sqrt{\psi_n(k_1)-k_{0rn}^2}=k_{2c}, \quad |k_1|>k_{0rn}, \quad n=1,2 \qquad (2)$$

where ψ_1 and ψ_2 are even functions of k_1 and are obtained from the equations $g_1=0$ and $g_2=0$, respectively, after expressing k_2 in terms of k_1. The function ψ_n must be equal to k_{0rn}^2 when k_1 equals $\pm k_{0rn}$. In Eq. (2), k_{2c} can be pure imaginary or complex depending on the material properties and the range of k_1 chosen, and the real and imaginary parts of $k_{2c}\geqslant 0$, for $(x_1,x_2)>0$. In reality, analytical expressions for g_1 and g_2 cannot be found directly from g using the general plate theory, and for given k_1, k_2 in Eq. (2), must be obtained numerically by setting $g=0$. The integration of Eq. (1) on k_2 can now be carried by contour integration as

$$\int_{-\infty}^{\infty}\frac{f(k_1,k_2,\omega)}{g(k_1,k_2,\omega)}e^{i(k_1x_1+k_2x_2)}dk_2=2\pi iF(k_1,k_{2r},\omega)e^{i(k_1x_1+k_{2r}x_2)};$$

$$|k_1|<k_{0rn}=2\pi iG(k_1,k_{2c},\omega)e^{i(k_1x_1+k_{2c}x_2)}; \quad |k_1|>k_{0rn} \qquad (3)$$

where

$$F(k_1,k_{2r},\omega)=\frac{f(k_1,k_{2r},\omega)}{\left.\dfrac{dg(k_1,k_2,\omega)}{dk_2}\right|_{k_2=k_{2r}}}$$

and

$$G(k_1,k_{2c},\omega)=\frac{f(k_1,k_{2c},\omega)}{\left.\dfrac{dg(k_1,k_2,\omega)}{dk_2}\right|_{k_2=k_{2c}}}$$

Thus, the double integration is transformed into a single integral in k_1 and can be explicitly written as

$$\begin{aligned}I=\sum_n \frac{2\pi i}{4\pi^2}\Bigg[&\int_0^{k_{0rn}} F(k_1,k_{2r},\omega)e^{i(k_1x_1+k_{2r}x_2)}dk_1\\&+\int_0^{k_{0rn}} F(-k_1,k_{2r},\omega)e^{i(-k_1x_1+k_{2r}x_2)}dk_1\\&+\int_{k_{0rn}}^{\infty} G(k_1,k_{2c},\omega)e^{i(k_1x_1+k_{2c}x_2)}dk_1\\&+\int_{k_{0rn}}^{\infty} G(-k_1,k_{2c},\omega)e^{i(-k_1x_1+k_{2c}x_2)}dk_1\Bigg]\end{aligned} \tag{4}$$

Since f, g, k_{2r}, k_{2c} and the derivatives of g with respect to k_2 are all even functions of k_1, F and G are also even functions of k_1. Therefore, the four integrals in Eq. (4) reduce to

$$\begin{aligned}I=\sum_n \frac{2\pi i}{4\pi^2}\Bigg[&2\int_0^{k_{0rn}} F(k_1,k_{2r},\omega)e^{ik_{2r}x_2}\cos(k_1x_1)dk_1\\&+2\int_{k_{0rn}}^{\infty} G(k_1,k_{2c},\omega)e^{ik_{2c}x_2}\cos(k_1x_1)dk_1\Bigg]\end{aligned} \tag{5}$$

The integral in Eq. (5) can be evaluated numerically by using any suitable integration scheme. However, it should be noted that its integrand is highly oscillatory, especially at high frequencies and large distances from the source. In addition, there is an integrable singularity at $k_1=k_{0rn}$ that appears from the derivative of g; it is best handled by expressing F and G in terms of polynomials in $(k_{0rn}-k_1)$ and (k_1-k_{0rn}), respectively, near this point, and integrating out exactly. Furthermore, G is a decaying function of k_1 and the exponential term associated with it gives additional decay for nonzero x_2. As a consequence, the contribution of the second integrand for large values of k_1 is negligible. It will be shown later that the contribution of the second integral in Eq. (5) is concentrated within a very small region beyond k_{0rn} for large values x_2, and one need not even calculate the complex roots. Thus, one major advantage of the present scheme would be to split the positive x_1-x_2 plane into two halves by the line $\theta=45$ deg, where θ is measured counter clockwise from the x_1 axis. The integration on k_1 can then be performed as described earlier for the observation points located in $\theta>45$ deg. In order to obtain the solution for the field points located in $\theta<45$ deg, the order of the integration needs to be reversed. The basic procedure remains same. The current integration scheme will work both in presence and absence of material dissipation. In a mildly dissipative material, the real roots will have a small imaginary part, which can be obtained by means of a number of available techniques (e.g., Muller's method).

In the next section, we use the new method to calculate the response in a number of simple model problems.

2.2 Guided Waves in a Thin Anisotropic Plate (CPT). Assuming that the material of the plate is transversely isotropic with its symmetry axis along its surface, the vertical surface displacement of the plate due to a normal concentrated force $f(t)$ at the origin can be expressed in the form [10]

$$\overline{u}_3(x_1,x_2,0,\omega)=\frac{F(\omega)}{4\pi^2}\int_{-\infty}^{\infty}\int_{-\infty}^{\infty}\frac{1}{D_{11}k_1^4+2(D_{12}+2D_{55})k_1^2k_2^2+D_{22}k_2^4-\rho\omega^2H}e^{i(k_1x_1+k_2x_2)}dk_1dk_2 \tag{6}$$

where, D_{11}, D_{12}, D_{22}, and D_{55} are functions of the elastic constants of the plate material and $F(\omega)$ is the Fourier transform of the load.

Thus,

$$f=1,\quad g=D_{11}k_1^4+2(D_{12}+2D_{55})k_1^2k_2^2+D_{22}k_2^4-\rho\omega^2H \tag{7}$$

Setting $g=0$,

$$k_2^2=-bk_1^2\pm\sqrt{b^2k_1^4-ck_1^4+\frac{\rho\omega^2H}{D_{22}}} \tag{8}$$

where

$$b=\frac{D_{11}+2D_{55}}{D_{22}},\quad c=\frac{D_{11}}{D_{22}}$$

In order to obtain the real roots, for a given k_1, the positive sign must be chosen for the second term in the right-hand side of Eq. (8). Hence,

$$k_2^2=-bk_1^2+\sqrt{b^2k_1^4-ck_1^4+ck_{0r1}^4} \tag{9}$$

where $k_{0r1}=[\rho\omega^2H/D_{11}]^{1/4}$ gives only one propagating mode.

Thus, Eq. (9) can be expressed in the form

$$k_2^2=k_{0r1}^2-\psi_1(k_1) \tag{10}$$

where

$$\psi_1(k_1)=k_{0r1}^2+bk_1^2-\sqrt{b^2k_1^4-ck_1^4+ck_{0r1}^4}$$

Using Eq. (3),

$$F(k_1,k_{2r},\omega)=\frac{1}{4D_{22}\alpha(k_1)\sqrt{k_{0r1}^2-\psi_1(k_1)}},$$

$$G(k_1,k_{2c},\omega)=\frac{1}{4D_{22}\alpha(k_1)i\sqrt{\psi_1(k_1)-k_{0r1}^2}} \tag{11}$$

where

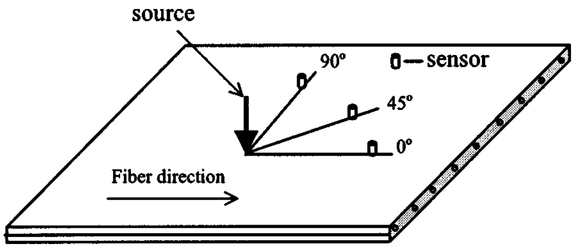

Fig. 2 Schematic of a loaded unidirectional composite plate showing position of the sensors with respect to the fiber direction

$$\alpha(k_1)=[k_{0r1}^2-\psi_1(k_1)+bk_1^2]$$

The rest of the calculation can be carried out in a straightforward manner starting from Eq. (4) of Sec. 2.1.

If the plate is isotropic, $b=c=1$, so that $\psi_1(k_1)=k_1^2$. Thus, the first of Eq. (2) produces an equation of a circle in the k_1-k_2 plane with radius k_{0r1} centered at the origin. Thus from Eq. (11),

$$F(k_1,k_{2r},\omega)=\frac{A}{\sqrt{k_{0r1}^2-k_1^2}},\quad G(k_1,k_{2c},\omega)=\frac{A}{i\sqrt{k_1^2-k_{0r1}^2}} \tag{12}$$

where

$$A=\frac{1}{4D_{22}k_{0r1}^2}$$

Thus, from Eqs. (5) and (6),

Table 1 Material constants of graphite/epoxy composite material

Thickness (mm)	Density (g/cm^3)	C_{11} (GPa)	C_{12} (GPa)	C_{22} (GPa)	C_{23} (GPa)	C_{55} (GPa)
1	1.578	160.73	6.44	13.92	6.92	7.07

$$\overline{u_3}(x_1,x_2,0,\omega)=F(\omega)iAH_0^1(k_{0r1}r) \tag{13}$$

where H_0^1 is the Hankel function of first kind and $r=\sqrt{x_1^2+x_2^2}$. It can be further shown that the surface displacement in the frequency domain obtained using exact theory [6], and following the same procedure, has the same form as Eq. (13). However, a sum on all propagating modes, k_{0rn}, where n is the number of propagating modes, should be taken in Eq. (13) and A will be a function of k_{0rn} and the material properties. The time domain response can be obtained after performing inverse Fourier transform on Eq. (13).

3 Numerical Results

Numerical results are presented for a unidirectional graphite/epoxy composite plate subjected to a vertical dynamic point load on its top surface. A loaded unidirectional composite plate with surface mounted sensors is shown in Fig. 2. The elastic properties of the material used in the calculations are given in Table 1.

3.1 Typical Behavior of the Integrand of Wavenumber Integral.

The integrand of the approximate solution given in Eq. (10) is plotted in Fig. 3 for propagation at 45 deg to the fibers for

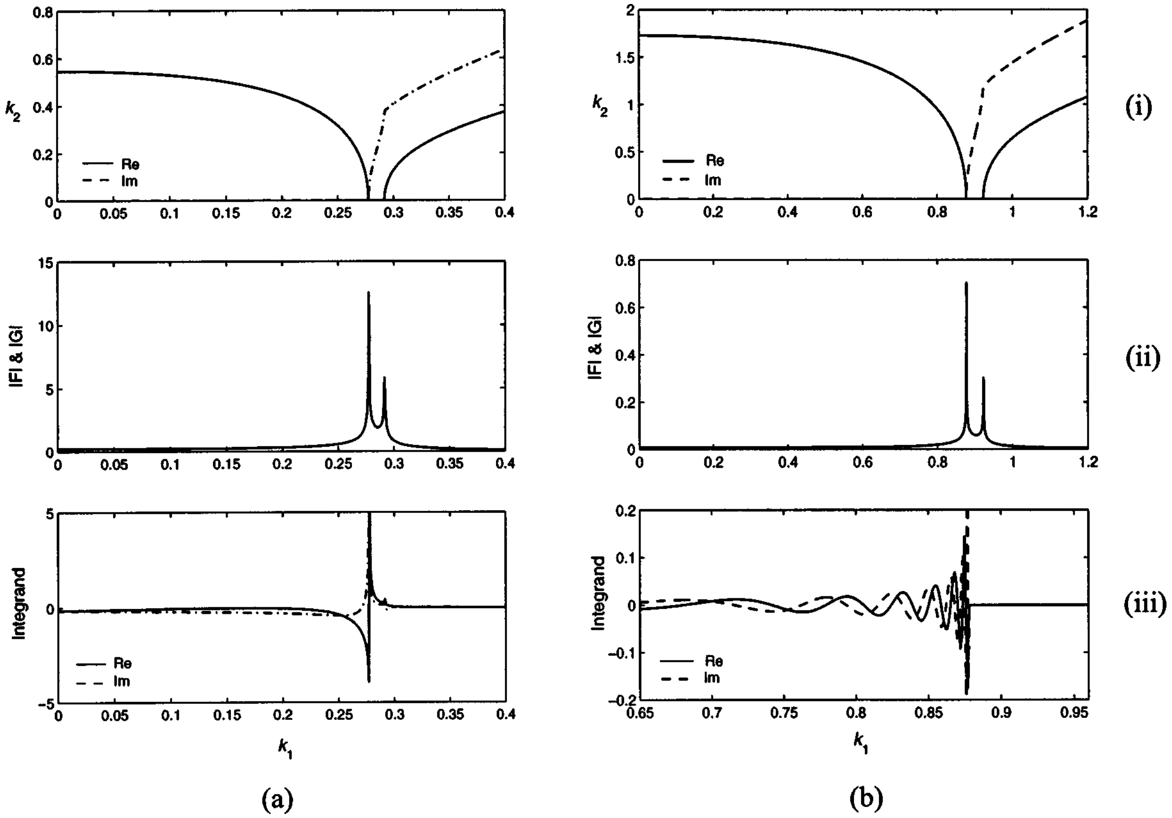

Fig. 3 Kernel behavior for a unidirectional graphite/epoxy composite plate of thickness 1 mm for propagation along 45 degh for two cases: (a) at a distance 10 mm from the source at 0.1 MHz and (b) at a distance 50 mm from the source at 1.0 MHz (CPT). (i) Locus of real (k_{2r}) and imaginary roots (k_{2c}) of $g(k_1,k_2)$ in the k_1-k_2 plane, (ii) absolute plot of Eq. (3), and (iii) real and imaginary parts of the integrand in Eq. (5).

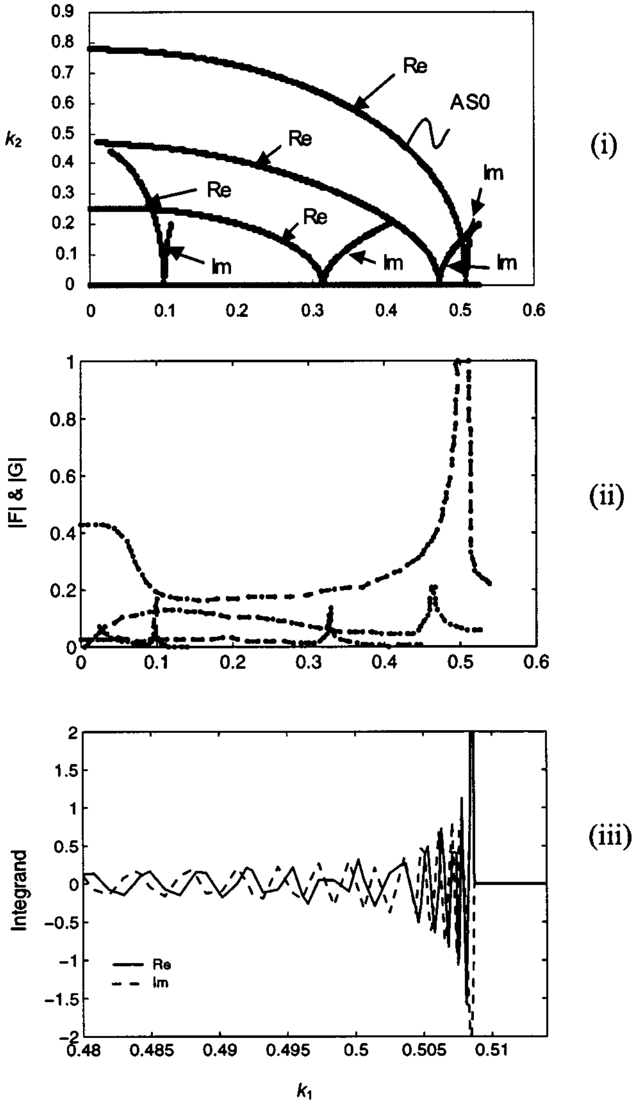

Fig. 4 Kernel behavior for a unidirectional graphite/epoxy composite plate of thickness 1 mm for propagation along 90 deg at a distance 50 mm from the source at 1 MHz (exact theory). (i), (ii), and (iii) are the same as that of Fig. 3.

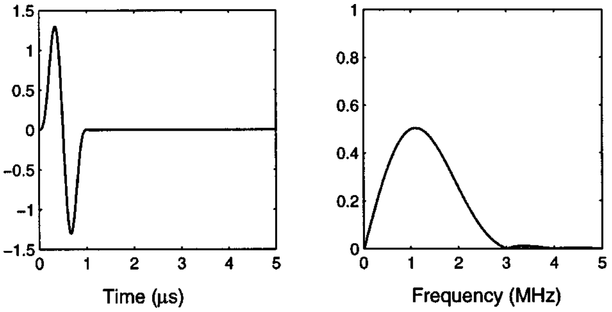

Fig. 5 Time history and spectrum of the source

two cases: (a) at a distance of 10 mm from the source at 0.1 MHz, and (b) at a distance of 50 mm from the source at 1.0 MHz. From the first plots of cases (a) and (b), it can be seen that k_2 is purely imaginary within a small region beyond k_{0r1}, and becomes complex afterwards. An increase in the amplitude of the function $|G|$ (Eq. (15)) is observed in both cases (second plots) when k_2 becomes complex. However, as shown in the third plots of Fig. 3, the contributions from the complex values of k_2 are very small at all frequencies of interest. The contribution is negligible for large distances and high frequencies as shown in case (b). As indicated earlier, the integrand is highly oscillatory at higher frequencies.

A typical plot of the behavior of the integrand in Eq. (5), using exact theory [6] is presented in Fig. 4, for the same plate at 1 MHz, for propagation along 90 deg at a distance of 50 mm from the source. The complex roots are not shown in the plots. The same features are found in this case as well. It can be seen that most of the contribution towards the integral comes from the AS0 mode only.

3.2 Evaluation of the Wave Number Integral. The calculations are carried out for a concentrated vertical surface load in the form [8]

$$F(x_1,x_2,t)=f(t)\,\delta(x_1)\,\delta(x_2) \tag{14}$$

where

$$f(t)=\sin\left(\frac{2\pi t}{\tau}\right)-0.5\sin\left(\frac{4\pi t}{\tau}\right),\quad 0<t<\tau \tag{15}$$

The time dependence of the load, $f(t)$, and its Fourier transform, $F(\omega)$, are plotted for $\tau=1$ μs in Fig. 5. The source spectrum is maximum around 1.1 MHz and becomes negligibly small beyond 3 MHz.

The new integration scheme has also been implemented on the exact theory to obtain the time histories of the vertical surface displacement. The results are compared with those from FEM for propagation along 0 deg, 30 deg, 60 deg, and 90 deg with respect to the fiber direction at a number of field points in Figs. 6(*a*)–6(*d*). Since the displacements calculated from the CPT diverge greatly from the exact and FEM solutions, the results are omitted for brevity. A third-order elliptic digital filter [19] with a pass band of0.05–0.65 MHz is applied to all calculated spectra to eliminate high frequency numerical noise. The agreement between the results from the two models is excellent in almost all cases. The time histories of surface motion from the exact theory show the strong influence of the higher order modes at high frequencies, which are absent in those from FEM. This requires further investigation. The arrival time of the peak in the two sets of signals, however, coincides. A recently discovered behavior of the wave forms, namely, phase reversal of the main pulse with propagation distance [20] caused by the strong dispersion of the AS0 mode is also present in the results.

4 Concluding Remarks

The time histories of the vertical surface displacement calculated from FEM and exact theory show excellent agreement. The two methods can be combined for efficient and accurate calculation of the wave forms in both near and far fields. The new integration scheme for the evaluation of the double wave-number integral representation of the field involves the numerical computation of only one of the integrals, thus reducing the computational effort significantly. Another major advantage of the current method is that the integration scheme can be exploited to obtain the solution for any specific propagating mode by using a suitable numerical approach. As an example, if only the AS0 mode is chosen for evaluation, the computational effort will be extremely small. The approach can be used for rapid calculation of the elastic waves generated by impact and fatigue damage in plates and should be useful in real time heath monitoring of critical structural components. Extension of the current work to thicker laminates and laboratory experiments are currently underway.

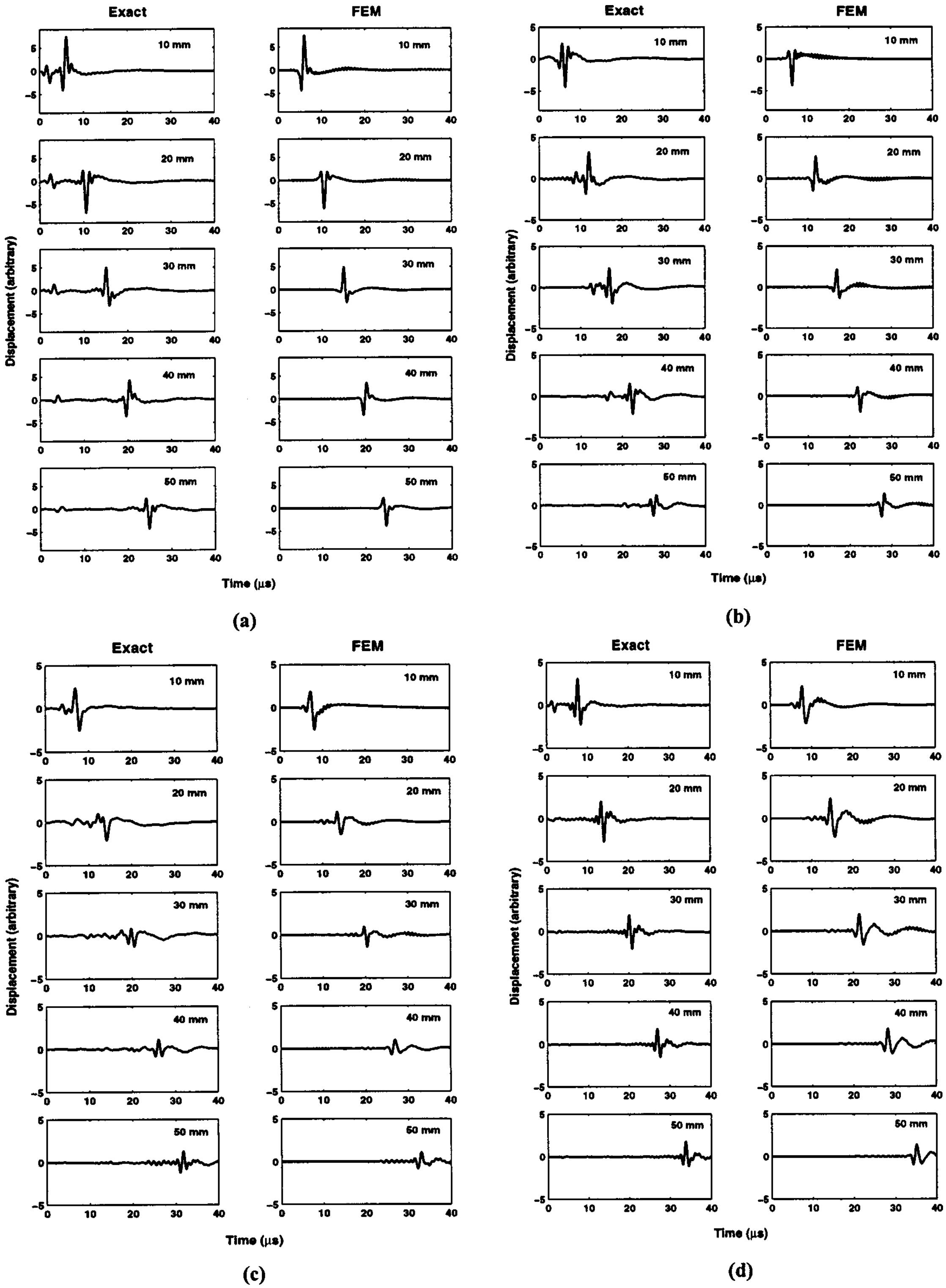

Fig. 6 Time history of vertical surface displacement in a 1 mm thick unidirectional graphite/epoxy composite plate subjected to a point load from exact theory (first column) and FEM (second column), (a) 0 deg propagation, (b) 30 deg propagation, (c) 60 deg propagation, and (d) 90 deg propagation

Acknowledgment

This research was supported by NASA Langley Research Center under Grant No. NAG-1-02036.

References

[1] Achenbach, J. D., 1978, *Wave Propagation in Elastic Solids*, North-Holland, New York.

[2] Nayfeh, A. H., 1995, *Wave Propagation in Layered Anisotropic Media: With Applications to Composites*, Elsevier Science, Amsterdam.

[3] Rose, J. L., 1999, *Ultrasonic Waves in Solid Media*, Cambridge University Press, New York.

[4] Kundu, T., and Mal, A. K., 1985, "Elastic Waves in a Multilayered Solid Due to a Dislocation Source," Wave Motion, **7**, pp. 459–471.

[5] Guo, D., Mal, A. K., and Ono, K., 1996, "Wave Theory of Acoustic Emission in Composite Laminates," J. Acoust. Emiss., **14**, S19–S46.

[6] Mal, A. K., 1988, ‘‘Wave Propagation in Layered Composite Laminates Under Periodic Surface Loads,’’ Wave Motion, **10**, pp. 257–266.
[7] Mal, A. K., and Lih, S. S., 1992, ‘‘Elastodynamic Response of a Unidirectional Composite Laminate to Concentrated Surface Loads, Parts I & II,’’ ASME J. Appl. Mech., **55**, pp. 878–892.
[8] Lih, S. S., and Mal, A. K., 1996, ‘‘Response of Multilayered Composite Laminates to Dynamic Surface Loads,’’ Composites, Part B, **27B**, pp. 633–641.
[9] Reddy, J. N., 1984, ‘‘A Simple Higher-Order Theory for Laminated Composite Plates,’’ ASME J. Appl. Mech., **51**, pp. 745–752.
[10] Lih, S. S., and Mal, A. K., 1995, ‘‘On the Accuracy of Approximate Plate Theories for Wave Field Calculations in Composite Laminates,’’ Wave Motion, **21**, pp. 17–34.
[11] Chimenti, D. E., 1997, ‘‘Guided Waves in Plates and Their Use in Material Characterization,’’ Appl. Mech. Rev., **50**, pp. 247–284.
[12] Abrate, S., 1998, *Impact on Composite Structures*, Cambridge University Press, New York.
[13] Xu, P. C., and Mal, A. K., 1985, ‘‘An Adaptive Integration Scheme for Irregularly Oscillating Functions,’’ Wave Motion, **7**, pp. 235–243.
[14] Dravinski, M., and Mossessian, T. K., 1988, ‘‘On the Evaluation of the Green’s Functions for Harmonic Line Loads in a Viscoelastic Half-Space,’’ Int. J. Numer. Methods Eng., **26**, pp. 823–841.
[15] Gary, J., and Hamstad, M., 1994, ‘‘On the Far-Field Structure of Waves Generated by a Pencil Break on a Thin Plate,’’ J. Acoust. Emiss., **12**(3–4), pp. 157–170.
[16] Hamstad, M. A., Gary, J., and O’Gallagher, A., 1996, ‘‘Far-Field Acoustic Emission Waves by Three-Dimensional Finite Element Modeling of Pencil Breaks on a Thick Plate,’’ J. Acoust. Emiss., **14**(2), pp. 103–114.
[17] Prosser, W. H., Hamstad, M. A., Gary, J., and O’Gallagher, A., 1999, ‘‘Comparison of Finite Element and Plate Theory Methods for Modeling Acoustic Emission Waveforms,’’ J. Nondestruct. Eval., **18**(3), pp. 83–90.
[18] Vasudevan, N., and Mal, A. K., 1985, ‘‘Response of an Elastic Plate to Localized Transient Sources,’’ ASME J. Appl. Mech., **107**, pp. 356–362.
[19] MATLAB 6.5, Release 13.
[20] Banerjee, S., Prosser, W. H., and Mal, A. K., 2004, ‘‘Analysis of Transient Lamb Waves Generated by Dynamic Surface Sources in Thin Composite Plates,’’ J. Acoust. Soc. Am., **115**, pp. 1905–1911.

Steady Mechanics of Belt-Pulley Systems

Lingyuan Kong
Research Assistant

Robert G. Parker[1]
e-mail: parker.242@osu.edu
Mem. ASME

Department of Mechancial Engineering,
The Ohio State University,
206 W. 18th Avenue,
Columbus, OH 43210

Steady state analysis of a two-pulley belt drive is conducted where the belt is modeled as a moving Euler-Bernoulli beam with bending stiffness. Other factors in the classical creep theory, such as elastic extension and Coulomb friction with the pulley, are retained, and belt inertia is included. Inclusion of the bending stiffness leads to nonuniform distribution of the tension and speed in the belt spans and alters the belt departure points from the pulley. Solutions for these quantities are obtained by a numerical iteration method that generalizes to n-pulley systems. The governing boundary value problem (BVP), which has undetermined boundaries due to the unknown belt-pulley contact points, is first converted to a standard fixed boundary form. This form is readily solvable by general purpose BVP solvers. Bending stiffness reduces the wrap angles, improves the power efficiency, increases the span tensions, and reduces the maximum transmissible moment.

[DOI: 10.1115/1.1827251]

1 Introduction

Belt-pulley drives have been widely used to transmit power for hundreds of years. The power is transmitted from the driver pulley to the driven pulleys through friction between the belt and the pulleys. The belt-pulley mechanics are important in industrial applications as they impact belt tension, belt life, power transmission efficiency, maximum transmissible moment, and noise. Considerable research has been done in the field of belt mechanics. Fawcett [1] gives a comprehensive review of belt mechanics up to 1981. Two different theories have been used to describe the belt behavior. One is known as creep theory, which assumes that the belt is elastically extensible, friction is developed due to the relative slip motion between the belt and pulley, and a Coulomb law describes the belt-pulley friction. Another model is the shear theory, which addresses shearing deformation of the belt and assumes that the belt is inextensible. The shear theory is developed recently in [2,3]. Alciatore and Traver [4] give a comparison between these two different theories. In this paper the creep theory is adopted with the refinement of incorporating belt bending stiffness.

Johnson [5] gives a review of the classic creep theory. Gerbert [6] analyzes a symmetric system with no belt bending stiffness where the driver and driven pulleys have the same radius. Recently, by considering inertial effects, Bechtel et al. [7] update the classic creep theory to include belt inertia and present a complete solution for a two-pulley belt drive. Independently, Rubin [8] investigates the effects of the same inertia terms and presents a method to find solutions for general multi-pulley systems. Although the derivations in [7,8] seem different, the analysis and main conclusions are essentially the same. The main contribution of these two papers is that they include belt inertia terms and determine the relative errors of prior creep theories that neglect these terms.

In both [7,8], the belt is treated as a string and belt bending stiffness is not considered. Bending stiffness introduces additional, nonuniform tension in the belt due to the induced curvatures in the spans, leads to nonuniform speed along the belt spans, alters the wrap angles, and influences performance criteria such as maximum transmissible moment and efficiency. When bending stiffness is appreciable compared to tension stiffness (especially for thick, low tension, or short span belts), the effects of bending stiffness are more significant than the inertia terms introduced in [7,8]. The main concern of this study is to investigate the influence of bending stiffness on the steady motion while keeping belt inertia.

The belt is modeled as a moving Euler-Bernoulli beam. Even in the belt spans, the distributions of tension and speed are no longer uniform and there is no explicit analytical solutions for the ordinary differential equations (ODEs) governing the belt spans, in contrast to the string models [7,8]. Furthermore, inclusion of the bending stiffness makes the contact points between the belt and pulleys (boundaries for the ODEs) not known a priori. Consequently, the steady motion analysis is governed by boundary value problem with unknown domain. This presents one of the main obstacles. By suitable transformation using ordinary differential equation conversion techniques, however, this problem is formulated as a standard BVP with fixed boundaries. This form is accepted by general-purpose two-point BVP solvers. No spatial discretization (e.g., Galerkin, Ritz) is used; the final result can be viewed as numerically exact. Although the iteration method is presented for two-pulley belt drives, it can be readily extended to multi-pulley drives.

In related works, Wang and Mote [9] and Hwang and Perkins [10] consider belt bending stiffness while investigating a band/wheel system with two identical pulleys. The steady state analysis in this work and those in [7,8] are different in spirit from those in [9,10], where calculation of the steady state is mainly for subsequent linearized free vibration analysis. The problems discussed here, like the nonuniform tension and speed distributions, belt slip on the pulleys, power transmission efficiency, and maximum transmissible torque, are not addressed in [9,10]. Correspondingly, some simplifying assumptions are adopted in [9,10]. For example, the belt speed is assumed to be uniform throughout the system, variations of belt tension along a span and on the pulleys are not considered, friction between the pulley and belt is neglected, and no energy is dissipated during steady power transmission. In [9], the boundaries of the spans are fixed at the belt-pulley contact points of the string model. In [10], although the belt-pulley contact points are not fixed, the belt is assumed to be inextensible.

Note the present analysis is only an approximation for V-belt drives because V-belt systems have deep grooves that generate seating and unseating zones not modeled here.

Section 2 presents the governing differential equations of the moving Euler-Bernoulli beam in the steady state. Section 3 intro-

---

[1] To whom correspondence should be addressed.

Contributed by the Applied Mechanics Division of THE AMERICAN SOCIETY OF MECHANICAL ENGINEERS for publication in the ASME JOURNAL OF APPLIED MECHANICS. Manuscript received by the Applied Mechanics Division, July 1, 2003; final revision; February 19, 2004. Associate Editor: M. P. Mignolet. Discussion on the paper should be addressed to the Editor, Prof. Robert M. McMeeking, Journal of Applied Mechanics, Department of Mechanical and Environmental Engineering, University of California—Santa Barbara, Santa Barbara, CA 93106-5070, and will be accepted until four months after final publication in the paper itself in the ASME JOURNAL OF APPLIED MECHANICS.

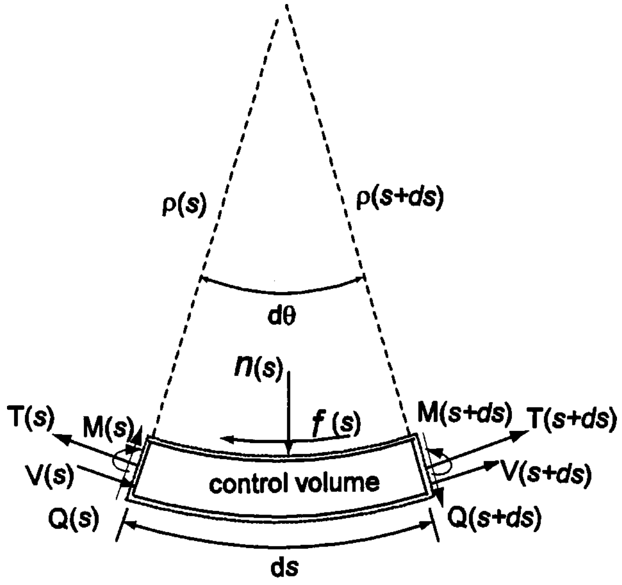

Fig. 1 Free body diagram of a moving curved beam

duces techniques to transform the unknown boundary BVP to fixed-boundary form. These techniques are presented for the case where a single belt span wraps around two pulleys. This solution is a fundamental building block for the overall belt-pulley system solution. Section 4 presents the steady state analysis for a two-pulley belt drive system. Two different problems are considered. One finds the steady motion when the moments on the pulleys are specified. The second problem finds the maximum transmissible moment that can be exerted on the pulleys. Section 5 presents numerical results corresponding to these two problems.

2 Nonlinear Equations of a Moving Curved Beam

Figure 1 shows the free body diagram of an extensible belt, which is modeled as a moving Euler-Bernoulli beam. Rotary inertia and shear deformation are ignored. An Eulerian formulation is adopted for the control volume. The radius of curvature $\rho(s)$ is a function of the arclength coordinate. $f(s)$ and $n(s)$ are contact forces per unit length exerted on the belt.

For steady motions, conservation of mass requires that

$$G = m(s)V(s) = \text{const} \tag{1}$$

where $m(s)$ is the belt mass density per unit length. Euler-Bernoulli beam theory requires

$$M = EI\kappa \tag{2}$$

where EI is the bending stiffness and κ is the curvature of the beam. κ equals the varying rate of inclination of the beam

$$\kappa = d\theta/ds \tag{3}$$

where the inclination angle θ is measured from the due east direction (Fig. 2). The balance of angular momentum with respect to the center of mass of the control volume yields

$$dM - Q ds = 0, \quad Q = dM/ds = EI(d\kappa/ds) \tag{4}$$

Balance of linear momentum projected in the tangential direction leads to

$$dT - f ds = G dV - Q d\theta \tag{5}$$

Substitution of (2)–(4) into (5) leads to

$$(T - GV)' + EI\kappa\kappa' = f \tag{6}$$

where $(\;)'$ denotes differentiation with respect to the arclength s. Balance of linear momentum projected in the normal direction yields

$$n ds = (T - GV) d\theta - dQ \tag{7}$$

Substitution of (4) leads to

$$(T - GV)\kappa - EI\kappa'' = n \tag{8}$$

The above derivation assumes that $d\theta \ll 1$, $\cos(d\theta/2) \approx 1$, $\sin(d\theta/2) \approx d\theta/2$, and products of infinitesimal quantities are negligible.

For the belt in the spans, the contact forces f and n are zero, and Eqs. (6) and (8) become

$$(T - GV)' + EI\kappa\kappa' = 0, \quad (T - GV)\kappa - EI\kappa'' = 0 \tag{9}$$

This converges to the string model [7] when the bending stiffness is zero. Because the curvature is constant for the belt on the pulleys, Eqs. (6) and (8) in these contact regions become

$$(T - GV)' = f, \quad (T - GV)/R = n \tag{10}$$

The governing equations (10) are the same as for a string model [7,8].

3 BVP Solver Based Method for Problem With Unknown Boundaries

Figure 2 presents a single belt span stretched between two fixed pulleys. This boundary value problem has unknown boundaries; the belt departure points from the pulleys are determined in the analysis. This case is a key step in the subsequent solution for general belt-pulley systems. Furthermore, it shows the techniques for converting the problem with unknown boundaries into a standard form [11] that can be solved by general purpose BVP solvers.

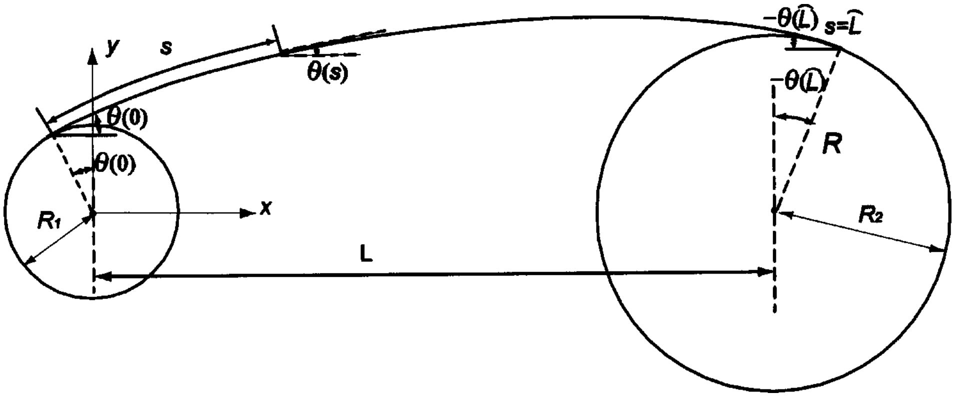

Fig. 2 Single span boundary value problem with unknown boundaries

For this reduced problem, the belt speed is zero. This reduces (9) to

$$T' + EI\kappa\kappa' = 0, \quad T\kappa - EI\kappa'' = 0 \tag{11}$$

Three boundary conditions are needed. For reasons to be evident later, the tension at the start point is assumed to be known

$$T(0) = T_0 \tag{12}$$

The curvatures κ at the two boundaries are specified by the geometric relations (Fig. 2)

$$\kappa(0) = -1/R_1, \quad \kappa(s = \hat{L}) = -1/R_2 \tag{13}$$

where $\hat{L}$ is the total arclength of the belt in the span. What makes the problem unusual is that $\hat{L}$ is not known a priori. The geometric requirement is that the curved belt should contact and be tangent with both pulleys.

By applying ODE conversion techniques, the above system is transformed into a standard form defined on the interval (0,1). This formulation is readily accepted by most general-purpose BVP solvers. First, the following nondimensional variables are introduced

$$\hat{s} = \frac{s}{\hat{L}}, \quad \hat{x} = \frac{x}{\hat{L}}, \quad \hat{y} = \frac{y}{\hat{L}}, \quad \hat{\kappa} = \hat{L}\kappa, \quad \hat{p} = \frac{T\hat{L}^2}{EI} \tag{14}$$

where $x(s)$ and $y(s)$ are the rectangular coordinates of belt particles (Fig. 2). Substitution of (14) into (11) yields

$$\frac{d\hat{p}}{d\hat{s}} + \hat{\kappa}\frac{d\hat{\kappa}}{d\hat{s}} = 0, \quad \frac{d^2\hat{\kappa}}{(d\hat{s})^2} - \hat{p}\hat{\kappa} = 0, \quad 0 < \hat{s} < 1 \tag{15}$$

The boundary conditions (12) and (13) become

$$\hat{p}(0) = T_0\hat{L}^2/EI, \quad \hat{\kappa}(0) = -\hat{L}/R_1, \quad \hat{\kappa}(1) = -\hat{L}/R_2 \tag{16}$$

The unknown constant $\hat{L}$ is defined as the function $\hat{L} = \hat{L}(\hat{s})$, governed by

$$\frac{d\hat{L}}{d\hat{s}} = 0, \quad 0 < \hat{s} < 1 \tag{17}$$

Geometric relations lead to

$$\frac{d\theta}{d\hat{s}} = \hat{\kappa}, \quad \frac{d\hat{x}}{d\hat{s}} = \cos\theta, \quad \frac{d\hat{y}}{d\hat{s}} = \sin\theta, \quad 0 < \hat{s} < 1 \tag{18}$$

The corresponding boundary conditions are

$$[\hat{L}(0)\hat{x}(0)]^2 + [\hat{L}(0)\hat{y}(0)]^2 = R_1^2, \quad \hat{L}(0)\hat{x}(0) = -R_1\sin\theta(0) \tag{19}$$

$$[\hat{L}(1)\hat{x}(1) - L]^2 + [\hat{L}(1)\hat{y}(1)]^2 = R_2^2,$$
$$-R_2\sin\theta(1) = \hat{L}\hat{x}(1) - L \tag{20}$$

where L is the known distance between the centers of the two fixed pulleys (Fig. 2). Equations (19) and (20) ensure that the belt contacts and is tangent to the bounding pulleys. Tangency is imposed by the angles on the pulleys to the contact points being equal to the span inclination angles $\theta(0)$ and $-\theta(1)$.

The seven boundary conditions (16), (19), and (20) equal the total order of the six differential equations (15), (17), and (18). Equation (15) involving higher derivatives can be reduced to standard first order form with the definitions $q_1(\hat{s}) = \hat{\kappa}(\hat{s})$, $q_2(\hat{s}) = \hat{\kappa}'(\hat{s})$, $q_1'(\hat{s}) = y_2(\hat{s})$. The problem is cast entirely on the interval $\hat{s} \in (0,1)$ even though the problem involves unknown boundaries. This standard form is readily accepted by general-purpose, two-point BVP solvers.

There are several advantages of the BVP solver based method: 1) Because there is no spatial discretization and because of the high quality and robustness of state-of-the-art BVP solver codes, the results can be viewed as numerically exact. 2) It is easy to implement with minimal programming. 3) It not only gives the tension and curvature of the belt but also gives the contact points and explicit positions of the entire belt $[x(s)$ and $y(s)]$ simultaneously.

Further, the method can be extended to other problems that do not seem amenable to a general-purpose BVP solver at first sight. In Section 4, two additional required ODE conversion techniques are presented. One shows how to incorporate an integral term in the BVP system. The other shows how to incorporate an algebraic equation.

4 Steady State Analysis of Belt Pulley Drives: An Iteration Method

In this part, the steady motion analysis is presented for a general two pulley belt drive with different pulley radii. Following [7], the specified parameters are driver pulley radius R_1, driven pulley radius R_2, center distance between the two fixed pulleys L, belt longitudinal stiffness EA, constant rotation speed ω_1 of the driver pulley, coefficients of friction μ_1 and μ_2 on the two pulleys, static tension of the belt T_{ini} of the *reference state* (where there is no moment exerted on the pulleys and the belt speed is zero), and belt mass flow rate G. Due to consideration of the bending stiffness, the reference state tensions are no longer uniform along the belt; T_{ini} is assumed to be the tension at the midpoints of the spans. (Note that in the string model of [8], instead of specifying ω_1 and G, the undeformed belt mass per unit length m_0 and $c = G/m_0$ are the chosen parameters. In Section 5.2 and the Appendix, these definitions are shown to be equivalent.)

Two problems are considered: (1) If the moment M_2 on the driven pulley is specified, one finds the driving moment, distributions of tension, speed, and friction along the belt as well as the slip and adhesion angles on the two pulleys, and (2) the moments on the pulleys are not specified, and one first finds the maximum transmissible moment and then calculates the corresponding steady state mechanics; the implicit condition here is that one or both of the adhesion angles vanishes and no additional moment can be transmitted.

The governing equations for the spans are (9). In the contact zones, the governing equations are (10). On the boundaries between the spans and contact zones, the tension, curvature, and speed must be continuous. To complete the problem, a constitutive law is needed. Following [12], a differential belt element with undeformed length ds_o has deformed length

$$ds = (1 + T/EA)ds_o \tag{21}$$

and the mass density per unit length $m(s)$ becomes

$$m(s) = \frac{m_0 ds_o}{ds} = \frac{m_0}{1 + T/EA} \tag{22}$$

Substitution of (22) into (1) leads to

$$G = m(s)V(s) = \frac{m_0}{1 + T/EA}V(s) \tag{23}$$

So, the constitutive law is

$$T = EA(V/V_{ref} - 1), \quad V_{ref} = G/m_0 \tag{24}$$

as used in [7]. Note that V_{ref} is not known a priori because only one of m_0 and G is specified; V_{ref} is determined in the solution. Finally, the system must satisfy the compatibility condition

$$L_T^{(0)} + L_S^{(0)} + L_{\beta_1}^{(0)} + L_{\beta_2}^{(0)} + L_{\alpha_1}^{(0)} + L_{\alpha_2}^{(0)} = L^{(0)} \tag{25}$$

where $L_T^{(0)}$ and $L_S^{(0)}$ are the unstretched lengths for the tight and slack spans, $L_{\alpha_1}^{(0)}$ and $L_{\alpha_2}^{(0)}$ are the unstretched lengths of the adhesion zones on the driver and driven pulleys, $L_{\beta_1}^{(0)}$ and $L_{\beta_2}^{(0)}$ are the unstretched lengths of the slip zones on the driver and driven pulleys, and $L^{(0)}$ is the unstretched length of the total belt when it

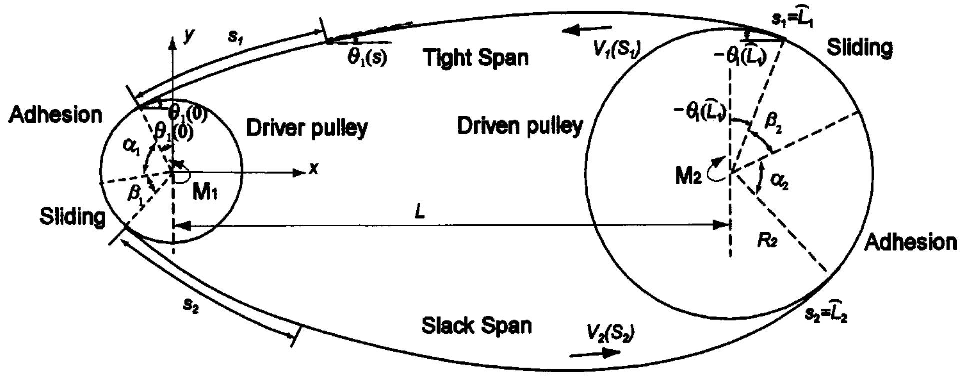

Fig. 3 Two-pulley belt drive with inclusion of belt bending stiffness

is removed from the pulleys. $L^{(0)}$ can be calculated from the reference state. Physically, the compatibility equation (25) means that the unstretched length computed from the steady state should equal that computed from the reference state, guaranteeing that the same belt is considered [8].

The compatibility equation (25) is that used in [8] and prior belt drive analysis [13]. In [7], the compatibility equation is mistakenly omitted and this makes the derivation inconsistent. Equation (17) in [7] leads to $T_t - T_s = M/r$. This contradicts their equation (3), which requires that, after integration, $(T_t - GV_t) - (T_s - GV_s) = M/r$.

4.1 Regular Moment Transmission Problem. In this problem, the moment M_2 exerted on the driven pulley is a specified value less than the maximum transmissible moment.

To find the driving moment and distributions of tension, speed, and friction along the belt loop, an iteration method is used. The iteration starts from the tight span, which has the following governing ODE

$$(T_1 - GV_1)' + EI\kappa_1\kappa_1' = 0 \tag{26}$$

$$(T_1 - GV_1)\kappa_1 - EI\kappa_1'' = 0 \tag{27}$$

where the subscript 1 represents the tight span (subscript 2 represents the slack span). First, the tension at the left boundary (contact point between the driver pulley and the tight span) is assigned an initial guess

$$T_1(0) = T_{1\_0} \tag{28}$$

At the same boundary of the tight span $(s_1 = 0)$, the speed of the belt is the same as the driver pulley

$$V_1(0) = \omega_1 R_1 \tag{29}$$

Substitution of (28) and (29) into the constitutive law (24) leads to

$$V_{ref} = \frac{\omega_1 R_1}{1 + (T_{1\_0}/EA)} \tag{30}$$

Thus the relationship between the tension T_1 and speed V_1 can be completely determined from (24) (for the assumed T_{1_0}), and $T_1 - GV_1$ can be treated as one unknown field variable. Equations (28) and (29) give the boundary condition for this unknown field variable. The other two boundary conditions for the governing equations (26) and (27) are

$$\kappa_1(0) = -1/R_1, \quad \kappa_1(\hat{L}_1) = -1/R_2 \tag{31}$$

where $\hat{L}_1$ is the total arclength of the tight span, which is to be determined. This single span problem with unknown boundary $\hat{L}_1$ is of the form discussed previously. By adopting the ODE conversion techniques presented earlier, the solution for the tight span can be found.

For the belt in the belt-pulley contact zones, the governing equation (10) is the same as for the string models. All relations for these segments of the belt derived from prior string models [7,8] still hold. For the adhesion zones, the tension and speed are constant. For the sliding zone on the driver pulley (see Fig. 3), (10) and $f = \mu_1 n$ lead to

$$\beta_1 = \frac{1}{\mu_1} \ln \frac{T_1(0) - GV_1(0)}{T_2(0) - GV_2(0)} \tag{32}$$

where $T_2(0)$ and $V_2(0)$ are the as yet unknown boundary values of tension and speed for the slack span. For steady operation, the balance of angular momentum on the driver and driven pulleys leads to

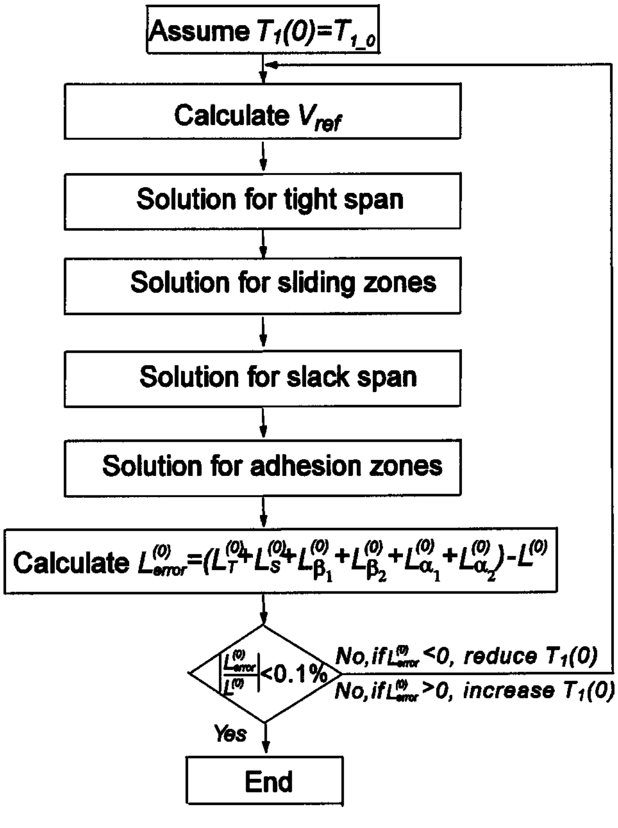

Fig. 4 Flowchart of the iteration for the regular transmission problem

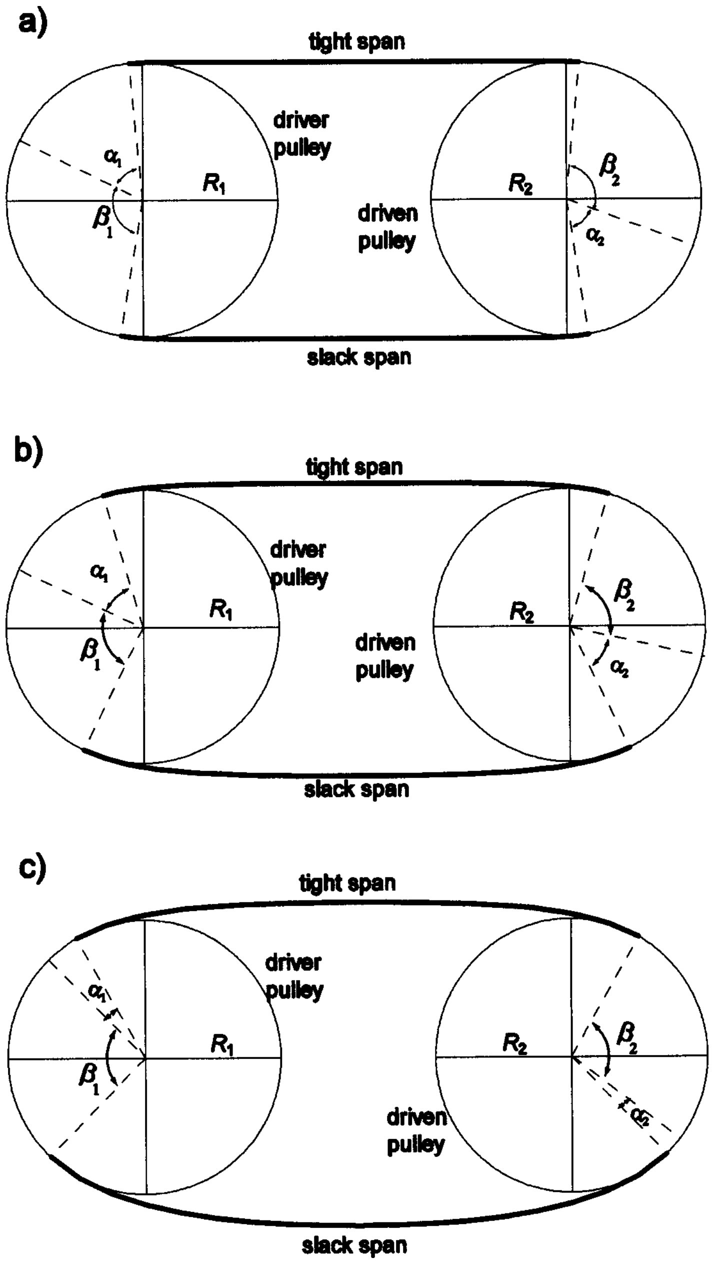

Fig. 5 Steady solutions for the system properties specified in Table 1. (*a*) *EI*=0.0015, (*b*) *EI*=0.015, and (*c*) *EI*=0.05 N·m².

$$M_1/R_1=\int_0^{\beta_1 R_1} f_1\,ds=[T_1(0)-GV_1(0)]-[T_2(0)-GV_2(0)] \tag{33}$$

$$M_2/R_2=[T_1(\hat{L}_1)-GV_1(\hat{L}_1)]-[T_2(\hat{L}_2)-GV_2(\hat{L}_2)] \tag{34}$$

The governing equations for the slack span are

$$(T_2-GV_2)'+EI\kappa_2\kappa_2'=0, \quad (T_2-GV_2)\kappa_2-EI\kappa_2''=0 \tag{35}$$

Two boundary conditions for (35) are

$$\kappa_2(0)=1/R_1, \quad \kappa_2(\hat{L}_2)=1/R_2 \tag{36}$$

where $\hat{L}_2$ is the total arclength of the slack span (to be determined).

Integration of (26) and the first of (35) yields

$$\Big[(T_2(s_2)-GV_2(s_2)]-\Big[(T_1(s_1)-GV_1(s_1)] \\ =-\frac{1}{2}EI\kappa_2^2(s_2)+\frac{1}{2}EI\kappa_1^2(s_1)+D \tag{37}$$

where D is a constant. Taking the two choices $s_1=0$, $s_2=0$ and then $s_1=\hat{L}_1$, $s_2=\hat{L}_2$ in (37), subtracting the two resulting equations, and using (31) and (36) gives

Table 1 Physical properties of the belt drive with two identical pulleys

$R_1=R_2=0.05$ m	$L=\pi R_1=0.1571$ m	$EA=25$ kN	$\mu_1=\mu_2=0.6$
$T_{ini}=50$ N (midspan)	$\omega_1=500$ rad/s	$M_2=2$ N·m	$G=0.5$ kg/s

Table 2 Numerical results for the belt drive specified in Table 1

EI ($\mathrm{N\cdot m^2}$)	$\beta_1=\beta_2$ (deg)	$\alpha_1=\alpha_2$ (deg)	$\theta_1(0)$ $[-\theta_1(\hat{L}_1)]$ (deg)	$-\theta_2(0)$ $[\theta_2(\hat{L}_2)]$ (deg)	$\hat{L}_1/L$	$\hat{L}_2/L$
0	109.4	70.60	0	0	1	1
0.0015	100.2	64.67	5.645	9.503	1.063	1.106
0.0150	87.18	50.05	16.86	25.92	1.189	1.293
0.0500	90.26	15.91	29.82	44.00	1.339	1.511

$$\begin{aligned}&[T_2(\hat{L}_2)-GV_2(\hat{L}_2)]-[T_1(\hat{L}_1)-GV_1(\hat{L}_1)]\\&\quad=[T_2(0)-GV_2(0)]-[(T_1(0)-GV_1(0))]\end{aligned} \tag{38}$$

Comparison of (33), (34), and (38) yields $M_1=(R_1/R_2)M_2$ for steady operation.

Using (28)–(30), (33), $M_1=(R_1/R_2)M_2$ and the constitutive law (24) gives two equations for $T_2(0)$ and $V_2(0)$, fixing the field variable T_2-GV_2 at $s_2=0$. This gives a third boundary condition, in addition to (36), for the governing equations (35) of the slack span. Again, this boundary value problem has the form discussed previously for the single span case and can be solved by a general purpose BVP solver. The sliding angle β_2 on the driven pulley is calculated from (10) and $f=\mu_2 n$ as $\beta_2=(1/\mu_2)\ln\{[T_1(\hat{L}_1)-GV_1(\hat{L}_1)]/[T_2(\hat{L}_2)-GV_2(\hat{L}_2)]\}$.

For the adhesion zones of the belt on pulleys, the adhesion angles are

$$\alpha_1=\pi-\beta_1-\theta_1(0)+\theta_2(0),\qquad \alpha_2=\pi-\beta_2+\theta_1(\hat{L}_1)-\theta_2(\hat{L}_2) \tag{39}$$

Thus, the steady motion has been calculated for the assumed tension T_{1_0}. This includes the torque on the driver pulley M_1, the span lengths $(\hat{L}_1,\hat{L}_2)$, the deflected belt shapes in the spans $(x_1(s_1),y_1(s_1),x_2(s_2),y_2(s_2))$, the tension and speed distributions along the belt $(T_1(s_1),V_1(s_1),T_2(s_2),V_2(s_2))$, the belt-pulley contact points $(\theta_1(0),\theta_1(\hat{L}_1),\theta_2(0),\theta_2(\hat{L}_2))$, and the adhesion and slip zones $(\alpha_1,\alpha_2,\beta_1,\beta_2)$.

The calculated result for the assumed tension T_{1_0} is a possible steady state that can physically exist. But whether or not it is the same belt specified in the reference state, which has the unstretched length $L^{(0)}$, depends on if the system satisfies the compatibility equation (25). To check the compatibility condition, one must find the unstretched length of the total belt for the assumed $T_1(0)=T_{1\_0}$.

For the adhesion and slip zones, the unstretched lengths are

$$L_{\alpha_1}^{(0)}=\frac{\alpha_1 R_1}{1+T_1(0)/EA},\qquad L_{\alpha_2}^{(0)}=\frac{\alpha_2 R_2}{1+T_2(\hat{L}_2)/EA} \tag{40}$$

$$\begin{aligned}L_{\beta_1}^{(0)}&=\int_0^{\beta_1 R_1}\frac{1}{1+T(s^*)/EA}\,ds^*\\&=\left(1-\frac{GV_{ref}}{EA}\right)\frac{R_1}{\mu_1}\\&\quad\times\ln\frac{1+EA/[T_1(0)-GV_1(0)-M_1/R_1]}{1+EA/[T_1(0)-GV_1(0)]}\end{aligned} \tag{41}$$

$$L_{\beta_2}^{(0)}=\left(1-\frac{GV_{ref}}{EA}\right)\frac{R_2}{\mu_2}\ln\frac{1+EA/[T_1(\hat{L}_1)-GV_1(\hat{L}_1)-M_2/R_2]}{1+EA/[T_1(\hat{L}_1)-GV_1(\hat{L}_1)]} \tag{42}$$

where s^* is the local arclength for the slip zone of the belt. The unstretched length of the tight span is

$$L_T^{(0)}=\int_0^{\hat{L}_1}\frac{1}{1+T_1(s_1)/EA}\,ds_1 \tag{43}$$

To calculate this term, direct integration method could be used because the distribution of the tension $T_1(s_1)$ and the total arclength of the tight span $\hat{L}_1$ have been calculated. Instead we use an alternative method that integrates the integral term into the standard BVP form for the tight span with little additional effort. We define $I_T(s)=\int_0^s\{1/[1+T_1(s_1)/EA]\}ds_1$ and add an additional ODE and boundary condition to the corresponding BVP standard form for the tight span

$$\frac{dI_T(s)}{ds}=\frac{1}{1+T_1(s)/EA},\qquad 0<s<\hat{L}_1\ \text{ with }\ I_T(0)=0 \tag{44}$$

Then $I_T(\hat{L}_1)$ is equivalent to the desired integral term $L_T^{(0)}$ and is a natural product of the BVP solution. Although the added ODE and boundary condition (44) are written in the dimensional form over the range $(0,\hat{L}_1)$, (14) transforms them into the necessary form on (0,1). Similar operations can be performed on the BVP for the slack span to obtain the unstretched belt length $L_S^{(0)}$.

The error between the unstretched length for the assumed T_{1_0} and the actual unstretched length $L^{(0)}$ (discussed below) is

$$L_{error}^{(0)}=(L_T^{(0)}+L_S^{(0)}+L_{\beta_1}^{(0)}+L_{\beta_2}^{(0)}+L_{\alpha_1}^{(0)}+L_{\alpha_2}^{(0)})-L^{(0)} \tag{45}$$

Physically, if $L_{error}^{(0)}<0$, the assumed T_{1_0} is larger than the true $T_1(0)$ and should be reduced in the next iteration step; $L_{error}^{(0)}>0$ implies T_{1_0} is smaller than the true $T_1(0)$. $L_{error}^{(0)}$ is a monotonically decreasing function of the assumed tension T_{1_0}. This property allows use of the bisection method in the iteration loop. This gives rapid convergence of the iteration to the true solution.

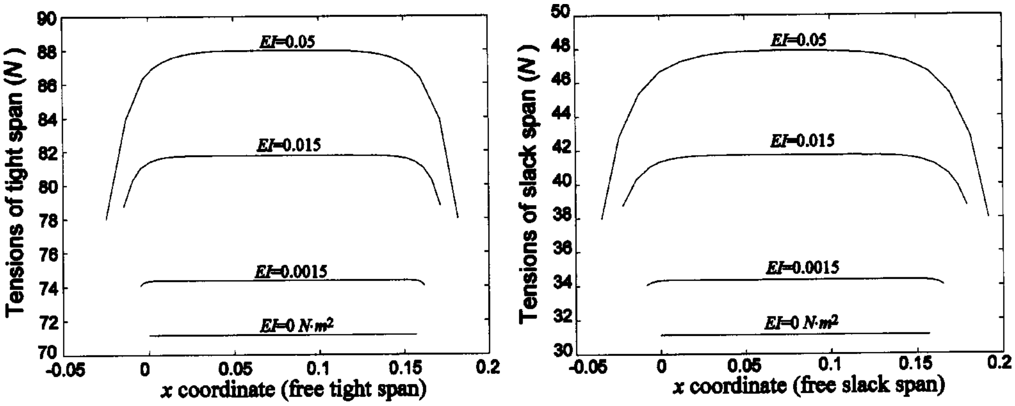

Fig. 6 Variations of tension in the tight and slack spans for the belt-pulley drive in Table 1

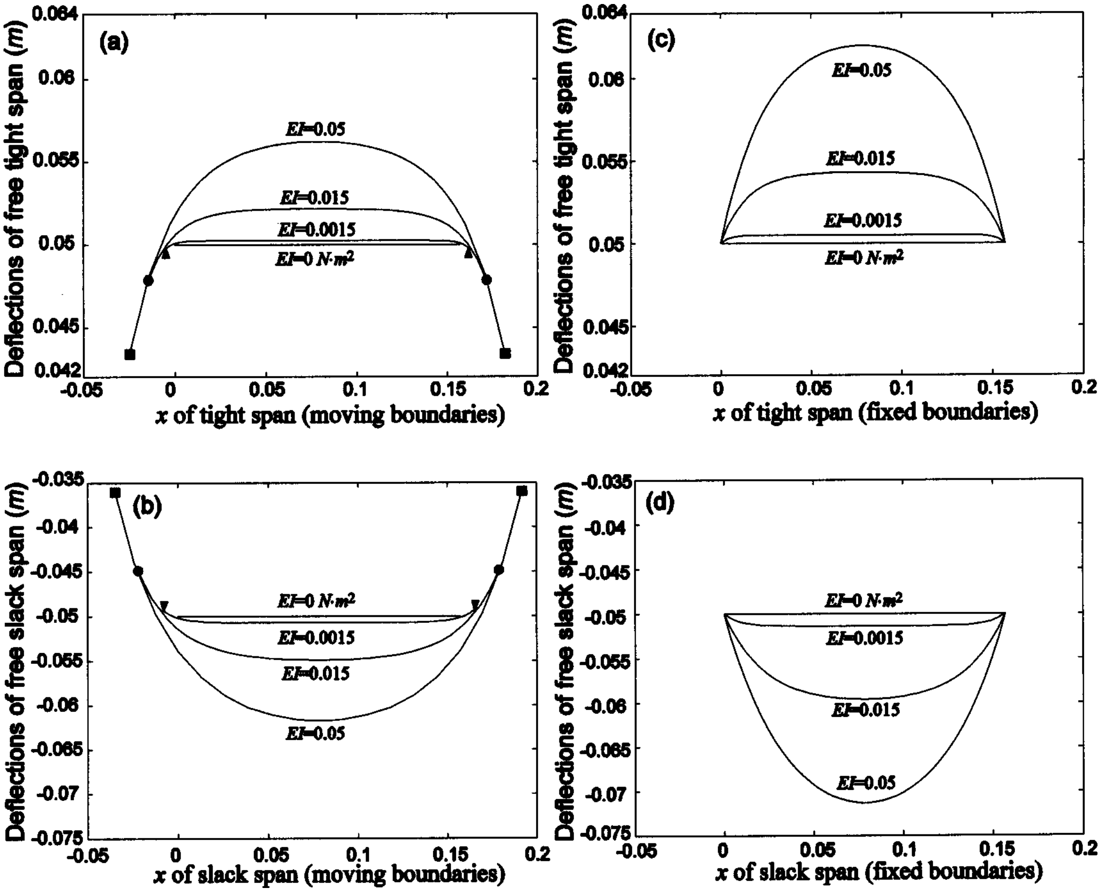

Fig. 7 Deflections of the spans for two different belt-pulley models. (*a*) and (*b*) correspond to the current model (symbols denote span endpoints); (*c*) and (*d*) correspond to the fixed boundary model in [15]. The system is specified in Table 1.

In this study, the results converge such that $|L_{error}^{(0)}/L^{(0)}|<0.1\%$. The above iteration procedure is summarized in the flowchart in Fig. 4.

The unstretched length of the total belt $L^{(0)}$ must be calculated from the reference state when the analysis follows those in [7,8] and the reference state tension T_{ini} in a chosen span is specified (instead of $L^{(0)}$). Because the span tensions are nonuniform in the reference state when bending stiffness is modeled, this condition is modified such that T_{ini} is given at an arbitrary point in the belt loop. A similar iteration method as already presented can be applied to obtain $L^{(0)}$ with the only difference that during the trial-and-error process, instead of checking the compatibility condition (25), one checks if the calculated tension at the appropriate point equals the specified value T_{ini}. In practical applications, the more appropriate problem formulation provides the unstretched belt length $L^{(0)}$ instead of T_{ini}. In that case, the iteration to determine $L^{(0)}$ is not necessary.

4.2 Maximum Transmissible Moment Problem. The above iteration method is valid for the case of specified pulley moments. How is this extended to calculate the maximum moment that can be transmitted? One obvious solution is to first specify a small moment M_2 exerted on the driven pulley and calculate the steady motion by using the above iteration method, then increase the specified moment M_2 towards the unknown maximum transmissible moment $M_{2\_\max}$ until one of the adhesion angles reaches zero. This method is feasible, but it involves two iteration loops. In the following analysis, a modification of the above iteration method is introduced that only involves one iteration loop.

As in the specified moment case, the tension $T_1(0)$ changes in each iteration loop. The first step is also the same, namely calculating the steady mechanics for the tight span using the single span BVP building block. After this step, instead of addressing the belt in the contact zones and the belt in the slack span successively, we address both of them simultaneously to find $M_{2\_\max}$ (for the assumed T_{1_0}) as follows.

The unknown $M_{2\_\max}$ is defined as a field variable $M_{2\_\max}=M_{2\_\max}(s_2)$ governed by

$$\frac{dM_{2\_\max}(s_2)}{ds_2}=0 \tag{46}$$

forcing $M_{2\_\max}$ to be a constant. This ODE is added to the BVP (with unknown boundaries) for the slack span. Correspondingly, one additional boundary condition is needed to make the ODE system complete. Because $M_{2\_\max}$ is constant along the domain, the boundary value of $M_{2\_\max}(0)$ at $s_2=0$ equals the maximum transmissible moment. Substitution of (33) and $M_1=(R_1/R_2)M_{2\_\max}$ into (32) yields

$$\beta_1=-\frac{1}{\mu_1}\ln\left[1-\frac{M_{2\_\max}(s_2=0)/R_2}{T_1(0)-GV_1(0)}\right] \tag{47}$$

Similarly, for the belt on the driven pulley,

$$\beta_2=-\frac{1}{\mu_2}\ln\left[1-\frac{M_{2\_\max}(s_2=0)/R_2}{T_1(\hat{L}_1)-GV_1(\hat{L}_1)}\right] \tag{48}$$

Table 3 Physical properties of the belt drive with two different pulleys

$R_1=0.01$ m	$R_2=0.05$ m	$EA=40$ kN	$\mu_1=\mu_2=1$
$T_{ini}=800$ N (midspan)	$m_0=\rho_0^* A=0.0056$ kg/s	$L=0.1$ m	$c_{cr}=374$ m/s

Without loss of generality, we assume that full slip appears first on the driver pulley ($\alpha_1=0$). Substitution of (47) into the first of (39) yields

$$\pi+\frac{1}{\mu_1}\ln\left[1-\frac{M_{2\_\max}(s_2=0)/R_2}{T_1(0)-GV_1(0)}\right]-\theta_1(0)+\theta_2(0)=0 \quad (49)$$

where $\theta_1(0)$ has been calculated in the last step when solving the BVP for the tight span. Equation (49) serves as the required additional boundary condition for the ODE (46). The rest of the iteration process is the same as discussed previously. $M_{2\_\max}$ emerges naturally as part of the solution along with all other quantities giving the mechanics for $M_2=M_{2\_\max}$.

Since most general-purpose BVP solvers can not directly handle coupled BVP/algebraic equations, this conversion technique is useful in general for addressing such coupled systems.

5 Results and Discussion

Two example two-pulley belt drives are examined. The first is for the regular moment transmission problem. Except for the bending stiffness, all specified data of this drive (Fig. 5) are the same as for the string model example in [7]. The second example is for the maximum transmissible moment problem. Except for the bending stiffness, all specified data of this drive (Fig. 8) are the same as in [8]. The uniform reference state span tensions specified in [7] and [8] are taken to be midspan tensions in the present analysis where span tension is nonuniform.

Three different belt bending stiffness values are considered in the examples ($EI=0.0015, 0.015, 0.05\ \mathrm{N\cdot m^2}$). All are within practical estimates for poly-ribbed belts. For V-belts, the bending stiffness can be much larger.

5.1 Example of Regular Moment Transmission Problem. The data for this system are specified in Table 1. The calculated results for slip/adhesion zones, belt-pulley departure points $\theta_{1,2}(0)$, and span lengths are presented in Table 2 for three values of bending stiffness. The deflected belt shapes are shown in Fig. 5, where the strokes of the belt in the spans are thickened. Bending stiffness decreases the wrap angles. For appreciable bending stiffness, the adhesion angles are reduced significantly. Notice that the belt transverse deflections are significantly increased for large bending stiffness. Figure 6 shows the tension variations in the spans. When $EI=0$, this converges to the string model where the tension and speed are uniform throughout the spans [7,8]. Large percentage increases in belt tension result with increased bending stiffness, and this impacts belt life. Comparing line lengths in Fig. 6 shows the increased span lengths for increased bending stiffness. Note the variations of speed in the spans, which are easily calculated from (24), are low (<0.04%) because EA is very large. In the adhesion zones, the tension and speed are uniform; in the sliding zones, the tension and speed are exponentially distributed, similar to the string models.

Figures 7*a*,*b* give the span deflections. The boundaries of the spans change as the bending stiffness changes. In the literature, an alternative theory concerning bending stiffness in belt-pulley systems has been used [9,14–16]. These works assume that the boundaries of the spans are fixed at the belt-pulley contact points of the string model, the speed is uniform throughout the system, the tensions are uniform throughout the spans, and at the boundaries the beam displacement satisfies $EIw_{,xx}|_{BC}=\pm EI/r$, where r is the radius of the pulley. Figures 7*c*,*d* give the deflections of the spans derived from the fixed boundary analysis of Kong and Parker [15]. Comparison of results from these two theories shows that as the bending stiffness increases, the differences are pronounced.

5.2 Example of Maximum Transmissible Moment Problem. Following [8], the data are specified in Table 3. c_{cr} is the critical speed for the string model, that is, the speed where the belt expands such that the maximum transmissible moment vanishes. Note that in the string model of [8], instead of specifying ω_1 and G, m_0 and c (or $C=c/c_{cr}$, $0\leqslant C\leqslant 1$) are specified. This does not change the definition of the problem because $c=V_{ref}$ and $m_0=G/V_{ref}$ [see Eq. (24) and the Appendix for the reasoning]. For

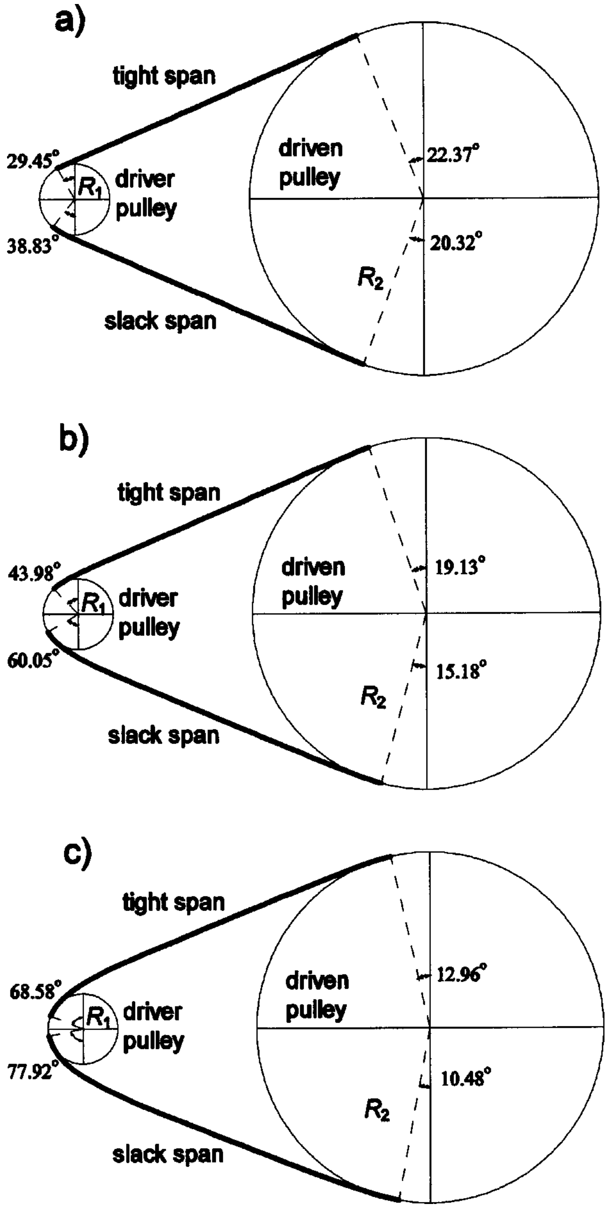

Fig. 8 Steady solutions for the system properties specified in Table 3. Full slip occurs on the driver pulley. (*a*) $EI=0.0015$, (*b*) $EI=0.015$, and (*c*) $EI=0.05\ \mathrm{N\cdot m^2}$.

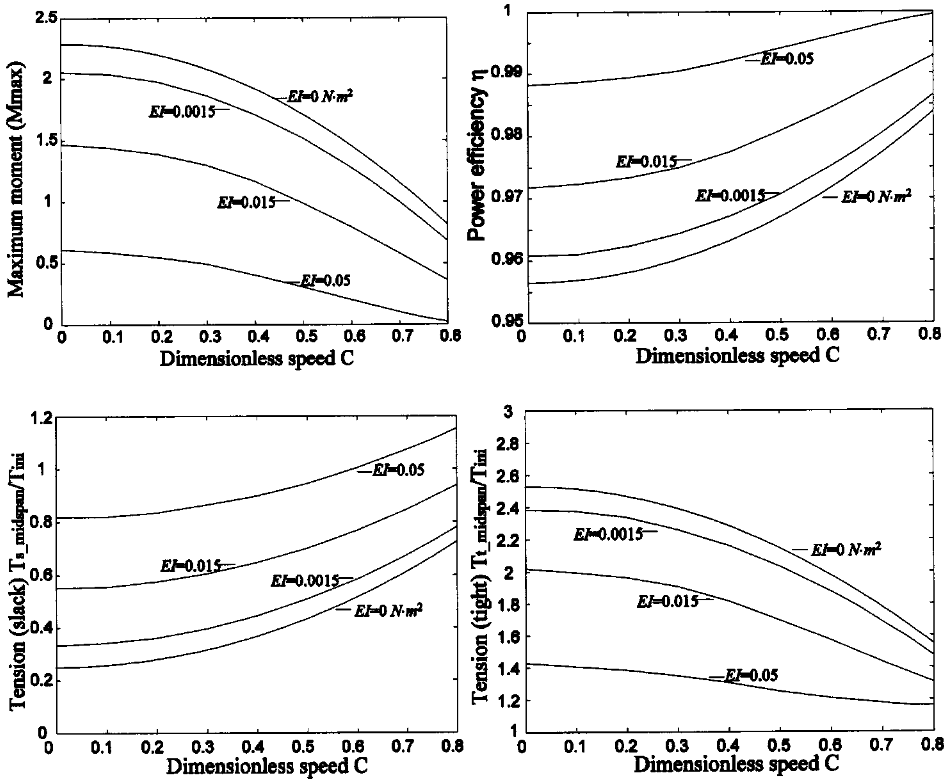

Fig. 9 Comparison of maximum transmitted moment $M_{\max}=M_{2\_\max}/T_{ini}R_2$, power efficiency η, $T_{t\_midspan}/T_{ini}$, and $T_{s\_midspan}/T_{ini}$ between the string and beam models for the belt drive in Table 3

any assumed T_{1_0}, c and m_0 can be obtained from G and ω_1, or vice versa. For example, suppose c and m_0 are specified. Then $G=m_0c$ and, using (30),

$$\omega_1=\frac{V_{ref}}{R_1}\left(1+\frac{T_{1\_0}}{EA}\right)=\frac{c}{R_1}\left(1+\frac{T_{1\_0}}{EA}\right)$$

Figure 8 depicts the steady states of the belt drive transmitting maximum moment at $c=c_{cr}/2$; full slip occurs on the driver pulley, $\alpha_1=0$. When $EI=0$, the results are for the string model. Especially for pulleys of small radius, the wrap angle is reduced significantly with increasing bending stiffness as shown by the belt-pulley departure angles listed on the figure. Because generally it is the small pulley that first reaches the full slip state, and this determines the maximum transmissible moment, inclusion of the bending stiffness can greatly reduce the maximum transmissible moment, as shown in Fig. 9.

In Fig. 9, four nondimensional variables are plotted with respect to $C=c/c_{cr}$ at different bending stiffness values: $M_{\max}=M_{2\_\max}/(T_{ini}R_2)$, $T_{t\_midspan}/T_{ini}$, $T_{s\_midspan}/T_{ini}$, and η, where $T_{t\_midspan}$ and $T_{s\_midspan}$ are tensions at the midpoints of the tight and slack spans, respectively, and the power efficiency η is defined as the ratio between the power of the driven pulley and the driver pulley

$$\eta=\frac{M_2\omega_2}{M_1\omega_1}=\frac{V_2(\hat{L}_2)}{V_1(0)}=\frac{1+(T_2(\hat{L}_2)/EA)}{1+(T_1(0)/EA)} \tag{50}$$

Figure 9 shows that increasing the bending stiffness significantly decreases the maximum transmissible moment and increases the power efficiency η. The significant overestimation of the maximum transmissible moment using the string model can lead to poor performance and unanticipated full belt slip, especially for belts with appreciable bending stiffness. Bending stiffness reduces the effects of belt speed C on the steady motion; variations of the nondimensional variables over the same range of C are decreased for increasing bending stiffness.

6 Conclusions

Belt bending stiffness is included in the steady state analysis of belt-pulley systems where belt inertia is also modeled. An iterative solution is presented to determine the deflections of the belt, belt-pulley contact points, span lengths, and the distributions of speed, tension, and friction along the belt. Inclusion of bending stiffness leads to initially unknown belt-pulley contact points, yielding a governing boundary value problem (BVP) with undetermined boundaries. This requires a transformation of the governing equations to a standard ODE form with fixed boundaries. This form is readily accepted by general-purpose BVP solver codes. The main conclusions include:

1. Inclusion of bending stiffness leads to nonuniform speed and tension in the spans and reduces the belt wrap angles on pulleys, especially for small radii. Span tensions, which directly impact belt life, increase markedly with bending stiffness.
2. Bending stiffness decreases the wrap angles, causes earlier full slip of the belt on the pulleys, increases the power efficiency η, and decreases the maximum transmissible moment. Some of these effects are pronounced for appreciable bending stiffness and may cause poor performance in systems designed based on string model analysis.
3. The effects of belt speed on the steady motion are reduced as the bending stiffness increases.

Acknowledgments

The authors thank Mark IV Automotive/Dayco Corporation and the National Science Foundation for support of this research.

Appendix: Relationship With Results of [8]

Because in [8], Eq. $(16)_4$ is $d_i = 1 + T_i/EA$ and Eq. $(23)_2$ is $\omega_i = c d_i / R_i$,

$$T_i = EA(\omega_i R_i / c - 1) \tag{A1}$$

Comparison of (24), (29), and (*A*1) leads to

$$c = V_{ref} \tag{A2}$$

Equations (24) and (*A*2) yield $G = m_0 c$.

References

[1] Fawcett, J. N., 1981, ‘‘Chain and Belt Drives—a Review,’’ Shock Vib. Dig., **13**(5), pp. 5–12.

[2] Firbank, T. C., 1970, ‘‘Mechanics of Belt Drives,’’ Int. J. Mech. Sci., **12**, pp. 1053–1063.

[3] Gerbert, G. G., 1991, ‘‘On Flat Belt Slip,’’ Veh. Tribol. Ser., **16**, pp. 333–339.

[4] Alciatore, D. G., and Traver, A. E., 1995, ‘‘Multipulley Belt Drive Mechanics: Creep Theory vs Shear Theory,’’ ASME J. Mech. Des., **117**, pp. 506–511.

[5] Johnson, K. L., 1985, *Contact Mechanics*, Cambridge University Press, Cambridge.

[6] Gerbert, G., 1999, *Traction Belt Mechanics*, Chalmers University of Technology, Sweden.

[7] Bechtel, S. E., Vohra, S., Jacob, K. I., and Carlson, C. D., 2000, ‘‘The Stretching and Slipping of Belts and Fibers on Pulleys,’’ ASME J. Appl. Mech., **67**, pp. 197–206.

[8] Rubin, M. B., 2000, ‘‘An Exact Solution for Steady Motion of an Extensible Belt in Multipulley Belt Drive Systems,’’ ASME J. Mech. Des., **122**, pp. 311–316.

[9] Wang, K. W., and Mote, C. D. Jr., 1986, ‘‘Vibration Coupling Analysis of Band/Wheel Mechanical Systems,’’ J. Sound Vib., **109**, pp. 237–258.

[10] Hwang, S. J., and Perkins, N. C., 1994, ‘‘High Speed Stability of Coupled Band/Wheel Systems: Theory and Experiment,’’ J. Sound Vib., **169**(4), pp. 459–483.

[11] Ascher, U., and Russell, R., 1981, ‘‘Reformulation of Boundary Value Problems Into ‘Standard’ Form,’’ SIAM Rev., **23**, pp. 238–254.

[12] Leamy, M. J., 2005, ‘‘On a New Perturbation Method for the Analysis of Unsteady Belt-Drive Operation,’’ ASME J. Appl. Mech., in press.

[13] Beikmann, R. S., Perkins, N. C., and Ulsoy, A. G., 1996, ‘‘Design and Analysis of Automotive Serpentine Belt Drive Systems for Steady State Performance,’’ ASME J. Mech. Des., **119**, pp. 162–168.

[14] Mote, C. D., Jr., and Wu, W. Z., 1985, ‘‘Vibration Coupling in Continuous Belt and Band Systems,’’ J. Sound Vib., **102**, pp. 1–9.

[15] Kong, L., and Parker, R. G., 2003, ‘‘Equilibrium and Belt-Pulley Vibration Coupling in Serpentine Belt Drives,’’ ASME J. Appl. Mech., **70**(5), pp. 739–750.

[16] Kong, L., and Parker, R. G., ‘‘Coupled Belt-Pulley Vibration in Serpentine Drives With Belt Bending Stiffness,’’ ASME J. Appl. Mech., **71**, pp. 109–119.

Lin-Quan Yao
School of Mathematics Science,
Suzhou University,
Suzhou 215006, P. R. China;
and Singapore-MIT Alliance,
Advanced Materials for Micro- and
Nano-Systems Program,
4 Engineering Drive 3,
Singapore 117576, Singapore

Li Lu[1]
Singapore-MIT Alliance,
Advanced Materials for Micro- and
Nano-Systems Program,
4 Engineering Drive 3,
Singapore 117576, Singapore;
and Department of Mechanical Engineering,
National University of Singapore,
9 Engineering Drive 1,
Singapore 117576, Singapore

An Electric Node Concept for Solid-Shell Elements for Laminate Composite Piezoelectric Structures

The eight-node solid-shell finite element models have been developed for the analysis of laminated composite plate/shell structures embedded with piezoelectric actuators and sensors. To resolve the locking problems of the solid-shell elements in laminated materials and improve accuracy, the assumed natural strain method and hybrid stress method are employed. Introduction of the concept of the electric nodes can effectively eliminate the burden of constraining the equality of the electric potential for the nodes lying on the same electrode. Furthermore, the nonlinear electric potential distribution in piezoelectric layer is described by introducing internal electric potential. The developed finite element models, especially electric potential node model, are simpler over other models but can still obtain same accuracy as exact solution described. Several examples are studied and compared with exact solution and other predicted results to illustrate the accuracy of the present model, and efficacy and effect caused by nonlinear electric potential distribution on frequency and electric fields in smart structure modeling. [DOI: 10.1115/1.1827249]

1 Introduction

Piezoelectric materials have attracted significant attention due to their potential application in sensors and actuators because piezoelectric materials are coupled with mechanical and electrical properties. Recent advances in design and manufacturing technologies have greatly enhanced the use of advanced fiber-reinforced composite materials in aircraft and aerospace structural applications. As a consequence, the integration of composite materials and adaptive structures with the smart system could potentially result in significant improvement in the performance and reliability of aircrafts, space structures, satellites, and other advanced structures. Such materials will combine the superior mechanical properties of composite materials as well as inherent capability to sense and adapt their static and dynamic responses. However, this effort requires the development of admissible mechanics entailing capabilities to model the unified electromechanical response of sensory/active structures including the coupling between sensors and actuators. For smart structures, experimental models, and prototypes are limited to relatively simple structures, such as beams and plates. Thus, in practical applications, finite element techniques provide the versatilities in modeling, simulation, and analysis of engineering designs in modern smart/intelligent material and structures.

There have been many theories and models proposed for the analysis of laminated composite plates containing active and passive piezoelectric layers [1–19]. Owing to the geometric complexity of surfaces bonded with sensors and actuators which are most conveniently be modeled by continuum elements (no rotational d.o.f.), many of the developed finite element models are continuum in nature [7–11]. However, strict considerations of locking deficiencies are often lacking in the course of developing these finite element models. It is unfortunate that solid elements, when applied to plate and shell analyses, can be plagued by the largest number of finite element deficiencies which include shear, membrane, trapezoidal, thickness, and dilatational lockings. Hence, solid-to-plate/shell transition elements may have to be adopted whereas excessive aspect ratios of the solid and transition elements must be avoided. Alternatively, transition elements can be avoided by introducing numerical constraints to tie up the rotations in plate/shell elements with the translations in the solid elements. This practice is tedious and also adversely affects the condition of the system equation. Moreover, for piezoelectric element, most of researchers use simplified approximations attempting to replicate the electric field generated by a piezoelectric layer under an external electric field or applied load. Very often the electric potential distribution is assumed to vary linearly in through-thickness of piezoelectric layer. An exact solution for piezoelectric laminate plates has shown that the distribution of electric field given by Heyliger and Saravanos [12] is often poorly modeled using simplified theories. According to the results of this exact solution, the electric field distribution in piezoelectric layer is not constant. For the finite element model reported by Saravanos et al. [3], each layer is modeled using independent approximations for the in-plane displacement components and the electrostatic potential in a unified representation, as mandated by the linear theory of piezoelectricity. The predicted results reported by Saravanos et al. [3] are well closer with exact solution, indicating that electric field distribution through-thickness in piezoelectric layer is not constant.

In this paper, an eight-node hybrid stress and assumed strain (ANS) solid-shell element for laminate composite structures is used. Since piezoelectric patches are always coated with electrons, which constitute equal-potential surfaces, the concept of electric nodes is introduced. The introduction of the electric nodes can effectively eliminate the burden of constraining the equality of the electric potential for the nodes lying. To model the distribution of electric field through thickness in piezoelectric layer, the electric potential distribution is assumed to vary second-order or to be linear instead of constant through thickness in the piezoelectric layer by introducing internal electric potential of piezoelectric element.

---

[1] To whom correspondence should be addressed. e-mail: mpeluli@nus.edu.sg

Contributed by the Applied Mechanics Division of THE AMERICAN SOCIETY OF MECHANICAL ENGINEERS for publication in the ASME JOURNAL OF APPLIED MECHANICS. Manuscript received by the Applied Mechanics Division, July 1, 2003; final revision, March 15, 2004. Associate Editor: B. M. Moran. Discussion on the paper should be addressed to the Editor, Prof. Robert M. McMeeking, Journal of Applied Mechanics, Department of Mechanical and Environmental Engineering, University of California, Santa Barbara, Santa Barbara, CA 93106-5070, and will be accepted until four months after final publication in the paper itself in the ASME JOURNAL OF APPLIED MECHANICS.

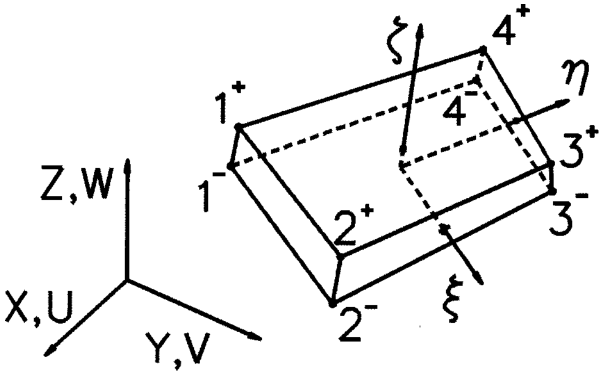

Fig. 1 An eight-node thin hexahedral solid element

2 Geometric and Kinematic Interpolation

Figure 1 shows an eight-node hexahedral element in which ξ, η, and ζ are the natural coordinates. Let ζ be aligned with the transverse direction of the shell; the geometric and displacement interpolation can be expressed as:

$$\begin{aligned}\mathbf{X}(\xi,\eta,\zeta)&=\sum_{i=1}^{4} N_i(\xi,\eta)\left(\frac{1+\zeta}{2}\mathbf{X}_i^+ + \frac{1-\zeta}{2}\mathbf{X}_i^-\right)\\ &=(\mathbf{a}_0+\mathbf{a}_1\xi+\mathbf{a}_2\eta\xi+\mathbf{a}_3\eta)+\zeta(\mathbf{b}_0+\mathbf{b}_1\xi+\mathbf{b}_2\eta\xi+\mathbf{b}_3\eta)\\ &=\mathbf{X}_0+\zeta\mathbf{X}_n, \end{aligned} \tag{1}$$

$$\begin{aligned}\mathbf{U}(\xi,\eta,\zeta)&=\sum_{i=1}^{4} N_i(\xi,\eta)\left(\frac{1+\zeta}{2}\mathbf{U}_i^+ + \frac{1-\zeta}{2}\mathbf{U}_i^-\right)\\ &=\mathbf{N}(\xi,\eta)\mathbf{q}_0+\zeta\mathbf{N}(\xi,\eta)\mathbf{q}_n=\mathbf{U}_0+\zeta\mathbf{U}_n, \end{aligned} \tag{2}$$

where $N_1=(1-\xi)(1-\eta)/4$, $N_2=(1+\xi)(1-\eta)/4$, $N_3=(1+\xi)\times(1+\eta)/4$, $N_4=(1-\xi)(1+\eta)/4$, $\mathbf{X}$, $\mathbf{X}_i^+$, and $\mathbf{X}_i^-$ are the coordinate vectors, its value at the i^+ and i^- nodes of the element, respectively. U, $\mathbf{U}_i^+$, and $\mathbf{U}_i^-$ are the displacement vectors with respect to the global Cartesian coordinates, its value at the i^+ and i^- nodes of the element, respectively,

$$\mathbf{N}(\xi,\eta)=[N_1\mathbf{I}_3, N_2\mathbf{I}_3, N_3\mathbf{I}_3, N_4\mathbf{I}_3],\qquad \mathbf{q}_0=\frac{1}{2}\begin{Bmatrix}\mathbf{U}_1^+ + \mathbf{U}_1^-\\ \mathbf{U}_2^+ + \mathbf{U}_2^-\\ \mathbf{U}_3^+ + \mathbf{U}_3^-\\ \mathbf{U}_4^+ + \mathbf{U}_4^-\end{Bmatrix},$$

$$\mathbf{q}_n=\frac{1}{2}\begin{Bmatrix}\mathbf{U}_1^+ - \mathbf{U}_1^-\\ \mathbf{U}_2^+ - \mathbf{U}_2^-\\ \mathbf{U}_3^+ - \mathbf{U}_3^-\\ \mathbf{U}_4^+ - \mathbf{U}_4^-\end{Bmatrix},$$

where $\mathbf{I}_m$ is the mth order identity matrix.

To resolve the trapezoidal and shear locking in the eight-node elemen [5,20–24], ANS is employed. Truncating the first- and second-order ζ-terms in transverse shear strains and the tangential strains, respectively, the physical strains can be expressed as:

$$\begin{Bmatrix}\boldsymbol{\varepsilon}_{=}\\ \varepsilon_{\|}\end{Bmatrix}=\begin{Bmatrix}\varepsilon_x\\ \varepsilon_y\\ \gamma_{xy}\\ \varepsilon_z\end{Bmatrix}=\begin{Bmatrix}\boldsymbol{\varepsilon}_m+\zeta\boldsymbol{\varepsilon}_b\\ \boldsymbol{\varepsilon}_{\|}\end{Bmatrix}=\begin{bmatrix}\mathbf{B}_m+\zeta\mathbf{B}_b\\ \mathbf{B}_{\|}\end{bmatrix}\mathbf{q}^e,$$

$$\boldsymbol{\gamma}=\begin{Bmatrix}\gamma_{zx}\\ \gamma_{zy}\end{Bmatrix}=\mathbf{B}_t\mathbf{q}^e, \tag{3}$$

where $\mathbf{B}$'s are independent of ζ and $\mathbf{q}^e$ is the element displacement vector.

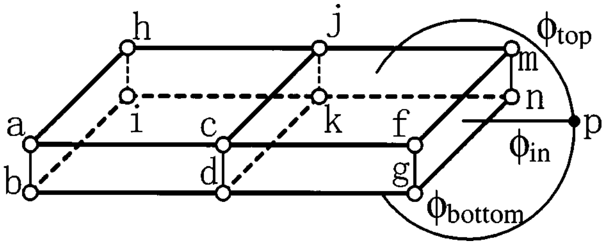

Fig. 2 The solid elements modeling the same piezoelectric patch/film share the same electric node, i.e., connectivity for l.h. element: [a,c,j,h,b,d,k,i,p]; connectivity for rh element: [c,f,m,j,d,g,n,k,p]

3 Solid-Shell Element for Piezoelectric Patches

Although it is often assumed that the distribution of electric potential varies linearly through thickness in piezoelectric layer, an exact solution for piezoelectric laminate plates given by Heyliger and Saravanos [12] has shown the nonlinear distribution of electric potential. Moreover, the electric potential distributed in piezoelectric material is generally function of place space. Practically, electropolar direction is perpendicular to in-plane of the piezoelectric patch as sensor and/or actuator. Thus, the same piezoelectric patch/film (i.e., it has the same electrode) has the same electric potential on its same surface. For generic piezoelectric solid elements, each node is equipped with three translations and one electric potential as the nodal d.o.f.s. It is necessary to constrain the equality of the electric d.o.f.s of the nodes on the same electrode. To avoid this task, the electric d.o.f.s are separated from the kinetic nodes. It should be noted that unlike kinetic nodes, electric nodes have no coordinates.

Figure 2 shows two elements modeling the same piezoelectric patch in which two elements only need three electric d.o.f.s grouped under the electric node "p." To model real through-thickness electric field distribution in piezoelectric layer, the electric potential distribution is assumed to vary with second-order through thickness by introducing internal electric potential of piezoelectric element. Electric potential ϕ can, hence, be expressed as:

$$\begin{aligned}\phi&=\frac{1}{2}(1+\zeta)\phi_{\text{top}}+\frac{1}{2}(1-\zeta)\phi_{\text{bottom}}+(1-\zeta^2)\phi_{\text{in}}^e\\ &=\begin{bmatrix}\dfrac{1+\zeta}{2} & \dfrac{1-\zeta}{2}\end{bmatrix}\boldsymbol{\Phi}^e+(1-\zeta^2)\phi_{\text{in}}^e, \end{aligned} \tag{4}$$

where $\boldsymbol{\Phi}^e=\{\phi_{\text{top}},\phi_{\text{bottom}}\}^T$ is the electric potential of node "p," ϕ_{top}, ϕ_{bottom}, and ϕ_{in}^e are the top, bottom, and internal electric potential of the piezoelectric patch. The electric field in the transverse direction with respect to the local Cartesian system is derived from the above potential expression as:

$$\begin{aligned}E_z&=-\phi_{,z}=-\frac{1}{\|\mathbf{X}_n\|}\left(\begin{bmatrix}\dfrac{1}{2} & -\dfrac{1}{2}\end{bmatrix}\boldsymbol{\Phi}^e-2\zeta\phi_{in}^e\right)=-\mathbf{B}_e\boldsymbol{\Phi}^e-\zeta B_{ei}\phi_{in}^e\\ &=E_C+\zeta E_L, \end{aligned} \tag{5}$$

where $\mathbf{B}_e$ is the electric field–electric potential matrix in the transverse direction.

Furthermore, transverse shear response is assumed to be uncoupled from the others. Since two of the electric field components vanish and the poling direction is always aligned with the transverse direction, the piezoelectric constitutive relation can therefore be expressed as

$$\begin{Bmatrix} \sigma_= \\ \sigma_\parallel \\ D_z \end{Bmatrix} = \begin{bmatrix} \mathbf{C}_= & \mathbf{C}_\times & -\mathbf{e}_=^T \\ \mathbf{C}_\times^T & C_\parallel & -e_{33} \\ \mathbf{e}_= & e_{33} & \kappa_{33}^\varepsilon \end{bmatrix} \begin{Bmatrix} \boldsymbol{\varepsilon}_= \\ \varepsilon_\parallel \\ E_z \end{Bmatrix},$$

$$\text{or} \quad \begin{Bmatrix} \boldsymbol{\varepsilon}_= \\ \varepsilon_\parallel \\ D_z \end{Bmatrix} = \begin{bmatrix} \mathbf{S}_= & \mathbf{S}_\times & \mathbf{d}_=^T \\ \mathbf{S}_\times^T & \mathbf{S}_\parallel & d_{33} \\ \mathbf{d}_= & d_{33} & \kappa_{33}^\sigma \end{bmatrix} \begin{Bmatrix} \boldsymbol{\sigma}_= \\ \boldsymbol{\sigma}_\parallel \\ E_z \end{Bmatrix},$$

$$\boldsymbol{\tau} = \begin{Bmatrix} \tau_{zx} \\ \tau_{zy} \end{Bmatrix} = \mathbf{C}_t \begin{Bmatrix} \gamma_{zx} \\ \gamma_{zy} \end{Bmatrix} = \mathbf{C}_t \boldsymbol{\gamma}, \tag{6}$$

where

$$\boldsymbol{\sigma}_= = \{\sigma_x, \sigma_y, \tau_{xy}\}^T, \quad \boldsymbol{\varepsilon}_= = \{\varepsilon_x, \varepsilon_y, \gamma_{xy}\}^T,$$

$$\begin{bmatrix} \mathbf{S}_= & \mathbf{S}_\times \\ \mathbf{S}_\times^T & S_\parallel \end{bmatrix} = \begin{bmatrix} \mathbf{C}_= & \mathbf{C}_\times \\ \mathbf{C}_\times^T & C_\parallel \end{bmatrix}^{-1}$$

in which $\mathbf{e}_= = (e_{31}, e_{32}, e_{36})$, e_{33}, $\mathbf{d}_= = (d_{31}, d_{32}, d_{36})$, d_{33} is piezoelectric coefficient, and D_z and $\kappa_{33}^\varepsilon\,(\kappa_{33}^\sigma)$ are the electric displacement and the permittivity coefficient in the transverse direction, respectively.

4 Solid-Shell Element for Laminated Materials

The average thickness strain can be calculated by first rewriting Eq. (6) as:

$$\begin{Bmatrix} \boldsymbol{\sigma}_= \\ \varepsilon_\parallel \\ D_z \end{Bmatrix} = \begin{bmatrix} \mathbf{A} & \mathbf{B} & \mathbf{G} \\ -\mathbf{B}^T & D & F \\ -\mathbf{G}^T & F & R \end{bmatrix} \begin{Bmatrix} \boldsymbol{\varepsilon}_= \\ \boldsymbol{\sigma}_\parallel \\ E_z \end{Bmatrix} = \begin{bmatrix} \mathbf{S}_=^{-1} & -\mathbf{S}_=^{-1}\mathbf{S}_\times & -\mathbf{S}_=^{-1}\mathbf{S}_\times e_{33} - \mathbf{e}_=^T \\ \mathbf{S}_\times^T \mathbf{S}_=^{-1} & S_\parallel - \mathbf{S}_\times^T \mathbf{S}_=^{-1} \mathbf{S}_\times & (S_\parallel - \mathbf{S}_\times^T \mathbf{S}_=^{-1}\mathbf{S}_\times) e_{33} \\ \mathbf{S}_\times^T \mathbf{S}_=^{-1} e_{33} + \mathbf{e}_= & (S_\parallel - \mathbf{S}_\times^T \mathbf{S}_=^{-1}\mathbf{S}_\times) e_{33} & \kappa_{33}^\varepsilon + (S_\parallel - \mathbf{S}_\times^T \mathbf{S}_=^{-1}\mathbf{S}_\times) e_{33}^2 \end{bmatrix} \begin{Bmatrix} \boldsymbol{\varepsilon}_= \\ \boldsymbol{\sigma}_\parallel \\ E_z \end{Bmatrix}. \tag{7}$$

Note, that $\boldsymbol{\varepsilon}_m$, $\boldsymbol{\varepsilon}_b$, $\boldsymbol{\varepsilon}_h$, and E_z [see Eqs. (3) and (5)] are independent of ζ, and the element thickness stress $\boldsymbol{\sigma}_\square$ is assumed to be independent of ζ. To achieve higher computational efficiency, the second-order ζ terms in the in-plane strain are often truncated whereas only the zero order ζ term is retained in the Jacobian determinant that following will turn up. From Eqs. (3), (5), and (7) we have

$$\overline{\varepsilon_\parallel} = \frac{1}{2}\int_{-1}^{+1} \left([-\mathbf{B}^T \;\; D \;\; F] \begin{Bmatrix} \boldsymbol{\varepsilon}_= \\ \boldsymbol{\sigma}_\parallel \\ E_z \end{Bmatrix} \right) \mathrm{d}\zeta$$

$$= \frac{1}{2}\int_{-1}^{+1} [-\mathbf{B} \;\; D \;\; -\zeta\mathbf{B} \;\; F \;\; \zeta F]\,\mathrm{d}\zeta \cdot \begin{Bmatrix} \boldsymbol{\varepsilon}_m \\ \boldsymbol{\sigma}_\parallel \\ \boldsymbol{\varepsilon}_b \\ E_C \\ E_L \end{Bmatrix},$$

$$\begin{Bmatrix} \overline{\boldsymbol{\sigma}_m} \\ \overline{\boldsymbol{\sigma}_b} \\ \overline{D_C} \\ \overline{D_L} \end{Bmatrix} = \frac{1}{2}\int_{-1}^{+1} \begin{Bmatrix} \boldsymbol{\sigma}_= \\ \zeta\boldsymbol{\sigma}_= \\ D_z \\ \zeta D_z \end{Bmatrix} \mathrm{d}\zeta$$

$$= \frac{1}{2}\int_{-1}^{+1} \begin{bmatrix} \mathbf{A} & \mathbf{B} & \zeta\mathbf{A} & \mathbf{G} & \zeta\mathbf{G} \\ \zeta\mathbf{A} & \zeta\mathbf{B} & \zeta^2\mathbf{A} & \zeta\mathbf{G} & \zeta^2\mathbf{G} \\ -\mathbf{G}^T & F & -\zeta\mathbf{G}^T & R & \zeta R \\ -\zeta\mathbf{G}^T & \zeta F & -\zeta^2\mathbf{G}^T & \zeta R & \zeta^2 R \end{bmatrix} \mathrm{d}\zeta$$

$$\cdot \begin{Bmatrix} \boldsymbol{\varepsilon}_m \\ \boldsymbol{\sigma}_\parallel \\ \boldsymbol{\varepsilon}_b \\ E_C \\ E_L \end{Bmatrix}$$

which can be collected as:

$$\begin{Bmatrix} \bar{\boldsymbol{\sigma}} \\ \bar{\mathbf{D}}_\parallel \end{Bmatrix} = \left[\begin{array}{c|cc} \bar{\mathbf{C}}_\perp & -\bar{\mathbf{e}}_0^T & -\bar{\mathbf{e}}_1^T \\ \hline \bar{\mathbf{e}}_0 & \bar{\boldsymbol{\kappa}}_0^\varepsilon & \bar{\boldsymbol{\kappa}}_{01}^\varepsilon \\ \bar{\mathbf{e}}_1 & \bar{\boldsymbol{\kappa}}_{01}^\varepsilon & \bar{\boldsymbol{\kappa}}_1^\varepsilon \end{array} \right] \begin{Bmatrix} \boldsymbol{\varepsilon} \\ \mathbf{E}_\parallel \end{Bmatrix} = \begin{bmatrix} \bar{\mathbf{C}}_\perp & -\bar{\mathbf{e}}^T \\ -\bar{\mathbf{e}} & \bar{\boldsymbol{\kappa}}^\varepsilon \end{bmatrix} \begin{Bmatrix} \boldsymbol{\varepsilon} \\ \mathbf{E}_\parallel \end{Bmatrix}, \tag{8}$$

where

$$\overline{\boldsymbol{\sigma}} = \begin{Bmatrix} \overline{\boldsymbol{\sigma}_m} \\ \overline{\sigma_\parallel} \\ \overline{\boldsymbol{\sigma}_b} \end{Bmatrix}, \quad \boldsymbol{\varepsilon} = \begin{Bmatrix} \boldsymbol{\varepsilon}_m \\ \overline{\varepsilon_\parallel} \\ \boldsymbol{\varepsilon}_b \end{Bmatrix}, \quad \overline{\mathbf{D}}_\parallel = \begin{Bmatrix} \overline{D_C} \\ \overline{D_L} \end{Bmatrix}, \quad \mathbf{E}_\parallel = \begin{Bmatrix} E_C \\ E_L \end{Bmatrix},$$

$$\overline{\mathbf{C}}_\perp = \begin{bmatrix} \mathbf{A}_0 + \mathbf{B}_0\mathbf{B}_0^T/D_0 & \mathbf{B}_0/D_0 & \mathbf{A}_1 + \mathbf{B}_0\mathbf{B}_1^T/D_0 \\ \mathbf{B}_0^T/D_0 & 1/D_0 & \mathbf{B}_1^T/D_0 \\ \mathbf{A}_1 + \mathbf{B}_1\mathbf{B}_0^T/D_0 & \mathbf{B}_1/D_0 & \mathbf{A}_2 + \mathbf{B}_1\mathbf{B}_1^T/D_0 \end{bmatrix},$$

$$\overline{\mathbf{e}}_0 = \{-\mathbf{G}_0^T + F_0\mathbf{B}_0^T/D_0 \;\; F_0/D_0 \;\; -\mathbf{G}_1^T + F_0\mathbf{B}_1^T/D_0\},$$

$$\overline{\mathbf{e}}_1 = \{-\mathbf{G}_1^T + F_1\mathbf{B}_0^T/D_0 \;\; F_1/D_0 \;\; -\mathbf{G}_2^T + F_1\mathbf{B}_1^T/D_0\},$$

$$\overline{\boldsymbol{\kappa}}_0^\varepsilon = R_0 - F_0F_0/D_0, \quad \overline{\boldsymbol{\kappa}}_{01}^\varepsilon = R_1 - F_0F_1/D_0,$$

$$\overline{\boldsymbol{\kappa}}_1^\varepsilon = R_2 - F_1F_1/D_0,$$

$$[\mathbf{A}_0, \mathbf{A}_1, \mathbf{A}_2] = \frac{1}{2}\int_{-1}^{+1} [1, \zeta, \zeta^2]\mathbf{A}\,\mathrm{d}\zeta,$$

$$[\mathbf{B}_0, \mathbf{B}_1] = \frac{1}{2}\int_{-1}^{+1} [1, \zeta]\mathbf{B}\,\mathrm{d}\zeta, \quad D_0 = \frac{1}{2}\int_{-1}^{+1} D\,\mathrm{d}\zeta,$$

$$[\mathbf{G}_0, \mathbf{G}_1, \mathbf{G}_2] = \frac{1}{2}\int_{-1}^{+1} [1, \zeta, \zeta^2]\mathbf{G}\,\mathrm{d}\zeta,$$

$$[F_0, F_1] = \frac{1}{2}\int_{-1}^{+1} [1, \zeta] F\,\mathrm{d}\zeta,$$

$$[R_0, R_1, R_2] = \frac{1}{2}\int_{-1}^{+1} [1, \zeta, \zeta^2] R\,\mathrm{d}\zeta,$$

and from Eq. (6), obtain

$$\overline{\boldsymbol{\tau}} = \frac{1}{2}\int_{-1}^{+1} \boldsymbol{\tau}\,\mathrm{d}\zeta = \frac{1}{2}\int_{-1}^{+1} \mathbf{C}_t\,\mathrm{d}\zeta \cdot \boldsymbol{\gamma} = \overline{\mathbf{C}}_T\boldsymbol{\gamma}, \tag{9}$$

where $\overline{\mathbf{C}}_\perp$, $\overline{\mathbf{C}}_T$, $\overline{\mathbf{e}}$'s, and $\overline{\kappa^\varepsilon}$'s are termed as the modified generalized laminate stiffness matrices which are associated with the generalized element stress and strain, the generalized piezostrain coefficients, and the generalized permittivity coefficient in the transverse direction, respectively. It is worth noting two cases: (a) the element only contains laminated material where piezoelectric coefficients are assumed to be zero and permittivity coefficient of each layer is the same; (b) the element only contains one layer piezoelectric material. In both cases, the generalized stiffness matrices in the Eq. (8) can, respectively, be reduced to:

$$\begin{Bmatrix}\bar{\boldsymbol{\sigma}}\\ \bar{\mathbf{D}}_{\Box}\end{Bmatrix}=\left[\begin{array}{c|cc}\bar{\mathbf{C}}_{\perp} & 0 & \\ \hline & \kappa_{33}^{\varepsilon} & 0\\ 0 & & \\ & 0 & \frac{1}{3}\kappa_{33}^{\varepsilon}\end{array}\right]\begin{Bmatrix}\boldsymbol{\varepsilon}\\ \mathbf{E}_{\parallel}\end{Bmatrix},$$

$$\begin{Bmatrix}\bar{\boldsymbol{\sigma}}\\ \bar{\mathbf{D}}_{\parallel}\end{Bmatrix}=\left[\begin{array}{ccc|cc}\mathbf{C}_{=} & \mathbf{C}_{\times} & 0 & -\mathbf{e}_{=}^{T} & 0\\ \mathbf{C}_{\times}^{T} & C_{\parallel} & 0 & -e_{33} & 0\\ 0 & 0 & \frac{1}{3}\mathbf{S}_{=}^{-1} & 0 & \frac{1}{3}\mathbf{G}\\ \hline \mathbf{e}_{=} & e_{33} & 0 & \kappa_{33}^{\varepsilon} & 0\\ 0 & 0 & -\frac{1}{3}\mathbf{G}^{T} & 0 & \frac{1}{3}R\end{array}\right]\begin{Bmatrix}\boldsymbol{\varepsilon}\\ \mathbf{E}_{\parallel}\end{Bmatrix}. \tag{10}$$

Using the following generalized elementwise potential energy function:

$$\Pi^{e}=\frac{1}{2}\int_{-1}^{+1}\int_{-1}^{+1}\left(\begin{Bmatrix}\boldsymbol{\varepsilon}\\ -\mathbf{E}_{\parallel}\end{Bmatrix}^{T}\begin{bmatrix}\overline{\mathbf{C}}_{\perp} & \overline{\mathbf{e}}^{T}\\ \overline{\mathbf{e}} & -\overline{\boldsymbol{\kappa}}^{\varepsilon}\end{bmatrix}\begin{Bmatrix}\boldsymbol{\varepsilon}\\ -\mathbf{E}_{\parallel}\end{Bmatrix}\right.$$

$$\left.+\boldsymbol{\gamma}^{T}\overline{\mathbf{C}}_{T}\boldsymbol{\gamma}\right)2J_{0}d\xi\mathrm{d}\eta-P^{e}, \tag{11}$$

where P^{e} is the element load potential due to mechanical force and surface charge, $J_{0}=J|_{\zeta=0}$ in which J is the Jacobian determinant, from Eq. (11), the following static equations of the piezoelectric elementwise can be derived:

$$\begin{bmatrix}\mathbf{k}_{mm}^{e} & \mathbf{k}_{me0}^{e} & \mathbf{k}_{me1}^{e}\\ (\mathbf{k}_{me0}^{e})^{T} & \mathbf{k}_{ee0}^{e} & 0\\ (\mathbf{k}_{me1}^{e})^{T} & 0 & k_{ee1}^{e}\end{bmatrix}\begin{Bmatrix}\mathbf{q}^{e}\\ \boldsymbol{\Phi}^{e}\\ \phi_{\mathrm{in}}^{e}\end{Bmatrix}=\begin{Bmatrix}\mathbf{f}_{f}^{e}\\ \mathbf{f}_{Q}^{e}\\ 0\end{Bmatrix}, \tag{12}$$

where

$$\mathbf{k}_{mm}^{e}=2\int_{-1}^{+1}\int_{-1}^{+1}(\mathbf{B}_{\perp}^{T}\overline{\mathbf{C}}_{\perp}\mathbf{B}_{\perp}+\mathbf{B}_{t}^{T}\overline{\mathbf{C}}_{T}\mathbf{B}_{t})J_{0}d\xi d\eta,$$

$$k_{me0}^{e}=2\int_{-1}^{+1}\int_{-1}^{+1}\mathbf{B}_{\perp}^{T}\overline{\mathbf{e}}_{0}^{T}\mathbf{B}_{e}J_{0}d\xi d\eta,$$

$$\mathbf{k}_{me1}^{e}=2\int_{-1}^{+1}\int_{-1}^{+1}\mathbf{B}_{\perp}^{T}\overline{\mathbf{e}}_{1}^{T}\mathbf{B}_{e}J_{0}d\xi d\eta$$

$$\mathbf{k}_{ee0}^{e}=-2\int_{-1}^{+1}\int_{-1}^{+1}\mathbf{B}_{e}^{T}\overline{\kappa}_{0}^{\varepsilon}\mathbf{B}_{e}J_{0}d\xi d\eta,$$

$$\mathbf{k}_{ee1}^{e}=-2\int_{-1}^{+1}\int_{-1}^{+1}B_{ei}\overline{\kappa}_{1}^{\varepsilon}B_{ei}J_{0}d\xi d\eta,\qquad \mathbf{B}_{\perp}=(\mathbf{B}_{m},\mathbf{B}_{\parallel},\mathbf{B}_{b})^{T},$$

$\mathbf{f}_{f}^{e}$ is the elementwise mechanical force due to the body force and surface traction, $\mathbf{f}_{Q}^{e}$ is the elementwise electric force vector due to the charge density.

5 Hybrid Stress Solid-Shell Element for Laminated Materials

To apply hybrid stress (HS) formulation to the above ANS solid-shell element to improve the latter's in-plane response, the following elementwise modified Hellinger–Reissner functional can be used [25]:

$$\Pi_{HR}^{e}=\int_{-1}^{+1}\int_{-1}^{+1}\left(\frac{-1}{2}\begin{Bmatrix}\overline{\boldsymbol{\sigma}}\\ -\mathbf{E}_{\parallel}\end{Bmatrix}^{T}\begin{bmatrix}\overline{\mathbf{S}}_{\perp} & -\overline{\mathbf{d}}^{T}\\ -\overline{\mathbf{d}} & \overline{\boldsymbol{\kappa}}^{\sigma}\end{bmatrix}\begin{Bmatrix}\overline{\boldsymbol{\sigma}}\\ -\mathbf{E}_{\parallel}\end{Bmatrix}+\overline{\boldsymbol{\sigma}}^{T}\boldsymbol{\varepsilon}\right.$$

$$\left.-\frac{1}{2}\overline{\boldsymbol{\tau}}^{T}\overline{\mathbf{C}}_{T}^{-1}\overline{\boldsymbol{\tau}}+\overline{\boldsymbol{\tau}}^{T}\boldsymbol{\gamma}\right)J_{0}\mathrm{d}\xi\mathrm{d}\eta-P^{e} \tag{13}$$

where $\overline{\mathbf{S}}_{\perp}=\overline{\mathbf{C}}_{\perp}^{-1}$, $\overline{\mathbf{d}}=\overline{\mathbf{e}}\overline{\mathbf{C}}_{\perp}^{-1}$ and $\overline{\boldsymbol{\kappa}}^{\sigma}=\overline{\boldsymbol{\kappa}}^{\varepsilon}+\overline{\mathbf{e}}\overline{\mathbf{d}}^{T}$.

The following orthogonal constant and nonconstant stress nodes are chosen in a way similar to that of Pian's eight-node element [26,27]:

$$\begin{Bmatrix}\overline{\boldsymbol{\sigma}}_{m}\\ \overline{\sigma}_{\parallel}\\ \overline{\boldsymbol{\sigma}}_{b}\end{Bmatrix}=\begin{bmatrix}\mathbf{I}_{4} & \mathbf{0}_{4\times3} & \mathbf{P}_{\mathrm{NH}} & \mathbf{0}_{4\times2}\\ \mathbf{0}_{3\times4} & \mathbf{I}_{3} & \mathbf{0}_{3\times5} & \mathbf{P}_{\mathrm{MH}}\end{bmatrix}\begin{Bmatrix}\boldsymbol{\beta}_{\mathrm{NC}}\\ \boldsymbol{\beta}_{\mathrm{MC}}\\ \boldsymbol{\beta}_{\mathrm{NH}}\\ \boldsymbol{\beta}_{\mathrm{MH}}\end{Bmatrix},$$

$$\overline{\boldsymbol{\tau}}=[\mathbf{I}_{2}\ \ \mathbf{P}_{\mathrm{TH}}]\begin{Bmatrix}\boldsymbol{\beta}_{\mathrm{TC}}\\ \boldsymbol{\beta}_{\mathrm{TH}}\end{Bmatrix}, \tag{14}$$

where

$$\mathbf{P}_{\mathrm{NH}}=\frac{1}{J_{0}}\begin{bmatrix}\xi\overline{x}_{\eta}\overline{x}_{\eta} & 0 & \eta\overline{x}_{\xi}\overline{x}_{\xi} & 0 & 0\\ \xi\overline{y}_{\eta}\overline{y}_{\eta} & 0 & \eta\overline{y}_{\xi}\overline{y}_{\xi} & 0 & 0\\ \xi\overline{x}_{\eta}\overline{y}_{\eta} & 0 & \eta\overline{x}_{\xi}\overline{y}_{\xi} & 0 & 0\\ 0 & \xi & 0 & \eta & \xi\eta\end{bmatrix},$$

$$\mathbf{P}_{\mathrm{MH}}=\frac{1}{J_{0}}\begin{bmatrix}\xi\overline{x}_{\eta}\overline{x}_{\eta} & \eta\overline{x}_{\xi}\overline{x}_{\xi}\\ \xi\overline{y}_{\eta}\overline{y}_{\eta} & \eta\overline{y}_{\xi}\overline{y}_{\xi}\\ \xi\overline{x}_{\eta}\overline{y}_{\eta} & \eta\overline{x}_{\xi}\overline{y}_{\xi}\end{bmatrix},\qquad \mathbf{P}_{\mathrm{TH}}=\frac{1}{J_{0}}\begin{bmatrix}\xi\overline{x}_{\eta} & \eta\overline{x}_{\xi}\\ \xi\overline{y}_{\eta} & \eta\overline{y}_{\xi}\end{bmatrix},$$

$$J_{0}=J|_{\xi=\eta=\zeta=0},\quad \overline{x}_{\xi}=x_{\xi}|_{\xi=\eta=\zeta=0},\quad \overline{y}_{\xi}=y_{\xi}|_{\xi=\eta=\zeta=0},$$

$$\overline{x}_{\eta}=x_{\eta}|_{\xi=\eta=\zeta=0},\quad \overline{y}_{\eta}=y_{\eta}|_{\xi=\eta=\zeta=0}.$$

Substituting Eq. (14) into Eq. (13), and condensing $\boldsymbol{\beta}$'s with the stationary conditions of Π_{HR}^{e} with respect to $\boldsymbol{\beta}$'s, Eq. (13) can be expressed as:

$$\Pi_{\mathrm{HR}}^{e}=\frac{1}{2}\begin{Bmatrix}\mathbf{q}^{e}\\ \boldsymbol{\Phi}^{e}\\ \phi_{in}^{e}\end{Bmatrix}^{T}\begin{bmatrix}\mathbf{k}_{mm}^{e} & \mathbf{k}_{me0}^{e} & \mathbf{k}_{me1}^{e}\\ (\mathbf{k}_{me0}^{e})^{T} & \mathbf{k}_{ee0}^{e} & 0\\ (\mathbf{k}_{me1}^{e})^{T} & 0 & k_{ee1}^{e}\end{bmatrix}\begin{Bmatrix}\mathbf{q}^{e}\\ \boldsymbol{\Phi}^{e}\\ \phi_{in}^{e}\end{Bmatrix}$$

$$-\begin{Bmatrix}\mathbf{f}_{f}^{e}\\ \mathbf{f}_{Q}^{e}\\ 0\end{Bmatrix}^{T}\begin{Bmatrix}\mathbf{q}^{e}\\ \boldsymbol{\Phi}^{e}\\ \phi_{\mathrm{in}}^{e}\end{Bmatrix}, \tag{15}$$

where

$$\mathbf{k}_{mm}^{e}=\frac{1}{v}\begin{bmatrix}\mathbf{G}_{\mathrm{NC}}\\ \mathbf{G}_{\mathrm{MC}}\end{bmatrix}^{T}\overline{\mathbf{C}}_{\perp}\begin{bmatrix}\mathbf{G}_{\mathrm{NC}}\\ \mathbf{G}_{\mathrm{MC}}\end{bmatrix}+\begin{bmatrix}\mathbf{G}_{\mathrm{NH}}\\ \mathbf{G}_{\mathrm{MH}}\end{bmatrix}^{T}\mathbf{H}_{\perp}^{-1}\begin{bmatrix}\mathbf{G}_{\mathrm{NH}}\\ \mathbf{G}_{\mathrm{MH}}\end{bmatrix}+\frac{1}{v}\mathbf{G}_{\mathrm{TC}}^{T}\overline{\mathbf{C}}_{T}\mathbf{G}_{\mathrm{TC}}$$

$$+\mathbf{G}_{\mathrm{TH}}^{T}\mathbf{H}_{T}^{-1}\mathbf{G}_{\mathrm{TH}}$$

$$\mathbf{k}_{me0}^{e}=\frac{1}{v}\begin{Bmatrix}\mathbf{G}_{\mathrm{NC}}\\ \mathbf{G}_{\mathrm{MC}}\end{Bmatrix}^{T}\overline{\mathbf{C}}_{\perp}\mathbf{E}_{\mathrm{CC}}+\begin{Bmatrix}\mathbf{G}_{\mathrm{NH}}\\ \mathbf{G}_{\mathrm{MH}}\end{Bmatrix}^{T}\mathbf{H}_{\perp}^{-1}\mathbf{E}_{\mathrm{CH}},$$

$$\mathbf{k}_{me1}^{e}=\frac{1}{v}\begin{Bmatrix}\mathbf{G}_{\mathrm{NC}}\\ \mathbf{G}_{\mathrm{MC}}\end{Bmatrix}^{T}\overline{\mathbf{C}}_{\perp}\mathbf{E}_{\mathrm{HC}}+\begin{Bmatrix}\mathbf{G}_{\mathrm{NH}}\\ \mathbf{G}_{\mathrm{MH}}\end{Bmatrix}^{T}\mathbf{H}_{\perp}^{-1}\mathbf{E}_{\mathrm{HH}},$$

$$\mathbf{k}_{ee0}^{e}=\frac{1}{v}\mathbf{E}_{\mathrm{CC}}^{T}\overline{\mathbf{C}}_{\perp}\mathbf{E}_{\mathrm{CC}}+\mathbf{E}_{\mathrm{CH}}^{T}\mathbf{H}_{\perp}^{-1}\mathbf{E}_{\mathrm{CH}}-\mathbf{A}_{p0},$$

$$\mathbf{k}_{ee1}^{e}=\frac{1}{v}\mathbf{E}_{\mathrm{HC}}^{T}\overline{\mathbf{C}}_{\perp}\mathbf{E}_{\mathrm{HC}}+\mathbf{E}_{\mathrm{HH}}^{T}\mathbf{H}_{\perp}^{-1}\mathbf{E}_{\mathrm{HH}}-\mathbf{A}_{p1},$$

$$v=2\int_{-1}^{+1}\int_{-1}^{+1}J_{0}d\xi d\eta,$$

$$\mathbf{H}_{\perp}=2\int_{-1}^{+1}\int_{-1}^{+1}\begin{bmatrix}\mathbf{P}_{\mathrm{NH}} & \mathbf{0}_{4\times 2}\\ \mathbf{0}_{3\times 5} & \mathbf{P}_{\mathrm{MH}}\end{bmatrix}^{T}\overline{\mathbf{S}}_{\perp}\begin{bmatrix}\mathbf{P}_{\mathrm{NH}} & \mathbf{0}_{4\times 2}\\ \mathbf{0}_{3\times 5} & \mathbf{P}_{\mathrm{MH}}\end{bmatrix}J_0 d\xi d\eta,$$

$$\mathbf{H}_T=2\int_{-1}^{+1}\int_{-1}^{+1}\mathbf{P}_{\mathrm{TH}}^{T}\overline{\mathbf{C}}_T^{-1}\mathbf{P}_{\mathrm{TH}}J_0 d\xi d\eta,$$

$$\mathbf{G}_{\mathrm{NC}}=2\int_{-1}^{+1}\int_{-1}^{+1}\begin{bmatrix}\mathbf{B}_m\\ \mathbf{B}_{\parallel}\end{bmatrix}J_0 d\xi d\eta,$$

$$\mathbf{G}_{\mathrm{MC}}=2\int_{-1}^{+1}\int_{-1}^{+1}\mathbf{B}_b J_0 d\xi d\eta,$$

$$\mathbf{G}_{\mathrm{NH}}=2\int_{-1}^{+1}\int_{-1}^{+1}\mathbf{P}_{\mathrm{NH}}^{T}\begin{bmatrix}\mathbf{B}_m\\ \mathbf{B}_{\parallel}\end{bmatrix}J_0 d\xi d\eta,$$

$$\mathbf{G}_{\mathrm{MH}}=2\int_{-1}^{+1}\int_{-1}^{+1}\mathbf{P}_{\mathrm{MH}}^{T}\mathbf{B}_b J_0 d\xi d\eta,$$

$$\mathbf{G}_{\mathrm{TC}}=2\int_{-1}^{+1}\int_{-1}^{+1}\mathbf{B}_t J_0 d\xi d\eta,\quad \mathbf{G}_{\mathrm{TH}}=2\int_{-1}^{+1}\int_{-1}^{+1}\mathbf{P}_{\mathrm{TH}}^{T}\mathbf{B}_t J_0 d\xi d\eta,$$

$$\mathbf{E}_{\mathrm{CC}}=2\int_{-1}^{+1}\int_{-1}^{+1}\overline{\mathbf{d}}_0^{T}\mathbf{B}_e J_0 d\xi d\eta,$$

$$\mathbf{E}_{\mathrm{HC}}=2\int_{-1}^{+1}\int_{-1}^{+1}\overline{\mathbf{d}}_1^{T}B_{ei}J_0 d\xi d\eta,$$

$$\mathbf{E}_{\mathrm{CH}}=2\int_{-1}^{+1}\int_{-1}^{+1}\mathbf{P}_{\mathrm{NH}}^{T}\overline{\mathbf{d}}_0^{T}\mathbf{B}_e J_0 d\xi d\eta,$$

$$\mathbf{E}_{\mathrm{HH}}=2\int_{-1}^{+1}\int_{-1}^{+1}\mathbf{P}_{\mathrm{NH}}^{T}\overline{\mathbf{d}}_1^{T}B_{ei}J_0 d\xi d\eta,$$

$$\mathbf{A}_{p0}=2\int_{-1}^{+1}\int_{-1}^{+1}\kappa_0^{\sigma}\mathbf{B}_e^{T}\mathbf{B}_e J_0 d\xi d\eta,$$

$$A_{p1}=2\int_{-1}^{+1}\int_{-1}^{+1}\kappa_1^{\sigma}B_{ei}B_{ei}J_0 d\xi d\eta,$$

$$\overline{\mathbf{d}}=\begin{pmatrix}\overline{\mathbf{d}}_0\\ \overline{\mathbf{d}}_1\end{pmatrix},\quad \overline{\boldsymbol{\kappa}}^{\sigma}=\begin{bmatrix}\overline{\kappa}_0^{\sigma} & 0\\ 0 & \overline{\kappa}_1^{\sigma}\end{bmatrix}.$$

The elementwise static equation having the same form as Eq. (12) can be obtained from Eq. (15).

6 System and Eigenequations

Assembling the elemental matrices gives the global system matrices. The resulting dynamic equation becomes

$$\begin{bmatrix}\mathbf{M} & 0 & 0\\ 0 & 0 & 0\\ 0 & 0 & 0\end{bmatrix}\begin{Bmatrix}\ddot{\mathbf{q}}\\ \ddot{\boldsymbol{\Phi}}\\ \ddot{\boldsymbol{\phi}}_{\mathrm{in}}\end{Bmatrix}+\begin{bmatrix}\mathbf{C}_p & 0 & 0\\ 0 & 0 & 0\\ 0 & 0 & 0\end{bmatrix}\begin{Bmatrix}\dot{\mathbf{q}}\\ \dot{\boldsymbol{\Phi}}\\ \dot{\boldsymbol{\phi}}_{\mathrm{in}}\end{Bmatrix}$$
$$+\begin{bmatrix}\mathbf{K}_{mm} & \mathbf{K}_{me0} & \mathbf{K}_{me1}\\ (\mathbf{K}_{me0})^T & \mathbf{K}_{ee0} & 0\\ (\mathbf{K}_{me1})^T & 0 & \mathbf{K}_{ee1}\end{bmatrix}\begin{Bmatrix}\mathbf{q}\\ \boldsymbol{\Phi}\\ \boldsymbol{\phi}_{\mathrm{in}}\end{Bmatrix}=\begin{Bmatrix}\mathbf{F}_f\\ \mathbf{F}_Q\\ 0\end{Bmatrix},\quad (16)$$

where $\mathbf{M}$ is mass matrix, $\mathbf{C}_p$ is proportional passive matrix, $\mathbf{q}$, $\boldsymbol{\Phi}$ and $\boldsymbol{\phi}_{\mathrm{in}}$ are, respectively, the system vectors of nodal displacement and electric potentials, and $\mathbf{F}_f$ and $\mathbf{F}_Q$ are, respectively, the system vectors of mechanical force and electric force.

Since the internal DOF $\boldsymbol{\phi}_{\mathrm{in}}$ does not have physical significance, it can be condensed from the system equations in order to improve the computation efficiency. One can obtain the modified matrix equations as

$$\begin{bmatrix}\mathbf{M} & 0\\ 0 & 0\end{bmatrix}\begin{Bmatrix}\ddot{\mathbf{q}}\\ \ddot{\boldsymbol{\Phi}}\end{Bmatrix}+\begin{bmatrix}\mathbf{C}_p & 0\\ 0 & 0\end{bmatrix}\begin{Bmatrix}\dot{\mathbf{q}}\\ \dot{\boldsymbol{\Phi}}\end{Bmatrix}+\begin{bmatrix}\tilde{\mathbf{K}}_{mm} & \mathbf{K}_{me0}\\ \mathbf{K}_{me0}^{\mathbf{T}} & \mathbf{K}_{ee0}\end{bmatrix}\begin{Bmatrix}\mathbf{q}\\ \boldsymbol{\Phi}\end{Bmatrix}=\begin{Bmatrix}\mathbf{F}_f\\ \mathbf{F}_Q\end{Bmatrix},\quad (17)$$

and

$$\boldsymbol{\phi}_{\mathrm{in}}=-\mathbf{K}_{ee1}^{-1}\mathbf{K}_{me1}^{T}\mathbf{q},\quad (18)$$

where,

$$\tilde{\mathbf{K}}_{mm}=\mathbf{K}_{mm}-\mathbf{K}_{me0}\mathbf{K}_{ee1}^{-1}\mathbf{K}_{me1}^{T}\,.$$

If the actuators and sensors are embedded in a structure, it is convenient to partition the system vector of electric potential $\boldsymbol{\Phi}$ into $\boldsymbol{\Phi}^A$ of the actuators and $\boldsymbol{\Phi}^S$ of the sensors. Since there is no electric loading applied to the sensors, Eq. (17) can be written as:

$$\mathbf{M}\ddot{\mathbf{q}}+\mathbf{C}_p\dot{\mathbf{q}}+\tilde{\mathbf{K}}_{mm}\mathbf{q}+\mathbf{K}_{me}^{A}\boldsymbol{\Phi}^A+\mathbf{K}_{me}^{S}\boldsymbol{\Phi}^S=\mathbf{F}_f\,,\quad (19)$$

$$\boldsymbol{\Phi}^A=(\mathbf{K}_{ee}^{A})^{-1}[\mathbf{F}_Q^{A}-(\mathbf{K}_{me}^{A})^T\mathbf{q}],\quad (20)$$

$$\boldsymbol{\Phi}^S=-(\mathbf{K}_{ee}^{S})^{-1}(\mathbf{K}_{me}^{S})^T\mathbf{q},\quad (21)$$

where

$$\begin{Bmatrix}\boldsymbol{\Phi}^A\\ \boldsymbol{\Phi}^S\end{Bmatrix}=\boldsymbol{\Phi},\quad \begin{bmatrix}(\mathbf{K}_{ee}^{A})^{-1} & \mathbf{0}\\ \mathbf{0} & (\mathbf{K}_{ee}^{S})^{-1}\end{bmatrix}=\mathbf{K}_{ee0}^{-1},$$

$$[\mathbf{K}_{me}^{A},\mathbf{K}_{me}^{S}]=\mathbf{K}_{me0}\,,\quad \begin{Bmatrix}\mathbf{F}_Q^{A}\\ 0\end{Bmatrix}=\mathbf{F}_Q\,.$$

In particular, $\mathbf{K}_{ee0}$ is block diagonal because the host structure is nonpiezoelectric, i.e., $\boldsymbol{\Phi}^A$ and $\boldsymbol{\Phi}^S$ do not couple. Substitution of Eq. (21) into Eq. (19) results in:

$$\mathbf{M}\ddot{\mathbf{q}}+\mathbf{C}_p\dot{\mathbf{q}}+[\tilde{\mathbf{K}}_{mm}-\mathbf{K}_{me}^{S}(\mathbf{K}_{ee}^{S})^{-1}(\mathbf{K}_{me}^{S})^T]\mathbf{q}=\mathbf{F}_f-\mathbf{K}_{me}^{A}\boldsymbol{\Phi}^A.\quad (22)$$

With the control algorithm known and by virtue of Eq. (21), $\boldsymbol{\Phi}^A$ can be expressed in terms of $\mathbf{q}$ and thus all the electric d.o.f.s in Eq. (21) can be condensed and a standard eigenvalue equation can be obtained as

$$[(\tilde{\mathbf{K}}_{mm}-\mathbf{K}_{me0}\mathbf{K}_{ee0}^{-1}\mathbf{K}_{me0}^{T})-\omega^2\mathbf{M}]\mathbf{q}=0,\quad (23)$$

where ω is eigen frequency. Eigenvalues and mode shapes can be calculated and defined accordingly.

7 Numerical Examples

7.1 Laminated Simply Supported Square Plate

7.1.1 Modeling. The plates used in this simulation are square in shape with simply supported edges. Three different lamination schemes are considered. The first is layup of [1/2/2/1], and second [2/1/1/2], where digitals 1 and 2 denote the orthotropic PVDF and the transversely isotropic PZT-4, respectively, as shown as Table 1. Each layer has equal thickness of $0.25h$, where h is the total thickness of the laminated plate. The both lamination plates are composed of two dissimilar materials with a mismatch in both elastic and electric properties. The third one is a five-ply laminate [p/0/90/0/p]. The laminate configuration consists of a [0/90/0] Gr/Epoxy, denoted as 4 in Table 1, cross-ply sublaminate with composite plies each $0.8h/3$ thick. Two continuous PZT-4's, denoted as 2 in Table 1, layers of thickness $0.1h$ each are also bonded to the upper and lower surfaces of the laminate. To comply with the reported results of exact solution, all layers were assumed to have equal density ($\rho=1$ kg/m^3). Two aspect ratios of thick plate ($a/h=4$) and thin plate ($a/h=50$) are considered, where letter a denotes the length of the square plate. The outer surfaces of the piezoelectric layers were forced to remain always grounded. Based on this, two sets of electric boundary conditions were considered for the inner surface of the piezoelectric layers:

(a) a closed-circuit condition, with the electric potential forced to remain zero (grounded), and

Table 1 Material properties ($\varepsilon_0 = 8.85\ 10^{-12}$ farad/m, electric permittivity of air)

Property	1 (PVDF)	2 (PZT-4)	3 (PZT-4)	4 (Gr/epoxy)	5 (Gr/epoxy)
Elastic properties:					
E_1 (GPa)	237.0	81.3	63.0	132.38	150.0
E_2	23.2	81.3	63.0	10.756	9.0
E_3	10.5	64.5	63.0	10.756	9.0
G_{44}	2.15	25.6	24.231	3.606	7.1
G_{55}	4.4	25.6	24.231	5.6537	7.1
G_{66}	6.43	30.6	24.231	5.6537	7.1
v_{12}	0.154	0.329	0.3	0.24	0.3
v_{13}	0.178	0.432	0.3	0.24	0.3
v_{23}	0.177	0.432	0.3	0.49	0.3
Piezoelectric	−0.13	−5.20	44.367	0	0
coefficient (C/m^2):					
e_{31}	−0.14	−5.20	44.367	0	0
e_{32}	−0.28	15.08	50.182	0	0
e_{33}	−0.01	12.72	14.151	0	0
e_{24}					
Electric permittivity:	12.5	1475	1728.8	0	0
$\varepsilon_{11}/\varepsilon_0$	11.98	1475	1728.8	0	0
$\varepsilon_{22}/\varepsilon_0$	11.98	1300	6362.7	0	0
$\varepsilon_{33}/\varepsilon_0$	1800.0	7600.0	7600.0	1578.0	1600.0
Mass density ρ (kg/m^3)					

(b) an open-circuit condition, where the electric potential remains free (zero electric displacements). Three elements are meshed through thickness direction.

7.1.2 Fundamental Natural Frequency. The normalized natural frequencies for three laminated schemes plates are shown in Tables 2–4. In the tables, the exact results reported by Heyliger and Saravanos [12] are nondimension by $f_1 a^2/(h\rho^{1/2}10^3)$. The letters ND and LD in these tables denote about through-thickness electric potential nonlinear distributions and linear distributions, respectively. That is, the electric potential ϕ_{in} in Eq. (4) is considered for nonlinear distribution and not considered for linear distribution. FER in Table 4 denotes the finite element results reported by Saravanos et al. [3] in the case of three discrete-layers. According to the Tables 2–4, the predicted natural frequencies by means of both displacement element (D) and hybrid-stress element methods (HS) consistently converge above and below the values of the exact solution depending on the type of electric boundary conditions for both thick $(a/h=4)$ and thin $(a/h=50)$ plates. The differences between D and HS in all results are very small. The natural frequency is little higher under the case of ND than of LD. The frequency differences between ND and LD are the highest in the first laminated [1/2/2/1] among three laminated plates, about 1%. The differences in case of another two laminated plates are very small. This shows that the effect on natural frequency caused by through-thickness nonlinear electric potential distribution is generally very small. However, this effect should be considered when the piezoelectric layer is thick and its electric properties are strong. On the side, although predicted natural frequencies are very good in most cases, the predicted results are lower than the exact solution in the case of aspect ratios $a/h=50$ and closed-circuit electric boundary condition, as shown as Tables 3 and 4. This reason remains a subject of investigation.

Table 2 The normalized natural frequencies of three layers piezoelectric plate (1/2/2/1)

Aspect ratios		$a/h=4$				$a/h=50$			
		Closed circuit		Open circuit		Closed circuit		Open circuit	
Mesh	Method	ND	LD	ND	LD	ND	LD	ND	LD
4×4	D	1.0464	1.0362	1.0465	1.0363	1.0740	1.0640	1.0741	1.0642
	HS	1.0446	1.0343	1.0447	1.0344	1.0719	1.0620	1.0720	1.0621
8×8	D	1.0056	0.9963	1.0057	0.9963	1.0140	1.0051	1.0141	1.0052
	HS	1.0052	0.9958	1.0053	0.9959	1.0136	1.0046	1.0137	1.0047
12×12	D	0.9983	0.9891	0.9983	0.9891	1.0035	0.9947	1.0036	0.9948
	HS	0.9981	0.9889	0.9982	0.9889	1.0033	0.9945	1.0034	0.9946
Exact		183.791		183.834		252.029		252.057	

Table 3 The normalized natural frequencies of three layers piezoelectric plate (2/1/1/2)

Aspect ratios		$a/h=4$				$a/h=50$			
		Closed circuit		Open circuit		Closed circuit		Open circuit	
Mesh	Method	ND	LD	ND	LD	ND	LD	ND	LD
4×4	D	1.0207	1.0145	1.0319	1.0259	1.0040	1.0019	1.0534	1.0515
	HS	1.0184	1.0123	1.0297	1.0238	0.9994	0.9973	1.0489	1.0470
8×8	D	0.9874	0.9819	0.9985	0.9933	0.9482	0.9463	0.9939	0.9923
	HS	0.9868	0.9814	0.9980	0.9927	0.9472	0.9453	0.9928	0.9911
12×12	D	0.9813	0.9760	0.9924	0.9872	0.9384	0.9365	0.9831	0.9815
	HS	0.9811	0.9758	0.9921	0.9870	0.9379	0.9361	0.9825	0.9809
Exact		148.329		148.597		288.556		288.565	

Table 4 The normalized natural frequencies of five-ply composite piezoelectric plate (p/0/90/0/p)

Aspect ratios		$a/h=4$				$a/h=50$			
		Closed circuit		Open circuit		Closed circuit		Open circuit	
Mesh	Method	ND	LD	ND	LD	ND	LD	ND	LD
	D	1.0402	1.0398	1.0576	1.0571	1.0204	1.0202	1.0601	1.0599
4×4	HS	1.0383	1.0379	1.0559	1.0554	1.0164	1.0162	1.0561	1.0560
	FER	1.0273		1.0634		1.0314		1.1230	
	D	1.0053	1.0050	1.0225	1.0221	0.9635	0.9633	1.0003	1.0002
8×8	HS	1.0049	1.0045	1.0220	1.0216	0.9626	0.9624	0.9993	0.9992
	FER	1.0064		1.0453		0.9743		1.0641	
	D	0.9990	0.9986	1.0160	1.0156	0.9535	0.9533	0.9896	0.9894
12×12	HS	0.9988	0.9984	1.0157	1.0154	0.9531	0.9529	0.9891	0.9890
	FER	1.0023		1.0423		0.9643		1.0558	
Exact		145.339		145.377		245.941		245.942	

7.1.3 Electric Potential Distribution. Figures 3–6 illustrate the through-thickness electric potential fundamental mode for the laminated [1/2/2/1] and [2/1/1/2] plates for two aspect ratios under open-circuit condition, respectively. The linear electric potential distributions are also included in the figures to compare purpose. Plots of through-thickness electric potential fundamental mode for laminated [p/0/90/0/p] for both electric boundary conditions are shown in Fig. 7 for $a/h=4$ and in Fig. 8 for $a/h=50$. The curves in these figures have very similar shape with the exact solutions reported by Heyliger and Saravanos [12] and part FE results reported by Saravanos et al. [3]. As seen from Figs. 7 and 8, it is interesting to note that electric fields exist in the piezoelectric layers even with the closed-circuit conditions. Although the electric potential in piezoelectric layer is much lower in closed-circuit condition than in open-circuit-condition, it should not be neglected when the piezoelectric layer is thicker. It can be seen that

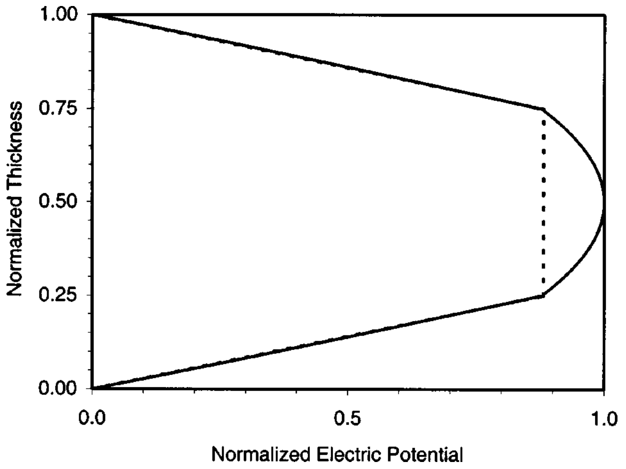

Fig. 3 Through-thickness electric potential distributions for three-ply [1/2/2/1], a/h=4 (——) nonlinear distribution, (- - - -) linear distribution

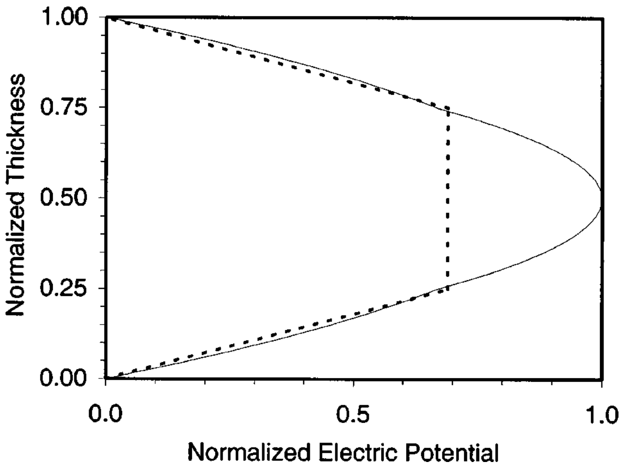

Fig. 4 Through-thickness electric potential distributions for three-ply [1/2/2/1], a/h=50 (——) nonlinear distribution, (- - - -) linear distribution

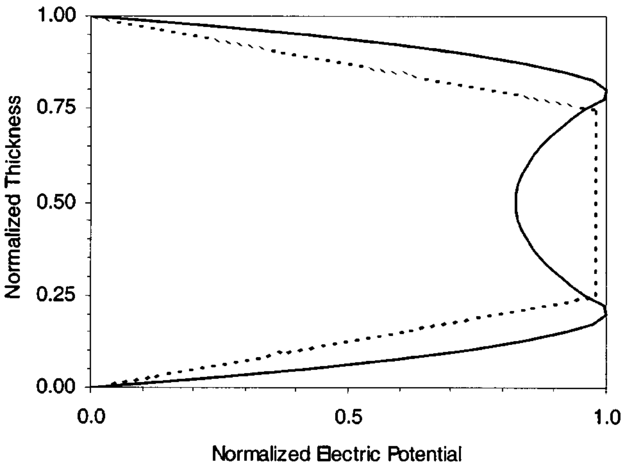

Fig. 5 Through-thickness electric potential distributions for three-ply [2/1/1/2], a/h=4 (——) nonlinear distribution, (- - - -) linear distribution

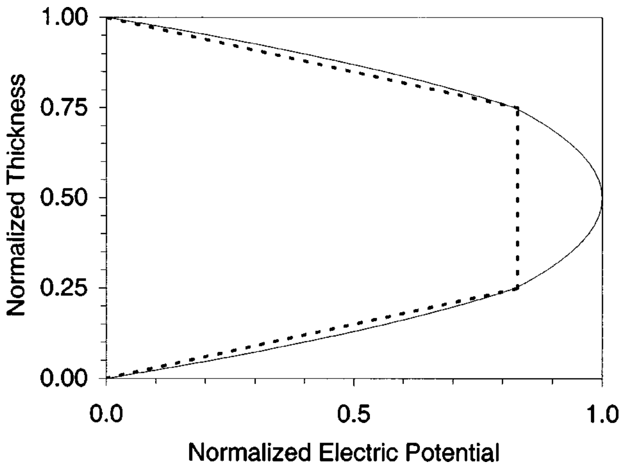

Fig. 6 Through-thickness electric potential distributions for three-ply [2/1/1/2], a/h=50 (——) nonlinear distribution, (- - - -) linear distribution

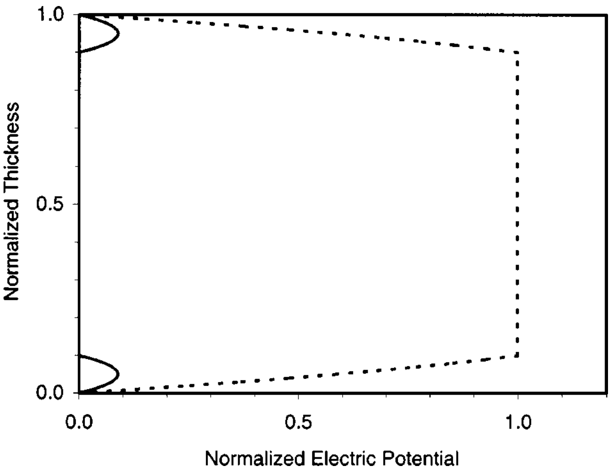

Fig. 7 Through-thickness electric potential distributions for five-ply [p/0/90/0/p] for a/h=4 (——) closed-circuit; (- - - -) open-circuit

the electric fields in piezoelectric layers have considerable difference between linear distribution (LD) and nonlinear distribution (ND), especially, for electric field in middle piezoelectric layer. However, the difference is very small for the third laminated plate.

7.2 Cantilever Composite Plate With Distributed Actuators. Figure 9 shows a composite cantilever plate with twenty-two square and eight nonsquare surface bonded piezoelectric ceramic patches, material properties denoted as 3 in Table 1. Stacking of the composite plate is [0°/±45°]s and the plate is made of graphite/epoxy unidirectional laminate, material properties denoted as 5 in Table 1. The geometric size of the plate and the corresponding meshes are shown in Fig. 9. The deflections are induced by an applied uniform electric field of 394 V/mm, of opposite polarity at the upper and lower piezoelectric patches. The following nondimensional deflection parameters are computed by the present element model (HS) and shown in Figs. 10–12:

$$W_L = w_2/C, \quad W_T = [w_2 - (w_1 + w_3)/2]/C$$

$$\text{and} \quad W_R = (w_3 - w_1)/C,$$

which correspond to longitudinal bending, transverse bending and lateral twisting deflections. In the above equations, w_2, w_1, and w_3 are the transverse displacement along the midline and the two edges, respectively, and C is the width of the plate. For comparative purpose, the experimental results of Crawly and Lazarus [28] and the finite element predictions of Ha et al. [7] are also included in the figures. The element models developed by Ha et al. [7] are eight-node solid elements with nine incompatible displacement modes. These incompatible elements suffer from shear locking when the elements are not in the form of rectangular prisms [29]. Despite the regular geometry of the elements in this example, W_R predicted by the incompatible models are apparently smaller than that obtained by the present model and the experimental measurement.

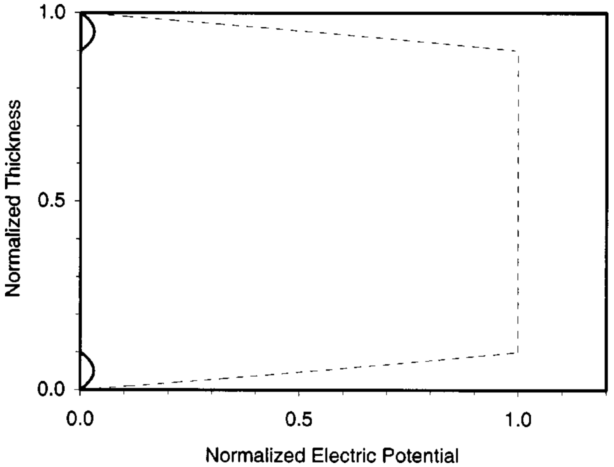

Fig. 8 Through-thickness electric potential distributions for five-ply [p/0/90/0/p] for a/h=50 (——) closed-circuit; (????) open-circuit

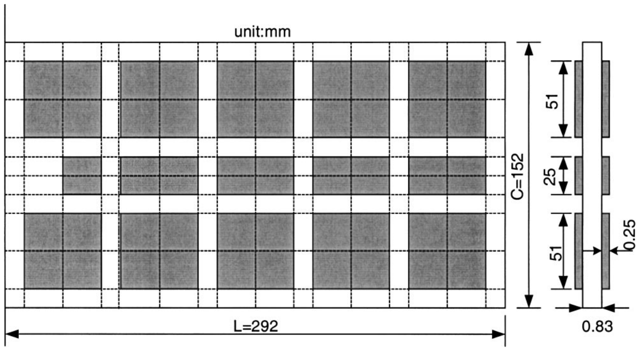

Fig. 9 A cantilever composite plate with thirty surface-bonded piezoelectric actuators

8 Conclusions

In this paper, an eight-node hexahedral solid-shell element for laminated composite structures is employed. The generalized laminate stiffness matrices are derived by the assumed natural

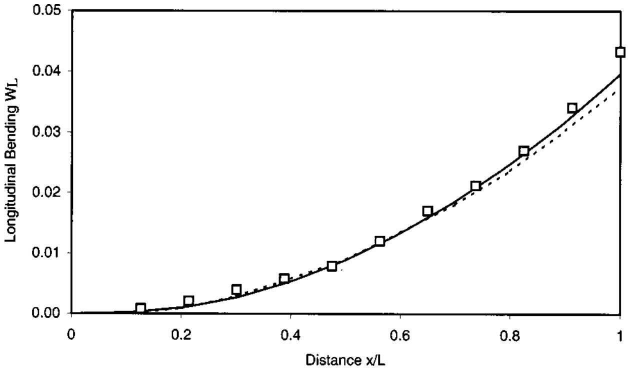

Fig. 10 Nondimensional longitudinal bending deflection of cantilever plate in Fig. 9. (——) present results; (- - - -) Ha et al. [7]; (□) experiment [Crawly and Lazarus [21]].

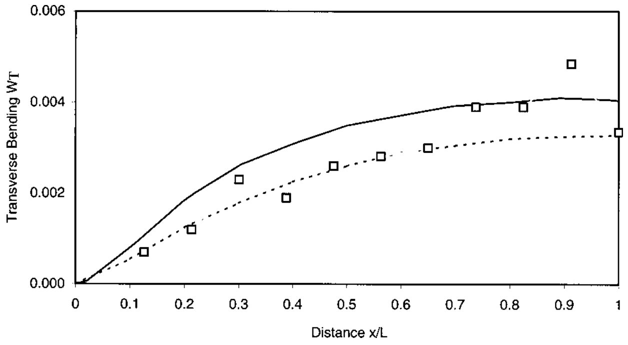

Fig. 11 Nondimensional transverse bending deflection of the cantilever plate in Fig. 9. (——) present result; (- - - -) Ha et al. [7]; (□) experiment [Crawly and Lazarus [21]].

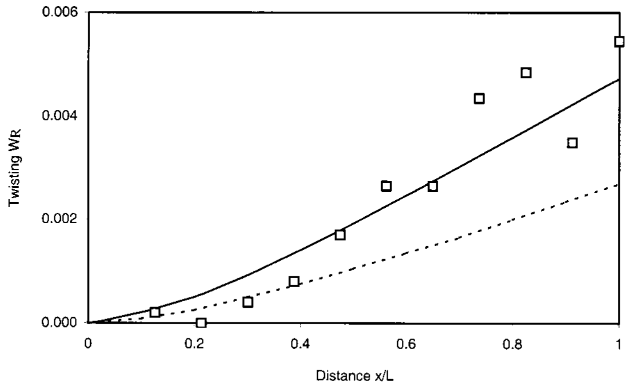

Fig. 12 Nondimensional lateral twisting deflection of the cantilever plate in Fig. 9. (——) present result; (- - - -) Ha et al. [7]; (□) experiment [Crawly and Lazarus [21]].

strain method and hybrid stress method. The developed finite element models can resolve thickness locking and some abnormalities of the solid-shell elements in laminated materials. The solid-shell elements are then generalized for modeling piezoelectric materials by including the electromechanical coupling. Unlike the conventional piezoelectric elements, the nonlinear electric potential distribution in the piezoelectric layer is described by introducing internal electric potential. Moreover, the notion of electric nodes is introduced that can conveniently take into account the equipotential effect induced by the electrodes. The developed finite element models, especially, electric node model, have the advantages of simpler modeling and can obtain same effect that exact solution described. The predicted results show that the effect on natural frequency and electric field caused by through-thickness nonlinear electric potential distribution is very small, especially, in the case of thin plate and laminate composite structure with surface bonded piezoelectric patches.

References

[1] Chandrashekhara, K., and Agarwal, A. N., 1993, "Active Vibration Control of Laminated Composite Plates Using Piezoelectric Devices: A Finite Element Approach," J. Intell. Mater. Syst. Struct., **4**, pp. 496–508.

[2] Detwiler, D. T., Shen, M. H., and Venkayya, V. B., 1995, "Finite Element Analysis of Laminated Composite Structures Containing Distributed Piezoelectric Actuators and Sensors," Finite Elem. Anal. Design, **20**, pp. 87–100.

[3] Saravanos, D. A., Heyliger, P. R., and Hopkins, D. A., 1997, "Layerwise Mechanics and Finite Element for the Dynamic Analysis of Piezoelectric Composite Plates," Int. J. Solids Struct., **34**, pp. 359–378.

[4] Hwang, W. S., and Park, H. C., 1993, "Finite Element Modelling of Piezoelectric Sensors and Actuators," AIAA J., **31**, pp. 930–937.

[5] Sze, K. Y., and Yao, L. Q., 2000, "Modeling Smart Structures With Segmented Piezoelectric Sensors and Actuators," J. Sound Vib., **235**, pp. 495–520.

[6] Sze, K. Y., Yao, L. Q., and Yi, S., 2000, "A Hybrid-Stress ANS Solid-Shell Element and Its Generalization for Smart Structure Modeling—Part II: Smart Structure Modeling," Int. J. Numer. Methods Eng., **48**, pp. 565–582.

[7] Ha, S. K., Keilers, C., and Chang, F. K., 1992, "Finite Element Analysis of Composite Structures Containing Distributed Piezoelectric Sensors and Actuators," AIAA J., **30**, pp. 772–780.

[8] Kim, J., Varadan, V. V., and Varadan, V. K., 1997, "Finite Element Modelling of Structures Including Piezoelectric Active Devices," Int. J. Numer. Methods Eng., **40**, pp. 817–832.

[9] Tzou, H. S., and Ye, R., 1996, "Analysis of Piezoelectric Structures With Laminated Piezoelectric Triangle Shell Elements," AIAA J., **34**, pp. 110–115.

[10] Tzou, H. S., Tseng, C. I., and Bahrami, H., 1994, "A Thin Piezoelectric Hexahedron Finite Element Applied to Design of Smart Continua," Finite Elem. Anal. Design, **16**, pp. 27–42.

[11] Rao, S. S., and Sunar, M., 1993, "Analysis of Distributed Thermopizoelectric Sensors and Actuators in Advanced Intelligent Structures," Am. Inst. Aeronautics Astron. J., **31**, pp. 1280–1286.

[12] Heyliger, P. R., and Saravanos, D. A., 1995, "Exact Free-Vibration Analysis of Laminated Plates With Embedded Piezoelectric Layers," J. Acoust. Soc. Am., **98**, pp. 1547–1557.

[13] Lee, H. J., and Saravanos, D. A., 1997, "Generalized Finite Element Formulation for Smart Multilayered Thermal Piezoelectric Composite Plates," Int. J. Solids Struct., **34**, pp. 3355–3371.

[14] Saravanos, D. A., and Heyliger, P. R., 1994, "Coupled Layerwise Analysis of Composite Beams With Embedded Piezoelectric Sensors and Actuators," J. Intell. Mater. Syst. Struct., **6**, pp. 350–363.

[15] Heyliger, P. R., Ramirez, G., and Saravanos, D. A., 1994, "Coupled Discrete-Layer Finite Elements for Laminated Piezoelectric Plates," Commun. Numer. Methods Eng., **10**, pp. 971–981.

[16] Reddy, J. N., 1999, "On Laminated Composite Plates With Integrated Sensors and Actuators," Eng. Struct., **21**, pp. 568–593.

[17] Lammering, R., 1991, "The Application of a Finite Shell Element for Composites Containing Piezoelectric Polymers in Vibration Control," Comput. Struct., **41**, pp. 1101–1109.

[18] Wang, Z. D., Chen, S. H., and Han, W. Z., 1997, "The Static Shape Control for Intelligent Structures," Finite Elem. Anal. Design, **26**, pp. 303–314.

[19] Lee, C. K., 1990, "Theory of Laminated Piezoelectric Plates for the Design of Distributed Sensors/Actuators. Part I: Governing Equations and Reciprocal Relationships," J. Appl. Mech., **57**, pp. 434–441.

[20] Sze, K. Y., and Yao, L. Q., 2000, "A Hybrid-Stress ANS Solid-Shell Element and its Generalization for Smart Structure Modeling. Part I: Solid-Shell Element Formulation," Int. J. Numer. Methods Eng., **48**, pp. 545–564.

[21] Park, K. C., and Stanley, G. M., 1986, "A Curved C0 Shell Element Based on Assumed Natural Coordinate Strains," J. Appl. Mech., **53**, pp. 278–290.

[22] Hauptmann, R., and Schweizerhof, K., 1988, "A Systematic Development of Solid-Shell Element Formulations for Linear and Nonlinear Analysis Employing Only Displacement Degrees of Freedom," Int. J. Numer. Methods Eng., **42**, pp. 49–69.

[23] Sze, K. Y., and Zhu, D., 1999, "A Quadratic Assumed Natural Strain Curved Triangular Shell Element," Comput. Methods Appl. Mech. Eng., **174**, pp. 57–71.

[24] Sze, K. Y., Yi, S., and Tay, M. H., 1997, "An Explicit Hybrid-Stabilized Eighteen-Node Solid Element for Thin Shell Analysis," Int. J. Numer. Methods Eng., **40**, pp. 1839–1856.

[25] Sze, K. Y., and Pan, Y. S., 1999, "Hybrid Finite Element Models for Piezoelectric Materials," J. Sound Vib., **26**, pp. 519–547.

[26] Pian, T. H. H., 1985, "Finite Elements Based on Consistently Assumed Stresses and Displacements," Finite Elem. Anal. Design, **1**, pp. 131–140.

[27] Sze, K. Y., 1992, "Efficient Formulation of Robust Hybrid Elements Using Orthogonal Stress/Strain Interpolants and Admissible Matrix Formulation," Int. J. Numer. Methods Eng., **35**, pp. 1–20.

[28] Crawly, J. L., and Lazarus, K. B., 1991, "Induced Strain Actuation of Isotropic and Anisotropic Plate," Am. Inst. Aeronautics Astron. J., **29**, pp. 944–951.

[29] Sze, K. Y., and Ghali, A., 1993, "An Hexahedral Element for Plates, Shells and Beams by Selective Scaling," Int. J. Numer. Methods Eng., **36**, pp. 1519–1540.

Axisymmetric Plane Stress States of an Annulus Subject to Displacive Shear Transformation

Yuwei Chi
Thomas J. Pence
Hungyu Tsai

Department of Mechanical Engineering,
Michigan State University,
East Lansing, MI 48824

We study the equilibrium stress field in an annulus composed of a material that admits stress-induced displacive phase transformation that preserves volume. A standard example is the austenite to martensite transformation in shape memory alloys. Attention is restricted to isothermal and axisymmetric load increase. The constitutive model follows a standard J_2 formulation appropriate for small strains and incorporates a single internal variable (the martensite phase fraction). A plane-stress boundary value problem is analyzed so as to determine the partitioning of the annulus into regions of (pure) austenite, (pure) martensite, and austenite/martensite mixture. Structure maps are presented, giving concise descriptions of the phase partitioning as the loads increase.

[DOI: 10.1115/1.1828062]

1 Introduction

This paper presents a detailed examination of axisymmetric stress, strain and phase fraction fields in an equilibrated annulus composed of a material that undergoes displacive shear transformation. This includes the case of shape memory alloys, which accounts for the basic interest in this problem. In view of standard notions of plane stress, we regard the annulus as a thin, flat plate. Attention is restricted to isothermal load increase at a temperature for which the more ordered crystal structure (austenite) is either stable or metastable at zero stress. In the context of shape memory materials this corresponds to temperatures above the martensite-start temperature M_s. The plate is traction free on its upper and lower faces, and subject to uniform normal traction $\sigma_{rr}=-p_i$ on its inner edge $r=r_i$, and uniform normal traction $\sigma_{rr}=-p_o$ on its outer edge $r=r_o$. This type of problem for the case of an infinite shape memory plate subject to far-field equi-biaxial load and a traction free inner edge was recently the subject of Birman [1] and so corresponds to the specializations $(r_o\rightarrow\infty, p_i=0)$ for the problem considered here. In addition to generalizing the geometry and the loading conditions of Birman [1], we utilize a more standard model for the determination of transformation strain. This more standard model does not constrain the radial normal transformation strain to be equal to the azimuthal normal transformation strain and so is in keeping with conventional J_2 style formulations. Like Birman [1], solutions involving nonconstant phase fractions require a numerical treatment, however by employing a Nadai transformation we achieve a more concise analytical formulation that in turn gives rise to certain efficiencies in the numerical treatment of the resulting two-point boundary value problem.

Engineering scale models for shape memory behavior typically introduce one or more phase fraction internal variables in order to track the transformation between the austenite phase and the martensite phase that is responsible for the shape memory effect. At present there exist a variety of such models, and the reader is referred to one of the various reviews on this subject (e.g., [2,3]). For a simpler geometry corresponding to uniaxial load, many of the most common models can be put in close equivalence with each other provided that the loading is not reversed. Loading is associated with what is typically referred to as the forward transformation (austenite to martensite). Such equivalences break down in unloading after full or partial completion of the forward transformation. This is due to the different treatments in the various models for the hysteresis associated with the reverse transformation (martensite to austenite).

For more complicated loading geometries, similar close equivalences occur in loading so long as only the forward transformation is activated. Here the work of Bondaryev and Wayman [4] evidently provides the first useful and general multi-dimensional model of such thermomechanical behavior. Their work gives what can be viewed as the J_2-style flow generalization of an infinitesimal strain uniaxial treatment. In particular, so long as unloading is not at issue, this provides a conceptual setting that in effect would apply to many current J_2-style models for displacive shear transformation. For multi-axial load, the utility of J_2-based models as a useful first approximation is apparent from experiments on shape memory alloys by Gall et al. [5] and Lim and McDowell [6] among others.

Isothermal loading response of shape memory materials has been extensively studied and modeled in the one-dimensional setting of uniaxial tension such as is appropriate for thin wires. As shown by the schematic diagram in Fig. 1(*a*), the stress-strain curve for loading is then characterized by a loading plateau as the material converts from austenite to martensite. This conversion takes place over a relatively small stress interval from $\sigma_s^{FT}(T)$ to $\sigma_f^{FT}(T)$ which depends on temperature (hence the argument T). The superscript FT denotes "forward transformation," while the subscripts refer to "start" and "finish." This is referred to as pseudoelastic behavior. The threshold stresses σ_s^{FT} and σ_f^{FT} increase with temperature at an essentially constant rate, as indicated in Fig. 1(*b*), so as to be consistent with the Clausius-Clapeyron relation. The associated modeling considerations are reviewed, for example, in [3].

Again with reference to Fig. 1(*a*), the stress-strain curve for unloading in uniaxial tension at $T>A_f$ is also characterized by a pseudoelastic unloading plateau (below the loading plateau) as the material converts martensite back to austenite (the reverse transformation). Let $\sigma_s^{RT}(T)$ and $\sigma_f^{RT}(T)$ denote the associated threshold stresses. In particular, $\sigma_f^{RT}(A_f)=0$, which is due to the fact that unloading at temperatures below A_f results in an incomplete reverse transformation. The temperature ordering $M_f<M_s<A_s<A_f$ implies for $T>A_f$ that $\sigma_f^{RT}(T)<\sigma_s^{RT}(T)<\sigma_s^{FT}(T)<\sigma_f^{FT}(T)$.

Contributed by the Applied Mechanics Division of THE AMERICAN SOCIETY OF MECHANICAL ENGINEERS for publication in the ASME JOURNAL OF APPLIED MECHANICS. Manuscript received by the Applied Mechanics Division, July 8, 2003; final revision, August 16, 2004. Associate Editor: K. Ravi-Chandar. Discussion on the paper should be addressed to the Editor, Prof. Robert M. McMeeking, Journal of Applied Mechanics, Department of Mechanical and Environmental Engineering, University of California—Santa Barbara, Santa Barbara, CA 93106-5070, and will be accepted until four months after final publication in the paper itself in the ASME JOURNAL OF APPLIED MECHANICS.

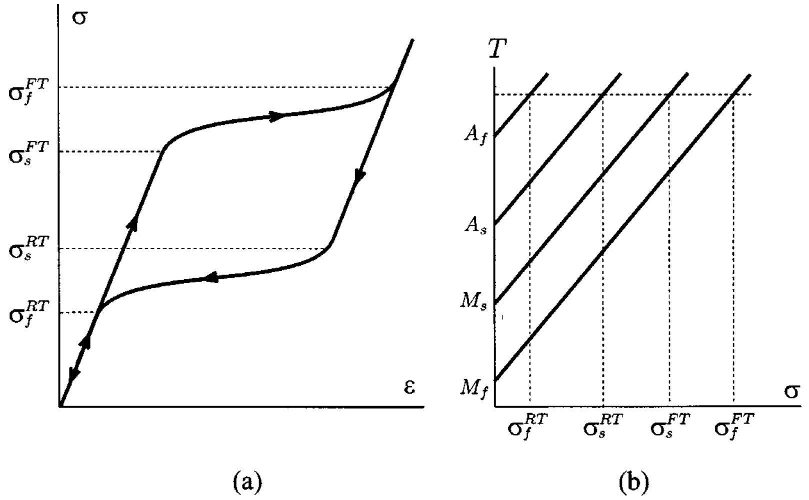

Fig. 1 (*a*) **Typical one-dimensional stress-strain curve for $T>A_f$. (*b*) Temperature dependence of threshold stresses σ_s^{FT}, σ_f^{FT}, σ_s^{RT} and σ_f^{RT}.**

Since the stress is essentially uniform in a thin wire, the conversion of austenite to martensite takes place over a relatively small load interval. For more complicated geometries, such as the plate geometry considered in this paper, the conversion of the entire structure from the austenite to the martensite state may take place over an appreciable range of load. Over this load range, it is necessary to describe the partitioning of the structure into regions of austenite, martensite and their mixture. For this purpose, it is standard practice to employ a field variable, here ξ, for the volumetric phase fraction of martensite within a general mixture of austenite and martensite. From the viewpoint of continuum mechanics, ξ is an internal variable as it describes additional microstructure features at each point in the continuum. At each radial value r, the phase fraction ξ is determined from the effective stress. If the temperature is not constant, then the phase fraction ξ is determined from both effective stress and temperature.

It is to be noted that certain shape memory models further refine such a phase fraction field variable so as to distinguish different types or different variants of martensite and to properly account for the directionality of transformation strain. The same effect can typically be achieved in J_2 theories without such refinement by specifying transformation strain in terms of the stress deviator [4].

We do not consider unloading issues associated with the reverse transformation from martensite back to austenite even though the present modeling framework is sufficiently general to accommodate this extension. If both forward and reverse transformations occur, then the phase fraction ξ depends not only on the current values of effective stress and temperature but also on their past history. It is at this juncture that the various models exhibit marked differences in the treatment of the associated phase fraction hysteresis. Further brief commentary on such extended modeling is presented in the next section.

In the next section we also formulate the boundary value problem for the annulus. Similar boundary value problems have been considered for materials that admit dilatational martensitic transformation [7] instead of the shearing martensitic transformation considered here. Dilatational martensitic transformation is responsible for transformation toughening in certain ceramic materials [8]. On the other hand, the martensitic transformations associated with shape memory behavior in metal alloys have little, if any, volume change and the associated continuum models invoke transformation strains that are volume preserving.

The boundary value problem of interest here reduces to two ordinary differential equations; one follows from the stress equations of equilibrium and the other follows from the dependence of ξ upon effective stress. No additional assumptions are introduced, such as the assumption in [1] which postulates that the ratio $\sigma_{rr}/\sigma_{\theta\theta}$, as a function of r, shares the same formula as that of the elastic solution. Indeed we find that such an assumption is not obeyed, due to a significant redistribution of stress associated with the martensitic transformation.

Additional analytical simplification follows by employing a change of variables due to Nadai [9]. The associated boundary value problem admits simple closed form solutions for the case in which no transformation takes place anywhere within the plate. In all other cases we find it necessary to employ a numerical procedure to obtain solutions. However, in all cases it does follow analytically that the effective stress is a nonincreasing function of r. Thus the martensite phase fraction is also nonincreasing with r. The most general phase distribution involves a plate that is partitioned into an inner martensite ring ($r_i<r<r_{\mathcal{M}}$), an intermediate ring involving phase coexistence ($r_{\mathcal{M}}<r<r_{\mathcal{A}}$), and an outer ring of austenite ($r_{\mathcal{A}}<r<r_o$) as shown in Fig. 2. Less complicated phase arrangements involve only one or two such rings. In this

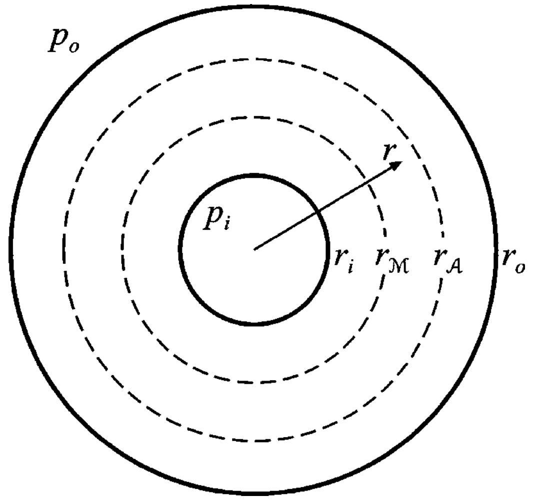

Fig. 2 Generic phase distribution within the shape memory alloy annulus. The inner ring $\mathcal{M}$ ($r_i \leq r \leq r_{\mathcal{M}}$) consists of martensite. The outer ring $\mathcal{A}$ ($r_{\mathcal{A}} \leq r \leq r_o$) consists of austenite. The intermediate ring $\mathcal{C}$ ($r_{\mathcal{M}}<r<r_{\mathcal{A}}$) consists of an austenite/martensite mixture.

setting a quasi-static program of increasing loads (p_i, p_o) results in the original austenite ring for $(p_i, p_o)=(0,0)$ giving way to a two-ring structure via the emergence of the mixture zone at the inner boundary. The emergence itself corresponds to the special case wherein $r_{\mathcal{A}}=r_i$. The particular combinations (p_i, p_o) associated with the emergence of the mixture zone can be computed analytically.

Further increase in (p_i, p_o) causes the interface $r=r_{\mathcal{A}}$ to advance from the inner radius into the interior of the plate. Eventually the loads (p_i, p_o) may increase to values such that the interface $r=r_{\mathcal{A}}$ encounters the outer boundary $r=r_o$. The loads may also increase to values such that the second interface $r=r_{\mathcal{M}}$ emerges at the inner boundary $r=r_i$, heralding the conclusion of the austenite to martensite transformation at that location. Continued load increase now also advances the second front into the plate. At a fixed radius r, passage of the first front initiates the austenite-to-martensite transformation and passage of the second front completes this transformation.

Values of (p_i, p_o) associated with either scenario $r_{\mathcal{A}}=r_o$ or $r_{\mathcal{M}}=r_i$ can be obtained numerically. Either scenario may occur first, depending on the geometry (characterized by r_i and r_o) and on the constitutive parameters. Similar ring shaped zones describe configurations associated with dilatant phase transformations, and the work of Giannakopoulos and Olson [7] shows how the development of such zones is sensitive to various modeling assumptions on the nature of the dilitant transformation. For the displacive shear transformations considered here the partitioning of the plate into various pure and mixed phase regions is described with the aid of structure maps in the (p_i, p_o) plane. The structure map is completed by determining the loads associated with the disappearance of the second front $r=r_{\mathcal{M}}$ at the plate outer boundary $r=r_o$. Thus a general structure map consists of four closed curves in the (p_i, p_o) plane associated with the conditions $r_{\mathcal{A}}=r_i$, $r_{\mathcal{A}}=r_o$, $r_{\mathcal{M}}=r_i$, and $r_{\mathcal{M}}=r_o$. Examples of various structure maps are presented in Sec. 6.

2 Problem Statement

Following a standard development [10] we consider a plate of constant thickness in the shape of an annulus with inner radius r_i and outer radius r_o (Fig. 2). It is held at a constant temperature and prior to loading is everywhere in the austenite phase. It is subject to uniform edge thrusts described by

$$\begin{aligned} \sigma_{rr}&=-p_o \quad \text{at } r=r_o, \\ \sigma_{rr}&=-p_i \quad \text{at } r=r_i. \end{aligned} \tag{1}$$

There is no shear traction on the boundaries. This setting is consistent with axisymmetric radial displacement $u_r(r)$ and vanishing azimuthal displacement $u_\theta=0$. A plane stress solution of the plate involves only σ_{rr} and $\sigma_{\theta\theta}$, both functions of r only.

The equilibrium equations reduce to the single equation

$$\frac{d\sigma_{rr}}{dr}+\frac{\sigma_{rr}-\sigma_{\theta\theta}}{r}=0. \tag{2}$$

Attention is restricted to infinitesimal strains. The polar coordinate system provides a principal frame in which the in-plane strains are given by

$$\varepsilon_{rr}=\frac{du_r}{dr} \qquad \text{and} \qquad \varepsilon_{\theta\theta}=\frac{u_r}{r}. \tag{3}$$

The out-of-plane strain ε_{zz} need not enter the problem formulation, but can be determined from the constitutive description as shown in what follows. To maintain compatibility, the in-plane strain components in (3) must satisfy

$$\varepsilon_{rr}=\frac{d(r\varepsilon_{\theta\theta})}{dr}. \tag{4}$$

The plate is composed of a material capable of transforming between the two distinct phases of martensite and austenite. The martensite phase fraction is denoted by ξ so that $\xi=1$ corresponds to martensite and $\xi=0$ corresponds to austenite, while $0<\xi<1$ indicates a state of austenite/martensite mixture. In general ξ varies with radial location. The strains are additively decomposed into two parts, the elastic part which can be expressed in terms of stresses, and the inelastic part consisting of the transformation strains that result from phase transformation:

$$\begin{aligned} \varepsilon_{rr}&=(\sigma_{rr}-\nu\sigma_{\theta\theta})/E+\varepsilon_r^{\text{tran}}, \\ \varepsilon_{\theta\theta}&=(\sigma_{\theta\theta}-\nu\sigma_{rr})/E+\varepsilon_\theta^{\text{tran}}, \\ \varepsilon_{zz}&=-\nu(\sigma_{rr}+\sigma_{\theta\theta})/E+\varepsilon_z^{\text{tran}} \end{aligned} \tag{5}$$

where E is the Young's modulus, ν is the Poisson's ratio, and $\varepsilon_r^{\text{tran}}$, $\varepsilon_\theta^{\text{tran}}$ and $\varepsilon_z^{\text{tran}}$ are the transformation strains. In the present analysis, the elastic moduli are taken to be the same in both austenite and martensite. Conventional thermal expansion is not considered here as the analysis is isothermal.

Let $\boldsymbol{\tau}$ be the stress tensor and $\mathbf{1}$ be the identity tensor so that $\mathbf{S}=\boldsymbol{\tau}-1/3(\text{tr}\,\boldsymbol{\tau})\mathbf{1}$ is the deviatoric stress tensor and $J_2=1/2\text{tr}(\mathbf{S}^T\mathbf{S})$. The transformation strain tensor $\boldsymbol{\varepsilon}^{\text{tran}}$ is taken to be in the same direction as $\mathbf{S}$ and proportional to ξ, specifically

$$\boldsymbol{\varepsilon}^{\text{tran}}=\frac{\mathbf{S}}{\sqrt{\text{tr}(\mathbf{S}^T\mathbf{S})}}\sqrt{3/2}\,\alpha\xi. \tag{6}$$

Note that $\text{tr}\,\boldsymbol{\varepsilon}^{\text{tran}}=0$, indicating that the phase transformation by itself is volume preserving in the present small strain setting. The material constant α in (6) corresponds to the axial transformation strain under uniaxial load for complete conversion of austenite to martensite. Namely if $\boldsymbol{\tau}=\sigma_{xx}\mathbf{e}_1\otimes\mathbf{e}_1$ then $\boldsymbol{\varepsilon}^{\text{tran}}=\alpha\xi(\mathbf{e}_1\otimes\mathbf{e}_1-1/2\mathbf{e}_2\otimes\mathbf{e}_2-1/2\mathbf{e}_3\otimes\mathbf{e}_3)$ so that $\varepsilon_{xx}^{\text{tran}}=\alpha$ if the forward transformation is complete ($\xi=1$). The expression (6) is a deformation version of the flow rule in the model of Bondaryev and Wayman [4]. Namely, their model gives the specification of $d\boldsymbol{\varepsilon}^{\text{tran}}$ rather than $\boldsymbol{\varepsilon}^{\text{tran}}$. The present deformation version follows closely the recent formulation of Briggs and Ostrowski [11]. It is expected that J_2-style theories would generally involve either a formulation like (6) or else an associated rate version (see for example (3.25) of [12]). Recently, for example, Briggs and Ponte Castaneda [13] have employed such a model to estimate the effective behavior of shape memory alloy fiber composites.

Specializing (6) to the case of plane stress gives

$$\begin{aligned} \varepsilon_r^{\text{tran}}&=\frac{2\sigma_{rr}-\sigma_{\theta\theta}}{2\sigma}\alpha\xi, \\ \varepsilon_\theta^{\text{tran}}&=\frac{2\sigma_{\theta\theta}-\sigma_{rr}}{2\sigma}\alpha\xi, \\ \varepsilon_z^{\text{tran}}&=-\frac{\sigma_{\theta\theta}+\sigma_{rr}}{2\sigma}\alpha\xi, \end{aligned} \tag{7}$$

where σ is the effective stress given by

$$\sigma=\sqrt{\sigma_{rr}^2-\sigma_{rr}\sigma_{\theta\theta}+\sigma_{\theta\theta}^2}. \tag{8}$$

The effective stress σ for general three-dimensional analysis is $\sqrt{3\text{tr}(\mathbf{S}^T\mathbf{S})/2}=\sqrt{3J_2}$ and so reduces to (8) for our problem. Note from (7) that $\varepsilon_r^{\text{tran}}\neq\varepsilon_\theta^{\text{tran}}$ if $\sigma_{rr}\neq\sigma_{\theta\theta}$. This differs from the constitutive assumption $\varepsilon_r^{\text{tran}}=\varepsilon_\theta^{\text{tran}}$ employed in [1] [Eq. (5)]. The effective stress can be regarded as a scalar representation of the shear character resident in the stress tensor. That this dictates the martensite phase fraction is consistent with experiments on shape memory alloys showing for these materials that shear is the predominant factor in stress induced martensitic transformation [14].

For J_2-style theories the dependence of ξ on $\boldsymbol{\tau}$ is only through J_2 or equivalently only through σ. Starting from a state of pure austenite ($\xi=0$), let $g^{FT}(\sigma,T)$ give the phase fraction ξ for uninterrupted forward transformation. Any J_2-style theory will define such a function, which for our purposes is referred to as the forward envelope function. In a similar fashion, the reverse envelope function $g^{RT}(\sigma,T)$ gives ξ for uninterrupted reverse transformation starting from a state of pure martensite ($\xi=1$). An example of such a σ-ξ curve for $T>A_f$ is shown in Fig. 3. Such envelope functions play a role that is analogous to yield surface functions in traditional plasticity theory. A useful approximation for $g^{FT}(\sigma,T)$ and $g^{RT}(\sigma,T)$ is then (cf. [15])

$$g^{FT}(\sigma,T)=\begin{cases}1 & \text{for } \sigma\geqslant\sigma_f^{FT}(T),\\ \dfrac{1}{2}\left[1-\cos\left(\dfrac{\sigma-\sigma_s^{FT}(T)}{\sigma_f^{FT}(T)-\sigma_s^{FT}(T)}\,\pi\right)\right] & \text{for } \sigma_s^{FT}(T)<\sigma<\sigma_f^{FT}(T),\\ 0 & \text{for } \sigma\leqslant\sigma_s^{FT}(T),\end{cases} \tag{9}$$

with similar construction for $g^{RT}(\sigma,T)$. This framework is sufficient for the description of complete transformation behavior, but incompletely posed for the description of partial transformation behavior associated with subloops. Extensions that allow for the description of subloops due to partial transformation followed by transformation reversal can be accomplished in this framework, but such extensions are highly model dependent. For example, Duhem-Madelung hysteresis models extend the above framework using history dependent kinetic rules framed in terms of differential equations that depend on the envelope functions [16]. Other models, such as those using a Preisach algorithm, are not quite so conveniently described [3]. As the present study restricts attention only to the forward transformation starting from pure austenite, such considerations are not germane.

In this paper, attention is restricted to the case of isothermal loading beginning from pure austenite as may occur for $T>M_s$. Loading here refers to conditions such that effective stress σ at each location r is increasing with time (or keeps the same value) whereupon the reverse transformation is never activated. Under such circumstances, temperature can be dropped from the notation and only the forward transformation need be considered. Hence Eq. (9) is rewritten as

$$g(\sigma)=\begin{cases}1 & \text{for } \sigma\geqslant\sigma_f,\\ \dfrac{1}{2}\left[1-\cos\left(\dfrac{\sigma-\sigma_s}{\sigma_f-\sigma_s}\,\pi\right)\right] & \text{for } \sigma_s<\sigma<\sigma_f,\\ 0 & \text{for } \sigma\leqslant\sigma_s\end{cases} \tag{10}$$

by employing the following replacement:

$$g^{FT}(\sigma,T)\to g(\sigma),\quad \sigma_s^{FT}(T)\to\sigma_s,\quad \sigma_f^{FT}(T)\to\sigma_f. \tag{11}$$

In this convention, we have $\xi=g(\sigma)$ with $\xi=0$ if $\sigma\leqslant\sigma_s$ and $\xi=1$ if $\sigma\geqslant\sigma_f$. In general the martensite fraction function $g(\sigma)$ is a continuous, differentiable and nondecreasing function, obeying $0\leqslant g(\sigma)\leqslant 1$. This definition of ξ together with (5) and (7) implies tension/compression symmetry for such purely J_2-style models. A useful extension that allows tension/compression asymmetry in an otherwise initially isotropic setting involves the refinement $g=g(\sigma,J_3)$, where $J_3=\det\mathbf{S}$ as considered, for example, in [12,17].

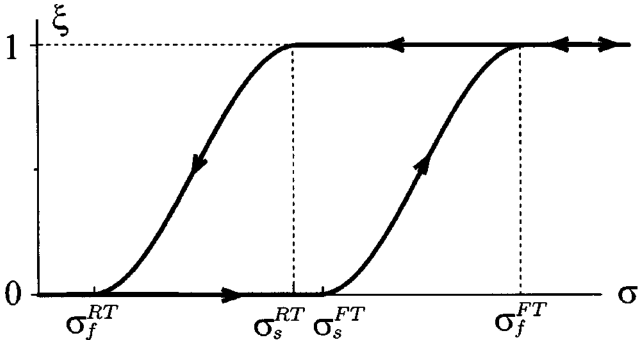

Fig. 3 Martensite phase fraction as a function of effective stress for $T>A_f$

The framework presented above is sufficient for the determination of how the plate transforms from austenite to martensite due to change in the thrusts p_i and p_o. If the applied thrusts (p_i,p_o) are regarded as functions of time, then the stresses, strains and phase fraction are also functions of time. It is assumed that the thrust loads change slowly so that the effect of inertia on the deformation and phase transformation can be neglected. This allows for the interpretation in terms of quasi-static phase evolution within the plate as discussed in the Introduction.

In the present treatment $\xi(r)$ is a continuous function of r obeying $0\leqslant\xi(r)\leqslant 1$. For fixed p_i and p_o the plate can be in one of three broad phase states: a fully austenite state denoted by $\mathcal{A}$ meaning that $\xi(r)$ is identically zero, a fully martensite state denoted by $\mathcal{M}$ meaning that $\xi(r)$ is identically 1, or some kind of combined state denoted through the use of $\mathcal{C}$ meaning that there is at least one value of r such that $0<\xi(r)<1$.

3 A Useful Reformulation

Equations (5) and (7) lead to the following expression for the in-plane strains

$$\begin{aligned}\varepsilon_{rr}&=\frac{1}{E}(\sigma_{rr}-\nu\sigma_{\theta\theta})+\left(\frac{1}{E_s(\sigma)}-\frac{1}{E}\right)\left(\sigma_{rr}-\frac{1}{2}\sigma_{\theta\theta}\right),\\ \varepsilon_{\theta\theta}&=\frac{1}{E}(\sigma_{\theta\theta}-\nu\sigma_{rr})+\left(\frac{1}{E_s(\sigma)}-\frac{1}{E}\right)\left(\sigma_{\theta\theta}-\frac{1}{2}\sigma_{rr}\right),\end{aligned} \tag{12}$$

where $E_s(\sigma)$ is the secant modulus given by

$$E_s(\sigma)=\frac{1}{1/E+\alpha\xi/\sigma}=\frac{1}{1/E+\alpha g(\sigma)/\sigma}. \tag{13}$$

Substituting from (12) into the compatibility condition (4) now gives

$$\frac{\mathrm{d}}{\mathrm{d}r}(\sigma_{rr}+\sigma_{\theta\theta})-\frac{2\sigma_{\theta\theta}-\sigma_{rr}}{2E_s(\sigma)}\frac{\mathrm{d}}{\mathrm{d}r}E_s(\sigma)=0, \tag{14}$$

in which the equilibrium equation (2) has been used to eliminate the terms involving the Poisson's ratio. The absence of the Poisson's ratio is not unexpected for the case of plane stress as discussed for example by Budiansky [18] in the context of what is known as the extended Michell's theorem. This theorem gives that the stress field for a traction boundary value problem is independent of Poisson's ratio for the type of problems under consideration here. Rather than directly substituting from (8) into (14), we introduce the following change of variables due to Nadai [9]:

$$\begin{aligned}\sigma_{rr}&=\frac{2\sigma}{\sqrt{3}}\sin\left(\beta+\frac{\pi}{6}\right),\\ \sigma_{\theta\theta}&=\frac{2\sigma}{\sqrt{3}}\sin\left(\beta-\frac{\pi}{6}\right),\end{aligned}\qquad (\sigma>0) \tag{15}$$

where β is a function of r and for convenience is taken as obeying $0\leqslant\beta<2\pi$. Notice that the stresses given by (15) automatically satisfy (8).

By virtue of the definition of $E_s(\sigma)$ given in (13), the equilibrium (2) and the compatibility (14) can be written in terms of $\sigma=\sigma(r)$ and $\beta=\beta(r)$ as

$$\begin{gathered}\sin\left(\beta+\frac{\pi}{6}\right)\frac{\mathrm{d}\sigma}{\mathrm{d}r}+\sigma\cos\left(\beta+\frac{\pi}{6}\right)\frac{\mathrm{d}\beta}{\mathrm{d}r}=-\frac{\sigma\cos\beta}{r},\\ \left[\sin\beta-\frac{E\alpha(g-\sigma g')}{2(E\alpha g+\sigma)}\sin(\beta-\pi/3)\right]\frac{\mathrm{d}\sigma}{\mathrm{d}r}+\sigma\cos\beta\,\frac{\mathrm{d}\beta}{\mathrm{d}r}=0,\\ (\sigma>0)\end{gathered} \tag{16}$$

where for simplicity $g(\sigma)$ is written as g and $g'=g'(\sigma)$ denotes the derivative $\mathrm{d}g/\mathrm{d}\sigma$. Solving (16) for $\mathrm{d}\sigma/\mathrm{d}r$ and $\mathrm{d}\beta/\mathrm{d}r$ gives

$$\begin{aligned}\frac{\mathrm{d}\sigma}{\mathrm{d}r}&=-\frac{\sigma^2\cos^2\beta}{r\Delta},\\ \frac{\mathrm{d}\beta}{\mathrm{d}r}&=\frac{\sigma\cos\beta}{r\Delta}\left[\sin\beta-\frac{E\alpha(g-\sigma g')}{2(E\alpha g+\sigma)}\sin(\beta-\pi/3)\right]\end{aligned}\qquad(\sigma>0) \tag{17}$$

with Δ given by

$$\Delta=\frac{\sigma}{2}\left[1-\frac{E\alpha(g-\sigma g')}{E\alpha g+\sigma}\cos^2(\beta+\pi/6)\right]. \tag{18}$$

Note that the dependence of governing equations (17) and (18) on parameters E and α is solely through the product $E\alpha$ which serves as a basic measure of complete transformation stress in the sense of a one-dimensional description.

By definition $\sigma>0$ and E, α, g, and g' are non-negative, therefore $\Delta>0$. It follows from (17) with $\Delta>0$ that

$$\frac{\mathrm{d}\sigma}{\mathrm{d}r}\leqslant 0. \tag{19}$$

Thus the maximum effective stress $\sigma_{\max}$ occurs at $r=r_i$ and the minimum effective stress $\sigma_{\min}$ occurs at $r=r_o$. Accordingly $\mathrm{d}\xi/\mathrm{d}r\leqslant 0$ whereupon there are six possible phase distributions: $\mathcal{A}$, $\mathcal{M}$, $\mathcal{C}$, $\mathcal{AC}$, $\mathcal{CM}$, $\mathcal{ACM}$, as follows:

$$\begin{aligned}&\mathcal{A}:\quad \xi(r_i)=0\Leftrightarrow\sigma(r_i)\leqslant\sigma_s,\\ &\mathcal{AC}:\quad 1>\xi(r_i)>0,\ \xi(r_o)=0\Leftrightarrow\sigma_f>\sigma(r_i)>\sigma_s,\ \sigma(r_o)\leqslant\sigma_s,\\ &\mathcal{ACM}:\quad \xi(r_i)=1,\ \xi(r_o)=0\Leftrightarrow\sigma(r_i)\geqslant\sigma_f,\ \sigma(r_o)\leqslant\sigma_s,\\ &\mathcal{C}:\quad 1>\xi(r_i)>0,\ \xi(r_o)>0\Leftrightarrow\sigma_f>\sigma(r_i)\geqslant\sigma(r_o)>\sigma_s,\\ &\mathcal{CM}:\quad \xi(r_i)=1,\ 1>\xi(r_o)>0\Leftrightarrow\sigma(r_i)\geqslant\sigma_f,\ \sigma_f>\sigma(r_o)>\sigma_s,\\ &\mathcal{M}:\quad \xi(r_o)=1\Leftrightarrow\sigma(r_o)\geqslant\sigma_f.\end{aligned} \tag{20}$$

The phase distribution $\mathcal{AC}$ involves an austenite outer ring on $r_{\mathcal{A}}<r<r_o$ and a mixture zone on an inner ring $r_i<r<r_{\mathcal{A}}$. The separating interface $r=r_{\mathcal{A}}$ is associated with satisfaction of the condition $\sigma(r_{\mathcal{A}})=\sigma_s$. The phase distribution $\mathcal{CM}$ involves a mixture zone on an outer ring $r_{\mathcal{M}}<r<r_o$ and a martensite inner ring $r_i<r<r_{\mathcal{M}}$. The separating interface $r=r_{\mathcal{M}}$ is associated with satisfaction of the condition $\sigma(r_{\mathcal{M}})=\sigma_f$. The phase distribution $\mathcal{ACM}$ involves three rings: an austenite outer ring $r_{\mathcal{A}}<r<r_o$, a mixture zone on an intermediate ring $r_{\mathcal{M}}<r<r_{\mathcal{A}}$, and a martensite inner ring $r_i<r<r_{\mathcal{M}}$. These are the same type of structures as obtained in [1].

From the first equation of (17), it follows that a constant effective stress field requires either $\beta=\pi/2$ or $\beta=3\pi/2$. These correspond to uniform equi-biaxial stress solutions $\sigma_{rr}(r)=\sigma_{\theta\theta}(r)=-p$ so that $\sigma=|p|$. Such solutions occur if and only if $p_o=p_i$ and are the only solutions with effective stress $\sigma(r)=\text{const}$. Here $p_i=p_o=p>0$ gives $\beta=3\pi/2$ and $p_i=p_o=p<0$ gives $\beta=\pi/2$. The phase distribution for uniform equi-biaxial stress is respectively of type $\mathcal{A}$, $\mathcal{C}$, $\mathcal{M}$ according to whether $|p|\leqslant\sigma_s$, $\sigma_s<|p|<\sigma_f$, $|p|\geqslant\sigma_f$.

For the generic case $p_o\neq p_i$, it follows that (19) holds with strict inequality. To obtain the effective stress distribution requires integration of (17). Note for example that, if $(\sigma^*(r),\beta^*(r))$ is a solution of (17) corresponding to boundary conditions $\sigma_{rr}=-p_i^*$ at $r=r_i$ and $\sigma_{rr}=-p_o^*$ at $r=r_o$, then $(\sigma^*(r),\beta^*(r)+\pi)$ is a solution corresponding to boundary conditions $\sigma_{rr}=+p_i^*$ at $r=r_i$ and $\sigma_{rr}=+p_o^*$ at $r=r_o$. Therefore in the (p_i,p_o) plane, two load pairs that are related to each other by a 180 deg rotation about the origin will produce the same distribution of effective stress and hence the same phase configuration in the plate. This symmetric property is inherent in the constitutive model in view of its tension/compression symmetry.

Now if σ and β are specified at some location r, then Eqs. (17) can in principle be integrated for $\sigma=\sigma(r)$, $\beta=\beta(r)$. However, boundary conditions in the original form (1) do not generate conditions for (σ,β) at any one point. Generally, the iterated shooting method [19] can be used in the case of two-point boundary conditions such as (1). The iterated shooting method can be avoided for the case of alternative boundary conditions wherein both σ and σ_{rr} are specified at one boundary. In particular this provides a direct procedure for studying the four special conditions $r_{\mathcal{A}}=r_i$, $r_{\mathcal{A}}=r_o$, $r_{\mathcal{M}}=r_i$, $r_{\mathcal{M}}=r_o$ that are associated with transitions between the different phase distribution types in (20).

4 A Fully Austenitic Plate ($\mathcal{A}$ Phase Distribution)

This section considers plates that are completely in the austenite phase and so correspond to a phase distribution of type $\mathcal{A}$ in (20). This requires $\sigma\leqslant\sigma_s$ everywhere in the plate, hence $g=g'=0$, $\Delta=\sigma/2$ and Eq. (17) reduces to

$$\frac{\mathrm{d}\sigma}{\mathrm{d}r}=-\frac{2\sigma\cos^2\beta}{r}\quad\text{and}\quad\frac{\mathrm{d}\beta}{\mathrm{d}r}=\frac{2\sin\beta\cos\beta}{r}. \tag{21}$$

The solution to Eq. (21) is given by

$$\begin{gathered}\sigma\sin\beta=c_1\quad\text{and}\quad\sin\beta/\cos\beta=c_2r^2\quad\text{for }\cos\beta\neq 0,\\ \sigma=c_3\quad\text{for }\cos\beta=0\end{gathered} \tag{22}$$

where c_1, c_2, and c_3 are constants to be determined by the boundary conditions. Radial stress σ_{rr} and hoop stress $\sigma_{\theta\theta}$ can be obtained by substituting (22) into (15) as

$$\begin{gathered}\sigma_{rr}=c_1+\frac{c_1}{\sqrt{3}c_2r^2}\quad\text{and}\quad\sigma_{\theta\theta}=c_1-\frac{c_1}{\sqrt{3}c_2r^2}\quad\text{for }\cos\beta\neq 0,\\ \sigma_{rr}=\sigma_{\theta\theta}=\pm c_3\quad\text{for }\cos\beta=0\end{gathered} \tag{23}$$

and it follows from this equation that $\cos\beta=0$ if and only if $p_i=p_o$.

If $p_i\neq p_o$, then the constants c_1 and c_2 can be obtained from the first equation of (23) as

$$c_1=\frac{p_ir_i^2-p_or_o^2}{r_o^2-r_i^2}\quad\text{and}\quad c_2=\frac{p_ir_i^2-p_or_o^2}{\sqrt{3}(p_o-p_i)r_i^2r_o^2}\quad\text{for }p_i\neq p_o. \tag{24}$$

If instead $p_i=p_o=p$, then the second equation of (23) gives $c_3=|p|$ whereupon

$$\sigma_{rr}(r)=\sigma_{\theta\theta}(r)=-p, \quad \sigma(r)=|p| \quad \text{for } p_i=p_o. \tag{25}$$

Equations (23)–(25) together retrieve the classical linear elastic solution, with in-plane stress given by

$$\begin{aligned}\sigma_{rr}&=\frac{p_ir_i^2-p_or_o^2}{r_o^2-r_i^2}+\frac{(p_o-p_i)r_i^2r_o^2}{(r_o^2-r_i^2)r^2},\\ \sigma_{\theta\theta}&=\frac{p_ir_i^2-p_or_o^2}{r_o^2-r_i^2}-\frac{(p_o-p_i)r_i^2r_o^2}{(r_o^2-r_i^2)r^2}.\end{aligned} \tag{26}$$

The effective stress is given by

$$\sigma=\hat{\sigma}(r):=\frac{\sqrt{(r_o^2p_o-r_i^2p_i)^2+3r_i^4r_o^4(p_i-p_o)^2/r^4}}{r_o^2-r_i^2}. \tag{27}$$

The maximum and minimum effective stresses are given by $\sigma_{\max}=\hat{\sigma}(r_i)$ and $\sigma_{\min}=\hat{\sigma}(r_o)$, respectively.

The validity of this solution requires $\sigma_{\max}\leqslant\sigma_s$. The case $\sigma_{\max}=\sigma_s$ is associated with parameter values obeying

$$(r_i^4+3r_o^4)p_i^2-2r_o^2(r_i^2+3r_o^2)p_ip_o+4r_o^4p_o^2=(r_o^2-r_i^2)^2\sigma_s^2. \tag{28}$$

Equation (28) defines an ellipse in the (p_i,p_o) plane containing the origin $(p_i,p_o)=(0,0)$. Values (p_i,p_o) internal to this ellipse are associated with an $\mathcal{A}$ phase distribution. This ellipse will be referred to as the *fully austenitic loop* (FAL) in the (p_i,p_o) plane and corresponds to the transitional condition $r_{\mathcal{A}}=r_i$. The FAL is symmetric with respect to 180° rotation about the origin, a consequence of the tension/compression symmetry in the modeling description. In the sequel additional curves will be constructed in the (p_i,p_o) plane, thus giving rise to a fully articulated *structure map* that distinguishes between the phase distribution possibilities (20).

An alternative way of obtaining the FAL is to solve (21) subject to a requirement $\sigma(r_i)=\sigma_s$. If $\beta(r_i)=\beta_0\neq\pi/2,\ 3\pi/2$, then according to (22) c_1 and c_2 are given by $c_1=\sigma_s\sin\beta_0$ and $c_2=\tan\beta_0/r_i^2$, hence the stresses are given by

$$\begin{aligned}\sigma_{rr}&=\sigma_s[\sin\beta_0+r_i^2\cos\beta_0/(\sqrt{3}r^2)],\\ \sigma_{\theta\theta}&=\sigma_s[\sin\beta_0-r_i^2\cos\beta_0/(\sqrt{3}r^2)],\\ \sigma&=\sigma_s\sqrt{\sin^2\beta_0+r_i^4\cos^2\beta_0/r^4}.\end{aligned} \tag{29}$$

Applied thrusts p_i and p_o are then given by

$$p_i=-\left(\sin\beta_0+\frac{\cos\beta_0}{\sqrt{3}}\right)\sigma_s$$

$$\text{and} \quad p_o=-\left(\sin\beta_0+\frac{\cos\beta_0 r_i^2}{\sqrt{3}r_o^2}\right)\sigma_s. \tag{30}$$

Equation (30) defines an ellipse in parametric form within the (p_i,p_o) plane where β_0 is the varying parameter. Solving (30) gives $\sin\beta_0$ and $\cos\beta_0$ as

$$\sin\beta_0=\frac{p_ir_i^2-p_or_o^2}{(r_o^2-r_i^2)\sigma_s} \quad \text{and} \quad \cos\beta_0=\frac{\sqrt{3}(p_o-p_i)r_o^2}{(r_o^2-r_i^2)\sigma_s}, \tag{31}$$

whereupon the identity $\sin^2\beta_0+\cos^2\beta_0=1$ retrieves (28). The use of β as a varying parameter in obtaining loops associated with the remaining transitional cases $r_{\mathcal{A}}=r_o$, $r_{\mathcal{M}}=r_i$, $r_{\mathcal{M}}=r_o$ is central to the remaining development.

5 A Fully Martensitic Plate ($\mathcal{M}$ Phase Distribution)

We now consider plates that are completely in the martensite phase, whereupon $g=1$ and $g'=0$, and Eq. (17) reduces to

$$\begin{aligned}\frac{\mathrm{d}\sigma}{\mathrm{d}r}&=-\frac{\sigma^2\cos^2\beta}{r\Delta_{\mathcal{M}}},\\ \frac{\mathrm{d}\beta}{\mathrm{d}r}&=\frac{\sigma\cos\beta}{r\Delta_{\mathcal{M}}}\left[\sin\beta-\frac{E\alpha}{2(E\alpha+\sigma)}\sin(\beta-\pi/3)\right]\end{aligned} \tag{32}$$

where $\Delta_{\mathcal{M}}$ is obtained from (18) as

$$\Delta_{\mathcal{M}}=\frac{\sigma}{2}\left[1-\frac{E\alpha}{E\alpha+\sigma}\cos^2(\beta+\pi/6)\right]. \tag{33}$$

A closed form solution to (32) is not obvious, hence prompting a numerical approach. Such solutions are valid provided $\sigma(r_o)\geqslant\sigma_f$.

As an example, Fig. 4 displays the radial variation of σ, σ_{rr} and $\sigma_{\theta\theta}$ for a plate with $E=50$ GPa, $\alpha=0.05$, $\sigma_s=75$ MPa, $\sigma_f=300$ MPa, $r_o/r_i=2$, $p_o=5\sigma_s$ and $p_i=\sigma_s$. The corresponding stress distributions for an elastic material ($\alpha=0$) subject to the same edge thrusts p_i and p_o are plotted as dashed lines. Note that the σ_{rr} distributions for these two materials are similar, but the $\sigma_{\theta\theta}$ distributions are quite different. In particular the two materials give different ratios $\sigma_{rr}/\sigma_{\theta\theta}$, therefore raising questions with respect to any assumption that such a ratio is preserved.

The equality case for the validity condition $\sigma(r_o)\geqslant\sigma_f$ defines the *fully martensitic loop* (FML) in the (p_i,p_o) plane. The FML at fixed σ_f, $E\alpha$ and r_o/r_i can be obtained from integrating Eq. (32) with boundary condition $(\sigma(r_o),\beta(r_o))=(\sigma_f,\beta_0)$ upon varying β_0 from 0 to 2π. Like the FAL, the FML is also symmetric with respect to 180° rotation about the origin. The FML corresponds to the transitional condition $r_{\mathcal{M}}=r_o$, and the region exterior to the FML corresponds to loads (p_i,p_o) that generate an $\mathcal{M}$ phase distribution. The FML will surround the FAL in the (p_i,p_o) plane, although unlike the FAL, the FML is generally not an ellipse. The region between the FAL and the FML corresponds to loads (p_i,p_o) that generate one of the phase distributions containing a mixture zone: $\mathcal{C}$, $\mathcal{AC}$, $\mathcal{CM}$ or $\mathcal{ACM}$.

Although the FML is usually determined numerically, it will pass through $(p_i,p_o)=\pm(\sigma_f,\sigma_f)$ which provides the uniform equi-biaxial stress solutions on the FML. More generally, the line $p_i=p_o$ provides the uniform equi-biaxial stress solutions in the (p_i,p_o) plane. On this line $\sigma_{rr}(r)=\sigma_{\theta\theta}(r)=-p$, giving a uniform effective stress $\sigma(r)=|p|$ and hence a phase fraction field $\xi(r)$ that is also independent of r and determined directly from p as $\xi=g(|p|)$. Hence such loading results in a phase distribution of either type $\mathcal{A}$, $\mathcal{C}$ or $\mathcal{M}$.

Figure 5 displays both the FAL and the FML for the parameters $E=50$ GPa, $\alpha=0.05$, $\sigma_s=75$ MPa, $\sigma_f=300$ MPa, and $r_o/r_i=2$. Note that the region enclosed by the FML is not convex for these parameters. Note also that the FML is highly elongated in the p_i direction compared with the p_o direction. In this case the external thrust p_o is significantly more efficient than the internal thrust p_o in promoting an $\mathcal{M}$ phase distribution. For example, a traction free inner boundary requires an outer thrust $p_o=3.39\sigma_s$ to fully martensitize the plate, whereas a traction free outer boundary requires an inner thrust $p_i=27.74\sigma_s$.

The FML is completely determined by the parameters σ_f, $E\alpha$ and r_o/r_i. Figure 6 shows the effect of varying σ_f at fixed $E\alpha$ and r_o/r_i. In particular, this figure displays a family of seven FMLs corresponding to $\sigma_f/\sigma_s=1$, 2, 3, 4, 6, 8, 10, with the other parameters set at $E=50$ GPa, $\alpha=0.05$, $\sigma_s=75$ MPa and $r_o/r_i=2$. As one would anticipate, the FMLs are nested with respect to increasing σ_f. The small internal ellipse is the common FAL. Note that the FML corresponding to $\sigma_f/\sigma_s=1$ intersects the FAL at the uniform equi-biaxial stress solutions $(p_i,p_o)=\pm(\sigma_f,\sigma_f)$. Thus if $\sigma_f=\sigma_s$, then equi-biaxial loading such that $p_i=p_o=p$ results in a uniform phase distribution of type $\mathcal{A}$ transitioning directly to a uniform phase distribution of type $\mathcal{M}$ as the common thrust value p passes through the common threshold stress $\sigma_f=\sigma_s$.

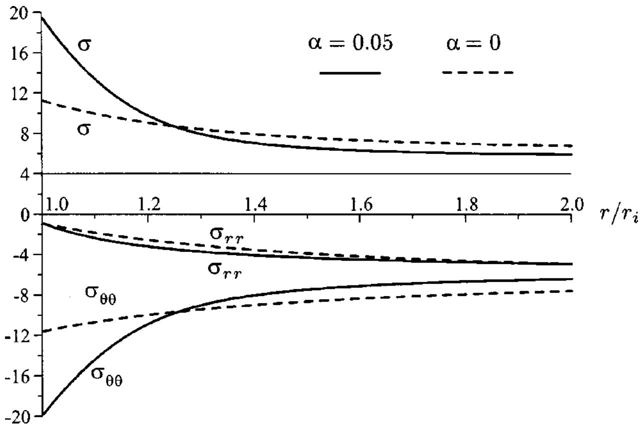

Fig. 4 Typical stress distributions (normalized by σ_s) for a plate with $\mathcal{M}$ phase distribution $[\sigma(r)\geqslant\sigma_f]$. Here $E=50$ GPa, $\sigma_f=4\sigma_s=300$ MPa, $r_o/r_i=2$ and $(p_i,p_o)=(1,5)\sigma_s$. Solid lines represent the case of $\alpha=0.05$. For comparison, stresses for an elastic solution ($\alpha=0$) under the same boundary conditions are plotted as dashed lines.

6 A Plate Containing Mixtures of Martensite and Austenite (Phase Distributions of Type: $\mathcal{AC}$, $\mathcal{ACM}$, $\mathcal{CM}$ and $\mathcal{C}$)

We now turn to consider the remaining types of phase distribution given in (20). The structure map is useful in this discussion, as all such phase distributions occur in the region between the FAL and the FML. The phase distribution in this region is ensured to be of type $\mathcal{C}$ on the line of uniform equi-biaxial load $(p_i,p_o)=(p,p)$, $\sigma_s<|p|<\sigma_f$. However, off of this line it is not yet clear what type of phase distribution occurs. To make this determination it is useful to complete the structure map via the construction of two additional curves.

The first such curve is the *austenite disappearing loop* (ADL) that is associated with solutions obeying $\sigma(r_o)=\sigma_s$ or, equivalently, $r_{\mathcal{A}}=r_o$. Austenite (unmixed with martensite) can only be present at locations on the structure map inside of the ADL. Inside the ADL the phase distribution must be of type $\mathcal{A}$, $\mathcal{AC}$, or $\mathcal{ACM}$. Outside of the ADL the phase distribution must be of type $\mathcal{C}$, $\mathcal{M}$, or $\mathcal{CM}$. The ADL is strictly within the FML so long as $\sigma_f>\sigma_s$. The ADL is also external to the FAL except at the two points of intersection $(p_i,p_o)=\pm(\sigma_s,\sigma_s)$ which are on the equi-biaxial load line of the structure map.

The final curve for completing the structure map is the *martensite emerging loop* (MEL) that is associated with solutions obeying $\sigma(r_i)=\sigma_f$ or, equivalently, $r_i=r_{\mathcal{M}}$. Martensite (unmixed with austenite) can only be present at locations on the structure map outside of the MEL. Outside the MEL the phase distribution must be of type $\mathcal{M}$, $\mathcal{CM}$, or $\mathcal{ACM}$. Inside of the MEL the phase distribution must be of type $\mathcal{C}$, $\mathcal{AC}$, or $\mathcal{A}$. The MEL is strictly outside the FAL so long as $\sigma_f>\sigma_s$. The MEL is also internal to the FML except at the two points of intersection $(p_i,p_o)=\pm(\sigma_f,\sigma_f)$ which are on the equi-biaxial load line of the structure map.

With the exception of locations on the equi-biaxial line, both the ADL and the MEL are determined numerically. This is most easily accomplished using the same procedure that generates the FML upon replacing the FML condition $\sigma(r_o)=\sigma_f$ with either the ADL condition $\sigma(r_o)=\sigma_s$ or the MEL condition $\sigma(r_i)=\sigma_f$. Like the FML, both the ADL and the MEL are generally not elliptical. Like the FAL and the FML, both the ADL and the MEL are symmetric with respect to 180 deg rotation about the origin, hence the symmetry of structure map follows.

Two examples of fully articulated structure maps are presented in Figs. 7 and 8. Both correspond to material parameters $E=50$ GPa, $\alpha=0.05$, $\sigma_s=75$ MPa, and $\sigma_f=300$ MPa. Their difference is due to differing values of r_o/r_i, namely $r_o/r_i=2$ for Fig. 7 and $r_o/r_i=5$ for Fig. 8. Each structure map is partitioned into various regions by the four loops FAL, FML, ADL and MEL. Each region corresponds to a distinct phase distribution type as also displayed in Figs. 7 and 8.

The qualitative difference between these two structure maps is that in Fig. 7 the ADL is strictly inside the MEL while in Fig. 8 it is not. We shall refer to the former as a *type I structure map* and to the latter as a *type II structure map*. A type II structure map has two symmetric regions corresponding to an $\mathcal{ACM}$ phase distribution whereas a type I structure map does not involve this type of phase distribution. To within unit scaling, the structure map is determined by the material parameter combinations $E\alpha$, σ_f, σ_s and geometry parameter ratio r_o/r_i. For fixed material parameters $E\alpha$, σ_f, σ_s one finds that the structure map is of type I for small r_o/r_i but is of type II for large r_o/r_i. The condition r_o sufficiently greater than r_i makes possible a situation supporting the condition $r_i<r_{\mathcal{M}}<r_{\mathcal{A}}<r_o$ that is associated with the phase distribution $\mathcal{ACM}$.

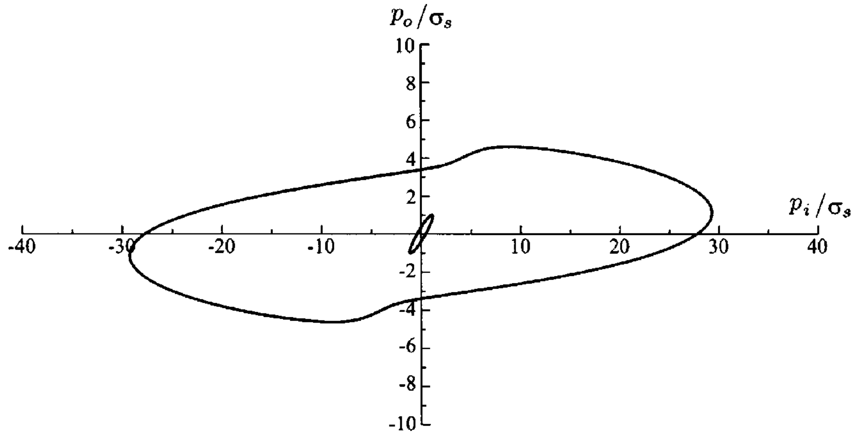

Fig. 5 The FML (fully martensitic loop) and FAL (fully austenitic loop) for $E=50$ GPa, $\alpha=0.05$, $\sigma_f=4\sigma_s=300$ MPa and $r_o/r_i=2$. Thrusts inside the smaller ellipse (FAL) produce a fully austenitic plate, while thrusts outside the bigger loop (FML) produce a fully martensitic plate.

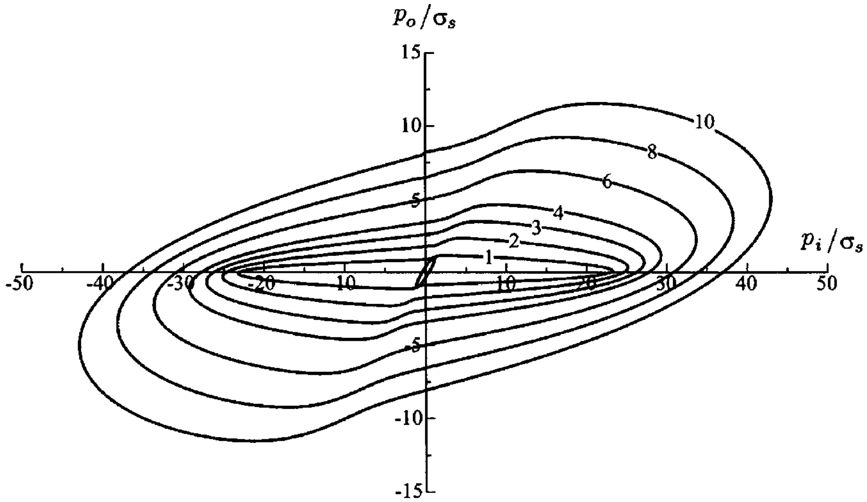

Fig. 6 FMLs for various σ_f values. Here $E=50$ GPa, $\alpha=0.05$, $\sigma_s=75$ MPa and $r_o/r_i=2$. The smallest loop is the common FAL, and the other curves are FMLs, each marked with corresponding value of σ_f/σ_s.

For given $E\alpha$ and σ_f, σ_s there is thus a special value of r_o/r_i such that the structure map is of type I below the special value but of type II above the special value. For the material parameters associated with Figs. 7 and 8 ($E\alpha/\sigma_s=100/3$, $\sigma_f/\sigma_s=4$), this special transitional value is found to be $r_o/r_i=3.58$. The structure map for $E\alpha/\sigma_s=100/3$, $\sigma_f/\sigma_s=4$, $r_o/r_i=3.58$ is plotted in Fig. 9 showing how the ADL osculates the MEL.

The stress distribution for the phase distributions under discussion can be determined numerically on the basis of (17) using the iterated shooting method, in a similar fashion to this determination for a fully martensitic plate. For example, Fig. 10 displays the radial variation of σ, σ_{rr}, $\sigma_{\theta\theta}$ for the $\mathcal{CM}$ phase distribution associated with the load $(p_i,p_o)=(5,0.5)\sigma_s$ represented by the dot in Fig. 7 ($E\alpha/\sigma_s=100/3$, $\sigma_f/\sigma_s=4$, $r_o/r_i=2$). A mixture of austenite and martensite obtains on the outer plate boundary $r=r_o$. This mixture becomes progressively richer in martensite as r decreases to $r=r_{\mathcal{M}}=1.29r_i$ within which the plate is in the martensite phase. This solution could in principle be obtained by many quasi-static load paths in the (p_i,p_o) plane so long as the effective stress at each point in the plate remains nondecreasing. In particular the proportional loading path $(p_i,p_o)=(5,0.5)\sigma_s k$, where k is a load path parameter, is associated with an initial phase distribution of type $\mathcal{A}$. There will then be three values of $k<1$, say $k_1<k_2<k_3$, associated respectively with transitions through the sequence of phase distributions: $\mathcal{A}$, $\mathcal{AC}$, $\mathcal{C}$, $\mathcal{CM}$. Here $k=k_1$ is associated with the emergence of the $\mathcal{AC}$ front $r_{\mathcal{A}}$ at the inner plate boundary. This front proceeds through the plate as k increases until it merges with the outer boundary when $k=k_2$. The $\mathcal{CM}$ front $r_{\mathcal{M}}$ then emerges at the inner plate boundary when $k=k_3$ and continued loading drives this front to $r=1.29r_i$ when $k=1$. Further loading will then drive this front to the outer boundary, resulting in a phase distribution of type $\mathcal{M}$.

Figure 11 shows the stress distributions at the same load $(p_i,p_o)=(5,0.5)\sigma_s$ as in Fig. 10 but for the structure map of Fig. 8. In this case the larger value of r_o ($r_o=5r_i$) gives rise to a phase distribution of type $\mathcal{ACM}$ with $r_{\mathcal{A}}=4.84r_i$ and $r_{\mathcal{M}}=1.24r_i$. In this case the proportional loading path $(p_i,p_o)=(5,0.5)\sigma_s k$ passes through phase distribution states of type $\mathcal{A}$, $\mathcal{AC}$, $\mathcal{ACM}$ with the transitions taking place at two special k values that are analogous to k_1 and k_3 of the previous example associated with Fig. 10.

A final set of stress distributions is shown in Fig. 12. These correspond to the osculation point of ADL with MEL at $(p_i,p_o)=(3.565,0.995)\sigma_s$. Along the proportional loading line from the origin through this point, this solution is associated with the disappearance of the pure austenite phase at the outer plate edge ($r_{\mathcal{A}}=r_o$) that is simultaneous with the appearance of the pure martensite phase at the inner plate edge ($r_{\mathcal{M}}=r_i$).

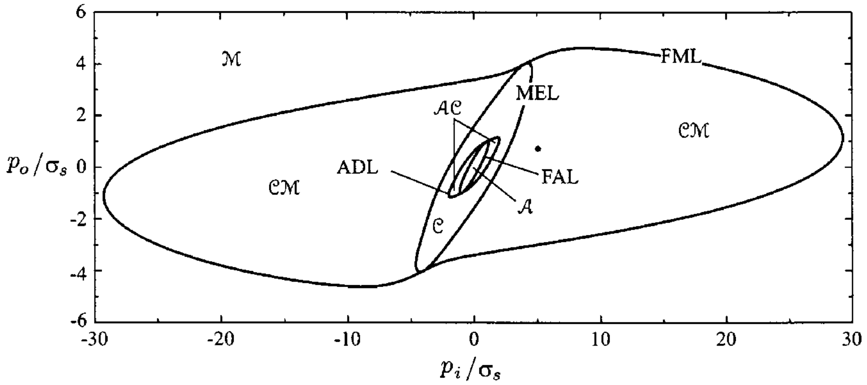

Fig. 7 Structure map (type I) for $r_o/r_i=2$. Here $E=50$ GPa, $\alpha=0.05$ and $\sigma_f=4\sigma_s=300$ MPa. Note that there is no $\mathcal{ACM}$ region. Thrust pair $(p_i,p_o)=(5,0.5)\sigma_s$, marked as a dot, produces a $\mathcal{CM}$ phase distribution. The resulting stresses are shown in Fig. 10.

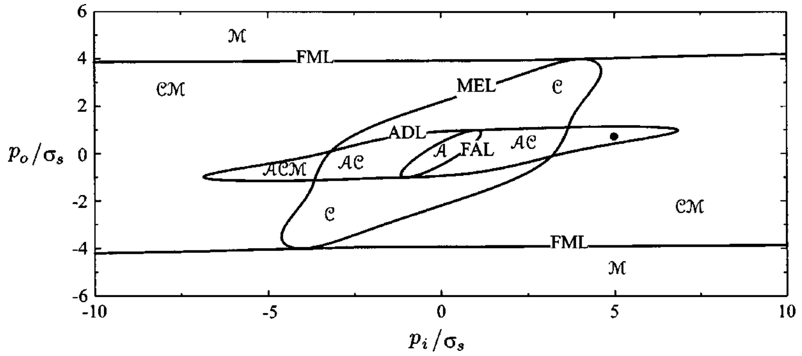

Fig. 8 Structure map (type II) for $r_o/r_i=5$. Here $E=50$ GPa, $\alpha=0.05$ and $\sigma_f=4\sigma_s=300$ MPa. All six types of phase distributions are present. Thrust pair $(p_i,p_o)=(5,0.5)\sigma_s$, marked as a dot, produces a $\mathcal{ACM}$ phase distribution. The resulting stresses are shown in Fig. 11.

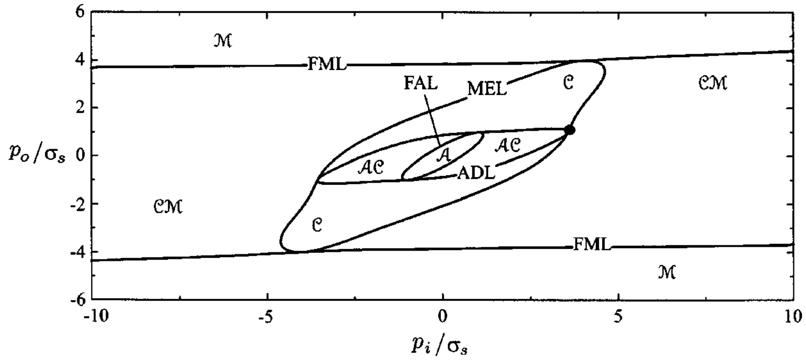

Fig. 9 Structure map for the special value $r_o/r_i=3.58$. Lower values produce type I structure maps, while higher values produces type II. Here $E=50$ GPa, $\alpha=0.05$ and $\sigma_f=4\sigma_s=300$ MPa. There is no $\mathcal{ACM}$ region, and ADL contacts MEL at two points. One of the two points (shown as a dot) represents $(p_i,p_o)=(3.565,0.995)\sigma_s$, producing a $\mathcal{C}$ phase distribution with $\sigma(r_i)=\sigma_f$ and $\sigma(r_o)=\sigma_s$. The resulting stresses are shown in Fig. 12.

7 Conclusions

In this paper, a boundary value problem is formulated and solved for the equilibrium stress and strain fields in an annulus composed of a material undergoing displacive shear transformation. The description allows for mixtures of austenite and martensite as described by a single phase fraction field variable. Each point in the annulus may be either in a state of austenite $\mathcal{A}$, martensite $\mathcal{M}$ or their mixture $\mathcal{C}$. Transformation strain is assumed to be proportional to the stress deviator. The properties of the solutions to the governing equations are studied and the stress distributions are obtained when the annulus is subject to normal edge loads p_i and p_o on the inner and outer boundaries. The effective

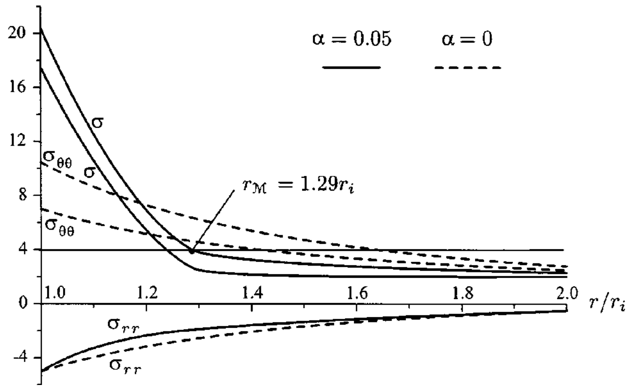

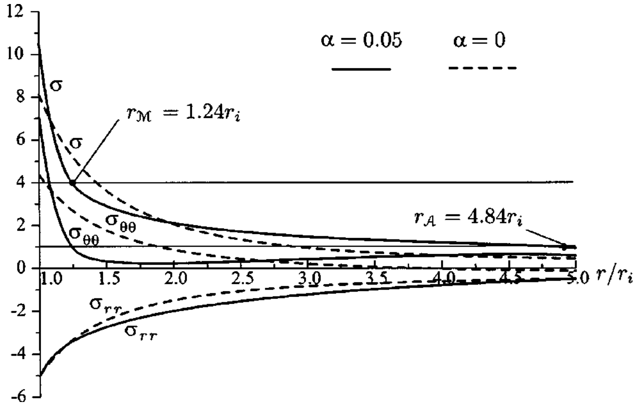

Fig. 10 Stresses (normalized by σ_s) for a $\mathcal{CM}$ phase distribution. Here $E=50$ GPa, $\alpha=0.05$, $\sigma_f=4\sigma_s=300$ MPa, $r_o/r_i=2$ and $(p_i,p_o)=(5,0.5)\sigma_s$. An elastic solution ($\alpha=0$) is shown for comparison (dashed lines).

Fig. 11 Stresses (normalized by σ_s) for a $\mathcal{ACM}$ phase distribution. Here $E=50$ GPa, $\alpha=0.05$, $\sigma_f=4\sigma_s=300$ MPa, $r_o/r_i=5$ and $(p_i,p_o)=(5,0.5)\sigma_s$. An elastic solution ($\alpha=0$) is shown for comparison (dashed lines).

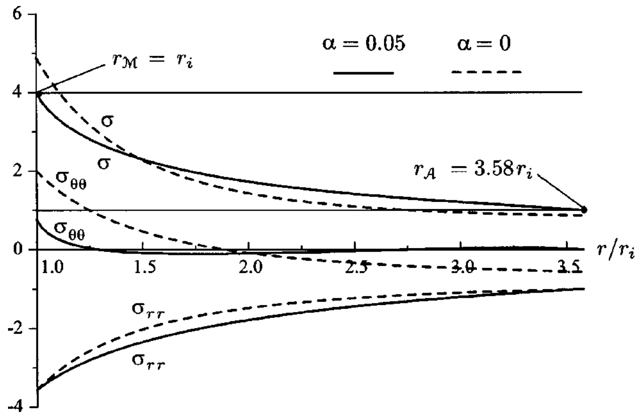

Fig. 12 Stresses (normalized by σ_s) for a special $\mathcal{C}$ phase distribution with $r_{\mathcal{M}}=r_i$ and $r_{\mathcal{A}}=r_o$, for $E=50$ GPa, $\alpha=0.05$, $\sigma_f=4\sigma_s=300$ MPa, $r_o/r_i=3.58$ and $(p_i,p_o)=(3.565,0.995)\sigma_s$. An elastic solution ($\alpha=0$) is shown for comparison (dashed lines).

stress and the martensite phase fraction are each shown to be a nonincreasing function of r. This restricts the phase partitioning to be one of six generic types: $\mathcal{A}$, $\mathcal{C}$, $\mathcal{M}$, $\mathcal{AC}$, $\mathcal{CM}$, and $\mathcal{ACM}$, the latter three of which correspond to various ring structures. The phase partitioning is described by structure maps in the (p_i, p_o) plane that provide a straightforward guide for finding loads that are required to produce a desired phase partitioning. Parametric studies show how geometry and material properties affect the structure maps. Such information would generally be useful for systems involving device control by means of shape memory alloy plates and tubes. If warranted, the strain and displacement fields are easily obtained from the stress distribution using Eqs. (5) and (3). The boundary value problems studied in detail here apply to situations involving isothermal loading. The role of temperature in such an isothermal process is simply to determine the values of the "start" and "finish" effective stresses, σ_s and σ_f. However, the modeling framework is presented in a sufficiently general manner so as to permit further studies on unloading behavior, load cycling and temperature variation as would be valuable in developing shape memory applications in such plate and tube geometries.

References

[1] Birman, V., 1999, "Analysis of an Infinite Shape Memory Alloy Plate With a Circular Hole Subjected to Biaxial Tension," Int. J. Solids Struct., **36**(1), pp. 167–178.
[2] Birman, V., 1997, "Review of Mechanics of Shape Memory Alloy Structures," Appl. Mech. Rev., **50**(11), pp. 629–645.
[3] Bernardini, D., and Pence, T. J., 2002, "Shape-Memory Materials, Modeling," *Encyclopedia of Smart Materials*, M. Schwartz, ed., J. Wiley & Sons, New York, pp. 964–979.
[4] Bondaryev, E. N., and Wayman, C. M., 1988, "Some Stress-Strain-Temperature Relationships for Shape Memory Alloys," Metall. Trans. A, **19A**(10), pp. 2407–2413.
[5] Gall, K., Sehitoglu, H., Maier, H. J., and Jacobus, K., 1998, "Stress-Induced Martensitic Phase Transformation in Polycrystalline CuZnAl Shape Memory Alloys Under Different Stress States," Metall. Mater. Trans. A, **29A**(3), pp. 765–773.
[6] Lim, T. J., and McDowell, D. L., 1999, "Mechanical Behavior of an Ni-Ti Shape Memory Alloy Under Axial-Torsional Proportional and Nonproportional Loading," ASME J. Eng. Mater. Technol., **121**(1), pp. 9–18.
[7] Giannakopoulos, A. E., and Olsson, M., 1993, "Axisymmetric Deformation of Transforming Ceramic Rings," Mech. Mater., **16**(3), pp. 295–316.
[8] Budiansky, B., Hutchinson, J. W., and Lambropoulos, J. C., 1983, "Continuum Theory of Dilitant Transformation Toughening in Ceramics," Int. J. Solids Struct., **19**(4), pp. 337–355.
[9] Nadai, A., 1950, *Theory of Flow and Fracture of Solids*, McGraw–Hill, New York, pp. 472–481.
[10] Chi, Y., Pence, T. J., and Tsai, H., 2003, "Plane Stress Analysis of a Shape Memory Annular Plate Subject to Edge Pressure," J. Phys. IV, **112**, pp. 245–248.
[11] Briggs, J. P., and Ostrowski, J. P., 2002, "Experimental Feedforward and Feedback Control of a One-Dimensional SMA Composite," Smart Mater. Struct., **11**(1), pp. 9–23.
[12] Qidwai, M. A., and Lagoudas, D. C., 2000, "On Thermomechanics and Transformation Surfaces of Polycrystalline NiTi Shape Memory Alloy Material," Int. J. Plast., **16**, pp. 1309–1343.
[13] Briggs, J. P., and Ponte Castaneda, P., 2002, "Variational Estimates for the Effective Response of Shape Memory Alloy Actuated Fiber Composites," ASME J. Appl. Mech., **69**(4), pp. 470–480.
[14] Delaey, L., Krishnan, R. V., Tas, H., and Warlimont, H., 1974, "Review: Thermoelasticity, Pseudoelasticity and the Memory Effects Associated With Martensitic Transformations. Part 1: Structural and Microstructural Changes Associated With the Transformations," J. Mater. Sci., **9**, pp. 1521–1535.
[15] Liang, C., and Rogers, C. A., 1990, "One-Dimensional Thermomechanical Constitutive Relations for Shape Memory Materials," J. Intell. Mater. Syst. Struct., **1**, pp. 207–234.
[16] Ivshin, Y., and Pence, T. J., 1994, "A Constitutive Model for Hysteretic Phase Transition Behavior," Int. J. Eng. Sci., **32**(4), pp. 681–704.
[17] Gillet, Y., Meunier, M. A., Brailovski, V., Trochu, F., Patoor, E., and Berveiller, M., 1995, "Comparison of Thermomechanical Models for Shape Memory Alloy," J. Phys. IV, **5**(C8), pp. 1165–1170.
[18] Budiansky, B., 1958, "Extension of Michell's Theorem to Problems of Plasticity and Creep," Q. Appl. Math., **16**, pp. 307–309.
[19] Roberts, S. M., and Shipman, J. S., 1972, *Two-Point Boundary Value Problems: Shooting Methods*, American Elsevier, New York.

Jen-San Chen
Professor
e-mail: jschen@ccms.ntu.edu.tw

Chun-Yi Liao
Graduate Student,

Department of Mechanical Engineering,
National Taiwan University,
Taipei, Taiwan 10617

Experiment and Analysis on the Free Dynamics of a Shallow Arch After an Impact Load at the End

In this paper we consider a sinusoidal arch with one end pinned in space while the other end attached to a mass and supported by a spring. The supporting wall of the spring is moved a distance quasi-statically to initiate preload in the arch and the spring. The assembly is then set in motion by an impact at the attached mass. The condition under which the arch may snap to the other side dynamically depends on the initial speed of the attached mass due to impact. Sufficient condition on the initial speed against dynamic snap-through is formulated based on the concept of minimum energy barrier. The effects of damping on the transient response of the assembly are also discussed. An experimental setup is designed to measure the transient response of the arch following the impact and the critical initial speed of the attached mass. The experimental results are in good agreement with theoretical predictions. [DOI: 10.1115/1.1827245]

1 Introduction

An arch subjected to lateral loads may become elastically unstable. If the initial height of the arch is of the same order as the span of the arch, the buckling deformation is nearly inextensional. On the other hand, an arch is termed shallow if the initial height is much smaller than the span. When the lateral load of a shallow arch reaches a critical value the deformed shape may undergo a sudden jump called snap-through buckling. The buckling deformation of a shallow arch will be extensional rather than inextensional. Depending on how the lateral load is applied, the snap-through buckling of a shallow arch can be divided into two categories, i.e., static buckling and dynamic buckling. In the case of static buckling, the lateral load is applied in a quasi-static manner. The first theoretical prediction on the static critical load was conducted by Timoshenko in 1935 [1], in which a pinned sinusoidal arch was subjected to a uniformly distributed load. Fung and Kaplan [2] extended the research by considering a flexibly supported shallow arch under various kinds of lateral loading. Fung and Kaplan also conducted a series of experiments on the pin-ended arches having rigid simple supports. Gjelsvik and Bonder [3] presented a complete theoretical and experimental analysis on a clamped arch under a central concentrated load. Franciosi et al. [4] extended the conventional limit analysis to the collapse of arches under repeated loading. Schreyer and Masur [5] analyzed a clamped circular arch and demonstrated that the existence of a bifurcation of the equilibrium state is not an adequate condition for the use of the asymmetric buckling criterion. Lee and Murphy [6] considered the inelastic buckling of a clamped circular arch made of work-hardening material. Simitses [7] studied the effect of an elastic foundation on the critical loads of a sinusoidal arch. Roorda [8] conducted a series of experiments to study the effect of small imperfection on the buckling of elastic structures, including a laterally loaded circular arch.

In the case when the lateral load is applied suddenly instead of in quasi-static manner, the phenomenon is dynamic and much more complicated. Generally speaking, the methodologies used in estimating dynamic critical loads of elastic structures can be classified in two groups [9]. The first approach is to study the total energy and the phase plane of the system. By this method sufficient conditions for dynamic stability may be established. The first theoretical prediction of dynamic buckling load was conducted by Hoff and Bruce in 1954 [10], in which they studied the stability of a sinusoidal arch under unit step loading and ideal impulsive loading. Hsu [11,12] and Hsu et al. [13] studied the effects various parameters on the stability of a flexibly supported sinusoidal arch under impulsive and other types of time-varying loads. Xu et al. [14] considered a shallow arch elastically supported at both ends in the lateral direction and under impulsive loading. This approach provides a lower bound of the dynamic critical load.

The second approach is to solve the equations of motion numerically to obtain the system response and identify the critical load for specified system parameters. This approach provides a more accurate prediction of the critical load at the expense of large amount of calculation. Humphreys [15] performed both numerical and experimental studies on the dynamic snap-through of a circular arch under uniform impulsive loading. Lock [16] used a numerical integration method and an infinitesimal stability analysis to predict the dynamic critical load of a sinusoidal arch under a step loading. Huang and Nachbar [17] added the effects of geometric imperfection and viscoelastic behavior. Ariaratnam and Sankar [18] studied the dynamic buckling of a shallow arch under stochastic loads. Fulton and Barton [19] introduced a different criterion for dynamic stability. Sundararajan and Kumani [20] investigated the dynamic stability of a shallow arch under inclined loads. Lo and Masur [21] presented a hybrid method for snap-through stability analysis, which incorporates an integral equation formulation in conjunction with a finite element method. Johnson and Mclvor [22] investigated numerically the effects of the spatial distribution of impulsive loads and damping [23] on the dynamic snap-through of a shallow arch. Huang and Plaut [24] studied the dynamic stability of a shallow arch under pulsating loads. Gregory and Plaut [25] and Donaldson and Plaut [26] discussed the stability boundaries for arches that are loaded by two independent sets of dynamic loads.

It is noted from the earlier literature review that while theoretical development on dynamic snap-through of shallow arches is quite well-established, experimental investigation [15] is relatively rare compared to the static case, partly because of the difficulty in applying prescribed time-varying lateral force. In this paper we will investigate, both theoretically and experimentally, a dynamic problem which involves an elastically supported arch subjected to impact at the end, as shown in Fig. 1. One end of the arch is pinned in space, while the other end is attached to a mass

---

Contributed by the Applied Mechanics Division of THE AMERICAN SOCIETY OF MECHANICAL ENGINEERS for publication in the ASME JOURNAL OF APPLIED MECHANICS. Manuscript received by the Applied Mechanics Division, July 15, 2003; final revision, March 18, 2004. Associate Editor: N. Sri Namachchivaya. Discussion on the paper should be addressed to the Editor, Prof. Robert M. McMeeking, Journal of Applied Mechanics, Department of Mechanical and Environmental Engineering, University of California—Santa Barbara, Santa Barbara, CA 93106-5070, and will be accepted until four months after final publication in the paper itself in the ASME JOURNAL OF APPLIED MECHANICS.

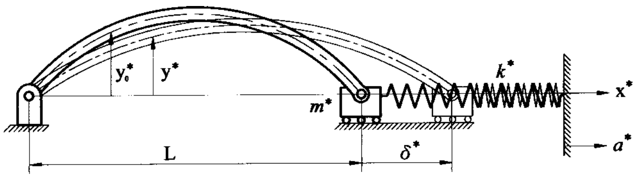

Fig. 1 Schematic diagram of a flexibly supported arch under impact at the end

and supported by a spring. The arch is not subjected to any lateral load. After a quasi-static movement of the supporting wall to preload the arch and the spring, the attached mass is subjected to an impact and attains a substantial initial speed. The arch-mass-spring assembly is then set in motion. The question we are interested in this paper is whether the arch will snap to the other side before it settles to a steady state position. Intuitively, if the impact is minor the arch will return to its original position after the vibration following impact is damped out. On the other hand, if the impact is more severe and the initial speed of the attached mass reaches a critical value, the arch may snap to the other side. Theoretical prediction of the critical initial speed will be presented and verified later by an experiment. By adjusting the stiffness of the supporting spring and the height of the arch, the assembly can be used as a mechanical warning device against severe impact.

2 Equations of Motion

Figure 1 shows a flexibly supported shallow arch, with one end pinned in space while the other end attached to a mass m^* and supported by a spring with spring constant k^*. We assume that both the arch and the spring are in unstrained state initially. The initial shape of the arch when it is unstrained is $y_0^*(x^*)$ with the two ends being separated by a distance L. Before time $t^*=0$ we move quasi-statically the supporting wall of the spring a distance a^* to the right. The arch-mass-spring system is then in a stable equilibrium position with the distance of the two ends of the arch being increased by an amount δ_i^*, while the spring being stretched a distance $\delta_i^* - a^*$. The shape of the prestressed arch is denoted by $y_i^*(x^*)$. The axial thrust throughout the arch and the spring is p_i^*. If the supporting wall of the spring is moved to the left then a^* is negative. We assume that at time $t^*=0$ the attached mass of the prestressed assembly is under impact by an object and attains an initial speed $\dot{\delta}^*(0)=v_i^*$. The arch-mass-spring system is then set in motion with the shape of the vibrating arch being denoted by $y^*(x^*,t^*)$. The equation of motion of the arch can be written as

$$\rho A y^*_{,t^*t^*} = -EI(y^*-y_0^*)_{,x^*x^*x^*x^*} + (p^* - m^*\ddot{\delta}^*)y^*_{,x^*x^*} \quad (1)$$

The parameters E, ρ, A, and I are Young's modulus, mass density, area, and area moment of inertia of the cross section of the arch. The comma represents partial differentiation, while the overhead dot represents the derivative with respect to time. In writing Eq. (1) we assume that the curvature of the arch is small and can be approximated by $-(y^*-y_0^*)_{,x^*x^*}$. An arch is termed high arch when its curvature cannot be treated as small. We also assume that the effects of rotary inertia and shearing deformations are neglected. Strains are assumed to remain within the elastic limit and Hooke's law is valid. The term $p^* - m^*\ddot{\delta}^*$ is the axial thrust in the arch, while p^* alone is the axial force in the spring

$$p^* = -k^*(\delta^* - a^*) \quad (2)$$

We assume that the axial thrust is constant along the arch and is thus a function only of the time. The moving distance δ^* of the attached mass from its initial rest position before the quasi-static wall movement can be related to the arch shape $y^*(x^*,t^*)$ by considering the equilibrium of the attached mass as

$$\delta^* = \frac{(p^* - m^*\ddot{\delta}^*)L}{EA} + \frac{1}{2}\int_0^L [(y^*_{0,x^*})^2 - (y^*_{,x^*})^2]dx^* \quad (3)$$

The first term on the right-hand side of Eq. (3) represents the effect of extensibility of the arch, while the second term represents the effect of shape change (mainly due to rotation). From Eqs. (2) and (3) we can derive p^* as

$$p^*(t) = \frac{k^*}{EA + k^*L}\left\{Lm^*\ddot{\delta}^* + EAa^* - \frac{EA}{2}\int_0^L [(y^*_{0,x^*})^2 - (y^*_{,x^*})^2]dx^*\right\} \quad (4)$$

The parameters δ_i^*, p_i^*, and function $y_i^*(x^*)$, which refer to the mass position, axial force, and deformed shape of the arch before impact, can be calculated from Eqs. (1), (3), and (4) by ignoring all the terms involving differentiation with respect to time.

Equations (1) and (4) can be nondimensionalized to the forms

$$y_{,tt} = -(y-y_0)_{,xxxx} + (p - m\ddot{\delta})y_{,xx} \quad (5)$$

$$p = \frac{k}{2\pi}\int_0^\pi (y_{,x}^2 - y_{0,x}^2)dx + a + km\ddot{\delta} \quad (6)$$

where

$$y = \frac{y^*}{r}, \quad y_0 = \frac{y_0^*}{r}, \quad x = \frac{\pi x^*}{L}, \quad t = \frac{\pi^2 t^*}{L^2}\sqrt{\frac{EI}{A\rho}},$$

$$p = \frac{p^* L^2}{\pi^2 EI}, \quad k = \frac{k^*}{k^* + EA/L}$$

$$\delta = \frac{L\delta^*}{\pi^2 r^2(1-k)}, \quad a = \frac{kLa^*}{\pi^2 r^2}, \quad m = \frac{(1-k)I\pi^4 m^*}{L^3A^2\rho},$$

$$v_i = \frac{L^3 v_i^*}{\pi^4 r^3(1-k)}\sqrt{\frac{\rho}{E}}$$

As a general rule in this paper, a variable without asterisk is a dimensionless counterpart of the one with asterisk. r is the radius of gyration of the cross section of the arch. $p=1$ corresponds to the Euler buckling load for a perfectly straight simply supported beam. The dimensionless spring constant k ranges from 0 ($k^*=0$) to 1 ($k^* \to \infty$). The boundary conditions for y at $x=0$ and π are

$$y(0)-y_0(0) = y_{,xx}(0) - y_{0,xx}(0) = y(\pi) - y_0(\pi)$$
$$= y_{,xx}(\pi) - y_{0,xx}(\pi) = 0 \quad (7)$$

The initial shape of the unstrained arch is assumed to be in the form

$$y_0(x) = h\sin x \quad (8)$$

h is the initial height of the arch. It is assumed that the shape of the arch can be expanded as

$$y(x,t) = y_0 + \sum_{n=1}^{\infty}\alpha_n(t)\sin nx \quad (9)$$

After substituting Eqs. (8) and (9) into (5) and (6) we obtain the equations governing the generalized coordinates α_n:

$$\ddot{\alpha}_1 = -\alpha_1 - (p - m\ddot{\delta})(h + \alpha_1) \quad (10)$$

$$\ddot{\alpha}_n = -n^4\alpha_n - n^2(p - m\ddot{\delta})\alpha_n \quad n = 2,3,\ldots \quad (11)$$

where

$$p = k\left(\frac{h}{2}\alpha_1 + \frac{1}{4}\sum_{i=1}^{\infty} i^2\alpha_i^2\right) + a + km\ddot{\delta} \quad (12)$$

It is noted that the parameter $\ddot{\delta}$ in Eqs. (10), (11), and (12) is still unknown. To obtain the additional equation of motion accounting for δ we substitute Eq. (4) into Eq. (3), nondimensionalize, and discretize by using Eq. (9):

$$m\ddot{\delta} = -\delta - \left(\frac{h}{2}\alpha_1 + \frac{1}{4}\sum_{i=1}^{\infty} i^2\alpha_i^2 \right) + \frac{a}{1-k} \tag{13}$$

Equations (10)–(13) are the discretized equations of motion of the assembly.

3 Equilibrium Configurations

We first study the equilibrium configurations of the prestressed arch-mass-spring assembly following the quasi-static wall movement a. The shape of the prestressed arch can be determined from Eqs. (10) and (11) by neglecting all the acceleration terms. There are two different types of equilibrium configurations, i.e., one-mode and two-mode solutions. It can be easily shown that Eqs. (10) and (11) do not admit an equilibrium configuration with more than two modes.

One-Mode Solution $y = y_0 + \alpha_1 \sin x$.

α_1 satisfies the following cubic equation

$$a(\alpha_1 + h) = -\frac{\alpha_1}{4}(k\alpha_1^2 + 3kh\alpha_1 + 2kh^2 + 4) \tag{14}$$

After defining parameter a_1 as

$$a_1 = \frac{kh^2}{4} - \frac{3}{4}(4kh^2)^{1/3} - 1 \tag{15}$$

we can make the following observations.

1. If $a > a_1$, then there is only one equilibrium configuration denoted by P_0.
2. If $a < a_1$, then there are three equilibrium configurations P_0, P_1^+, and P_1^-, where

$$\alpha_1(P_1^-) < -h - \left(\frac{2h}{k}\right)^{1/3} < \alpha_1(P_1^+) < -h < \alpha_1(P_0) \tag{16}$$

3. If $a = a_1$, then the configurations P_1^+ and P_1^- coincide. We denote this special one-mode configuration as P_1. Also

$$\alpha_1(P_1) = -h - \left(\frac{2h}{k}\right)^{1/3} \tag{17}$$

Two-Mode Solution $y = y_0 + \alpha_1 \sin x + \alpha_j \sin jx$.

It can be shown that a two-mode solution always contains the first mode $\alpha_1 \sin x$. For this case the solutions can be written explicitly

$$\alpha_1 = \frac{-j^2 h}{j^2 - 1} \tag{18}$$

$$\alpha_j = \pm\frac{2}{j}\sqrt{\frac{a_j - a}{k}} \tag{19}$$

where

$$a_j = \frac{(j^2-2)j^2h^2k}{4(j^2-1)^2} - j^2 \tag{20}$$

These configurations are denoted by P_{1j}^+ and P_{1j}^-, which exist only when

$$a < a_j \tag{21}$$

It is noted that in both Eqs. (15) (for a_1) and (20) (for a_j) the parameters k and h appear together in the form kh^2. By comparing Eqs. (15) and (20) we observe that

$$a_1 \geqslant a_j \tag{22}$$

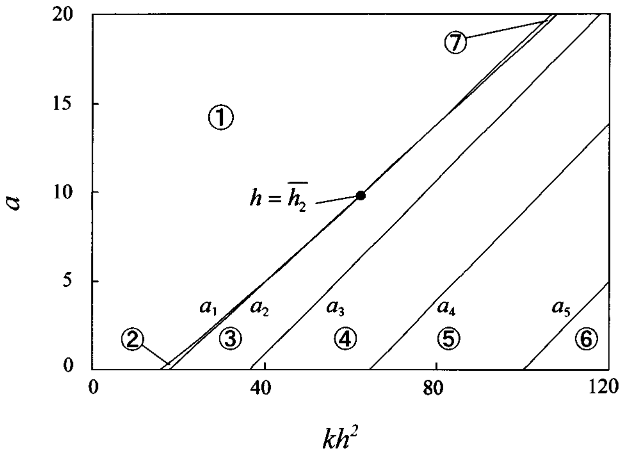

Fig. 2 a_j curves on the kh^2-a plane

The special initial height which renders $a_1 = a_j$ is denoted by $\overline{h}_j$, where

$$k\overline{h}_j^2 = 2(j^2-1)^3 \quad j = 2,3,4,\ldots \tag{23}$$

The values of some of $k\overline{h}_j^2$ are $k\overline{h}_2^2 = 54$, $k\overline{h}_3^2 = 1024$, etc. Figure 2 shows the a_j curves in the kh^2-a plane. These a_j curves divide the kh^2-a plane into several regions. The black dot at $h = \overline{h}_2$ signifies the touching point between a_1 and a_2 curves. For a given set of kh^2 and a, we can determine the number of equilibrium configurations. For instance, if the point (kh^2, a) fall in the region 1, then there is only one equilibrium configuration P_0. For the parameter ranges in Fig. 2 there are seven regions, whose equilibrium configurations are listed in Table 1.

4 Stability of Equilibrium Configurations

First of all, the dimensionless total energy H of any configuration can be calculated as

$$H = \frac{2}{\pi}\int_0^{\pi}[(y_{,t})^2 + (y_{,xx} - y_{0,xx})^2]dx + 2(p - m\ddot{\delta})^2 + \frac{2p^2(1-k)}{k} + 2m\dot{\delta}^2(1-k) \tag{24}$$

The two terms in the integral represent the kinetic energy and the bending strain energy. The second term is the strain energy due to the axial force. The third term is the strain energy of the spring. The last term is the kinetic energy of mass. For an equilibrium configuration corresponding to a specified wall movement a, the kinetic energy is zero and the total energy consists of only the strain energy U:

$$U = \frac{2}{\pi}\int_0^{\pi}(y_{,xx} - y_{0,xx})^2 dx + \frac{2p^2}{k} \tag{25}$$

Table 1 Equilibrium configurations in various regions of Fig. 2

Region	Equilibrium configuration	Stability of P_1^-
1	P_0	
2	P_0, $P_1^\pm$	Stable
3	P_0, $P_1^\pm$, $P_{12}^\pm$	Stable
4	P_0, $P_1^\pm$, $P_{12}^\pm$, $P_{13}^\pm$	Stable
5	P_0, $P_1^\pm$, $P_{12}^\pm$, $P_{13}^\pm$, $P_{14}^\pm$	Stable
6	P_0, $P_1^\pm$, $P_{12}^\pm$, $P_{13}^\pm$, $P_{14}^\pm$, $P_{15}^\pm$	Stable
7	P_0, $P_1^\pm$	Unstable

For the two-mode configurations P_{1j}^{+} and P_{1j}^{-} the strain energy are equal, and can be written as

$$U(P_{1j}^{+})=U(P_{1j}^{-})=\frac{1}{k}\left(\frac{j^4kh^2}{j^2-1}-2j^4-4j^2a\right) \tag{26}$$

For the one-mode solutions the strain energy is

$$U=\alpha_1^2+\frac{2p^2}{k} \tag{27}$$

where α_1 and p are the generalized coordinate and the axial thrust of the one-mode solution. The physical total energy H^* and strain energy U^* are related to H and U by

$$H=\frac{4AL^3H^*}{\pi^2EI^2}, \quad U=\frac{4AL^3U^*}{\pi^2EI^2} \tag{28}$$

In order to study the stability of the equilibrium configuration with shape $\overline{y}$, we perturb the equilibrium shape by a small amount $\varepsilon\hat{y}$ to examine how the strain energy changes. ε is a small positive number. The strain energy U of the perturbed configuration can be expanded in terms of ε as

$$\begin{aligned}U(\overline{y}+\varepsilon\hat{y})-U(\overline{y})&=\varepsilon\left\{\frac{4}{\pi}\int_0^{\pi}[(\overline{y}_{,xx}-y_{0,xx})\hat{y}_{,xx}+\overline{p}\overline{y}_{,x}\hat{y}_{,x}]dx\right\}\\&\quad+\varepsilon^2\left\{\frac{2}{\pi}\int_0^{\pi}[(\hat{y}_{,xx})^2+\overline{p}(\hat{y}_{,x})^2]dx\right.\\&\quad\left.+\frac{2k}{\pi^2}\left[\int_0^{\pi}\overline{y}_{,x}\hat{y}_{,x}dx\right]^2\right\}\\&\quad+\varepsilon^3\left\{\frac{2k}{\pi^2}\left[\int_0^{\pi}\overline{y}_{,x}\hat{y}_{,x}dx\right]\left[\int_0^{\pi}(\hat{y}_{,x})^2dx\right]\right\}\\&\quad+\varepsilon^4\left\{\frac{k}{2\pi^2}\left[\int_0^{\pi}(\hat{y}_{,x})^2dx\right]^2\right\}\end{aligned} \tag{29}$$

$\overline{p}$ is the axial force of the equilibrium configuration $\overline{y}$, and can be calculated from Eq. (10) as

$$\overline{p}=\frac{-\alpha_1}{\alpha_1+h} \tag{30}$$

To prove that an equilibrium shape $\overline{y}$ is stable we have to show that the energy difference $U(\overline{y}+\varepsilon\hat{y})-U(\overline{y})$ is positive for any $\hat{y}\neq 0$. On the other hand, to prove that $\overline{y}$ is an unstable equilibrium shape, we only need to find one $\hat{y}\neq 0$ which renders $U(\overline{y}+\varepsilon\hat{y})-U(\overline{y})$ negative. After integrating by parts and using the fact that $\overline{y}$ satisfies the static equilibrium equations it can be shown that the coefficient of ε in Eq. (29) is zero. To determine the stability we next examine the second variation of the strain energy

$$\delta^2U=\frac{2}{\pi}\int_0^{\pi}[(\hat{y}_{,xx})^2+\overline{p}(\hat{y}_{,x})^2]dx+\frac{2k}{\pi^2}\left[\int_0^{\pi}\overline{y}_{,x}\hat{y}_{,x}dx\right]^2 \tag{31}$$

In some cases δ^2U is zero identically, and higher order variation is needed. More details of the above energy method can be found in Ref. [27], and the conclusions are summarized in the following.

One-Mode Solutions: P_0 is always stable. P_1^{+} is always unstable. If $h\leqslant\overline{h_2}$, then P_1^{-} is stable if and only if $a<a_1$. On the other hand, if $h>\overline{h_2}$, then P_1^{-} is stable if and only if $a<a_2$.

Two-Mode Solutions: P_{1j}^{+} and P_{1j}^{-} are always unstable.

From the earlier analysis, we know that for any combination of a and kh^2 there are at most two stable configurations. One of them is always P_0, and the other possible stable configuration is P_1^{-}. In Table 1 we also identify the regions with stable P_1^{-}. For those quasi-static wall movements a, which result in only one stable equilibrium position P_0, the assembly will return to the original position following impact. On the other hand, for those wall movements which render the existence of two stable positions P_0 and P_1^{-}, then it is possible for the arch to snap and settle to P_1^{-} following the impact. It is the purpose of this paper to determine the lowest possible initial speed of the impacted mass, below which the arch-mass-spring assembly is in no danger to snap. This lowest initial speed is called the critical initial speed.

5 Snap-Through Criterion

While it is in general difficult to determine the necessary and sufficient condition for dynamic snap-through to occur, we can establish the sufficient conditions against dynamic snap-through in terms of the dimensionless total energy H of the vibrating arch-mass-spring assembly following the impact. The basic idea of the snap-through criterion is that if the total energy gained by the assembly from the impact is smaller than the minimum energy barrier lying between the nearest stable equilibrium position and the distant stable one, then the arch has no chance to snap dynamically. The energy barrier can be proved to be the strain energy of either the unstable configuration P_1^{+} or $P_{12}^{\pm}$, depending on the parameters k, h and a [27]. The sufficient conditions against dynamic snap-through from P_0 to P_1^{-} can then be stated in the following.

Case (1) $h\leqslant\overline{h_2}$ and $a_2\leqslant a<a_1$: The sufficient condition against snap-through is $H_i<U(P_1^{+})$, where H_i is the total energy immediately following impact.

Case (2) $a<a_2$: The sufficient condition against snap-through is $H_i<U(P_{12}^{\pm})$.

Figures 3(*a*), 3(*b*), and 3(*c*) show the equilibrium positions and strain energy contours for three typical situations. In Fig. 3(*a*) $k=0.4$, $h=10$, and $a=3$, which falls in region 3 of Fig. 2. There are five equilibrium positions in this region, among them $P_{12}^{\pm}$ are the saddle points whose strain energy is the energy barrier preventing the system from snapping from position P_0 to another stable position P_1^{-}. In Fig. 3(b) $k=0.2$, $h=10$, and $a=0.6$, which falls in region 2 of Fig. 2. There are three equilibrium positions in this region, among them P_1^{+} is a saddle point whose strain energy serves as the energy barrier. In Fig. 3(*c*) $k=0.8$, $h=10$, and $a=13.8$, which falls in region 7 of Fig. 2. There are three equilibrium positions in this region, among them P_0 is the only stable equilibrium position. P_1^{-} becomes a saddle point in this case.

6 Effect of Damping

Figures 4(*a*), 4(*b*), and 4(*c*) show the deformation history of an arch with $h=10$, $k=0.4$, $a=3$, and $m=0.001$, which falls in region 3 of Fig. 2. In calculating the response we modify Eq. (10) by adding a damping parameter μ:

$$\ddot{\alpha}_1=-\mu\dot{\alpha}_1-\alpha_1-(p-m\ddot{\delta})(h+\alpha_1) \tag{32}$$

The relation between μ and its physical counterpart μ^* is

$$\mu=\frac{\mu^*L^2}{\pi^2\rho Ar}\sqrt{\frac{\rho}{E}} \tag{33}$$

The initial speed v_i is set to be 110. The damping μ used in Figs. 4(*a*), 4(*b*), and 4(*c*) are 0.2, 0.3, and 0.6, respectively. The initial conditions are

$$\begin{aligned}&\alpha_i(0)=0, \quad i=1,2,3,\ldots\\&\dot{\alpha}_1(0)=-\frac{2v_i}{h},\\&\dot{\alpha}_i(0)=0, \quad i=2,3,4,\ldots\end{aligned} \tag{34}$$

For the small damping case in Fig. 4(*a*) the energy gained by the assembly is large enough to surpass the energy barrier $U(P_{12}^{\pm})$ and

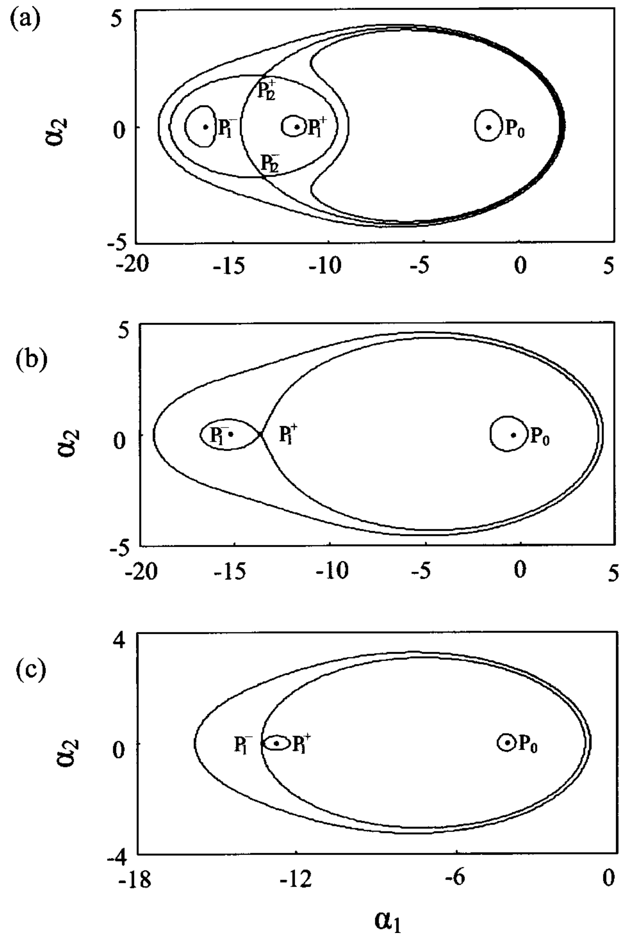

Fig. 3 Strain energy contours for (*a*) $k=0.4$, $h=10$, $a=3$, (*b*) $k=0.2$, $h=10$, $a=0.6$, (*c*) $k=0.8$, $h=10$, $a=13.8$

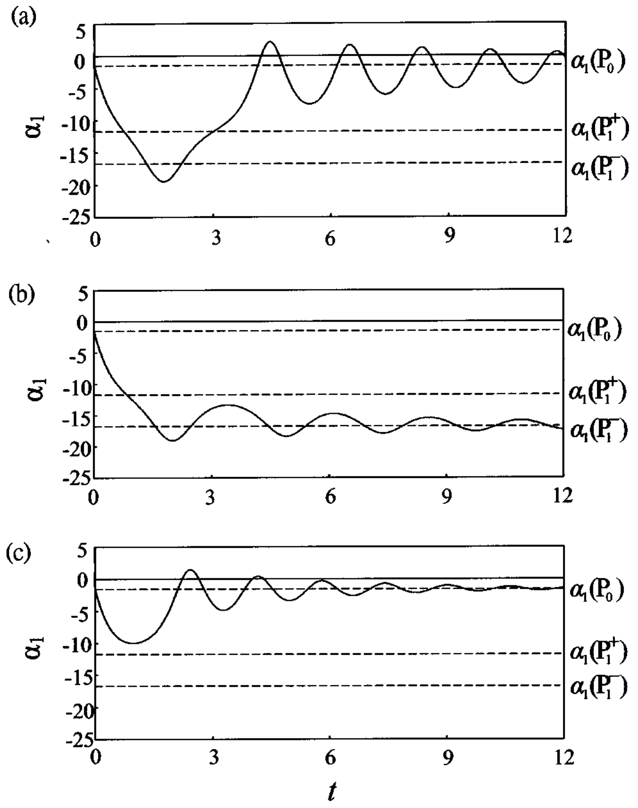

Fig. 4 Effect of damping μ on the response of the assembly with $h=10$, $k=0.4$, $a=3$, $v_i=110$, $m=0.001$. (*a*) $\mu=0.2$, (*b*) $\mu=0.3$, (*c*) $\mu=0.6$.

α_1 can reach $\alpha_1(P_1^-)$. However, due to small damping, the arch is snapped back and finally settles to position P_0. For the medium damping case in Fig. 4(*b*), the assembly not only gains enough energy to surpass $U(P_{12}^{\pm})$ and α_1 can reach $\alpha_1(P_1^-)$, the damping also prevents it from snapping back to P_0. The arch settles to P_1^- eventually. In Fig. 4(*c*) the damping is so large that it prevents the arch from surpassing $U(P_{12}^{\pm})$, and the arch has no choice but to settle to P_0. The existent equilibrium positions are plotted as dashed horizontal lines for reference. These examples demonstrate that damping plays an important role in dynamic snap-through when the total energy of the assembly gained from impact is greater than the energy barrier.

7 Critical Initial Speed

Another important factor in determining whether snap-through will occur is the end initial speed. Apparently, for very small initial speed no snap-through is possible. As v_i increases, on the other hand, snap-through might occur. It is therefore possible to define a critical initial speed v_{cr} below which no snap-through is possible even if there exist two stable equilibrium positions. From the snap-through criterion discussed previously, we can derive the expression of the critical initial speed as follows.

For the case when $h \leqslant \overline{h_2}$ and $a_2 \leqslant a < a_1$ the energy barrier is $U(P_1^+)$. From the condition $H_i(v_{cr}) = U(P_1^+)$, where $H_i(v_{cr})$ is the total energy of the system immediately after the attached mass attains initial speed v_{cr} from the impact, it can be found that the critical initial speed v_{cr} for this case is

$$v_{\mathrm{cr}} = \frac{h[k\alpha_1^2(P_1^+) - k\alpha_1^2(P_0) + 2p^2(P_1^+) - 2p^2(P_0)]^{1/2}}{[2mh^2k(1-k)+4k]^{1/2}} \tag{35}$$

$p(P_0)$ and $p(P_1^+)$ are the axial thrust of the assembly in the equilibrium positions P_0 and P_1^+, respectively. For the case when $a < a_2$ the energy barrier is $U(P_{12}^{\pm})$. From the condition $H_i(v_{\mathrm{cr}}) = U(P_{12}^{\pm})$ it can be found that the critical initial speed v_{cr} for this case is

$$v_{\mathrm{cr}} = \frac{h[16kh^2 - 96 - 48a - 3k\alpha_1^2(P_0) - 6p^2(P_0)]^{1/2}}{[6mh^2k(1-k)+12k]^{1/2}} \tag{36}$$

It is noted that the one-mode solution P_0 and P_1^+ cannot be solved explicitly when $a \neq 0$. Therefore, the parameters $\alpha_1(P_0)$, $\alpha_1(P_1^+)$, $p(P_0)$, and $p(P_1^+)$ in Eqs. (35) and (36) can only be calculated numerically. On the other hand when $a=0$, i.e., the assembly is unstrained before impact, Eqs. (35) and (36) can be expressed in the following closed forms. For the case $18 > kh^2 > 16$:

$$v_{\mathrm{cr}} = \frac{h^2(3-c)}{4(1-c)} \left\{ \frac{16 + 2kh^2(1-c)^2}{kh^2[mh^2(1-k)+2]} \right\}^{1/2},$$

$$\text{where } c = \sqrt{1 - \frac{16}{kh^2}} \tag{37}$$

For the case $kh^2 > 18$:

$$v_{\mathrm{cr}} = \frac{h}{2} \left[\frac{32h^2k - 192}{3mh^2k(1-k)+6k} \right]^{1/2} \tag{38}$$

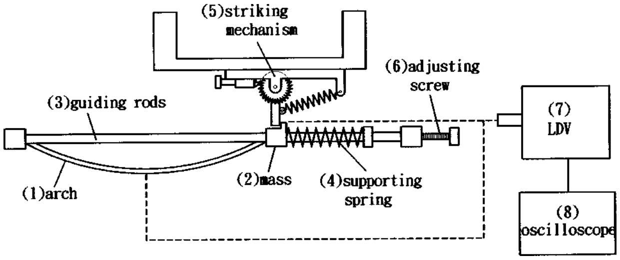

Fig. 5 Schematic diagram of the experimental setup

8 Experimental Setup

An experimental setup is designed to verify the earlier theoretical prediction. The schematic diagram of the setup is shown in Fig. 5. The function of each component in the setup is explained as follows. (1) The arch is made of aluminum strip with Young's modulus 70 GPa and mass density 2800 kg/m^3. The length L of the arch is 40 cm and the cross section is 25 mm×1.5 mm. (2) Attached mass, which consists of a roller bearing and a linear bearing at the end, is scaled at $m^*=473$ g. The roller bearing is installed to simulate the pinned condition, while the linear bearing is to reduce the friction when the mass slides on the guiding rods (3). (4) Spring to support the arch in the axial direction, whose spring constant can be adjusted in the range $k^*=200-400$ N/cm by changing its working length. (5) A lock-and-release striking mechanism, which consists of a striking hammer and a spring to store the striking power. (6) An adjustable screw mechanism to control the quasi-static wall movement a^*. (7) An LDV system made by Polytec Co. (optical measurement head OFV-508 and electronic signal processor OFV-2802) to measure the speed of the sliding mass in the axial direction or the lateral speed at the midpoint (one at a time) of the arch. The converting ratio of the LDV signal is 1 V to 125 mm/s. The instrument can record a signal up to 15 V. Displacement can be obtained by integrating the speed signal. (8) A digital oscilloscope is used to visually monitor and record the signals from the LDV system. A photograph of the laboratory setup is shown in Fig. 6.

9 Transient Response Measurements

Figure 7 shows the measured speed history of the attached mass following the impact. The parameters of the assembly are initial height $h^*=2.80$ cm ($h=65$), spring constant $k^*=327$ N/cm ($k=0.0050$), wall movement $a^*=0$. The complicated impact phenomenon between the striking hammer and the metallic flange on the sliding mass is not of our interest. Instead, we focus our attention to the initial speed gained by the sliding mass after the impact. The initial speed is measured at $v_i^*=1.72$ m/s ($v_i=2860$) and is signified by a black dot in the figure. The rise time from impact to the speed peak is about 0.0005 s. In this experiment snap-through occurs with the arch passing through the horizontal position at 0.015 s (the first crossing of the $\dot{\delta}^*=0$ line). For easy reference we present the results with both physical parameters (with asterisk) and the dimensionless ones (without asterisk). The same labeling style is adopted in the following figures.

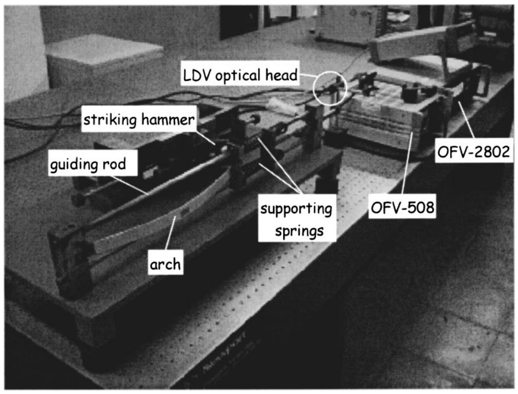

Fig. 6 A photograph of the experimental setup in the laboratory

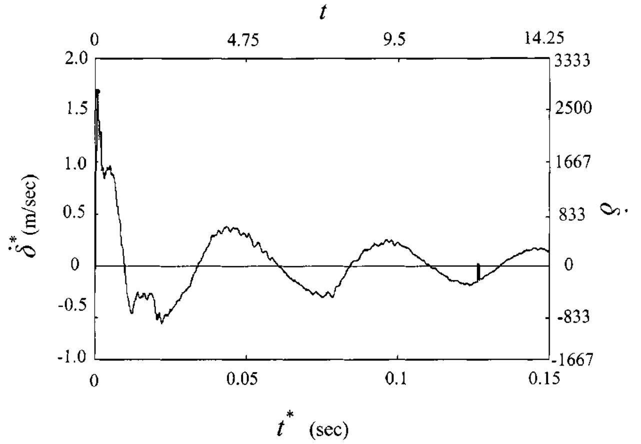

Fig. 7 Measured speed history of the attached mass following the impact. Parameters of the assembly are $h^*=2.80$ cm, $k^*=327$ N/cm, $a^*=0$.

The solid lines in Fig. 8 represent the measured lateral deflection history at the midpoint of the arch following the impact. The parameters of the assembly in Fig. 8(*a*) are $h^*=3.46$ cm ($h=80$), $k^*=206$ N/cm ($k=0.0034$), $v_i^*=1.44$ m/s ($v_i=2400$).

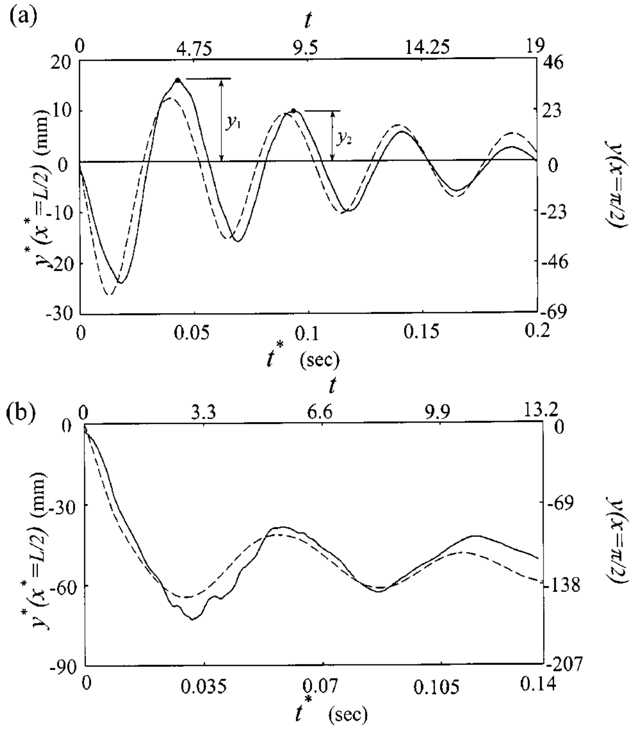

Fig. 8 Deflection history at the midpoint of the arch following the impact. The solid lines are the measured response while the dashed lines are the numerical results. (*a*) $h^*=3.46$ cm, $k^*=206$ N/cm, $v_i^*=1.44$ m/s. (*b*) $h^*=3.00$ cm, $k^*=333$ N/cm, $v_i^*=1.79$ m/s.

No snap-through occurs in this case and the arch settles to the original shape eventually. Figure 8(*b*) shows the deflection history of another assembly with parameters $h^*=3.00\,\text{cm}\,(h=70)$, $k^*=333\,\text{N/cm}\,(k=0.0051)$, $v_i^*=1.79\,\text{m/s}\,(v_i=2975)$. Snap-through occurs in Fig. 8(*b*) and the arch settles eventually to the other side.

To simulate the motion of the assembly numerically, we have to estimate the damping of the system. The dissipating mechanism of the system comes from the friction in the moving parts and the material damping in the arch and the spring. We assume that the first mode is dominant in the dynamic response in Fig. 8(*a*). The damping factor may be estimated from the decaying rate of the two peaks as signified by black dots. The heights of the two peaks are measured at $y_1=38$ and $y_2=24$. The ratio of the damping of the system μ in Eq. (32) to a critical damping μ_c is [28]

$$\frac{\mu}{\mu_c}=\frac{\ln(y_1/y_2)}{\{(2\pi)^2+[\ln(y_1/y_2)]^2\}^{1/2}} \tag{39}$$

The damping ratio in Eq. (39) is calculated as 0.07. The critical damping μ_c is estimated numerically by adjusting the damping parameter μ in Eq. (32) until the response α_1 ceases to oscillate. In this way the dimensionless critical damping μ_c is estimated as 10. As a consequence the damping of the assembly is estimated as $\mu=0.7$ ($\mu^*=9.8$ N s/m). It is noted that the concept of critical damping and the logarithmic decrement approach is for a linear oscillator. We assume that the similar concept can be extended to a nonlinear system with a linear viscous damping such as Eq. (32). Although this estimate may appear somewhat engineering-oriented, it is believed that the damping factor in our experimental setup is about this order. Whether this approach is satisfactory is examined by experimental results. The dashed lines in Figs. 8(*a*) and 8(*b*) are the deflection history from numerically integrating Eq. (32). The short rise time from impact to the peak speed as explained in Fig. 7 is ignored. It is noted that the actual response as measured in the experiment may contain multiple-mode components, while the numerical simulation contains only a single mode α_1 because of the initial conditions (34). The actual multi-mode response may result from imperfect initial shape of the arch. The good agreement between the experiment and the numerical simulation as demonstrated in Figs. 8(*a*) and 8(*b*) confirms that the one-mode solution $\alpha_1(t)\sin x$ is indeed the dominant component.

10 Critical Speed Measurements

Figure 9 shows the results from a series of experiments on the critical initial speed. Figure 9(*a*) shows the relation between the critical initial speed v_{cr}^* and the wall movement a^*. The fixed parameters of the assembly is $h^*=3.46\,\text{cm}\,(h=80)$, $k^*=206\,\text{N/cm}\,(k=0.0034)$. The symbol×represents the measured critical initial speed. In the experiment we increase the striking power of the hammer incrementally until snap-through occurs. The increment in the corresponding initial speed change is about 0.0125 m/s, which may be considered as the accuracy of the critical speed measurement. Each experiment is repeated three times. Therefore, there are three×clustered for each specified a^*. The solid line represents the theoretical predictions. The two black dots represent the wall movement corresponding to a_1 and a_2. In the range $a_2<a<a_1$ the theoretical critical initial speed is given by Eq. (35). In the range $a<a_2$ the theoretical critical initial speed is given by Eq. (36). In the range $a>a_1$ no snap-through is possible because there exist only one stable equilibrium position P_0. It is noted that the wall movement a in the experiment ranges from negative to positive values. It is observed that the critical initial speed decreases as the wall movement a increases until the point $a=a_1$.

Figure 9(*b*) shows the critical initial speed as a function of the supporting spring constant k^*. The fixed parameters of the assembly is $h^*=3.46\,\text{cm}\,(h=80)$, $a^*=0$. The two points signified by black dots are $k_1=16/h^2$ and $k_2=18/h^2$. In the range $k_1<k<k_2$ the theoretical critical initial speed is given by Eq. (37). In the range $k<k_2$ the theoretical critical initial speed is given by Eq. (38). It is observed that the critical initial speed increases as the spring constant k^* increases. Figure 9(*c*) shows the critical initial speed as a function of the initial height h^* of the arch. The fixed parameters of the assembly is $k^*=208\,\text{N/cm}\,(k=0.0035)$, $a^*=0$. The two points corresponding to a_1 and a_2 are outside the range of this figure. The critical initial speed increases as the initial height of the arch increases. Generally speaking, the experimental results of the critical initial speeds are satisfactory compared to the theoretical predictions.

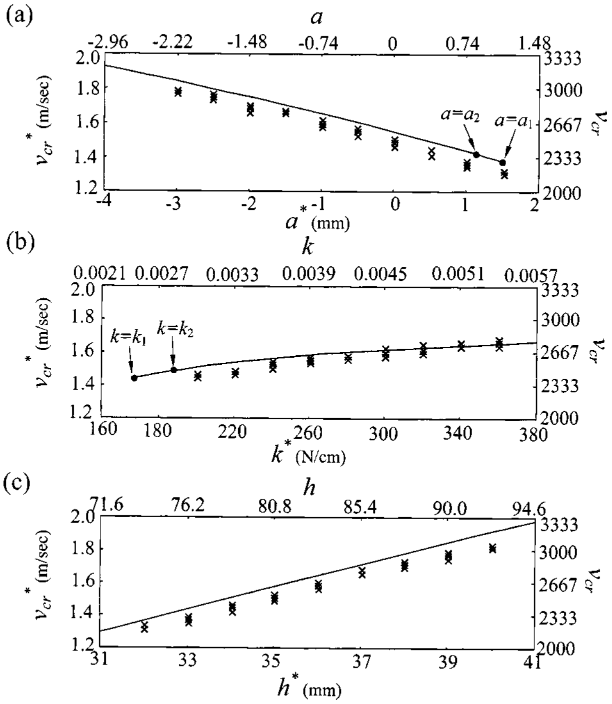

Fig. 9 Critical initial speed v_{cr}^* as a function of (*a*) wall movement a^*, (*b*) supporting spring constant k^*, (*c*) initial height h^* of the arch. Symbol×represents the measured data, while the solid lines are the theoretical predictions.

11 Conclusions

In this paper we consider a shallow arch with initial height *h*. One end of the arch is attached to a mass *m* and supported by a spring with constant *k*. After the supporting wall is moved quasi-statically a distance *a* to preload the arch-mass-spring assembly, the attached mass is subjected to impact and attains initial speed v_i. We are interested in the conditions under which the arch will snap to the other side dynamically. Some results can be summarized in the following.

(1) There are at most two stable equilibrium configurations for any given combination of *a*, *h* and *k*. One of them is P_0, which is always stable. The other is P_1^-, which is stable only in certain range of *a* and kh^2.

(2) When $h\leqslant\overline{h_2}$ and $a_2\leqslant a<a_1$, the energy barrier preventing the arch from snapping from P_0 to P_1^- is the strain energy of P_1^+. In the case when $a<a_2$ the energy barrier is the strain energy of $P_{12}^{\pm}$.

(3) The assembly is safe from dynamic snap-through as long as the initial speed of the attached mass from the impact is smaller than a critical speed. This critical initial speed can be predicted analytically and confirmed by experiments.

(4) Generally speaking the critical initial speed decreases as a increases, while it increases as k and h increase.

Acknowledgment

The results presented here were obtained in the course of research supported by a grant from the National Science Council of the Republic of China.

References

[1] Timoshenko, S. P., 1935, ''Buckling of Flat Curved Bars and Slightly Curved Plates,'' ASME J. Appl. Mech., **2**, pp. 17–20.
[2] Fung, Y. C., and Kaplan, A., 1952, ''Buckling of Low Arches or Curved Beams of Small Curvature,'' NACA Technical Note 2840.
[3] Gjelsvik, A., and Bonder, S. R., 1962, ''The Energy Criterion and Snap Buckling of Arches,'' J. Eng. Mech. Div., **88**, pp. 87–134.
[4] Franciosi, V., Augusti, G., and Sparacio, R., 1964, ''Collapse of Arches Under Repeated Loading,'' ASCE J. Struct. Div., **90**, pp. 165–201.
[5] Schreyer, H. L., and Masur, E. F., 1966, ''Buckling of Shallow Arches,'' J. Eng. Mech. Div., **92**, pp. 1–19.
[6] Lee, H. N., and Murphy, L. M., 1968, ''Inelastic Buckling of Shallow Arches,'' J. Eng. Mech. Div., **94**, pp. 225–239.
[7] Simitses, G. J., 1973, ''Snapping of Low Pinned Arches on an Elastic Foundation,'' ASME J. Appl. Mech., **40**, pp. 741–744.
[8] Roorda, J., 1965, ''Stability of Structures With Small Imperfections,'' J. Eng. Mech. Div., **91**, pp. 87–106.
[9] Simitses, G. J., 1990, *Dynamic Stability of Suddenly Loaded Structures*, Springer, New York.
[10] Hoff, N. J., and Bruce, V. G., 1954, ''Dynamic Analysis of the Buckling of Laterally Loaded Flat Arches,'' J. Math. Phys., **32**, pp. 276–288.
[11] Hsu, C. S., 1967, ''The Effects of Various Parameters on the Dynamic Stability of a Shallow Arch,'' ASME J. Appl. Mech., **34**, pp. 349–358.
[12] Hsu, C. S., 1968, ''Stability of Shallow Arches Against Snap-Through Under Timewise Step Loads,'' ASME J. Appl. Mech., **35**, pp. 31–39.
[13] Hsu, C. S., Kuo, C. T., and Lee, S. S., 1968, ''On the Final States of Shallow Arches on Elastic Foundations Subjected to Dynamical Loads,'' ASME J. Appl. Mech., **35**, pp. 713–723.
[14] Xu, J.-X., Huang, H., Zhang, P.-Z., and Zhou, J.-Q., 2002, ''Dynamic Stability of Shallow Arch With Elastic Supports—Application in the Dynamic Stability Analysis of Inner Winding of Transformer During Short Circuit,'' Int. J. Non-Linear Mech., **37**, pp. 909–920.
[15] Humphreys, J. S., 1966, ''On Dynamic Snap Buckling of Shallow Arches,'' AIAA J., **4**, pp. 878–886.
[16] Lock, M. H., 1966, ''The Snapping of a Shallow Sinusoidal Arch Under a Step Pressure Load,'' AIAA J., **4**, pp. 1249–1256.
[17] Huang, N. N., and Nachbar, W., 1968, ''Dynamic Snap-Through of Imperfect Viscoelastic Shallow Arches,'' ASME J. Appl. Mech., **35**, pp. 289–296.
[18] Ariaratnam, S. T., and Sankar, T. S., 1968, ''Dynamic Snap-Through of Shallow Arches Under Stochastic Loads,'' AIAA J., **6**, pp. 798–802.
[19] Fulton, R. E., and Barton, F. W., 1971, ''Dynamic Buckling of Shallow Arches,'' J. Eng. Mech. Div., **97**, pp. 865–877.
[20] Sundararajan, V., and Kumani, D. S., 1972, ''Dynamic Snap-Buckling of Shallow Arches Under Inclined Loads,'' AIAA J., **10**, pp. 1090–1091.
[21] Lo, D. L. C., and Masur, E. F., 1976, ''Dynamic Buckling of Shallow Arches,'' J. Eng. Mech. Div., **102**, pp. 901–917.
[22] Johnson, E. R., and Mclvor, I. K., 1978, ''The Effect of Spatial Distribution on Dynamic Snap-Through,'' ASME J. Appl. Mech., **45**, pp. 612–618.
[23] Johnson, E. R., 1980, ''The Effect of Damping on Dynamic Snap-Through,'' ASME J. Appl. Mech., **47**, pp. 601–606.
[24] Huang, K. Y., and Plaut, R. H., 1982, ''Snap-Through of a Shallow Arch Under Pulsating Load,'' *Stability in the Mechanics of Continua*, F. H. Schroeder, ed., Springer, Berlin, pp. 215–223.
[25] Gregory, Jr., W. E., and Plaut, R. H., 1982, ''Dynamic Stability Boundaries for Shallow Arches,'' J. Eng. Mech. Div., **108**, pp. 1036–1050.
[26] Donaldson, M. T., and Plaut, R. H., 1983, ''Dynamic Stability Boundaries for a Sinusoidal Arch Under Pulse Loads,'' AIAA J., **21**, pp. 469–471.
[27] Liao, C.-Y., 2003, ''Experiment and Analysis of a Flexibly Supported Arch Under Impact at the End,'' Master thesis, Department of Mechanical Engineering, National Taiwan University, Taipei, Taiwan.
[28] Rao, S. S., 1995, *Mechanical Vibrations*, 3rd ed., Addision-Wesley, Reading, MA.

A Plane Stress Perfectly Plastic Mode I Crack Solution With Continuous Stress Field

David J. Unger
Department of Mechanical and Civil Engineering,
University of Evansville,
1800 Lincoln Avenue,
Evansville, IN 47722
e-mail: du2@evansville.edu
Mem. ASME

A statically admissible solution for a perfectly plastic material in plane stress is presented for the mode I crack problem. The yield condition employed is an alternative type first proposed by von Mises in order to approximate his original yield condition for plane stress while eliminating most of the elliptic region as pertaining to partial differential equations. This yield condition is composed of two intersecting parabolas rather than a single ellipse in the principal stress space. The attributes of this particular solution of the mode I problem over that previously obtained are that it contains neither stress discontinuities nor compressive stresses anywhere in the field. [DOI: 10.1115/1.1828061]

The mode I perfectly plastic solution for the plane stress crack problem under the von Mises yield condition [1] has a discontinuous radial stress in the trailing portion of the plastic zone. Beyond this stress discontinuity and extending to the crack face lies a region under compression, which is a counterintuitive feature for a crack subject to tensile loads. In contrast, neither this stress discontinuity nor compressive region is found in the analogous plane strain crack problem (see, e.g., [2]). These features are likely inherent to the plane stress problem because of the extended regions of the yield surface where the governing differential equations are elliptic. In the analogous plane strain problem, only hyperbolic partial differential equations govern over the entire yield surface.

Cognizant of the innate mathematical difficulties that arise with ellipticity in plasticity theory, von Mises [3] proposed an alternative yield condition for plane stress. This yield condition approximates the shape of the original surface in the principal stress plane, while eliminating most of the elliptic region of the yield surface—the exceptions being just two points. Using this alternative yield criterion, it will be shown that a continuous stress field is derivable for the perfectly plastic mode I crack problem under plane stress loading conditions.

The traditional von Mises yield condition [3] assumes the following form for a plane stress, nonwork hardening material

$$\sigma_1^2+\sigma_2^2-\sigma_1\sigma_2=\sigma_0^2=3k^2, \tag{1}$$

where σ_1 and σ_2 are the first and second principal stresses ($\sigma_3=0$), σ_0 is the tensile yield stress, and k is the yield stress in pure shear. A plot of the corresponding yield surface in Fig. 1 shows that the curve itself in principal stress space is an ellipse. Regions VW and UZ on the yield surface are governed by hyperbolic partial differential equations [2], while regions UV and WZ are governed by elliptic equations. At the transition points U, V, W, and Z, parabolic partial differential equations govern.

For purposes of comparison, inscribed in the von Mises yield condition in Fig. 1 is the Tresca yield surface, which is hexagonal in shape. Regions NP and ST on the Tresca have hyperbolic partial differential equations as governing equations [2]. Regions MN, MT, PQ, and QS have parabolic partial differential equations. At points M and Q the equations become elliptic. The relationship between the tensile yield stress σ_0 and that in shear k differs from the von Mises yield condition and has the form $\sigma_0=2k$.

The alternative von Mises yield condition [3] is defined below for plane stress

$$\frac{\sigma_1-\sigma_2}{k}=\pm\frac{1}{1+\sqrt{2}}\left[(1+\sqrt{2})^2-\left(\frac{\sigma_1+\sigma_2}{2k}\right)^2\right]. \tag{2}$$

Its plot in Fig. 2 reveals it is comprised of two intersecting parabolas. The positive sign in (2) corresponds to the solid parabola shown in the figure, while the negative sign corresponds to the broken parabola. For the solid parabola, the slope $d\sigma_2/d\sigma_1$ is zero at the lowest point of the defining curve Q' and infinite at the highest point of the defining curve M'. The converse is true for the dashed line portion. The associated governing partial differential equations are hyperbolic, except where the slope is zero or infinity. At these extreme points M' and Q' on the diagonal line, the equations are elliptic. These points are similar mathematically to corresponding points on the Tresca yield condition M and Q, which are also located at extreme points along the diagonal line. For the alternative von Mises yield condition, the tensile yield stress $\sigma_0=2k$; however, k is no longer interpreted as the yield stress in pure shear.

To gain insight into the varying predictions of these three different yield criteria, the mode I linear elastic, small scale yielding stresses [2] have been substituted into the various criteria and plotted in Fig. 3, which is a normalized XY plane with a crack situated to the left of the origin. In this plane, the dimensionless coordinates are of the form $X=2\pi x\sigma_0^2/K_I^2$, etc., where K_I is the mode I stress intensity factor, and x is the standard Cartesian coordinate. It can be seen that the yield locus of the alternative von Mises yield condition is similar in size to the traditional von Mises yield criterion. However, the alternative von Mises yield criterion seems to resemble the shape of the Tresca yield condition more than the traditional von Mises yield condition.

To date, no analytical elastic-plastic solution of the mode I problem has been found. However, plastic stresses [2,4,5] have been continued analytically across the prescribed elastic-plastic boundary that is shown in Fig. 3 for the Tresca yield condition. The associated slip line nets found in these analyses are shown in Fig 4. It is curious to note that along slipline DF a biaxial state of stress of magnitude $2k$ is determined. This state of stress corresponds to point M on the Tresca yield surface (Fig. 1), which is governed by an elliptic partial differential equation. One could infer by symmetry that a similar slip line, which is the reflection of DF, exists on the opposite side of the crack axis. Thus the analytical continuation of stresses across the leading edge of the

---

Contributed by the Applied Mechanics Division of THE AMERICAN SOCIETY OF MECHANICAL ENGINEERS for publication in the ASME JOURNAL OF APPLIED MECHANICS. Manuscript received by the Applied Mechanics Division, July 21, 2003; final revision, August 13, 2004. Associate Editor: K. Ravi-Chandar. Discussion on the paper should be addressed to the Editor, Prof. Robert M. McMeeking, Journal of Applied Mechanics, Department of Mechanical and Environmental Engineering, University of California–Santa Barbara, Santa Barbara, CA 93106-5070, and will be accepted until four months after final publication in the paper itself in the ASME JOURNAL OF APPLIED MECHANICS.

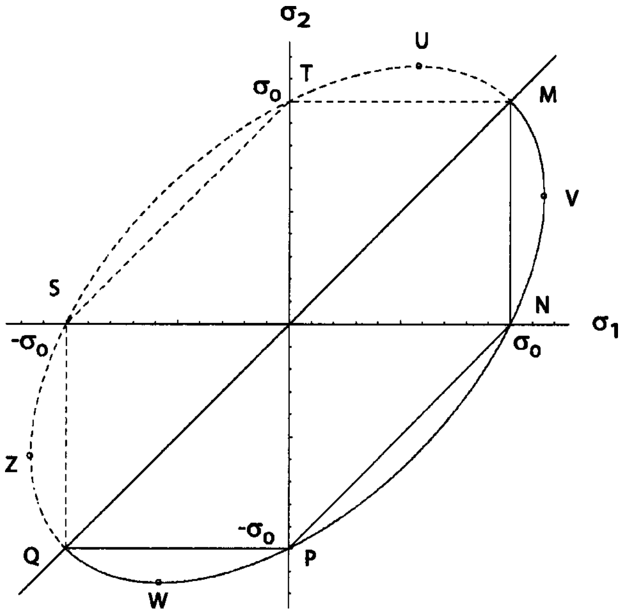

Fig. 1 The von Mises yield condition (elliptically shaped) with inscribed Tresca yield condition. After [3].

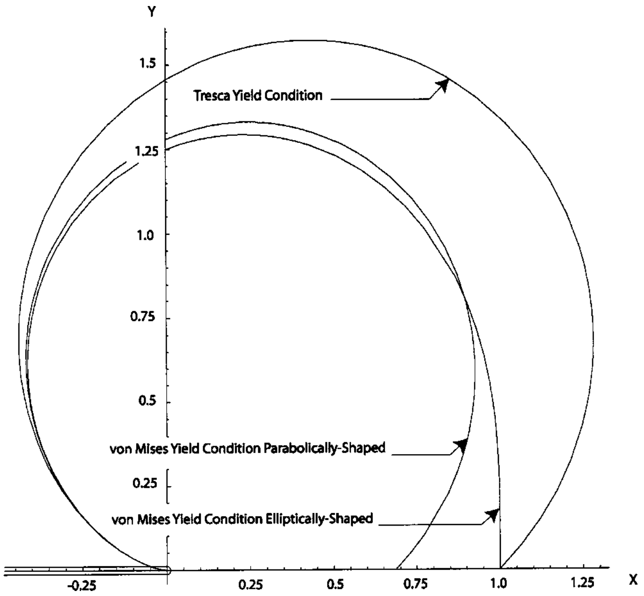

Fig. 3 Predicted elastic-plastic boundaries around a crack tip for different yield criteria using the elastic stress field

plastic zone suggests that a biaxial state of stress might be present in front of the crack tip for the elastic-plastic problem.

In the context of a perfectly plastic material under the Tresca yield condition, a stress field having a biaxial state of stress $2k$ ahead of the crack and a uniaxial state of stress of magnitude $2k$ along the crack faces is statically admissible. This would require a stress discontinuity to form at the crack tip and continue to $\pm\infty$ along the Y-axis, for a crack oriented along the negative X-axis as in Fig. 4. No concentrated fan of slip lines is admissible within the Tresca yield condition in plane stress (the Appendix gives some indication of why this is true); otherwise, it would seem natural to try to eliminate this stress discontinuity through an intervening fan connecting these two regions of uniform stress. It will be shown that the alternative von Mises allows a stress field to be developed which has a biaxial state of stress in front of the crack tip, a uniaxial state of stress adjacent to the crack faces, and a concentrated fan of characteristics in-between the other two regions.

The characteristics for the most commonly used perfectly plastic model for plane stress are shown in Fig. 5, which was developed in [1] for comparison with a power-law hardening material. (Note the crack in [1] was oriented to the left rather than to the right, as shown in Fig. 5.) The dashed line along OB of Fig. 5 indicates a stress discontinuity. The associated stress field is independent of the radius r from crack tip. Its variation with the polar angle θ, measured counterclockwise from OA, is provided in Fig. 6.

Analysis

A solution of a mode I perfectly plastic solution for plane stress is found in this section using the alternative von Mises yield con-

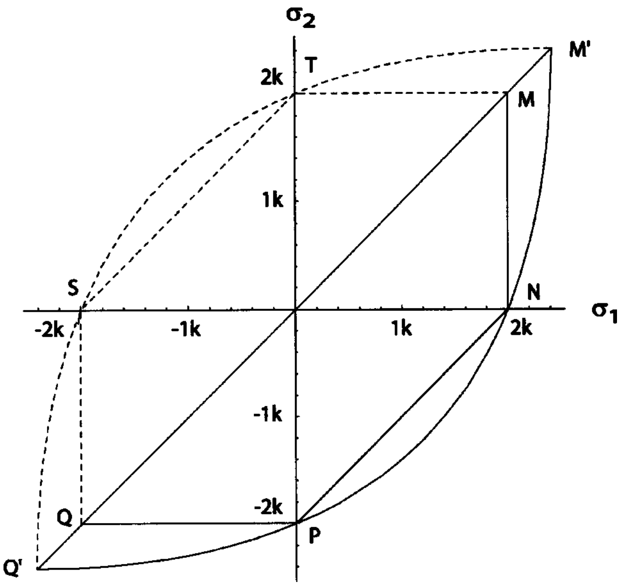

Fig. 2 The alternative von Mises yield condition (parabolically shaped) compared to the Tresca yield condition. After [3].

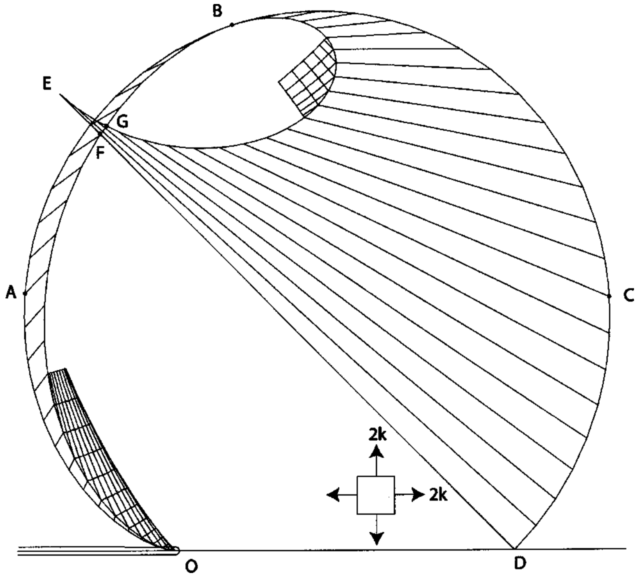

Fig. 4 Slip lines across an elastic-plastic boundary under the Tresca yield condition. After [2,4,5].

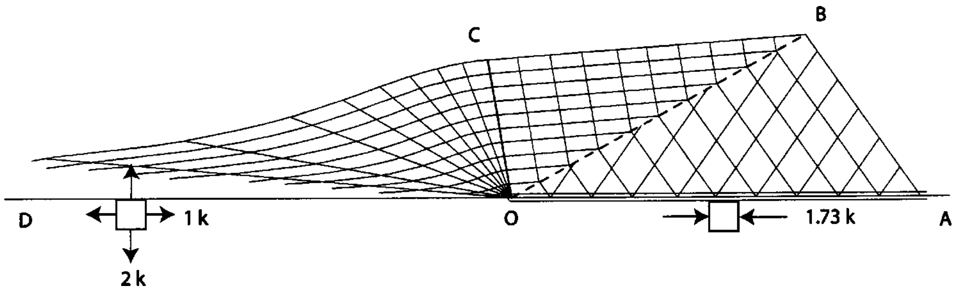

Fig. 5 Characteristics for plane stress mode I crack under the von Mises yield condition (elliptically shaped). After [1].

dition. The first step will be to solve the associated differential equation generated by (2) for a stress field independent of the radius r for a body in equilibrium.

Solving (2) for σ_2 gives

$$\sigma_2 = 2ak + 2\sqrt{2ak(ak-\sigma_1)} - \sigma_1, \quad \text{where} \quad a = 1+\sqrt{2}. \tag{3}$$

Note the branch of the multiple-valued function was chosen in (2) to represent quadrant one of the principal stress plane for the solid-line segment of the yield surface of Fig. 2.

The following elementary transformations are used to relate the stresses in polar coordinates (r,θ) to the principal stresses in the yield condition (3)

$$\sigma_1 = (\sigma_r + \sigma_\theta)/2 + \sqrt{(\sigma_r - \sigma_\theta)^2 + 4\tau_{r\theta}^2}/2, \tag{4}$$

$$\sigma_2 = (\sigma_r + \sigma_\theta)/2 - \sqrt{(\sigma_r - \sigma_\theta)^2 + 4\tau_{r\theta}^2}/2. \tag{5}$$

Introducing a stress function of the form

$$\phi = r^2 f(\theta) \tag{6}$$

allows for stresses which automatically satisfy the equilibrium equations in the plane.

Further, the particular form of (6) defines a stress field, which is independent of the coordinate r, which can be deduced from the relationships given below relating ϕ to stresses in polar coordinates

$$\sigma_r = \frac{1}{r^2}\frac{\partial^2\phi}{\partial\theta^2} + \frac{1}{r}\frac{\partial\phi}{\partial r} = f''(\theta) + 2f(\theta), \tag{7}$$

$$\sigma_\theta = \frac{\partial^2\phi}{\partial r^2} = 2f(\theta), \tag{8}$$

$$\tau_{r\theta} = -\frac{\partial}{\partial r}\left(\frac{1}{r}\frac{\partial\phi}{\partial\theta}\right) = -f'(\theta). \tag{9}$$

Upon substitution of (7)–(9) into (4) and (5) and subsequently the resulting expressions for σ_1 and σ_2 into (3), one finds that the governing ordinary differential equation for $f(\theta)$ is

$$f''(\theta) + 4f(\theta) = 2ak + 2\sqrt{2ak\left\{ak - \left[\frac{f''(\theta)+4f(\theta)}{2} + \frac{1}{2}\sqrt{(f''(\theta))^2 + 4(f'(\theta))^2}\right]\right\}}. \tag{10}$$

Applying the standard technique for reducing the order of an ordinary differential equation lacking the explicit appearance of the independent variable, i.e.,

$$f'(\theta) = p, \quad f''(\theta) = p\frac{dp}{df}, \tag{11}$$

produces the expression

$$\left[\frac{1}{8ak}\left(p\frac{dp}{df} + 4f - 2ak\right)^2 + \frac{1}{2}p\frac{dp}{df} + 2f - ak\right]^2 = \frac{1}{4}\left[\left(p\frac{dp}{df}\right)^2 + 4p^2\right], \tag{12}$$

after both sides have been squared repetitively in such a way as to eliminate both radical signs appearing in (10).

An additional substitution of the form

$$Q = \tfrac{1}{2}p^2 + 2f^2 \tag{13}$$

further reduces the equation to

$$\left[\frac{1}{8ak}\left(\frac{dQ}{df} - 2ak\right)^2 + \frac{1}{2}\frac{dQ}{df} - ak\right]^2 = \frac{1}{4}\left[\left(\frac{dQ}{df}\right)^2 - 8f\frac{dQ}{df} + 8Q\right]. \tag{14}$$

Let us now introduce the following notation into (14)

$$q(f) = \frac{dQ(f)}{df} = Q'(f). \tag{15}$$

Upon expansion of the bracketed terms in (14), the equation assumes the form

$$fq(f) - Q(f) = -\frac{a^2k^2}{8} + \frac{3}{16}q^2(f) - \frac{1}{128a^2k^2}q^4(f). \tag{16}$$

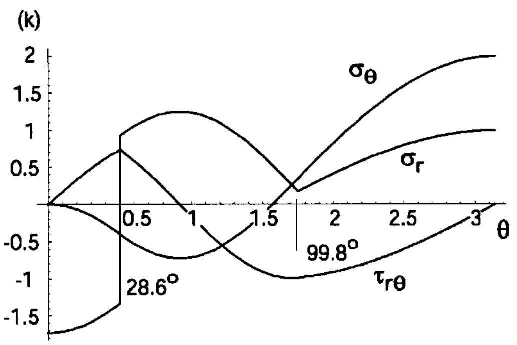

Fig. 6 Stress field for plane stress mode I crack under the von Mises yield condition (elliptically shaped). After [1].

On the surface, (16) appears to be a formidable differential equation to solve being of quartic degree. Typically, a first order differential equation of degree higher than one requires as an intermediate step a solution of an algebraic equation of the same degree as that of the equation itself. However, in this case the left-hand side of (16) has the form of a Clairaut equation [6], which will simplify the solution process considerably. The operational procedure to solve a Clairaut equation is to substitute an arbitrary constant for the first derivative appearing in the equation, and solve the expression for the dependent variable. The solution of the differential equation in this case is the dependent variable Q, where c is the constant of integration. Upon applying this procedure to (16), it becomes

$$fc-Q(f)=-\frac{a^2k^2}{8}+\frac{3}{16}c^2-\frac{1}{128a^2k^2}c^4. \tag{17}$$

Now reverting to the original definition for $Q(f)$, i.e., (13), one finds from (17) that

$$fc-\frac{1}{2}p^2-2f^2=-\frac{a^2k^2}{8}+\frac{3}{16}c^2-\frac{1}{128a^2k^2}c^4. \tag{18}$$

By substituting the definition of p from (11) into (18), the solution to the original second order differential equation is reduced to quadrature, i.e.,

$$\pm\theta+\frac{\alpha}{2}=\int\frac{df}{\sqrt{a^2k^2/4-\frac{3}{8}c^2+c^4/64a^2k^2+2cf-4f^2}}, \tag{19}$$

where α represents the second constant of integration. The integral in (19) can be evaluated using either an integral table or using a symbolic computer program with the result being an inverse trigonometric function of f. Upon inversion of this elementary function, one finds the explicit form of the general solution of (10) as

$$f(\theta)=\frac{c}{4}\pm\left(\frac{ak}{4}-\frac{c^2}{16ak}\right)\sin(2\theta+\alpha). \tag{20}$$

It can be shown that $f(\theta)$ of (20) represents a class of solutions of (10), which generate uniform states of stress.

Another possible type of solution of the original differential equation (10) is a singular solution. Singular solutions represent envelopes of general solutions. However, they cannot be derived from the general solution by simply selecting particular values of the arbitrary constants. For Clairaut's equation, a method of finding singular solutions (if they exist) is described in [6] and will be used here. In order to find the singular solution, one must first take a derivative of the governing equation (16) with respect to the independent variable f, i.e.,

$$Q''(f)\left(f-\frac{3}{8}q-\frac{1}{32a^2k^2}q^3\right)=0. \tag{21}$$

This procedure sets up a specific relationship between q and f related to the envelope of the general solution. Next the term in the parentheses in (21) is set equal to zero and the expression solved for $q(f)$. The only real-valued solution of this cubic algebraic equation for $q(f)$ is

$$q(f)=2\sqrt[3]{\sqrt{4a^4k^4f^2-a^6k^6}-2a^2k^2f}+\frac{2a^2k^2}{\sqrt[3]{\sqrt{4a^4k^4f^2-a^6k^6}-2a^2k^2f}}. \tag{22}$$

When (22) is substituted for q into the original differential equation and solved, a singular solution is obtained.

Upon substituting the definition of $Q(f)$ into (16), one finds that

$$p=\frac{df}{d\theta}=\pm\sqrt{\frac{a^2k^2}{4}-\frac{3}{8}q^2(f)+\frac{q^4(f)}{64a^2k^2}+2q(f)f-4f^2}, \tag{23}$$

where $q(f)$ is given by (22). From (23) one further infers by separating variables and integrating that

$$\pm\theta+\beta=\int\frac{df}{\sqrt{a^2k^2/4-\frac{3}{8}q^2(f)+q^4(f)/64a^2k^2+2q(f)f-4f^2}}, \tag{24}$$

where β is a constant of integration.

The implicit form of a singular solution of (10) is obtained from (24), provided the integral exists. However, evaluating the integral analytically is difficult in its present form due to the complicated expression $q(f)$. Nevertheless, it can be accomplished by noting a simple parametric representation of (22) exists in the form

$$f=\frac{ak}{2}\sin\psi=\frac{ak}{4i}(e^{i\psi}-e^{-i\psi}),$$

$$q=4ak\sin\frac{\psi}{3}=\frac{2ak}{i}(e^{i\psi/3}-e^{-i\psi/3}). \tag{25}$$

By substituting the complex representations of both f and q from (25) into (24) produces a simplified form of the integral

$$\pm\theta+\beta=\frac{1}{2}\int_0^{\psi}\frac{(1+e^{2i\psi})d\psi}{(1-e^{2i\psi/3}+e^{4i\psi/3})^{3/2}}. \tag{26}$$

The symbolic computer program Mathematica® (Wolfram Research, Urbana, IL) was used to integrate (26) to yield

$$\theta+\beta=\tfrac{3}{4}ig(\psi),\quad \text{where}$$

$$g(\psi)=-2\psi i/3+\ln(2-e^{2i\psi/3}+2\sqrt{1-e^{2i\psi/3}+e^{4i\psi/3}})+\sinh^{-1}\left(\frac{1-2e^{2i\psi/3}}{\sqrt{3}}\right)+\sinh^{-1}3^{-1/2}-\ln 3,\quad \text{and} \tag{27}$$

$$\psi=\sin^{-1}\left(\frac{2f_s}{ak}\right),$$

where the ambiguous ± sign in front of θ in (26) has been made positive in anticipation of the application to follow.

Equation (27) represents a singular solution f_s of (10) in implicit form.[1] The constant β in (27) represents physically a rigid body motion. Although the notation of (27) contains imaginary numbers the result is actually real-valued.

From the general solution (20) and the singular solution (27) a statically admissible stress field representing the mode I plane stress problem for a perfectly plastic material will be found.

A solution will be sought having a uniaxial tensile state of stress along the crack faces of magnitude $2k$, as indicated in Fig. 7. The boundary condition of zero traction ($\sigma_\theta=0,\tau_{r\theta}=0$) is satisfied along the crack faces by choosing the negative sign indicated in (20) and adjusting the arbitrary constants to be

$$c=2k,\quad \alpha=\pi/2,\quad \rightarrow f_{OAB}=k\sin^2\theta, \tag{28}$$

where the subscript on f indicates the sector over which this solution applies in Fig. 7.

---

[1] See Appendix B for an explicit form of the singular solution of (10).

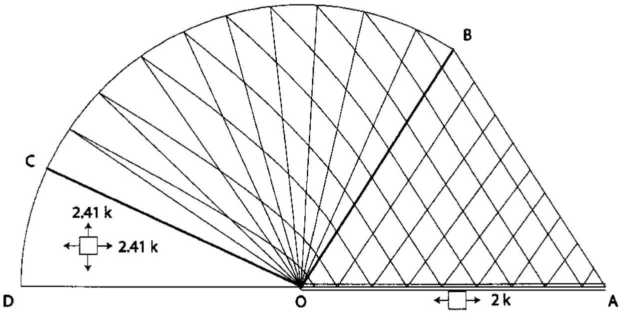

Fig. 7 Characteristics for plane stress mode I crack under the alternative von Mises yield condition (parabolically shaped)

Similarly, a biaxial state of tensile stress of magnitude ak (point M' of Fig. 2) is desired ahead of the crack, where a is defined in (3). The following choice of the constant c in (20) generates this biaxial state of stress for region OCD of Fig. 7

$$c = 2ak \rightarrow \quad f_{OCD} = ak/2. \tag{29}$$

Now an attempt will be made to connect the two uniform states of stress in regions OAB and OCD with a fan defined by the singular solution (27). A requirement for equilibrium across boundaries OB and OC is that $f(\theta)$ and $f'(\theta)$ be continuous, i.e., four boundary conditions.

First, θ_{OB} and f_{OB} are found numerically from the two simultaneous equations generated by equating $p(f_{OBC})$ from (23) to $f'_{OAB}(\theta)$ determined from (28), together with $f_{OAB}(\theta) = f_{OBC}$. Next, the phase angle β of the fan follows by substituting the now known values of f_{OB} and θ_{OB} into (27). Following this, the angle θ_{OC} is determined from (27) by substituting the known value of β together with the value of f_{OCD} from (29). The results are summarized below

$$\theta_{OB} = 57.2 \text{ deg}, \quad \beta = -20.5 \text{ deg}, \quad \theta_{OC} = 155.5 \text{ deg}. \tag{30}$$

It should be pointed out that the system is over determined and one now needs to check that the fourth boundary condition for equilibrium is also satisfied. The fourth boundary condition requires that the fan derivative p of (23) be zero at $\theta_{OC} = 155.5$ deg because f_{OCD} is constant throughout its domain. This is verified by substituting the value of f_{OCD} from (29) into (23).

The stress fields associated with functions f_{OAB}, f_{OBC}, and f_{OCD} by (7)–(9) are plotted in Fig. 8. One notes that all stresses are continuous throughout the entire domain. In addition, there is no compressive region anywhere in the field.

To the best of the author's knowledge, the solutions of the fan stresses have not been previously solved for the alternative von Mises yield condition. However, the characteristics related to the fan have previously appeared in the literature [7,8], and as such their derivation will not be repeated here. The curved characteristics in the fan are of the form

$$r = r_0 / \sin^{3/2}\left(\frac{2\gamma + \pi}{3}\right), \quad -\pi/2 \leq \gamma \leq \pi \tag{31}$$

where r_0 is constant along a characteristic and γ is a varying parameter $(d\theta = d\gamma)$.

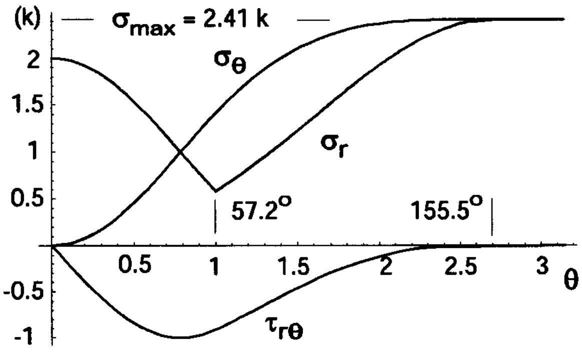

Fig. 8 Stress field for plane stress mode I crack under alternative von Mises yield condition (parabolically shaped)

This family of characteristics asymptotically approaches line OC in Fig. 7 $(\gamma = \pi)$, as the stress field approaches the biaxial state ak, which is an elliptic point on the yield surface. Being related to hyperbolic equations, there is also a second family of characteristics in the fan, which are radial lines. At the interface OB both families of characteristics have smooth transitions as the stress fields are continuous. Thus the characteristics in the uniform stress region OAB make angles of 57.2 deg and 122.8 deg with the crack line OA, as determined from (30) and (31).

Discussion

In the context of a perfectly plastic solid, a stress discontinuity represents physically the last remnant of an elastic region. Indeed, the stress discontinuity observed in the perfectly plastic limit of the plane stress mode I power law solution [1] can be eliminated under the conventional von Mises yield condition provided one generalizes the problem to include linear elastic sectors in addition to perfectly plastic sectors, as in [9]. Thus the formation of a stress discontinuity in the plastic region of a plane stress mode I crack problem under the von Mises yield condition depends on certain a priori assumptions about the neighboring regions.

References [9,10] address the more general mixed mode crack problem, where the mode I problem is considered as a special case. In [9] the plane stress linear elastic/perfectly plastic mode I problem is examined both analytically and numerically using asymptotic methods and finite element analyses. For the analytical portion, a statically admissible solution was found which is independent of the radial distance from the crack tip. For validation of the analytical solution, a finite element analysis employing Prandtl-Reuss flow theory was employed. The analytical and numerical results of [9] agree very well with one another near the crack tip. No stress discontinuity was indicated in either analysis. In contrast, a numerically determined stress distribution only slightly different from the discontinuous stress field of [1] forms as a power law material approaches the perfectly plastic state under the von Mises yield condition [10]. A fully plastic state without a stress discontinuity and without elastic regions was found in [9] only for a pure mode II loading. The results of [9] also concur with those of an earlier elastic-plastic finite element analysis in [11] for the pure mode I problem. That study involved the development of independent finite element programs for both linear elastic/perfectly plastic materials and linear elastic/power law hardening materials employing flow theory under the von Mises yield condition.

The issue of completeness for the conventional plane stress von Mises yield condition in regard to the mode I crack problem was addressed in [12]. The alternative von Mises yield condition does not have the same limitation as the traditional von Mises in this regard. As such it admits the continuous stress field derived here for the mode I crack problem within a perfectly plastic analysis. The disadvantage of the using the alternative von Mises yield condition instead of the conventional is the significant increase in the degree of the governing ordinary or partial differential equation and hence the difficulty of solving it analytically.

The solution presented in this paper for a semi-infinite length crack is readily extended to the case of the finite length crack. One need only position a second crack tip at point A of Fig. 7, introduce a second characteristic fan centered at A, and a second biaxial stress region to the right. The stress field follows immediately from the semi-infinite crack solution using symmetry. Concerning this extension, a rigid elastic region would need to be introduced at point B of Fig. 7, with the rigid elastic/perfectly plastic boundary following two different curved characteristics to the left and to the right. Lacking a stress discontinuity, a kinematically admissible velocity field is readily found for this particular stress field. A presentation of this velocity analysis will appear in a future publication. The author is unaware of the existence of a compatible velocity field for the stress field plotted in Fig. 6.

Whether or not a power-law type material can be developed for the alternative von Mises yield condition is an open question and seems worthy of consideration in the future. The solution presented here would serve as a comparison as a limiting case of a perfectly plastic material for a mode I crack problem.

It is curious to note that the stress field derived in this paper resembles the Prandtl and Hill stress fields for plane strain (see, e.g., [2]), more than the Hutchinson solution [1] for plane stress, in that the fan lies between two regions of uniform stress, rather than lying ahead of two uniform stress regions. This geometry change might have important implications regarding the strength of the strain singularity in steady-state crack propagation problems [13,14].

Concerning elastic-plastic problems, the solution presented here is consistent with a state of stress with indeterminate principal directions ($\sigma_x=\sigma_y, \tau_{xy}=0$) found ahead of the mode I crack tip along the crack line as determined using Westergaard potentials (see, e.g., [2]) for linear elastic materials. For a steadily moving crack, an elliptic region of plastic stress was noted in front of the crack tip in [15].

Appendix A

The technique used to solve the governing differential equation (10) for the alternative von Mises yield condition in this paper can also be used to solve analogous problems for the traditional von Mises yield condition and the Tresca yield condition in plane stress.

For the von Mises, the equivalent of (10) is

$$\frac{3}{4}\{[f''(\theta)]^2+4[f'(\theta)]^2\}=3k^2-\left[\frac{f''(\theta)+4f(\theta)}{2}\right]^2. \qquad (A1)$$

Note that the terms in the braces and brackets are exactly the same form as those appearing in (10). Hence the substitution of Q from (13) will also simplify (A1). The result of this substitution is another equation of the Clairaut type. A class of solutions related to uniform states of stress can be found from (A1) in much the same way as (20) was found for the alternative von Mises yield condition.

Concerning the singular solution of (A1), the relationship analogous to (22) is

$$q=3f. \qquad (A2)$$

Using (A2) its singular solution follows as

$$f_s^M=\pm k\cos(\theta+\beta). \qquad (A3)$$

Solution (A3) generates the stress field of the fan OCD in Fig. 5.

For the Tresca yield condition, the ordinary differential equation for the parabolic region MN of the yield condition of Fig. 1 is

$$\sqrt{[f''(\theta)]^2+4[f'(\theta)]^2}=4k-[f''(\theta)+4f(\theta)]. \qquad (A4)$$

Again the substitution of Q from (13) will reduce the equation to the Clairaut type, and a simple general solution related to uniform states of stress can be found. However, when a singular solution is attempted, the result analogous to (22) is independent of q, i.e.,

$$f_s^T=k. \qquad (A5)$$

No fan of slip lines is generated by f_s^T. Instead a biaxial state of stress of magnitude $2k$ is determined from (A5).

Appendix B

Subsequent to submitting this manuscript for publication, a simple explicit form of the singular solution of (10) was obtained as

$$f_s(\theta)=\frac{ak}{4}\left[3-\sin^2\frac{2}{3}(\theta+\beta)\right]\sin\frac{2}{3}(\theta+\beta). \qquad (B1)$$

References

[1] Hutchinson, J. W., 1968, "Plane Stress and Strain Fields at the Crack Tip," J. Mech. Phys. Solids, **16**, pp. 337–347.

[2] Unger, D. J., 2001, *Analytical Fracture Mechanics*, Dover Publications, Mineola, NY.

[3] von Mises, R., 1949, "Three Remarks on the Theory of the Ideal Plastic Body," *Reissner Anniversary Volume, Contributions to Applied Mechanics*, J. W. Edwards, Publisher, Inc., Ann Arbor, MI, pp. 415–429.

[4] Unger, D. J., 1990, "Analytic Continuation of Stresses across a Mode I Elastoplastic Interface," Eng. Fract. Mech., **36**, pp. 763–776.

[5] Unger, D. J., 1998, "Stress across an Elastoplastic Boundary of a Mode I Crack Parabolic to Hyperbolic Plasticity Transition," Theor. Appl. Fract. Mech., **30**, pp. 195–208.

[6] Zwillinger, D., 1989, *Handbook of Differential Equations*, Academic Press, San Diego.

[7] Freudenthal, A. M., and Geiringer, H., 1958, "The Mathematical Theories of the Inelastic Continuum," Elasticity and Plasticity, *Handbuch der Physik*, **VI**, Flügge, S., ed., Springer-Verlag, Berlin, pp. 229–433.

[8] Geiringer, H., 1973, "Ideal Plasticity," Mechanics of Solids III, *Handuch der Physik*, **VIa/3**, Truesdell, C., ed., Springer-Verlag, Berlin, pp. 403–533.

[9] Dong, P., and Pan, J., 1990, "Plane-Stress Mixed-Mode Near-Tip Fields in Elastic Perfectly Plastic Solids," Eng. Fract. Mech., **37**, pp. 43–57.

[10] Shih, C. F., 1973, *Elastic-Plastic Analysis of the Combined Mode Crack Problem*, PhD thesis, Harvard University, Cambridge.

[11] Narasimhan, R., and Rosakis, A. J., 1988, "A Finite Element Analysis of Small-Scale Yielding near a Stationary Crack under Plane Stress," J. Mech. Phys. Solids, **36**, pp. 77–117.

[12] Sham, T.-L., and Hancock, J. W., 1999, "Mode I Crack Tips with Incomplete Crack Tip Plasticity in Plane Stress," J. Mech. Phys. Solids, **47**, pp. 2011–2027.

[13] Rice, J. R., 1982, "Elastic-Plastic Crack Growth," *Mechanics of Solids*, H. G., Hopkins, and M. J., Sewell, eds., Pergamon Press, Oxford, pp. 539–562.

[14] Broberg, K. B., 1999, *Cracks and Fracture*, Academic Press, San Diego.

[15] Narasimhan, R., Rosakis, A. J., and Hall, J. F., 1987, "A Finite Element Study of Stable Crack Growth under Plane Stress Conditions: Part I-Elastic Perfectly-Plastic Solids," ASME J. Appl. Mech., **54**, pp. 838–845.

The Coupled Thermoelastic Transversely Isotropic Bimaterial: Interface Crack Extension

L. M. Brock
Department of Mechanical Engineering,
University of Kentucky,
Lexington, KY 40506
e-mail: brock@engr.uky.edu
Fellow ASME

A semi-infinite crack grows at a constant subcritical speed along the interface of rigidly bonded, dissimilar transversely isotropic, coupled thermoelastic half-spaces. Shear and normal loads that move on the crack faces drive the process. A dynamic steady state of plane strain is considered. Robust asymptotic full-field solutions for the related problem of translating interface disturbances are first obtained. These lead to coupled singular integral equations for the crack problem that are solved analytically. Expressions for the crack opening components and discontinuity in temperature between crack faces, the traction and temperature change ahead of the crack, and debonding energy rate are presented. These show that the critical crack speed is the minimum of the two Rayleigh speeds and, if it exists, the Stoneley speed. The case of zinc bonded to a thermally inert rigid solid is examined, and calculations for interface temperature change and debonding energy rate given. Apart from any fracture criterion, these parameters show sensitivity to crack speed and to the extent which compressive crack face loading dominates shear loading. Indeed, interface temperature change may decrease in magnitude with crack speed when shear loading dominates. [DOI: 10.1115/1.1825435]

1 Introduction

The interface crack in equilibrium has been considered [1–3] for an isotropic bimaterial and asymptotic dynamic [4] and transient [5] studies also exist. The equilibrium interface crack in an anisotropic bimaterial [6–8], and the dynamic case for an orthotropic or transversely isotropic bimaterial [9,10] have been considered. These treatments are isothermal, and so this article presents a study of interface crack extension in a bimaterial consisting of rigidly bonded, transversely isotropic, coupled thermoelastic half-spaces. A dynamic steady state of plane strain is assumed, in which a semi-infinite interface crack grows at a constant rate under the action of translating crack face loads.

In part I, general results for a disturbance moving on a transversely isotropic, coupled thermoelastic half-space are given. These are used to obtain full-field solution expressions for translation of a strip of displacement and temperature discontinuity along the interface of rigidly-bonded dissimilar half-spaces. The translation speed is constant and subcritical, and a dynamic steady state of plane strain is examined. The findings of part I then form the basis for Part II—analysis of interface crack extension.

1.1 Basic Equations in the Half-Space.

Consider a half-space at rest at a uniform (absolute) temperature T_0. It is transversely isotropic, with Cartesian coordinates (x,y,z) defining the plane (xz) and axis (y) of material symmetry. The half-space surface is taken to be $y=0$, and the half-space itself can be either $y>0$ or $y<0$. If a boundary disturbance induces a state of plane strain with respect to (x,y), then, from results for anisotropic elasticity [11–15] and coupled thermoelasticity [16,17], the relevant field variables are the (x,y)-components of displacement (u_x,u_y), change in absolute temperature θ, and tractions $(\sigma_x,\sigma_y,\sigma_z,\sigma_{xy})$. The relevant material properties are elastic constants $(c_{11},c_{12},c_{13},c_{22},c_{44})$, mass density ρ, specific heat (at constant strain) c_v, thermal expansion coefficients (α_x,α_y), and thermal conductivity parameters (K_x,K_y). These obey constraints [13,16]

$$c_{11}>|c_{13}|, \quad (c_{11}+c_{13})c_{22}>2c_{12}^2, \quad c_{44}>0 \tag{1a}$$

$$(K_x,K_y)>0, \quad (\alpha_x,\alpha_y)>0, \quad \rho>0, \quad c_v>0 \tag{1b}$$

The plane strain disturbance on the surface is confined to a region of fixed dimensions that translates in the positive x-direction with constant subcritical speed v. A dynamic steady state ensues, so that it is convenient to translate the Cartesian system with the region. The independent variables are then (x,y), and time differentiation in the inertial frame can be written as $-v(\,)_{,x}$; the operation $(\,)_{,s}$ denotes s-differentiation.

It is convenient to introduce the Lame' shear modulus symbol, rotational wave speed, thermoelastic characteristic length and average conductivity

$$\mu=c_{44}, \quad v_r=\sqrt{\frac{\mu}{\rho}}, \quad h=\frac{K_x+K_y}{2\rho c_v v_r}, \quad \tilde{\alpha}=\tfrac{1}{3}(2\alpha_x+\alpha_y) \tag{2}$$

nondimensionalized disturbance speed

$$c=\frac{v}{v_r} \tag{3}$$

and, after [13], dimensionless constants

$$a=\frac{c_{22}}{c_{44}}, \quad b=\frac{c_{11}}{c_{44}}, \quad m=1+\frac{c_{12}}{c_{44}},$$

$$m_3=1+\frac{c_{13}}{c_{44}}, \quad \gamma=1+ab-m^2 \tag{4}$$

Dimensionless constants

$$\varepsilon=\frac{T_0}{c_v}(\tilde{\alpha}v_r)^2, \quad C_s=\frac{2K_s}{K_x+K_y} \tag{5a}$$

$$\Gamma_x=(b+m_3-1)\frac{\alpha_x}{\tilde{\alpha}}+(m-1)\frac{\alpha_y}{\tilde{\alpha}}, \quad \Gamma_y=2(m-1)\frac{\alpha_x}{\tilde{\alpha}}+a\frac{\alpha_y}{\tilde{\alpha}} \tag{5b}$$

Contributed by the Applied Mechanics Division of THE AMERICAN SOCIETY OF MECHANICAL ENGINEERS for publication in the ASME JOURNAL OF APPLIED MECHANICS. Manuscript received by the Applied Mechanics Division, October 28, 2003; final revision, May 28, 2004. Associate Editor: H. Gao. Discussion on the paper should be addressed to the Editor, Professor Robert M. McMeeking, Journal of Applied Mechanics, Department of Mechanical and Environmental Engineering, University of California-Santa Barbara, Santa Barbara, CA 93106-5070, and will be accepted until four months after final publication in the paper itself in the ASME JOURNAL OF APPLIED MECHANICS.

are also introduced. From [11–17] the governing equations in the absence of body forces can then be written as

$$(b-c^2)u_{x,xx}+u_{x,yy}+mu_{y,xy}-\tilde{\alpha}\Gamma_x\theta_{,x}=0 \tag{6a}$$

$$mu_{x,xy}+(1-c^2)u_{y,xx}+au_{y,yy}-\tilde{\alpha}\Gamma_y\theta_{,y}=0 \tag{6b}$$

$$h(C_x\theta_{,xx}+C_y\theta_{,yy})+c\left[\theta+\frac{\varepsilon}{\tilde{\alpha}}(\Gamma_x u_{x,x}+\Gamma_y u_{y,y})\right]_{,x}=0 \tag{6c}$$

Similarly, the constitutive relations take the form

$$\begin{bmatrix}\sigma_x\\ \sigma_y\\ \sigma_z\\ \sigma_{xy}\end{bmatrix}=\mu\begin{bmatrix}b & m-1 & \Gamma_x & 0\\ m-1 & a & \Gamma_y & 0\\ m_3-1 & m-1 & \Gamma_x & 0\\ 0 & 0 & 0 & 1\end{bmatrix}\begin{bmatrix}u_{x,x}\\ u_{y,y}\\ -\tilde{\alpha}\theta\\ u_{x,y}+u_{y,x}\end{bmatrix} \tag{7}$$

1.2 Transform Solution in Half-Space. A bilateral Laplace transform and inverse can be defined as [18]

$$\hat{f}=\int_{-\infty}^{\infty}f(x)e^{-px}dx, \quad f(x)=\frac{1}{2\pi i}\int\hat{f}e^{px}dp \tag{8}$$

Transform variable p is imaginary in the first (transform) integral, and the second (inversion) integration is taken over a Bromwich contour in the p-plane. Application of the transform integral to (6) in view of (7) and the requirement that (u_x, u_y, θ) be bounded as $\sqrt{x^2+y^2}\rightarrow\infty$ gives the general transforms

$$p\hat{u}_x=\tilde{\alpha}\sum(\Gamma_x B^2+k_y q_i^2)\psi_i e^{-pq_i|y|} \tag{9a}$$

$$p\hat{u}_y=-\tilde{\alpha}\,\mathrm{sgn}(y)\sum(k_x+\Gamma_y q_i^2)q_i\psi_i e^{-pq_i|y|} \tag{9b}$$

$$\hat{\theta}=a\sum T(q_i)\psi_i e^{-pq_i|y|} \tag{9c}$$

for $y\neq 0$. Summation is over index $i=(1,2,3)$ and the ψ_i are coefficients to be determined by imposing conditions consistent with the surface disturbance. The dimensionless term

$$T(q)=q^4+(\Delta_0+A_0^2+B^2)q^2+A_0^2B^2 \tag{10}$$

and dimensionless parameters

$$\sqrt{a}A_0=\sqrt{b-c^2}, \quad B=\sqrt{1-c^2} \tag{11a}$$

$$k_x=(b-c^2)\Gamma_y-m\Gamma_x, \quad k_y=a\Gamma_x-m\Gamma_y \tag{11b}$$

$$a\Delta_0=(a-1)(b-1)-m^2 \tag{11c}$$

The anisotropy coefficient $\Delta_0=0$ in the isotropic limit. Dimensionless quantities q_i^2 are the three roots of

$$\left(C_x+C_y q^2+\frac{c}{hp}\right)T(q)+\frac{c\varepsilon}{ahp}[\Gamma_x^2B^2+(k_x\Gamma_y+k_y\Gamma_x)q^2+\Gamma_y^2q^4] \tag{12}$$

Equation (12) and the cubic root formula [19] imply that the form of q_i may require inversion of (9) by numerical quadrature. Therefore, robust asymptotic expansions of the roots of (12), (9) and corresponding stress transforms are used. Specifically, a transform valid for $|hp|\ll 1$ has an inverse valid for $|x/h|\gg 1$. Isotropic calculations [17] show that $h\approx O(10^{-8})$ m. Expansions can then be made for small $|p|$ and only lowest-order terms kept. The roots of (12) become

$$(q_1,q_2)=\frac{\sqrt{-p}}{\sqrt{p}}(A',B'), \quad q_3=\frac{1}{p}\sqrt{\frac{-p}{h'}} \tag{13}$$

Length h' and dimensionless terms (A',B') are defined by (2)–(5) and

$$h'=\frac{aC_y}{a_\varepsilon c}h, \quad A'=\Omega+\omega, \quad B'=\Omega-\omega \tag{14a}$$

$$2(\Omega,\omega)=\sqrt{\Delta_\varepsilon+(A_\varepsilon\pm B)^2}, \quad A'B'=A_\varepsilon B \tag{14b}$$

$$\sqrt{a_\varepsilon}A_\varepsilon=\sqrt{b_\varepsilon-c^2}, \quad a_\varepsilon\Delta_\varepsilon=(a_\varepsilon-1)(b_\varepsilon-1)-m_\varepsilon^2 \tag{14c}$$

These expressions feature

$$a_\varepsilon=a+\varepsilon_x, \quad b_\varepsilon=b+\varepsilon_y, \quad m_\varepsilon=m+\sqrt{\varepsilon_x\varepsilon_y} \tag{15a}$$

$$m_{3\varepsilon}=m_3+\varepsilon_y, \quad \gamma_\varepsilon=1+a_\varepsilon b_\varepsilon-m_\varepsilon^2 \tag{15b}$$

$$\varepsilon_s=\varepsilon\Gamma_s^2 \tag{15c}$$

The $(\varepsilon_x, \varepsilon_y)$ are thermoelastic coupling constants [17] for transverse isotropy. Like its isothermal counterpart in (11c), anisotropy coefficient $\Delta_\varepsilon=0$ in the isotropic limit, as does the anisotropy factor Δ defined by (11b) and

$$\Delta=\Gamma_x\Gamma_yB^2-k_xk_y, \quad c^2\Delta=N_xN_yB^2-M_xM_y \tag{16a}$$

$$M_s=k_s+\Gamma_sB^2, \quad N_s=k_s+\Gamma_s \tag{16b}$$

It can also be shown that (Δ, k_s, M_s, N_s) are invariant under the isothermal-thermoelastic transformation $(a,b,m)\rightarrow(a_\varepsilon, b_\varepsilon, m_\varepsilon)$.

1.3 Bounded Solutions: Material Characterization Study of (11a) and (14) shows that $c=\pm(1,\sqrt{b},\sqrt{b_\varepsilon})$ are branch points of (B,B'), A_0 and (A_ε, A'), respectively, in the c-plane. In light of (2)–(5) $(v_r, \sqrt{b}v_r, \sqrt{b_\varepsilon}v_r)$ are the rotational, isothermal dilatational, and thermoelastic dilatational wave speeds in the material symmetry plane. Because [13] $b_\varepsilon>b>1$, terms (A_0, A_ε, B) are purely real for all subsonic $(0<v<v_r)$ disturbance speeds. Terms (A',B') share the branch cuts of (A_ε, B), respectively, but, through their components (Ω,ω), exhibit others as well. Modification [20] of a system for isothermal transverse isotropy [13] gives

$$\text{Category 1:} \quad 2\sqrt{a_\varepsilon b_\varepsilon}\leqslant\gamma_\varepsilon\leqslant 1+a_\varepsilon b_\varepsilon \ \ (1<b_\varepsilon<a_\varepsilon)$$

$$a_\varepsilon+b_\varepsilon\leqslant\gamma_\varepsilon\leqslant 1+a_\varepsilon b_\varepsilon \ \ (1<a_\varepsilon<b_\varepsilon)$$

$$2a_\varepsilon\leqslant\gamma_\varepsilon\leqslant 1+a_\varepsilon^2 \ \ (1<b_\varepsilon=a_\varepsilon)$$

$$\text{Category 2:} \quad 1+b_\varepsilon<\gamma_\varepsilon<a_\varepsilon+b_\varepsilon, \quad \gamma_\varepsilon^2-4a_\varepsilon b_\varepsilon<0$$

$$\text{Category 3:} \quad \gamma_\varepsilon<1+b_\varepsilon, \quad \gamma_\varepsilon^2-4a_\varepsilon b_\varepsilon<0$$

In the c-plane, Ω and ω exhibit, respectively, for category 3 the branch points

$$c=\pm c_0, \quad c_0=\sqrt{1-\left(\frac{a_\varepsilon\sqrt{-\Delta_\varepsilon}-m_\varepsilon}{a_\varepsilon-1}\right)^2} \tag{17a}$$

$$c=\pm i\overline{c_0}, \quad \overline{c_0}=\sqrt{\left(\frac{a_\varepsilon\sqrt{-\Delta_\varepsilon}+m_\varepsilon}{a_\varepsilon-1}\right)^2-1} \tag{17b}$$

Term ω exhibits branch points

$$c=\pm c_c, \quad c_c=\sqrt{\left[\frac{m_\varepsilon(\pm)ia_\varepsilon\sqrt{\Delta_\varepsilon}}{a_\varepsilon-1}\right]^2-1} \tag{18}$$

for category 1, and (17b) for category 2. These points collapse to the origin and $(A',B')\rightarrow(A_\varepsilon, B)$ in the isotropic limit $(\Delta_\varepsilon=0)$. The nonreal branch points (17b) and (18) do not arise for positive real disturbance speeds. Thus, for category 1 and 2 (A',B',Ω) are given by (14) and are positive-real for $0<|c|<1$ on the Re(c)-axis for subsonic v. However $0<c_0<1$ in (17a), so that (A',B',Ω) for category 3 are all positive-real only for $c_0<|c|<1$, i.e., v is in the subsonic range $c_0v_r<v<v_r$. For v in the range $0<v<c_0v_r$, Ω remains positive-real for $0<|c|<c_0$, but (14a) is replaced by

$$A'=\Omega\mp i\overline{\omega}, \quad B'=\Omega\pm i\overline{\omega}, \quad \overline{\omega}=\sqrt{-\Delta_\varepsilon-(A_\varepsilon-B)^2} \tag{19}$$

for $\mathrm{Im}(c)=0\pm$, $0<|c|<c_0$. In light of all this and the fact that $\Omega>(\omega,\overline{\omega})\geqslant 0$, Eq. (9) is bounded as $|y|\to\infty$ for all subsonic v when $\mathrm{Re}(\sqrt{\pm p})\geqslant 0$ in the p-plane with, respectively, branch cuts $\mathrm{Im}(p)=0$, $\mathrm{Re}(p)<0$ and $\mathrm{Im}(p)=0$, $\mathrm{Re}(p)>0$.

1.4 Translating Interface Strip of Discontinuity. Now consider two such half-spaces of dissimilar properties, rigidly bonded along interface $y=0$. This bimaterial is at rest at a common uniform (absolute) temperature T_0 when an interface strip of discontinuity in displacement and temperature appears and translates in the positive x-direction with a constant subcritical speed v. The strip is of infinite extent in the z-direction, but of fixed width, and the discontinuities vary only with location across the width. The situation is one of plane strain, and we assume that a dynamic steady state is achieved.

Therefore, the basic equations presented above hold for each half-space, with only T_0 being the same in each set. In particular, (6) and (7) govern, and (u_x, u_y, θ) are bounded for $\sqrt{x^2+y^2}\to\infty$. Now, however, interface conditions

$$u_{x1}-u_{x2}=U_x(x), \quad u_{y1}-u_{y2}=U_y(x); \quad \theta_1-\theta_2=\Theta(x) \tag{20a}$$

$$\sigma_{xy1}-\sigma_{xy2}=\sigma_{y1}-\sigma_{y2}=\theta_{1,y}-\theta_{2,y}=0 \tag{20b}$$

hold for $y=0$. Subscripts (1,2) signify, respectively, half-space $(y>0, y<0)$, and discontinuity functions $(U_x, U_y, \Theta)\equiv 0$, $x\notin L$, where L denotes the strip region. The functions are continuous except perhaps at isolated locations for $x\in L$; (U_x, U_y) in particular vanish continuously at the strip edges.

Transforms (9) are also valid for each half-space. The two coefficient sets (ψ_{i1}, ψ_{i2}) are obtained by substitution of (9) and their traction counterparts for each half-space into the transform of (20). Use of asymptotic results (13)–(16) gives, for example, the coefficients for half-space 1 $(y>0)$ as

$$\psi_{11}=\frac{1}{S}\left[\frac{a_\varepsilon}{B\Delta(A'-B')}\right]_1\left(-X_B p\hat{U}_x+Y_B\frac{\sqrt{-p}}{\sqrt{p}}p\hat{U}_y\right) \tag{21a}$$

$$\psi_{21}=\frac{1}{S}\left[\frac{a_\varepsilon}{B\Delta(A'-B')}\right]_1\left(X_A p\hat{U}_x+Y_A\frac{\sqrt{-p}}{\sqrt{p}}p\hat{U}_y\right) \tag{21b}$$

$$\begin{aligned}\psi_{31}=&\frac{p^2\hat{U}_x}{\sqrt{h_1'}+\sqrt{h_2'}}\frac{h_1'^{3/2}}{a_1}\frac{1}{S}\left[\left(\frac{\varepsilon}{\tilde{\alpha}}\right)_2\tilde{\alpha}_1 X_{12}+\varepsilon_1 X_{21}\right]\\&+\frac{p^2\hat{U}_y}{\sqrt{h_1'}+\sqrt{h_2'}}\frac{h_1'^{3/2}}{a_1}\frac{2}{S}\frac{\sqrt{-p}}{\sqrt{p}}\left[\left(\frac{\varepsilon}{\tilde{\alpha}}\right)_2\tilde{\alpha}_1 Y_{12}-\varepsilon_1 Y_{21}\right]\\&+\frac{p\hat{\Theta}}{\sqrt{h_1'}+\sqrt{h_2'}}\frac{h_1'^{3/2}\tilde{\alpha}}{a_1}\end{aligned} \tag{21c}$$

In (21) the dimensionless terms

$$X_s=\frac{\mu_2}{\mu_1}R_2V_{1s}+2(a_\varepsilon A_\varepsilon\Omega)_2\Sigma_{1s}+N_2T_{1s} \tag{22a}$$

$$Y_s=\frac{\mu_2}{\mu_1}R_2U_{1s}+2(a_\varepsilon B\Omega)_2T_{1s}+N_2\Sigma_{1s} \tag{22b}$$

$$X_{ik}=\frac{\mu_i}{\mu_k}R_iK_k+4(a_\varepsilon A_\varepsilon\Omega)_i(B\Omega N_y)_k+N_iP_k \tag{22c}$$

$$Y_{ik}=\frac{\mu_i}{\mu_k}R_i(B\Gamma_y\Omega)_k+(a_\varepsilon B\Omega)_iP_k+N_i(BN_y\Omega)_k \tag{22d}$$

$$\begin{aligned}S=&\frac{\mu_1}{\mu_2}R_1M_2+\frac{\mu_2}{\mu_1}R_2M_1+2N_1N_2+4(a_\varepsilon\Omega)_1(a_\varepsilon\Omega)_2(A_{\varepsilon1}B_2\\&+A_{\varepsilon2}B_1)\end{aligned} \tag{22e}$$

Additional subscripts (1,2) are understood for dimensionless quantities

$$\begin{aligned}&U_{(A,B)}=\Gamma_xB^2-k_y(A',B')^2,\\&V_{(A,B)}=(A',B')[k_x-\Gamma_y(A',B')^2]\end{aligned} \tag{23a}$$

$$\begin{aligned}&\Sigma_{(A,B)}=N_xB^2-M_y(A',B')^2,\\&T_{(A,B)}=(A',B')[M_x-N_y(A',B')^2]\end{aligned} \tag{23b}$$

that exhibit (A', B'), and dimensionless terms

$$K=k_yA_\varepsilon+\Gamma_xB, \quad P=M_yA_\varepsilon+N_xB \tag{24a}$$

$$M=a_\varepsilon A_\varepsilon+B, \quad N=a_\varepsilon A_\varepsilon+(1-m_\varepsilon)B \tag{24b}$$

$$R=-a_\varepsilon c^2A_\varepsilon+[a_\varepsilon^2A_\varepsilon^2-(m_\varepsilon-1)^2]B \tag{24c}$$

that exhibit (A_ε, B). Terms R and S are factored forms of Rayleigh and Stoneley functions associated with the common plane (xz) of material symmetry. Their forms are actually simpler than isothermal isotropic results often used [21,22]. The factorizations minimize dependence on the anisotropy factor Δ and (asymptotic) cubic roots (A', B'). In particular, (9) and (21) show that these terms appear only in expressions for the corresponding half-space, i.e., the category of one half-space has limited effect on transform solutions for the other. Moreover, even for category 3 case (19), the real-valued nature of strip speed dependence in transform solutions is maintained because contributions corresponding to (ψ_1, ψ_2) for the given half-space are complex conjugates with respect to c for that half-space. It can be shown that

$$R=a_\varepsilon b_\varepsilon-(m_\varepsilon-1)^2>0, \;\; R=-\sqrt{a_\varepsilon(b_\varepsilon-1)}<0, \;\; R=0 \tag{25}$$

for $v=(0, \pm v_r, \pm c_Rv_r)$, respectively, where $0<c_R<1$. In light of (2), then, $v_R=c_Rv_r$ is the thermoelastic Rayleigh speed in the material symmetry plane. Similarly,

$$\begin{aligned}S=&\sqrt{a_{\varepsilon1}\Delta_{\varepsilon1}+(\sqrt{a_{\varepsilon1}}+\sqrt{b_{\varepsilon1}})^2}\sqrt{a_{\varepsilon2}\Delta_{\varepsilon2}+(\sqrt{a_{\varepsilon2}}+\sqrt{b_{\varepsilon2}})^2}\\&\times(\sqrt{a_{\varepsilon1}b_{\varepsilon2}}+\sqrt{a_{\varepsilon2}b_{\varepsilon1}})+(\sqrt{a_\varepsilon b_\varepsilon}+m_\varepsilon-1)_1\\&\times\left[\frac{\mu_1}{\mu_2}(\sqrt{a_\varepsilon b_\varepsilon}+1-m_\varepsilon)_1\sqrt{a_{\varepsilon2}b_{\varepsilon2}}+(\sqrt{a_\varepsilon b_\varepsilon}+1-m_\varepsilon)_2\right]\\&+(\sqrt{a_\varepsilon b_\varepsilon}+m_\varepsilon-1)_2\left[\frac{\mu_2}{\mu_1}(\sqrt{a_\varepsilon b_\varepsilon}+1-m_\varepsilon)_2\sqrt{a_{\varepsilon1}b_{\varepsilon1}}\right.\\&\left.+(\sqrt{a_\varepsilon b_\varepsilon}+1-m_\varepsilon)_1\right]\end{aligned} \tag{26a}$$

$$\begin{aligned}S=&\sqrt{a_{\varepsilon1}(b_{\varepsilon1}-1)}\left(\frac{\mu_2}{\mu_1}R_2-\frac{\mu_1}{\mu_2}M_2+2N_2\right)\\&+2(a_\varepsilon B\Omega)_2\sqrt{b_{\varepsilon1}-1}\sqrt{a_{\varepsilon1}\Delta_{\varepsilon1}+b_{\varepsilon1}-1}\end{aligned} \tag{26b}$$

for $v=0$ and $v=v_{r1}<v_{r2}$, respectively. The corresponding result for $v=v_{r2}<v_{r1}$ follows from (26*b*) upon interchange of subscripts (1,2). It can be shown that (26*a*) is non-negative, but (26*b*) and its counterpart are either both positive, or of different sign. In the latter instance, a thermoelastic Stoneley speed v_S exists, where $0<v_S<\min(v_{r1}, v_{r2})$.

1.5 Full-Field Expressions. In light of (9) and (21) the imaginary p-axis can serve as the Bromwich contour in the inversion integral of (8). Indeed, integration can be performed with a standard table [23]. As illustration, consider the displacement components (u_{x1}, u_{y1}) in half-space $y>0$. For all subsonic, i.e., $0<v<\min(v_{r1}, v_{r2})$, speeds for category 1 and 2 and for the subsonic range $(c_0v_r)_1<v<\min(v_{r1}, v_{r2})$ for category 3,

$$\begin{aligned} u_{x1}=&\frac{1}{2\pi S}\Bigg(U_{\Omega 1}+\frac{U_{\tau 1}}{\omega_1}\Bigg)\int_L\frac{A_1'yU_x(t)}{\tau^2+A_1'^2y^2}dt+\frac{1}{\pi S}\Bigg(U_{\tau 1}'\\ &+\frac{U_{\Omega 1}'}{2\omega_1}\Bigg)\int_L\frac{\tau U_y(t)}{\tau^2+A_1'^2y^2}dt+\frac{1}{2\pi S}\Bigg(U_{\Omega 1}\\ &-\frac{U_{\tau 1}}{\omega_1}\Bigg)\int_L\frac{B_1'yU_x(t)}{\tau^2+B_1'^2y^2}dt+\frac{1}{\pi S}\Bigg(U_{\tau 1}'\\ &-\frac{U_{\Omega 1}'}{2\omega_1}\Bigg)\int_L\frac{\tau U_y(t)}{\tau^2+B_1'^2y^2}dt \end{aligned} \tag{27a}$$

$$\begin{aligned} u_{y1}=&\frac{1}{\pi S}\Bigg(\frac{V_{\tau 1}'}{2\omega_1}-V_{\Omega 1}'\Bigg)\int_L\frac{\tau U_x(t)}{\tau^2+A_1'^2y^2}dt+\frac{1}{2\pi S}\Bigg(V_{\Omega 1}\\ &-\frac{V_{\tau 1}}{\omega_1}\Bigg)\int_L\frac{A_1'yU_y(t)}{\tau^2+A_1'^2y^2}dt-\frac{1}{\pi S}\Bigg(\frac{V_{\tau 1}'}{2\omega_1}\\ &+V_{\Omega 1}'\Bigg)\int_L\frac{\tau U_x(t)}{\tau^2+B_1'^2y^2}dt+\frac{1}{2\pi S}\Bigg(V_{\Omega 1}\\ &+\frac{V_{\tau 1}}{\omega_1}\Bigg)\int_L\frac{B_1'yU_y(t)}{\tau^2+B_1'^2y^2}dt \end{aligned} \tag{27b}$$

Here L signifies integration over the strip width and

$$\tau=t-x \tag{28}$$

In the speed range $0<v<(c_0v_r)_1$ for category 3, however,

$$\begin{aligned} u_{x1}=&\frac{-U_{\tau 1}}{2\pi S\overline{\omega}_1}\int_L\left(\frac{\tau_{1+}}{\tau_{1+}^2+\Omega_1^2y^2}-\frac{\tau_{1-}}{\tau_{1-}^2+\Omega_1^2y^2}\right)U_x(t)dt\\ &+\frac{U_{\Omega 1}}{2\pi S}\int_L\left(\frac{\Omega_1y}{\tau_{1+}^2+\Omega_1^2y^2}+\frac{\Omega_1y}{\tau_{1-}^2+\Omega_1^2y^2}\right)U_x(t)dt\\ &+\frac{U_{\Omega 1}'}{2\pi S\overline{\omega}_1}\int_L\left(\frac{\Omega_1y}{\tau_{1+}^2+\Omega_1^2y^2}-\frac{\Omega_1y}{\tau_{1-}^2+\Omega_1^2y^2}\right)U_y(t)dt\\ &+\frac{U_{\tau 1}'}{\pi S}\int_L\left(\frac{\tau_{1+}}{\tau_{1+}^2+\Omega_1^2y^2}+\frac{\tau_{1-}}{\tau_{1-}^2+\Omega_1^2y^2}\right)U_y(t)dt \end{aligned} \tag{29a}$$

$$\begin{aligned} u_{y1}=&\frac{V_{\Omega 1}'}{2\pi S\overline{\omega}_1}\int_L\left(\frac{\Omega_1y}{\tau_{1+}^2+\Omega_1^2y^2}-\frac{\Omega_1y}{\tau_{1-}^2+\Omega_1^2y^2}\right)U_x(t)dt\\ &-\frac{V_{\tau 1}'}{\pi S}\int_L\left(\frac{\tau_{1+}}{\tau_{1+}^2+\Omega_1^2y^2}+\frac{\tau_{1-}}{\tau_{1-}^2+\Omega_1^2y^2}\right)U_x(t)dt\\ &+\frac{V_{\tau 1}}{2\pi S\overline{\omega}_1}\int_L\left(\frac{\tau_{1+}}{\tau_{1+}^2+\Omega_1^2y^2}-\frac{\tau_{1-}}{\tau_{1-}^2+\Omega_1^2y^2}\right)U_y(t)dt\\ &+\frac{V_{\Omega 1}}{2\pi S}\int_L\left(\frac{\Omega_1y}{\tau_{1+}^2+\Omega_1^2y^2}+\frac{\Omega_1y}{\tau_{1-}^2+\Omega_1^2y^2}\right)U_y(t)dt \end{aligned} \tag{29b}$$

In both (29*a*), (29*b*),

$$\tau_{1\pm}=t-x\mp\overline{\omega}_1y \tag{30}$$

In (27*a*) and (29*a*) dimensionless quantities

$$\begin{aligned} U_{\tau 1}=&\Omega_1M_1'\frac{\mu_2}{\mu_1}R_2+\Omega_1N_1'N_2+B_1[a_\varepsilon^2A_\varepsilon^2+c^2-(m_\varepsilon\\ &-1)^2]_1(a_\varepsilon A_\varepsilon\Omega)_2 \end{aligned} \tag{31a}$$

$$U_{\Omega 1}=4(a_\varepsilon B\Omega)_1(a_\varepsilon A_\varepsilon\Omega)_2+N_1N_2+M_1\frac{\mu_2}{\mu_1}R_2 \tag{31b}$$

$$U_{\tau 1}'=(a_\varepsilon B\Omega)_1N_2+N_1(a_\varepsilon B\Omega)_2 \tag{31c}$$

$$\begin{aligned} U_{\Omega 1}'=&2\Omega_1N_1'(a_\varepsilon B\Omega)_2+m_{\varepsilon 1}B_1\frac{\mu_2}{\mu_1}R_2+\frac{1}{2}B_1[a_\varepsilon^2A_\varepsilon^2+c^2-(m_\varepsilon\\ &-1)^2]_1N_2 \end{aligned} \tag{31d}$$

In (27*b*) and (29*b*) dimensionless quantities

$$\begin{aligned} V_{\tau 1}=&\Omega_1M_1'\frac{\mu_2}{\mu_1}R_2+\Omega_1N_1'N_2+A_{\varepsilon 1}[a_\varepsilon^2A_\varepsilon^2+c^2-(m_\varepsilon\\ &-1)^2]_1(a_\varepsilon B\Omega)_2 \end{aligned} \tag{32a}$$

$$V_{\Omega 1}=4(a_\varepsilon A_\varepsilon\Omega)_1(a_\varepsilon B\Omega)_2+N_1N_2+M_1\frac{\mu_2}{\mu_1}R_2 \tag{32b}$$

$$V_{\tau 1}'=(a_\varepsilon A_\varepsilon\Omega)_1N_2+N_1(a_\varepsilon A_\varepsilon\Omega)_2 \tag{32c}$$

$$\begin{aligned} V_{\Omega 1}'=&2\Omega_1N_1'(a_\varepsilon A_\varepsilon\Omega)_2+m_{\varepsilon 1}A_{\varepsilon 1}\frac{\mu_2}{\mu_1}R_2+\frac{1}{2}A_{\varepsilon 1}[a_\varepsilon^2A_\varepsilon^2+c^2-(m_\varepsilon\\ &-1)^2]_1N_2 \end{aligned} \tag{32d}$$

In addition to parameters in (24), dimensionless terms (M_1',N_1') appear in (31) and (32) where, with additional subscript (1,2) understood,

$$M'=a_\varepsilon A_\varepsilon-B,\quad N'=a_\varepsilon A_\varepsilon+(m_\varepsilon-1)B \tag{33}$$

The study of (27)–(33) shows that the anisotropy factor Δ_1 in the denominators of (21) cancels from field variable expressions. It can be shown that (27) and (29) are identical when $y=0$ because the denominator terms $(\omega_1,\overline{\omega_1})$ cancel out. They are also identical when $c_1=c_{01}$. Then $(\omega_1,\overline{\omega_1})=0$, but results are finite because the factors of $(1/\omega_1,1/\overline{\omega_1})$, respectively, vanish themselves when $(\omega_1,\overline{\omega_1})=0$. The function S in (27) and (29), however, does imply singular behavior at v_S, if it exists. Therefore, the subcritical speed requirement for the translating interface strip should be

$$0<v<\min(v_{r1},v_{r2},v_S) \tag{34}$$

2.1 Interface Crack Problem. Consider two dissimilar transversely isotropic, coupled thermoelastic half-spaces. In terms of Cartesian coordinates (x,y,z) they have interface $y=0$, and are rigidly bonded over the portion $y=0$, $x>0$. The interface (xz) plane and its normal (y-direction) coincide with, respectively, the plane and axis of material symmetry for both half-spaces. These are at rest at uniform (absolute) temperature T_0 when opposing shear and normal forces (line loads in the z-direction) (F_x,F_y) are applied to the half-space surfaces in the separation zone $y=0$, $x<0$. These are translated in the positive x-direction with subcritical speed v, thereby inducing debonding. A dynamic steady state of plane strain ensues, in which the interface crack also extends with speed v, and the forces maintain a fixed distance L from the crack edge. It is convenient to translate the Cartesian system with the crack, so that $(x,y)=0$ always locates its edge. Equation (6) and (7) hold for each half-space, and the interface conditions are

$$\sigma_{xy1}-\sigma_{xy2}=\sigma_{y1}-\sigma_{y2}=\theta_{1,y}-\theta_{2,y}=0\quad(y=0) \tag{35a}$$

$$\begin{gathered} \sigma_{xy1}=-F_x\delta(x+L),\quad\sigma_{y1}=-F_y\delta(x+L),\\ \theta_{1,y}=0\quad(y=0,x<0) \end{gathered} \tag{35b}$$

$$u_{x1}-u_{x2}=u_{y1}-u_{y2}=\theta_1-\theta_2=0\quad(y=0,x>0) \tag{35c}$$

where δ is the Dirac function. The last condition in (35*b*) implies negligible heat flux across crack faces. Comparison of (35) with (20) shows that, if (U_x,U_y) and Θ are interpreted as, respectively, the crack opening and discontinuity in temperature between crack faces, and can be found such that (35*b*) is satisfied, then the part I results also serve as the interface crack solution.

2.2 Integral Equations. Setting $y=0$ in counterparts for the far-field results (27) and (29) yields, upon substitution into (35*b*), coupled integral equations

$$\frac{\sqrt{\mu_1\mu_2}}{S}\left(-D\frac{dU_y}{dx}+\frac{D_A}{\pi}(vp)\int_{-\infty}^{0}\frac{dU_x}{dt}\frac{dt}{t-x}\right)=-F_x\delta(x+L) \tag{36a}$$

$$\frac{\sqrt{\mu_1\mu_2}}{S}\left(D\frac{dU_x}{dx}+\frac{D_B}{\pi}(vp)\int_{-\infty}^{0}\frac{dU_y}{dt}\frac{dt}{t-x}\right)=-F_y\delta(x+L) \tag{36b}$$

$$\frac{1}{\sqrt{h_1'}+\sqrt{h_2'}}\frac{d}{dx}\int_x^0\frac{dt}{\sqrt{\pi(t-x)}}\left(\Theta-\frac{T_x}{S}\frac{dU_x}{dx}+\frac{2T_y}{\pi S}(vp)\int_{-\infty}^{0}\frac{dU_y}{d\tau}\frac{d\tau}{\tau-t}\right)=0 \tag{36c}$$

for $x<0$, where (vp) signifies Cauchy principal value integration. Dimensionless terms

$$D_A=2\sqrt{\frac{\mu_1}{\mu_2}}R_1(a_\varepsilon A_\varepsilon\Omega)_2+2\sqrt{\frac{\mu_2}{\mu_1}}R_2(a_\varepsilon A_\varepsilon\Omega)_1 \tag{37a}$$

$$D_B=2\sqrt{\frac{\mu_1}{\mu_2}}R_1(a_\varepsilon B\Omega)_2+2\sqrt{\frac{\mu_2}{\mu_1}}R_2(a_\varepsilon B\Omega)_1 \tag{37b}$$

$$D=\sqrt{\frac{\mu_1}{\mu_2}}R_1N_2-\sqrt{\frac{\mu_2}{\mu_1}}R_2N_1 \tag{37c}$$

appear in (36*a*), (36*b*), while (36*c*) exhibits dimensionless quantities

$$T_x=\left(\frac{\varepsilon}{\tilde{\alpha}}\right)_2X_{12}+\left(\frac{\varepsilon}{\tilde{\alpha}}\right)_1X_{21} \tag{38a}$$

$$T_y=\left(\frac{\varepsilon}{\tilde{\alpha}}\right)_2Y_{12}-\left(\frac{\varepsilon}{\tilde{\alpha}}\right)_1Y_{21} \tag{38b}$$

2.3 Solution. The weak coupling of unknowns (U_x,U_y,Θ) in (36) allows (36*a*), (36*b*) to be treated separately. Application of singular integral equation techniques [24], after [9], gives the eigenvalue equation

$$D_AD_B\cos^2\pi v+D^2\sin^2\pi v=0 \tag{39}$$

supported by the observation that $(D_A,D_B)\geqslant 0$ for $0<v<\min(v_{R1},v_{R2})$ and results

$$D_AD_B-D^2=R_1R_2S,\quad q=\frac{D}{\sqrt{D_AD_B}} \tag{40}$$

In light of (40) and the discussion above, $|q|<1$ for $0<v<\min(v_{R1},v_{R2},v_S)$. Then (39) gives dimensionless complex conjugate eigenvalues

$$v_\pm=-\frac{1}{2}\pm i\zeta,\quad 2\pi\zeta=\ln\frac{1-q}{1+q} \tag{41}$$

and it is noted that (ζ,D) are of opposite sign. If, however, v lies between the minimum and the minimum of the remaining two speeds, then $|q|>1$ and (39) gives

$$v_\pm=\pm i\bar{\zeta},\quad 2\pi\bar{\zeta}=\ln\frac{q-1}{q+1} \tag{42}$$

This imaginary result implies purely sinusoidal eigenfunctions for (36*a*), (36*b*). Thus, in what follows, subcritical interface crack extension is defined by

$$0<v<\min(v_{R1},v_{R2},v_S) \tag{43}$$

It is noted that (43) is more restrictive than the part I condition (34). It should also be noted that results for isothermal anisotropy [25] and isotropic thermoelasticity [26] indicate that $(v_{R1},v_{R2})<v_S$ when the Stoneley speed exists. In view of (39)–(41), the analytical solutions to (36*a*), (36*b*) are

$$\frac{dU_x}{dx}=\frac{\sqrt{D_B}}{\pi R_1R_2}\frac{1}{x+L}\sqrt{\frac{L}{|x|}}\frac{\bar{F}}{\sqrt{\mu_1\mu_2}}\sin\left(\phi-\zeta\ln\frac{L}{|x|}\right)+\frac{DF_y}{R_1R_2\sqrt{\mu_1\mu_2}}\delta(x+L) \tag{44a}$$

$$\frac{dU_y}{dx}=\frac{\sqrt{D_A}}{\pi R_1R_2}\frac{1}{x+L}\sqrt{\frac{L}{|x|}}\frac{\bar{F}}{\sqrt{\mu_1\mu_2}}\cos\left(\phi-\zeta\ln\frac{L}{|x|}\right)-\frac{DF_x}{R_1R_2\sqrt{\mu_1\mu_2}}\delta(x+L) \tag{44b}$$

for $x<0$, where the amplitude and phase angle are

$$\bar{F}=\sqrt{D_BF_x^2+D_AF_y^2},\quad \phi=\tan^{-1}\sqrt{\frac{D_B}{D_A}}\frac{F_x}{F_y}\left(-\frac{\pi}{2}<\phi<\frac{\pi}{2}\right) \tag{45}$$

Equation (36*c*) gives an Abel integral equation that, in view of (36*a*), (36*b*) and (44), yields

$$\Theta=\frac{1}{\pi R_1R_2S}\left(T_x+\frac{2D}{D_B}T_y\right)\frac{\sqrt{D_B}}{x+L}\sqrt{\frac{L}{|x|}}\frac{\bar{F}}{\sqrt{\mu_1\mu_2}}\sin\left(\phi-\zeta\ln\frac{L}{|x|}\right)-\left[\frac{2T_y}{D_B}+\frac{1}{R_1R_2S}\left(T_x+\frac{2D}{D_B}T_y\right)\right]\frac{F_y}{\sqrt{\mu_1\mu_2}}\delta(x+L)+\frac{C}{\sqrt{\pi|x|}} \tag{46}$$

Because its term shows weaker decay as $|x|\rightarrow\infty$, we set the integration constant $C\equiv 0$. For the single isotropic material limit, additional terms in the asymptotic integral transforms developed in Part I allow stronger coupling of (U_x,U_y,Θ) than that displayed in (36). An exact solution for the isotropic limit case [27,28] gives more complicated forms than (44) and (46), but behavior indicates that the stronger coupling has marginal effects, especially away from the crack edge.

2.4 Interface Functions. The same procedure that gives (36) yields, upon substitution of (44*a*), (44*b*) and use of Cauchy residue theory, the analytical results

$$\sigma_{xy}^0=\frac{\bar{F}}{\pi\sqrt{R_1R_2S}}\frac{\sqrt{D_A}}{x+L}\sqrt{\frac{L}{x}}\sin\left(\phi-\zeta\ln\frac{L}{x}\right) \tag{47a}$$

$$\sigma_y^0=\frac{\bar{F}}{\pi\sqrt{R_1R_2S}}\frac{\sqrt{D_B}}{x+L}\sqrt{\frac{L}{x}}\cos\left(\phi-\zeta\ln\frac{L}{x}\right) \tag{47b}$$

$$\theta^0=\frac{-1}{\pi\sqrt{R_1R_2S}}\frac{\sqrt{h_1'h_2'}}{\sqrt{h_1'}+\sqrt{h_2'}}\left(\frac{\varepsilon_2}{\tilde{\alpha}_2\sqrt{h_2'}}Y_{12}+\frac{\varepsilon_1}{\tilde{\alpha}_1\sqrt{h_1'}}Y_{21}\right)\times\frac{\bar{F}}{\sqrt{\mu_1\mu_2D_B}}\frac{1}{x+L}\sqrt{\frac{L}{x}}\cos\left(\phi-\zeta\ln\frac{L}{x}\right) \tag{47c}$$

for $y=0$, $x>0$. The superscript indicates that functions are valid for both half-spaces. The oscillatory behavior in (44), (46), and

(47) is typical for interface cracks [1–3]. In (44*b*) and (47*b*), it implies crack face interpenetration and a compressive normal interface stress, unless x is restricted by

$$-\frac{\pi}{2}<\phi-\zeta\ln\frac{L}{|x|}<\frac{\pi}{2} \tag{48}$$

For example, when $(\zeta>0, F_x=0)$, (48) gives

$$e^{-\pi/2\zeta}<\frac{|x|}{L}<e^{\pi/2\zeta} \tag{49}$$

Isothermal results [9,10] indicate that $|\zeta|\approx O(10^{-1})$. Thus, (48) shows that the aberrant behavior occurs either at great distances (as a multiple of L) from, or in small regions near (as a fraction of L), the moving crack edge. Moreover, certain field variable combinations are free of oscillations: (44*a*), (44*b*) and (47*a*), (47*b*) give, respectively,

$$\sqrt{D_A\left(\frac{dU_x}{dx}\right)^2+D_B\left(\frac{dU_y}{dx}\right)^2}=\frac{\sqrt{D_AD_B}}{\pi R_1R_2}\frac{\bar{F}}{\overline{\sqrt{\mu_1\mu_2}}}\sqrt{\frac{L}{|x|}}\frac{1}{x+L}(x<0, x+L\neq 0) \tag{50a}$$

$$\sqrt{D_B(\sigma_{xy}^0)^2+D_A(\sigma_y^0)^2}=\frac{\sqrt{D_AD_B}}{\pi\sqrt{R_1R_2S}}\frac{\bar{F}}{x+L}\sqrt{\frac{L}{x}}(x>0) \tag{50b}$$

Similarly, derivation of the debonding energy rate (per unit length of crack edge) in the manner of [29] yields the positive result

$$E_d=\frac{v}{\pi L}\frac{\sqrt{D_AD_B}}{\overline{\sqrt{R_1R_2S}}}\frac{\bar{F}^2}{\overline{\sqrt{\mu_1\mu_2}}} \tag{51}$$

Equation (51) shows that the upper limit in (43) produces an unbounded energy rate, whether that limit is a Rayleigh speed or, if it exists, a Stoneley speed.

2.5 Illustration: Rigid-Elastic Bimaterial. Consider half-space 2 $(y<0)$ to be rigid, but capable of conducting heat. Then (44) and (46) for $y=0$, $x<0$ can be written as

$$\frac{\mu_1}{\bar{\sigma}}\frac{dU_x}{dx}=\frac{2}{\pi}\left(\frac{a_\varepsilon\Omega\sqrt{B}}{R}\right)_1\frac{\bar{f}}{1+x/L}\sqrt{\frac{L}{|x|}}\sin\left(\phi-\zeta\ln\frac{L}{|x|}\right)-\left(\frac{N}{R}\right)_1 f_yL\,\delta(x+L) \tag{52a}$$

$$\frac{\mu_1}{\bar{\sigma}}\frac{dU_y}{dx}=\frac{2}{\pi}\left(\frac{a_\varepsilon\Omega\sqrt{A_\varepsilon}}{R}\right)_1\frac{\bar{f}}{1+x/L}\sqrt{\frac{L}{|x|}}\cos\left(\phi-\zeta\ln\frac{L}{|x|}\right)+\left(\frac{N}{R}\right)_1 Lf_x\delta(x+L) \tag{52b}$$

$$\frac{\Theta}{\bar{\theta}}=\frac{2}{\pi}\left(\frac{\varepsilon\Omega N_y\sqrt{B}}{R}\right)_1\frac{\bar{f}}{1+x/L}\sqrt{\frac{L}{|x|}}\sin\left(\phi-\zeta\ln\frac{L}{|x|}\right)-\left(\frac{\varepsilon P}{R}\right)_1 f_yL\,\delta(x+L) \tag{52c}$$

where (41) and (43) give

$$2\pi\zeta=\ln\left(\frac{2a_\varepsilon\Omega\sqrt{A_\varepsilon B}+N}{2a_\varepsilon\Omega\sqrt{A_\varepsilon B}-N}\right)_1 \tag{53a}$$

$$\bar{f}=\sqrt{A_\varepsilon f_y^2+Bf_x^2},\quad \phi=\tan^{-1}\sqrt{\frac{B}{A_\varepsilon}}\frac{f_x}{f_y}\left(-\frac{\pi}{2}<\phi<\frac{\pi}{2}\right) \tag{53b}$$

For $y=0$, $x>0$ results (47) take the form

$$\frac{\sigma_{xy}^0}{\bar{\sigma}}=\frac{2}{\pi}\left(\frac{a_\varepsilon\Omega\sqrt{A_\varepsilon}}{\sqrt{MR}}\right)_1\frac{\bar{f}}{1+x/L}\sqrt{\frac{L}{x}}\sin\left(\phi-\zeta\ln\frac{L}{x}\right) \tag{54a}$$

$$\frac{\sigma_{y}^0}{\bar{\sigma}}=\frac{2}{\pi}\left(\frac{a_\varepsilon\Omega\sqrt{B}}{\sqrt{MR}}\right)_1\frac{\bar{f}}{1+x/L}\sqrt{\frac{L}{x}}\cos\left(\phi-\zeta\ln\frac{L}{x}\right) \tag{54b}$$

$$\frac{\theta^0}{\bar{\theta}}=-\frac{2}{\pi}\left(\frac{\varepsilon\Omega\Gamma_y\sqrt{B}}{\sqrt{MR}}\right)_1\frac{\bar{f}}{\overline{1+\sqrt{\left(\frac{\rho c_v}{K_y}\right)_2\left(\frac{aC_y}{a_\varepsilon}hv_r\right)_1}}}\times\frac{1}{1+x/L}\sqrt{\frac{L}{x}}\cos\left(\phi-\zeta\ln\frac{L}{x}\right) \tag{54c}$$

and debonding energy rate (51) becomes

$$\frac{E_d}{\bar{E}}=\frac{4}{\pi}\left(\frac{a_\varepsilon\Omega\sqrt{c}}{\sqrt{R_4}}\right)_1^2\sqrt{\left(\frac{A_\varepsilon B}{MR}\right)_1}\bar{f}^2 \tag{55}$$

Use of dimensionless loading parameters

$$(f_x, f_y)=\frac{(F_x, F_y)}{\overline{\sqrt{F_x^2+F_y^2}}}(f_x^2+f_y^2=1) \tag{56}$$

and, respectively, the stress, temperature and energy rate amplitudes

$$\bar{\sigma}=\frac{1}{L}\sqrt{F_x^2+F_y^2},\quad \bar{\theta}=\frac{\bar{\sigma}}{(\mu\tilde{\alpha})_1},\quad \bar{E}=\frac{L\bar{\sigma}^2}{\overline{\sqrt{(\mu\rho)_1}}} \tag{57}$$

allow the right-hand sides of (54) and (55) to serve as dimensionless measures of interface traction and temperature and energy rate. These measures themselves depend on dimensionless variables $(c_1, x/L, (f_x, f_y))$, i.e., the crack speed, distance from crack edge, and relative strength of normal and shear crack face loading. These last two are not independent, so that either one can characterize relative strength, e.g., $f_y=0$ signifies pure shear and $f_y=1$ signifies pure compression (tensile loading of bimaterial).

Equation (54*c*) shows that the thermal properties of the rigid half-space affect the interface temperature change. If the rigid half-space is also thermally inert, then the denominator of the $\bar{f}$-term becomes unity. We now consider this case, with half-space 1 $(y>0)$ being the hexagonal material, zinc. Its properties are [30]

$$c_{11}=162.8\ \text{GPa},\quad c_{22}=62.7\ \text{GPa},\quad c_{12}=50.8\ \text{GPa},$$

$$c_{13}=36.2\ \text{GPa},\quad c_{44}=38.5\ \text{GPa}$$

$$\rho=7140\ \text{kg/m}^3$$

$$c_v=390\ \text{J/kg}\,^\circ\text{C},\quad K_x=K_y=124\ \text{W/m}\,^\circ\text{C}$$

$$\alpha_x=5.818(10^{-6})1/^\circ\text{C},\quad \alpha_y=15.35(10^{-6})1/^\circ\text{C}$$

at room temperature $(T_0=294\,\text{K})$. These values give, in view of (2)–(4) and (15), the dimensionless solution parameters

$$a=1.6286,\quad b=4.2301,\quad m=2.3195,$$

$$m_3=1.9403,\quad \gamma=2.506$$

$$a_\varepsilon=1.7203,\quad b_\varepsilon=4.3024,\quad m_\varepsilon=2.4019,$$

$$m_{3\varepsilon}=2.0144,\quad \gamma_\varepsilon=2.6354$$

$$c_0=0.999,\quad c_R=0.8833$$

$$\Gamma_x=4.6018,\quad \Gamma_y=5.1181,\quad \varepsilon=0.003485$$

and values

$$h=1.9178(10^{-8})\ \text{m},\quad v_r=2322\ \text{m/s}$$

Table 1 Eigenvalue parameter ζ versus dimensionless crack speed c_1

c_1	0	0.1	0.2	0.3	0.4	0.5	0.6	0.7	0.8
ζ	0.0913	0.093	0.096	0.1014	0.11	0.1234	0.1447	0.1826	0.2688

As noted in part I, $c_0 v_r$ is a speed that arises for category 3 materials, but does not affect solution behavior on the interface plane. The value of c_0 given here, moreover, puts the speed beyond the subcritical range. The isothermal parameters (a,b,m,m_3,γ) and their ε-subscripted thermoelastic counterparts are seen to be, in keeping with linear coupled thermoelasticity theory [16,17], perturbations of each other. As noted at the outset, isothermal results [9,10] involved a smaller class of transversely isotropic materials; specifically, only the category 1 class defined in Part I.

For the present bimaterial, Table 1 gives the dimensionless eigenvalue parameter ζ for subcritical values of c_1. Values are seen to be of $O(10^{-1})$ and to increase with crack speed. Similar behavior arises for isothermal category I results [9,10].

A criterion for which interface crack extension occurs is not imposed in this study. However, some insight into solution behavior is possible by examining the dimensionless energy rate $E_d/\overline{E}$ for subcritical c_1 and f_y in the range (0,1). Calculations of (55) are presented in Table 2, and show increases with both parameters. That is, higher crack speeds are associated with higher energy rates, and energy rate increases as the compression component of crack face loading dominates.

Similarly, data for the dimensionless change in interface temperature (54c) is presented for subcritical c_1 and f_y in the range (0,1) at locations $x=(0.5L,L,2L)$ in, respectively, Tables 3–5. All entries are negative, indicating that interface temperature drops with interface crack extension. That the drop magnitude for a given (c_1,f_y) decreases with x is predicted by the form of S+C. Tables 3 and 4 give magnitudes that, like Table 2 entries, increase with crack speed and dominance by compressive loading. Table 5 shows, however, that further from the crack edge, magnitude may decrease with crack speed, especially when shear dominates crack face loading. This represents a stronger coupling of speed and loading mode effects.

Table 2 Dimensionless energy rate $E_d/\overline{E}$ versus dimensionless crack speed c_1 and loading parameter f_y

c_1	$f_y=0.1$	$f_y=0.3$	$f_y=0.7$	$f_y=0.9$
0	0.0	0.0	0.0	0.0
0.1	0.0225	0.0241	0.0294	0.0337
0.2	0.0468	0.049	0.0605	0.0693
0.3	0.0723	0.076	0.0943	0.1098
0.4	0.101	0.1068	0.1345	0.1568
0.5	0.1362	0.1446	0.1864	0.2198
0.6	0.1848	0.1978	0.2633	0.3157
0.7	0.271	0.2943	0.4107	0.5037
0.8	0.2956	0.329	0.496	0.6296

Table 3 Dimensionless interface temperature change $\theta^0/\overline{\theta}$ at $x=0.5L$ versus dimensionless crack speed c_1 and loading parameter f_y

c_1	$f_y=0.1$	$f_y=0.3$	$f_y=0.7$	$f_y=0.9$
0	−0.000486	−0.001127	−0.002382	−0.002984
0.1	−0.000489	−0.00113	−0.002385	−0.002987
0.2	−0.000495	−0.001137	−0.002395	−0.002997
0.3	−0.000505	−0.00115	−0.002413	−0.003016
0.4	−0.000524	−0.001177	−0.002452	−0.003059
0.5	−0.000547	−0.001206	−0.002489	−0.003097
0.6	−0.000591	−0.001265	−0.002574	−0.003189
0.7	−0.000677	−0.001386	−0.002753	−0.003386
0.8	−0.000928	−0.00175	−0.003318	−0.004014

Table 4 Dimensionless interface temperature change $\theta^0/\overline{\theta}$ at $x=L$ versus dimensionless crack speed c_1 and loading parameter f_y

c_1	$f_y=0.1$	$f_y=0.3$	$f_y=0.7$	$f_y=0.9$
0	−0.000172	−0.000516	−0.001204	−0.001548
0.1	−0.0001721	−0.0005163	−0.0012047	−0.001549
0.2	−0.0001726	−0.0005178	−0.0012082	−0.001553
0.3	−0.0001735	−0.0005205	−0.001245	−0.001573
0.4	−0.0001758	−0.0005274	−0.0012306	−0.001582
0.5	−0.0001776	−0.0005328	−0.001243	−0.001598
0.6	−0.0001824	−0.0005472	−0.001277	−0.001642
0.7	−0.0001929	−0.000579	−0.00135	−0.001736
0.8	−0.0002274	−0.000682	−0.001592	−0.002047

3 Comments

This article was a two-part study of dynamic interface crack extension in an unbounded bimaterial formed from rigidly bonded dissimilar transversely isotropic, coupled thermoelastic half-spaces. The half-spaces were initially at rest at a common uniform temperature, and crack extension was caused by the translation of normal and shear forces on the crack faces. A dynamic steady state of plane strain was treated, in which forces and crack edge move at the same constant subcritical speed. The interface and its normal coincided with, respectively, the plane and axis of material symmetry, and crack face insulation was assumed.

Part I of the article presented full-field results for the related problem of a translating strip of discontinuity in interface displacement and temperature. The use of robust asymptotic forms of the corresponding integral transforms led to expressions that were analytic to within single weighted integrals of the discontinuity functions. This feature was exploited in Part II to yield analytical formulas for crack opening and discontinuity in crack face temperature, interface traction and temperature change, and debonding energy rate. The formulas showed that the critical crack speed is the minimum of the two Rayleigh speeds and if it exists, the Stoneley speed.

For the special case of a rigid solid-zinc bimaterial, calculations for the problem eigenvalue parameter, nondimensionalized debonding energy rate and change in interface temperature were given. The eigenvalue parameter was seen to behave like its isothermal counterpart. The debonding energy rate increased both with crack speed and the degree to which crack face loading is dominated by compression. Interface temperature was seen to drop, and the drop magnitudes also increased with speed and compression dominance near the crack edge. However, as distance from the crack edge increased, drop magnitude could actually decrease with speed, especially when shear loading is dominant.

Table 5 Dimensionless interface temperature change $\theta^0/\overline{\theta}$ at $x=2L$ versus dimensionless crack speed c_1 and loading parameter f_y

c_1	$f_y=0.1$	$f_y=0.3$	$f_y=0.7$	$f_y=0.9$
0	−0.00004036	−0.0002039	−0.0005374	−0.0007107
0.1	−0.00003969	−0.0002033	−0.0005371	−0.0007106
0.2	−0.00003872	−0.000203	−0.0005482	−0.0007121
0.3	−0.00003699	−0.000202	−0.0005391	−0.0007147
0.4	−0.00003459	−0.0002018	−0.0005439	−0.0007226
0.5	−0.00002997	−0.000199	−0.0005455	−0.0007273
0.6	−0.00002328	−0.0001351	−0.0005541	−0.0007427
0.7	−0.00001109	−0.0001948	−0.0005746	−0.0007772
0.8	−0.00002133	−0.0001946	−0.0006465	−0.0008926

4 Future Efforts

Equations (44) and (48) indicate that interface crack closure could occur at large distances from the crack edge, thereby limiting the applicability of the semi-infinite crack model. This feature has been studied in the isothermal isotropic bimaterial for transonic interface crack speeds, i.e., between the rotational and dilatational values [4,31]. More recent [32] results for Mode I crack extension in a single transversely isotropic thermoelastic material show that smooth crack closure without interpenetration can occur for subcritical crack speed. The general results [9,10] for interface crack extension in the isothermal category 1 transversely isotropic bimaterial consider any constant crack speed. The results [9,10,32] are currently serving as guides in the extension of the present analysis beyond the subcritical range and the consideration of crack closure.

The restriction (43) for subcritical crack speed was based only on the fact that the Stoneley speed, if it exists, and both Rayleigh speeds are subsonic. As noted above, studies of bimaterials for the isothermal, anisotropic elastic [25] and isotropic thermoelastic [26] cases indicate that the Stoneley speed exceeds both Rayleigh speeds. The isothermal and thermoelastic rotational wave speeds in the material symmetry plane were seen in part I to be identical, and data for zinc indicated that the two dilatational wave speeds are perturbations of one another. This suggests that the observations of [25,26] generalize to the bimaterial considered here. Clearly, however, the aforementioned extension to supercritical speeds should specifically consider the Stoneley–Rayleigh speed relation.

References

[1] England, A. H., 1965, ''A Crack Between Dissimilar Media,'' ASME J. Appl. Mech., **32**, pp. 400–402.

[2] Erdogan, F., 1965, ''Stress Distributions in Bonded Dissimilar Materials With Cracks,'' ASME J. Appl. Mech., **32**, pp. 403–410.

[3] Rice, J. R., and Sih, G. C., 1965, ''Plane Problems of Cracks in Dissimilar Materials,'' ASME J. Appl. Mech., **32**, pp. 418–423.

[4] Liu, C., Huang, Y., and Rosakis, A. J., 1995, ''Shear Dominated Interfacial Crack Growth in a Bimaterial—II. Asymptotic Fields and Favorable Velocity Regimes,'' J. Mech. Phys. Solids, **43**, pp. 189–206.

[5] Brock, L. M., 1976, ''Interface Flaw Extension Under In-Plane Loadings,'' Int. J. Eng. Sci., **14**, pp. 963–974.

[6] Ting, T. C. T., 1990, ''Interface Cracks in Anisotropic Materials,'' J. Mech. Phys. Solids, **38**, pp. 505–513.

[7] Ni, L., and Nemat-Nasser, S., 1991, ''Interface Crack in Anisotropic Dissimilar Materials: An Analytic Solution,'' J. Mech. Phys. Solids, **39**, pp. 113–144.

[8] Ni, L., and Nemat-Nasser, S., 1992, ''Interface Cracks in Anisotropic Dissimilar Materials: General Case,'' Q. Appl. Math., **1**, pp. 305–322.

[9] Brock, L. M., 2002, ''Interface Crack Extension at any Constant Speed in Orthotropic or Transversely Isotropic Bimaterals—I. General Exact Solution,'' Int. J. Solids Struct., **39**, pp. 1163–1182.

[10] Brock, L. M., and Hanson, M. T., 2002, ''Interface Crack Extension at any Constant Speed in Orthotropic or Transversely Isotropic Bimaterials—II. Two Important Examples,'' Int. J. Solids Struct., **39**, pp. 1183–1198.

[11] Kraut, E. A., 1963, ''Advances in the Theory of Anisotropic Elastic Wave Propagation,'' Rev. Geophys., **1**, pp. 401–448.

[12] Scott, R. A., and Miklowitz, J., 1967, ''Transient Elastic Waves in Anisotropic Plates,'' ASME J. Appl. Mech., **34**, pp. 104–110.

[13] Payton, R. G., 1983, *Elastic Wave Propagation in Transversely Isotropic Materials*, Martinus Nijhoff, The Hague.

[14] Lekhnitski, S. G., 1963, *Theory of Elasticity of an Anisotropic Elastic Body*, Holden-Day, San Francisco.

[15] Ting, T. C. T., 1995, *Anisotropic Elasticity*, Oxford Science, New York.

[16] Boley, B. A., and Weiner, J. W., 1985, *Theory of Thermal Stresses*, Krieger, Malabar, FL.

[17] Chadwick, P. C., 1960, ''Thermoelasticity, the Dynamical Theory,'' in *Progress in Solid Mechanics*, Sneddon, I. N. and Hill, R., North–Holland, Amsterdam, Vol. 1.

[18] van der Pol, B., and Bremmer, H., 1950, *Operational Calculus Based on the Two-Sided Laplace Integral*, Cambridge University Press, Cambridge, UK.

[19] Abramowitz, M. A., and Stegun, I. A. (eds.), 1972, *Handbook of Mathematical Functions*, Dover, New York.

[20] Brock, L. M., 2003, ''Rapid Sliding Indentation With Friction on a Transversely Isotropic Thermoelastic Half-Space,'' Int. J. Solids Struct., **40**, pp. 3195–3210.

[21] Cagniard, L., 1962, *The Reflection and Refraction of Progressive Seismic Waves*, McGraw–Hill, New York.

[22] Achenbach, J. D., 1973, *Wave Propagation in Elastic Solids*, North–Holland, Amsterdam.

[23] Foster, R. M., and Peirce, B. O., 1956, *A Short Table of Integrals*, Blaisdell, Waltham, MA.

[24] Erdogan, F., 1976, ''Mixed Boundary Value Problems in Mechanics,'' in *Mechanics Today*, edited by Nemat-Nasser, S., Pergamon Press, NY, Vol. 4.

[25] Barnett, D. M., Gavazza, S. D., Lothe, J., and Musgrave, M. J. P., 1985, ''Considerations of the Existence of Interfacial (Stoneley) Waves in Bonded Anisotropic Elastic Half-Spaces,'' Proc. R. Soc. London, Ser. A, **402**, pp. 153–166.

[26] Brock, L. M., 1997, ''Some Results for Rayleigh and Stoneley Signals in Thermoelastic Solids,'' Indian J. Pure Appl. Math., **28**, pp. 835–850.

[27] Brock, L. M., 1999, ''Rapid Crack Growth in a Thermoelastic Solid Under Mixed-Mode Thermomechanical Loading,'' IMA J. Appl. Math., **62**, pp. 31–44.

[28] Brock, L. M., 2000, ''Partially-Coupled Integral Equations for a Dynamic Fracture Problem in Coupled Thermoelasticity,'' J. Integral Equ. Appl., **12**, pp. 31–38.

[29] Achenbach, J. D., 1970, ''Extension of a Crack by a Shear Wave,'' Z. Angew. Math. Phys., **21**, pp. 887–900.

[30] Sharma, J. N., and Sharma, P. K., 2002, ''Free Vibration of Homogeneous Transversely Isotropic Cylindrical Panel,'' J. Therm. Stresses, **25**, pp. 169–182.

[31] Huang, Y., Wang, W., Liu, C., and Rosakis, A. J., 1998, ''Intersonic Crack Growth in Bimaterial Interfaces: An Investigation of Crack Face Contact,'' J. Mech. Phys. Solids, **46**, pp. 2233–2259.

[32] Brock, L. M., 2004, ''Dynamic Fracture of Transversely Isotropic Coupled-Thermoelastic Solids: Wedging by a Cylinder With Friction,'' J. Thermal Stresses **27**, pp. 1053–1073.

D. Krajcinovic
Life Fellow ASME

A. Rinaldi

Mechanical and Aerospace Engineering,
Arizona State University,
Tempe, AZ 85287-6106

Statistical Damage Mechanics—Part I: Theory

Statistical damage mechanics in this work establishes the connection between damaged random heterogeneous micromaterial and the system macroparameter. Renormalization group theory provides the bridge from the microscale to the macroscale. Delaunay lattices, which simulate and capture the role of the disordered microstructure in damage process, substitute a polycrystal specimen assuming that microcracks are grain-boundaries cracks. The macroparameters of the system, in the form of algebraic functions, are obtained applying the Family–Vicsek scaling relation on simulation data. [DOI: 10.1115/1.1825434]

1 Introduction

Simple mathematical theory of the thermomechanical process is based on the four constitutive equations for the stress, $\overline{\sigma}_{ij}(X,t)$, heat flux, $\overline{q}_{ij}(X,t)$, internal energy and local entropy production, $\overline{\eta}_{ij}(X,t)$ [1]. Above, X is the position of the point, t is present time and the bar above the symbol indicates the macrosymbols. And ‘‘principle of local action, according to which the response at a X is determined if the conditions are known in an arbitrarily small neighborhood of X, the motion outside being disregarded’’ [1]. Kellogg [2] also used X to determine the ‘‘continuum particle.’’ Most classical continuous models are based on the property of locality. In [3,4] Kunin provides the connection between the nonlocal, weakly nonlocal models and quasicontinuum. In nonlocal continuum models used for damage mechanics [5] the position of microcracks in the ‘‘representative volume’’ is irrelevant.

Materials, such as ceramics, are on macroscale homogeneous, ordered and isotropic in pristine state. On the microscale, the texture of this ceramic is random heterogeneous [6]. The distribution of the position and geometry of grains, i.e., number of edges and faces per cell, surfaces, interfaces, boundaries, microcracks are random variables. As the microcracks nucleate, enlarge, and cluster with each other, the random variables become different. Thus, the effect of random heterogeneous ‘‘continuum particles’’ must be smaller as the microcracks grow.

But physics, thermodynamics, and mathematics provide, as always, the tools. The first tool is thermodynamics, which is empirically based science that requires no knowledge of microscopic interaction. The second tool is the statistical mechanics that ‘‘establishes a connection between the microscopic and thermodynamic description of a system’’ [7]. Thus, statistical mechanics models establish connection between macroparameters, such as the macroscale the components of generalized Hooke’s law, $\overline{C}^{\alpha\beta\gamma\delta}$, in the form $\overline{\sigma}^{\alpha\beta}=\overline{C}^{\alpha\beta\gamma\delta}(\overline{D})\overline{\varepsilon}_{\gamma\delta}$, when $\overline{D}$ is the macrodamage parameter. The third tool is the fractal geometry.

2 From Continuum to Quantum Mechanics?

Apparently it is Boscovich (1763) who ‘‘assumed that, between every two ultimate particles and along the line connecting them, forces act which are attractive for some distances and repulsive for other’’ (Timoshenko, S.P., *History of Strength of Materials*, Dover Publications, Inc., New York, p. 104). A proper model is dependent on the short-range intermolecular forces between molecular particles and on the body forces of longer-range that are acting on the interior of the specimen [8]. Continuum models of engineering cannot be used when the short-range intermolecular forces become longer-range forces, as the microcracks become macrocracks.

The model of this work can be used from continuous to molecular medium. But, in this work is restricted only to macroscale and microscale. The macroscale matter is contiguous. The resolution length of the microscale is ℓ, defined as the length of the grain-boundary. The microstructure of a polycrystal, such a ceramics, can be modeled by the lattice, i.e., a simplicial graph in which a Voronoi froth is perpendicular to the grain boundaries and the Delaunay graph, dual graph to the Voronoi froth, is of honeycomb geometry (Fig. 1). For the solid mechanics design the scaling process from microcracks to the macroparameters is most needed.

3 Damage “Micromechanics”

The task of ‘‘micromechanics’’ (in ‘‘micromechanics’’ material properties depend on macroscopic averages defects and not on the defects position in space) is to estimate the effective stiffness tensor of heterogeneous material. Mura [9], Nemat-Nasser and Hori [10], and Krajcinovic [11] have the same task, i.e., to estimate overall properties by ‘‘micromechanics’’ models under some circumstances. But, ‘‘micromechanics’’ considered only the statistical homogeneity of the matter at the microscale. Hence, the overall properties do not depend on the position of the microcracks, i.e., the process is ergodic. As microcrack density enlarges the interaction of two or more microcracks, their positions become more relevant. At threshold failure a large cluster of interacting microcracks become a macrocrack. Finally, the form of the failure depends on the fractal or multifractal geometry and density of the macrocrack.

3.1 Damage Scalar Model. The first, two-dimensional and time-independent, damage model [12,13] related the macrostress, $\overline{\sigma}$, and macrostrain, $\overline{\varepsilon}$, as

$$\overline{\sigma}=\overline{E}^0(1-\overline{D})\overline{\varepsilon}. \tag{1}$$

In (1) is the macrostress, $\overline{E}^0$ is the elastic modulus of pristine state, and $\overline{D}$ is the damage parameter. The bar over the parameter signifies a macroparameter.

The brittle loose bundle model [14,15] is the simplest damage model (1). The expression (1) can be obtained assuming that extant links share equally the tensile load, $\overline{\sigma}$, N is the number of all links, n is the number of all broken links, and f_r is the link rupture strength. All N links have identical stiffness $k=K/N$ when K is

---

Contributed by the Applied Mechanics Division of THE AMERICAN SOCIETY OF MECHANICAL ENGINEERS for publication in the ASME JOURNAL OF APPLIED MECHANICS. Manuscript received by the Applied Mechanics Division, November 1, 2003; final revision, May 28, 2004. Associate Editor: H. Gao. Discussion on the paper should be addressed to the Editor, Professor Robert M. McMeeking, Journal of Applied Mechanics, Department of Mechanical and Environmental Engineering, University of California, Santa Barbara, Santa Barbara, CA 93106-5070, and will be accepted until four months after final publication in the paper itself in the ASME JOURNAL OF APPLIED MECHANICS.

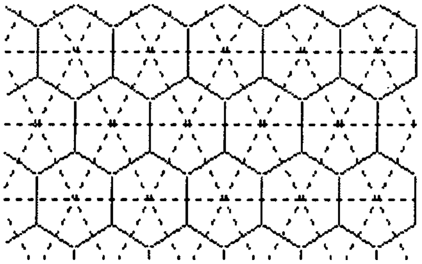

Fig. 1 Perfect two-dimensional honeycomb Voronoi and triangular Delaunay lattices

the stiffness of the model in the pristine state. The random variable is defined by $p(f_r)=(f_{\max})^{-1}=\text{const}$. The damage density is then

$$\bar{D}=\frac{n}{N}. \tag{2}$$

A different rate of damage variable is the quotient obtained by rate of unbroken bars divided by the number of the unbroken bars. In this measure the damage rate is [16]

$$\delta\bar{D}_n=\frac{\delta n}{N-n} \quad \text{or} \quad \bar{D}_n=\ln\left(\frac{N}{N-n}\right). \tag{3}$$

The damage density in expression (1) can be written as

$$\bar{D}=\frac{\bar{E}^0-\bar{E}}{\bar{E}^0} \quad \text{and} \quad \bar{D}_n=\ln\frac{\bar{E}^0}{\bar{E}}, \tag{4}$$

where $\bar{E}=\bar{E}^0(1-\bar{D})$ is the Young's elastic modulus of the damaged specimen.

The force versus displacements curve is a parabola for $p(f_r)=(f_{\max})^{-1}$ when the displacement is controlled. The hardening and softening parts are mirror-same over the directrix. Hence, the softening part of the brittle loose bundle model cannot be trusted.

3.2 Damage Model Based on Fracture Mechanics. Budiansky and O'Connell [17] proposed the first damage model based on the fracture mechanics. By assuming that the continuum is isotropic and homogeneous, damage is isotropic, cracks penny-shaped and damage density insignificant, and the damage parameter is

$$\bar{D}=\frac{1}{V^0}\langle a^3\rangle, \tag{5}$$

where a is the crack radius and V^0 is the volume of the specimen.

Krajcinovic [11] considered a single penny crack in effective properties of elastic, isotropic, homogeneous, and continuous specimen using fracture mechanics. The energy release rate, G, for homogeneous and isotropic elastic solid is

$$G=J=\frac{1-\nu}{2\mu}(K_{\mathrm{I}}^2+K_{\mathrm{II}}^2)+\frac{\nu}{2\mu}K_{\mathrm{III}}^2. \tag{6}$$

In (6) J is the integral for homogeneous and isotropic elastic solid, ν and μ is the Poisson's ratio and shear modulus, and K_m is the vector of stress intensity factors when $m=1,2,3$. After some tensor transformations ([11], pp. 253–258), the effective (average) compliance, $\bar{S}_{ijmn}$, is

$$\bar{S}_{ijmn}=\bar{S}^0_{ijmn}+\bar{S}^*_{ijmn}. \tag{7}$$

In (7) $\bar{S}^0_{ijmn}$ is the compliance of a pristine specimen. The compliance that is attributable to the presence of a single penny shaped crack embedded in a homogeneous, isotropic and elastic material is $\bar{S}^*_{ijmn}$. To facilitate the analytical and computational manipulations of the effective stiffness and compliance tensors it is advantageous to introduce a set of six fourth order tensors. These tensors represent the irreducible integrity basis for all fourth order tensor invariant to permutations of first and second pair of indices defined by the symmetries $\bar{S}_{ijmn}\equiv\bar{S}_{jimn}\equiv\bar{S}_{ijnm}\equiv\bar{S}_{mnij}$. The dyadic products of a unit vector **n** and the Kronecker delta function that define the two components of these six tensors [4] are

$$I^5_{ijmn}=\tfrac{1}{2}(n_in_m\delta_{jn}+n_in_n\delta_{jm}+n_jn_m\delta_{in}+n_jn_n\delta_{im}) \quad \text{and}$$

$$I^6_{ijmn}=n_in_jn_nn_m. \tag{8}$$

If the normal stress at the crack surface is tensile, the expression for the compliance that is attributable to a single, planar, penny-shaped crack of radius a has a very simple form

$$\bar{S}^{(\alpha)}_{ijmn}=\frac{16}{3V}\frac{1-\nu}{2-\nu}\frac{1}{2\mu}a^3\{2I^5_{ijmn}(m)-\nu I^6_{ijmn}(m)\}, \tag{9}$$

that is expressed in terms of the global (or specimen) coordinate system [11]. The unit vector m identifies the crack plane and can be expressed in the global coordinate system as $m=\{\cos\phi\cos\theta,\cos\phi\sin\theta,\sin\phi\}$ in terms of trigonometric functions of the Euler angles. Following the arguments in [10,11,18,19] where (9) is used as a Green's function, the compliance of a solid containing N penny-shaped microcracks is

$$\bar{S}^*_{ijmn}=\frac{16}{3}\frac{1-\nu}{2-\nu}\frac{1}{2\mu}\int_{a^-}^{a^+}a^3\vartheta(a)da$$
$$\times\int_0^{2\pi}\int_{-\pi/2}^{\pi/2}\bar{F}_{ijmn}(\theta,\phi)\rho(\theta,\phi)\cos\phi\, d\theta\, d\phi. \tag{10}$$

where $\vartheta(a)$ and $\rho(\theta,\phi)$ are statistical distributions of size and orientation and $\bar{F}_{ijnm}(\theta,\phi)$ is defined by the expression within the curly bracket in (9). This result is based on the assumptions that all cracks are penny-shaped, the crack growth is self-similar, the principle of superposition holds and that the distributions of orientation and size are independent. The set of restrictions makes this model close to be useless because the validity is confined to small damage density.

4 Statistical Damage Mechanics

Statistical mechanics establishes the theoretical bridge between the microscopic and macroscopic thermodynamics description of a system. Also, "thermodynamics is an empirically based science that requires no knowledge of the microscopic and macroscopic interactions" (Chaikin and Lubensky [7]).

4.1 Mean-Field Theory. Lev Davidovic Landau's works in mathematics and physics are the foundation of mean-field theory and statistical mechanics. He provided the mathematical tools for the statistical mechanics to establish the connection between random heterogeneous microstructure and macroscopic properties. Statistical mechanics literature, such as Chandler [20], Chaikin and Lubensky [7], Garrod [21], Cardy [22], Fujimoto [23], Kadanoff [24], Chowdhury and Stauffer [25] etc., was forgotten in solid mechanics research. The first mean-field model, by Landau in 1937 (see [21]), is the phase transition from the ferromagnetic phase to the paramagnetic phase as the temperature increases.

4.1.1 Correlation Length. The quantity $\xi(n)$ is the correlation length, i.e., the upper bound of the distance over interacting microcracks. The correlation length is the distance over which the fluctuations of the microscopic degrees of freedom (geometry, distance, Euler angles, specimen dimension, random microtexture, etc.) are significantly correlated with each other [22]. During the damage process the fluctuations of the microaffinities increase with the microcrack density. Thus, the number of degrees of freedom of strongly correlated microcracks is the correlation length.

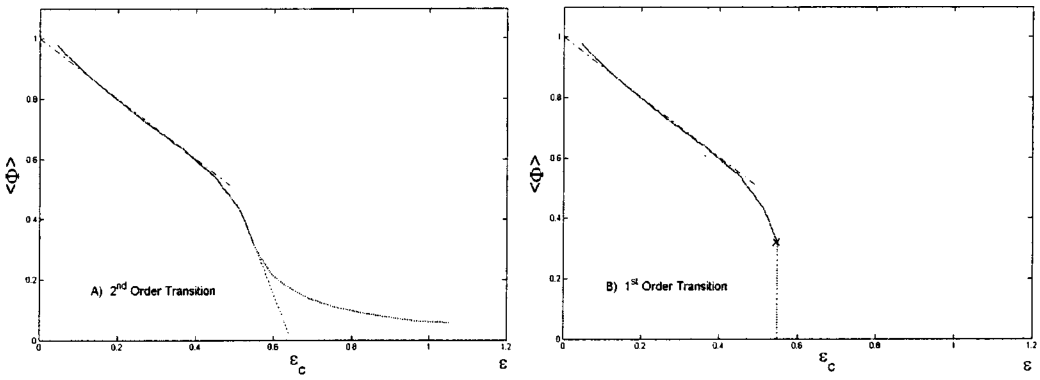

Fig. 2 Order Parameter. The second and first order chase transitions.

The closer the phase transition, where the largest cluster of the microcracks drives the process, the more the correlation length approaches the specimen characteristic size.

4.1.2 Order Parameter. Order parameters distinguish an ordered from a disordered phase. Even more, the "order parameter is a quantitative measure of the relevant 'order' in the system" [25]. Finally, "the order parameter is the average, $\langle\phi\rangle$, of an operator, ϕ, which is a function of the dynamical variable in the system Hamiltonian" (Chaikin and Lubensky [7]). The phase transition can be of first or second order. The order of the phase transition depends on the order parameter continuity.

During a brittle deformation of a specimen, under *uniaxial* extension in x direction, when the damage density is insignificant and correlation length is inferior to the specimen length L, L. M. Kachanov's model in (1) can be accepted. For each value of $\bar{D}$, the current effective secant stiffness modulus of the system is $\bar{E} = E(\bar{D}) = E^0(1-\bar{D})$. The order parameter, $\langle\phi\rangle = \langle 1-\bar{D}\rangle$, is a time-independent scalar, which is sufficient for the model in this paper. From (1) the relation between macrostrain and macrostress is

$$\frac{\bar{\sigma}}{E^0\bar{\varepsilon}_c} = \langle 1-\bar{D}\rangle\frac{\bar{\varepsilon}}{\bar{\varepsilon}_c} \quad \text{or} \quad \hat{\sigma} = \langle 1-\bar{D}\rangle\hat{\varepsilon} = \langle\phi\rangle\hat{\varepsilon}, \qquad (11)$$

with $\bar{\varepsilon}_c$ being the macrostrain at the specimen failure.

From (11) the order parameter, $\langle\phi\rangle$, is zero when the strain $\hat{\varepsilon} = \bar{\varepsilon}/\bar{\varepsilon}_c$ is unit. Vice versa, when the strain is zero, $\hat{\varepsilon}=0$, the order parameter, $\langle\phi\rangle$, is unit. At both of these states the normalized macrostress $\bar{\sigma}/E^0$ is zero. If $\langle\phi\rangle$ reaches continuously the zero value, the phase transition, $\hat{\varepsilon} = \bar{\varepsilon}/\bar{\varepsilon}_c = 1$, is of the *second order* [Fig. 2(*a*)]. If $\langle\phi\rangle$ goes discontinuously from zero to a nonzero value at $\hat{\varepsilon} = \bar{\varepsilon}/\bar{\varepsilon}_c < 1$, the phase transition is of the *first order* [Fig. 2(*b*)]. Figures 2(*a*) and 2(*b*) refer to a 2D quasibrittle lattice.

4.2 Mean Field Theory: Critical Behavior. The importance and utility of mean field approach consist of the robustness to the details underlying the interactions. The mean-field theory at critical behavior is based on two concepts.

1. *Universality* designates that a problem belongs to a universality class. Universality class is the set of all systems that have same critical properties and fixed points (Kadanoff [24]).
2. *Scaling* refers to the power law relations that are observed between various quantities (Kardar [26]). The fragmentations, earthquakes (Gutenberg–Richter relation) and fracture of quasibrittle materials (Weibull theory) indicate that the system is invariant under the transformation $\mathbf{r}\to\lambda\mathbf{r}$, when $\mathbf{r}$ is position.

These two concepts support the bridging between the microscopic and macroscopic parameters. This bridge is the *renormalization group theory*, that is a transformation involving thinning of degrees of freedom (coarse graining) coupled with a change in the length scale [7,22,27,28].

4.3 Thermodynamics of Griffith Cracks and Thermodynamic Potentials. Experiments demonstrate that isolated systems spontaneously tend to states that are known as equilibrium states, defined by a "small" number of *system* parameter [20]. The specimen is in contact with heat reservoir to maintain the temperature at $\bar{T} = \bar{T}_o = \text{const}$ [29] during the damage process. If the system elongation, $\bar{\varepsilon}_{ij}$, is controlled, equilibrated thermodynamic states of the process are defined by the manifolds $\{\bar{\sigma}, \bar{D}, \bar{T}_o\}_{\bar{\varepsilon}}$ on the macroscale. When the elongation, $\bar{\varepsilon}_{ij}$, increases, the macrostress and macrodamage parameters increase as well, i.e., the manifold is $\{\bar{\sigma}+\delta\bar{\sigma}, \bar{D}+\delta\bar{D}, \bar{T}_o\}_{\bar{\varepsilon}}$. This quasistatically damage process can be partitioned in a sequence of many two-steps operations [29]. The two steps are the following:

1. Separating reversibly two surfaces pulling against cohesive forces until two surfaces are not jointed. "By definition of the quantity 2γ as the reversible work of (isothermal) separation per unit area, the contribution to the free energy Φ is $2\gamma\ell$" [29].
2. Deforming elastically and quasistatically each element of the damaged specimen so that such elements have the same equilibrated strain-state as that actually induced in the specimen when the microcrack is ℓ and the imposed displacement is $\delta\bar{\varepsilon}$.

In polycrystal specimen microcracks will nucleate and propagate either along the grain-boundaries or through the grain. In this work, the resistance energy at the grain-boundary, $2\gamma_{\mathrm{gb}}n\ell$, is smaller than in the bulk of the grain and the cracking is purely intergranular.

The Gibbs' potential, $\bar{\psi}$, (per unit volume), defined as the Legendre transformation of the Helmholtz free energy density, $\bar{\upsilon}$, [30]

$$\bar{\psi}(\bar{\sigma},\bar{T},\bar{H}) = \bar{\sigma}:\bar{\varepsilon} - \upsilon(\bar{\varepsilon},\bar{T},\bar{H}) = \bar{\sigma}:\bar{\varepsilon} - \tilde{u} - \bar{T}\bar{\eta}. \qquad (12)$$

In (12) $\bar{T}$ is the absolute temperature, $\tilde{u}$ is internal energy density, $d\tilde{u} = \bar{\sigma}_{mn}d\bar{\varepsilon}_{mn}$, $\bar{H}$ is the history recording parameter, and $\bar{\eta}$ is entropy. Complementary expressions for the average stress and strain (at fixed $\bar{H}$) are

$$\bar{\sigma}_{ij} = \frac{\partial\bar{\upsilon}(\bar{\varepsilon},\bar{T},\bar{H})}{\partial\bar{\varepsilon}_{ij}} \quad \text{and} \quad \bar{\varepsilon}_{ij} = \frac{\partial\bar{\psi}(\bar{\sigma},\bar{T},\bar{H})}{\partial\bar{\sigma}_{ij}}. \qquad (13)$$

The inelastic (irreversible) changes of Gibbs' potential (per unit volume) occur during processes characterized by the change of the recorded history.

The inelastic (irreversible) changes of two potentials that occur during processes are characterized by the change of the recorded history. The change in the Gibbs' energy density associated with a change of state (isothermal and load-controlled) is [29]

$$\delta^i \overline{\psi} = \frac{1}{V^0} \sum_{\alpha} f_{\alpha} \delta \vartheta_{\alpha} = \frac{1}{V^0} \sum_{\alpha} \oint_{L_{\alpha}} [G(\sigma,a) - R(\ell)] \delta a(\ell) d\ell. \tag{14}$$

In (14) $\delta a(\ell)$ is the "distance" that a point on the microcrack front advanced during the transition between two neighboring states and $\overline{\psi} \equiv V^0 \psi$. Since the entropy production rate is nonnegative the integral in (14) is

$$\int_{\text{c.f.}} f \dot{\ell} ds \equiv \int_{\text{c.f.}} (G-R) \dot{\ell} ds \equiv \int_{\text{c.f.}} \mathcal{A} \dot{\ell} ds \geqslant 0. \tag{15}$$

In (15) "c.f." stands for "crack front" and the integral with respect to the arc length s is carried over all extending parts of the microcracking front [29]. Finally, analogously to the Griffith's theory, G is the energy release rate, R is the material resistance to crack extension, and $\mathcal{A}$ is the thermodynamic affinity

$$\mathcal{A} = G - R. \tag{16}$$

The thermodynamic crack-extension "force" per unit length along the locus of all microcrack fronts, $\overline{F}$ (N/m), is (Rice [31])

$$\overline{F} = \sum_{N} (G_i - R_i). \tag{17}$$

The part of the Gibbs' free energy required for damage increase is

$$d^i \overline{\Psi} = \sum_{n} (G_i - R_i) da_i \geqslant 0. \tag{18}$$

In (18) N is number of microcracks, n number of microcracks that increased, and a the microcrack radius. This formulation can be applied to continuum or discrete models but requires thermodynamic equilibrium.

5 Mean-Field Theory of Damage

Mean-field theory, at infinite and finite dimensions (see in [7,20,21–25]), provides a tool for considering many processes at phase transitions and at critical states. But, most of those models and procedures do not consider process in materials, which are at microscale random and heterogeneous, and on the macroscale "continuous." Close to the phase transitions and critical states, most continuous engineering materials, such as ceramics, concrete, rock, cementitious composites, etc., become discontinuous on the macroscale. Thus, the material at pristine state and at threshold of failure is not the same.

Research in the statistical physics models is not frequently found in books and journals of engineering mechanics of continuous medium. Weibull's publication in 1939 of the paper "A statistical theory of the strength of material" [32] shows that the threshold of failure scales with the size of the specimen. This engineering work provides the foundation of the "weakness" of material but was published, without any mention of the mean-field theory of Landau in 1937. The other shortcoming of that genre of engineering literature that will benefit by considering mean-field theory is fatigue. Behaviors of small fatigue flaws (of the size from a fraction of millimeter to several millimeters) are still called *anomalous*. What is "anomalous" is that the models of continuous medium from fracture mechanics are used in fatigue models, even though that material at microscale is heterogeneous [33] and discontinuous.

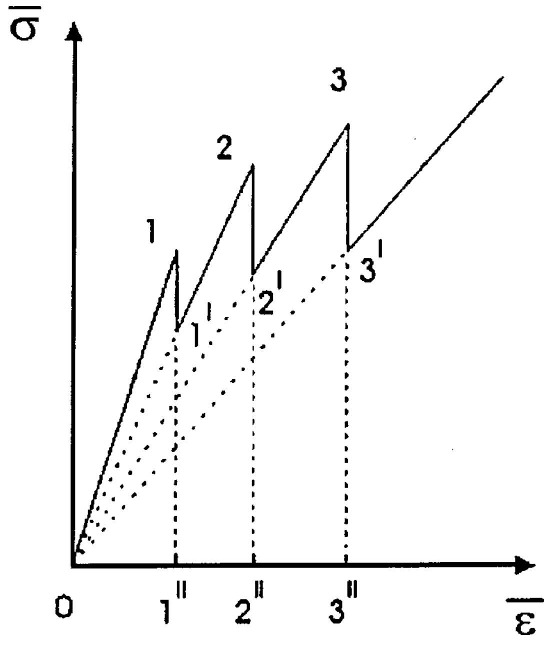

Fig. 3 Saw-toothed stress versus strain curve during the damage process

5.1 Disordered Matter: Lattice Simulations. A damage tolerant material, that has random heterogeneous microstructure, is modeled in a simple way by a lattice. On the microscale the geometry of a disordered material, either a polycrystal or an amorphous one, can be thought as a random-close-packed particle structure where each particle is connected to the others. In a general sense, each particle can be an atom, a molecule or a grain depending on the specific problem. By assuming to know the nature of the interactions, the matrix of Hamilton's equations of such structure would be full and the simulations laborious. However, the primacy of the "short-range order is very much in evidence in the structure of amorphous solids" (Zallen [34]) and polycrystal material. Limiting the model to the short-range makes large simulations become possible. The x-ray scattering data on amorphous metallic glass, amorphous silicon, amorphous metal and other materials demonstrate that short-range order provides good models and useful data [34]. In this case each atom is connect only to few closer atoms.

In this paper a two-dimension lattice (or network) is used to model the polycrystal material. The sites represent the grain masses and the bonds (links) connect each grain with six close sites. The link consists of a spring of given stiffness that breaks when the load reaches a random tensile threshold. The load is imparted through rigid bars that are applied on the free surfaces of the lattice and are free to translate along given directions. The lattice is rectangular and the macro-strain is homogeneous. Irregular Wigner–Seitz cells can be used to the approximate the grain of fully dense polycrystalline ceramic on the microscale. To simulate the random heterogeneous geometry of real microstructure, the lattice must be irregular.

By a mechanical viewpoint, either finite elements or molecular dynamics can be used to solve spring network, which is indeterminate and globally stable. The latter is used here.

In a displacement controlled monotonic loading, the macrostress versus macrostrain curve resembles a smooth parabola. On the microscale the model the stress versus strain curve is sawtoothed as shown in Fig. 3. The radial segments of the macrostress versus macrostrain curve are linear elastic. The macroparameter manifold for the radial segments are, $\{(\overline{\sigma}_i + \delta\overline{\sigma}_i), \overline{D}_i, \overline{T}_o\}_{\overline{\varepsilon}_i + \delta\overline{\varepsilon}_i}$, when the system elongation passes from $\overline{\varepsilon}_i$ to $\overline{\varepsilon}_i + \overline{\varepsilon}_{i+1}$. The vertical segments, in Fig. 3, are nonstationary and nonequilibrated. In fact the "vertical" segments are not vertical at all.

In reality, microcracks formation and growth are dynamic processes during which shock waves attenuate, interact and reflect within the random material. Damping properties of materials depend on the chemical composition, constitution, homogeneity effects, damage, aging, solid-state transformations, state of internal stress and stress imposed by service conditions (including environmental conditions) [35] that are not known.

5.2 Phase Transitions. The mechanisms of damage evolution on the microscale are the nucleation, propagation, and clustering of microcracks. As the density of microcracks evolves, the effective macrostiffness declines. The rate of damage that evolves depends on the primary mechanism of the damage. If the nucleation is the primary mechanism of damage evolution, the rate of the damage evolution and the reduction of the effective macrostiffness are slower. The rate of macrostiffness decline and damage evolution is higher when the microcracks clustering is the primary mechanism.

A faster decline of the macrostiffness becomes obvious when the process is close to the critical state. Thus, by measuring the rate of the effective macrostiffness, at "pristine" and current states, one can estimate the residual strength and durability of the specimen. Since the damage grows as a stochastic process and the material is randomly heterogeneous on the microscale, the critical state is a random variable. Consequently, residual strength and durability are also random variables. Accordingly, statistical damage mechanics provide the only possible fundamental models of the damage tolerance principles of airplane design [36].

5.3 Phases. There are two phases during the process of damage accumulation from its pristine state to the failure of the specimen. The two phases, hardening and softening, are the reflections of the primary mechanism of damage growth.

Hardening Phase:

a. Damage density develops by microcracks nucleation at the weak links or spots. It is unlikely that the distance between two or more microcracks is small. The amplifying interaction effect of microcracks is insignificant.
b. The specimen is statistically homogeneous and the damage nucleation microcracks is the paramount mechanism of damage rate increase. Close to the peak of the macrostress versus macrostrain, the propagation and clustering mechanisms become dominant. The result is the large reduction of the effective stiffness of the system.
c. The specimen is statistically homogeneous only in part of the hardening phases. This part of the hardening phases may be small. But, when the macrotraction vector is applied, the failure threshold depends on the rate of reduction of the effective system stiffness in that part of the macrostress versus macrostrain curve.

Thus, "micromechanics" models, Section 3.2 in this paper, may provide good data in the hardening phase. However this model cannot furnish any estimate of specimen failure.

During the hardening phase, including the peak, the form of the macrostress versus macrostrain curve does not depend on whether the macrotraction or the conjugate macrodisplacement is applied to the specimen. The experimental data indicate that macroparameters are fractals at the failure [4,37–42].

Softening Phase:

a. The damage process in softening phase depends on the large cluster, formed at the peak of the macrostress versus macrostrain curve, of the microcracks of correlation length, $\xi(\overline{D})$, that spans the specimen. This cluster is known as macrocrack or fault [40,42].
b. Correlation length is a fractal and/or multifractal.
c. The specimen is random heterogeneous.
d. Macroparameters are fractal and/or multifractal.
e. The failure is of the avalanche class [41,43].

When the macrotraction is applied to the specimen, failure happens at the peak of the macrostress versus macrostrain curve, i.e., the softening phase does not exist. Then, the process has only one phase transition namely the failure when $d\overline{\sigma}=0$. This phase is identical to the first phase transition when the conjugate macrodisplacement is applied. For this case there are two phases, i.e., before and after the peak. Thus, it is sufficient to study the process when the macrodisplacement is applied. Finally, when the traction, $\overline{\sigma}$, is applied to the specimen, the failure at the peak is a first-order phase transition [Fig. 2(*b*)]. When the displacement, $\overline{\varepsilon}$, is controlled, the failure is a second-order phase transition [Fig. 2(*a*)] and happens at $\overline{\sigma}=0$.

5.4 Phase Transition. "Phase transition between two equilibrium phases of matter whose signature is a singularity or discontinuity in some observable quantity" is the phase transition [7]. By considering a specimen loaded under uniaxial tension, the order parameter in (11) can be used:

$$\langle\phi\rangle=\frac{\overline{E}}{E_0}=\langle 1-\overline{D}\rangle \quad \text{or} \quad \langle\phi\rangle=e^{-\hat{D}} \tag{19}$$

This order parameter denotes "a fluctuating variable the average value of which provides a signature of the order or broken symmetry in the system" [20].

The Delaunay triangular lattice, used in this work, may furnish good data when the process approaches failure, but not as good as one would desire to predict reliably the failure. This is due to the many approximations in the specific lattice model. Far from the softening phase, the correlation length approaches the specimen length, i.e. coherence length $\xi(\overline{D})\rightarrow L^{\beta}$, and in reality the largest cluster also grows through the grains. During the same part of the process, the damage increases by avalanches. The macrocrack increases by larger numbers of the microcracks and the affinities of the microcracks in the rest of the specimen stagnate or become lesser (shielding and crack closure).

At the threshold of failure, the order parameter $\langle 1-\overline{D}(\overline{\varepsilon})\rangle$ depends on the damage tolerance of the material, the process dynamics, the damping properties of the matter and the temperature. All these parameters should be embedded in the lattice model. Hence, the lattice in this work cannot simulate correctly the part of the process when the specimen secant effective stiffness is close to zero, $K^{*}\approx 0$, and the order parameter $\langle\phi\rangle\approx 0$. In Fig. 2(*a*) the order parameter curve terminates with dashed lines. Wannier considered a similar problem, in [23], on two distinct magnetizations.

5.5 Hardening Phase: Macro Parameters. The goal of statistical mechanics is to estimate macroparameters, required in engineering, from microscopic descriptions of a system. Scaling concepts provide the tool for the goal. From Weibull to this day tests determined that "power laws are fundamental constants, robust to the details of the underlying interactions" [32]. In this work a two-dimensional triangular lattice substitutes a damage tolerant specimen, i.e., a ceramic in which the microcracks nucleate and propagate along the grain-boundaries.

The simulation data provide the macro-behavior of four lattices of size $L=\{23,47,95,191\}$. From [15], the damage response of the lattice is of the form

$$\overline{\sigma}=\overline{E}^{0}(1-\overline{D})\overline{\varepsilon} \quad \text{or} \quad \overline{\sigma}=\overline{E}^{0}e^{-\hat{D}}\overline{\varepsilon} \tag{20}$$

where $\overline{D}$ and $\hat{D}$ is the damage parameters. Thus, the relation $\overline{D}$ versus $\overline{\varepsilon}$ fully describes the stochastic part of process. In this process the order parameter, $\langle 1-\overline{D}(\overline{\varepsilon})\rangle$, depends on the scaling function, $\overline{D}(\overline{\varepsilon})$. The damage parameter for the lattice is

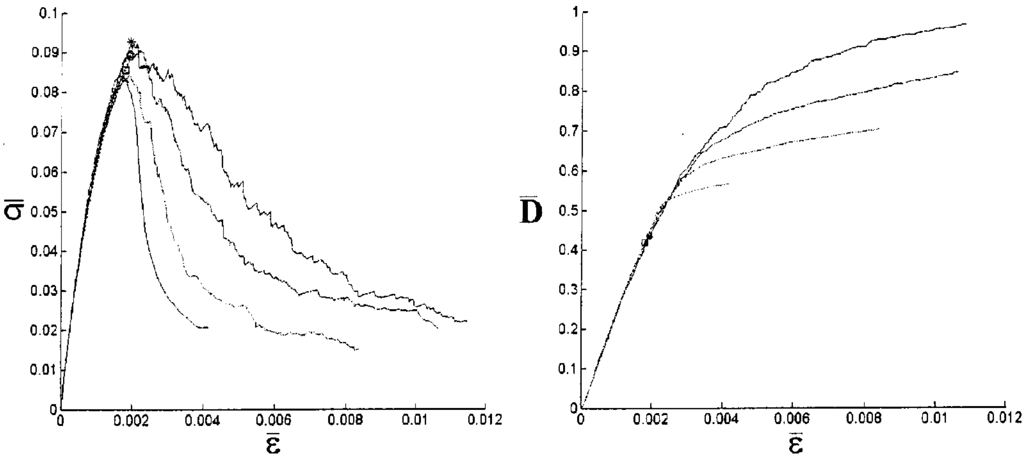

Fig. 4 The $\bar{\sigma}$ versus $\bar{\varepsilon}$ and $\bar{D}$ versus $\bar{\varepsilon}$ curves from simulation data

$$\bar{D} \sim \frac{n}{L^2}, \tag{21}$$

where n is the number of broken bonds from simulations. The macrostress versus macrostrain curves, $\bar{\sigma}$ versus $\bar{\varepsilon}$, and the damage versus macrostrain curves, $\bar{D}$ versus $\bar{\varepsilon}$ are shown in Fig. 4 (curves in Fig. 4 are mean curves of a sample of 10 replicates per lattice size). The collapse of simulation data in Fig. 5(*b*) is obtained when relation (21) is $\bar{D}=(2e^{-1.6})^{-1}nL^{-2}$. The number of broken bonds at the force peak, N_p, is a fractal quantity (already in [43]) and the curve N_p versus L is a straight line in the log–log plot. The exponent -1.6 of the exponential in the latter expression equals the intercept of such straight line (plot not shown). Markers in Fig. 4 correspond to the values of damage at the peak of the curves $\bar{\sigma}$ versus $\bar{\varepsilon}$. The location of such peak points is different for each lattice.

In this paper, the Family–Vicsek scaling relations in [28] are reinterpreted to make the damage curves collapse on a single curve throughout the hardening regime. The relations are

$$\bar{D}(\bar{\varepsilon},L)=L^{\alpha}f\left(\frac{\bar{\varepsilon}}{L^{\gamma}}\right) \quad \text{and} \quad \gamma=\frac{\alpha}{\beta} \tag{22}$$

where α, γ, β are, respectively, the scaling exponent of $\bar{D}$, the scaling exponent of $\bar{\varepsilon}$ and the exponent of the power law that fits the data better at the origin. In lieu of the linearity of Fig. 5(*b*) in the beginning, $\beta=1$ and $\gamma=\alpha$. Thus, there is only one degree of freedom, α, and (22) can be rewritten as

$$\bar{D}(\bar{\varepsilon},L)=L^{\alpha}f\left(\frac{\bar{\varepsilon}}{L^{\alpha}}\right) \tag{23}$$

The data of the hardening phase, shown in Fig. 5 by dashed lines, collapsed for $\alpha=-0.035$ and the peak points clustered around $(\bar{\varepsilon}/L^{\alpha},\bar{D}/L^{\alpha})_p=(0.0021,0.5)$ remarkably well for all lattice sizes. This is important in deducing the macroparameter and the macrostress versus macrostrain relations from pristine state to failure. The scaling (23) is feasible because the damage at the peak is a fractal quantity that plays the role of the saturation threshold in [28]. In the beginning the simulation data are close to a straight line but deviate progressively at the peak. The simple analytical formula for the damage parameter,

$$\bar{D}=a\bar{\varepsilon}+b\,\frac{\bar{\varepsilon}^2}{L^{\alpha}}, \tag{24}$$

captures the data simulation of the hardening phase (solid line in Fig. 5). The coefficients a and b are deduced from simulations. The parameter, a, is the nucleation damage rate (Fig. 5, dashed–dotted line) and b governs the rate of data deviation from the straight line, i.e., the effect of the interaction of microcracks at the threshold of the transition. For the fitted model in Fig. 6, a set of parameters is $a=\partial\bar{D}/\partial\bar{\varepsilon}\rceil_0=275$ and $b=L^{\alpha}/2\bar{\varepsilon}_p(\partial\bar{D}/\partial\bar{\varepsilon}\rceil_p-\partial\bar{D}/\partial\bar{\varepsilon}\rceil_0)=-14{,}862$.

The selection of the order parameter is correct if the macrodamage parameter, $\bar{D}(\bar{\varepsilon})$ versus $\bar{\varepsilon}$, collapses on a single curve for all sample averages of specimen sizes. This test of the selection of the order parameter, $\langle 1-\bar{D}\rangle$, was passed as shown in Fig. 5.

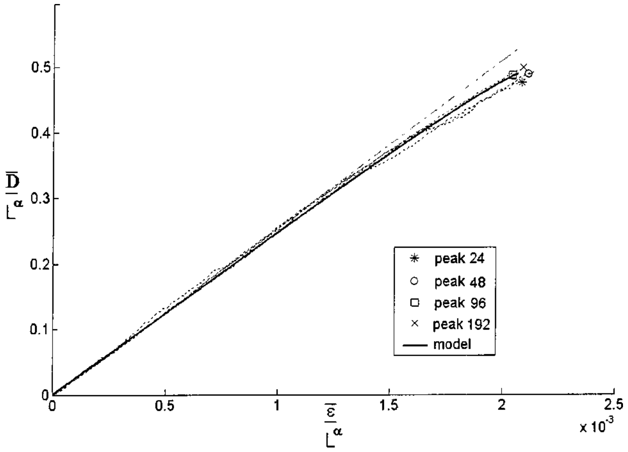

Fig. 5 Simulation data in the hardening phase after the scaling

5.6 Softening Phase: Macro Parameters. The requirement of a non-negative entropy production rate, as the temperature is positive, is

$$\sum_i (G_i-R_i)\ell_i=\bar{\mathcal{A}}\ell\geqslant 0. \tag{25}$$

In (25) $\bar{\mathcal{A}}=\Sigma_i(G_i-R_i)$ is the affinity defined earlier that determines the damage or thermodynamic force that drive the evolution (link rupture). For an increment of applied displacement $\Delta\bar{\varepsilon}$, the increment of length is $\Delta\ell$. As the affinity of a link reaches zero, the link breaks. The smallest increment of damage is when only one link breaks. The force that the broken link was carrying

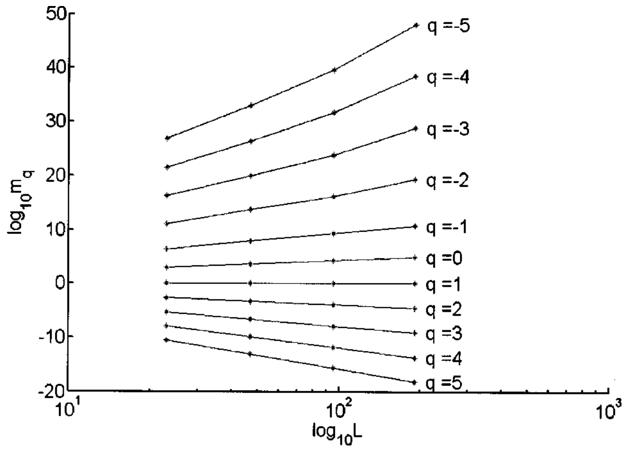

Fig. 6 Multifractal distribution of the *q*th moments of the microaffinity distribution

is distributed to the other links such that the complementary work and the minimum value of the complementary energy are satisfied. The force of the dismembered link is distributed to the links of negative affinity, in accordance with equilibrium and compatibility conditions. At that point, defined by the applied macrodisplacement, $\overline{\varepsilon}_x$, the survival links carry the force of the broken links and their affinities is $(\mathcal{A}_i+\Delta\mathcal{A}_i)<0$. Thus, on microscale there are only two processes: (1) $\max(\mathcal{A}_i+\Delta\mathcal{A}_i)<0$ and (2) $\max(\mathcal{A}_i+\Delta\mathcal{A}_i)\geqslant 0$. Process (1) dominates the hardening phase as the damage grows by one link at time. Process (2) dominates the softening phase as the damage grows by two or more link at the time. The number of links at damage grows is the order of bursts.

Hemmer and Hansen in [44] ascertained that this evolution of the process involves a sequence of bursts (avalanches) during which a group of links fails in the simulation. They derived the analytical expression for the distribution law for bursts and also determined that the distribution of numbers of broken links during the simulation is a fractal.

At the threshold of failure, one may conclude that small numbers of links at the tip of the largest cluster carry the largest force. However, the material of the cluster tip is heterogeneous. Generally, the macroenergy release rate, *G*, drives the damage process and the material resistance, *R*, determines the geometry of the clusters. The microaffinity intrinsically accounts for this difference by definition (25) and has a strong physical significance. In the large microaffinities, $\mathcal{A}\Rightarrow O$, is concentrated at tip of the largest cluster similar to the "Barenblatt strip" [45]. The affinities of the links in the "singularity dominated zone" [46] are large but not as large as those in the "Barenblatt strip." Therefore, the distribution of links affinities is a multifractal, because the on position in space and their strength of "Barenblatt strip," "singularity dominated zone" and other zones, which is fractals. Thus, bases of the softening process are the two discontinuous fields, namely the distributions of microtexture of the specimen and the distribution of link affinities.

These fields are in accord with the multifractal measures where "knowledge of the fractal dimension of a set, is insufficient to characterize its geometry, and, all the more so, any physical phenomenon occurring on this set" (Gouyet [47]). Multifractal analysis is the proper tool when links breakdown into a "collection of sets having different singularities" (Hansen and Roux [43]).

Following Gouyet [47] the "multifractal character is connected with the heterogeneous nature of the distribution." The scaling law of $\langle\mathcal{M}(\mathcal{R})\rangle$, where mass is $\mathcal{M}(\mathcal{R})$ and $\mathcal{R}$ is the radius of sphere centered on the fractal at x_i, is $\mathcal{R}^{\kappa}$. If all moments modulate like as $\langle\mathcal{M}(\mathcal{R})^q\rangle\propto\langle\mathcal{M}(\mathcal{R})\rangle^q$, for all *q*, the fractal distribution is characterization by the sole exponent κ, and the fractal distribution is homogeneous. For heterogeneous fractals of broad distribution, $P(\mathcal{M})$, of the masses the sole exponent κ is not sufficient. In this case the quantities $f(\alpha)$ and $\tau(q)$ "characterize the distributing heterogeneity's of the measures known as multifractal measures" [47].

The entropy production rate in a heterogeneous (or discontinuous) system is

$$\Lambda=\frac{1}{T}\sum_i (G_i-R_i)\dot{\ell}_i=\frac{1}{T}\sum_i \mathcal{A}_i\dot{\ell}_i=\frac{1}{T}\overline{\mathcal{A}}\overline{\dot{\ell}} \tag{26}$$

In relation (26) $\overline{\mathcal{A}}$ total affinity and $\overline{\dot{\ell}}$ is the total rate of the damage parameter

$$\overline{\mathcal{A}}=\sum_i \mathcal{A}_i=\sum_i (G_i-R_i) \quad \text{and} \quad \overline{\dot{\ell}}=\sum_i \dot{\ell}_i. \tag{27}$$

Since the absolute temperature, *T*, is non-negative the entropy production rate will also be non-negative.

The statistical moments of the distribution of link affinities in the asymptotic neighborhood of the phase transition can be written in the form [11]

$$M_k(L)=\sum_j \mathcal{A}_j^k n(\mathcal{A}_j,L)\cong\int_0^1 \mathcal{A}^k n(\mathcal{A}_j,L)d\mathcal{A}. \tag{28}$$

In (28) $\mathcal{A}_j$ is the normalized affinity carried by the *j*th link, while $n(\mathcal{A}_j,L)$ is the number of links conducting an affinity $\mathcal{A}_j(-\infty<\mathcal{A}_j\leqslant 0)$ in lattice of size *L*. Using the relation in (28) the problem of the determination of the distribution of affinity transmitted by individual links of a lattice is reduced to the determination of a set of exponents $z(k)$. These exponents must be size-independent to be useful in analyses. For a finite *k* the product $n(\mathcal{A}_k,L)\mathcal{A}^k$ is very small for both $\mathcal{A}\rightarrow-\infty$ and $\mathcal{A}\rightarrow 0$. For $\mathcal{A}=-\infty$ and finite *n* this product is obviously equal to zero. Moreover, the fraction of cutting links $n(\mathcal{A}_k\rightarrow 0,L)$, which carry the affinities close to zero, is a minuscule part of the total affinity. Thus, the product $n(\mathcal{A}_k,L)\mathcal{A}^k$ peaks at an intermediate value of the affinity $\mathcal{A}_i$ of the normalized affinity *i*. All peaks become sharper with the increase of lattice size *L*. Assuming that the peak is very steep, the sum in (28) can be approximated by a single (dominant) term as

$$M_k\approx n(\mathcal{A}_k,L)\mathcal{A}_k^k. \tag{29}$$

Mathematically, the expression (29) can also be interpreted as an estimate of the integral equation in (28) derived by using the method of steepest descent (or the saddle point). The approximation (29) is consistent with the conjecture that each statistical moment of the current distribution in the lattice is supported by a different fractal subset of the backbone. The affinity, $\mathcal{A}_k$, at which the integrand of (28) peaks, is determined in a traditional way by setting to zero its first derivative.

Employing the stratagem in [43] for the currents in the electrical network, assume that local affinities, $\mathcal{A}$, scale as $\mathcal{A}\propto L^{\alpha}$, and that their support is a fractal object, as in the "Barenblatt" strip, of dimension *f*, $n(\mathcal{A})\propto L^f$. Thus, the moment (29) of order *q* in the softening phase is

$$M(q)\propto L^f L^{\alpha q}=L^{\chi(q)} \quad \text{when} \quad \chi(q)=\alpha q+f. \tag{30}$$

Since the function $\chi(q)$ is not affine in α Hansen and Roux assumed "that instead of a single set of such currents, there exist a large number of such values of α, and for each of them a corresponding $f(\alpha)$ dimension." Thereupon, the function $\chi(q)$ is

$$\chi(q)=\max_{\alpha}[\alpha q+f(\alpha)]. \tag{31}$$

Thus, the exponent χ can be computed for the selected function $f(\alpha)$. Using the extremum condition, the function in (31) leads to

$$f'(\alpha)=-q. \tag{32}$$

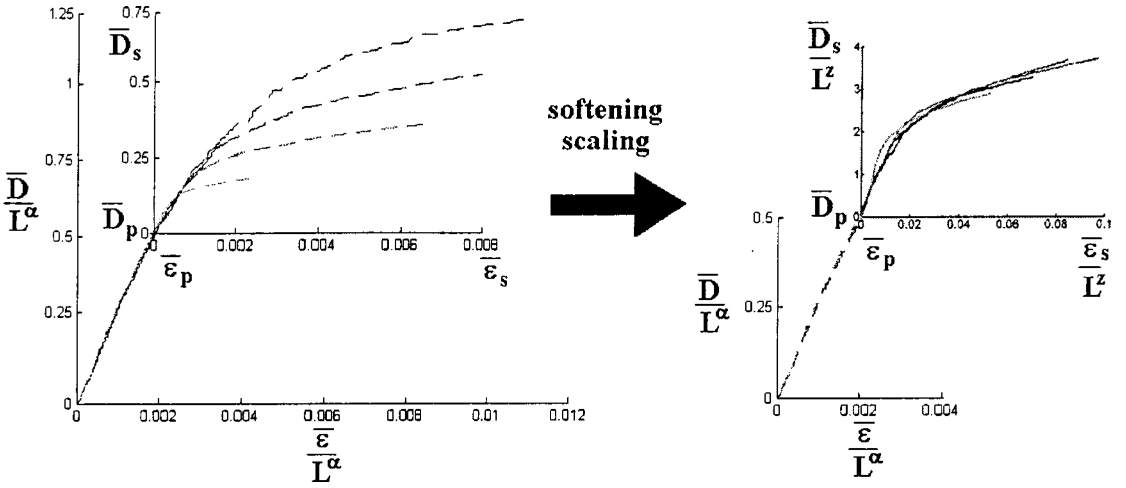

Fig. 7 Scaling procedure of the data in the softening regime

The condition (32) designates the value of α that contributes most importantly to the scaling of the qth moment. With this value of $\alpha=\alpha(q)$ the function in (31) is

$$\chi(q)=q\alpha(q)+f(\alpha(q)). \tag{33}$$

The derivative of χ function with respects to q is

$$\frac{d\chi(q)}{dq}=\alpha(q)+[q+f'(\alpha(q))]\frac{d\alpha(q)}{dq}. \tag{34}$$

From (32), $\alpha(q)$ and $f(q)$ are

$$\alpha(q)=\frac{d\chi(q)}{dq} \quad \text{and} \quad f(\alpha(q))=\chi(q)-q\alpha(q). \tag{35}$$

Gouyet derived the same expression (35) for multinomial fractal measures. Hence, knowing the function $\chi(q)$ in (30) is equivalent to the knowledge of (35). By virtue of (30), since the qth moments plot on straight lines in Fig. 6, the distribution of microaffinities is multifractal.

Relations (35) are similar to a Legendre transform. The parameter q allows selecting subsets E_α of the set E, i.e., $E=\cup_\alpha E_\alpha$. The two functions $f(\alpha)$ and $\chi(q)$ are related by the Legendre transform in (33). The properties of the multifractal spectrum, $f(\alpha)$, are:

1. The determination of the scaling exponent of the moment or order q takes one single set of links from (30) and is tangent to the spectrum that has slope $-q$ [43].
2. The maximum of $f(\alpha)$ corresponds to a uniform measure on the support [47]. From (33) the exponent α is maximum.
3. The Legendre transform allows one to pass from the equation $f=f(\alpha)$ to a plane curve to the equation $\tau=\tau(q)$, of the same curve, by elimination α between $q=df/d\alpha$ and $\tau=f-q\alpha$ [47].

The scaling (23) takes care only of the first part of the process. In the softening regime the damage curves are, indeed, still scattered [Fig. 7(*a*)]. It is possible to scale the data also in the softening phase because of the existence of fractal sets. The new scaling is applied only to the data of the softening regime and new coordinates, $\bar{D}_s$ and $\bar{\varepsilon}_s$ are defined as

$$\begin{cases} \bar{\varepsilon}_s=\dfrac{\Delta\bar{\varepsilon}}{L^\alpha}=\dfrac{\bar{\varepsilon}-\bar{\varepsilon}_p}{L^\alpha} \\ \bar{D}_s=\dfrac{\Delta\bar{D}}{L^\alpha}=\dfrac{\bar{D}}{L^\alpha}-0.5 \end{cases} \tag{36}$$

with respect to a new frame of reference. In Fig. 7(*a*), the origin of the new coordinates is the point $(\bar{\varepsilon}_p,\bar{D}_p)=(0.0021,0.5)$, where the peak points collapsed in Fig. 5.

There are some similarities between the crystal-growth phenomena in [28] and the propagation/clustering mechanisms in the softening regime. Hence, a scaling similar to (23) is used. Since the new set of data, $\bar{D}_s$ versus $\bar{\varepsilon}_s$, does not have a large curvature at the origin, $\beta=1$ is assumed and the new scaling relation is

$$\bar{D}_s(\bar{\varepsilon}_s,L)=L^z g\left(\frac{\bar{\varepsilon}_s}{L^z}\right). \tag{37}$$

The result of (37) is shown in Fig. 7(*b*), with $z=-0.52$. The data collapse is evident and provides a useful piece of information in deducing the macroparameters and the threshold of failure. The analytical function for the damage parameter

$$\bar{D}=L^\alpha\bar{D}_p+a_1L^\alpha\bar{\varepsilon}_s+b_1L^\alpha L^z(1-e^{-c_1(\bar{\varepsilon}_s/L^z)}) \tag{38}$$

describes very well the softening data as shown in Fig. 8. The three parameters a_1,b_1,c_1 are determined from simulations but

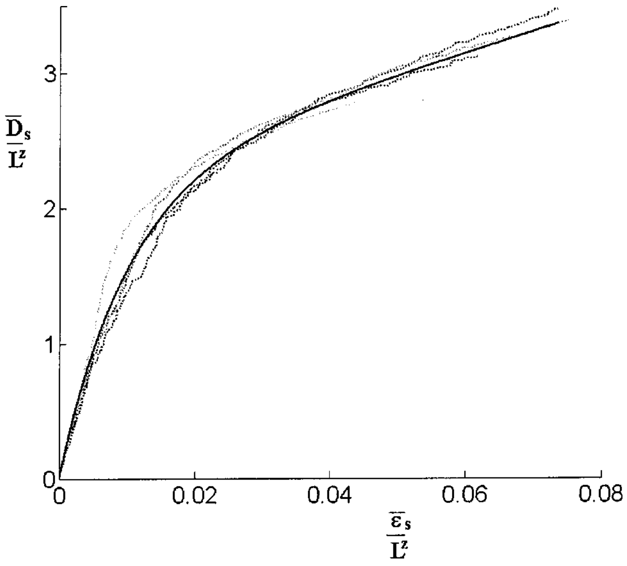

Fig. 8 Data in the softening regime after scaling

they are not independent. After the scaling (37), the softening data maintain C^1 continuity with the hardening data from (23) [Fig. 7(*b*)]. This provides the first condition

$$a_1 + b_1 c_1 = \left.\frac{\partial \overline{D}}{\partial \overline{\varepsilon}}\right|_{\overline{\varepsilon}_p}. \tag{39}$$

At the end of the transition, characterized by a continuous slope change, the softening data collapse on a straight line of slope $a_1 = \partial \overline{D}/\partial \overline{\varepsilon}|_{\text{failure}}$. Hence, given a_1 and (39), only one degree of freedom is left in (38). The pair $\{b_1, c_1\}$ is chosen to optimize the data fit. (A nonlinear regression analysis is needed to this purpose.) When the transition is complete at the saturation, the third term in (39) tends to the constant b_1. For the data in Fig. 8(*b*), the values are $a_1 = 15.80$, $b_1 = 2.2$, and $c_1 = 100$.

The usage of analytical expression (24) and (39) allows the estimates of the damage parameter in the entire range of the damage process and for any lattice size.

''Fractal geometry is a mathematical tool dealing with complex system that have no characteristic length scale'' [47]. One of those complex systems is the specimen whose macroparameter changes as the damage increases.

The macroproperties of systems in ''micromechanics'' models [9–12], is based on the *averaging* models, such as the self-consistent and differential methods, and Hashin–Shtrikman variational principle. However, the damage process is ergodic only when the damage density is not at the residual strength and failure. The model based on the statistical mechanics, thermodynamics, fractal and multifractal measure of random geometry can be used when the damage process is ergodic and not ergodic. Moreover, the principle of local action, in the introduction of this paper, is a principle only when the affinity, $\mathcal{A}$, is the measure of ''generalized forces,'' and the entropy production rate conjugate to the rate of the damage, $\Delta \overline{D}$. Finally, the order parameter, $\langle 1 - \overline{D} \rangle$, is the measure of the influence of the damage on the specimen.

6 Conclusion and Summary

Progress in engineering technology and design depends on the research in physics, mathematics, materials sciences, testing and measurement models, and computational science. In recent years the goal of aeronautical and power plant engineering is to formulate methods based on damage tolerance principles, i.e., durability of a system, whose performance is diminished by ''multiple site damage.''

The first principle of aeronautical design is the structural airworthiness. The ''redundancy of the fail-safe structures is desirable to the extent that is economically feasible to provide structural safety'' [36]. Structural characteristics, such as the damage tolerance and durability, of aeronautical and all technology, cannot be measured. Fundamental goal of the durability of a structure is its fatigue life [33,42]. For most of the total life of a fatigue crack, its length is of grain boundary size or smaller. However, microcracks, as in this paper, grow much less than macrocracks. The appellation *anomalous* for small fatigue cracks is not correct [33]. Fatigue cracks are microcracks, or short cracks, most of the time and it is the fatigue analysis that is anomalous. A short crack, sees material as being a random heterogeneous matter. ''Micromechanics'' models see the material as statistical homogeneity and the process ergodic. As the largest affinity is always larger than the average affinity, the micromechanics model will always overpredict the residual strength. The overstate prediction of structural strength and durability is larger when the structure is larger.

To estimate the damage growth, needed for structural maintenance and durability, one needs a model that conforms to the physical process and the material on the microscale. Most of the materials are continuous on the macroscale but random heterogeneous on all other scales. The microscale geometry changes are not insignificant as damage grows in a random heterogeneous crystalline solid. As the microgeometry changes, fresh microcracks nucleate, old microcracks grow and/or crystal deforms and rotates, and the set of number of degrees of freedom is very large. The solution of the large number of degrees of freedom problem asks for statistical physics and fractal geometry.

Durability and residual strength are two parameters, which define the microcracks order and density at the specimen passage to the failure. The goal of the method in this paper, composed by solid mechanics, statistical physics and thermodynamics, is to estimate the durability and residual strength of systems from airplanes to semiconductors. This method establishes the connection between macroparameters and the random processes on all scale using the renormalization group transformation. In this work macroparameters are deduced from the microcracks and random heterogeneity of the material.

Acknowledgments

This research is sponsored by the Mathematical, Information and Computational Science Division of Office of Advanced Scientific Computing Research, U.S. Department of Energy under Contract No. DE-AC05-00OR22725 with UT-Battelle, LLC. The authors wish to give a special thanks to Dr. S. Simunovic for valuable discussions that improved our work and Dr. I. Krajcinovic for help in editing this paper.

References

[1] Billington, E. W., and Tate, A., 1981, *The Physics of Deformation and Flow*, McGraw–Hill Inc., NY.

[2] Kellogg, O. D., 1953, *Foundations of Potential Theory*, Dover, NY.

[3] Kunin, I. A., 1982, *Elastic Media with Microstructure I—One-Dimensional Models*, Springer-Verlag, Berlin.

[4] Kunin, I. A., 1983, *Elastic Media with Microstructure II—Three-Dimensional Models*, Springer-Verlag, Berlin.

[5] Bazant, Z. P., and Planas, P., 1998, *Fracture and Size Effect in Concrete and Other Quasibrittle Materials*, CRC Press, Boca Raton.

[6] Torquato, S., 2002, *Random Heterogeneous Material, Microstructure and Macroscopic Properties*, Springer, NY.

[7] Chaikin, P. M., and Lubensky, T. C., 1995, *Principles of Condensed Matter Physics*, Cambridge University Press, Cambridge, Great Britain.

[8] Malvern, L. E., 1969, *Introduction to the Mechanics of a Continuous Medium*, Prentice–Hall, Inc., Englewood Cliffs, NJ.

[9] Mura, T., 1982, *Micromechanics of Defects in Solids*, Martinus Nijhoff Publishers, The Hague.

[10] Nemat-Nasser, S., and Hori, M., 1993, *Micromechanics: Overall Properties of Heterogeneous Material*, North–Holland, Amsterdam, The Netherlands.

[11] Krajcinovic, D., 1996, *Damage Mechanics*, North-Holland, Amsterdam, The Netherlands.

[12] Kachanov, L. M., 1958, ''On the Time to Failure Under Creep Conditions,'' Izv. Akad. Nauk SSSR, Otd. Tekh. Nauk, Metall. Topl., **8**, pp. 26–31.

[13] Lemaitre, J., and Chaboche, J.-L., 1985, *Mecanique des Materiaux Solides*, Dunod, Paris.

[14] Krajcinovic, D., and Silva, M. A. G., 1982, ''Statistical Aspects of the Continuous Damage Theory,'' Int. J. Solids Struct., **18**, pp. 551–562.

[15] Krajcinovic, D., Lubarda, V., and Sumarac, D., 1993, ''Some Fundamental Aspects of the Brittle Cooperative Phenomena—Effective Continua Models,'' Mech. Mater., **15**, pp. 99–115.

[16] Janson, J., and Hult, J., 1977, ''Fracture Mechanics and Damage Mechanics—A Combined Approach,'' J. Mec. Theor. Appl., **1**, pp. S18–S28.

[17] Budiansky, B., and O'Connell, R. J., 1976, ''Elastic Moduli of a Cracked Solid,'' Int. J. Solids Struct., **12**, pp. 81–97.

[18] Kachanov, M., 1993, ''Elastic Solids With Many Cracks and Related Problems,'' in *Advances in Applied Mechanics*, edited by Hutchinson, J. and Wu, T., Academic Press, NY, Vol. 29, pp. 259–445.

[19] Lubarda, V., and Krajcinovic, D., 1994, ''Tensorial Representation of the Effective Elastic Properties of the Damage Material,'' Int. J. Damage Mech., **3**, pp. 38–56.

[20] Chandler, D., 1987, *Introduction to Modern Statistical Mechanics*, Oxford University Press, NY.

[21] Garrod, C., 1995, *Statistical Mechanics and Thermodynamics*, Oxford University Press, NY.

[22] Cardy, J., 1996, *Scaling and Renormalization in Statistical Physics*, Cambridge University Press, Cambridge.

[23] Fujimoto, M., 1997, *The Physics of Structural Phase Transitions*, Springer, NY.

[24] Kadanoff, L. O., 2001, *Statistical Physics—Statics, Dynamics and Renormalization*, World Scientific, Singapore.

[25] Chowhury, D., and Stauffer, D., 2000, *Principles of Equilibrium Statistical Mechanics*, Wiley–VCH, Weinheim.

[26] Kardar, M., 1990, ''Fluctuations of Interfaces and Fronts,'' in *Disorder and*

Fracture, edited by Charmet, J. C., Roux, S., and Guyon, E., Plenum Press, NY.

[27] Wilson, K. G., and Kogut, J., 1974, ''The Renormalization Group and the *e* Expansion,'' Phys. Rep., **12**, pp. 75–200.

[28] Barabasi, A.-L., and Stanley, H. E., 1995, *Fractal Concepts in Surface Growth*, Cambridge University Press, Cambridge.

[29] Rice, J. R., 1978, ''Thermodynamics of the Quasi-Static Growth of Griffith Cracks,'' J. Mech. Phys. Solids, **26**, pp. 61–78.

[30] Weiner, J. H., 1983, *Statistical Mechanics of Elasticity*, Wiley–Interscience John Wiley and Sons, NY.

[31] Rice, J. R., 1975, ''Continuum Mechanics and Thermodynamics of Plasticity in Relation to Microscale Deformation Mechanisms,'' in *Constitutive Equation in Plasticity*, edited by A. S. Argon, MIT Press, Cambridge, MA.

[32] Weibull, W., 1939, ''A Statistical Theory of the Strength of Materials,'' *Inst. Eng. Res.*, Stockholm, **151**, pp. 1–45.

[33] Suresh, S., 1991, *Fatigue of Materials*, Cambridge University Press, Cambridge.

[34] Zallen, R., 1983, *The Physics of Amorphous Solids*, John Wiley and Sons, NY.

[35] Goodman, L. E., 1976, ''Material Damping and Slip Damping,'' in *Shock and Vibration Handbook*, edited by C. M. Harris and C. E. Crede, McGraw–Hill Book Company, NY, Vol. 36, pp. 1–28.

[36] Goranson, U. G., 1993, Damage Tolerance; Facts and Fiction, Commercial Airplane Group, Boeing Commercial Airplane Group, U.S.A.

[37] Hansen, A., Roux, S., and Herrmann, H. J., 1989, ''Rupture of Central-Force Lattices,'' J. Phys. (France), **50**, pp. 517–522.

[38] Krajcinovic, D., and Basista, M., 1991, ''Rupture of Central-Force Lattices,'' J. Phys. I, **1**, pp. 241–245.

[39] Bunde, A., and Havlin, S., eds., 1994, *Fractals in Science*, Springer-Verlag, Berlin.

[40] Reches, Z., and Lockner, D. A., 1994, ''Nucleation and Growth of Faults in Brittle Rock,'' J. Geophys, Res., **99**(B9), pp. 18.159–18.173.

[41] Turcotte, D. L., 1992, *Fractal and Chaos in Geology and Geophysics*, Cambridge University Press, Cambridge.

[42] Krajcinovic, D., and Vujosevic, M., 1998, ''Strain Localization—Short to Long Correlation Length Transition,'' Int. J. Solids Struct., **35**, pp. 4147–4166.

[43] Hansen, A., and Roux, S., 2000, ''Statistics Toolbox for Damage and Fracture,'' in *Damage and Fracture of Disordered Materials*, edited by D. Krajcinovic and J. V. Mier, Springer, Wien, pp. 17–102.

[44] Hemmer, P. C., and Hansen, A., 1992, ''The Distribution of Simultaneous Fiber Failures in Fiber Bundles,'' ASME J. Appl. Mech., **59**, pp. 909–915.

[45] Barenblatt, G. I., 1962, ''Mathematical Theory of Equilibrium Cracks in Brittle Fracture,'' Adv. Appl. Mech., **7**, pp. 590–129.

[46] Anderson, T. L., 1995, *Fracture Mechanics*, 2nd ed., CRC Press, Boca Raton, FL.

[47] Gouyet, J.-F., 1996, *Physics and Fractal Structures*, Masson, Paris.

Thermoelastic Fields in Boundary Layers of Isotropic Laminates

Christian Mittelstedt[1]
Siegen University,
Department of Mechanical Engineering,
Paul-Bonatz-Strasse 9-11, D-57068 Siegen,
Germany
e-mail: christian.mittelstedt@uni-siegen.de

Wilfried Becker
Darmstadt University of Technology,
Department of Mechanics, Hochschulstrasse 1,
D-64289 Darmstadt, Germany

An approximate approach to the calculation of displacements, strains, and stresses near edges and corners in symmetric rectangular layered plates of dissimilar isotropic materials under thermal load is presented. In the thickness direction the plate is discretized into an arbitrary number of sublayers/mathematical layers. A layerwise linear displacement field is formulated such that the terms according to classical laminate plate theory are upgraded with unknown in-plane functions and a linear interpolation scheme through the layer thickness in order to describe edge and corner perturbations. By virtue of the principle of minimum potential energy the governing coupled Euler–Lagrange differential equations are derived, which in the case of free-edge effects allow a closed-form solution for the unknown inplane functions. Free-corner effects are investigated by combining the displacement formulations of the two interacting free-edge effects. Hence, all state variables in the plate are obtained in a closed-form manner. Boundary conditions of traction free plate edges are satisfied in an integral sense. The present methodology is easily applied and requires only reasonable computational expenses. [DOI: 10.1115/1.1827247]

1 Introduction

The application of layered materials in the field of structural mechanics requires adequate means of calculation for all state variables, i.e., displacements, strains, and stresses. The most common analysis tool is the Classical Laminate Plate Theory (short: CLPT, see, e.g., [1]) which can be considered as an extension of Kirchhoff's plate theory. CLPT is widely used but fails to predict accurate results in the vicinity of edges and corners of layered structures where due to the discontinuous change of material properties in the layer interfaces localized three-dimensional and singular interlaminar stress fields occur (so-called free-edge effects [2–49] and free-corner effects [50–56]) that may lead to interlaminar failure modes like, e.g., delaminations. Free-edge effects in composite laminates have a good tradition in scientific research throughout more than 30 years. Numerical, closed-form and experimental approaches employing a broad variety of methodologies are reported. In the following we give a short selective review concerning scientific developments on free-edge effects.

Early numerical works employing the finite difference method were reported by Pipes/Pagano [2] and Altus et al. [3], wherein the work [2] must be especially appreciated as a pioneering contribution which triggered countless other investigations in the years to come: Note, that the free-edge effect is often referred to as "Pipes–Pagano-problem." Standard displacement based finite element methods were employed by Wang/Crossman [4], Raju/Crews [5], Whitcomb et al. [6], or Wu [7]. Due to the singular stress concentrations at the free-edge interface point, mesh refinements around the singularity center were applied. Especially adjusted element formulations were employed by, e.g., Spilker/Chou [8], Wang/Yuan [9], Robbins/Reddy [10], Gaudenzi et al. [11], or Mannini/Gaudenzi [12]. Other numerical approaches like, e.g., the boundary element method or the scaled boundary finite element method for the investigation of free-edge stress concentrations were also reported (Davi [13], Lindemann/Becker [14]). Purely numerical investigations of singular stress concentration problems usually require high computational effort, hence approximate analytic methods which capture free-edge and free-corner effects adequately are of particular interest and practical importance, especially since until today there is no exact elasticity solution of the free-edge problem available. In 1967, Hayashi [15] published an approximate closed-form analytical study concerning interlaminar shear stress concentrations in crossply laminates. Consideration of equilibrium requirements between the anisotropic laminate layers led to simple trigonometric hyperbolic functions for the interlaminar shear stress distributions. To the best of the authors' knowledge, Hayashi's work is an early publication available on free-edge stress concentration phenomena. A quite similar early study based on simple equilibrium formulations was published by Puppo/Evensen [16]. Pagano [17] used a single layer theory employing the kinematic assumptions of Mindlin's plate theory with an additional linear thickness term and calculated interlaminar normal stresses in the symmetry plane of crossply laminates. Pipes/Pagano [18] derived an approximate elasticity solution for angle-ply laminates under uniaxial extension by expanding the displacements as Fourier-series. Tang [19] and Tang/Levy [20] as well as Hsu/Herakovich [21] employed perturbation techniques. Pagano [22,23] proposed a variational model based on inplane stress assumptions for the stress analysis in arbitrary composite laminates and outlined a specialization of his general theory to the free-edge problem. Kassapoglou/Lagace [24] introduced the so-called force balance method which is based on assumptions for the inplane stresses in the form of exponential inplane terms and polynomials through the thickness, with a subsequent application of the principle of minimum complementary energy. It is worth noting that due to its simplicity yet astonishing accuracy this method has been adapted and refined by a good number of authors. A single layer theory approach with polynomial thickness terms was utilized by Krishna Murty/Hari Kumar [25]. Rose/Herakovich [26] presented a refined version of the force balance method upgraded by additional stress functions which explicitly take into account the mismatches of the material properties of adjacent dissimilar laminate layers. Yin [27] investigated laminates with arbitrary layup under uniaxial extension, bending, and torsion and employed Lekhnitskii's stress functions and the principle of minimum complementary potential for the description of free-edge stress fields. Becker [28,29] employed single layer higher order displacement based theories for symmetric crossply and angle-ply layups and formulated trigonometric thickness warping terms especially adapted to the considered free-edge situations. Zhu/Lam [30] used a Rayleigh–Ritz formulation in con-

---

[1] To whom correspondence should be addressed.

Contributed by the Applied Mechanics Division of THE AMERICAN SOCIETY OF MECHANICAL ENGINEERS for publication in the JOURNAL OF APPLIED MECHANICS. Manuscript received by the Applied Mechanics Division, November 2, 2003; final revision, June 17, 2004. Associate Editor: D. A. Kouris. Discussion on the paper should be addressed to the Editor, Prof. Robert M. McMeeking, Journal of Applied Mechanics, Department of Mechanical and Environmental Engineering, University of California - Santa Barbara, Santa Barbara, CA 93106-5070, and will be accepted until four months after final publication in the paper itself in the ASME JOURNAL OF APPLIED MECHANICS.

junction with a layerwise displacement field in the form of products of in-plane and thickness terms. Tahani/Nosier [31] used layerwise linear displacement formulations and a variational principle for free-edge effects in pure crossply layups. The asymptotic analysis of the state variables in the vicinity of singular free-edge interface points has also been the topic of thorough investigations and is relevant until this very day. A selection of works is given with, e.g., Ting/Chou [32], Wang/Choi [33,34], Zwiers et al. [35], Delale [36], Bar-Yoseph/Avrashi [37], Ding/Kumosa [38], Gu/Belytschko [39], Kim/Im [40], Chaudhuri/Xie [41] or Chue/Liu [42]. Finally, experimental studies on free-edge effects are also of interest. Let us cite the works of, e.g., Pipes/Daniel [43], Whitney/Browning [44], Herakovich et al. [45], or Herakovich [46,47]. The interested reader may also refer to exhaustive review papers available on free-edge stress concentration problems, see, e.g., Herakovich [46], Kant/Swaminathan [48], or the present authors [49].

Compared to the amount of available investigations on free-edge effects, the number of works that are concerned with free-corner effects is considerably lower. Becker et al. [50] presented an expanded version of the force-balance method for the investigation of rectangular corners in crossply plates under uniform thermal load. Dimitrov et al. [51,52] investigated the orders of the occurring stress singularities for a good number of free-corner geometries and laminate layups by employing a variational formulation with a subsequent finite element boundary discretization. A similar numerical approach was presented by Labossiere/Dunn [53] for the three-dimensional asymptotic study of free corners in bimaterial joints consisting of isotropic materials. Mittelstedt/Becker [54] considered crossply laminates under thermal load and presented a simple higher order displacement approach based on a single layer theory employing trigonometric thickness warping terms. In 2003 and 2004, the same authors [55,56] expanded the method presented in [50] on angle-ply laminates and arbitrary nonorthotropic layups.

In all it can be concluded that there is an obvious lack of knowledge about what exactly happens in the vicinity of free laminate corners. Hence, in the present paper we develop a displacement based approach for free-corner effects in thermally loaded symmetric layered plates consisting of isotropic layers. The plate is supposed to include rectangular corners and is subdivided into an arbitrary number of mathematical layers through the thickness. The applied layerwise displacement formulation consists of CLPT terms combined with special perturbation terms and employs a linear thickness interpolation scheme between the interfaces of the mathematical layers in which unknown displacement functions with respect to the inplane coordinates are defined. As the thickness distribution of the displacements is assumed a priori, the actual three-dimensional problem is reduced to a two-dimensional one. The unknown interface in-plane functions are determined by employing the principle of minimum potential energy. The resultant governing Euler-Lagrange differential equations allow a closed-form solution since due to some simplifying assumptions we are able to uncouple the problem with respect to the two inplane coordinates. The boundary conditions of traction free plate edges are fulfilled in an average sense by utilizing an integral formulation. The method requires only reasonable computational resources, can be run on every standard personal computer employing standard programming languages and enables an important insight into the underlying mechanics of free-corner effects in isotropic laminates which to the best of the authors' knowledge has not been done before.

The use of displacement based layerwise theories for the computation of displacements and stresses in layered structures for a broad variety of analysis purposes has been reported in a good number of publications, whereas these higher order theories have been mostly applied to problems of bending, free vibration, or buckling of layered plates or shells. Excellent review works are available [57–61]. In general, the strategy of such layerwise theories is to simplify the three-dimensional theory of elasticity to a two-dimensional problem by postulating a displacement field in the form of a priori assumed displacement shapes with respect to the thickness coordinate whereas the in-plane displacement functions remain unknown and are the objectives of the actual computations. The governing equations are then usually derived by application of variational principles. The advantage of variationally consistent theories is that such formulations naturally lead to adequate finite element formulations in a straightforward way for numerical evaluations of the given theory. This is, however, not the objective of the present paper. The displacement formulations require at least C^0-continuity. The application of layerwise theories has a good tradition for more than the last three decades as the works of Whitney [62], Mau [63], Srinivas [64], and Sun/Whitney [65] show. A frequent employment of layerwise theories for laminated structures can be detected since the 1980s. Selecting some publications found in the open literature, it is noted that the employed layerwise theories do not only differ with respect to the utilized displacement formulations but can also be subdivided according to the applied requirements of continuity for the interlaminar stresses in the layer interfaces, the neglect or consideration of interlaminar normal stresses and the treatment of the transverse displacements. Since the number of publications concerning layerwise higher order theories for laminated structures is impressingly high, the following overview is a selective one. In 1987, Reddy [66] introduced a general higher order theory for plane layered structures allowing for arbitrary approximations with respect to the thickness direction. From the general expressions included therein, many of the known higher order theories can be derived as special cases, which is also true for the present method. Theories which apply linear thickness terms for the displacements and which are of special interest within the scope of the present contribution were applied by a good number of researchers. Di Sciuva [67] investigated bending, buckling, and free vibration of layered plates. Murakami [68] assumed layerwise linear displacement shapes in conjunction with a global approach applying Mindlin kinematics. The shear stresses were assumed as quadratic functions. The governing equations were derived by application of Reissner's variational functional. Reddy/Savoia [69] investigated the buckling and postbuckling behavior of layered cylindrical shells. In 1993, Nosier et al. [70] studied the dynamic behavior of crossply laminates. Wisniewski/Schrefler [71] used a layerwise linear approach in conjunction with Tschebyschew and Taylor polynomials of arbitrary order for the description of the mechanical behavior of composite beams. Reddy/Starnes [72] studied the buckling behavior of layered cylindrical shells with discrete stiffeners. Cho/Parmerter [73,74] used a combination of a global cubic displacement variation through the laminate thickness and a layerwise linear approach for the investigation of symmetric und unsymmetric lamination schemes. In 1994, He [75] applied a layerwise linear approach in conjunction with a global cubic equivalent single layer formulation. Liu et al. [76] employed layerwise linear displacement shapes in conjunction with Legendre polynomials. Chattopadhyay/Gu [77] investigated the buckling behavior of cylindrical shells with delaminations. Kam/Jan [78] numerically investigated the first ply failure of laminates with arbitrary layup by developing an eight noded finite element. Di/Rothert [79] in 1995 applied a global cubic displacement variation through the entire laminate thickness in conjunction with a linear layerwise displacement formulation and investigated cylindrical shells with arbitrary layups. Khatri/Asnani [80] conducted dynamic analyses of conical crossply shells with elastic and viscoelastic layers. Ossadzow et al. [81] employed layerwise linear displacement shapes with global trigonometric functions. In 1996, He/Zhang [82] investigated the bending of simply supported rectangular unsymmetric angle-ply plates. Kassegne/Reddy [83] applied a linear layerwise approach for the buckling and vibration analysis of discretely stiffened cylindrical shells. For the investigation of laminated plates under thermal and/or mechanical load,

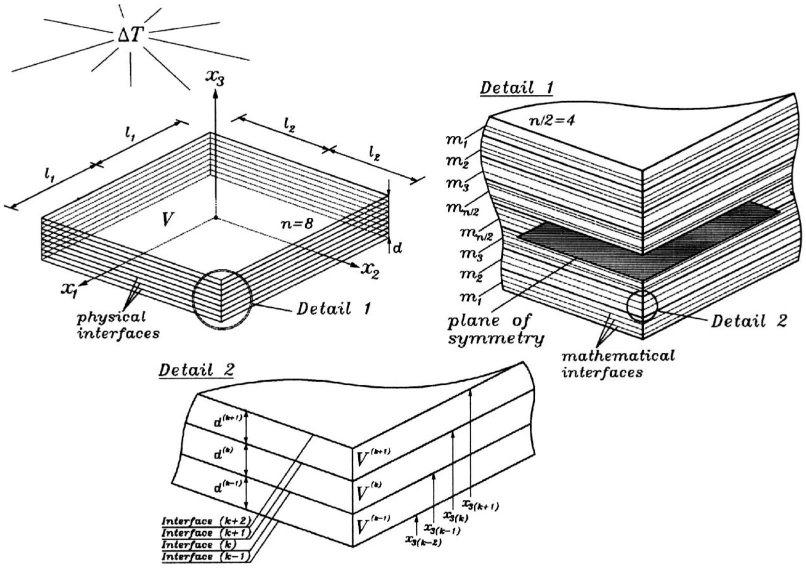

Fig. 1 Exemplary layered plate, discretization scheme, nomenclature

Ali et al. [84] used a global cubic and layerwise linear displacement approach for the in-plane displacements whereas the transverse displacement was assumed to be of a global parabolic form. In 2000, Cho/Averill [85] used linear layerwise approaches for arbitrary lamination schemes and developed a corresponding finite element formulation.

A further study of the literature on layerwise higher order theories shows that a good number of the applied theories neglects the dependence of the transverse displacement component on the thickness coordinate. Furthermore, in some of the investigated theories the interlaminar normal stress is also neglected. As long as we consider problems like, e.g., the bending, vibration, or buckling of layered plates or shells, these might be adequate simplifications. However, these typical assumptions are improper when stress concentration phenomena like free-edge and free-corner effects in composite laminates are to be considered. Hence, for the purposes of the present paper we must find a layerwise displacement formulation that involves a fully three-dimensional displacement field and a fully engaged stress tensor yet which allows closed-form computations with reasonable effort and accuracy.

2 Analysis Approach

2.1 Prerequisites. Consider a rectangular layered plate (Fig. 1) with total thickness d, in-plane dimensions $2l_1$ and $2l_2$ and symmetric lamination scheme $[m_1,m_2,\ldots,m_{n/2}]_S$ consisting of n physical isotropic plies with the materials $m_1, m_2, \ldots, m_{n/2}$ under a uniform thermal load ΔT. Let us subdivide each physical layer into an arbitrary number of mathematical layers, resulting in an overall number of n_L mathematical plies in the entire plate. The orthonormal reference axes x_1, x_2, x_3 are situated in the laminate middle plane (which is also the plane of symmetry), with x_3 being the thickness direction. The mathematical layer (k) with the thickness $d^{(k)}=x_{3(k)}-x_{3(k-1)}$ is bounded by the lower interface (k) with the thickness coordinate $x_3=x_{3(k-1)}$ and the upper interface $(k+1)$ at $x_3=x_{3(k)}$. The volume of the plate is denoted as V, the layer (k) has the volume $V^{(k)}$.

2.2 Constitutive CLPT Plate Behavior. The constitutive law for a layered plate according to CLPT can be written as follows [1]:

$$\begin{pmatrix}\underline{N}\\ \underline{M}\end{pmatrix}=\begin{bmatrix}\underline{\underline{A}} & \underline{\underline{B}}\\ \underline{\underline{B}} & \underline{\underline{D}}\end{bmatrix}\begin{pmatrix}\underline{\varepsilon}^0\\ \underline{\kappa}^0\end{pmatrix}\text{resp.}\begin{pmatrix}N_{11}\\ N_{22}\\ N_{12}\\ M_{11}\\ M_{22}\\ M_{12}\end{pmatrix}$$

$$=\begin{bmatrix}A_{11} & A_{12} & A_{16} & B_{11} & B_{12} & B_{16}\\ A_{12} & A_{22} & A_{26} & B_{12} & B_{22} & B_{26}\\ A_{16} & A_{26} & A_{66} & B_{16} & B_{26} & B_{66}\\ B_{11} & B_{12} & B_{16} & D_{11} & D_{12} & D_{16}\\ B_{12} & B_{22} & B_{26} & D_{12} & D_{22} & D_{26}\\ B_{16} & B_{26} & B_{66} & D_{16} & D_{26} & D_{66}\end{bmatrix}\begin{pmatrix}\varepsilon_{11}^0\\ \varepsilon_{22}^0\\ \gamma_{12}^0\\ \kappa_{11}^0\\ \kappa_{22}^0\\ \kappa_{12}^0\end{pmatrix}. \qquad (1)$$

The quantities $N_{\alpha\beta}$ and $M_{\alpha\beta}$ (α,β=1,2) are normal/shear forces and bending/twisting moments per length unit. The quantities $\varepsilon_{\alpha\alpha}^0$ and γ_{12}^0 are the in-plane normal/shear strains. Plate curvatures/torsions are denoted as $\kappa_{\alpha\alpha}^0$ and κ_{12}^0. A superscripted "0" denotes quantities according to CLPT. The components A_{op}, B_{op}, and D_{op} of the constitutive matrix in Eq. (1) read (with o, $p=1$, 2, and 6):

$$[A_{op},B_{op},D_{op}]=\int_d Q_{op}[1,x_3,x_3^2]\mathrm{d}x_3, \qquad (2)$$

or in the special case of layerwise constant material properties with $\xi_m^{(k)}=x_{3(k)}^m-x_{3(k-1)}^m$:

$$[A_{op},B_{op},D_{op}]=\sum_{r=1}^{r=n}Q_{op}^{(r)}\left[\xi_1^{(r)},\frac{1}{2}\xi_2^{(r)},\frac{1}{3}\xi_3^{(r)}\right]. \qquad (3)$$

Herein, the $Q_{op}^{(k)}$ are the reduced stiffness components. They can be derived from three-dimensional Hooke's law by imposing a plane state of stress. The resultant layerwise CLPT normal and shear stresses $\sigma_{\alpha\alpha}^{0(k)}$ and $\sigma_{12}^{0(k)}$ are calculated as $\underline{\sigma}^{0(k)}=\underline{\underline{Q}}^{(k)}(\underline{\varepsilon}^0+x_3\underline{\kappa}^0-\Delta T\underline{\alpha}_t^{0(k)})$, or:

$$\begin{pmatrix} \sigma_{11}^{0(k)} \\ \sigma_{22}^{0(k)} \\ \sigma_{12}^{0(k)} \end{pmatrix} = \begin{bmatrix} Q_{11}^{(k)} & Q_{12}^{(k)} & Q_{16}^{(k)} \\ Q_{12}^{(k)} & Q_{22}^{(k)} & Q_{26}^{(k)} \\ Q_{16}^{(k)} & Q_{26}^{(k)} & Q_{66}^{(k)} \end{bmatrix} \left[\begin{pmatrix} \varepsilon_{11}^{0} \\ \varepsilon_{22}^{0} \\ \gamma_{12}^{0} \end{pmatrix} + x_3 \begin{pmatrix} \kappa_{11}^{0} \\ \kappa_{22}^{0} \\ \kappa_{12}^{0} \end{pmatrix} - \Delta T \begin{pmatrix} \alpha_{11t}^{(k)} \\ \alpha_{22t}^{(k)} \\ \alpha_{12t}^{(k)} \end{pmatrix} \right], \tag{4}$$

where in the case of isotropic layer material the stiffnesses $Q_{\alpha 6}^{(k)}$ are vanishing. The stiffnesses $Q_{op}^{(k)}$ are interrelated to the common engineering constants—Young's modulus $E^{(k)}$, Poisson's ratio $\nu^{(k)}$, and shear modulus $G^{(k)}$—as:

$$Q_{\alpha\alpha}^{(k)} = \frac{E^{(k)}}{1-\nu^{(k)^2}}, \quad Q_{12}^{(k)} = \frac{\nu^{(k)} E^{(k)}}{1-\nu^{(k)^2}}, \quad Q_{\alpha 6}^{(k)} = 0, \quad Q_{66}^{(k)} = G^{(k)}. \tag{5}$$

The thermal forces $N_{\alpha\beta}^{T}$ and moments $M_{\alpha\beta}^{T}$ read:

$$[\underline{N}, \underline{M}] = \int_d \Delta T \underline{\underline{Q}}\, \underline{\alpha}_t [1, x_3] \mathrm{d}x_3 . \tag{6}$$

Since $Q_{\alpha 6}^{(k)} = 0$, $\alpha_{\alpha\alpha t}^{(k)} = \alpha_t^{(k)}$, and $\alpha_{12t}^{(k)} = 0$ hold for isotropic materials, we obtain $N_{12}^{T} = 0$. The nonvanishing normal forces are identical and read:

$$N_{\alpha\alpha}^{T} = N^{T} = \Delta T \sum_{r=1}^{r=n} d^{(r)} E^{(r)} \alpha_t^{(r)} \frac{1+\nu^{(r)}}{1-\nu^{(r)^2}} . \tag{7}$$

Furthermore, the matrix components $A_{\alpha 6}$ in Eq. (1) result in zero values and the relation $A_{11} = A_{22}$ holds. Due to the given symmetry all moments $M_{\alpha\beta}^{T}$ vanish and for the coupling terms in Eq. (1) $B_{op} = 0$ holds. Hence, no plate curvatures $\kappa_{\alpha\alpha}^{0}$ or torsions κ_{12}^{0} occur and Eq. (1) finally reduces to:

$$\begin{pmatrix} N^{T} \\ N^{T} \end{pmatrix} = \begin{bmatrix} A_{11} & A_{12} \\ A_{12} & A_{11} \end{bmatrix} \begin{pmatrix} \varepsilon_{11}^{0} \\ \varepsilon_{22}^{0} \end{pmatrix} . \tag{8}$$

The remaining matrix components A_{11} and A_{12} read:

$$[A_{11}, A_{12}] = \sum_{r=1}^{r=n} \frac{E^{(r)} d^{(r)}}{1-\nu^{(r)^2}} [1, \nu^{(r)}] . \tag{9}$$

The resultant inplane strains $\varepsilon_{\alpha\alpha}^{0}$ are identical and can be calculated from Eq. (8) as:

$$\varepsilon_{\alpha\alpha}^{0} = \varepsilon^{0} = \frac{N_t}{A_{11} + A_{12}} . \tag{10}$$

The resultant in-plane normal stresses $\sigma_{\alpha\alpha}^{0(k)}$ are also identical and with Eq. (4) result as:

$$\sigma_{\alpha\alpha}^{0(k)} = \frac{E^{(k)}}{1-\nu^{(k)}} (\varepsilon^{0} - \alpha_t^{(k)} \Delta T) . \tag{11}$$

No in-plane shear stresses $\sigma_{12}^{0(k)}$ occur in the present situation. The layerwise inplane CLPT displacements can be calculated by integration of the inplane strain ε^{0}:

$$u_{\alpha}^{0(k)} = \int_0^{x_\alpha} \varepsilon^{0} \mathrm{d}\hat{x}_{\alpha} . \tag{12}$$

The transverse displacement $u_3^{0(k)}$ results from layerwise integration of the transverse normal strain $\varepsilon_{33}^{0(k)}$:

$$u_3^{0(k)} = \int_0^{x_3} \varepsilon_{33}^{0(k)} \mathrm{d}\hat{x}_3 . \tag{13}$$

Herein, $\varepsilon_{33}^{0(k)}$ can be calculated from the assumption that the interlaminar normal stress $\sigma_{33}^{(k)}$ vanishes in the inner laminate regions which with three-dimensional Hooke's law leads to:

$$\varepsilon_{33}^{0(k)} = \frac{2\nu^{(k)}}{1-\nu^{(k)}} (\alpha_t^{(k)} \Delta T - \varepsilon^{0}) + \alpha_t^{(k)} \Delta T . \tag{14}$$

2.3 Linear Layerwise Displacement Approach. The physical layers of the plate are discretized into n_L mathematical plies. Let us postulate a layerwise C^1-continuous displacement field for each mathematical layer (k):

$$u_{\alpha}^{(k)} = u_{\alpha}^{0(k)} + u_{\alpha}^{1(k)} , \tag{15a}$$

$$u_3^{(k)} = u_3^{0(k)} + u_3^{11(k)} + u_3^{12(k)} . \tag{15b}$$

The layerwise terms $u_1^{1(k)}$, $u_2^{1(k)}$, $u_3^{11(k)}$, and $u_3^{12(k)}$ are defined as:

$$u_{\alpha}^{1(k)} = U_{\alpha}^{(k)}(x_\alpha) \psi_1^{(k)}(x_3) + U_{\alpha}^{(k+1)}(x_\alpha) \psi_2^{(k)}(x_3) , \tag{16a}$$

$$u_3^{1\alpha(k)} = U_{3\alpha}^{(k)}(x_\alpha) \psi_1^{(k)}(x_3) + U_{3\alpha}^{(k+1)}(x_\alpha) \psi_2^{(k)}(x_3) . \tag{16b}$$

Herein, we have introduced additional unknown displacement functions $U_1^{(k)}(x_1)$, $U_2^{(k)}(x_2)$, $U_{31}^{(k)}(x_1)$, $U_{32}^{(k)}(x_2)$ in the kth interface and $U_1^{(k+1)}(x_1)$, $U_2^{(k+1)}(x_2)$, $U_{31}^{(k+1)}(x_1)$, $U_{32}^{(k+1)}(x_2)$ in the interface $(k+1)$. This formulation takes free-edge perturbations of displacements and stresses into account and is supposed to blend into CLPT in the inner laminate regions where $U_1^{(k)} \to 0$ and $U_2^{(k)} \to 0$ as well as $U_{31}^{(k)} \to 0$ and $U_{32}^{(k)} \to 0$ must hold. The interface functions are interpolated by linear Lagrangian interpolation functions $\psi_1^{(k)}(x_3)$ and $\psi_2^{(k)}(x_3)$:

$$\psi_1^{(k)}(x_3) = \psi^{(k)}(x_{3(k)} - x_3) , \tag{17a}$$

$$\psi_2^{(k)}(x_3) = \psi^{(k)}(x_3 - x_{3(k-1)}) , \tag{17b}$$

with $\psi^{(k)} = (x_{3(k)} - x_{3(k-1)})^{-1}$. Note, that $\psi_1^{(k)}(x_3)$ and $\psi_2^{(k)}(x_3)$ have the properties $\psi_1^{(k)}(x_{3(k-1)}) = 1$, $\psi_1^{(k)}(x_{3(k)}) = 0$ and $\psi_2^{(k)}(x_{3(k-1)}) = 0$, $\psi_2^{(k)}(x_{3(k)}) = 1$ which makes the displacement formulation C^0-continuous across layer interfaces. Also note that by virtue of the a priori assumed linear thickness shape of all three displacement components the actual three-dimensional problem is reduced to a two-dimensional one, i.e., we have to solve for $4(n_L + 1)$ unknown interface functions $U_1^{(k)}(x_1)$, $U_2^{(k)}(x_2)$, $U_{31}^{(k)}(x_1)$, and $U_{32}^{(k)}(x_2)$. Assuming geometrical linearity, we may use the well-known kinematical relation between the displacements and the components of the linearized strain tensor, i.e., normal and shear strains $\varepsilon_{ii}^{(k)}$ and $\gamma_{ij}^{(k)}$ (i, $j = 1$, 2, and 3):

$$\varepsilon_{\alpha\alpha}^{(k)} = u_{\alpha,\alpha}^{(k)} = \varepsilon_{\alpha\alpha}^{0} + U_{\alpha,\alpha}^{(k)} \psi_1^{(k)} + U_{\alpha,\alpha}^{(k+1)} \psi_2^{(k)} , \tag{18a}$$

$$\varepsilon_{33}^{(k)} = u_{3,3}^{(k)} = \varepsilon_{33}^{0(k)} + (U_{31}^{(k)} + U_{32}^{(k)}) \psi_{1,3}^{(k)} + (U_{31}^{(k+1)} + U_{32}^{(k+1)}) \psi_{2,3}^{(k)} , \tag{18b}$$

$$\begin{aligned} \gamma_{\alpha 3}^{(k)} = u_{3,\alpha}^{(k)} + u_{\alpha,3}^{(k)} = U_{\alpha}^{(k)} \psi_{1,3}^{(k)} + U_{\alpha}^{(k+1)} \psi_{2,3}^{(k)} + U_{3\alpha,\alpha}^{(k)} \psi_1^{(k)} \\ + U_{3\alpha,\alpha}^{(k+1)} \psi_2^{(k)} , \end{aligned} \tag{18c}$$

$$\gamma_{12}^{(k)} = u_{2,1}^{(k)} + u_{1,2}^{(k)} = 0 . \tag{18d}$$

A subscripted index behind a comma denotes a derivative with respect to x_i, i.e., $(\ \ldots\ )_{,i} = \partial / \partial x_i$. Note that in the present situation no inplane shear strains $\gamma_{12}^{(k)}$ occur. Considering physical linearity, generalized Hooke's law applies which for a thermoelastic material in the kth layer reads $\underline{\sigma}^{(k)} = \underline{\underline{C}}^{(k)} (\underline{\varepsilon}^{(k)} - \underline{\alpha}_t^{(k)} \Delta T)$ in a contracted vector-matrix notation, or:

$$\begin{pmatrix}\sigma_{11}^{(k)}\\ \sigma_{22}^{(k)}\\ \sigma_{33}^{(k)}\\ \sigma_{23}^{(k)}\\ \sigma_{13}^{(k)}\\ \sigma_{12}^{(k)}\end{pmatrix}=\begin{bmatrix}c_{11}^{(k)} & c_{12}^{(k)} & c_{13}^{(k)} & 0 & 0 & 0\\ c_{12}^{(k)} & c_{22}^{(k)} & c_{23}^{(k)} & 0 & 0 & 0\\ c_{13}^{(k)} & c_{23}^{(k)} & c_{33}^{(k)} & 0 & 0 & 0\\ 0 & 0 & 0 & c_{44}^{(k)} & 0 & 0\\ 0 & 0 & 0 & 0 & c_{55}^{(k)} & 0\\ 0 & 0 & 0 & 0 & 0 & c_{66}^{(k)}\end{bmatrix}\left[\begin{pmatrix}\varepsilon_{11}^{(k)}\\ \varepsilon_{22}^{(k)}\\ \varepsilon_{33}^{(k)}\\ \gamma_{23}^{(k)}\\ \gamma_{13}^{(k)}\\ \gamma_{12}^{(k)}\end{pmatrix}-\begin{pmatrix}\alpha_t^{(k)}\Delta T\\ \alpha_t^{(k)}\Delta T\\ \alpha_t^{(k)}\Delta T\\ 0\\ 0\\ 0\end{pmatrix}\right]. \tag{19}$$

The components of the symmetric stiffness matrix $\underline{\underline{C}}^{(k)}$ can be expressed in terms of the engineering constants in the isotropic case as:

$$c_{11}^{(k)}=c_{22}^{(k)}=c_{33}^{(k)}=c_1^{(k)}=\frac{(1-\nu^{(k)})E^{(k)}}{(1+\nu^{(k)})(1-2\nu^{(k)})}, \tag{20a}$$

$$c_{12}^{(k)}=c_{13}^{(k)}=c_{23}^{(k)}=c_2^{(k)}=\frac{\nu^{(k)}E^{(k)}}{(1+\nu^{(k)})(1-2\nu^{(k)})}, \tag{20b}$$

$$c_{44}^{(k)}=c_{55}^{(k)}=c_{66}^{(k)}=c_3^{(k)}=G^{(k)}. \tag{20c}$$

Using Eq. (18), the stress field in the kth layer reads with Eqs. (19) and (20):

$$\begin{aligned}\sigma_{11}^{(k)}=&\,c_1^{(k)}(U_{1,1}^{(k)}\psi_1^{(k)}+U_{1,1}^{(k+1)}\psi_2^{(k)})+c_2^{(k)}(U_{2,2}^{(k)}\psi_1^{(k)}+U_{2,2}^{(k+1)}\psi_2^{(k)})\\ &+c_2^{(k)}[(U_{31}^{(k)}+U_{32}^{(k)})\psi_{1,3}^{(k)}+(U_{31}^{(k+1)}+U_{32}^{(k+1)})\psi_{2,3}^{(k)}]+\sigma_{11}^{0(k)},\end{aligned} \tag{21a}$$

$$\begin{aligned}\sigma_{22}^{(k)}=&\,c_2^{(k)}(U_{1,1}^{(k)}\psi_1^{(k)}+U_{1,1}^{(k+1)}\psi_2^{(k)})+c_1^{(k)}(U_{2,2}^{(k)}\psi_1^{(k)}+U_{2,2}^{(k+1)}\psi_2^{(k)})\\ &+c_2^{(k)}[(U_{31}^{(k)}+U_{32}^{(k)})\psi_{1,3}^{(k)}+(U_{31}^{(k+1)}+U_{32}^{(k+1)})\psi_{2,3}^{(k)}]+\sigma_{22}^{0(k)},\end{aligned} \tag{21b}$$

$$\begin{aligned}\sigma_{33}^{(k)}=&\,c_2^{(k)}(U_{1,1}^{(k)}\psi_1^{(k)}+U_{1,1}^{(k+1)}\psi_2^{(k)})+c_2^{(k)}(U_{2,2}^{(k)}\psi_1^{(k)}+U_{2,2}^{(k+1)}\psi_2^{(k)})\\ &+c_1^{(k)}[(U_{31}^{(k)}+U_{32}^{(k)})\psi_{1,3}^{(k)}+(U_{31}^{(k+1)}+U_{32}^{(k+1)})\psi_{2,3}^{(k)}],\end{aligned} \tag{21c}$$

$$\sigma_{23}^{(k)}=c_3^{(k)}(U_2^{(k)}\psi_{1,3}^{(k)}+U_2^{(k+1)}\psi_{2,3}^{(k)}+U_{32,2}^{(k)}\psi_1^{(k)}+U_{32,2}^{(k+1)}\psi_2^{(k)}), \tag{21d}$$

$$\sigma_{13}^{(k)}=c_3^{(k)}(U_1^{(k)}\psi_{1,3}^{(k)}+U_1^{(k+1)}\psi_{2,3}^{(k)}+U_{31,1}^{(k)}\psi_1^{(k)}+U_{31,1}^{(k+1)}\psi_2^{(k)}), \tag{21e}$$

$$\sigma_{12}^{(k)}=0. \tag{21f}$$

Note that while the resultant transverse strains $\varepsilon_{33}^{(k)}$, $\gamma_{23}^{(k)}$, and $\gamma_{13}^{(k)}$ are discontinuous across layer interfaces, there is the theoretical possibility for the interlaminar stresses $\sigma_{i3}^{(k)}$ of becoming at least approximately continuous and thus fulfilling equilibrium also at the layer interfaces with an increasing degree of refinement of the computational model. This will be the subject of a convergence study later on.

2.4 Variational Statement, Decomposition of the Problem.

Due to the chosen form of the displacement approach the three-dimensional conditions of equilibrium with neglected volume forces

$$\sigma_{i1,1}^{(k)}+\sigma_{i2,2}^{(k)}+\sigma_{i3,3}^{(k)}=0 \tag{22}$$

cannot be fulfilled identically. However, we may resort to a weak form, i.e., let us use a variational statement such that we require a minimum of the total potential energy of the plate:

$$\begin{aligned}\Pi=\sum_{r=1}^{r=n_L}\Bigg(&\frac{1}{2}\int\int\int_{V^{(r)}}\underline{\varepsilon}^{(r)^T}\underline{\underline{C}}^{(r)}\underline{\varepsilon}^{(r)}\mathrm{d}V^{(r)}\\ &-\int\int\int_{V^{(r)}}\underline{\sigma}^{(r)^T}\underline{\alpha}_t^{(r)}\Delta T^{(r)}\mathrm{d}V^{(r)}\\ &+\frac{1}{2}\int\int\int_{V^{(r)}}\underline{\alpha}_t^{(r)^T}\Delta T^{(r)}\underline{\underline{C}}^{(r)}\underline{\alpha}_t^{(r)}\Delta T^{(r)}\mathrm{d}V^{(r)}\Bigg)=\mathrm{Min.}\end{aligned} \tag{23}$$

As the third integral term only contains constant terms and thus vanishes throughout all subsequent variation processes we will omit it in the further course of this work. An integral concerning the volume $V^{(k)}$ of one mathematical layer can be decomposed into an integral through the layer thickness and an integral with respect to the area $A^0=4l_1l_2$ of the middle plane of the plate, i.e.,

$$\int\int\int_{V^{(k)}}\mathrm{d}V^{(k)}=\int\int_{A^0}\int_{x_{3(k-1)}}^{x_{3(k)}}\mathrm{d}x_3\mathrm{d}A^0. \tag{24}$$

As we have a priori assumed the thickness distributions of all displacement components, the integrand $F^{(k)}$ of the functional that is subject to the minimization process in Eq. (23) is only dependent on the interface functions $U_1^{(k)}(x_1)$, $U_2^{(k)}(x_2)$, $U_{31}^{(k)}(x_1)$, $U_{32}^{(k)}(x_2)$ and their first order derivatives. Hence, we may rewrite Eq. (23) in the following form:

$$\Pi=\sum_{r=1}^{r=n_L}\int\int_{A^0}\int_{x_{3(r-1)}}^{x_{3(r)}}F^{(r)}(U_1^{(r)},U_{1,1}^{(r)},U_2^{(r)},U_{2,2}^{(r)},U_{31}^{(r)},U_{31,1}^{(r)},U_{32}^{(r)},U_{32,2}^{(r)})\mathrm{d}x_3\mathrm{d}A^0=\mathrm{Min.} \tag{25}$$

Note that the variational statement Eq. (23), respectively, Eq. (25) leads to a set of governing coupled differential equations for $U_1^{(k)}(x_1)$, $U_2^{(k)}(x_2)$, $U_{31}^{(k)}(x_1)$, $U_{32}^{(k)}(x_2)$ that cannot be solved in a closed-form analytical manner but requires numerical evaluation. However, previous investigations (see, e.g., [54,55]) on free-corner problems have shown that for the present class of layered plates it is sufficient in an approximate sense to consider the two interacting free-edge effects separately and to combine these later on into a free-corner solution. Note, however, that this does not necessarily hold for other kinds of laminate layups. For the present analysis this means that as a decomposition measure we formulate two separate displacement fields that correspond to the involved free-edge effects alongside the x_1 axis and parallel to the x_2 coordinate. This will allow for a closed-form solution of the given thermoelastic free-corner problem. Let us first refer to the free-edge problem parallel to the x_1 axis. We may achieve an appropriate displacement formulation for this situation by letting $x_1 \rightarrow 0$ in Eqs. (15) and (16), which corresponds to $U_1^{(k)} = U_{31}^{(k)} = 0$ and thus $u_1^{1(k)} = u_3^{11(k)} = 0$. The remaining layerwise displacement field then reads:

$$u_1^{(k)} = u_1^{0(k)}, \tag{26a}$$

$$u_2^{(k)} = u_2^{0(k)} + u_2^{1(k)}, \tag{26b}$$

$$u_3^{(k)} = u_3^{0(k)} + u_3^{12(k)}. \tag{26c}$$

This describes the free-edge problem of a thermally loaded laminated strip which is long in the x_1 direction. The according strains and stresses for this situation can be gained by letting $U_1^{(k)} = U_{1,1}^{(k)} = U_{31}^{(k)} = U_{31,1}^{(k)} = 0$ in Eqs. (18) and (21). As the only remaining higher order functions are $U_2^{(k)}$ and $U_{32}^{(k)}$ and their derivatives $U_{2,2}^{(k)}$ and $U_{32,2}^{(k)}$, the corresponding variational statement reduces to:

$$\Pi = \sum_{r=1}^{r=n_L} \int \int_{A^0} \int_{x_{3(r-1)}}^{x_{3(r)}} F^{(r)}(U_2^{(r)}, U_{2,2}^{(r)}, U_{32}^{(r)}, U_{32,2}^{(r)}) \mathrm{d}x_3 \mathrm{d}A^0 = \mathrm{Min}. \tag{27}$$

It is convenient to introduce some abbreviations for the thickness integrals (with β, γ, δ=1, 2):

$$[H_\beta^{(k)}, H_{\beta\gamma}^{(k)}, H_{\beta t}^{(k)}] = \int_{x_{3(k-1)}}^{x_{3(k)}} \sigma_{\beta\beta}^{0(k)} [1, \psi_\gamma^{(k)}, \alpha_t^{(k)} \Delta T^{(k)}] \mathrm{d}x_3, \tag{28a}$$

$$[I_{i\gamma 1}^{(k)}, I_{i\gamma 2}^{(k)}] = \int_{x_{3(k-1)}}^{x_{3(k)}} c_i^{(k)} \alpha_t^{(k)} \Delta T^{(k)} [\psi_\gamma^{(k)}, \psi_{\gamma,3}^{(k)}] \mathrm{d}x_3, \tag{28b}$$

$$[J_{i\gamma 1}^{(k)}, J_{i\gamma 2}^{(k)}] = \int_{x_{3(k-1)}}^{x_{3(k)}} c_i^{(k)} [\psi_\gamma^{(k)}, \psi_{\gamma,3}^{(k)}] \mathrm{d}x_3, \tag{28c}$$

$$\begin{aligned} &[K_{i\gamma\delta 1}^{(k)}, K_{i\gamma\delta 2}^{(k)}, K_{i\gamma\delta 3}^{(k)}] \\ &\quad = \int_{x_{3(k-1)}}^{x_{3(k)}} c_i^{(k)} [\psi_\gamma^{(k)} \psi_\delta^{(k)}, \psi_\gamma^{(k)} \psi_{\delta,3}^{(k)}, \psi_{\gamma,3}^{(k)} \psi_{\delta,3}^{(k)}] \mathrm{d}x_3, \end{aligned} \tag{28d}$$

$$[L_{i\gamma 1}^{(k)}, L_{i\gamma 2}^{(k)}] = \int_{x_{3(k-1)}}^{x_{3(k)}} c_i^{(k)} \varepsilon_{33}^{0(k)} [\psi_\gamma^{(k)}, \psi_{\gamma,3}^{(k)}] \mathrm{d}x_3. \tag{28e}$$

Using Eqs. (18) and (21), the integrand $F^{(k)}$ of the functional Eq. (27) with Eq. (28) reads:

$$\begin{aligned} F^{(k)} = {} & \frac{1}{2} \varepsilon^0 (H_1^{(k)} + H_2^{(k)}) - (H_{1t}^{(k)} + H_{2t}^{(k)}) \\ & + \left(\frac{1}{2} H_{21}^{(k)} - I_{111}^{(k)} - 2I_{211}^{(k)} + \frac{1}{2} \varepsilon^0 (J_{211}^{(k)} + J_{111}^{(k)}) + \frac{1}{2} L_{211}^{(k)} \right) U_{2,2}^{(k)} \\ & + \left(\frac{1}{2} H_{22}^{(k)} - I_{121}^{(k)} - 2I_{221}^{(k)} + \frac{1}{2} \varepsilon^0 (J_{221}^{(k)} + J_{121}^{(k)}) + \frac{1}{2} L_{221}^{(k)} \right) U_{2,2}^{(k+1)} \\ & + \left(-I_{112}^{(k)} - 2I_{212}^{(k)} + \varepsilon^0 J_{212}^{(k)} + \frac{1}{2} L_{112}^{(k)} \right) U_{32}^{(k)} \\ & + \left(-I_{122}^{(k)} - 2I_{222}^{(k)} + \varepsilon^0 J_{222}^{(k)} + \frac{1}{2} L_{122}^{(k)} \right) U_{32}^{(k+1)} + (K_{3112}^{(k)} U_{32,2}^{(k)} \\ & + K_{3212}^{(k)} U_{32,2}^{(k+1)}) U_2^{(k)} + (K_{3122}^{(k)} U_{32,2}^{(k)} + K_{3222}^{(k)} U_{32,2}^{(k+1)}) U_2^{(k+1)} \\ & + (K_{2112}^{(k)} U_{32}^{(k)} + K_{2122}^{(k)} U_{32}^{(k+1)}) U_{2,2}^{(k)} + (K_{2212}^{(k)} U_{32}^{(k)} \\ & + K_{2222}^{(k)} U_{32}^{(k+1)}) U_{2,2}^{(k+1)} + \frac{1}{2} K_{3113}^{(k)} U_2^{(k)^2} + K_{3123}^{(k)} U_2^{(k)} U_2^{(k+1)} \\ & + \frac{1}{2} K_{3223}^{(k)} U_2^{(k+1)^2} + \frac{1}{2} K_{1111}^{(k)} U_{2,2}^{(k)^2} + K_{1121}^{(k)} U_{2,2}^{(k)} U_{2,2}^{(k+1)} \\ & + \frac{1}{2} K_{1221}^{(k)} U_{2,2}^{(k+1)^2} + \frac{1}{2} K_{1113}^{(k)} U_{32}^{(k)^2} + K_{1123}^{(k)} U_{32}^{(k)} U_{32}^{(k+1)} \\ & + \frac{1}{2} K_{1223}^{(k)} U_{32}^{(k+1)^2} + \frac{1}{2} K_{3111}^{(k)} U_{32,2}^{(k)^2} + K_{3121}^{(k)} U_{32,2}^{(k)} U_{32,2}^{(k+1)} \\ & + \frac{1}{2} K_{3221}^{(k)} U_{32,2}^{(k+1)^2}. \end{aligned} \tag{29}$$

2.5 Governing Equations and Their Solution. We seek that array of functions $U_2^{(k)}$, $U_{2,2}^{(k)}$, $U_{32}^{(k)}$, and $U_{32,2}^{(k)}$ which minimizes the total potential energy of the plate. According to the calculus of variation, the following two governing Euler-Lagrange equations must be satisfied:

$$\frac{\partial}{\partial U_2^{(k)}} \left(\sum_{r=1}^{r=n_L} F^{(r)} \right) - \frac{d}{dx_2} \left[\frac{\partial}{\partial U_{2,2}^{(k)}} \left(\sum_{r=1}^{r=n_L} F^{(r)} \right) \right] = 0, \tag{30a}$$

$$\frac{\partial}{\partial U_{32}^{(k)}} \left(\sum_{r=1}^{r=n_L} F^{(r)} \right) - \frac{d}{dx_2} \left[\frac{\partial}{\partial U_{32,2}^{(k)}} \left(\sum_{r=1}^{r=n_L} F^{(r)} \right) \right] = 0, \tag{30b}$$

with $d/d(\ldots)$ and $\partial/\partial(\ldots)$ for derivatives. Performance of the variations (30) with respect to each interface leads to the following n_L+1 sets of coupled ordinary linear differential equations:

$$\begin{aligned} & (K_{3122}^{(k-1)} - K_{2212}^{(k-1)}) U_{32,2}^{(k-1)} + (K_{3222}^{(k-1)} - K_{2222}^{(k-1)} + K_{3112}^{(k)} - K_{2112}^{(k)}) U_{32,2}^{(k)} \\ & \quad + (K_{3212}^{(k)} - K_{2122}^{(k)}) U_{32,2}^{(k+1)} + K_{3123}^{(k-1)} U_2^{(k-1)} \\ & \quad + (K_{3223}^{(k-1)} + K_{3113}^{(k)}) U_2^{(k)} + K_{3123}^{(k)} U_2^{(k+1)} - K_{1121}^{(k-1)} U_{2,22}^{(k-1)} \\ & \quad - (K_{1221}^{(k-1)} + K_{1111}^{(k)}) U_{2,22}^{(k)} - K_{1121}^{(k)} U_{2,22}^{(k+1)} = 0, \end{aligned} \tag{31a}$$

$$\begin{aligned} & (K_{2122}^{(k-1)} - K_{3212}^{(k-1)}) U_{2,2}^{(k-1)} + (K_{2222}^{(k-1)} - K_{3222}^{(k-1)} + K_{2112}^{(k)} - K_{3112}^{(k)}) U_{2,2}^{(k)} \\ & \quad + (K_{2212}^{(k)} - K_{3122}^{(k)}) U_{2,2}^{(k+1)} + K_{1123}^{(k-1)} U_{32}^{(k-1)} \\ & \quad + (K_{1223}^{(k-1)} + K_{1113}^{(k)}) U_{32}^{(k)} + K_{1123}^{(k)} U_{32}^{(k+1)} - K_{3121}^{(k-1)} U_{32,22}^{(k-1)} \\ & \quad - (K_{3221}^{(k-1)} + K_{3111}^{(k)}) U_{32,22}^{(k)} - K_{3121}^{(k)} U_{32,22}^{(k+1)} \\ & \quad = I_{112}^{(k)} + 2I_{212}^{(k)} + I_{122}^{(k-1)} + 2I_{222}^{(k-1)} - \frac{1}{2} [2\varepsilon^0 (J_{222}^{(k-1)} + J_{212}^{(k)}) \\ & \qquad + (L_{122}^{(k-1)} + L_{112}^{(k)})]. \end{aligned} \tag{31b}$$

It is convenient to introduce a vector-matrix notation for Eq. (31) with the vectors $\underline{U}_2 = [U_2^{(k)}] \in \mathbb{R}^{(n_L+1)\times 1}$ and $\underline{U}_{32} = [U_{32}^{(k)}] \in \mathbb{R}^{(n_L+1)\times 1}$ including the functions $U_2^{(k)}$ and $U_{32}^{(k)}$ and their derivatives:

$$\underline{\underline{K}}_1 \underline{U}_2 + \underline{\underline{K}}_2 \underline{U}_{2,22} + \underline{\underline{K}}_3 \underline{U}_{32,2} = \underline{0}, \tag{32a}$$

$$\underline{\underline{K}}_4 \underline{U}_{32} + \underline{\underline{K}}_5 \underline{U}_{32,22} + \underline{\underline{K}}_6 \underline{U}_{2,2} = \underline{F}. \tag{32b}$$

The constant quadratic coefficient matrices $\underline{\underline{K}}_m = [K_{pqm}] \in \mathbb{R}^{(n_L+1)\times(n_L+1)}$ (with $m = 1,2,3,\ldots,6$ and $p,q = 1,2,3 \ldots n_L + 1$) can be found in detail in Appendix 1. The vector $\underline{F} \in \mathbb{R}^{(n_L+1)\times 1}$ contains the nonhomogeneous right-hand sides of Eq. (31*b*), $\underline{0} \in \mathbb{R}^{(n_L+1)\times 1}$ is a zero vector. A solution of Eq. (32) is possible by introducing some new notations for $U_2^{(k)}$ and $U_{32}^{(k)}$:

$$\overline{\underline{U}}_1 = (\overline{\underline{U}}_{11} \;\; \overline{\underline{U}}_{12})^T = (\underline{U}_{2,2} \;\; \underline{U}_{32})^T, \tag{33a}$$

$$\overline{\underline{U}}_2 = (\overline{\underline{U}}_{21} \;\; \overline{\underline{U}}_{22})^T = (\underline{U}_2 \;\; \underline{U}_{32,2})^T. \tag{33b}$$

Note that $\overline{\underline{U}}_{11} = \overline{\underline{U}}_{21,2}$ and $\overline{\underline{U}}_{22} = \overline{\underline{U}}_{12,2}$. Using these notations, after some algebra the governing Eqs. (32) can be rewritten as:

$$\overline{\underline{U}}_{1,22} - \overline{\underline{\underline{K}}}_1 \overline{\underline{\underline{K}}}_2 \overline{\underline{U}}_1 = \overline{\underline{\underline{K}}}_1 \overline{\underline{F}}, \tag{34a}$$

$$\overline{\underline{U}}_2=\overline{\underline{\underline{K}}}_1^{-1}\overline{\underline{U}}_{1,2}. \tag{34b}$$

The quantities $\overline{\underline{\underline{K}}}_1\in\mathbb{R}^{2(n_L+1)\times 2(n_L+1)}$, $\overline{\underline{\underline{K}}}_2\in\mathbb{R}^{2(n_L+1)\times 2(n_L+1)}$, and $\overline{\underline{F}}\in\mathbb{R}^{2(n_L+1)\times 1}$ read:

$$\overline{\underline{\underline{K}}}_1=\begin{pmatrix} -\underline{\underline{K}}_2^{-1}\underline{\underline{K}}_1 & -\underline{\underline{K}}_2^{-1}\underline{\underline{K}}_3 \\ \underline{\underline{0}} & \underline{\underline{E}} \end{pmatrix},$$

$$\overline{\underline{\underline{K}}}_2=\begin{pmatrix} \underline{\underline{E}} & \underline{\underline{0}} \\ -\underline{\underline{K}}_5^{-1}\underline{\underline{K}}_6 & -\underline{\underline{K}}_5^{-1}\underline{\underline{K}}_4 \end{pmatrix}, \quad \overset{=}{\underline{F}}\begin{pmatrix} \underline{0} \\ \underline{\underline{K}}_5^{-1}\underline{F} \end{pmatrix}, \tag{35}$$

wherein $\underline{\underline{E}}=[\delta_{pq}]\in\mathbb{R}^{(n_L+1)\times(n_L+1)}$ is the unity matrix with δ_{pq} being the Kronecker symbol, $\underline{\underline{0}}\in\mathbb{R}^{(n_L+1)\times(n_L+1)}$ is a zero matrix. A solution for the homogeneous Eq. (34*a*), i.e., for $\overline{\underline{U}}_{1,22}-\overline{\underline{\underline{K}}}_3\overline{\underline{U}}_1=\underline{0}$ with $\overline{\underline{\underline{K}}}_3=\overline{\underline{\underline{K}}}_1\overline{\underline{\underline{K}}}_2$, can be shown to be a system of hyperbolic functions:

$$\overline{\underline{U}}_1=\underline{\underline{\Gamma}}\,\underline{\underline{C}}_1\underline{b}_1+\underline{\underline{\Gamma}}\,\underline{\underline{S}}_1\underline{b}_2. \tag{36}$$

The quantities $\underline{\underline{C}}_1\in\mathbb{R}^{2(n_L+1)\times 2(n_L+1)}$ and $\underline{\underline{S}}_1\in\mathbb{R}^{2(n_L+1)\times 2(n_L+1)}$ are diagonal matrices of the form $\underline{\underline{C}}_1=[\delta_{st}\cosh(\lambda_s x_2)]$ and $\underline{\underline{S}}_1=[\delta_{st}\sinh(\lambda_s x_2)]$ with $s,t=1,2,3,\ldots,2(n_L+1)$. Therein, the quantities λ_s are the roots of the $2(n_L+1)$ eigenvalues λ_1^2, $\lambda_2^2,\ldots,\lambda_{(2n_L+2)}^2$ of $\underline{\underline{K}}_3$, the matrix $\underline{\underline{\Gamma}}=[\gamma_{st}]\in\mathbb{R}^{2(n_L+1)\times 2(n_L+1)}$ includes the corresponding eigenvectors of $\overline{\underline{\underline{K}}}_3$. The vectors $\underline{b}_1=[b_{1s}]\in\mathbb{R}^{2(n_L+1)\times 1}$ and $\underline{b}_2=[b_{2s}]\in\mathbb{R}^{2(n_L+1)\times 1}$ contain free constants. Using Eq. (34*b*) gives the homogeneous solution for $\overline{\underline{U}}_2$:

$$\overline{\underline{U}}_2=\underline{\underline{\Phi}}\,\underline{\underline{S}}_1\underline{b}_1+\underline{\underline{\Phi}}\,\underline{\underline{C}}_1\underline{b}_2, \tag{37}$$

with $\underline{\underline{\Phi}}=[\varphi_{st}]\in\mathbb{R}^{2(n_L+1)\times 2(n_L+1)}$ being defined as $\underline{\underline{\Phi}}=\overline{\underline{\underline{K}}}_1^{-1}\underline{\underline{\Gamma}}\,\underline{\underline{\Lambda}}$ and $\underline{\underline{\Lambda}}=[\delta_{st}\lambda_s]\in\mathbb{R}^{2(n_L+1)\times 2(n_L+1)}$. Utilizing Eqs. (36) and (37) for the unknown interface functions $U_2^{(k)}$ and $U_{32}^{(k)}$ and their derivatives according to Eq. (33) leads to the following homogeneous solution of Eq. (32):

$$U_2^{(k)}=\sum_{r=1}^{r=2(n_L+1)} b_{1r}\varphi_{kr}\sinh(\lambda_r x_2) + \sum_{r=1}^{r=2(n_L+1)} b_{2r}\varphi_{kr}\cosh(\lambda_r x_2), \tag{38a}$$

$$U_{2,2}^{(k)}=\sum_{r=1}^{r=2(n_L+1)} b_{1r}\gamma_{kr}\cosh(\lambda_r x_2)+\sum_{r=1}^{r=2(n_L+1)} b_{2r}\gamma_{kr}\sinh(\lambda_r x_2), \tag{38b}$$

$$U_{32}^{(k)}=\sum_{r=1}^{r=2(n_L+1)} b_{1r}\gamma_{\bar{k}r}\cosh(\lambda_r x_2)+\sum_{r=1}^{r=2(n_L+1)} b_{2r}\gamma_{\bar{k}r}\sinh(\lambda_r x_2), \tag{38c}$$

$$U_{32,2}^{(k)}=\sum_{r=1}^{r=2(n_L+1)} b_{1r}\varphi_{\bar{k}r}\sinh(\lambda_r x_2) + \sum_{r=1}^{r=2(n_L+1)} b_{2r}\varphi_{\bar{k}r}\cosh(\lambda_r x_2), \tag{38d}$$

with $\bar{k}=k+n_L+1$. As the nonhomogeneous right-hand side of Eq. (34*a*) is a constant quantity and an appropriate approach for a particular solution would be in the form of polynomial terms, a particular solution of Eq. (34*a*) and thus of Eq. (32) corresponds to rigid body motions and strain states. As the displacement solution Eqs. (12) and (13) according to CLPT already fully accounts for these states, the introduced CLPT terms correspond to the particular solution. Hence, the formulation Eq. (38) for $U_2^{(k)}$ and $U_{32}^{(k)}$ and their derivatives is complete and unique.

Due to the symmetry of the given situation it is convenient to restrict our investigations to one quarter of the plate containing two free edges merging into a rectangular corner, e.g., enclosed in the interval $0\leqslant x_1\leqslant l_1$, $0\leqslant x_2\leqslant l_2$, $-d/2\leqslant x_3\leqslant d/2$, and fulfill the boundary conditions of traction free plate edges for this quarter-piece. The remaining parts of the plate can be adequately taken account of by consideration of the symmetry of the given situation. Since $u_2^{(k)}$ must be an odd function of x_2, $U_2^{(k)}(x_2)=-U_2^{(k)}(-x_2)$ must hold as well which is achieved by neglecting the corresponding cosh functions in Eq. (38). Accordingly, $u_3^{(k)}$ and hence also $U_{32}^{(k)}$ must be an even function of x_2 which leads to the neglect of the corresponding sinh terms in Eq. (38). Summing up, the solutions in Eq. (38) are reduced to:

$$U_2^{(k)}=\sum_{r=1}^{r=2(n_L+1)} b_{1r}\varphi_{kr}\sinh(\lambda_r x_2), \tag{39a}$$

$$U_{2,2}^{(k)}=\sum_{r=1}^{r=2(n_L+1)} b_{1r}\gamma_{kr}\cosh(\lambda_r x_2), \tag{39b}$$

$$U_{32}^{(k)}=\sum_{r=1}^{r=2(n_L+1)} b_{1r}\gamma_{\bar{k}r}\cosh(\lambda_r x_2), \tag{39c}$$

$$U_{32,2}^{(k)}=\sum_{r=1}^{r=2(n_L+1)} b_{1r}\varphi_{\bar{k}r}\sinh(\lambda_r x_2). \tag{39d}$$

Finally we have to find a solution for the free-edge effect occurring parallel to the x_2 axis. Letting $x_2\to 0$ leads to $U_2^{(k)}=U_{32}^{(k)}=0$ and hence $u_2^{1(k)}=u_3^{12(k)}=0$. Analogous to the free-edge problem along the x_1 axis, the variational statement of the present free-edge problem leads to a set of governing equations for the unknown functions $U_1^{(k)}$ and $U_{31}^{(k)}$ and subsequently an eigenvalue problem that can be solved like the presented free-edge problem parallel to the x_1 axis. Note that due to the isotropic layer material properties the present situation is insensitive to a coordinate transformation regarding the right corner angle, hence all occurring eigenvalues and eigenvectors are identical for both free-edge problems. The solution for the remaining displacement functions $U_1^{(k)}$ and $U_{31}^{(k)}$ and their derivatives in the *k*th interface can be written similar to Eq. (39):

$$U_1^{(k)}=\sum_{r=1}^{r=2(n_L+1)} c_{1r}\varphi_{kr}\sinh(\lambda_r x_1), \tag{40a}$$

$$U_{1,1}^{(k)}=\sum_{r=1}^{r=2(n_L+1)} c_{1r}\gamma_{kr}\cosh(\lambda_r x_1), \tag{40b}$$

$$U_{31}^{(k)}=\sum_{r=1}^{r=2(n_L+1)} c_{1r}\gamma_{\bar{k}r}\cosh(\lambda_r x_1), \tag{40c}$$

$$U_{31,1}^{(k)}=\sum_{r=1}^{r=2(n_L+1)} c_{1r}\varphi_{\bar{k}r}\sinh(\lambda_r x_1). \tag{40d}$$

The quantities c_{1s} are free constants.

2.6 Stress Field and Boundary Conditions. Using the solutions (39) and (40), the stress field (21) in the *k*th layer for the coupled problem formulation reads:

$$\sigma_{11}^{(k)}=\sigma_{11}^{0(k)}+\sum_{r=1}^{r=2(n_L+1)}\left[c_{1r}(c_1^{(k)}\psi_{1r}^{(k)}+c_2^{(k)}\psi_{2r}^{(k)})\cosh(\lambda_r x_1) + b_{1r}c_2^{(k)}(\psi_{1r}^{(k)}+\psi_{2r}^{(k)})\cosh(\lambda_r x_2)\right], \tag{41a}$$

$$\sigma_{22}^{(k)}=\sigma_{22}^{0(k)}+\sum_{r=1}^{r=2(n_L+1)}\left[c_{1r}c_2^{(k)}(\psi_{1r}^{(k)}+\psi_{2r}^{(k)})\cosh(\lambda_r x_1)+b_{1r}(c_1^{(k)}\psi_{1r}^{(k)}+c_2^{(k)}\psi_{2r}^{(k)})\cosh(\lambda_r x_2)\right], \tag{41b}$$

$$\sigma_{33}^{(k)}=\sum_{r=1}^{r=2(n_L+1)}(c_2^{(k)}\psi_{1r}^{(k)}+c_1^{(k)}\psi_{2r}^{(k)})\left[c_{1r}\cosh(\lambda_r x_1)+b_{1r}\cosh(\lambda_r x_2)\right], \tag{41c}$$

$$\sigma_{23}^{(k)}=c_3^{(k)}\sum_{r=1}^{r=2(n_L+1)}b_{1r}\psi_{3r}^{(k)}\sinh(\lambda_r x_2), \tag{41d}$$

$$\sigma_{13}^{(k)}=c_3^{(k)}\sum_{r=1}^{r=2(n_L+1)}c_{1r}\psi_{3r}^{(k)}\sinh(\lambda_r x_1), \tag{41e}$$

$$\sigma_{12}^{(k)}=0, \tag{41f}$$

wherein

$$\psi_{1s}^{(k)}=\psi_1^{(k)}\gamma_{ks}+\psi_2^{(k)}\gamma_{(k+1)s}, \tag{42a}$$

$$\psi_{2s}^{(k)}=\psi_{1,3}^{(k)}\gamma_{(k+n_L+1)s}+\psi_{2,3}^{(k)}\gamma_{(k+n_L+2)s}, \tag{42b}$$

$$\psi_{3s}^{(k)}=\psi_1^{(k)}\varphi_{(k+n_L+1)s}+\psi_2^{(k)}\varphi_{(k+n_L+2)s}+\psi_{1,3}^{(k)}\varphi_{ks}+\psi_{2,3}^{(k)}\varphi_{(k+1)s}. \tag{42c}$$

These stresses have to fulfill the conditions of traction-free plate edges:

$$\sigma_{\alpha\alpha}^{(k)}(x_\alpha=l_\alpha)=0, \tag{43a}$$

$$\sigma_{\alpha 3}^{(k)}(x_\alpha=l_\alpha)=0. \tag{43b}$$

An identical fulfillment of Eq. (43) is not possible with the chosen form of a layerwise approach. However, an integrated form with respect to the plate interfaces using the same interpolation functions $\psi_1^{(k)}$ and $\psi_2^{(k)}$ as for the stresses can be utilized which leads to $4(n_L+1)$ equations for the $4(n_L+1)$ free constants b_{1s} and c_{1s}:

$$\int_0^{l_2}\int_{x_{3(k-2)}}^{x_{3(k-1)}}\sigma_{11}^{(k-1)}(x_1=l_1,x_2,x_3)\psi_2^{(k-1)}\mathrm{d}x_2\mathrm{d}x_3+\int_0^{l_2}\int_{x_{3(k-1)}}^{x_{3(k)}}\sigma_{11}^{(k)}(x_1=l_1,x_2,x_3)\psi_1^{(k)}\mathrm{d}x_2\mathrm{d}x_3=0, \tag{44a}$$

$$\int_0^{l_1}\int_{x_{3(k-2)}}^{x_{3(k-1)}}\sigma_{22}^{(k-1)}(x_1,x_2=l_2,x_3)\psi_2^{(k-1)}\mathrm{d}x_1\mathrm{d}x_3+\int_0^{l_1}\int_{x_{3(k-1)}}^{x_{3(k)}}\sigma_{22}^{(k)}(x_1,x_2=l_2,x_3)\psi_1^{(k)}\mathrm{d}x_1\mathrm{d}x_3=0, \tag{44b}$$

$$\int_0^{l_2}\int_{x_{3(k-2)}}^{x_{3(k-1)}}\sigma_{13}^{(k-1)}(x_1=l_1,x_2,x_3)\psi_2^{(k-1)}\mathrm{d}x_2\mathrm{d}x_3+\int_0^{l_2}\int_{x_{3(k-1)}}^{x_{3(k)}}\sigma_{13}^{(k)}(x_1=l_1,x_2,x_3)\psi_1^{(k)}\mathrm{d}x_2\mathrm{d}x_3=0, \tag{44c}$$

$$\int_0^{l_1}\int_{x_{3(k-2)}}^{x_{3(k-1)}}\sigma_{23}^{(k-1)}(x_1,x_2=l_2,x_3)\psi_2^{(k-1)}\mathrm{d}x_1\mathrm{d}x_3+\int_0^{l_1}\int_{x_{3(k-1)}}^{x_{3(k)}}\sigma_{23}^{(k)}(x_1,x_2=l_2,x_3)\psi_1^{(k)}\mathrm{d}x_1\mathrm{d}x_3=0. \tag{44d}$$

This eventually yields an ordinary system of $4(n_L+1)$ linear equations for the free constants b_{1s} and c_{1s}:

$$\sum_{r=1}^{r=2(n_L+1)}b_{1r}B_{1r}^{(k)}+\sum_{r=1}^{r=2(n_L+1)}c_{1r}C_{1r}^{(k)}=D_1^{(k)}, \tag{45a}$$

$$\sum_{r=1}^{r=2(n_L+1)}b_{1r}B_{2r}^{(k)}+\sum_{r=1}^{r=2(n_L+1)}c_{1r}C_{2r}^{(k)}=D_2^{(k)}, \tag{45b}$$

$$\sum_{r=1}^{r=2(n_L+1)}b_{1r}B_{3r}^{(k)}=0, \tag{45c}$$

$$\sum_{r=1}^{r=2(n_L+1)}c_{1r}C_{3r}^{(k)}=0. \tag{45d}$$

The coefficients $B_{1s}^{(k)}$, $B_{2s}^{(k)}$, $B_{3s}^{(k)}$, $C_{1s}^{(k)}$, $C_{2s}^{(k)}$, $C_{3s}^{(k)}$ and the right-hand terms $D_1^{(k)}$, $D_2^{(k)}$ are given in detail in Appendix 2. With that, the development of the higher order layerwise theory is completed.

3 Results and Discussion

3.1 Convergence Study. It is of basic interest to study the behavior of the present analysis method with varying degrees of discretization refinement of the computational model. For the sake of simplicity let us investigate a four-layered symmetric bimaterial plate with material 1 in the facings and material 2 in the inner two layers. Let us assume that the physical layers are identically subdivided into $m=1/4n_L$ mathematical layers whereas we will investigate the development of the solution for $m=3$, $m=6$, $m=9$, and $m=12$. Let us assume aluminum as material 1 with the elastic properties:

$$E^1=71{,}000\ \text{MPa},\quad \nu^1=0.34,\quad \alpha_t^1=24\times10^{-6}\ \text{K}^{-1}, \tag{46}$$

whereas material 2 is supposed to be nickel:

$$E^2=210{,}000\ \text{MPa},\quad \nu^2=0.31,\quad \alpha_t^2=13\times10^{-6}\ \text{K}^{-1}. \tag{47}$$

The individual physical layers of the $[\text{Al,Ni}]_S$ plate are assumed to have a thickness of 0.5 mm each which leads to a total plate thickness of $d=2.0$ mm. A similar layered plate under uniform thermal load has been considered by Becker et al. [50]. The load case is a uniform temperature drop of $\Delta T=-100$ K. CLPT predicts the nonvanishing in-plane stresses as

$$\sigma_{11}^{0(1)}=\sigma_{11}^{0(4)}=\sigma_{22}^{0(1)}=\sigma_{22}^{0(4)}=87.43\ \text{MPa}, \tag{48a}$$

$$\sigma_{11}^{0(2)}=\sigma_{11}^{0(3)}=\sigma_{22}^{0(2)}=\sigma_{22}^{0(3)}=-87.43\ \text{MPa}. \tag{48b}$$

The in-plane dimensions of the computational model are set to $l_1=l_2=2d=4.0$ mm. For evaluation purposes from now on let us refer to an orthonormal corner coordinate system $\bar{x}_1$, $\bar{x}_2$, $\bar{x}_3$ (see Fig. 2). Figure 3 depicts the resultant distribution of the interlaminar normal stress σ_{33} through the thickness at the corner tip $\bar{x}_1=0$, $\bar{x}_2=0$, $-d/2\leqslant\bar{x}_3\leqslant d/2$ for $m=3$, $m=6$, $m=9$, and $m=12$. We did not calculate mean values of σ_{33} at one interface coordinate $\bar{x}_3$ but have depicted both stress values of the respective two adjacent mathematical layers to gain an estimate of the convergence of the presented method with respect to the development of continuous interlaminar stresses in the mathematical interfaces. As could be expected, the quality of the stress results increases with

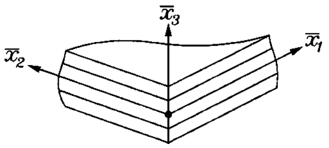

Fig. 2 Corner coordinate system $\bar{x}_1$, $\bar{x}_2$, $\bar{x}_3$

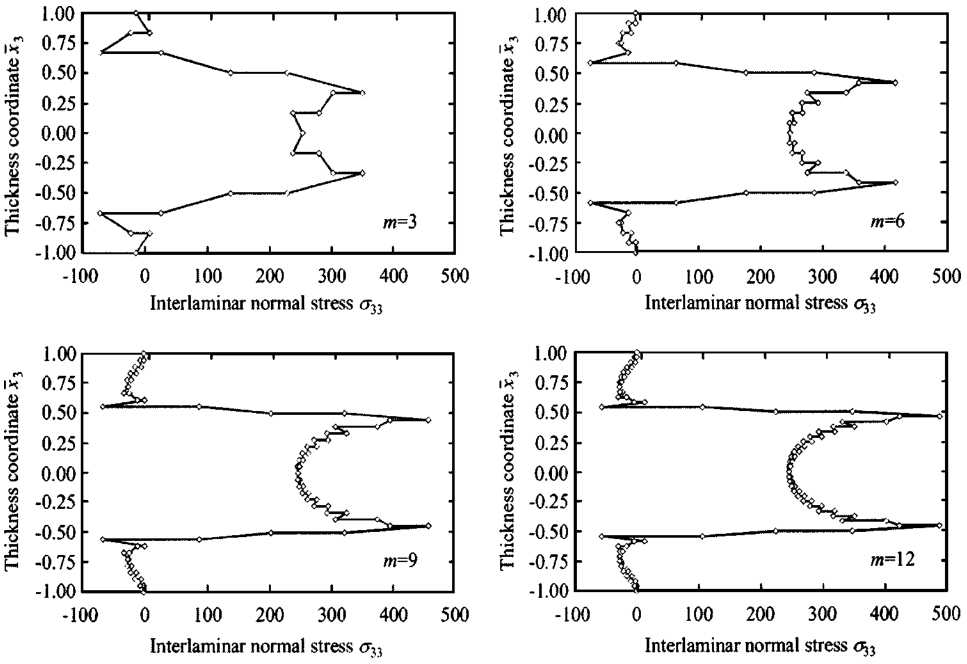

Fig. 3 Convergence study, σ_{33} through the thickness $-d/2\leqslant\bar{x}_3\leqslant d/2$ at the corner tip $\bar{x}_1=0$, $\bar{x}_2=0$ for $m=3$ (upper left portion), $m=6$ (upper right portion), $m=9$ (lower left portion), $m=12$ (lower right portion), $\bar{x}_3$ in mm, all stresses in MPa

higher values of m. In regions that are not dominated by singular influences, i.e., some distance away from the interfaces between two dissimilar physical layers at $\bar{x}_3=\pm d/4$, convergence of the stress distributions is rapid and almost continuous stresses in the mathematical interfaces are achieved. Close to the physical interfaces between the aluminum and nickel layers, however, no convergence of the solution can be observed as with higher values of m positive stress values are encountered that seem to increase without bound. This is a common effect when applying discretizing methods in the vicinity of physical interfaces between dissimilar plate layers at free edges and corners and hints of a distinct corner stress singularity as the comparison of σ_{33} at $\bar{x}_1=0$, $\bar{x}_2=0$, $\bar{x}_3=d/4$ for varying m (see Table 1 where the mean values of the two according interface values $\sigma_{33}^{\text{Tip}}=\sigma_{33}(\bar{x}_1=0,\bar{x}_2=0,\bar{x}_3=d/4)$ of the adjacent mathematical layers are given) also shows. Furthermore, in the regions close to the physical interfaces the continuity properties of σ_{33} remain somewhat poor for all m. Also note that the fulfillment of the boundary condition of traction free plate surfaces, i.e., here $\sigma_{33}(\bar{x}_1=0,\bar{x}_2=0,\bar{x}_3=\pm d/2)=0$, is significantly improved with increasing values of m (see also Table 1 where the numerical values of $\sigma_{33}^{\text{Bot}}=\sigma_{33}(\bar{x}_1=0,\bar{x}_2=0,\bar{x}_3=-d/2)$ at the bottom surface of the plate are given). This is all the more satisfactory as the fulfillment of this boundary condition is not part of the formulation of the layerwise theory, hence these results also render the presented method reliable with plausible results. The differences $\Delta\sigma_{33}^{\text{Tip}}$ and $\Delta\sigma_{33}^{\text{Bot}}$ between two stress values σ_{33}^{Tip} and σ_{33}^{Bot} for two sequent values of m, i.e., $\Delta\sigma_{33}^{\text{Tip}}=\sigma_{33}^{\text{Tip}}(m)-\sigma_{33}^{\text{Tip}}(m-1)$ and $\Delta\sigma_{33}^{\text{Bot}}=\sigma_{33}^{\text{Bot}}(m)-\sigma_{33}^{\text{Bot}}(m-1)$, are also given in Table 1. It is noted that the convergence rate is high for lower values of m and decreases with higher m.

The analytical method exhibits excellent convergence properties for the intralaminar CLPT stresses, accordingly Fig. 4, upper left portion, shows the distribution of $\sigma_{11}(\bar{x}_1=l_1,\bar{x}_2=l_2,-d/2\leqslant\bar{x}_3\leqslant d/2)$ in the center of the plate for $m=3$ only. Deviations between the analytical results and the CLPT predictions of about 1% are found for this stage of discretization.

Figure 4, upper right portion, shows the distribution of σ_{33} along the plate edge $\bar{x}_2=0$ in the range $0\leqslant\bar{x}_1\leqslant l_1/2$ at the thickness coordinate $\bar{x}_3=d/4$, i.e., directly at the interface between the upper aluminum ply and the nickel layer, for the discretizations $m=3$, $m=6$, $m=9$, and $m=12$. Since σ_{33} is dominated by a singularity along the entire structural line $0\leqslant\bar{x}_1\leqslant l_1$ directly at the interface at $\bar{x}_3=d/4$, no convergence of the stress results can be observed. With increasing values of m, higher stress values are found in the entire considered range. Note that the differences between the results of two sequent discretization stages m seem to be more pronounced in the closer corner regions which hints of a distinct corner singularity that will most probably exhibit characteristics different from the occurring edge singularities.

Figure 4, lower left portion, depicts the classical free-edge effect situation of σ_{33} at $\bar{x}_2=l_2$ in the range $0\leqslant\bar{x}_1\leqslant l_1/2$ at $\bar{x}_3=d/4$. Along this structural line, σ_{33} is dominated by a singularity only at the edge point $\bar{x}_1=0$, $\bar{x}_2=l_2$, $\bar{x}_3=d/4$. It is observed that

Table 1 Convergence study, $\sigma_{33}=\sigma_{33}^{\text{Tip}}$ at $\bar{x}_1=0$, $\bar{x}_2=0$ in the physical interface $\bar{x}_3=d/4$ and $\sigma_{33}=\sigma_{33}^{\text{Bot}}$ at $\bar{x}_1=0$, $\bar{x}_2=0$ at the bottom of the plate $\bar{x}_3=-d/2$ for several discretization stages m, differences between sequent discretization degrees, all stresses in MPa

m	3	4	5	6	7	8	9	10	11	12
σ_{33}^{Tip}	182.51	201.50	217.36	230.89	242.70	253.18	262.60	271.17	279.02	286.29
$\Delta\sigma_{33}^{\text{Tip}}$	⋯	18.99	15.86	13.53	11.81	10.48	9.42	8.57	7.85	7.27
σ_{33}^{Bot}	−15.20	−4.91	−5.07	−3.05	−2.32	−1.63	−1.19	−0.85	−0.61	−0.42
$\Delta\sigma_{33}^{\text{Bot}}$	⋯	10.29	−0.16	2.02	0.73	0.69	0.44	0.34	0.24	0.19

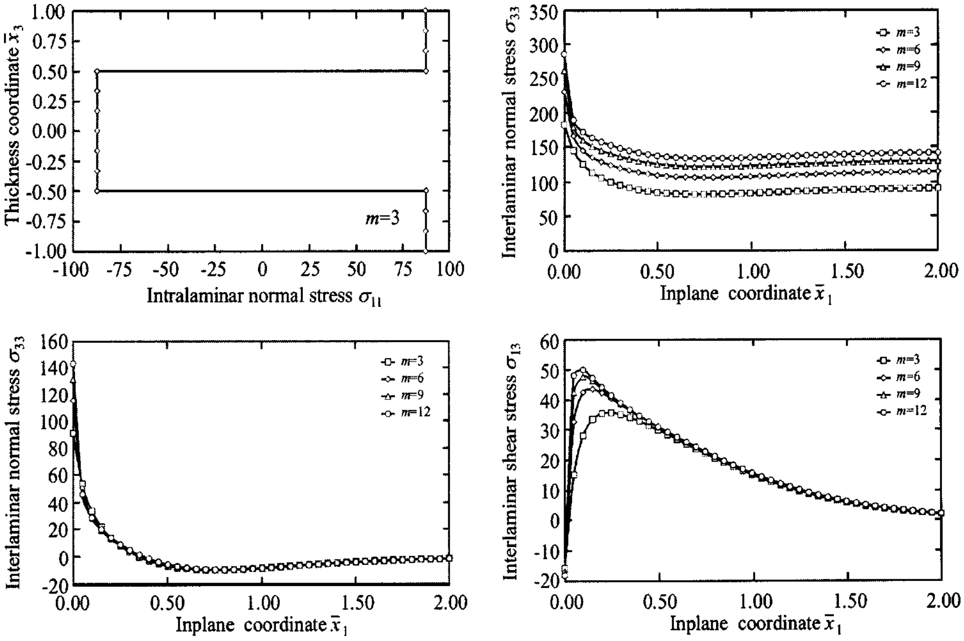

Fig. 4 Convergence study, σ_{11} through the thickness $-d/2\leqslant\bar{x}_3\leqslant d/2$ at the plate center point $\bar{x}_1=l_1$, $\bar{x}_2=l_2$ (upper left portion), σ_{33} at $\bar{x}_2=0$, $\bar{x}_3=d/4$ in the range $0\leqslant\bar{x}_1\leqslant l_1/2$ (upper right portion), σ_{33} at $\bar{x}_2=l_2$, $\bar{x}_3=d/4$ in the range $0\leqslant\bar{x}_1\leqslant l_1/2$ (lower left portion), σ_{13} at $\bar{x}_2=0$, $\bar{x}_3=d/4$ in the range $0\leqslant\bar{x}_1\leqslant l_1/2$ (lower right portion), $\bar{x}_1$ and $\bar{x}_3$ in mm, all stresses in MPa

the stress results for all applied discretization schemes in the entire investigated range agree well with the obvious exception of the close edge region where again no convergence of the results is found. Since this is a common observation with free-edge effects in layered plates this result is not unexpected.

Figure 4, lower right portion, shows the interlaminar shear stress σ_{13} at $\bar{x}_2=0$ in the range $0\leqslant\bar{x}_1\leqslant l_1/2$ at $\bar{x}_3=d/4$. Since σ_{13} is not dominated by singular influences for this class of plate layups, the peak values of σ_{13} some distance from the plate edge show convergent behavior, as between the discretization stages $m=9$ and $m=12$ only small deviations are observed. However, it must be noted that the fulfillment of the boundary conditions [Eq. (43*b*)] is only approximately achieved at this location. However, we will present results for σ_{13} later on where a satisfying fulfillment of Eq. (43*b*) is shown.

For the investigation of basic characteristics of thermoelastic free-corner problems, a discretization degree of at least $m=6$ is recommended. However, if there is interest in very accurate results, a value of $m=12$ mathematical layers per physical ply should be applied, which in all corresponds to $n_L=48$ mathematical layers in the present four-plied plate. As the convergence study has shown, this degree of refinement of the computational model is a reasonable compromise between the spent computational cost (note that one analysis at this degree of discretization takes several seconds on a standard personal computer) and the achieved accuracy of the analysis results. The value $m=12$ will also be applied in all subsequent computations.

3.2 Thermoelastic Stress Fields in a Bimaterial Plate. Let us further refer to the $[\mathrm{Al,Ni}]_S$ plate with $\Delta T=-100\,\mathrm{K}$ and first investigate the intralaminar normal stress σ_{11} in the plate middle plane $\bar{x}_3=0$ in the range $0\leqslant\bar{x}_1\leqslant l_1$, $0\leqslant\bar{x}_2\leqslant l_2$ as it is depicted in Fig. 5(*a*). Results for the second occurring in-plane normal stress σ_{22} are not given since these can be achieved from the results for σ_{11} by switching the axes $\bar{x}_1$, $\bar{x}_2$. The in-plane normal stress σ_{11} exhibits significant gradients with respect to $\bar{x}_1$ and $\bar{x}_2$ in the vicinity of both free plate edges and fulfills the given boundary condition Eq. (43*a*) reasonably well whereas some disruption is found in the closer corner region. In the inner plate regions CLPT holds true. Thus, the present stress localization problem is such that the in-plane stresses are rendered more harmless in comparison to their CLPT values.

Furthermore, let us investigate the distribution of the interlaminar shear stress σ_{13} in the interval $0\leqslant\bar{x}_1\leqslant l_1$, $0\leqslant\bar{x}_2\leqslant l_2$ at $\bar{x}_3$

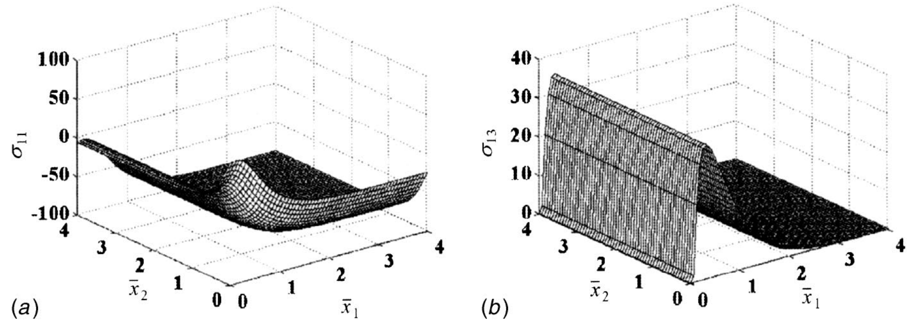

(*a*) (*b*)

Fig. 5 (*a*) σ_{11} at $\bar{x}_3=0$ in the range $0\leqslant\bar{x}_1\leqslant l_1$, $0\leqslant\bar{x}_2\leqslant l_2$, (*b*) σ_{13} at $\bar{x}_3=3/16d$ in the range $0\leqslant\bar{x}_1\leqslant l_1$, $0\leqslant\bar{x}_2\leqslant l_2$, and $\bar{x}_1$ and $\bar{x}_2$ in mm, all stresses in MPa

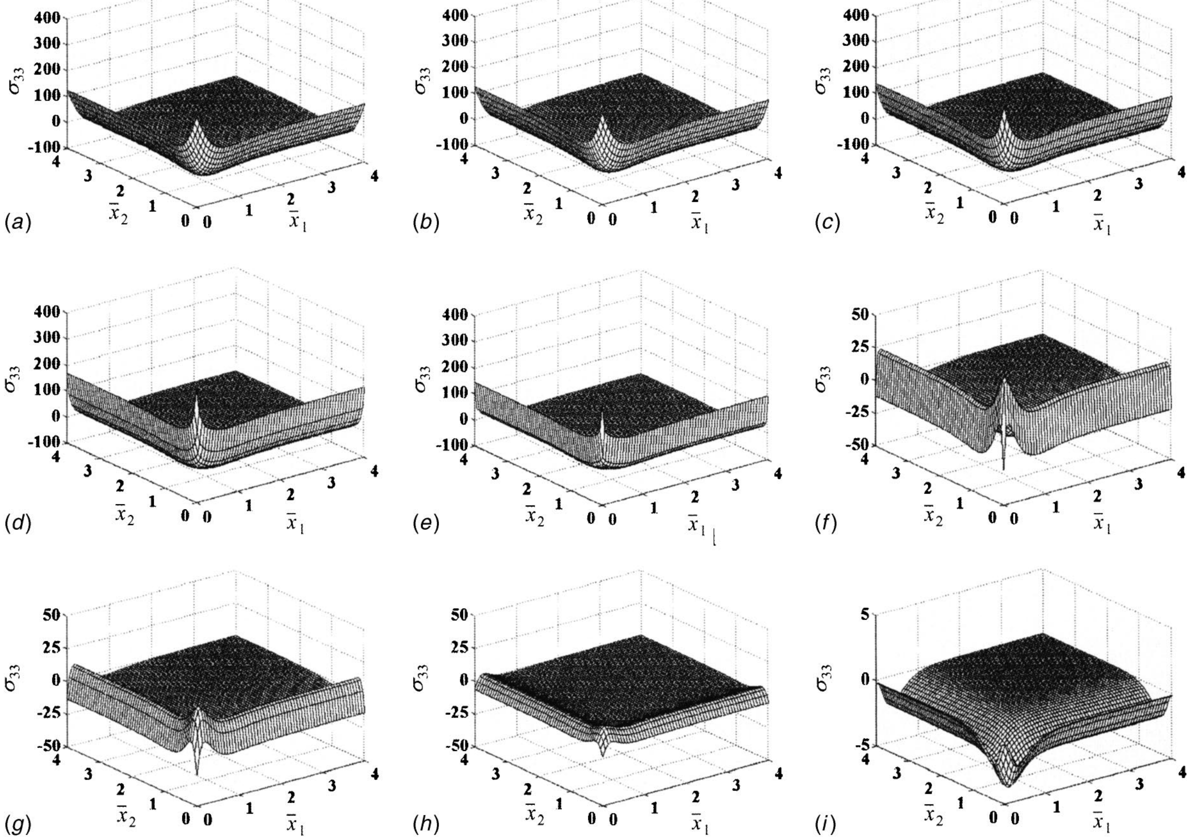

Fig. 6 (*a*)–(*i*) σ_{33} at several locations $\bar{x}_3$ in the range $0\leqslant\bar{x}_1\leqslant l_1$, $0\leqslant\bar{x}_2\leqslant l_2$, (*a*) σ_{33} at $\bar{x}_3=0$, (*b*) σ_{33} at $\bar{x}_3=d/16$, (*c*) σ_{33} at $\bar{x}_3=d/8$, (*d*) σ_{33} at $\bar{x}_3=3d/16$, (*e*) σ_{33} at $\bar{x}_3=d/4$, (*f*) σ_{33} at $\bar{x}_3=5d/16$, (*g*) σ_{33} at $\bar{x}_3=3d/8$, (*h*) σ_{33} at $\bar{x}_3=7d/16$, (*i*) σ_{33} at $\bar{x}_3=d/2$, $\bar{x}_1$ and $\bar{x}_2$ in mm, all stresses in MPa

$=3/16d$ (Fig. 5(*b*)). Due to the same symmetry reasons as for σ_{11} and σ_{22}, results for the second occurring interlaminar shear stress σ_{23} are not given. It is found that σ_{13} fulfills the boundary condition of traction-free plate edges (43*b*) in a convincing manner (a value of $\sigma_{13}=-0.21$ MPa is encountered at $\bar{x}_1=0$) and rises to a positive peak value at some distance from the free plate edge before falling to zero values in the inner plate regions. Note that as σ_{13} is coupled with the inplane normal stress σ_{11} by three-dimensional equilibrium (22) and since the gradient $\sigma_{11,1}$ is nonvanishing (Fig. 5(*a*)), the occurrence of nonconstant inplane stresses σ_{11} is mainly responsible for the occurrence of interlaminar corner stress concentrations of σ_{13}. Similar reasoning will also hold true for the relationship between σ_{22} and σ_{23}. Since the encountered peak value of σ_{13} at the present location is about half of the inplane normal stresses σ_{11}^{0} and σ_{22}^{0} according to CLPT and the peak value at $\bar{x}_3=d/4$ is even higher (see Fig. 4(*d*)), it is appropriate to talk about a serious stress concentration phenomenon.

In the course of the convergence study it was revealed that the occurring interlaminar normal stresses σ_{33} exhibit very high peak values in the vicinity of the free laminate corner and also along the free plate edges which characterizes the encountered free-edge effects and especially the free-corner effect as possibly critical stress concentration phenomena. Thus it is justified to discuss the occurring distributions of σ_{33} at some more length. Figures 6(*a*)–6(*i*) display the distributions of σ_{33} in the interval $0\leqslant\bar{x}_1\leqslant l_1$, $0\leqslant\bar{x}_2\leqslant l_2$ at several thickness locations $\bar{x}_3$ from the plate middle plane at $\bar{x}_3=0$ upward to the free plate surface at $\bar{x}_3=d/2$, namely between every third mathematical layer. In addition, Fig. 7 shows a thickness plot of the mean values of σ_{33} at the corner tip $\bar{x}_1=\bar{x}_2=0$ in all interfaces between the mathematical layers in the interval $0\leqslant\bar{x}_3\leqslant d/2$. Table 2 shows a relative comparison between the encountered corner stresses σ_{33} at $\bar{x}_1=\bar{x}_2=0$ and the CLPT in-plane normal stress $\sigma_{11}^{0(1)}$. As the shear stress gradients $\sigma_{13,1}$ and $\sigma_{23,2}$ are nonvanishing (see also Figs. 4(*d*) and 5(*b*)), the interlaminar normal stress σ_{33} has to arise due to three-dimensional equilibrium (22). Figures 6(*a*)–6(*i*) show that the encountered free-corner effect in essence consists of the superposition of the two corresponding free-edge effects that culminate in distinct stress peaks at the corner tip at $\bar{x}_1=\bar{x}_2=0$. This is encountered at all locations $\bar{x}_3$. Note that below the physical interface at $\bar{x}_3=d/4$ in the nickel layer, the encountered free-edge effects are

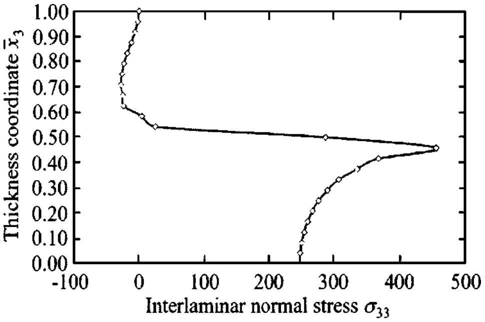

Fig. 7 Interlaminar normal stress σ_{33} through the thickness $0\leqslant\bar{x}_3\leqslant d/2$ at the corner tip $\bar{x}_1=0$, $\bar{x}_2=0$, $\bar{x}_3$ in mm, all stresses in MPa

Table 2 Mean values of σ_{33} at the corner tip $\bar{x}_1=0$, $\bar{x}_2=0$ at several locations $\bar{x}_3$, comparison with in-plane CLPT stresses, $\bar{x}_3$ in mm, all stresses in MPa

$\bar{x}_3$	0.000	0.042	0.083	0.125	0.167	0.208	0.250	0.292	0.333
$\sigma_{33}^{\mathrm{Tip}}$	246.52	247.22	249.34	253.00	258.37	265.82	275.70	289.22	306.43
$\dfrac{\sigma_{33}^{\mathrm{Tip}}}{\sigma_{11}^{0}(m_1)}$	2.82	2.83	2.85	2.89	2.96	3.04	3.15	3.31	3.50
$\bar{x}_3$	0.375	0.417	0.458	0.500	0.542	0.583	0.625	0.667	0.708
$\sigma_{33}^{\mathrm{Tip}}$	334.31	367.37	455.81	286.29	24.55	4.24	−23.43	−25.07	−27.88
$\dfrac{\sigma_{33}^{\mathrm{Tip}}}{\sigma_{11}^{0}(m_1)}$	3.82	4.20	5.21	3.27	0.28	0.05	−0.27	−0.29	−0.32
$\bar{x}_3$	0.750	0.792	0.833	0.875	0.917	0.958	1.000		
$\sigma_{33}^{\mathrm{Tip}}$	−26.16	−22.83	−17.86	−12.03	−6.28	−2.18	−0.42		
$\dfrac{\sigma_{33}^{\mathrm{Tip}}}{\sigma_{11}^{0}(m_1)}$	−0.30	−0.26	−0.20	−0.14	−0.07	−0.02	0.00		

possibly critical with high tensile stresses at the plate edges that are well above the stress values of CLPT. However, also note that the arising free-corner effects exhibit stress peaks at the corner tip that amount to approximately double values of the involved free-edge effects and thus make the immediate vicinity of the free corner tip in the interval $0 \leqslant \bar{x}_3 \leqslant d/4$ the most critical location with respect to the initiation of delamination. The encountered stress distributions above the physical interface at $\bar{x}_3=d/4$ are in contrast to those previously discussed. Here, σ_{33} reaches some positive peak values some distance from both free plate edges before falling to compressive edge and corner values. All encountered absolute values of σ_{33} are well below those in the range $0 \leqslant \bar{x}_3 \leqslant d/4$ as can also be concluded from Fig. 7 and Table 2. Figure 6(*i*) shows that the boundary condition of traction free plate surfaces is met with reasonable accuracy. The encountered stress values at $\bar{x}_3=d/2$ are negligible in comparison to those found at all other locations $\bar{x}_3$.

Becker et al. [50] investigated the free-corner effect in thermally loaded cross-ply plates and calculated stresses for the layup $[\mathrm{Ni,Al}]_S$ under a uniform thermal load of $\Delta T=100\,\mathrm{K}$ with the geometry data identical to those previously discussed. Figure 8 shows a comparison of the present method and the approach as described in [50] which consists of a variational principle and a layerwise stress shape assumption for the in-plane stresses in the form of exponential functions with unknown decaying rate. The finite element results reported in [50] are also depicted in Fig. 8. Results are generated at the thickness coordinate $\bar{x}_3=d/5$ in the range $0 \leqslant \bar{x}_1 \leqslant l_1$, $\bar{x}_2=0$. A reasonable agreement between both methods is found which lends credibility to the present approach. Furthermore, the present analysis compares well with the numerical results as given in [50]. The deviations between the present results and those from Becker et al. probably stem from the fact that in [50] a coarse finite element mesh was employed whereas the presently applied discretization scheme with 12 sublayers per physical layer means a quite high discretizational effort. Furthermore, the closed-form analysis performed in [50] is based on very simple stress shapes the choice of which is somewhat arbitrary so that it may be concluded that the presently applied displacement based approach probably yields results of higher accuracy. However, the overall qualitative agreement between [50] and the present approach is quite satisfying and thus renders the presented displacement based approach a trustworthy method.

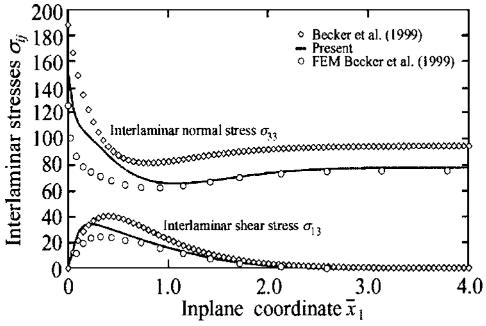

Fig. 8 Comparison of the present method with the results of Becker et al., σ_{13} and σ_{33} at $\bar{x}_2=0$, $\bar{x}_3=d/5$ in the range $0 \leqslant \bar{x}_1 \leqslant l_1$, $\bar{x}_1$ in mm, all stresses in MPa

4 Summary

We have presented a layerwise displacement based approach to the determination of displacements, strains, and stresses in the vicinity of free edges and corners of symmetric plates of isotropic layers under uniform thermal load. After the assumption of a linear interpolation scheme between introduced interface functions that only depend on the in-plane coordinates, the application of the principle of minimum elastic potential of the plate leads to the Euler-Lagrange differential equations that govern the interface functions. These equations allow a closed-form solution due to some simplifying considerations in the displacement formulations and the nature of the encountered free-corner effect. In conclusion, it can be stated that the occurring corner and edge perturbations are an utmost localized phenomenon and are found to be bounded to a small edge region. Especially, the occurrence of interlaminar normal stresses σ_{33} in the near field of the free plate corner is a highly critical stress concentration problem and should be considered with care whenever layered structural elements are involved under thermal influence.

Nomenclature

Subscripts

(k) = layer/interface index
$(\ldots)_{,i}$ = partial derivative with respect to x_i
$\alpha, \beta, \gamma, \delta$ = 1, 2
i, j = 1, 2, 3
o, p = 1, 2, 6
m = 1, 2, 3, . . . ,6
p, q = $1,2,3,\ldots,n_L+1$
s, t = $1,2,3,\ldots,2(n_L+1)$
r = summation index
$\underline{m}$ = auxiliary subscript
$\bar{k}$ = $k+n_L+1$, auxiliary subscript

Superscripts

(k) = layer/interface superscript
0 = quantity according to classical laminate plate theory (CLPT)

r = summation superscript
m = auxiliary superscript

Coordinates

x_1, x_2, x_3 = orthonormal reference axes, inplane coordinates x_1, x_2, and thickness coordinate x_3
$\overline{x_1}, \overline{x_2}, \overline{x_3}$ = orthonormal corner coordinate system

Basic Quantities

d, V, A^0 = total laminate thickness/volume/area of laminate middle plane
$2l_1, 2l_2$ = in-plane laminate dimensions
n, n_L = total number of physical layers/mathematical layers
m = number of mathematical layers per physical layer
$d^{(k)}, V^{(k)}$ = thickness/volume of layer (k)
$x_{3(k-1)}, x_{3(k)}$ = thickness coordinates of lower/upper interface $(k)/(k+1)$ of layer (k)
ΔT = uniform thermal load
$E^{(k)}, \nu^{(k)}$ = layerwise Young's modulus/Poisson's ratio
$G^{(k)}, \alpha_t^{(k)}$ = layerwise shear modulus/coefficient of thermal expansion
$c_{11}^{(k)}, c_{22}^{(k)}, c_{33}^{(k)}, c_{12}^{(k)}, c_{13}^{(k)}, c_{23}^{(k)}, c_{44}^{(k)}, c_{55}^{(k)}, c_{66}^{(k)}$ = layerwise three-dimensional stiffness components
$c_1^{(k)}, c_2^{(k)}, c_3^{(k)}$ = layerwise auxiliary three-dimensional stiffness components
$m_1, m_2, \ldots, m_{n/2}$ = isotropic materials of layers 1,2,3, . . . ,n/2 in a symmetric n-plied laminate
$d/d(\ldots), \partial/\partial(\ldots)$ = standard/partial derivative
δ_{pq} = Kronecker symbol

Quantities According to CLPT

$N_{\alpha\beta}, M_{\alpha\beta}$ = normal/shear forces and bending/twisting moments
$\varepsilon_{\alpha\alpha}^0, \gamma_{12}^0$ = normal/shear strains
ε^0 = normal strain of the isotropic plate
$\kappa_{\alpha\alpha}^0, \kappa_{12}^0$ = plate curvatures/torsion
A_{op}, B_{op}, D_{op} = membrane/coupling/plate stiffnesses
$Q_{op}^{(k)}$ = layerwise reduced stiffness components
$\sigma_{\alpha\alpha}^{0(k)}, \sigma_{12}^{0(k)}$ = layerwise normal/shear stresses
$\alpha_{\alpha\beta t}^{(k)}$ = layerwise coefficients of thermal expansion
$N_{\alpha\beta}^T, M_{\alpha\beta}^T$ = thermal forces/moments
N^T = thermal normal force
$u_\alpha^{0(k)}, u_3^{0(k)}$ = layerwise inplane/transverse displacements
$\varepsilon_{33}^{0(k)}$ = layerwise transverse normal strain
$\xi_m^{(k)}$ = layerwise auxiliary geometric quantity

Vectors and Matrices

$\underline{(\ldots)}$ = vector, one-dimensional array
$\underline{\underline{(\ldots)}}$ = matrix, two-dimensional array
$\underline{N}, \underline{M} \in \mathbb{R}^{3\times 1}$ = arrays of normal/shear forces and bending/twisting moments
$\underline{\varepsilon}^0, \underline{\kappa}^0 \in \mathbb{R}^{3\times 1}$ = arrays of CLPT normal/shear strains and plate curvatures/torsion
$\underline{\alpha}_t^{0(k)} \in \mathbb{R}^{3\times 1}$ = array of layerwise CLPT coefficients of thermal expansion
$\underline{\alpha}_t^{(k)} \in \mathbb{R}^{6\times 1}$ = array of layerwise three-dimensional coefficients of thermal expansion
$\underline{\sigma}^{0(k)} \in \mathbb{R}^{3\times 1}$ = array of layerwise CLPT normal/shear stresses
$\underline{\sigma}^{(k)}, \underline{\varepsilon}^{(k)} \in \mathbb{R}^{6\times 1}$ = arrays of layerwise three-dimensional normal/shear stresses and strains
$\underline{U}_\alpha \in \mathbb{R}^{(n_L+1)\times 1}$ = vectors of displacement functions $U_\alpha^{(k)}$
$\underline{U}_{3\alpha} \in \mathbb{R}^{(n_L+1)\times 1}$ = vectors of displacement functions $U_{3\alpha}^{(k)}$
$\underline{F} \in \mathbb{R}^{(n_L+1)\times 1}$ = vector of effective forces
$\underline{0} \in \mathbb{R}^{(n_L+1)\times 1}$ = zero vector
$\underline{b}_\alpha, \underline{c}_\alpha \in \mathbb{R}^{2(n_L+1)\times 1}$ = arrays of free constants
$\underline{U}_{\alpha\beta} \in \mathbb{R}^{(n_L+1)\times 1}$ = auxiliary displacement vectors
$\underline{U}_{\underline{\alpha}} \in \mathbb{R}^{2(n_L+1)\times 1}$ = auxiliary displacement vectors
$\underline{F} \in \mathbb{R}^{2(n_L+1)\times 1}$ = auxiliary effective force vector
$\underline{\underline{A}}, \underline{\underline{B}}, \underline{\underline{D}} \in \mathbb{R}^{3\times 3}$ = matrices of CLPT laminate membrane/coupling/plate stiffnesses
$\underline{\underline{Q}}^{(k)} \in \mathbb{R}^{3\times 3}$ = matrix of layerwise reduced stiffnesses
$\underline{\underline{C}}^{(k)} \in \mathbb{R}^{6\times 6}$ = matrix of layerwise three-dimensional stiffnesses
$\underline{\underline{K}}_m \in \mathbb{R}^{(n_L+1)\times(n_L+1)}$ = quadratic coefficient matrices
$\underline{\underline{E}} \in \mathbb{R}^{(n_L+1)\times(n_L+1)}$ = unity matrix
$\underline{\underline{0}} \in \mathbb{R}^{(n_L+1)\times(n_L+1)}$ = zero matrix
$\underline{\underline{C}}_1 \in \mathbb{R}^{2(n_L+1)\times 2(n_L+1)}$ = diagonal matrix containing hyperbolic cosines
$\underline{\underline{S}}_1 \in \mathbb{R}^{2(n_L+1)\times 2(n_L+1)}$ = diagonal matrix containing hyperbolic sines
$\overline{\underline{\underline{K}}}_i \in \mathbb{R}^{2(n_L+1)\times 2(n_L+1)}$ = auxiliary stiffness matrices
$\underline{\underline{\Gamma}} \in \mathbb{R}^{2(n_L+1)\times 2(n_L+1)}$ = matrix of eigenvectors of $\overline{\underline{\underline{K}}}_3$
$\underline{\underline{\Phi}}, \underline{\underline{\Lambda}} \in \mathbb{R}^{2(n_L+1)\times 2(n_L+1)}$ = auxiliary matrices

Quantities According to the Three-Dimensional Layerwise Linear Theory Approach

$\sigma_{ii}^{(k)}, \sigma_{ij}^{(k)}$ = layerwise normal/shear stresses
$u_\alpha^{(k)}, u_3^{(k)}$ = layerwise inplane/transverse displacements
$\varepsilon_{ii}^{(k)}, \gamma_{ij}^{(k)}$ = layerwise normal/shear strains
$u_\alpha^{1(k)}, u_3^{1\alpha(k)}$ = layerwise inplane/transverse higher order displacement terms
$U_\alpha^{(k)}, U_{3\alpha}^{(k)}$ = displacement functions in interface (k)
$U_\alpha^{(k+1)}, U_{3\alpha}^{(k+1)}$ = displacement functions in interface $(k+1)$
$\psi_\alpha^{(k)}$ = layerwise linear Lagrangian interpolation functions
Π = total potential energy of the laminate
$F^{(k)}$ = layerwise integrand of the energy functional
$H_\beta^{(k)}, H_{\beta\gamma}^{(k)}, H_{\beta t}^{(k)}, I_{i\gamma 1}^{(k)}, I_{i\gamma 2}^{(k)}, J_{i\gamma 1}^{(k)}, J_{i\gamma 2}^{(k)}, K_{i\gamma\delta 1}^{(k)}, K_{i\gamma\delta 2}^{(k)}, K_{i\gamma\delta 3}^{(k)}, L_{i\gamma 1}^{(k)}, L_{i\gamma 2}^{(k)}$ = layerwise stress and stiffness resultants
K_{pqm} = components of $\underline{\underline{K}}_m$
$\gamma_{st}, \varphi_{st}$ = components of $\underline{\underline{\Gamma}}/\underline{\underline{\Phi}}$
λ_s = roots of the $2(n_L+1)$ eigenvalues $\lambda_1^2, \lambda_2^2, \ldots, \lambda_{(2n_L+2)}^2$ of $\underline{\underline{K}}_3$
$b_{\alpha s}, c_{\alpha s}$ = free constants, components of $\underline{b}_\alpha$ and $\underline{c}_\alpha$
$B_{is}^{(k)}, C_{is}^{(k)}$ = coefficients in equation system resulting from boundary conditions

$D_\alpha^{(k)}$ = right-hand side terms in equation system resulting from boundary conditions
σ_{33}^{tip} = σ_{33} in the interface between two physical layers at the free corner tip
σ_{33}^{bot} = σ_{33} at the bottom of the laminate at the free corner tip
$\Delta\sigma_{33}^{\text{tip}},\ \Delta\sigma_{33}^{\text{bot}}$ = differences between values of $\sigma_{33}^{\text{tip}}/\sigma_{33}^{\text{bot}}$ for two sequent values of m
$\psi^{(k)},\ \psi_{is}^{(k)},\ \xi_{is}^{(k)}$ = auxiliary quantities

Appendix 1

The coefficient matrices $\underset{=}{K}_m$ read:

$$\underset{=}{K}_m=[K_{pqm}]=\begin{pmatrix} K_{11m} & K_{12m} & 0 & 0 & \cdots & 0 & 0 \\ K_{21m} & K_{22m} & K_{23m} & 0 & \cdots & 0 & 0 \\ 0 & K_{32m} & K_{33m} & K_{34m} & \cdots & 0 & 0 \\ 0 & 0 & K_{43m} & K_{44m} & \cdots & 0 & 0 \\ \vdots & \vdots & \vdots & \vdots & \ddots & \vdots & \vdots \\ 0 & 0 & 0 & 0 & \cdots & K_{n_L n_L m} & K_{n_L(n_L+1)m} \\ 0 & 0 & 0 & 0 & \cdots & K_{(n_L+1)n_L m} & K_{(n_L+1)(n_L+1)m} \end{pmatrix}. \tag{49}$$

Their nonvanishing components with $p=[q-1,q,q+1]$ can be written as:

$$K_{pq1}=[K_{3123}^{(q-1)},(K_{3223}^{(q-1)}+K_{3113}^{(q)}),K_{3123}^{(q)}], \tag{50a}$$

$$K_{pq2}=-[K_{1121}^{(q-1)},(K_{1221}^{(q-1)}+K_{1111}^{(q)}),K_{1121}^{(q)}], \tag{50b}$$

$$K_{pq3}=[(K_{3212}^{(q-1)}-K_{2122}^{(q-1)}),(K_{3222}^{(q-1)}-K_{2222}^{(q-1)}+K_{3112}^{(q)} \\ -K_{2112}^{(q)}),(K_{3122}^{(q)}-K_{2212}^{(q)})], \tag{50c}$$

$$K_{pq4}=[K_{1123}^{(q-1)},(K_{1223}^{(q-1)}+K_{1113}^{(q)}),K_{1123}^{(q)}], \tag{50d}$$

$$K_{pq5}=-[K_{3121}^{(q-1)},(K_{3221}^{(q-1)}+K_{3111}^{(q)}),K_{3121}^{(q)}], \tag{50e}$$

$$K_{pq6}=[(K_{2212}^{(q-1)}-K_{3122}^{(q-1)}),(K_{2222}^{(q-1)}-K_{3222}^{(q-1)}+K_{2112}^{(q)} \\ -K_{3112}^{(q)}),(K_{2122}^{(q)}-K_{3212}^{(q)})]. \tag{50f}$$

Appendix 2

The coefficients $B_{1s}^{(k)},\ B_{2s}^{(k)},\ B_{3s}^{(k)},\ C_{1s}^{(k)},\ C_{2s}^{(k)},\ C_{3s}^{(k)}$ and the right-hand terms $D_1^{(k)},\ D_2^{(k)}$ of the equation system (45) read:

$$B_{1s}^{(k)}=\lambda_s^{-1}\sinh(\lambda_s l_2)\,\xi_{1s}^{(k)}, \tag{51a}$$

$$B_{2s}^{(k)}=l_1\cosh(\lambda_s l_2)\,\xi_{2s}^{(k)}, \tag{51b}$$

$$B_{3s}^{(k)}=l_1\sinh(\lambda_s l_2)\,\xi_{3s}^{(k)}, \tag{51c}$$

$$C_{1s}^{(k)}=l_2\cosh(\lambda_s l_1)\,\xi_{2s}^{(k)}, \tag{51d}$$

$$C_{2s}^{(k)}=\lambda_s^{-1}\sinh(\lambda_s l_1)\,\xi_{1s}^{(k)}, \tag{51e}$$

$$C_{3s}^{(k)}=l_2\sinh(\lambda_s l_1)\,\xi_{3s}^{(k)}, \tag{51f}$$

$$D_1^{(k)}=-l_2(H_{12}^{(k-1)}+H_{11}^{(k)}), \tag{51g}$$

$$D_2^{(k)}=-l_1(H_{22}^{(k-1)}+H_{21}^{(k)}), \tag{51h}$$

where

$$\xi_{1s}^{(k)}=[K_{2121}^{(k-1)}\gamma_{(k-1)s}+(K_{2221}^{(k-1)}+K_{2111}^{(k)})\gamma_{ks}+K_{2121}^{(k)}\gamma_{(k+1)s} \\ +K_{2212}^{(k-1)}\gamma_{(k+n_L)s}+(K_{2222}^{(k-1)}+K_{2112}^{(k)})\gamma_{(k+n_L+1)s} \\ +K_{2122}^{(k)}\gamma_{(k+n_L+2)s}], \tag{52a}$$

$$\xi_{2s}^{(k)}=[K_{1121}^{(k-1)}\gamma_{(k-1)s}+(K_{1221}^{(k-1)}+K_{1111}^{(k)})\gamma_{ks}+K_{1121}^{(k)}\gamma_{(k+1)s} \\ +K_{2212}^{(k-1)}\gamma_{(k+n_L)s}+(K_{2222}^{(k-1)}+K_{2112}^{(k)})\gamma_{(k+n_L+1)s} \\ +K_{2122}^{(k)}\gamma_{(k+n_L+2)s}], \tag{52b}$$

$$\xi_{3s}^{(k)}=[K_{3121}^{(k-1)}\varphi_{(k+n_L)s}+(K_{3221}^{(k-1)}+K_{3111}^{(k)})\varphi_{(k+n_L+1)s} \\ +K_{3121}^{(k)}\varphi_{(k+n_L+2)s}+K_{3212}^{(k-1)}\varphi_{(k-1)s}+(K_{3222}^{(k-1)}+K_{3112}^{(k)})\varphi_{ks} \\ +K_{3122}^{(k)}\varphi_{(k+1)s}]. \tag{52c}$$

References

[1] Tsai, S. W., and Hahn, H. T., 1980, *Introduction to Composite Materials*, Technomic Publishing, Lancaster.
[2] Pipes, R. B., and Pagano, N. J., 1970, "Interlaminar Stresses in Composite Laminates Under Uniform Axial Extension," J. Compos. Mater., **4**, pp. 538–548.
[3] Altus, E., Rotem, A., and Shmueli, M., 1980, "Free Edge Effect in Angle Ply Laminates: A New Three Dimensional Finite Difference Solution," J. Compos. Mater., **14**, pp. 21–30.
[4] Wang, A. S. D., and Crossman, F. W., 1977, "Some New Results on Edge Effect in Symmetric Composite Laminates," J. Compos. Mater., **11**, pp. 92–106.
[5] Raju, I. S., and Crews, J. H., 1981, "Interlaminar Stress Singularities at a Straight Free Edge in Composite Laminates," Comput. Struct., **14**, pp. 21–28.
[6] Whitcomb, J. D., Raju, I. S., and Goree, J. G., 1982, "Reliability of the Finite Element Method for Calculating Free Edge Stresses in Composite Laminates," Comput. Struct., **15**, pp. 23–37.
[7] Wu, C. M. L., 1992, "Elasto-Plastic Analysis of Edge Effects in Metal Matrix Angle-Ply Laminates," Comput. Struct., **45**, pp. 273–280.
[8] Spilker, R. L., and Chou, S. C., 1980, "Edge Effects in Symmetric Composite Laminates: Importance of Satisfying the Traction Free Edge Condition," J. Compos. Mater., **14**, pp. 2–20.
[9] Wang, S. S., and Yuan, F. G., 1983, "A Singular Hybrid Finite Element Analysis of Boundary-Layer Stresses in Composite Laminates," Int. J. Solids Struct., **19**, pp. 825–837.
[10] Robbins, Jr., D. H., and Reddy, J. N., 1996, "Variable Kinematic Modelling of Laminated Composite Plates," Int. J. Numer. Methods Eng., **39**, pp. 2283–2317.

[11] Gaudenzi, P., Mannini, A., and Carbonaro, R., 1998, ''Multi-Layer Higher-Order Finite Elements for the Analysis of Free-Edge Stresses in Composite Laminates,'' Int. J. Numer. Methods Eng., **41**, pp. 851–873.
[12] Mannini, A., and Gaudenzi, P., 2003, ''Multi-Layer Higher-Order Finite Elements for the Analysis of Free-Edge Stresses in Piezoelectric Actuated Laminates,'' Compos. Struct., **61**, pp. 271–278.
[13] Davi, G., 1996, ''Stress Fields in General Composite Laminates,'' AIAA J., **34**, pp. 2604–2608.
[14] Lindemann, J., and Becker, W., 2000, ''Analysis of the Free-Edge Effect in Composite Laminates by the Boundary Finite Element Method,'' Mech. Compos. Mater., **36**, pp. 355–366.
[15] Hayashi, T., 1967, ''Analytical Study of Interlaminar Shear Stresses in a Laminated Composite Plate,'' Trans. Jpn. Soc. Aeronaut. Eng. Space Sci., **10**, pp. 43–48.
[16] Puppo, A. H., and Evensen, H. A., 1970, ''Interlaminar Shear in Laminated Composites Under Generalized Plane Stress,'' J. Compos. Mater., **4**, pp. 204–220.
[17] Pagano, N. J., 1974, ''On the Calculation of Interlaminar Normal Stress in Composite Laminate,'' J. Compos. Mater., **8**, pp. 65–81.
[18] Pipes, R. B., and Pagano, N. J., 1974, ''Interlaminar Stresses in Composite Laminates: An Approximate Elasticity Solution,'' J. Appl. Mech., **41**, pp. 668–672.
[19] Tang, S., 1975, ''A Boundary Layer Theory. Part I: Laminated Composites in Plane Stress,'' J. Compos. Mater., **9**, pp. 33–41.
[20] Tang, S., and Levy, A., 1975, ''A Boundary Layer Theory. Part II: Extension of Laminated Finite Strip,'' J. Compos. Mater., **9**, pp. 42–52.
[21] Hsu, P. W., and Herakovich, C. T., 1977, ''Edge Effects in Angle-Ply Composite Laminates,'' J. Compos. Mater., **11**, pp. 422–428.
[22] Pagano, N. J., 1978, ''Stress Fields in Composite Laminates,'' Int. J. Solids Struct., **14**, pp. 385–400.
[23] Pagano, N. J., 1978, ''Free Edge Stress Fields in Composite Laminates,'' Int. J. Solids Struct., **14**, pp. 401–406.
[24] Kassapoglou, C., and Lagace, P. A., 1986, ''An Efficient Method for the Calculation of Interlaminar Stresses in Composite Materials,'' J. Appl. Mech., **53**, pp. 744–750.
[25] Krishna Murty, A. V., and Hari Kumar, H. K., 1989, ''Modelling of Symmetric Laminates Under Extension,'' Compos. Struct., **11**, pp. 15–32.
[26] Rose, C. A., and Herakovich, C. T., 1993, ''An Approximate Solution for Interlaminar Stresses in Composite Laminates,'' Composites Eng., **3**, pp. 271–285.
[27] Yin, W.-L., 1994, ''Free-Edge Effects in Anisotropic Laminates Under Extension, Bending and Twisting, Part I: A Stress-Function-Based Variational Approach,'' J. Appl. Mech., **61**, pp. 410–415.
[28] Becker, W., 1993, ''Closed-Form Solution for the Free-Edge Effect in Cross-Ply Laminates,'' Compos. Struct., **26**, pp. 39–45.
[29] Becker, W., 1994, ''Closed-Form Analysis of the Free Edge Effect in Angle-Ply Laminates,'' J. Appl. Mech., **61**, pp. 209–211.
[30] Zhu, C., and Lam, Y. C., 1998, ''A Rayleigh-Ritz Solution for Local Stresses in Composite Laminates,'' Compos. Sci. Technol., **58**, pp. 447–461.
[31] Tahani, M., and Nosier, A., 2003, ''Free Edge Stress Analysis of General Cross-Ply Composite Laminates Under Extension and Thermal Loading,'' Compos. Struct., **60**, pp. 91–103.
[32] Ting, T. C. T., and Chou, S. C., 1981, ''Edge Singularities in Anisotropic Composites,'' Int. J. Solids Struct., **17**, pp. 1057–1068.
[33] Wang, S. S., and Choi, I., 1982, ''Boundary-Layer Effects in Composite Laminates, Part 1: Free-Edge Stress Singularities,'' J. Appl. Mech., **49**, pp. 541–548.
[34] Wang, S. S., and Choi, I., 1982, ''Boundary-Layer Effects in Composite Laminates, Part 2: Free-Edge Stress Solutions and Basic Characteristics,'' J. Appl. Mech., **49**, pp. 549–560.
[35] Zwiers, R. I., Ting, T. C. T., and Spilker, R. L., 1982, ''On the Logarithmic Singularity of Free-Edge Stress in Laminated Composites Under Uniform Extension,'' J. Appl. Mech., **49**, pp. 561–569.
[36] Delale, F., 1984, ''Stress Singularities in Bonded Anisotropic Materials,'' Int. J. Solids Struct., **20**, pp. 31–40.
[37] Bar-Yoseph, P., and Avrashi, J., 1988, ''On the Nature of the Free Edge Stress Singularity in Composite Laminated Plates,'' Int. J. Numer. Methods Eng., **26**, pp. 1507–1523.
[38] Ding, S., and Kumosa, M., 1994, ''Singular Stress Behavior at an Adhesive Interface Corner,'' Eng. Fract. Mech., **47**, pp. 503–519.
[39] Gu, L., and Belytschko, T., 1994, ''A Numerical Study of Stress Singularities in a Two-Material Wedge,'' Int. J. Solids Struct., **31**, pp. 865–889.
[40] Kim, T. W., and Im, S., 1995, ''Boundary Layers in Wedges of Laminated Composite Strips Under Generalized Plane Deformation. Part I: Asymptotic Solutions,'' Int. J. Solids Struct., **32**, pp. 609–628.
[41] Chaudhuri, R. A., and Xie, M., 1998, ''Free-Edge Stress Singularity in a Bimaterial Laminate,'' Compos. Struct., **40**, pp. 29–136.
[42] Chue, C.-H., and Liu, C.-I., 2002, ''Disappearance of Free-Edge Stress Singularity in Composite Laminates,'' Compos. Struct., **56**, pp. 111–129.
[43] Pipes, R. B., and Daniel, I. M., 1971, ''Moire Analysis of the Interlaminar Shear Edge Effect in Laminated Composites,'' J. Compos. Mater., **5**, pp. 255–259.
[44] Whitney, J. M., and Browning, C. E., 1972, ''Free-Edge Delamination of Tensile Coupons,'' J. Compos. Mater., **6**, pp. 300–303.
[45] Herakovich, C. T., Post, D., Buczek, M. B., and Czarnek, R., 1985, ''Free Edge Strain Concentrations in Real Composite Laminates: Experimental-Theoretical Correlation,'' J. Appl. Mech., **52**, pp. 787–793.
[46] Herakovich, C. T., 1989, ''Free Edge Effects in Laminated Composites,'' *Handbook of Composites*, Vol. 2. *Structure and Design*, edited by C. T. Herakovich and Y. M. Tarnopol'skii, Elsevier Science Publishers, Amsterdam, The Netherlands, pp. 187–230.
[47] Herakovich, C. T., 1989, ''Failure Modes and Damage Accumulation in Laminated Composites With Free Edges,'' Compos. Sci. Technol., **36**, pp. 105–119.
[48] Kant, T., and Swaminathan, K., 2000, ''Estimation of Transverse/Interlaminar Stresses in Laminated Composites: A Selective Review and Survey of Current Developments,'' Compos. Struct., **49**, pp. 65–75.
[49] Mittelstedt, C., and Becker, W., 2004, ''Interlaminar Stress Concentrations in Layered Structures. Part I: A Selective Literature Survey on the Free-Edge Effect Since 1967,'' J. Compos. Mater., **38**, pp. 1037–1062.
[50] Becker, W., Jin, P. P., and Neuser, P., 1999, ''Interlaminar Stresses at the Free Corners of a Laminate,'' Compos. Struct., **45**, pp. 155–162.
[51] Dimitrov, A., Andrae, H., and Schnack, E., 2001, ''Efficient Computation of Order and Mode of Corner Singularities in 3D Elasticity,'' Int. J. Numer. Methods Eng., **51**, pp. 1–24.
[52] Dimitrov, A., Andrae, H., and Schnack, E., 2002, ''Singularities Near Three-Dimensional Corners in Composite Laminates,'' Int. J. Fract., **115**, pp. 361–375.
[53] Labossiere, P. E. W., and Dunn, M. L., 2001, ''Fracture Initiation at Three-Dimensional Bimaterial Interface Corners,'' J. Mech. Phys. Solids, **49**, pp. 609–634.
[54] Mittelstedt, C., and Becker, W., 2003, ''Free-Corner Effects in Cross-Ply Laminates: An Approximate Higher-Order Theory Solution,'' J. Compos. Mater., **37**, pp. 2043–2068.
[55] Mittelstedt, C., and Becker, W., 2003, ''Three-Dimensional Closed-Form Analysis of the Stress Field at Rectangular Corners of Layered Plates,'' Arch. Appl. Mech., **73**, pp. 63–74.
[56] Mittelstedt, C., and Becker, W., 2004, ''Interlaminar Stress Concentrations in Layered Structures. Part II: Closed-Form Analysis of Stresses at Laminated Rectangular Wedges With Arbitrary Non-Orthotropic Layup,'' J. Compos. Mater., **38**, pp. 1063–1090.
[57] Noor, A. K., and Burton, W. S., 1989, ''Assessment of Shear Deformation Theories for Multilayered Composite Plates,'' Appl. Mech. Rev., **42**, pp. 1–13.
[58] Noor, A. K., and Burton, W. S., 1990, ''Assessment of Computational Models for Multilayered Anisotropic Plates,'' Compos. Struct., **14**, pp. 233–265.
[59] Reddy, J. N., 1990, ''A Review of Refined Theories of Laminated Composite Plates,'' Shock Vib. Dig., **22**, pp. 3–17.
[60] Reddy, J. N., 1990, ''On Refined Theories of Composite Laminates,'' Meccanica, **25**, pp. 230–238.
[61] Altenbach, H., 1998, ''Theories for Laminated and Sandwich Plates, A Review,'' Mech. Compos. Mater., **34**, pp. 243–252.
[62] Whitney, J. M., 1969, ''The Effect of Transverse Shear Deformation on the Bending of Laminated Plates,'' J. Compos. Mater., **3**, pp. 534–547.
[63] Mau, S. T., 1973, ''A Refined Laminated Plate Theory,'' J. Appl. Mech., **40**, pp. 606–607.
[64] Srinivas, S., 1973, ''A Refined Analysis of Composite Laminates,'' J. Sound Vib., **30**, pp. 495–507.
[65] Sun, C. T., and Whitney, J. M., 1973, ''Theories for the Dynamic Response of Laminated Plates,'' AIAA J., **11**, pp. 178–183.
[66] Reddy, J. N., 1987, ''A Generalization of Two-Dimensional Theories of Laminated Composite Plates,'' Commun. Appl. Numer. Methods, **3**, pp. 173–180.
[67] Di Sciuva, M., 1986, ''Bending, Vibration and Buckling of Simply Supported Thick Multilayered Orthotropic Plates: An Evaluation of a New Displacement Model,'' J. Sound Vib., **105**, pp. 425–442.
[68] Murakami, H., 1986, ''Laminated Composite Plate Theory With Improved In-Plane Responses,'' J. Appl. Mech., **53**, pp. 661–666.
[69] Reddy, J. N., and Savoia, M., 1992, ''Layer-Wise Shell Theory for Postbuckling of Laminated Circular Cylindrical Shells,'' AIAA J., **30**, pp. 2148–2154.
[70] Nosier, A., Kapania, R. K., and Reddy, J. N., 1993, ''Free Vibration Analysis of Laminated Plates Using a Layerwise Theory,'' AIAA J., **31**, pp. 2335–2346.
[71] Wisniewski, K., and Schrefler, B. A., 1993, ''Hierarchical Multi-Layered Element of Assembled Timoshenko Beams,'' Compos. Struct., **48**, pp. 255–261.
[72] Reddy, J. N., and Starnes, Jr., J. H., 1993, ''General Buckling of Stiffened Circular Cylindrical Shells According to a Layerwise Theory,'' Compos. Struct., **49**, pp. 605–616.
[73] Cho, M., and Parmerter, R. R., 1993, ''An Efficient Higher Order Plate Theory for Laminated Composites,'' Compos. Struct., **20**, pp. 113–123.
[74] Cho, M., and Parmerter, R. R., 1993, ''Efficient Higher Order Composite Plate Theory for General Lamination Configurations,'' AIAA J., **31**, pp. 1299–1306.
[75] He, L. H., 1994, ''A Linear Theory of Laminated Shells Accounting for Continuity of Displacements and Transverse Shear Stresses at Layer Interfaces,'' Int. J. Solids Struct., **31**, pp. 613–627.
[76] Liu, P., Zhang, Y., and Zhang, X., 1994, ''Improved High-Order Thermoelastic Response Theory for Analyzing Thermal Bending of Laminated Composite Plates,'' J. Therm. Stresses, **17**, pp. 163–190.
[77] Chattopadhyay, A., and Gu, H., 1995, ''Modeling of Delamination Buckling in Composite Cylindrical Shells With a New Higher-Order Theory,'' Compos. Sci. Technol., **54**, pp. 223–232.
[78] Kam, T. Y., and Jan, T. B., 1995, ''First-Ply Failure Analysis of Laminated Composite Plates Based on the Layerwise Linear Displacement Theory,'' Compos. Struct., **32**, pp. 583–591.
[79] Di, S., and Rothert, H., 1995, ''A Solution of Laminated Cylindrical Shells Using an Unconstrained Third-Order Theory,'' Compos. Struct., **32**, pp. 667–680.

[80] Khatri, K. N., and Asnani, N. T., 1995, ''Vibration and Damping Analysis of Multilayered Shells,'' Compos. Struct., **33**, pp. 143–157.
[81] Ossadzow, C., Muller, P., and Touratier, M., 1995, ''A General Doubly Curved Laminate Shell Theory,'' Compos. Struct., **32**, pp. 299–312.
[82] He, J. F., and Zhang, Z. Z., 1996, ''Bending Analysis of Antisymmetric Angle-Ply Laminated Plates Including Transverse Shear Effects,'' Compos. Struct., **34**, pp. 437–444.
[83] Kassegne, S. K., and Reddy, J. N., 1998, ''Local Behavior of Discretely Stiffened Composite Plates and Cylindrical Shells,'' Compos. Struct., **41**, pp. 13–26.
[84] Ali, J. S. M., Bhaskar, K., and Varadan, T. K., 1999, ''A New Theory for Accurate Thermal/Mechanical Flexural Analysis of Symmetric Laminated Plates,'' Compos. Struct., **45**, pp. 227–232.
[85] Cho, Y. B., and Averill, R. C., 2000, ''First-Order Zig–Zag Sublaminate Plate Theory and Finite Element Model for Laminated Composite and Sandwich Panels,'' Compos. Struct., **50**, pp. 1–15.

Solutions for the Inclined Borehole in a Porothermoelastic Transversely Isotropic Medium

Younane Abousleiman

Shailesh Ekbote[1]

Mewbourne School of Petroleum
and Geological Engineering,
School of Civil Engineering
and Environmental Science,
PoroMechanics Institute,
The University of Oklahoma,
Norman, OK 73019

A porothermoelastic solution of the general problem of the inclined borehole in a transversely isotropic porous material is presented herein and compared with the isotropic porothermoelastic solution. The governing equations are outlined for the case of general anisotropy and specialized for a transversely isotropic poroelastic material under nonhydrostatic and nonisothermal in situ conditions. A superposition scheme is employed to obtain the analytical solutions within the isotropic and transversely isotropic poromechanics theory. The borehole generator is assumed to coincide with the material axis of symmetry, in the case of transverse isotropy, yet subjected to a three-dimensional state of stress. A systematic analysis has been carried out to evaluate the effect of the anisotropy of the poromechanical material parameters as well as the thermal material properties on stress and pore pressure distributions and the potential impact on the overall stability of deep wellbore drilling. [DOI: 10.1115/1.1825433]

Introduction

A great deal of attention has been focused on coupled thermomechanical behavior of fluid-saturated porous media. Over the years, the theoretical developments in this area have matured from a simple extension of Biot's isotropic poroelastic theory [1–6] to a more general approach which can handle the coupling along with the material anisotropy [7]. Applications for these are found in diverse areas such as deep drilling and excavation, modeling of nuclear waste disposal facilities [8], and extraction of geothermal energy [9]. With the complex mechanisms that come into play, identification of various driving forces and the interaction between them presents a challenge in predicting an appropriate behavior at depth.

Following the work of Biot [1,2], considerable research has been carried out in the mechanics of fluid-saturated porous media. Fundamental aspects of Biot's theory of poroelasticity have been reformulated and presented in various forms [10–12]. Extension of this theory to incorporate thermal effects for the isotropic case has been addressed by several authors [3–6]. Consequently, solutions to boundary and initial value problems have been developed under various scenarios which demonstrate the effect of the thermohydromechanical coupling on the response [13–18].

At the same time, Biot's theory has been extended to account for material anisotropy [2,11]. The extension introduced various material constants which were identified and recast with straightforward physical interpretations [19,20]. Subsequently, analytical solutions for fundamental problems such as Mandel's problem [21], the borehole problem, and the cylinder problem [22] have been extended for the transversely isotropic case. It was found that analysis of the transversely isotropic poroelastic problems showed unpredicted results when compared to their elastic counterparts [21,22]. In addition to the time dependency of the flow and deformation fields, the anisotropic material coefficients play an important role in the calculation of the in-plane stresses. There is existing literature that addresses the thermal effects in anisotropic media, though the treatment in many cases is limited to coupled thermoelasticity [23–25]. A comprehensive treatment of the anisotropic porothermoelasticity has been addressed by Katsube [7].

In general, geoactivities are usually carried out in formations that can be broadly classified as transversely isotropic due to the simple natural deposition of sedimentary rocks which has occurred over a geological time scale. The deposition processes lead to development of formations with similar material properties across a cross section but with different characteristics in the direction perpendicular to it. In this paper, a porothermoelastic solution for an inclined borehole in a transversely isotropic medium is presented. Governing equations are developed first for general anisotropy and then specialized for the transversely isotropic and isotropic cases. The resulting system of equations is used to obtain the analytical solution for an infinitely long borehole where it is assumed that the borehole generator coincides with the material axis of symmetry.

General Formulations

Upon load application, the mechanical response of a fluid-saturated porous system is characterized by coupled diffusion–deformation attributed to the interdependence of change in pore volume and the pore fluid pressure. With the introduction of boundary temperatures, i.e., a nonisothermal state, both the pore fluid and pore volume are subject to differential expansion or contraction, resulting in additional coupling associated with the temperature change. The magnitude of the relative change in stress, pore pressure, and temperature is coupled and described by constitutive relations weighted by material coefficients. In this section, a full set of governing equations is developed for the general anisotropic case.

Constitutive Equations. The constitutive equations for linear porothermoelasticity are expressed as [5,6]

$$\sigma_{ij}=M_{ijkl}\epsilon_{kl}-\alpha_{ij}p-\beta_{ij}^{s}T \qquad (1a)$$

$$\zeta=p/M+\alpha_{ij}\epsilon_{ij}-\beta^{sf}T \qquad (1b)$$

Equations (1*a*) and (1*b*) are written using a tension positive convention. The above equations relate the response of the dynamic variables, σ_{ij} (total stress tensor), p (pore pressure), and T (temperature), to the kinematic quantities, ϵ_{ij} (solid strain tensor) and ζ (variation of fluid content). The connection between the dy-

---

[1] Now at Shell International Exploration and Production, Houston, TX 77025.

Contributed by the Applied Mechanics Division of THE AMERICAN SOCIETY OF MECHANICAL ENGINEERS for publication in the ASME JOURNAL OF APPLIED MECHANICS. Manuscript received by the Applied Mechanics Division, January 21, 2004; final revision, March 18, 2004. Editor: R. M. McMeeking. Discussion on the paper should be addressed to the Editor, Prof. Robert M. McMeeking, Journal of Applied Mechanics, Department of Mechanical and Environmental Engineering, University of California—Santa Barbara, Santa Barbara, CA 93106-5070, and will be accepted until four months after final publication in the paper itself in the ASME JOURNAL OF APPLIED MECHANICS.

namic and kinematic quantities is characterized by the material constants, M_{ijkl} (drained elastic modulus tensor), α_{ij} (Biot's effective stress coefficient tensor), M (Biot's modulus), β^s_{ij} (thermic coefficient tensor related to the solid skeleton), and β^{sf} (thermic coefficient related to the pore fluid). The thermic coefficient tensor, β^s_{ij}, provides a measure of the stress induced due to change in temperature. It is related to the thermal expansion coefficients and the drained elastic modulus tensors as follows [26,27]:

$$\beta^s_{ij}=M_{ijkl}\alpha^s_{kl} \tag{2}$$

where α^s_{ij} is the linear expansion coefficient tensor of the solid skeleton. The thermic coefficient, β^{sf}, on the other hand, is associated with the pore fluid and provides a measure of the pore pressure induced due to a change in temperature. It is related to the thermal expansion coefficients of the solid–fluid system, the porosity to the medium, and the Biot's effective stress coefficient tensor, and is given as [28,29]

$$\beta^{sf}=\alpha_{ij}\alpha^s_{ij}+(\alpha^f-\alpha^s_{kk})\phi \tag{3}$$

in which α^f is the volumetric expansion coefficient for the pore fluid, and ϕ is the porosity. Note that in writing Eqs. (1)–(3), the thermal expansion coefficients of the bulk drained material and that of the solid skeleton are assumed to be equal. The above equations give the complete anisotropic stress–strain response of a porothermoelastic material. For the most general anisotropic case, the behavior is described using 35 constants ($21\,M_{ijkl}$'s, $6\ \alpha_{ij}$'s, $1\ M$, $6\ \beta^s_{ij}$'s, and $1\ \beta^{sf}$) [30].

Mass Balance. Under isothermal coditions, Darcy's law, where the fluid flux is proposional to the pressure gradient, is well known [6]. For solid–fluid constituent porous system, where no fluid sources or sinks exist, the fluid mass balance equation is written as

$$\frac{\partial\zeta}{\partial t}+q_{i,i}=0 \tag{4}$$

where q is the specific discharge vector. Under nonisothermal conditions fluid transport within the system can be caused by a gradient in both the pore fluid pressure as well as temperature. A generalized expression for the specific discharge, q, is given as [15]

$$q_i=-\kappa_{ij}p_{,j}+\Gamma^q_{ij}T_{,j} \tag{5}$$

in which κ_{ij} is the anisotropic mobility coefficient tensor and Γ^q_{ij} is the coefficient tensor which relates the flux to the temperature gradient. The first term on the right-hand side in Eq. (5) corresponds to the fluid transport caused by the *Darcy* effect and the second term on the right-hand side corresponds to the fluid flux generated as a result of the *Soret* effect. The term associated with the *Soret* effect is ignored in this analysis, and Eq. (5) results in the well-known Darcy's law. The anisotropic mobility coefficient tensor, κ_{ij}, is related to the intrinsic permeability tensor, k_{ij}, and the pore fluid viscosity, μ, by $\kappa_{ij}=k_{ij}/\mu$.

Momentum Balance. Momentum balance yields the equilibrium equations which are given by

$$\sigma_{ij,j}=0 \tag{6}$$

Again, Eq. (6) has been written, in terms of the total stress approach, while ignoring any body and inertial forces.

Energy Balance. Within a continuum model, both the matrix and the pore fluid are assumed to occupy the same point in space and therefore one should introduce two temperatures to characterize the thermal state of the system. However, existing studies for thermomechanical behavior of porous media employ a common temperature for both the constituents of the porous system based on the assumption of instantaneous local temperature equilibrium [3,4,15,16,31]. In other words, it is assumed that the heat transport between the matrix and the pore fluid at the local level is much faster than the overall heat diffusion process. Neglecting the internal energy change due to viscous dissipation and compression, the energy balance equation is given as

$$\rho C_v\frac{\partial T}{\partial t}=-h_{i,i}-(\rho C_v q_i)T_{,i} \tag{7}$$

where ρC_v is the heat capacity of the solid–fluid mixture and h is the heat flux. In Eq. (7) the first term on the right-hand side corresponds to heat transport by conduction, whereas the second term represents the heat transport by convection. In addition, it is assumed that the porous material bears a low permeability and that the heat diffusion occurs much faster than the fluid diffusion, which indirectly results in the assumption of a small *Peclet* number. Under these circumstances, the term corresponding to convection can be dropped from (7), resulting in a linearized form of the energy balance given by

$$\rho C_v\frac{\partial T}{\partial t}+h_{i,i}=0 \tag{8}$$

Clearly, Eq. (8) is uncoupled from the pore pressure field.

The "bulk heat capacity," ρC_v, can be related to individual heat capacities of the solid and fluid constituents by [3,15]

$$\rho C_v=(1-\phi)\rho^s C^s_v+\phi\rho^f C^f_v \tag{9}$$

in which the superscripts s and f refer to the solid and fluid, respectively.

Analogous to the fluid mass transport, the heat flux in the most general case can be caused by gradients in pressure and temperature. A generalized equation for the heat flux is given by [15]

$$h_i=-\lambda_{ij}T_{,j}+\Gamma^h_{ij}p_{,j} \tag{10}$$

where λ_{ij} is the effective thermal conductivity of the solid–fluid system, and Γ^h_{ij} is the coefficient tensor associated with the heat flux caused by the pressure gradient. The first term on the right-hand side in Eq. (10) is the heat flux caused by the *Fourier* effect, whereas the second term gives the heat flux resulting from the *Dufour* effect. The *Dufour* effect is ignored in this analysis, thus giving the governing equation for the heat flux also known as Fourier's law.

As in Eq. (9) the "effective thermal conductivity" can also be obtained from the thermal conductivities of the solid and fluid constituents as a weighted average using the porosity, and is given as [3,15]

$$\lambda_{ij}=(1-\phi)\lambda^s_{ij}+\phi\lambda^f_{ij} \tag{11}$$

where λ^s_{ij} and λ^f_{ij} are the thermal conductivities of the solid and fluid constituents, respectively.

The above set of Eqs. (1)–(11) represents the porothermoelastic system in the general anisotropic form. These are specialized for a transversely isotropic material in the next section.

Transversely Isotropic Material

A transversely isotropic material is characterized by same properties in one plane and different properties in the direction normal to this plane. For the transversely isotropic material it is assumed that the z axis coincides with the axis of elastic symmetry. The transversely isotropic poroelastic material is characterized by 8 material constants [19,20]. These are given as E, E', ν, ν', G', α, α', and M, where the unprimed variables are material coefficients in the isotropic plane and the primed variables are material coefficients in the transverse direction. In the above, E is the drained elastic modulus, ν is the drained Poisson's ratio, G is the shear modulus, α is the Biot's effective stress coefficient, and M is the

Biot's modulus. With the introduction of nonisothermal effects three additional thermic constants, β^s, $\beta^{s'}$, β^{sf} are required to account for the differential volume change of the solid skeleton and pore fluid due to temperature changes. Hence, constitutive relations for the transversely isotropic material under nonisothermal conditions are given as follows:

$$\begin{Bmatrix} \sigma_{xx} \\ \sigma_{yy} \\ \sigma_{zz} \\ \tau_{xy} \\ \tau_{yz} \\ \tau_{zx} \\ p \end{Bmatrix} = \begin{bmatrix} \bar{M}_{11} & \bar{M}_{12} & \bar{M}_{13} & 0 & 0 & 0 & -\alpha M \\ \bar{M}_{12} & \bar{M}_{11} & \bar{M}_{13} & 0 & 0 & 0 & -\alpha M \\ \bar{M}_{13} & \bar{M}_{13} & \bar{M}_{33} & 0 & 0 & 0 & -\alpha' M \\ 0 & 0 & 0 & G & 0 & 0 & 0 \\ 0 & 0 & 0 & 0 & G' & 0 & 0 \\ 0 & 0 & 0 & 0 & 0 & G' & 0 \\ -\alpha M & -\alpha M & -\alpha' M & 0 & 0 & 0 & M \end{bmatrix} \begin{Bmatrix} \epsilon_{xx} \\ \epsilon_{yy} \\ \epsilon_{zz} \\ \gamma_{xy} \\ \gamma_{yz} \\ \gamma_{zx} \\ \zeta \end{Bmatrix} - \begin{bmatrix} \bar{\beta}^s \\ \bar{\beta}^s \\ \bar{\beta}^{s'} \\ 0 \\ 0 \\ 0 \\ M\beta^{sf} \end{bmatrix} T \tag{12}$$

where

$$\bar{M}_{11} = M_{11} + \alpha^2 M; \quad \bar{M}_{12} = M_{12} + \alpha^2 M \tag{13a}$$

$$\bar{M}_{13} = M_{13} + \alpha\alpha' M; \quad \bar{M}_{33} = M_{33} + \alpha'^2 M \tag{13b}$$

$$\bar{\beta}^s = \beta^s + \alpha M \beta^{sf}; \quad \bar{\beta}^{s'} = \beta^{s'} + \alpha' M \beta^{sf} \tag{13c}$$

In the above, the coefficients of the drained elastic modulus tensor can be related to the material constants E, E', ν, ν', and G' chosen to represent the transversely isotropic materials by the following relations [20–22]:

$$M_{11} = \frac{E(E' - E\nu'^2)}{(1+\nu)(E' - E'\nu - 2E\nu'^2)};$$

$$M_{12} = \frac{E(E'\nu + E\nu'^2)}{(1+\nu)(E' - E'\nu - 2E\nu'^2)} \tag{14a}$$

$$M_{13} = \frac{EE'\nu'}{(E' - E'\nu - 2E\nu'^2)}; \quad M_{33} = \frac{E'^2(1-\nu)}{(E' - E'\nu - 2E\nu'^2)} \tag{14b}$$

In addition, it has been shown that, with the assumption of microisotropy and microhomogeneity the coefficients α and α' can be related to components of the drained elastic tensor [19,20]. These relations are given as

$$\alpha = 1 - \frac{M_{11} + M_{12} + M_{13}}{3K_s} \tag{15a}$$

$$\alpha' = 1 - \frac{2M_{13} + M_{33}}{3K_s} \tag{15b}$$

where K_s is the grain bulk modulus of the solid constituent. Similarly, using Eqs. (2) and (3), expressions for β^s, $\beta^{s'}$, and β^{sf} are obtained as follows:

$$\beta^s = (M_{11} + M_{12})\alpha^s + M_{13}\alpha^{s'} \tag{16a}$$

$$\beta^{s'} = 2M_{13}\alpha^s + M_{33}\alpha^{s'} \tag{16b}$$

$$\beta^{sf} = 2\alpha\alpha^s + \alpha'\alpha^{s'} + (\alpha^f - 2\alpha^s - \alpha^{s'})\phi \tag{16c}$$

where α^s and $\alpha^{s'}$ are coefficients of linear expansion of the solid skeleton in the isotropic plane and transverse directions, respectively. In addition, the transversely isotropic material is characterized by different thermal conductivities (λ, λ') and mobility coefficients (κ, κ') in the isotropic plane and transverse directions. In line with the aforementioned discussion, governing equations for a three-dimensional case can be derived.

However, many problems in geomechanics are characterized by geometries in which boundary conditions do not change along the direction of their generators. Under such circumstances, a generalized plane strain idealization can be used which allows extrapolation of solutions developed in two-dimensional geometries to a general three-dimensional case [32,33].

It is assumed that the z direction is infinitely long and that boundary conditions are invariant along that direction. Hence, a generalized plane strain condition, as discussed above, manifests itself, resulting in all stress components, pore pressure, and temperature being z independent. Naturally, both heat and fluid flux components in the z direction vanish and all diffusion phenomena occur in the $x-y$ plane which is isotropic. It would therefore be useful to derive governing equations for a plane $(x-y)$ case which will be utilized in obtaining analytical solutions (two-dimensional) and subsequently extended to the three-dimensional case under the assumption of a generalized plane strain condition.

Combination of the equilibrium equations with the constitutive relations yields the Navier-type equations which are given as follows:

$$\tfrac{1}{2}(M_{11} - M_{12})u_{i,jj} + \tfrac{1}{2}(M_{11} + M_{12})u_{j,ji} = \alpha p_{,i} + \beta^s T_{,i} \quad (i,j = 1,2) \tag{17}$$

where u_i denotes the solid displacement. Note that the two-dimensional form of the equilibrium equations has been used to derive the above equation.

Combining the energy balance relation with Fourier's law yields the heat diffusion equation

$$\frac{\partial T}{\partial t} - c_h \nabla^2 T = 0 \tag{18}$$

where $c_h = \lambda/\rho C_v$ is the heat diffusivity in the isotropic plane.

Diffusion equations for the pore fluid are obtained combining the fluid mass balance relations with Darcy's law. These can be expressed in terms of the pore pressure, p, and the variation of the fluid content ζ, and are given as

$$\frac{\partial p}{\partial t} - \kappa M \nabla^2 p = -\alpha M \frac{\partial \epsilon}{\partial t} + \beta^{sf} M \frac{\partial T}{\partial t} \tag{19a}$$

$$\frac{\partial \zeta}{\partial t} - c_f[\nabla^2 \zeta + \bar{c}\nabla^2 T] = 0 \tag{19b}$$

where $\epsilon = \epsilon_{xx} + \epsilon_{yy}$ and $\bar{c}$ are, respectively, the fluid diffusivity and a coupling constant in accordance with

$$c_f = \frac{\kappa M M_{11}}{(M_{11} + \alpha^2 M)} \tag{20a}$$

$$\overline{c}=\frac{\alpha\beta^s-M_{11}\beta^{sf}}{M_{11}} \tag{20b}$$

In addition, the pore pressure diffusion equation [Eq. 19(*a*)] can be simplified assuming an irrotational displacement field and a semi-infinite domain, and is expressed as

$$\frac{\partial p}{\partial t}-c_f\nabla^2 p=c_{hf}\frac{\partial T}{\partial t} \tag{21}$$

where c_{hf} is a coupling constant given by

$$c_{hf}=\frac{c_f}{\kappa}\left(\beta^{sf}-\frac{\alpha\beta^s}{M_{11}}\right) \tag{22}$$

Notice that although governing equations are written here in their two-dimensional forms [Eqs. (17)–(22)], their coefficients are still dependent on the material elastic properties in the transverse direction. However, since the heat and fluid flux in the z direction vanish under a generalized plane strain idealization, the respective conductivities (κ' and λ') are redundant.

The Navier-type equations (17), heat diffusion equation (18), and the pore pressure diffusion equation in an irrotational displacement field, Eq. (21), constitute a set of complete equations which can be solved to obtain solutions at the stress level. Clearly, the heat diffusion equation is uncoupled from the fluid diffusion and deformation fields and can be solved independently to yield expressions for the temperature distribution. These expressions for the temperature field are then used in the pore pressure diffusion equation [Eq. (21)] to obtain expressions for the pore pressure which can in turn be used within the Navier-type equations [Eq. (17)] to obtain solutions for the stress field.

Isotropic Material

Under the special case where the material is isotropic, the material is identified by two elastic constants, G and ν, two poroelastic constants, α and M, and two thermic coefficients, β^s and β^{sf}. It can be shown that the constitutive equations reduce to

$$\sigma_{ij}=2G\epsilon_{ij}+\frac{2G\nu}{1-2\nu}\epsilon\delta_{ij}-\alpha p\delta_{ij}-\beta^s T\delta_{ij} \tag{23a}$$

$$p=M(\zeta-\alpha\epsilon+\beta^{sf}T) \tag{23b}$$

$$\beta^s=\frac{2G(1+\nu)}{(1-2\nu)}\alpha^s \tag{23c}$$

$$\beta^{sf}=3\alpha\alpha^s+(\alpha^f-3\alpha^s)\phi \tag{23d}$$

The other governing equations are given as

Heat Diffusion

$$\frac{\partial T}{\partial t}-c_h\nabla^2 T=0 \tag{24}$$

Fluid Diffusion

$$\frac{\partial p}{\partial t}-\kappa M\nabla^2 p=-\alpha M\frac{\partial\epsilon}{\partial t}+\beta^{sf}M\frac{\partial T}{\partial t} \tag{25a}$$

$$\frac{\partial\zeta}{\partial t}-c_f[\nabla^2\zeta+\overline{c}\nabla^2 T]=0 \tag{25b}$$

Under the assumptions of an irrotational displacement field and semi-infinite domain, the pore pressure diffusion equation [Eq. 25(*a*)] reduces to

$$\frac{\partial p}{\partial t}-c_f\nabla^2 p=c_{hf}\frac{\partial T}{\partial t} \tag{26}$$

Navier Equations

$$Gu_{i,jj}+\frac{G\nu}{1-2\nu}u_{j,ji}=\alpha p_{,i}+\beta^s T_{,i} \tag{27}$$

and c_f, c_{hf}, and $\overline{c}$ reduce to their isotropic counterparts and are given by

$$c_f=\frac{2G\kappa(1-\nu)(\nu_u-\nu)}{\alpha^2(1-2\nu)^2(1-\nu_u)} \tag{28a}$$

$$c_{hf}=\frac{c_f}{\kappa}\left(\beta^{sf}-\alpha\alpha^s\frac{(1+\nu)}{(1-\nu)}\right) \tag{28b}$$

$$\overline{c}=\left(\alpha\alpha^s\frac{(1+\nu)}{(1-\nu)}-\beta^{sf}\right) \tag{28c}$$

Inclined Borehole Problem

It is assumed that an infinitely long borehole is drilled perpendicular to the isotropic plane of a transversely isotropic poroelastic formation. The borehole is inclined and its axis deviated from the in situ stress orientation. A schematic of the inclined borehole is shown in Fig. 1(*a*). The formation, described using a Cartesian coordinate system $x'y'z'$, is characterized by in situ stresses $S_{x'}$, $S_{y'}$, and $S_{z'}$, virgin pore pressure p_0, and formation temperature T_0. The borehole deviation is measured by two angles φ_z and φ_y, which are the inclination and azimuth angles, respectively. A local coordinate system is chosen to represent the borehole in which the z axis is assumed to coincide with the borehole axis. The far-field in situ stresses in the $x'y'z'$ coordinate system are transformed to the local xyz coordinate system via a transformation matrix [32]. In the local coordinate system, the borehole is subject to normal as well as shear components of stress given as S_x, S_y, S_z, S_{xy}, S_{xz}, and S_{yz}, as shown in Fig. 1(*b*).

The boundary conditions of the problem can be imposed at the far field, $r\to\infty$

$$\sigma_{xx}=-S_x;\quad \sigma_{yy}=-S_y;\quad \sigma_{zz}=-S_z; \tag{29a}$$

$$\tau_{xy}=-S_{xy};\quad \tau_{yz}=-S_{yz};\quad \tau_{xz}=-S_{xz}; \tag{29b}$$

$$p=p_0;\quad T=T_0 \tag{29c}$$

and at the borehole wall, $r=R$

$$\sigma_{rr}=-p_w H(t);\quad \tau_{r\theta}=\tau_{rz}=0; \tag{30a}$$

$$p=p_w H(t);\quad T=T_w H(t) \tag{30b}$$

where p_w is the wellbore pressure, T_w is the wellbore fluid temperature, and $H(t)$ is the Heaviside unit step function.

Owing to linearity of the problem, the solution is obtained employing a superposition of three subproblems [32]. Of these, the first problem is a modified plane strain problem which accounts for the in-plane normal and shear stresses and the pore pressure and temperature perturbations. This problem shows full coupling of the fluid and heat diffusion processes with the deformation. The other two problems, which are described as the uniaxial problem and the anti-plane problem [33], are purely elastic since they do not trigger fluid or heat diffusion.

The boundary conditions in the decomposition scheme are given as follows:

Problem 1:

At far field ($r\to\infty$)

$$\sigma_{xx}=-S_x;\quad \sigma_{yy}=-S_y;\quad \tau_{xy}=-S_{xy} \tag{31a}$$

$$\sigma_{zz}=-\nu'(S_x+S_y)-(\alpha'-2\nu'\alpha)p_0-(\beta^{s'}-2\nu'\beta^s)T_0 \tag{31b}$$

$$\tau_{yz}=\tau_{xz}=0 \tag{31c}$$

$$p=p_0;\quad T=T_0 \tag{31d}$$

At the borehole wall ($r=R$)

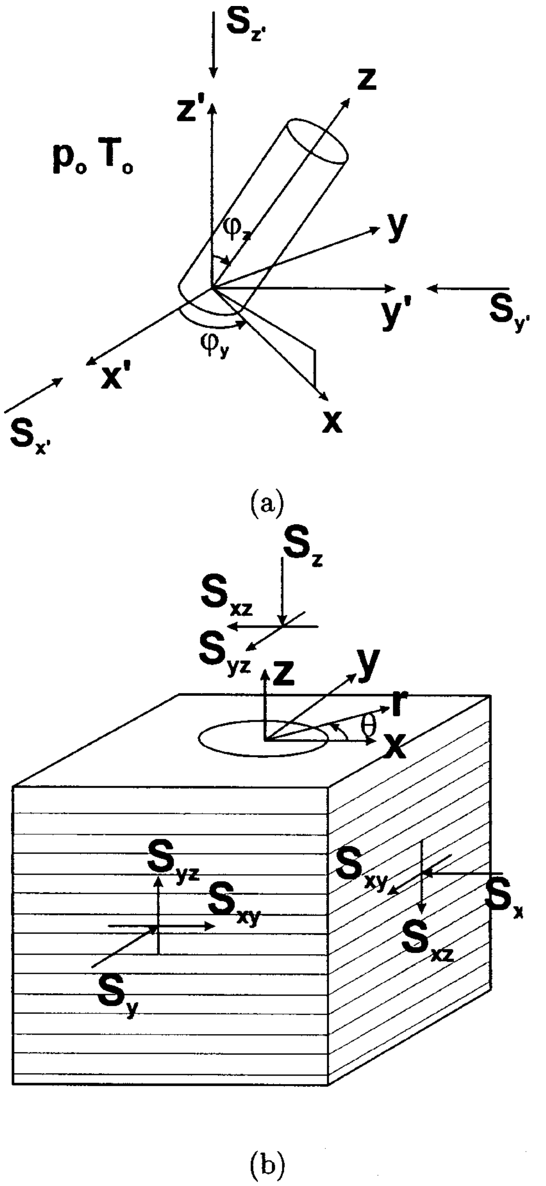

Fig. 1 (***a***) **Schematic of an inclined borehole;** (***b***) **Far-field stresses in the** ***xyz*** **coordinate system**

$$\sigma_{rr}=-p_wH(t);\quad p=p_wH(t);\quad T=T_wH(t) \tag{31e}$$

Problem 2:
At far field ($r\rightarrow\infty$)

$$\sigma_{zz}=-S_z+[\nu'(S_x+S_y)+(\alpha'-2\nu'\alpha)p_0+(\beta^{s'}-2\nu'\beta^s)T_0] \tag{32a}$$

$$\sigma_{xx}=\sigma_{yy}=\tau_{xy}=\tau_{yz}=\tau_{xz}=p=T=0 \tag{32b}$$

At borehole wall ($r=R$)

$$\sigma_{rr}=\tau_{r\theta}=\tau_{rz}=p=T=0 \tag{32c}$$

Problem 3:
At far field ($r\rightarrow\infty$)

$$\sigma_{xx}=\sigma_{yy}=\sigma_{zz}=\tau_{xy}=p=T=0 \tag{33a}$$

$$\tau_{xy}=-S_{xy};\quad \tau_{yz}=-S_{yz} \tag{33b}$$

At the borehole wall ($r=R$)

$$\sigma_{rr}=\tau_{r\theta}=\tau_{rz}=p=T=0 \tag{33c}$$

Table 1 Material parameters

Parameter	Units	Value
Elastic modulus (E)	GPa	9.474
Poisson's ratio (ν)	⋯	0.24
Grain bulk modulus (K_s)	GPa	27.5
Biot's modulus (M)	GPa	8.875
Permeability (k)	md	5.0×10^{-5}
Fluid viscosity (μ)	MPa·s	10^{-9}
Heat diffusivity·(c_h)	m^2/day	0.138 24
Linear expansion coefficient (solid skeleton, α^s)	/°C	6.0×10^{-6}
Volumetric expansion coefficient (fluid, α^s)	/°C	3.0×10^{-4}
Porosity (ϕ)	⋯	0.14

In addition, the solution for the modified plane strain problem is obtained by a decomposition of the boundary conditions into three contributing loading modes [32]. Of these, mode 1 accounts for the hydrostatic part of the boundary stresses, mode 2 accounts for both the pore pressure and temperature perturbations, and mode 3 takes into account the deviant part of the boundary stresses. Only modes 2 and 3 are time dependent, in that mode 2 is characterized by coupling between the pore fluid and heat diffusion processes. Although mode 3 shows characteristics of full poroelastic coupling it is still not affected by temperature perturbations. The boundary conditions at the borehole wall are as follows:

Mode 1:

$$\sigma_{rr}^{(1)}=P_0-p_w;\quad \sigma_{r\theta}^{(1)}=0;\quad p^{(1)}=0;\quad T^{(1)}=0; \tag{34a}$$

Mode 2:

$$\sigma_{rr}^{(2)}=0;\quad \sigma_{r\theta}^{(2)}=0;\quad p^{(2)}=(p_w-p_0);\quad T^{(2)}=(T_w-T_0) \tag{34b}$$

Mode 3:

$$\sigma_{rr}^{(3)}=-S_0\cos 2(\theta-\theta_r);\quad \sigma_{r\theta}^{(3)}=S_0\sin 2(\theta-\theta_r);$$

$$p^{(3)}=0;\quad T^{(3)}=0 \tag{34c}$$

where θ_r is given by

$$\theta_r=\tfrac{1}{2}\tan^{-1}[2S_{xy}/(S_x+S_y)] \tag{35}$$

The complete solution for the inclined borehole problem is obtained by a superposition and is given in the Appendix.

Numerical Examples

The solutions developed in the previous section are applied to assess the effect of the anisotropic parameters on the stress and pore pressure distribution in the vicinity of the borehole. The borehole orientation is given by two angles as shown in Fig. 1(*a*) which are the azimuth, $\varphi_y=30$ deg, and the inclination $\varphi_z=60$ deg. Comparisons with the corresponding isotropic porothermoelastic and the isotropic poroelastic cases are made to highlight the anisotropy effects on the results obtained.

A borehole of radius 0.1 m is assumed to be drilled in the formation characterized by in situ stress and pore pressure gradients given as: $S_{x'}=25$ kPa/m, $S_{y'}=22$ kPa/m, $S_{z'}=29$ kPa/m, $p_0=9.8$ kPa/m. A section at a depth of 1000 m is analyzed where the formation temperature is assumed to be $T_0=125°\mathrm{C}$. The borehole is assumed to be filled with a fluid maintained at a constant pressure given by $p_w=12.0$ MPa. The material properties used in the analysis are given in Table 1.

The degree of anisotropy of material parameters is modeled by selecting appropriate values for the ratios E/E', ν/ν', and $\alpha^s/\alpha^{s'}$. Numerical results are presented in Figs. 2–17, in which negative values of stresses are presented indicating that compression is denoted positive.

Effect of Temperature. The effect of temperature on the pore pressure and stress distributions is examined for the transversely

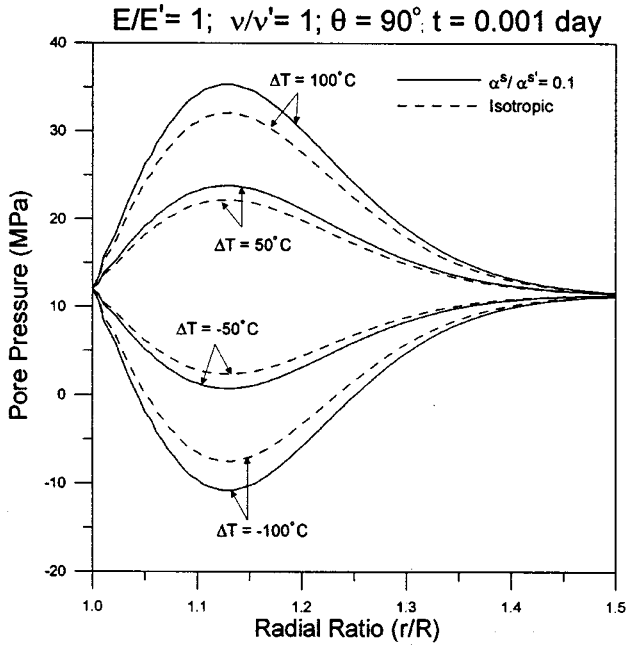

Fig. 2 Pore pressure varying with r/R along θ=90 deg at t=0.001 day for different values of ΔT

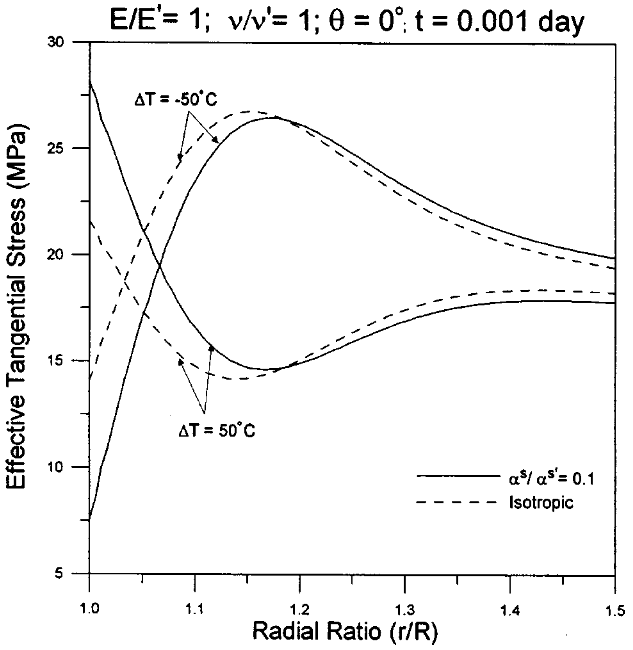

Fig. 4 Effective tangential stress varying with r/R along θ=90 deg at t=0.001 day for different values of ΔT

isotropic material and compared with the isotropic case. Only the anisotropy of thermic coefficients is modeled by fixing ratios for $E/E'=1$ and $\nu/\nu'=1$ and varying $\alpha^s/\alpha^{s'}$. The difference between the wellbore fluid and the formation temperature, ΔT, is varied where $\Delta T=T_w-T_0$. All the results shown in this regard are for a short time interval, i.e., $t=0.001$ day. Figures 2 and 3 show the pore pressure and the effective radial stress distributions, respectively, as a function of the radial distance along the θ=90 deg direction. Figure 2 shows that the temperature perturbation induces a higher pore pressure close the to borehole wall for the cases where ΔT is positive or when the wellbore fluid is at a higher temperature than the formation. On the other hand, a negative value of ΔT results in a reduction of the pore pressure. Also, both effects are more pronounced for the transversely isotropic case. The induced pore pressure (positive or negative) leads to a modification of the effective radial stresses. As presented in Fig. 3, the effective radial stresses are tensile when the wellbore fluid is at a higher temperature than the formation with the tensile magnitude being higher in the transversely isotropic material. In the case of a lower wellbore fluid temperature, the effective radial stresses are compressive in nature. Again, the compressive magnitude is higher for the transversely isotropic case. Figure 4 shows the effective tangential stress as a function of the radial distance along the θ=0 deg direction. As seen from Fig. 4, higher effective tangential stresses are observed when the wellbore fluid has a higher temperature. With a lower wellbore fluid temperature, the effective tangential stresses are reduced. This is also seen clearly in Fig. 5, which presents the variation of the effective tangential stresses around the borehole at $r/R=1$. Figure 5 has been generated using the data given by Li et al. [34] and is given in Table 2. However, as seen from Fig. 5, a lower wellbore fluid temperature leads to significant lowering of the effective tangential stress for the transversely isotropic case.

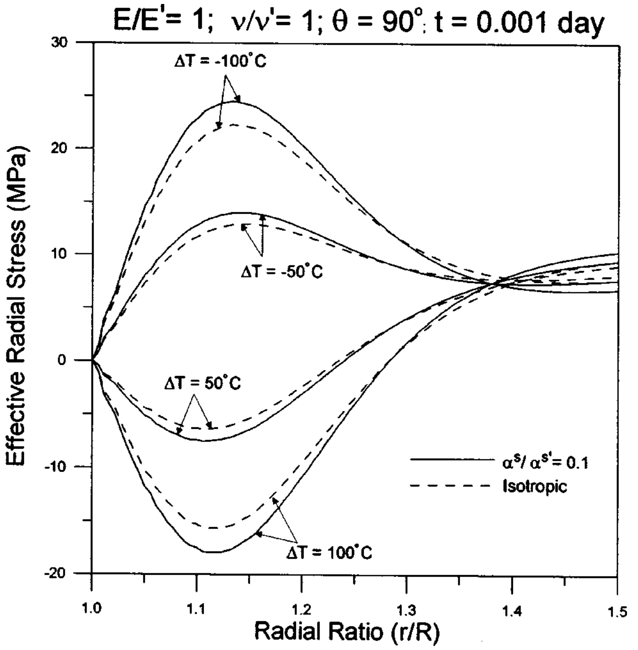

Fig. 3 Effective radial stress varying with r/R along θ=90 deg at t=0.001 day for different values of ΔT

Effect of Anisotropy of Thermic Coefficients. To evaluate the effect of the anisotropic nature of the thermic coefficients on the stress and pore pressure distributions, we fix the ratios for $E/E'=1$ and $\nu/\nu'=1$ and vary $\alpha^s/\alpha^{s'}$. In other words, we assume that material anisotropy is only because of a different $\alpha^{s'}$ value in the transverse direction. Notice that the above choice results only in the variation of values for the thermic coefficients β^s, $\beta^{s'}$, and β^{sf} with all other material coefficients (M_{ijkl}'s, α, and α') assuming their values as in the isotropic case. Data given in Table 1 are used for the analysis. The temperature difference between the wellbore fluid and the formation is assumed to be $\Delta T=50°\mathrm{C}$. Again, results are shown for a short time interval, i.e., $t=0.001$ day.

Figures 6 and 7 show the pore pressure profile as a function of the radial distance along the θ=90 deg direction. In Fig. 6 results are shown for lower thermic coefficient ratios $\alpha^s/\alpha^{s'}=0.1$, 0.5 along with the corresponding isotropic porothermoelastic and po-

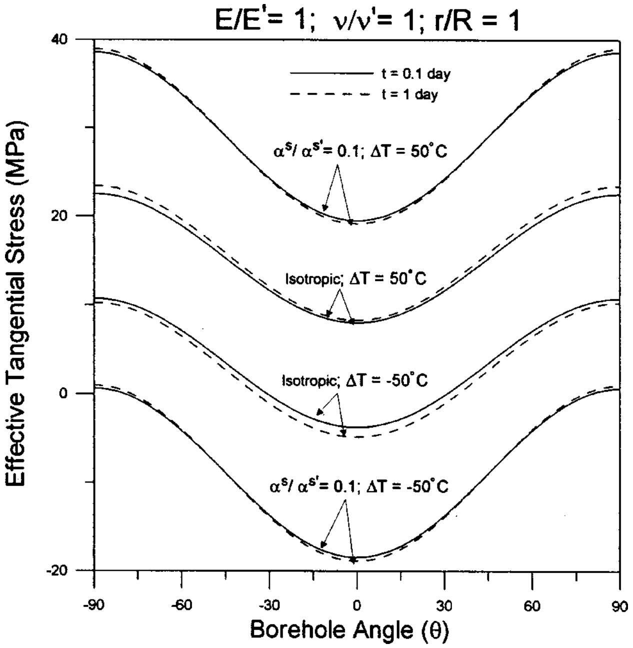

Fig. 5 Effective tangential stress around the wellbore at $r/R=1$ for different values of ΔT and $\alpha^s/\alpha^{s'}$. Curves generated using data given by Li et al., 1998 (Table 2).

roelastic cases. On the other hand, Fig. 7 show results corresponding to higher values of thermic coefficient ratios, i.e., $\alpha^s/\alpha^{s'}=2.0$, 5.0. First, the pore pressure profile in the poroelastic case exhibits the well-known Mandel–Cryer effect. In addition, all the porothermoelastic cases show an increased value of the pore pressure close to the region near the borehole wall.

Figures 8 and 9 show, respectively, the effective radial and tangential stress profiles for the two lower values of the thermic coefficient ratios, i.e., $\alpha^s/\alpha^{s'}=0.1$, 0.5. Tensile effective radial stresses are observed in the vicinity of the borehole which is a natural consequence of the high induced pore pressure as discussed above. Again, as observed in the earlier cases, the tensile magnitude of the stress is more predominant for the case with lower $\alpha^s/\alpha^{s'}$ ratio. In contrast, lower $\alpha^s/\alpha^{s'}$ ratios result in more compressive tangential stresses as can be seen from Fig. 9. However, at a short distance inside the formation, the effective tangential stresses are lowered, which may be again attributed to the effect of the induced pore pressure. The aforementioned observations can be directly linked to the effect of the $\alpha^s/\alpha^{s'}$ ratios on values of β^s, $\beta^{s'}$, and β^{sf}. A simple calculation shows that, for lower values of the $\alpha^s/\alpha^{s'}$ ratio ($\alpha^s/\alpha^{s'}<1.0$), the thermic coefficients β^s, $\beta^{s'}$, and β^{sf} assume higher values. As a result, a higher magnitude of the pore pressure is induced and the total stresses are more compressive.

Table 2 Material parameters (Li et al., 1998)

Parameter	Units	Value
Shear modulus (G)	GPa	8.88
Poisson's ratio (ν)	⋯	0.189
Undrained poisson's ratio (ν_u)	⋯	0.314
Skempton's coefficient (B)	GPa	0.596
Permeability (k)	md	5.0×10^{-5}
Fluid viscosity (μ)	MPa·s	10^{-9}
Heat diffusivity·(c_h)	m^2/s	1.6×10^{-6}
Volumetric expansion coefficient (solid skeleton, α^s)	/°C	18.0×10^{-6}
Volumetric expansion coefficient (fluid, α^s)	/°C	3.0×10^{-4}
Porosity (ϕ)	⋯	0.14
Wellbore fluid pressure	MPa	13.5

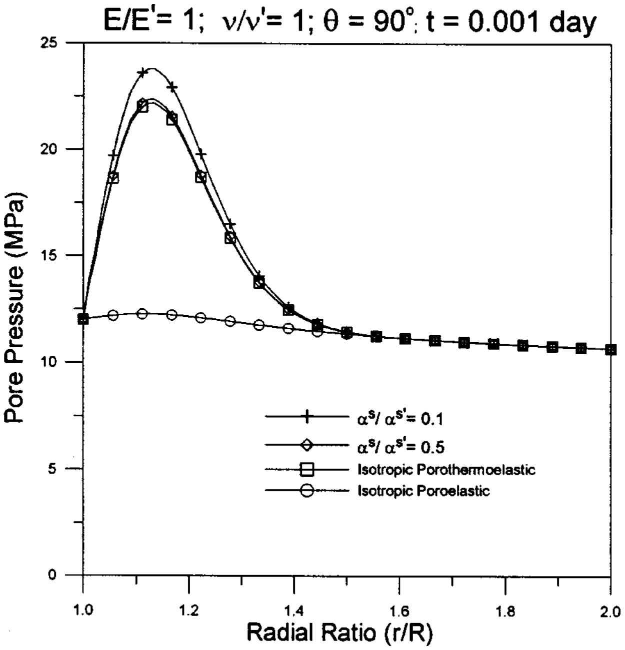

Fig. 6 Pore pressure varying with r/R along θ=90 deg at t=0.001 day

Next, we present results in the form of stress clouds to illustrate the shear failure potential. The "stress clouds" represent the amalgamation of the effective radial, tangential, and shear stresses presented in the $\sqrt{J_2}-S_p$ space, where $\sqrt{J_2}$ is the mean shear stress given by

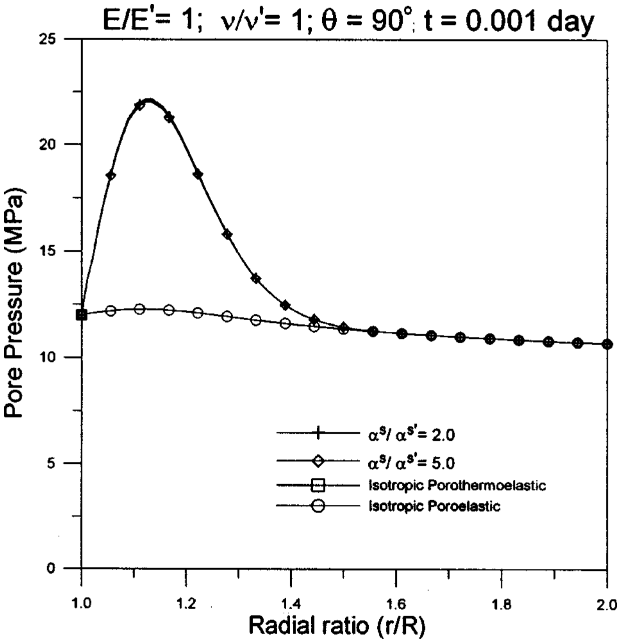

Fig. 7 Pore pressure varying with r/R along θ=90 deg at t=0.001 day

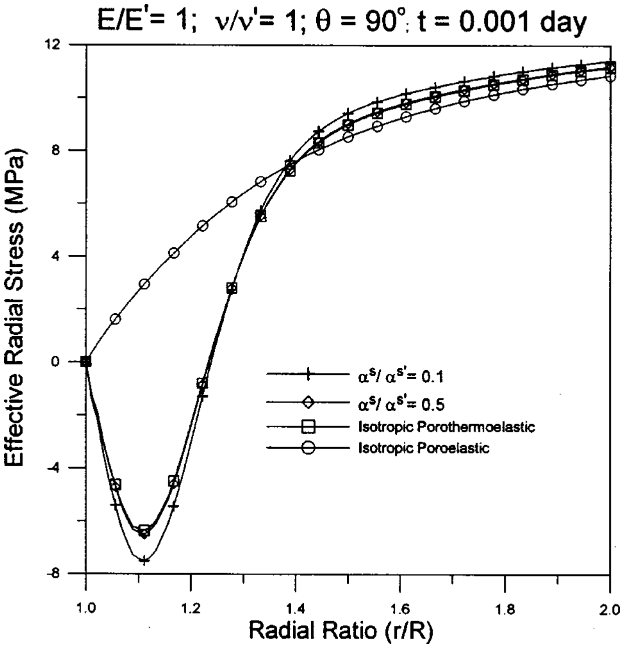

Fig. 8 Effective radial stress varying with r/R along θ=90 deg at t=0.001 day

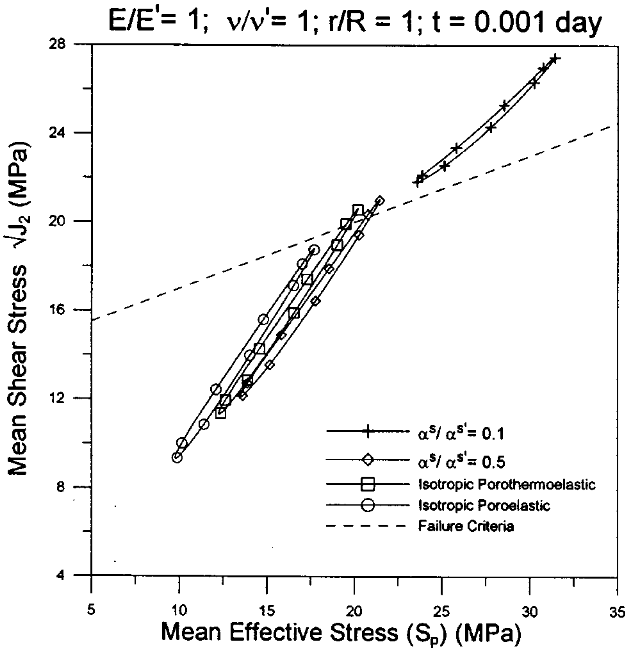

Fig. 10 Stress clouds at r/R=1 and t=0.001 day

$$J_2=\tfrac{1}{6}[(\sigma_{rr}-\sigma_{\theta\theta})^2+(\sigma_{\theta\theta}-\sigma_{zz})^2+(\sigma_{zz}-\sigma_{rr})^2]+\sigma_{r\theta}^2+\sigma_{rz}^2+\sigma_{\theta z}^2 \qquad (36)$$

and S_p is the mean effective stress given by

$$S_p=-\frac{\sigma_{rr}+\sigma_{\theta\theta}+\sigma_{zz}}{3}-p \qquad (37)$$

The stress cloud is obtained by evaluating pairs of $(S_p,\sqrt{J_2})$ by varying the angle around the borehole, θ for a fixed radial distance and time [32]. The stress cloud concept is used in conjunction with the Drucker–Prager criterion for a shear failure analysis. The Drucker–Prager criterion can be expressed as

$$\sqrt{J_2}=3AS_p+D \qquad (38)$$

where A and D are positive material constants. Values of $A=0.1$ and $D=14$ MPa are chosen to represent the failure envelope.

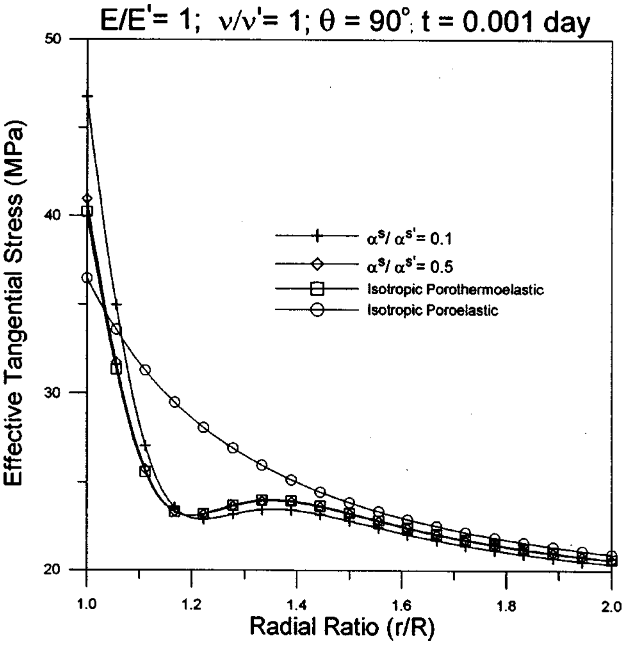

Fig. 9 Effective tangential stress varying with r/R along θ=90 deg at t=0.001 day

Figure 10 shows the stress clouds at the borehole wall, i.e., $r/R=1.0$. It is seen that, for a lower $\alpha^s/\alpha^{s'}$ ratio, the stress cloud moves to the right and higher, pushing it outside the failure envelope. At the borehole wall, the effective radial stresses are always zero. However, there is an increase in the effective tangential stress and the effective axial stress for the lower $\alpha^s/\alpha^{s'}$ ratio. This results in a higher difference between the stresses which causes the mean shear stress, $\sqrt{J_2}$, to increase. With higher effective tangential and axial stresses, the mean effective stress, S_p, is naturally higher. Hence, the stress cloud moves higher and to the right for the lower $\alpha^s/\alpha^{s'}$ ratio. Figure 11 shows the stress clouds at a fractional distance inside the formation given by $r/R=1.1$. The relative magnitudes of the stresses are still quite different for the lower $\alpha^s/\alpha^{s'}$ ratio, resulting in a cloud which is partially outside the failure envelope. Again, Figs. 10 and 11 show that higher thermal expansion coefficients in the transverse direction lead to a higher shear failure potential. Also shown in Fig. 12 are the variations of the effective tangential stresses as a function of the angle around the borehole, θ, at the borehole wall. The tangential stress is more compressive for lower values of the $\alpha^s/\alpha^{s'}$ ratio. A higher wellbore pressure would thus be required to produce tensile zones, indicating that a higher thermal coefficient in the transverse direction results in decreasing the fracturing failure potential.

Time-Dependent Effects. It is interesting to show the behavior of stresses and pore pressure as time progresses. In Figs. 13–15 we show their variation with radial distance, along the θ=90 deg direction for three time intervals, $t=0.001$, 0.01, and 0.1 day. Also, results are shown for two values of the thermal expansion coefficient ratios, i.e., $\alpha^s/\alpha^{s'}=0.1$ and 1.0. It is seen from Fig. 13 that the magnitude of the induced pore pressure

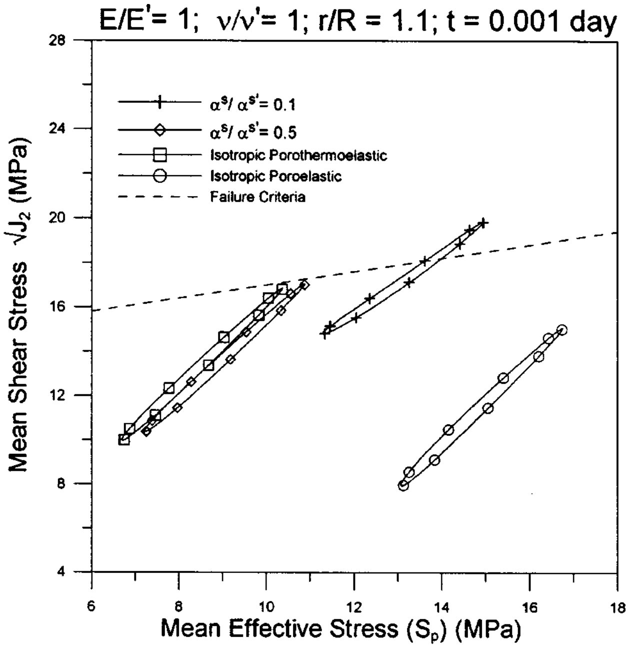

Fig. 11 Stress clouds at $r/R=1$ and $t=0.001$ day

progressively decreases with time. In addition, the location of the maximum pore pressure gradually moves into the formation and away from the borehole wall. The magnitude of the pore pressure for the lower $\alpha^s/\alpha^{s'}$ is, however, always higher. It is seen from Fig. 14 that with the passage of time effective radial stresses in the vicinity of the borehole change from tensile to compressive in nature as a result of the diffusion process. Correspondingly, as time progresses the effective tangential stresses become more compressive, as can be seen from Fig. 15. It may be expected that, as the induced pore pressure front progresses into the formation, it results in lowering the effective stresses, indicating that the potential shear failure zone gradually shifts into the formation.

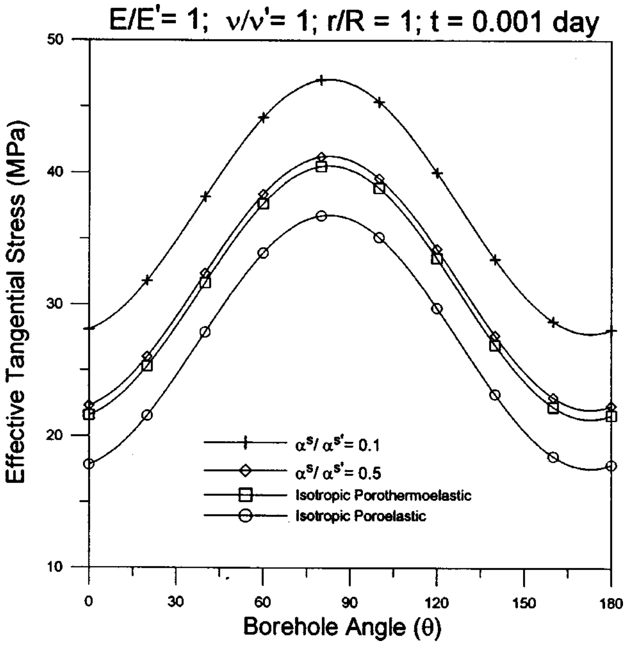

Fig. 12 Effective tangential stress varying with θ at $r/R=1$ and $t=0.001$ day

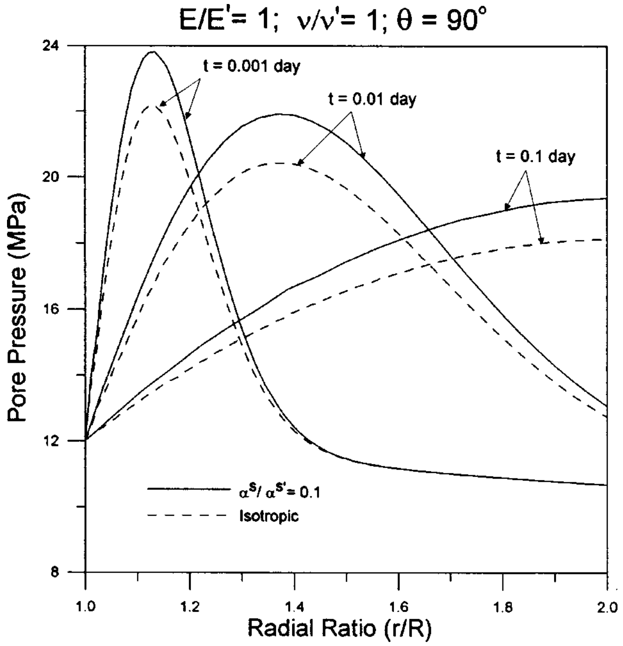

Fig. 13 Pore pressure varying with r/R for $\alpha_m/\alpha'_m=0.1, 1.0$, for $t=0.001, 0.01$, and 0.1 day

Combined Anisotropic Effects. The combined effect of the anisotropy of elastic parameters and the thermal expansion coefficient ratios is analyzed in Figs. 16–18. The pore pressure profiles for four sets of values of the E/E', ν/ν' and $\alpha^s/\alpha^{s'}$ ratios are shown in Fig. 16. It can be seen that for the two curves where $E/E'=2$, $\nu/\nu'=2$, the pore pressure induced is higher for the case when $\alpha^s/\alpha^{s'}=0.1$ as compared to that for the $\alpha^s/\alpha^{s'}=0.5$. In contrast, when $E/E'=0.5$, $\nu/\nu'=0.5$, the pore pressure is lower for the case where $\alpha^s/\alpha^{s'}=0.1$ than for $\alpha^s/\alpha^{s'}=0.5$. A similar observation is made about the tensile nature of the effective radial

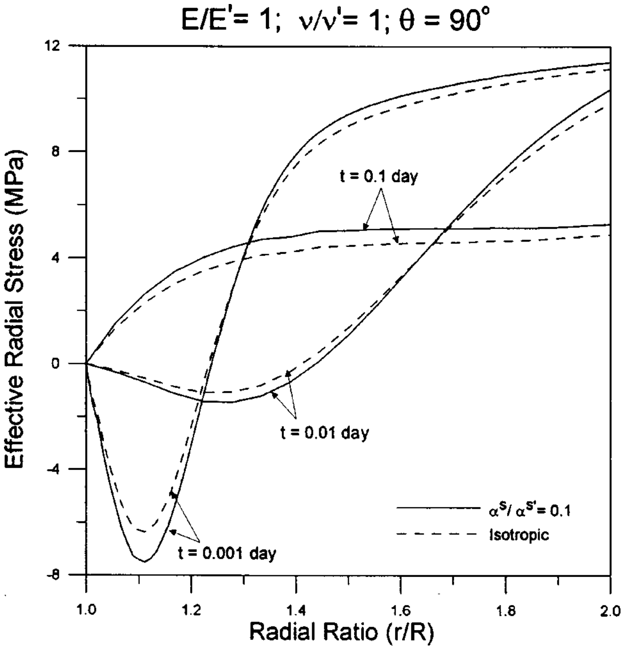

Fig. 14 Effective radial stress varying with r/R for $\alpha_m/\alpha'_m=0.1, 1.0$, for $t=0.001, 0.01$, and 0.1 day

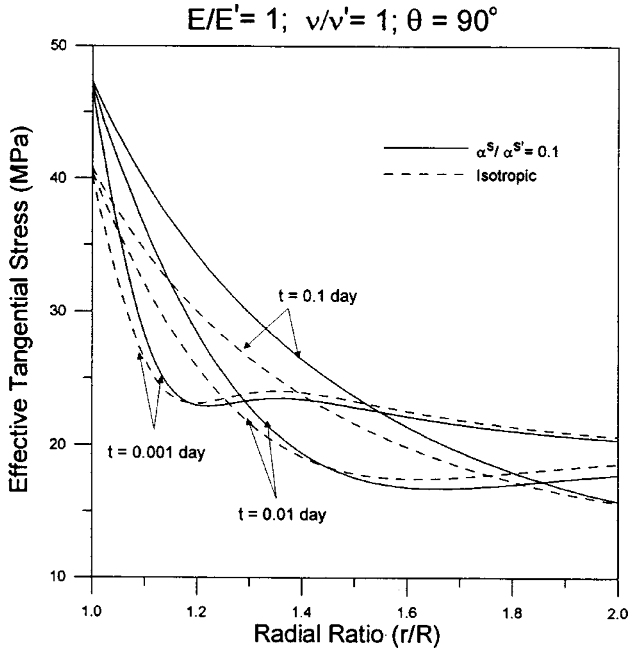

Fig. 15 Effective tangential stress varying with r/R for $\alpha_m/\alpha'_m=0.1$, 1.0, for $t=0.001$, 0.01, and 0.1 day

stresses, shown in Fig. 17. On the other hand, the effective tangential stress shown in Fig. 18 is most compressive for lower ratios of E/E', ν/ν', and $\alpha^s/\alpha^{s'}$. The combined effect of the anisotropy of both the material and thermal expansion coefficients results in complex behavior patterns. A consistent inference which relates the change in values for these ratios to behavior of the stresses and pore pressure may be difficult to draw. However, noting that a change in these ratios results in a corresponding modification of the values for β^s, $\beta^{s'}$, and β^{sf}, a fair prediction is plausible.

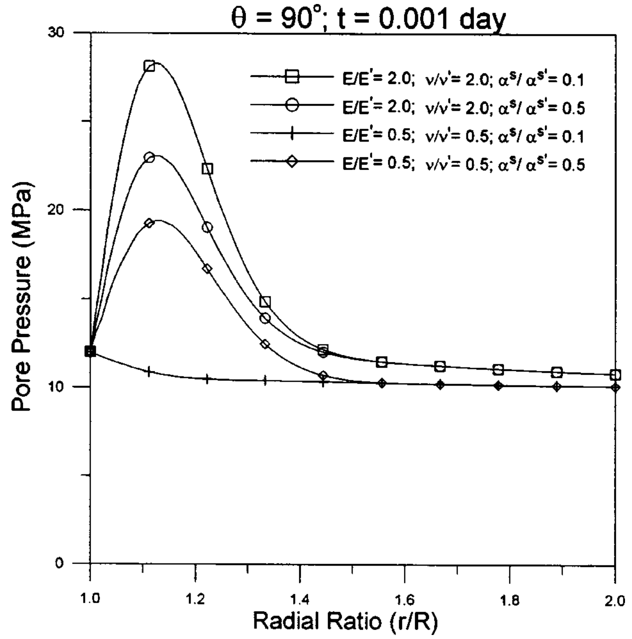

Fig. 16 Pore pressure varying with r/R at $t=0.001$ day for different combinations of E/E', ν/ν', and α_m/α'_m

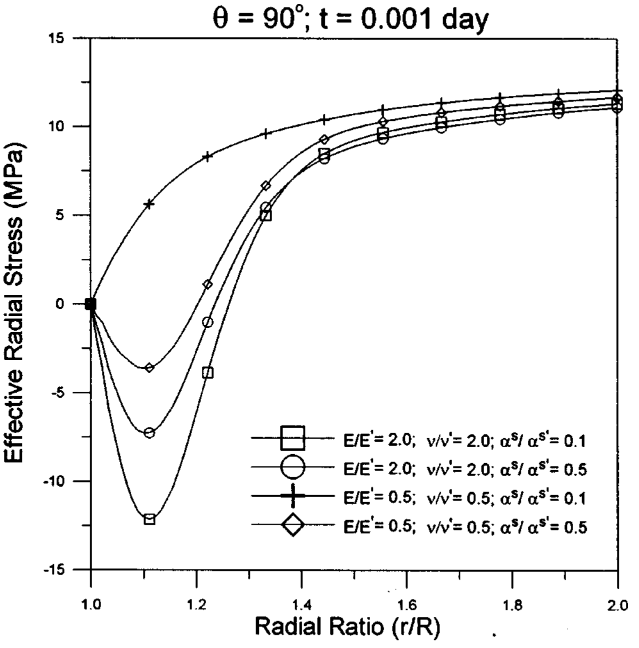

Fig. 17 Effective radial stress varying with r/R at $t=0.001$ day for different combinations of E/E', ν/ν', and α_m/α'_m

Conclusions

The solution for the inclined borehole problem in a transversely isotropic poroelastic medium under nonisothermal conditions has been presented in this paper. A superposition scheme, involving decomposition of the complex problem along with its boundary conditions into simpler problems which can be solved easily, has been used to arrive upon the solution. A parametric analysis has been presented to study the material anisotropy effect on the stress and pore pressure profiles.

The temperature difference leads to a modification of both the pore pressure and stress distributions. The effect of the anisotropy

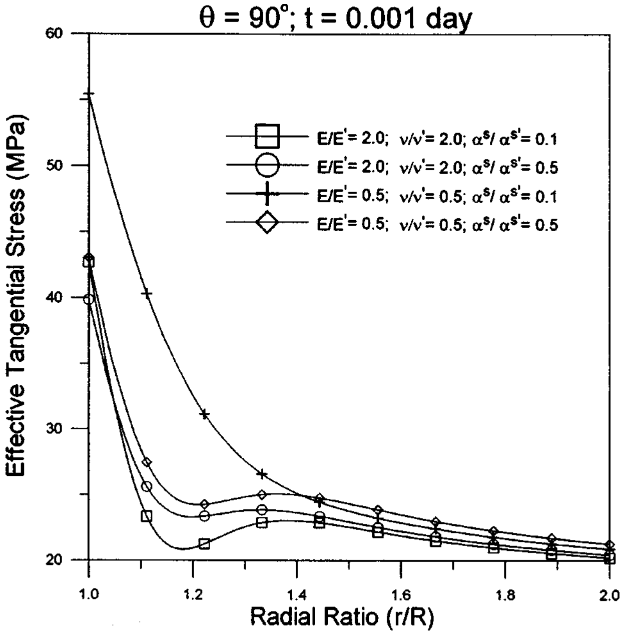

Fig. 18 Effective tangential stress varying with r/R at $t=0.001$ day for different combinations of E/E', ν/ν', and α_m/α'_m

of thermic coefficients has been studied varying the thermal expansion coefficients in the isotropic and transverse directions while keeping the mechanical parameters isotropic. It was found that the effects on the pore pressure and stress profiles are more pronounced when the material has a higher thermal expansion coefficient in the transverse direction. In contrast, the stress and pore pressure responses are more or less comparable to the isotropic case when the thermal expansion coefficients are lower in the transverse direction. The time-dependent variation of the induced pore pressure is characterized by a front which moves into the formation as time progresses. The effect of anisotropy of mechanical parameters has been studied varying E/E' and ν/ν'. It is interesting to note that for ratios of E/E', $\nu/\nu'>1$, the ratios of the thermal expansion coefficients affect the stress and pore pressure distributions in a manner similar to the case when the mechanical parameters are isotropic. On the other hand, when E/E', $\nu/\nu'<1$, the trend of these results (i.e., effect of $\alpha^s/\alpha^{s'}$) is reversed.

Again, it must be noted that applicability of the analytical solution may seem limited for the case where the isotropic plane is perpendicular to the borehole axis. Nevertheless, it serves as a unique tool in both understanding the underlying phenomena, and, validation of numerical analyses in which some of the assumptions may be relaxed subsequently [35,36].

Acknowledgments

The authors would like to thank Dr. Mazen Kanj and Dr. Rajesh Nair for the discussion pertaining to the results and constructive suggestions in preparing this manuscript. The financial support from the Rock Mechanics Consortium, at the PoroMechanics Institute, is also acknowledged.

Appendix

Transversely Isotropic Borehole Solution. The complete solution for the inclined borehole problem in a transversely isotropic medium and an isotropic medium are given.

$$\sigma_{rr}=-P_0+S_0\cos 2(\theta-\theta_r)+\sigma_{rr}^{(1)}+\sigma_{rr}^{(2)}+\sigma_{rr}^{(3)} \tag{A1a}$$

$$\sigma_{\theta\theta}=-P_0-S_0\cos 2(\theta-\theta_r)+\sigma_{\theta\theta}^{(1)}+\sigma_{\theta\theta}^{(2)}+\sigma_{\theta\theta}^{(3)} \tag{A1b}$$

$$\begin{aligned}\sigma_{zz}=&-S_z+[\nu'(S_x+S_y)+(\alpha'-2\nu'\alpha)p_0+(\beta'-2\nu'\beta)T_0]\\&+\nu'(\sigma_{rr}+\sigma_{\theta\theta})-(\alpha'-2\nu'\alpha)p-(\beta'-2\nu'\beta)T\end{aligned} \tag{A1c}$$

$$\sigma_{r\theta}=-P_0+S_0\sin 2(\theta-\theta_r)+\sigma_{r\theta}^{(3)} \tag{A1d}$$

$$\sigma_{rz}=-(S_{xz}\cos\theta+S_{yz}\sin\theta)[1-(R^2/r^2)] \tag{A1e}$$

$$\sigma_{\theta z}=(S_{xz}\sin\theta+S_{yz}\cos\theta)[1+(R^2/r^2)] \tag{A1f}$$

$$p=p_0+p^{(2)}+p^{(3)} \tag{A1g}$$

$$T=T_0+T^{(2)} \tag{A1h}$$

where $\sigma_{rr}^{(1)}$, $\sigma_{rr}^{(2)}$, $\sigma_{rr}^{(3)}$, $\sigma_{\theta\theta}^{(1)}$, $\sigma_{\theta\theta}^{(2)}$, $\sigma_{\theta\theta}^{(3)}$, $\sigma_{r\theta}^{(3)}$, $p^{(2)}$, $p^{(3)}$, and $T^{(2)}$ are obtained by solving the modified plane strain problem as indicated earlier. In the above, θ_r, P_0, and S_0 are given by

$$\theta_r=\tfrac{1}{2}\tan^{-1}[2S_{xy}/(S_x+S_y)] \tag{A2a}$$

$$P_0=(S_x+S_y)/2 \tag{A2b}$$

$$S_0=0.5\sqrt{(S_x-S_y)^2+4S_{xy}^2} \tag{A2c}$$

The expressions for $\sigma_{rr}^{(1)}$, $\sigma_{rr}^{(2)}$, $\sigma_{rr}^{(3)}$, $\sigma_{\theta\theta}^{(1)}$, $\sigma_{\theta\theta}^{(2)}$, $\sigma_{\theta\theta}^{(3)}$, $\sigma_{r\theta}^{(3)}$, $p^{(2)}$, $p^{(3)}$, and $T^{(2)}$ are obtained as follows [32,37]:

Solutions for Mode 1:

$$\sigma_{rr}^{(1)}=H(t)[P_0-p_w]\left(\frac{R^2}{r^2}\right) \tag{A3a}$$

$$\sigma_{\theta\theta}^{(1)}=-H(t)[P_0-p_w]\left(\frac{R^2}{r^2}\right) \tag{A3b}$$

Solutions for mode 2 and mode 3 are obtained in the Laplace domain and are inverted to the time-domain using the Stehfest algorithm [37].

Solutions for Mode 2:

$$s\tilde{T}^{(2)}=(T_w-T_0)\Phi(\omega) \tag{A4a}$$

$$s\tilde{p}^{(2)}=G_1\Phi(\xi)+G_2\Phi(\omega) \tag{A4b}$$

$$\begin{aligned}s\tilde{\sigma}_{rr}^{(2)}=&\,\alpha\left(1-\frac{M_{12}}{M_{11}}\right)\{\mathsf{F}_1\Psi(\xi)+\mathsf{F}_2\Psi(\omega)\}+\beta^s\left(1-\frac{M_{12}}{M_{11}}\right)\{(T_w\\&-T_0)\Psi(\omega)\}\end{aligned} \tag{A4c}$$

$$\begin{aligned}s\tilde{\sigma}_{\theta\theta}^{(2)}=&-\alpha\left(1-\frac{M_{12}}{M_{11}}\right)\{\mathsf{F}_1\Omega(\xi)+\mathsf{F}_2\Omega(\omega)\}-\beta^s\left(1-\frac{M_{12}}{M_{11}}\right)\{(T_w\\&-T_0)\Omega(\omega)\}\end{aligned} \tag{A4d}$$

Solutions for Mode 3:

$$\tilde{p}^{(3)}=\frac{S_0}{s}\left(\frac{c_f}{2G\kappa}C_1\mathrm{K}_2(\xi r)+A_1C_2\frac{R^2}{r^2}\right)\cos 2(\theta-\theta_r) \tag{A5a}$$

$$\begin{aligned}\tilde{\sigma}_{rr}^{(3)}=&\frac{S_0}{s}\left[A_1C_1\left(\frac{1}{\xi r}\mathrm{K}_1(\xi r)+\frac{6}{(\xi r)^2}\mathrm{K}_2(\xi r)\right)-A_2C_2\frac{R^2}{r^2}\right.\\&\left.-3C_3\frac{R^4}{r^4}\right]\cos 2(\theta-\theta_r)\end{aligned} \tag{A5b}$$

$$\begin{aligned}\tilde{\sigma}_{\theta\theta}^{(3)}=&\frac{S_0}{s}\left[-A_1C_1\left(\frac{1}{\xi r}\mathrm{K}_1(\xi r)\left(1+\frac{6}{(\xi r)^2}\right)\mathrm{K}_2(\xi r)\right)\right.\\&\left.+3C_3\frac{R^4}{r^4}\right]\cos 2(\theta-\theta_r)\end{aligned} \tag{A5c}$$

$$\begin{aligned}\tilde{\tau}_{r\theta}^{(3)}=&\frac{S_0}{s}2A_1C_1\left(\frac{1}{\xi r}\mathrm{K}_1(\xi r)+\frac{3}{(\xi r)^2}\mathrm{K}_2(\xi r)\right)-\frac{A_2}{2}C_2\frac{R^2}{r^2}\\&-3C_3\frac{R^4}{r^4}\sin 2(\theta-\theta_r)\end{aligned} \tag{A5d}$$

where K_n is the modified Bessel function of the second kind of order n. In the above

$$\Phi(x)=\left[\frac{\mathrm{K}_0(xr)}{\mathrm{K}_0(xR)}\right] \tag{A6a}$$

$$\Psi(x)=\left[\frac{\mathrm{K}_1(xr)}{xr\mathrm{K}_0(xR)}-\frac{R\mathrm{K}_1(xR)}{xr^2\mathrm{K}_0(xR)}\right] \tag{A6b}$$

$$\Omega(x)=\left[\frac{\mathrm{K}_1(xr)}{xr\mathrm{K}_0(xR)}-\frac{R\mathrm{K}_1(xR)}{xr^2\mathrm{K}_0(xR)}+\frac{\mathrm{K}_0(xr)}{\mathrm{K}_0(xR)}\right] \tag{A6c}$$

$$\mathsf{F}_1=\left[(p_w-p_0)-\left(\frac{c_{hf}}{(1-c_f/c_h)}\right)(T_w-T_0)\right] \tag{A6d}$$

$$\mathsf{F}_2=\left(\frac{c_{hf}}{(1-c_f/c_h)}\right)(T_w-T_0) \tag{A6e}$$

$$\omega=\sqrt{\frac{s}{c_h}};\quad \xi=\sqrt{\frac{s}{c_f}} \tag{A6f}$$

The constants C_1, C_2, C_3

$$C_1=\frac{4}{2A_1(B_3-B_2)-A_2B_1} \tag{A7a}$$

$$C_2=-\frac{4B_1}{2A_1(B_3-B_2)-A_2B_1} \tag{A7b}$$

$$C_3=\frac{2A_1(B_2+B_3)+3A_2B_1}{3[2A_1(B_3-B_2)-A_2B_1]} \tag{A7c}$$

in which

$$A_1=\frac{\alpha M}{M_{11}+\alpha^2 M} \tag{A8a}$$

$$A_2=\frac{M_{11}+M_{12}+2\alpha^2 M}{M_{11}+\alpha^2 M} \tag{A8b}$$

$$B_1=\frac{M_{11}}{2G\alpha}\mathrm{K}_2(\xi R) \tag{A8c}$$

$$B_2=\frac{1}{\xi R}\mathrm{K}_1(\xi R)+\frac{6}{(\xi R)^2}\mathrm{K}_2(\xi R) \tag{A8d}$$

$$B_3=2\left(\frac{1}{\xi R}\mathrm{K}_1(\xi R)+\frac{3}{(\xi R)^2}\mathrm{K}_2(\xi R)\right) \tag{A8e}$$

Isotropic Borehole Solution

Complete solution for the inclined borehole in an isotropic material is obtained using the same decomposition scheme and Eqs. (*A*1*a*)–(*A*1*h*), with the added condition that $\alpha=\alpha'$ and $\beta^s=\beta^{s'}$. Solutions for $\sigma_{rr}^{(1)}$, $\sigma_{rr}^{(2)}$, $\sigma_{rr}^{(3)}$, $\sigma_{\theta\theta}^{(1)}$, $\sigma_{\theta\theta}^{(2)}$, $\sigma_{\theta\theta}^{(3)}$, $\sigma_{r\theta}^{(3)}$, $p^{(2)}$, $p^{(3)}$, and $T^{(2)}$ for the inclined borehole in the isotropic medium were obtained by Li et al. [34]. Their solutions have been corrected for some of the typographical errors and reproduced for clarification below.

Solutions for Mode 1:

Solutions for $\sigma_{rr}^{(1)}$ and $\sigma_{\theta\theta}^{(1)}$ are the same as given in Eqs. (*A*3*a*) and (*A*3*b*).

Solutions for Mode 2:

$$s\tilde{T}^{(2)}=(T_w-T_0)\Phi(\omega) \tag{A9a}$$

$$s\tilde{p}^{(2)}=\mathsf{F}_1\Phi(\xi)+\mathsf{F}_2\Phi(\omega) \tag{A9b}$$

$$s\tilde{\sigma}_{rr}^{(2)}=\alpha\left(\frac{1-2\nu}{1-\nu}\right)\{\mathsf{F}_1\Psi(\xi)+\mathsf{F}_2\Psi(\omega)\}+\beta^s\left(\frac{1-2\nu}{1-\nu}\right)\{(T_w-T_0)\Psi(\omega)\} \tag{A9c}$$

$$s\tilde{\sigma}_{\theta\theta}^{(2)}=-\alpha\left(\frac{1-2\nu}{1-\nu}\right)\{\mathsf{F}_1\Omega(\xi)+\mathsf{F}_2\Omega(\omega)\}-\beta^s\left(\frac{1-2\nu}{1-\nu}\right)\{(T_w-T_0)\Omega(\omega)\} \tag{A9d}$$

The functions $\Phi(x)$, $\Psi(x)$, and $\Omega(x)$, F_1, F_2 are as defined in Eqs. (*A*6*a*)–(*A*6*c*).

Solutions for Mode 3:

$$\tilde{p}^{(3)}=\frac{S_0}{s}\left[\frac{B^2(1-\nu)(1+\nu_u)^2}{9(1-\nu_u)(\nu_u-\nu)}C_1\mathrm{K}_1(\xi r)+\frac{B(1+\nu_u)}{3(1-\nu_u)}C_2\frac{R^2}{r^2}\right]\cos 2(\theta-\theta_r) \tag{A10a}$$

$$\tilde{\sigma}_{rr}^{(3)}=\frac{S_0}{s}\left[\frac{B(1+\nu_u)}{3(1-\nu_u)}C_1\left(\frac{1}{\xi r}\mathrm{K}_1(\xi r)+\frac{6}{(\xi r)^2}\mathrm{K}_2(\xi r)\right)-\frac{1}{1-\nu_u}C_2\frac{R^2}{r^2}-3C_3\frac{R^4}{r^4}\right]\cos 2(\theta-\theta_r) \tag{A10b}$$

$$\tilde{\sigma}_{\theta\theta}^{(3)}=\frac{S_0}{s}\left[-\frac{B(1+\nu_u)}{3(1-\nu_u)}C_1\left(\frac{1}{\xi r}\mathrm{K}_1(\xi r)\left[1+\frac{6}{(\xi r)^2}\right]\mathrm{K}_2(\xi r)\right)+3C_3\frac{R^4}{r^4}\right]\cos 2(\theta-\theta_r) \tag{A10c}$$

$$\tilde{\tau}_{r\theta}^{(3)}=\frac{S_0}{s}\left[\frac{2B(1+\nu_u)}{3(1-\nu_u)}C_1\left(\frac{1}{\xi r}\mathrm{K}_1(\xi r)+\frac{3}{(\xi r)^2}\mathrm{K}_2(\xi r)\right)-\frac{1}{2(1-\nu_u)}C_2\frac{R^2}{r^2}-3C_3\frac{R^4}{r^4}\right]\sin 2(\theta-\theta_r) \tag{A10d}$$

where B is the Skempton's pore pressure coefficient, ν_u is the undrained Poisson's ratio, and K_n is the modified Bessel function of the second kind of order n.

The constants C_1, C_2, C_3 are given by

$$C_1=-\frac{12\xi R(1-\nu_u)(\nu_u-\nu)}{B(1+\nu_u)(D_2-D_1)} \tag{A11a}$$

$$C_2=\frac{4(1-\nu_u)D_2}{(D_2-D_1)} \tag{A11b}$$

$$C_3=-\frac{\xi R(D_2+D_1)+8(\nu_u-\nu)\mathrm{K}_2(\xi R)}{\xi R(D_2-D_1)} \tag{A11c}$$

in which the constants D_1 and D_2 are given by

$$D_1=2(\nu_u-\nu)\mathrm{K}_1(\xi R) \tag{A12a}$$

$$D_2=\xi R(1-\nu)\mathrm{K}_2(\xi R) \tag{A12b}$$

References

[1] Biot, M. A., 1941, "General Theory of Three-Dimensional Consolidation," J. Appl. Phys., **12**, pp. 155–164.
[2] Biot, M. A., 1955, "Theory of Elasticity and Consolidation of a Porous Anisotropic Solid," J. Appl. Phys., **26**, pp. 182–185.
[3] Bear, J., and Corapcioglu, M. Y., 1981, "A Mathematical Model for Consolidation in a Thermoelastic Aquifer Due to Hot Water Injection or Pumping," Water Resour. Res., **17**(3), pp. 723–736.
[4] Kurashige, M., 1989, "A Thermoelastic Theory of Fluid-Filled Porous Materials," Int. J. Solids Struct., **25**(9), pp. 1039–1052.
[5] Coussy, O., 1989, "A General Theory of Thermoporoelastoplasticity for Saturated Porous Materials," Transp. Porous Media, **4**, pp. 281–293.
[6] Coussy, O., 1995, *Mechanics of Porous Continua*, Wiley, New York.
[7] Katsube, N., 1988, "The Anisotropic Thermomechanical Constitutive Theory for Fluid-Filled Porous Materials With Solid/Fluid Outer Boundaries," Int. J. Solids Struct., **24**(4), pp. 375–380.
[8] Utsugida, Y., 1985, "Coupled Analysis of Flow and Heat Around a High-Level Nuclear Waste Repository," in Proc. 5th Int. Conf. Numerical Methods in Geomechanics, Nagoya, Balkema, Rotterdam, pp. 711–716.
[9] Brownell, Jr., D. H., Garg, S. K., and Pritchett, J. W., 1977, "Governing Equations for Geothermal Reservoirs," Water Resour. Res., **13**, pp. 929–934.
[10] Rice, J. R., and Cleary, M. P., 1976, "Some Basic Stress Diffusion Solutions for Fluid-Saturated Elastic Porous Media With Compressible Constituents," Rev. Geophys. Space Phys., **14**(4), pp. 227–241.
[11] Thompson, M., and Willis, J. R., 1991, "A Reformulation of the Equations of Anisotropic Poroelasticity," ASME J. Appl. Mech., **58**, pp. 612–616.
[12] Wang, H., 2000, *Theory of Linear Poroelasticity With Applications to Geomechanics and Hydrogeology*, Princeton University Press, Princeton.
[13] Booker, J. R., and Savvidou, C., 1984, "Consolidation Around a Spherical Heat Source," Int. J. Solids Struct., **20**, pp. 1079–1090.
[14] Booker, J. R., and Savvidou, C., 1985, "Consolidation Around a Point Heat Source," Int. J. Numer. Analyt. Meth. Geomech., **9**, pp. 173–184.
[15] McTigue, D. F., 1986, "Thermoelastic Response of Fluid-Saturated Porous Rock," J. Geophys. Res., **91**(B9), pp. 9533–9542.
[16] McTigue, D. F., 1990, "Flow to a Heated Borehole in Porous, Thermoelastic Rock: Analysis," Water Resour. Res., **26**(8), pp. 1763–1774.

[17] Kurashige, M., 1992, ‘‘Thermal Stresses of a Fluid-Saturated Poroelastic Hollow Cylinder,’’ JSME Int. J., **35**(4), pp. 386–391.
[18] Kodashima, T., and Kurashige, M., 1996, ‘‘Thermal Stresses in a Fluid-Saturated Poroelastic Hollow Sphere,’’ J. Therm. Stresses, **19**, pp. 139–151.
[19] Cheng, A. H.-D., 1998, ‘‘Material Coefficients of Anisotropic Poroelasticity,’’ Int. J. Rock Mech. Min. Sci., **34**, pp. 183–193.
[20] Abousleiman, Y., and Cui, L., 2000, ‘‘The Theory of Anisotropic Poroelasticity With Applications,’’ *Modeling and Applications in Geomechanics*, edited by M. Zaman, J. Booker, and G. Gioda, Wiley, New York.
[21] Abousleiman, Y., Cheng, A. H.-D., Cui, L., Detournay, E., and Roegiers, J.-C., 1996, ‘‘Mandel’s Problem Revisited,’’ Geotechnique, **46**(2), pp. 187–195.
[22] Abousleiman, Y., and Cui, L., 1998, ‘‘Poroelastic Solutions in Transversely Isotropic Media for Wellbore and Cylinder,’’ Int. J. Solids Struct., **35**(34/35), pp. 4905–4929.
[23] Li, X., 1992, ‘‘A Generalized Theory of Thermoelasticity for an Anisotropic Medium,’’ Int. J. Eng. Sci., **30**(5), pp. 571–577.
[24] Sharma, J. N., and Kumar, V., 1996, ‘‘On the Axisymmetric Problems of Generalized Anisotropic Thermoelasticity,’’ J. Therm. Stresses, **19**, pp. 781–794.
[25] Sharma, J. N., and Kumar, V., 1997, ‘‘Plane Strain Problems of Transverse Isotropic Thermoelastic Media,’’ J. Therm. Stresses, **20**, pp. 463–476.
[26] Nowacki, W., 1962, *Thermoelasticity*, Addison-Wesley, Reading, MA.
[27] Nowinski, J. L., 1978, *Theory of Thermoelasticity With Applications*, Sijthoff & Noordhoff, Groningen.
[28] Ekbote, S., Abousleiman, Y., and Zaman, M. M., 2000, ‘‘Porothermoelastic Solution for an Inclined Borehole in Transversely Isotropic Porous Media,’’ Fourth North American Rock Mechanics Symposium. Seattle, WA, Sept. 5–10.
[29] Ekbote, S., 2002, ‘‘Poromechanics Wellbore Stability: Theory and Applications,’’ Ph.D. dissertation, The University of Oklahoma.
[30] Abousleiman, Y., and Ekbote, S., 1999, ‘‘Porothermoelasticity in Transversely Isotropic Porous Materials,’’ The IUTAM Symposium on Theoretical and Numerical Methods in Continuum Mechanics of Porous Materials. Stuttgart, Germany, Sept. 5–10, pp. 145–152.
[31] Bird, R. B., Stewart, W. E., and Lightfoot, E. N., 1960, *Transport Phenomena*, Wiley, New York.
[32] Cui, L., Cheng, A. H.-D., and Abousleiman, Y., 1997, ‘‘Poroelastic Solution of an Inclined Borehole,’’ ASME J. Appl. Mech., **64**, pp. 32–38.
[33] Cheng, A. H.-D., 1997, ‘‘On Generalized Plane Strain Poroelasticity,’’ Int. J. Rock Mech. Min. Sci., **35**, pp. 199–205.
[34] Li, X., Cui, L., and Roegiers, J.-C., 1998, ‘‘Thermoporoelastic Modeling of Wellbore Stability in Non-Hydrostatic Stress Field,’’ Int. J. Rock Mech. Min. Sci., **34**(3/4), pp. 829–835.
[35] Nair, R., Abousleiman, Y., and Zaman, M. M., 2002, ‘‘A Finite Element Porothermoelastic Model for Dual-Porosity Media,’’ Int. J. Numer. Analyt. Meth. Geomech., **28**(9), pp. 875–898.
[36] Carslaw, H. S., and Jaegar, J. C., 1959, *Conduction of Heat in Solids*, Oxford University Press, New York.
[37] Stehfest, H., 1970, ‘‘Numerical Inversion of Laplace Transforms,’’ Commun. ACM, **13**, pp. 47–49; **13**, p. 624.

Y. J. Liu[1]

N. Nishimura

Y. Otani

Academic Center for Computing and Media Studies,
Kyoto University,
Kyoto 606-8501, Japan

T. Takahashi

Computational Astrophysics Labortory,
RIKEN,
Wako 351-0198, Japan

X. L. Chen

Department of Mechanical, Industrial and Nuclear Engineering,
University of Cincinnati,
Cincinnati, OH 45221-0072

H. Munakata

Academic Center for Computing and Media Studies,
Kyoto University,
Kyoto 6068501, Japan

A Fast Boundary Element Method for the Analysis of Fiber-Reinforced Composites Based on a Rigid-Inclusion Model

A new boundary element method (BEM) is developed for three-dimensional analysis of fiber-reinforced composites based on a rigid-inclusion model. Elasticity equations are solved in an elastic domain containing inclusions which can be assumed much stiffer than the host elastic medium. Therefore the inclusions can be treated as rigid ones with only six rigid-body displacements. It is shown that the boundary integral equation (BIE) in this case can be simplified and only the integral with the weakly-singular displacement kernel is present. The BEM accelerated with the fast multipole method is used to solve the established BIE. The developed BEM code is validated with the analytical solution for a rigid sphere in an infinite elastic domain and excellent agreement is achieved. Numerical examples of fiber-reinforced composites, with the number of fibers considered reaching above 5800 and total degrees of freedom above 10 millions, are solved successfully by the developed BEM. Effective Young's moduli of fiber-reinforced composites are evaluated for uniformly and "randomly" distributed fibers with two different aspect ratios and volume fractions. The developed fast multipole BEM is demonstrated to be very promising for large-scale analysis of fiber-reinforced composites, when the fibers can be assumed rigid relative to the matrix materials. [DOI: 10.1115/1.1825436]

1 Introduction

Modeling can play an important role in the analysis and design of fiber-reinforced composite materials. Mechanical properties and possible failure modes of these composites can be predicted early during the design stage using modeling techniques. However, modeling fiber-reinforced materials presents many challenges to numerical methods. Fibers in a composite can have different properties, shapes and sizes. They can be straight or curved, short or long, aligned or oriented arbitrarily, and distributed uniformly or randomly. All these factors make estimates of the mechanical properties of fiber-reinforced composites very difficult using the numerical methods. Often a representative volume element (RVE) containing only a few fibers may not be sufficient for accurately determining the effective properties of a composite. Large-scale models with hundreds or thousands of fibers may be deemed necessary in many situations. Unfortunately, modeling fibers, matrix, and possibly interphases between them as separate material domains in large-scale models is beyond the limit of current computing power. This has been the main reason that most of the current models of the fiber-reinforced composites based on the boundary integral equation and boundary element method (BIE/BEM) are two-dimensional ones with one or a few fibers considered in the RVEs (see, e.g., Refs. [1–8]). These models are adequate for the study of local properties, such as interfacial stresses and fractures, of a composite, but are often not sufficient for evaluating the overall mechanical properties of the composite. Therefore, models that can capture the overall behaviors of a composite without overwhelming computing resources are needed and will be beneficial in large-scale simulations. Using the rigid-inclusion model seems to be a feasible first step in large-scale simulations for investigating the interactions of fibers, load transfer mechanism and effective properties of a composite. The rigid-inclusion approximation is valid when the fibers have much higher values of stiffness compared with that of the matrix. This approximation can significantly reduce the modeling complexity for the analysis, as will be demonstrated in this paper.

There are two approaches regarding whether or not to further simplify the geometries for modeling rigid inclusions. One approach treats the rigid inclusions as they are without further simplifying their geometries, which consequently requires 3D models for rigid inclusions. The other approach treats slender rigid inclusions, as in the case of long-fiber-reinforced composites, as rigid-line inclusions, where the geometry of an inclusion is reduced to a *line*. This rigid-line inclusion model is valid when the aspect ratio of an inclusion is large. It is also efficient in modeling of rigid-line inclusions because of the simplified geometry. Only 2D models of rigid-line inclusions in a medium have been studied so far.

In the analysis of rigid-line inclusions, also called anticracks in a 2D elastic domain [9], many research results have been reported in the literature. Boundary integral equation and boundary element method have been found especially suitable for the analysis of rigid-line inclusions, since cracks in 2D, the counter part of rigid lines, have been studied intensively by using the BIEs. Many of the results for crack analysis can be extended readily to the analysis of rigid-line inclusions. In the early 1990s, the group of Hu, Chandra and Huang made considerable contributions to the study of rigid-line inclusions in a matrix using the boundary inte-

---

[1] Corresponding author. On leave from the Department of Mechanical, Industrial and Nuclear Engineering, University of Cincinnati, P.O. Box 210072, Cincinnati, OH 45221-0072. e-mail: yijun.liu@uc.edu

Contributed by the Applied Mechanics Division of THE AMERICAN SOCIETY OF MECHANICAL ENGINEERS for publication in the ASME JOURNAL OF APPLIED MECHANICS. Manuscript received by the Applied Mechanics Division, January 29, 2004; final revision; May 22, 2004. Associate Editor: M. Mukherjee. Discussion on the paper should be addressed to the Editor, Professor Robert M. McMeeking, Journal of Applied Mechanics, Department of Mechanical and Environmental Engineering, University of California-Santa Barbara, Santa Barbara, CA 93106-5070, and will be accepted until four months after final publication of the paper itself in the ASME JOURNAL OF APPLIED MECHANICS.

gral equation method for 2D cases. Some of their analytical and numerical results can be found in Refs. [10–14]. In these works, the rigid lines embedded in an infinite space are represented by distributions of tractions along the rigid lines (as compared to distributions of dislocations for cracks) and integral equations are established using the Green's functions. The interactions of rigid lines with cracks and the effects of rigid lines on the effective elastic material properties of composites were successfully studied using this approach for 2D models [10–14]. Extensive review of the earlier theoretical work on the elasticity study of rigid-line inclusions in a solid can also be found in Refs. [10–14]. Recently, there seems to be a renewed interest in the study of rigid-line inclusions using the BIEs. In Ref. [15], Leite, Coda, and Venturini reported a 2D BEM coupled with the finite elements that are used to model the bar inclusions in a matrix. These bar inclusions, representing fibers in a matrix, are assumed to be rigid within any cross section of a bar, but can deform along the axial direction in their models. The displacement and stress fields near the line inclusions are studied by this approach. In a recent work [16], Dong, Lo, and Cheung developed a hypersingular BIE approach for the analysis of interactions of rigid-line inclusions with cracks in a 2D elastic medium. Stress intensity factors at the tips of rigid lines are computed with this hypersingular BIE approach and compared with analytical solutions. In all the results mentioned above, only 2D models with a small number (less than 10) of rigid-line inclusions have been considered. Most recently, Nishimura and Liu [17] used the fast multipole BEM to solve rigid-line inclusion models in the context of 2D thermal analysis. The rigid-line concept in the thermal case means line inclusions with much higher thermal conductivities than that of the matrix material. A hypersingular BIE was employed and up to 10 000 line inclusions were studied. The effective thermal conductivity of a 2D medium (thin films) containing rigid lines were successfully evaluated using the 2D RVEs embedded in an infinite plane in Ref. [17].

In the case of modeling rigid inclusions as 2D or 3D objects without simplifying their geometries, Ingber and Papathanasiou's work [18] seems to be the only reported one using the boundary element method. The full conventional BIE for Navier's equation governing an *incompressible* medium containing rigid fibers is solved in [18] in order to determine the effective moduli of composites with different fiber volume fractions and aspect ratios. Constant boundary elements were employed to discretize the BIE which contains the singular as well as weakly-singular kernels. Parallel computing was used to solve the BEM equations. Up to 200 short, aligned rigid fibers, with the total degrees of freedom (DOFs) of about 12 000, were successfully solved by the developed BEM approach. Very good agreement of the evaluated effective moduli using their BEM approach and analytical results is reported in [18], which clearly demonstrates that the rigid-fiber model is very promising and the BEM is very efficient for analyzing fiber-reinforced composites. In the field of fluid mechanics, there are many research results concerning the flows of fluids around rigid solids. Two recent references using the boundary element method for modeling rigid bodies in fluids can be found in Refs. [19], [20]. In particular, in Ref. [19], an indirect BIE of the first kind using the single-layer potential is developed for solving Stokes equations and this approach is found to be very stable and more amenable to fast iterative solvers.

The boundary element method based on the BIEs is a natural way to model inclusion problems, due to its reduction of the dimension of the problem domain and high accuracy. With the development of the fast multipole methods (FMM) (see a recent review in Ref. [21]) for solving boundary integral equations, large models with several million degrees of freedom can be solved readily on a desktop computer. Rokhlin, Greengard, and coworkers, who pioneered the FMM, have done extensive research on the FMM for inclusion problems in the context of potential fields as well as elastic fields in two-dimensional domains (see, Ref. [22] and related papers in Refs. [23–25]). Rodin and coworkers [26] have formulated the BIE for 3D elastic inclusion problems using the FMM. Solutions for up to 343 spherical voids in an elastic domain were computed using their parallel FMM BEM code (with total DOFs about 400 000) [26]. Some other development of the fast multipole BEM can be found in Refs. [27], [28] for general elasticity problems, and in [29–31] for crack problems. With the advances of new composites, new modeling approaches that can handle even larger numbers of fibers in an RVE need to be developed. The rigid-inclusion approach seems to be a feasible first approximation with the current computing capabilities. All these demands in materials research and progresses in the BEM suggest that the rigid-inclusion models and the fast multipole BEM may play a significant role in the analysis of fiber-reinforced composites.

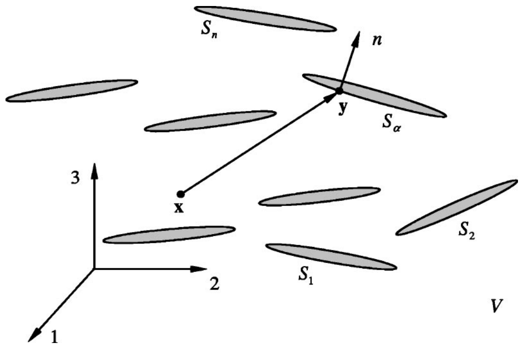

Fig. 1 A 3D infinite elastic medium (R^3) embedded with rigid inclusions

In this paper, a new BIE formulation is presented for the analysis of rigid inclusions in a general 3D isotropic elastic medium based on the general direct BIE formulation. The BIE contains only the displacement kernel and the influence of the traction kernel is implied in the coefficient of the free displacement term. Although this integral equation is essentially (not exactly) a Fredholm integral equation of the first kind, it is suitable for numerical solutions with iterative solvers because a good preconditioner is available. The BEM accelerated by the fast multipole method is used to solve the established BIE and the preconditioned system of equations is found to be well conditioned. The analytical solution of a rigid sphere in an infinite elastic domain is used to validate the developed BEM code and excellent agreement is achieved. Examples for modeling fiber-reinforced composites, with the number of fibers reaching above 5800 and total DOFs above 10 millions, are successfully solved by the developed fast multipole BEM. Effective Young's moduli of fiber-reinforced composites are evaluated for uniformly and "randomly" distributed and oriented fibers with two different aspect ratios and volume fractions. The developed fast multipole BEM is demonstrated to be very promising for large-scale analysis of fiber-reinforced composites, when the fibers can be assumed rigid relative to the matrix. It can also be applied to modeling other inclusion problems.

2 BIE Formulation for an Elastic Medium Containing Rigid Inclusions

The boundary integral equation for the analysis of an elastic domain containing rigid inclusions is derived in this section. This new and simplified BIE formulation contains only one integral with the displacement kernel and thus can facilitate more efficient computation. Consider a 3D infinite elastic domain V embedded with n rigid inclusions (Fig. 1). The matrix is loaded with a remote stress or displacement field. The displacement at a point inside the domain is given by the following direct representation integral (see, e.g., [32]):

$$\mathbf{u}(\mathbf{x}) = \int_S [\mathbf{U}(\mathbf{x},\mathbf{y})\mathbf{t}(\mathbf{y}) - \mathbf{T}(\mathbf{x},\mathbf{y})\mathbf{u}(\mathbf{y})]\,dS(\mathbf{y}) + \mathbf{u}^\infty(\mathbf{x}), \quad \forall \mathbf{x} \in V, \tag{1}$$

where $\mathbf{u}$ and $\mathbf{t}$ are the displacement and traction vectors, respectively; $S = \cup_\alpha S_\alpha$ with S_α being the boundary of the αth rigid inclusion (Fig. 1); and $\mathbf{u}^\infty$ the undisturbed displacement field when a remote stress or displacement field is applied and the rigid inclusions are not present (This term is similar to that for an incident wave in the elastodynamic case [33]). For a finite domain model, this term will not be present in Eq. (1). The two kernel functions $\mathbf{U}(\mathbf{x},\mathbf{y})$ and $\mathbf{T}(\mathbf{x},\mathbf{y})$ in Eq. (1) are the displacement and traction components in the fundamental solution (Kelvin's solution), respectively, which can be found in any BEM references (see, e.g., [34–37]).

Before we let the source point $\mathbf{x}$ approach the boundary S to derive the boundary integral equation, we first consider the rigid-body motions of each inclusion. For a rigid inclusion enclosed by S_α, the displacement at any point $\mathbf{y}$ can be described by the rigid-body motions as:

$$\mathbf{u}(\mathbf{y}) = \mathbf{d} + \boldsymbol{\omega} \times \mathbf{p}(\mathbf{y}), \tag{2}$$

where $\mathbf{d}$ is the rigid-body translational displacement vector, $\boldsymbol{\omega}$ the rotation vector, and $\mathbf{p}$ a position vector for point $\mathbf{y}$ measured from a reference point (such as the center of the inclusion). Consider a *complement* problem in the interior region enclosed by S_α and filled with the same material as that of domain V. Then the following representation integral holds:

$$\mathbf{0} = \int_{S_\alpha} [\tilde{\mathbf{U}}(\mathbf{x},\mathbf{y})\tilde{\mathbf{t}}(\mathbf{y}) - \tilde{\mathbf{T}}(\mathbf{x},\mathbf{y})\tilde{\mathbf{u}}(\mathbf{y})]\,dS(\mathbf{y}), \quad \forall \mathbf{x} \in V, \tag{3}$$

where $\tilde{\mathbf{u}}$ and $\tilde{\mathbf{t}}$ are the displacement and traction vectors, respectively, for this complement problem; $\tilde{\mathbf{U}} = \mathbf{U}$ and $\tilde{\mathbf{T}} = -\mathbf{T}$ as in Eq. (1) (the normal for the region enclosed by S_α is in the opposite direction of n shown in Fig. 1). Any rigid-body motion is a solution to the elasticity equations for the complement problem. Thus, the following solution:

$$\tilde{\mathbf{u}}(\mathbf{y}) = \mathbf{u}(\mathbf{y}) = \mathbf{d} + \boldsymbol{\omega} \times \mathbf{p}(\mathbf{y}), \quad \tilde{\mathbf{t}}(\mathbf{y}) = \mathbf{0}$$

satisfies the representation integral (3). Substituting these results into (3), we obtain:

$$\int_{S_\alpha} \mathbf{T}(\mathbf{x},\mathbf{y})[\mathbf{d} + \boldsymbol{\omega} \times \mathbf{p}(\mathbf{y})]\,dS(\mathbf{y}) = \mathbf{0}, \quad \forall \mathbf{x} \in V,$$

or

$$\int_{S_\alpha} \mathbf{T}(\mathbf{x},\mathbf{y})\mathbf{u}(\mathbf{y})\,dS(\mathbf{y}) = \mathbf{0}, \quad \forall \mathbf{x} \in V, \tag{4}$$

for the region enclosed by S_α $(\alpha = 1,2,\ldots,n)$. This is exactly the second integral with the $\mathbf{T}$ kernel in Eq. (1) on one inclusion. Therefore, the integral in Eq. (1) involving the $\mathbf{T}$ kernel vanishes and Eq. (1) reduces to:

$$\mathbf{u}(\mathbf{x}) = \int_S \mathbf{U}(\mathbf{x},\mathbf{y})\mathbf{t}(\mathbf{y})\,dS(\mathbf{y}) + \mathbf{u}^\infty(\mathbf{x}), \quad \forall \mathbf{x} \in V, \tag{5}$$

for all *rigid* inclusions $(S = \cup_\alpha S_\alpha)$. This representation integral can be applied to evaluate the displacement field at any point inside the domain V, once the tractions on the surfaces of the rigid inclusions are obtained. The stress field at any point in the domain can also be evaluated by taking derivatives of expression (5) and applying the Hook's law.

To obtain the traction values on surfaces of the rigid inclusions, we let the source point $\mathbf{x}$ approach the boundary S to arrive at the following boundary integral equation:

$$\mathbf{u}(\mathbf{x}) = \int_S \mathbf{U}(\mathbf{x},\mathbf{y})\mathbf{t}(\mathbf{y})\,dS(\mathbf{y}) + \mathbf{u}^\infty(\mathbf{x}), \quad \forall \mathbf{x} \in S = \bigcup_\alpha S_\alpha, \tag{6}$$

in which no jump term arises since the $\mathbf{U}$ kernel is only weakly singular [34–37]. This BIE for rigid-inclusion problems is extremely compact and simple, in which only the weakly-singular kernel needs to be handled. Analytical solutions for rigid-inclusion problems may be obtained for simple geometries by using this BIE formulation.

Although the BIE (6) for rigid inclusions are much simpler to handle than the BIE for elastic inclusions, it requires additional considerations, that is, the rigid-body motions of each inclusion, expressed by Eq. (2) that contains six unknowns ($\mathbf{d}$ and $\boldsymbol{\omega}$ vectors) for each inclusion. Additional equations are needed to supplement BIE (6). These equations can be obtained by considering the equilibrium of each inclusion, that is, the following (six scalar) equations:

$$\int_{S_\alpha} \mathbf{t}(\mathbf{y})\,dS(\mathbf{y}) = \mathbf{0}; \tag{7}$$

$$\int_{S_\alpha} \mathbf{p}(\mathbf{y}) \times \mathbf{t}(\mathbf{y})\,dS(\mathbf{y}) = \mathbf{0}; \tag{8}$$

for $\alpha = 1,2,\ldots,n$. Expression (7) represents the equilibrium of the forces, while expression (8) that of the moments, for the rigid inclusions. BIE (6) and Eqs. (2), (7), and (8) are simultaneously solved to obtain the unknown rigid-body motions $\mathbf{d}$ and $\boldsymbol{\omega}$, and traction $\mathbf{t}$ for all the inclusions.

It should be pointed out that BIE in (6) is essentially a Fredholm integral equation of the first kind, although not exactly since it contains additional finite number of unknowns $\mathbf{d}$ and $\boldsymbol{\omega}$ for each inclusion. Integral equations of the first kind are usually considered not suitable for numerical solutions with iterative solvers. This problem can be resolved in two ways. Namely, we either convert the BIE into an equivalent equation of the second kind, or use a preconditioner after the discretization. One may possibly replace BIE (6) by a second kind integral equation of the following form as one uses instead the traction equation corresponding to (6):

$$\tfrac{1}{2}\mathbf{t}(\mathbf{x}) = \int_S T\mathbf{U}(\mathbf{x},\mathbf{y})\mathbf{t}(\mathbf{y})\,dS(\mathbf{y}) + T\mathbf{u}^\infty(\mathbf{x}), \quad \forall \mathbf{x} \in S = \bigcup_\alpha S_\alpha,$$

where T is the traction operator which is applied to $\mathbf{x}$. Unfortunately, the solution to this equation is not unique. We therefore decided to use BIE (6) for the analysis since we can find a good preconditioner for the system obtained after discretization of (6), as we shall see later.

In 2D, BIE (6) will degenerate in the limit as the aspect ratio of an inclusion tends to infinity, that is, equations generated by using BIE (6) on the two opposing boundaries of a slender inclusion will be identical and thus not enough equations will be available for solving the BIE for separate tractions. In this case, the sum of tractions across the inclusion can be used as a new variable in BIE (6) to derive a new equation. Different Green's function formulations can also be employed to consider rigid lines based on the work in Refs. [9–15], which may turn out to be equivalent with the equation based on BIE (6). Like the crack cases, hypersingular BIE formulations can also be applied, as has been done recently in [16] for 2D elasticity, and in [17] for 2D thermal analysis of line inclusions. New BIE formulations for rigid-line inclusion problems in 3D, however, still remain to be developed.

3 The Fast Multipole Method

The fast multipole method [21–31] is employed to accelerate the BEM solution of the BIE for rigid inclusions. In recent years, the fast multipole method has been demonstrated to be especially good for solving problems with large numbers of cracks and inclusions in both 2D and 3D cases. Using the fast multipole method for the BEM, the solution time of a problem is reduced to order $O(N)$, instead of $O(N^2)$ as in the traditional BEM (with N here being the number of equations). The memory requirement is also reduced since the iterative solver (such as GMRES) does not require the storage of the entire matrix in the memory. Thus, large models that had to be solved on a supercomputer in the past can now be solved on a desktop computer.

In the following, we briefly list the main results of the fast multipole method for the developed BIE (6) to show the essence of this powerful approach to solving BIEs. Complete formulations and steps in implementations of the FMM for elastostatic problems can be found in Refs. [38,39]. Other formulations using different FMM approaches for general elasticity problems can be found in Refs. [26–28].

We start with the following form of the fundamental solution (index notation is employed here, where repeated indices imply summations):

$$U_{ij}(\mathbf{x},\mathbf{y})=\frac{1}{8\pi\mu}\left(\delta_{ij}\frac{2}{r}-\frac{\lambda+\mu}{\lambda+2\mu}\frac{\partial}{\partial x_i}\frac{x_j-y_j}{r}\right), \tag{9}$$

where λ and μ are the Lamé constants, δ_{ij} the Kronecker symbol, and $r=r(\mathbf{x},\mathbf{y})$ the distance between the source point $\mathbf{x}$ and field point $\mathbf{y}$. The following identity holds:

$$\frac{1}{r(\mathbf{x},\mathbf{y})}=\sum_{n=0}^{\infty}\sum_{m=-n}^{n}S_{n,m}(\overrightarrow{\mathbf{Ox}})\overline{R_{n,m}(\overrightarrow{\mathbf{Oy}})}, \tag{10}$$

for $|\overrightarrow{\mathbf{Oy}}|<|\overrightarrow{\mathbf{Ox}}|$, in which $\mathbf{O}$ represents a third point, $R_{n,m}$ and $S_{n,m}$ are solid harmonic functions defined in Refs. [38,39], and $\overline{(\ )}$ means the complex conjugate. Substituting (10) into (9), we arrive at:

$$U_{ij}(\mathbf{x},\mathbf{y})=\frac{1}{8\pi\mu}\sum_{n=0}^{\infty}\sum_{m=-n}^{n}[F_{ij,n,m}(\overrightarrow{\mathbf{Ox}})\overline{R_{n,m}(\overrightarrow{\mathbf{Oy}})}+G_{i,n,m}(\overrightarrow{\mathbf{Ox}})(\overrightarrow{\mathbf{Oy}})_j\overline{R_{n,m}(\overrightarrow{\mathbf{Oy}})}], \tag{11}$$

where,

$$F_{ij,n,m}(\overrightarrow{\mathbf{Ox}})=\frac{\lambda+3\mu}{\lambda+2\mu}\delta_{ij}S_{n,m}(\overrightarrow{\mathbf{Ox}})-\frac{\lambda+\mu}{\lambda+2\mu}(\overrightarrow{\mathbf{Ox}})_j\frac{\partial}{\partial x_i}S_{n,m}(\overrightarrow{\mathbf{Ox}}),$$

$$G_{i,n,m}(\overrightarrow{\mathbf{Ox}})=\frac{\lambda+\mu}{\lambda+2\mu}\frac{\partial}{\partial x_i}S_{n,m}(\overrightarrow{\mathbf{Ox}}).$$

The significance of expression (11) is that the kernel $U_{ij}(\mathbf{x},\mathbf{y})$ is now a sum of functions in the form of $k_n^{(1)}(\mathbf{x}-\mathbf{O})k_n^{(2)}(\mathbf{y}-\mathbf{O})$, which will facilitate integrations independent of the source point $\mathbf{x}$ and thus reduce the number of integrals to compute. To see this, consider the integral in BIE (6) on a subdomain S_o of S away from the source point $\mathbf{x}$. Applying expression (11), with point $\mathbf{O}$ being close to subdomain S_o, we obtain:

$$\int_{S_o}U_{ij}(\mathbf{x},\mathbf{y})t_j(\mathbf{y})dS(\mathbf{y})=\frac{1}{8\pi\mu}\sum_{n=0}^{\infty}\sum_{m=-n}^{n}[F_{ij,n,m}(\overrightarrow{\mathbf{Ox}})\overline{M_{j,n,m}(\mathbf{O})}+G_{i,n,m}(\overrightarrow{\mathbf{Ox}})\overline{M_{n,m}(\mathbf{O})}], \tag{12}$$

in which,

$$M_{j,n,m}(\mathbf{O})=\int_{S_o}R_{n,m}(\overrightarrow{\mathbf{Oy}})t_j(\mathbf{y})dS(\mathbf{y}), \tag{13}$$

$$M_{n,m}(\mathbf{O})=\int_{S_o}(\overrightarrow{\mathbf{Oy}})_jR_{n,m}(\overrightarrow{\mathbf{Oy}})t_j(\mathbf{y})dS(\mathbf{y}), \tag{14}$$

are called the *multipole moments* for given n and m. Note that these four moments are independent of the location of the source point $\mathbf{x}$ and thus only need to be calculated once for all locations of the source point away from S_o (S_o will be a cell in FMM and $\mathbf{O}$ will be the center of this cell). To evaluate the integral using Eq. (12), only a small number of terms are required in the expansion. For example, using ten terms for n in these expansions has been found sufficient for most problems. Further details of the FMM in the context of general 3D elastostatic problems and used in this work can be found in Refs. [38,39].

The fast multipole BEM code developed for the current analysis of rigid inclusions in 3D elastic media is based on the FMM BEM code that was developed at the Kyoto University for general elasticity problems [38]. This earlier FMM code has been tested on some large-scale stress analysis problems of regular structures. More details on the FMM for the BEM and its implementations in solving other types of problems can be found in Refs. [21], [39].

4 Discretization of the BIE

The boundary element method, accelerated by the fast multipole method, is applied to solve BIE (6) together with Eqs. (2), (7), and (8). In this paper, constant triangular boundary elements are used to discretize these equations over the surfaces of the inclusions. One node is placed on each surface element and the field variable (traction) is assumed to be constant over each element which is a flat triangular area defined by its three corner points. Although constant elements may not be as accurate as linear or quadratic surface elements, they have certain advantages over other higher-order elements. For example, all the integrals involved in using the constant elements can be evaluated analytically in both 2D and 3D cases. (As a matter of fact, it is not impossible to carry out analytical integrations for any planar elements with arbitrary polynomial basis functions. But the results will be quite complicated.) This avoids the use of any numerical integration in the BEM and hence guarantees the accuracy in the evaluation of all integrals when the source point $\mathbf{x}$ is very close to an element of integration (which happens when many inclusions are closely packed in a model).

If the nodes are grouped together for each inclusion, numbered on one inclusion after another, then a discretized form of the BIE (6) can be written as:

$$\begin{Bmatrix}\tilde{\mathbf{u}}_1\\ \tilde{\mathbf{u}}_2\\ \vdots\\ \tilde{\mathbf{u}}_n\end{Bmatrix}=\begin{bmatrix}\tilde{\mathbf{U}}_{11} & \tilde{\mathbf{U}}_{12} & \cdots & \tilde{\mathbf{U}}_{1n}\\ \tilde{\mathbf{U}}_{21} & \tilde{\mathbf{U}}_{22} & \cdots & \tilde{\mathbf{U}}_{2n}\\ \vdots & \vdots & \ddots & \vdots\\ \tilde{\mathbf{U}}_{n1} & \tilde{\mathbf{U}}_{n2} & \cdots & \tilde{\mathbf{U}}_{nn}\end{bmatrix}\begin{Bmatrix}\tilde{\mathbf{t}}_1\\ \tilde{\mathbf{t}}_2\\ \vdots\\ \tilde{\mathbf{t}}_n\end{Bmatrix}+\begin{Bmatrix}\tilde{\mathbf{u}}_1^{\infty}\\ \tilde{\mathbf{u}}_2^{\infty}\\ \vdots\\ \tilde{\mathbf{u}}_n^{\infty}\end{Bmatrix}, \tag{15}$$

where n is the total number of inclusions being considered; $\tilde{\mathbf{u}}_\alpha$ and $\tilde{\mathbf{t}}_\alpha$ the nodal displacement and traction vector for inclusion α, respectively; $\tilde{\mathbf{u}}_\alpha^{\infty}$ the given remote displacement vector evaluated on inclusion α; and $\tilde{\mathbf{U}}_{\alpha\beta}$ the coefficient matrix obtained from the (analytical) integration of the displacement kernel over inclusion β when the source point $\mathbf{x}$ is located on inclusion α. From Eq. (2), the nodal displacement vector on an inclusion α can be related to the rigid-body translation $\mathbf{d}$ and rotation $\boldsymbol{\omega}$ of that inclusion by the following expression:

$$\tilde{\mathbf{u}}_\alpha=\begin{Bmatrix}\mathbf{u}_1\\ \mathbf{u}_2\\ \vdots\\ \mathbf{u}_m\end{Bmatrix}=\begin{bmatrix}\mathbf{a}_1\\ \mathbf{a}_2\\ \vdots\\ \mathbf{a}_m\end{bmatrix}\boldsymbol{\varphi}_\alpha=\mathbf{A}_\alpha\boldsymbol{\varphi}_\alpha, \tag{16}$$

in which $\mathbf{u}_i$ is the nodal displacement vector at node i (with m being the number of nodes on inclusion α); $\mathbf{a}_i$ the transformation matrix for each node i on inclusion α given by [see Eq. (2)]:

$$\mathbf{a}_i=\begin{bmatrix}1 & 0 & 0 & 0 & p_3 & -p_2\\ 0 & 1 & 0 & -p_3 & 0 & p_1\\ 0 & 0 & 1 & p_2 & -p_1 & 0\end{bmatrix}, \tag{17}$$

with p_k being the component of the position vector $\mathbf{p}$ for node i; and finally in (16), $\boldsymbol{\varphi}_\alpha$ is the rigid-body displacement vector for inclusion α, defined by:

$$\boldsymbol{\varphi}_\alpha=[d_1\ \ d_2\ \ d_3\ \ \omega_1\ \ \omega_2\ \ \omega_3]^T, \tag{18}$$

for $\alpha = 1,2, \ldots ,n$. The system of equations (15) is supplemented with the following ones from discretizations of Eqs. (7) and (8) on each inclusion α:

$$\mathbf{B}_\alpha \tilde{\mathbf{t}}_\alpha = \mathbf{0}, \tag{19}$$

for $\alpha = 1,2, \ldots ,n$, in which $\mathbf{B}_\alpha$ is a $6 \times 3m$ coefficient matrix obtained by evaluating Eqs. (7) and (8) on inclusion α.

With results in (16)–(18), the discretized BIE (15) and Eq. (19) can now be combined to provide the following form of the system of equations:

$$\begin{bmatrix} -\tilde{\mathbf{U}}_{11} & -\tilde{\mathbf{U}}_{12} & \cdots & -\tilde{\mathbf{U}}_{1n} & \mathbf{A}_1 & \mathbf{0} & \cdots & \mathbf{0} \\ -\tilde{\mathbf{U}}_{21} & -\tilde{\mathbf{U}}_{22} & \cdots & -\tilde{\mathbf{U}}_{2n} & \mathbf{0} & \mathbf{A}_2 & \cdots & \mathbf{0} \\ \vdots & \vdots & \ddots & \vdots & \vdots & \vdots & \ddots & \vdots \\ -\tilde{\mathbf{U}}_{n1} & -\tilde{\mathbf{U}}_{n2} & \cdots & -\tilde{\mathbf{U}}_{nn} & \mathbf{0} & \mathbf{0} & \cdots & \mathbf{A}_n \\ \mathbf{B}_1 & \mathbf{0} & \cdots & \mathbf{0} & \mathbf{0} & \mathbf{0} & \cdots & \mathbf{0} \\ \mathbf{0} & \mathbf{B}_2 & \cdots & \mathbf{0} & \mathbf{0} & \mathbf{0} & \cdots & \mathbf{0} \\ \vdots & \vdots & \ddots & \vdots & \vdots & \vdots & \ddots & \vdots \\ \mathbf{0} & \mathbf{0} & \cdots & \mathbf{B}_n & \mathbf{0} & \mathbf{0} & \cdots & \mathbf{0} \end{bmatrix} \begin{Bmatrix} \tilde{\mathbf{t}}_1 \\ \tilde{\mathbf{t}}_2 \\ \vdots \\ \tilde{\mathbf{t}}_n \\ \boldsymbol{\varphi}_1 \\ \boldsymbol{\varphi}_2 \\ \vdots \\ \boldsymbol{\varphi}_n \end{Bmatrix} = \begin{Bmatrix} \tilde{\mathbf{u}}_1^\infty \\ \tilde{\mathbf{u}}_2^\infty \\ \vdots \\ \tilde{\mathbf{u}}_n^\infty \\ \mathbf{0} \\ \mathbf{0} \\ \vdots \\ \mathbf{0} \end{Bmatrix}. \tag{20}$$

There are $3N + 6n$ equations in the above system (with $N = m \times n$, being the total number of nodes on all inclusions), which are sufficient for solving the $6n$ unknown rigid-body displacements and rotations $(\boldsymbol{\varphi}_\alpha)$ of the n inclusions, and the $3N$ unknown traction components $(\tilde{\mathbf{t}}_\alpha)$ at the N boundary nodes over all the inclusions. Note that in the above system, the dimension for submatrix $\mathbf{A}_\alpha$ is $3m \times 6$ and for $\mathbf{B}_\alpha$ is $6 \times 3m$. Both are not square matrices (the number of nodes per inclusion m can be large). If all the inclusions are of the same size and shape, and meshed in the same way, then both the submatrices $\mathbf{A}_\alpha$ and $\mathbf{B}_\alpha$ can be computed only once for all the inclusions.

The iterative solver GMRES is used to solve the system of equations in Eq. (20), in which the multiplication of the (coefficient) matrix and (approximate solution) vector in each iteration are obtained by using the fast multipole method. In the FMM, the maximum depth of the oct-tree structure is below 10 levels. Direct integrations for near field interactions are computed during each iteration and are not stored to save the memory space. As for the preconditioner, we use the following (“diagonal”) matrix:

$$\mathbf{M} = \begin{bmatrix} -\tilde{\mathbf{U}}_{11} & \mathbf{0} & \cdots & \mathbf{0} & \mathbf{A}_1 & \mathbf{0} & \cdots & \mathbf{0} \\ \mathbf{0} & -\tilde{\mathbf{U}}_{22} & \cdots & \mathbf{0} & \mathbf{0} & \mathbf{A}_2 & \cdots & \mathbf{0} \\ \vdots & \vdots & \ddots & \vdots & \vdots & \vdots & \ddots & \vdots \\ \mathbf{0} & \mathbf{0} & \cdots & -\tilde{\mathbf{U}}_{nn} & \mathbf{0} & \mathbf{0} & \cdots & \mathbf{A}_n \\ \mathbf{B}_1 & \mathbf{0} & \cdots & \mathbf{0} & \mathbf{0} & \mathbf{0} & \cdots & \mathbf{0} \\ \mathbf{0} & \mathbf{B}_2 & \cdots & \mathbf{0} & \mathbf{0} & \mathbf{0} & \cdots & \mathbf{0} \\ \vdots & \vdots & \ddots & \vdots & \vdots & \vdots & \ddots & \vdots \\ \mathbf{0} & \mathbf{0} & \cdots & \mathbf{B}_n & \mathbf{0} & \mathbf{0} & \cdots & \mathbf{0} \end{bmatrix}. \tag{21}$$

The system in (20) is right-preconditioned with this matrix. The inverse of $\mathbf{M}$ is easily obtained as:

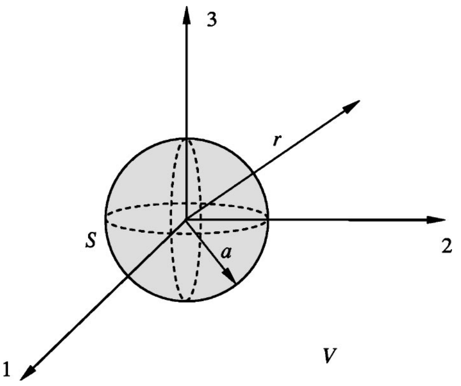

Fig. 2 A rigid sphere in an infinite elastic domain *V*

$$\mathbf{M}^{-1} = \begin{bmatrix} \mathbf{P}_1 & \mathbf{0} & \cdots & \mathbf{0} & \mathbf{Q}_1 & \mathbf{0} & \cdots & \mathbf{0} \\ \mathbf{0} & \mathbf{P}_2 & \cdots & \mathbf{0} & \mathbf{0} & \mathbf{Q}_2 & \cdots & \mathbf{0} \\ \vdots & \vdots & \ddots & \vdots & \vdots & \vdots & \ddots & \vdots \\ \mathbf{0} & \mathbf{0} & \cdots & \mathbf{P}_n & \mathbf{0} & \mathbf{0} & \cdots & \mathbf{Q}_n \\ \mathbf{R}_1 & \mathbf{0} & \cdots & \mathbf{0} & \mathbf{S}_1 & \mathbf{0} & \cdots & \mathbf{0} \\ \mathbf{0} & \mathbf{R}_2 & \cdots & \mathbf{0} & \mathbf{0} & \mathbf{S}_2 & \cdots & \mathbf{0} \\ \vdots & \vdots & \ddots & \vdots & \vdots & \vdots & \ddots & \vdots \\ \mathbf{0} & \mathbf{0} & \cdots & \mathbf{R}_n & \mathbf{0} & \mathbf{0} & \cdots & \mathbf{S}_n \end{bmatrix},$$

where

$$\begin{bmatrix} \mathbf{P}_i & \mathbf{Q}_i \\ \mathbf{R}_i & \mathbf{S}_i \end{bmatrix} = \begin{bmatrix} -\tilde{\mathbf{U}}_{ii} & \mathbf{A}_i \\ \mathbf{B}_i & \mathbf{0} \end{bmatrix}^{-1}, \quad \text{for inclusion } i = 1,2, \ldots ,n. \tag{22}$$

Physically speaking, inverting the matrix on the right-hand side of (22) means to solve a rigid-inclusion problem for the whole space just containing one inclusion (*i*th one). The inversion in (22) is a small operation which can be carried out efficiently with any direct solver for a matrix equation. With this preconditioning, the upper-right and lower-left submatrices in (20) reduce to zero matrices, while the lower-right submatrix and the block diagonals in the upper-left submatrix are converted into identity matrices. This is essentially equivalent to converting the original integral equation in (6) into another equation of the second kind whose solution is unique. The system thus obtained is well conditioned and the solutions are stable, as shown in the following numerical examples.

5 Numerical Examples

The developed fast BEM for the analysis of rigid inclusions is first validated using a test case of a single rigid sphere for which the analytical solution can be found readily. Then, the BEM code is applied to study the fiber-reinforced composites using the rigid-inclusion model.

5.1 A Rigid Sphere in an Infinite Elastic Medium. To validate the developed new BIE formulation and its BEM implementation for the study of rigid-inclusion models of fiber-reinforced composites, a rigid sphere in an infinite elastic medium is considered first (Fig. 2). The elastic medium containing the rigid sphere is loaded with a far-field triaxial stress σ^∞. The analytical solution for this axisymmetric problem can be obtained readily using basic elasticity theory [40] or the equivalent inclusion method [41]. The radial displacement, radial and tangential stresses in the elastic domain are found to be:

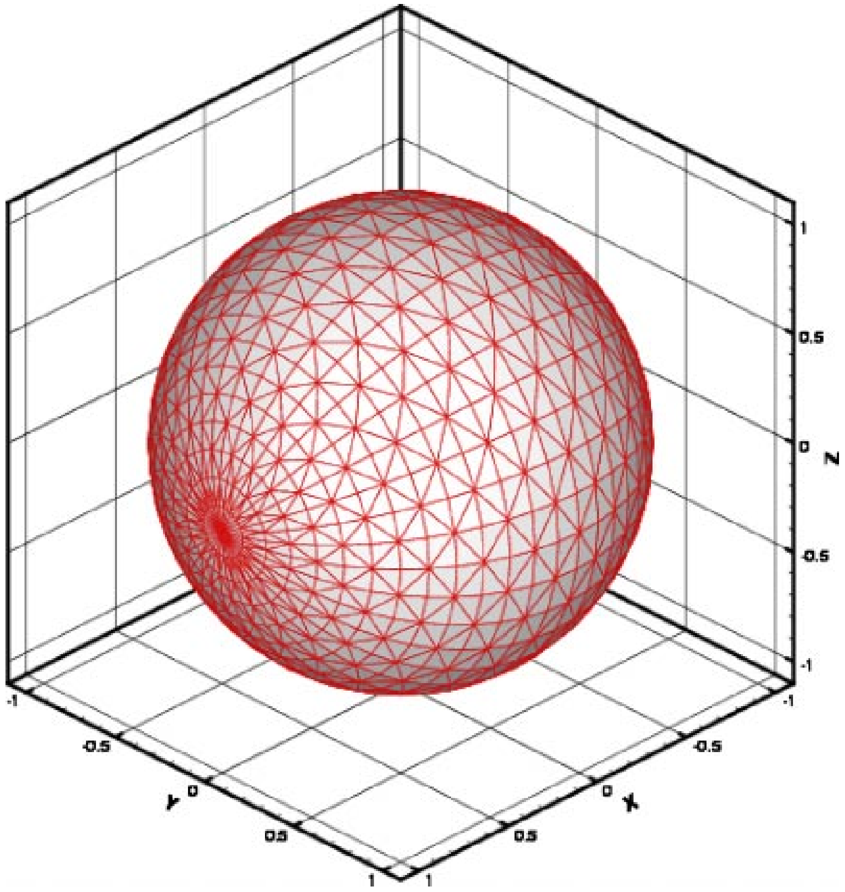

Fig. 3 A boundary element model of the sphere (with 1944 surface elements)

$$u_r(r) = \frac{(1-2\nu)\sigma^\infty}{E}\left(1-\frac{a^3}{r^3}\right)r, \tag{23}$$

$$\sigma_r(r) = \sigma^\infty\left[1+\frac{2(1-2\nu)}{1+\nu}\frac{a^3}{r^3}\right], \tag{24}$$

$$\sigma_\theta(r) = \sigma^\infty\left[1-\frac{1-2\nu}{1+\nu}\frac{a^3}{r^3}\right], \tag{25}$$

respectively, where a is the radius of the sphere, E the Young's modulus, and ν the Poisson's ratio of the elastic medium. Note that $u_r(a)=0$, which is the result for a rigid sphere.

The convergence of the BEM is studied with several boundary element meshes for the sphere. The finest mesh used (with 1944 elements) is shown in Fig. 3. The radial stress computed by the BEM on the surface is compared with the analytical solution [Eq. (24)] and the relative errors are plotted in Fig. 4 for different meshes with increasing numbers of elements. The error with the coarsest mesh (120 elements) is 4.93%, while that with the finest mesh (1944 elements) is 0.19%. The convergence of the BEM results is achieved. The field displacement and stresses within the elastic domain are plotted in Figs. 5 and 6, respectively, for the coarsest mesh (120 elements) to deliberately show the errors of the BEM. Even though the results on the surface for this coarse mesh contain a relatively larger error (4.93% for radial stress, Fig. 4), the results inside the domain (away from the surface) are quite good. This is one of the advantages of the BEM approach, which uses integral representation [e.g., Eq. (5)] for this calculation that tends to reduce the errors inside the domain. Note that both the radial and tangential stresses tend to the applied far-field stress σ^∞, as the distance r from the center of the sphere increases. The stress contour plot for σ_x on the surface (boundary of the medium) is given in Fig. 7 for the finest mesh (shown in Fig. 3). The boundary stress field is obtained by using the traction results and averaged at each corner node using results on the surrounding elements. Note the increase of the stress value on the surface (with a stress concentration factor of 1.6154) and its location due to the presence of the rigid sphere in the elastic medium.

The excellent agreement of the BEM results with the analytical solution for this example suggests that the developed new BIE formulation and its BEM implementation are correct and effective. Fiber-reinforced composite materials will be considered next using this rigid-inclusion model and the BEM approach.

5.2 Short-Fiber-Reinforced Composites. Modeling of fiber-reinforced composites using the rigid-inclusion model and the developed BEM is considered in this and next examples. Short fibers in a matrix are more likely to act like rigid rods [18] if their stiffness is more than an order of magnitude higher than that of the matrix. Several representative volume elements containing different numbers of fibers are used to study the interactions of the fibers and to estimate the effective properties of the composites. We limit our attention to short and moderately long fibers in a matrix, where the aspect ratio (length/diameter) of an inclusion is kept below 20. The main purpose of these examples is to show the capabilities and promises of the developed fast BEM in large-scale modeling of fiber-reinforced composites. The models studied here are simple and ideal in nature, with more realistic ones being left for future applications.

The RVEs considered in this study are of finite sizes and *embedded* in an infinite domain with the same material as that of the matrix (cf., similar inclusion models in 2D infinite space reported in Refs. [9–14,16,17]). In this way, the problem can be posed as

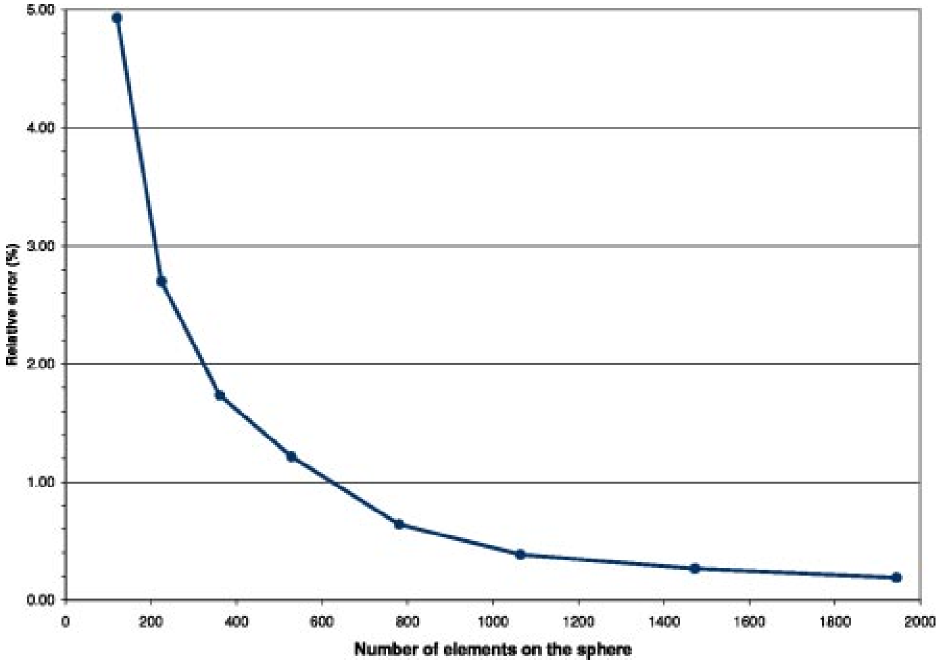

Fig. 4 Convergence of the BEM results for surface radial stress $\sigma_r(a)$

an infinite domain problem and the structure of Eq. (20) can be preserved. [A RVE model as a finite domain problem can be easily implemented with some modifications of Eq. (20) to consider direct loading on the surfaces of a RVE.] In the current embedded RVE models, a far-field uniaxial tensile stress is applied in the x-direction (Fig. 8). To estimate the effective Young's modulus of a composite in one direction (e.g., the fiber or x-direction), the displacements and stresses at some surfaces of the RVE, to be called data-collection surfaces (Fig. 8), are computed using Eq. (5) and its gradients, after the traction **t** is determined for each rigid inclusion by solving the BIE equations. The effective Young's modulus of the composite is estimated using the displacement and stress results at these data-collection surfaces by the following formula (which ignores the stresses on the lateral surfaces that have been found much smaller in value compared with σ_x in the cases studied):

$$E_{\text{eff}} = \frac{(\sigma_x)_{(\text{ave})} L}{(\Delta u_x)_{(\text{ave})}}, \tag{26}$$

where E_{eff} is the estimated effective Young's modulus of the composite in the x-direction (Fig. 8), and the displacement and stress averaged over the data-collection surfaces (Fig. 8) are obtained by:

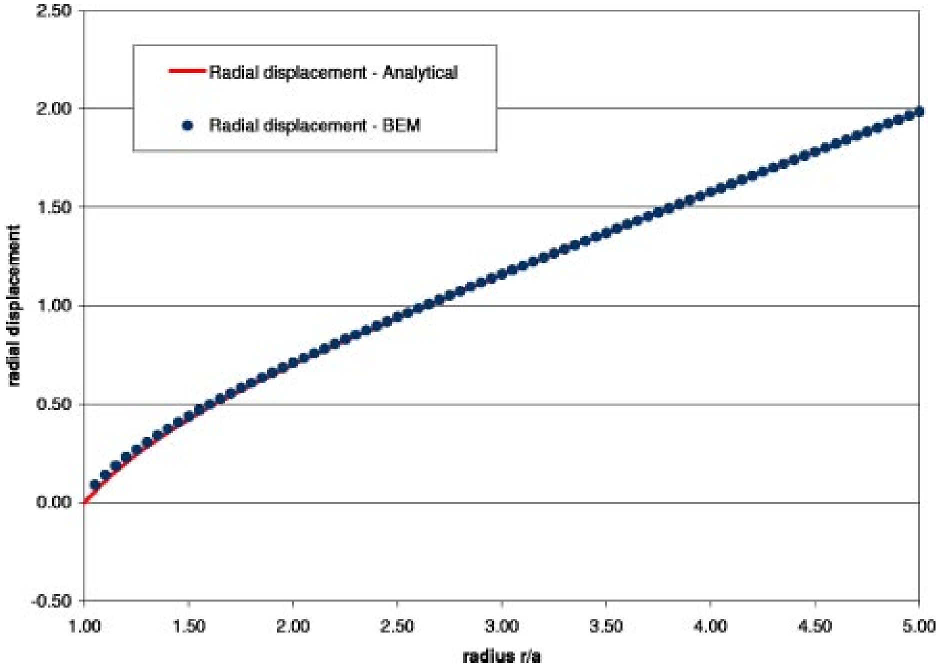

Fig. 5 Radial displacement ($\times \sigma^\infty a/E$) obtained by the BEM model with 120 elements

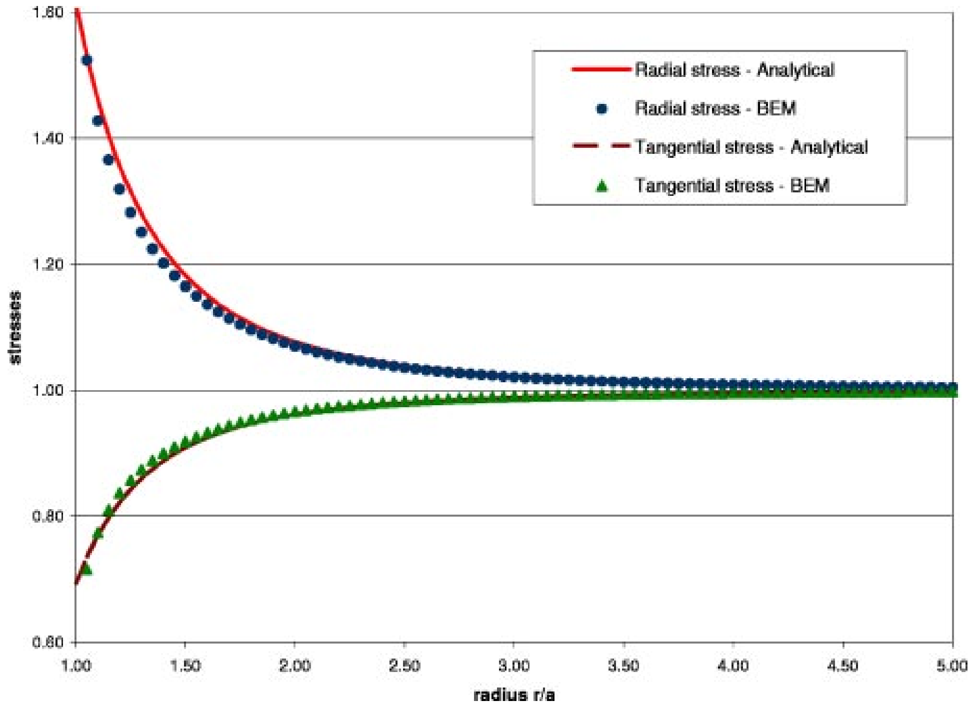

Fig. 6 Radial and tangential stresses $(\times\sigma^{\infty})$ obtained by the BEM model with 120 elements

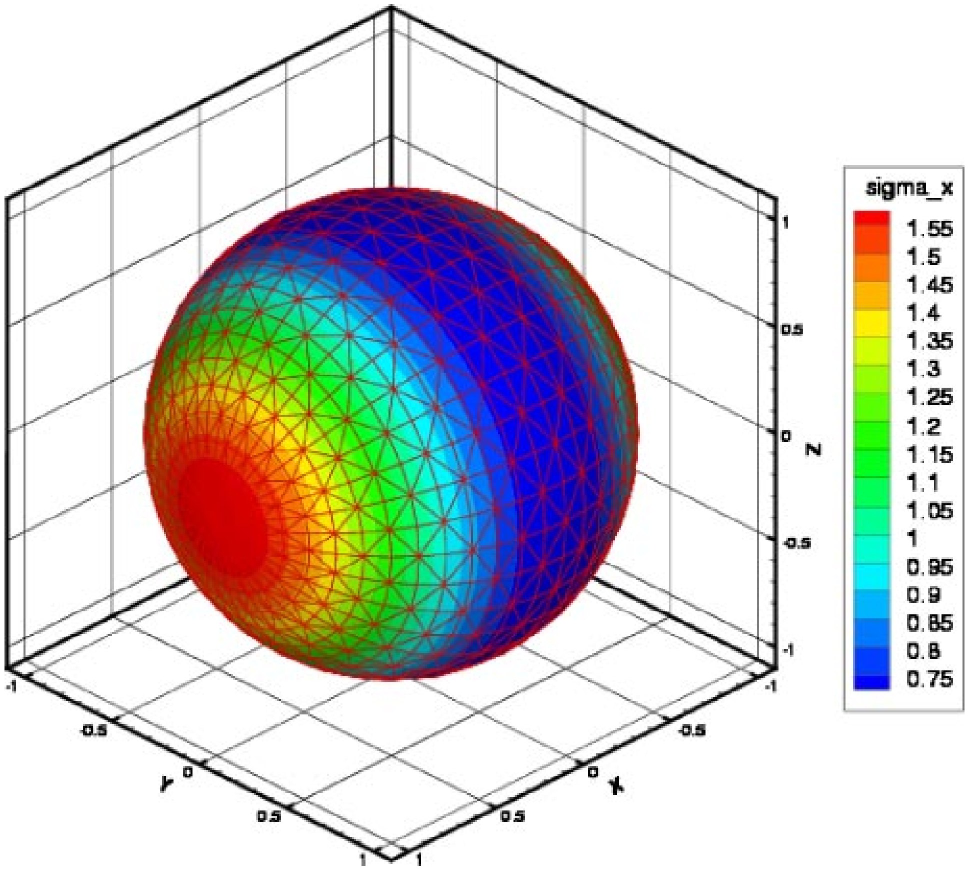

Fig. 7 Contour plot for stress $\sigma_x(\times\sigma^{\infty})$ on the surface of the rigid sphere

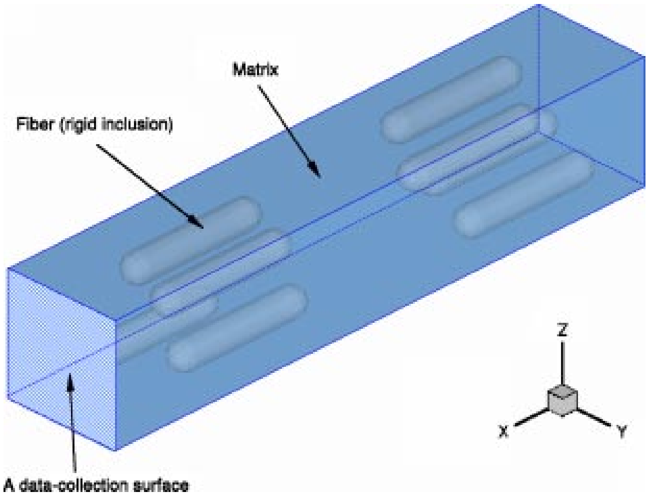

Fig. 8 A RVE of a short fiber-reinforced composite

$$(\Delta u_x)_{(\mathrm{ave})} = (u_x(x=L/2))_{(\mathrm{ave})} - (u_x(x=-L/2))_{(\mathrm{ave})}, \quad (27)$$

$$(\sigma_x)_{(\mathrm{ave})} = [(\sigma_x(x=L/2))_{(\mathrm{ave})} + (\sigma_x(x=-L/2))_{(\mathrm{ave})}]/2, \quad (28)$$

with L being the length of the RVE in the x direction Fig. 8, the origin of the coordinate system is located at the center of the RVE). In this way, the effective modulus is obtained as the local elastic constant of the volume with inclusions. One may argue that the effective modulus in (26) is an apparent property because it is obtained using an infinite domain that acts as part of the ''loading device.'' Indeed, the effectiveness of this approach with a RVE embedded in the infinite domain needs to be verified with other results and improved RVE models can also be developed. The reader is referred to Sec. 6 for further discussions and an attempt to verify the proposed approach.

A mesh with 456 boundary elements for a short, cylindrical fiber of an aspect ratio equal to 5 (length=50 and diameter=10) is shown in Fig. 9. This mesh is sufficient for obtaining converged results for the estimated effective moduli. The fiber is initially placed at the center of a box of dimensions 100×20×20 (chosen arbitrarily) and filled with the matrix material. This box is then repeated in the x-, y-, and z-directions to generate the multiple-fiber RVE models. Three different distributions and orientations of the fibers are considered. The first case is the uniform distribution of aligned fibers, to be called the *uniform* case. The second case is a ''random'' distribution of aligned fibers, where the fibers are still aligned in the x-direction, but their locations are shifted randomly in the x-, y-, and z-directions to such an extent that each fiber remains in its own box (territory) to avoid contact of the fibers. This case is called the *aligned random* case. The third case is a ''random'' distribution and ''random'' orientation of the fibers. Again the random distribution and (small angle) rotation of a fiber is limited to the extent that it remains in its own box. This case is named the *random* (or to be more precise, a *controlled* random) case. In all the cases, the volume fraction of the fiber is 9.16% based on the dimensions of the RVE and fibers. A Poisson's ratio of 0.3 is used for the matrix.

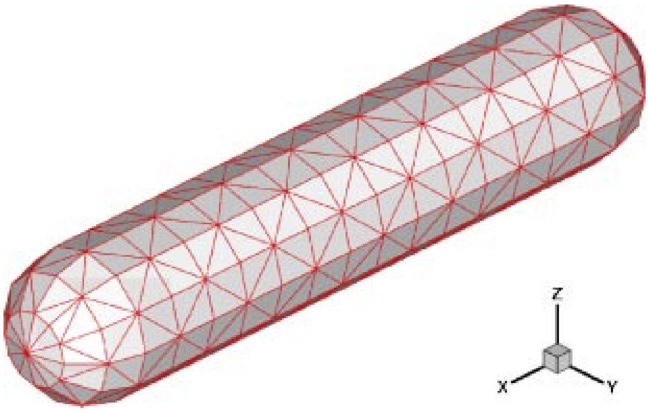

Fig. 9 A BEM mesh used for the short fiber inclusion (with 456 elements)

Figure 10 shows the contour plot of surface stress σ_x (in the matrix) for the RVE containing 216 ''random'' short fibers. For each fiber, high stresses occur around the two ends of the fiber, which is consistent with the theory that in the limit as the slender inclusion becomes a rigid line, singularity of stresses will arise at the two tips [9]. Values of these stresses are even higher when two fibers are closer to each other, suggesting closer interactions of the fibers. This stress plot is typical among all the studied RVEs containing $q\times q\times q$ fibers, with $q=2$, 3, 4, 6, 8, 10, 12, and 13 in this example. The largest RVE with 2197 (an array of 13×13×13) ''random'' fibers is shown in Fig. 11. The total degrees of freedom for the model in Fig. 11 is 3 018 678 $(=2197\times(6+456\times3))$.

The normalized Young's moduli $(E_{\mathrm{eff}}/E_{\mathrm{matrix}})$ of the composites, estimated with the three different fiber distributions and orientations using the above mentioned RVEs, are plotted in Fig. 12. The increase of the effective Young's modulus of the composite estimated by the RVEs with uniform distributions of aligned fibers ranges from 28.1% to 40.8% (a difference of 45.2%) as the number of fibers (or size of the RVEs) increases from 8 to 2197. The values of the modulus in this uniform case increase gradually and tend to a constant value. These results suggest that a RVE with a smaller number of short fibers is inefficient for obtaining the effective properties accurately with Eq. (26) even in the cases with uniform distributions of aligned fibers (without considering the periodic boundary conditions). The estimated increases of the Young's moduli in the *aligned random* and *random* cases range from 27.7% to 46.2% and oscillate within this range until approaching another constant. Surprisingly, the estimated moduli in the aligned random and random cases are higher for most RVEs than those in the corresponding uniform case. This may suggest that the load transfer may be improved by the ''random'' distributions of fibers in a short-fiber composite. However, in comparison, the values of the effective moduli are about 30% lower than those predicted by the theory and BEM (for incompressible materials) reported in Ref. [18] for the same fiber volume fraction and aspect ratio. This may be due to the fact that the fibers in the current models are confined within their own boxes and no ''relays'' occur in the fiber direction, even in the ''random'' case, which leads to ''weakest-link'' regions between two arrays of fibers. While in the models used in Ref. [18], aligned fibers are placed randomly in the RVE and therefore better load transfer are achieved. Further tests on the current BEM can be carried out with more realistic distributions of the fibers.

Figure 13 shows the CPU time used to obtain results in this short-fiber composite example, on a FUJITSU PRIMEPOWER HPC2500 machine (a shared memory machine with 96 CPUs and 384GB memory) and using four CPUs. In this example, no serious attempts have been made to parallelize the code except for the automatic parallelization made by the compiler. Contrary to the traditional BEM where the solution time is of $O(N^3)$ (with N here being the total number of DOFs), the CPU time required for solving a model using the fast multipole BEM is only of $O(N)$ as shown in Fig. 13 (a straight line with the slope close to unity). Furthermore, the memory required for solving a problem also increases linearly with the size of the problem for fast multipole BEM. Also, the number of iterations required to reach the convergence with a tolerance of 10^{-5} in using the GMRES is between 5 (for $N=10\,992$) and 7 (for $N=3\,018\,678$). Therefore, the fast

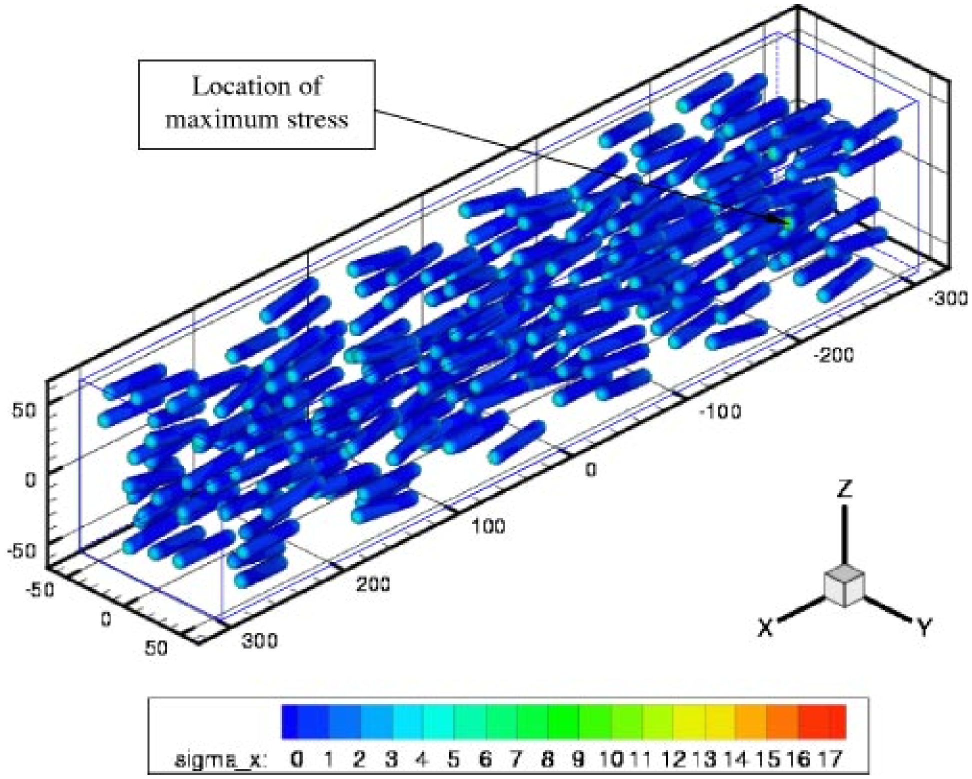

Fig. 10 Contour plot of surface stresses ($\times\sigma^{\infty}$) for a model with 216 "randomly" distributed and oriented short fibers

multipole BEM is much faster and more efficient as compared with the traditional BEM (further discussions and examples can be found in Refs. [21,39]).

These preliminary results in modeling short-fiber-reinforced composites clearly demonstrate the effectiveness and robustness of the developed fast multipole BEM based on the rigid-inclusion model.

5.3 Long-Fiber-Reinforced Composites. Composites reinforced with relatively long fibers, with an aspect ratio of 16 (length=80 and diameter=5), are studied using the developed BEM. Each fiber is discretized using 600 boundary elements and placed in a box of the same dimensions ($100\times20\times20$) as in the short-fiber example. This box is then repeated in the *x*-, *y*-, and *z*-directions to generate RVEs containing $q\times q\times q$ fibers, with q

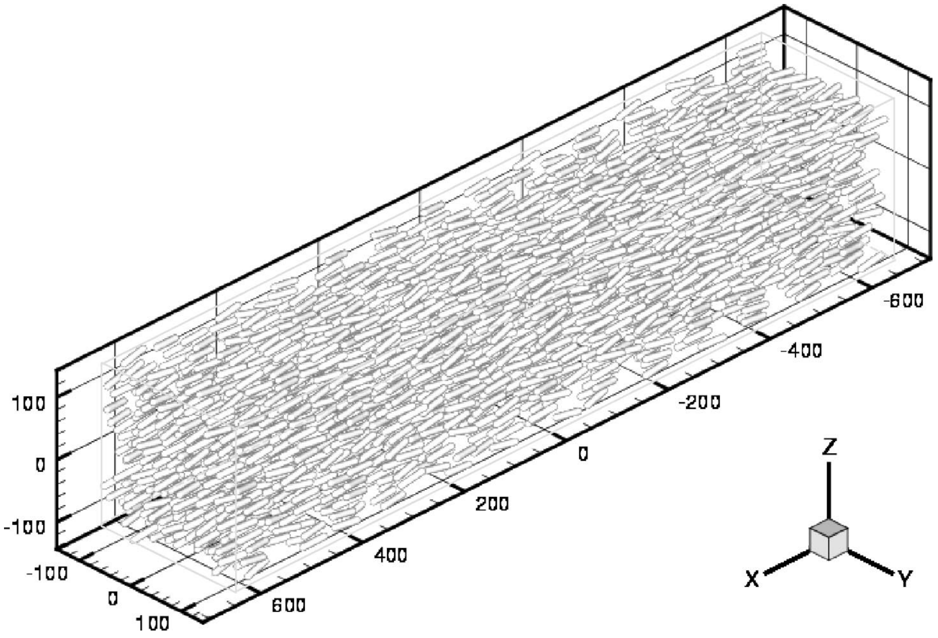

Fig. 11 A RVE containing 2197 short fibers with the total DOF=3 018 678

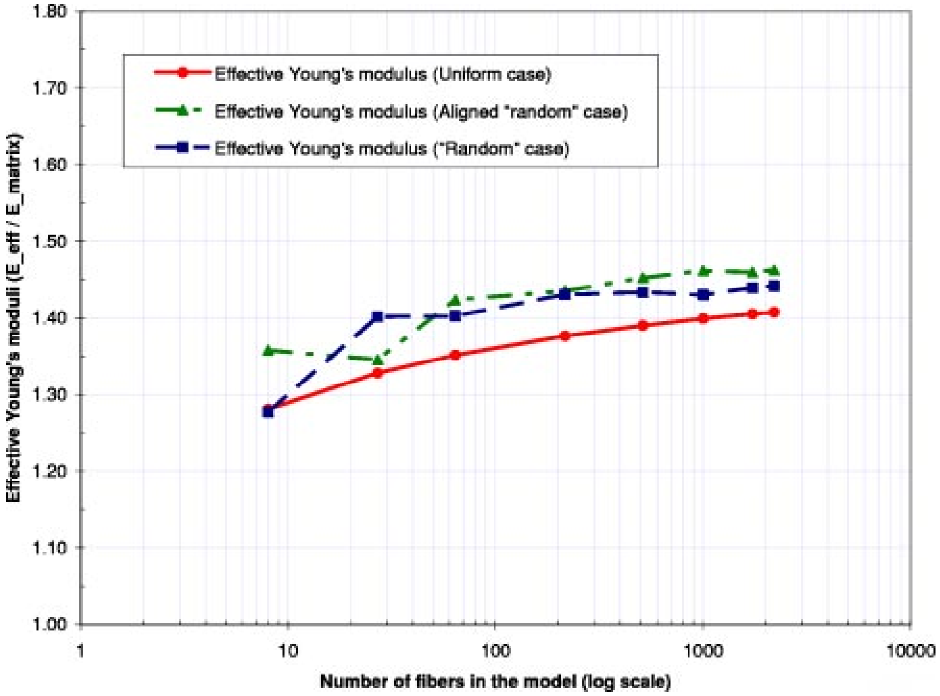

Fig. 12 **Estimated effective Young's moduli in the *x*-direction for the composite model with up to 2197 *short* rigid fibers (fiber volume fraction=9.16%)**

=2, 3, 4, 6, 8, 10, 12, 13, 15, and 18 in this example. The largest model with 5832 fibers and 10 532 592 DOFs (5832×(6+600×3)) is shown in Fig. 14. The fibers are arranged in the so called "random" manner as in the short-fiber RVEs. Again, these are "controlled random" distributions (each fiber within its own box) and orientations (with small rotation angles) of the fibers so that no contact among them occur in the RVEs. The volume fraction of the fiber is 3.85% for all the long-fiber models in this example. The Poisson's ratio for the matrix is 0.3.

Figure 15 shows the normalized effective Young's moduli ($E_{\text{eff}}/E_{\text{matrix}}$) computed for the composites with the relatively long fibers using the RVEs in the uniform and "random" cases. The increases of the computed effective moduli are about two times higher in these long-fiber cases than those in the short-fiber cases, even though the fiber volume fraction is lower. This is expected since aligned long fibers are better for load transfer in a composite. The increases in the values of the modulus range from 75.9% to 95.0% for the uniform case and from 65.4% to 87.6% for the

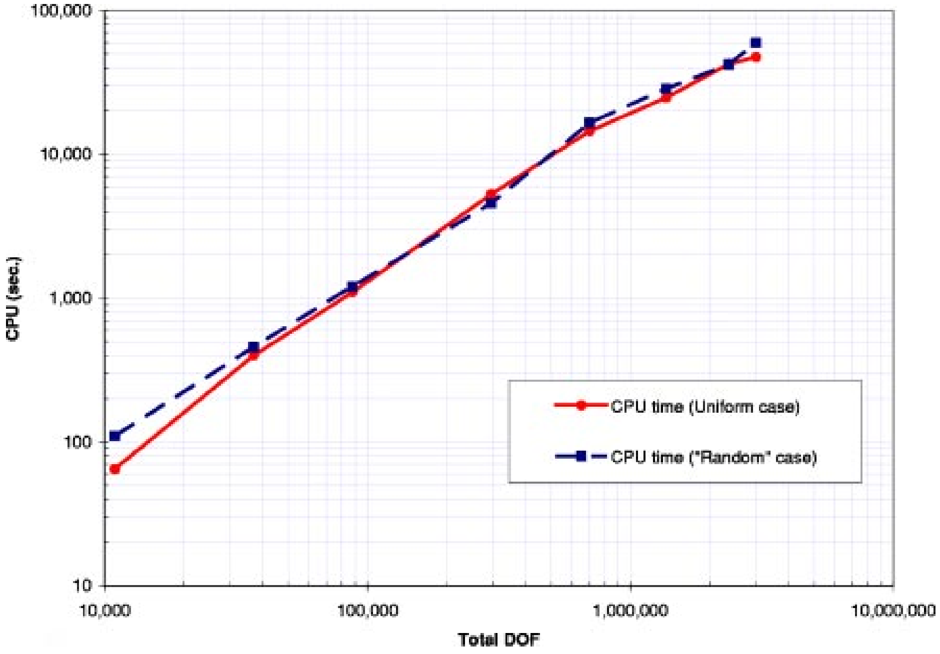

Fig. 13 **CPU time used for solving the BEM models for the short-fiber cases**

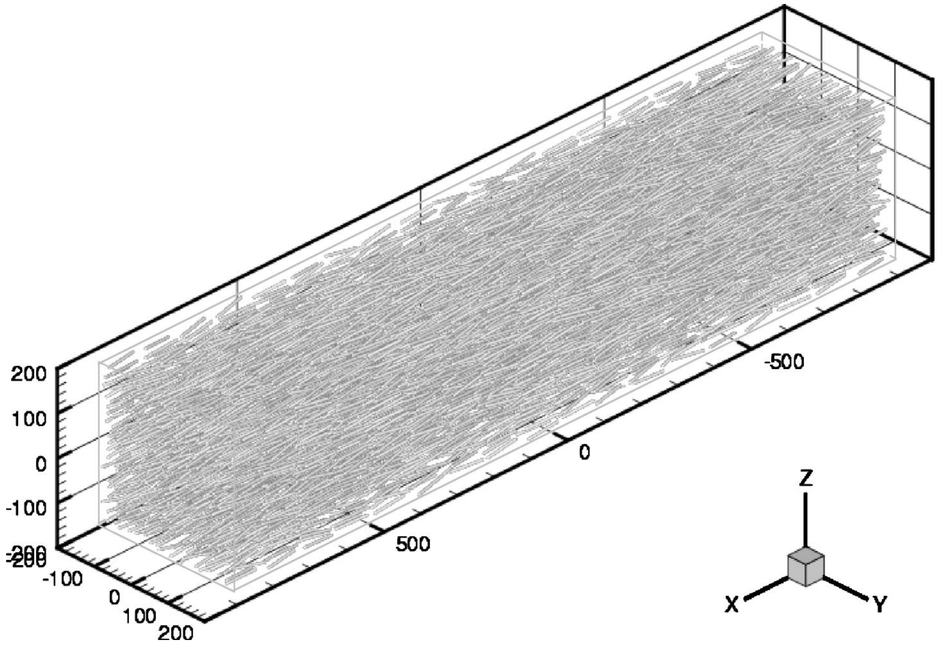

Fig. 14 A RVE containing 5832 long fibers with the total DOF=10 532 592

random case. Results for the uniform case increase gradually with the increase of the RVE sizes and tend to a constant value (95.0%). The values obtained for the "random" case fluctuate for the smaller RVEs and also approach a constant for the larger RVEs. However, the increases in the "random" case are about 8% lower than those in the uniform case in this long-fiber example. This suggests that even small misalignment and rotations of long fibers (which are uniformly and closely packed in the fiber direction initially) will offset the enhancement in the stiffness for long-fiber composites. The largest RVE model (with 5832 fibers and 10 532 592 DOFs) can be solved in 3 h and 40 min (wall-clock time) on the PRIMEPOWER HPC2500 computer using 32 CPUs, with a tolerance of 10^{-5} in the solution with GMRES and ten-term expansion in the FMM. The code used for this example was parallelized with minimum efforts using OpenMP and automatic parallelization option of the compiler.

Rapid convergence is achieved in this case also. The number of iterations in solving the preconditioned system using the GMRES iterative solver is between 5 (for $N = 14\,448$) and 11 (for $N = 10\,532\,592$) with a tolerance of 10^{-5}. This shows that the preconditioner in (22) works very well even in problems when the

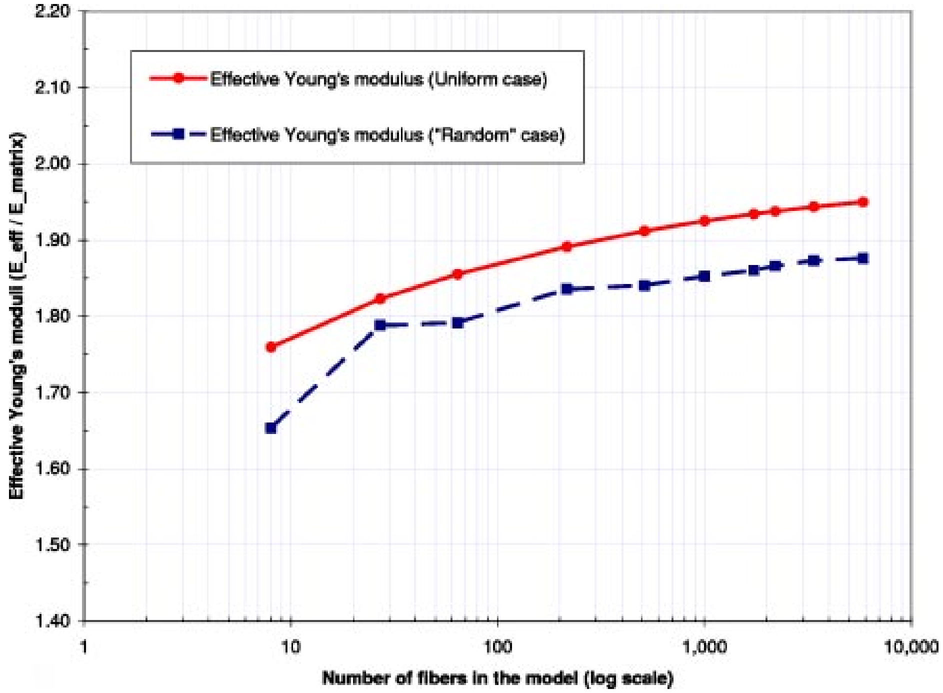

Fig. 15 Estimated effective Young's moduli in the *x*-direction for the composite model with up to 5832 *long* rigid fibers (fiber volume fraction=3.85%)

aspect ratio of the inclusions is as large as 16. The robustness of the developed BEM for modeling fiber-reinforced composites is demonstrated again by this example which has reached 10 million DOFs for the boundary element method.

6 Discussions

The developed fast multipole BEM for the analysis of fiber-reinforced composites based on the rigid-inclusion model has been demonstrated to be very effective and efficient for large scale models. Interactions of the fibers, load transfer mechanisms and effective properties of a composite can be investigated readily using the BEM code with different parameters, such as fiber aspect ratios, volume fractions, waviness, distributions, and orientations. However, further studies are needed regarding the effectiveness of the model and method for evaluating the effective properties of the composite materials, since the rigid-inclusion model has some obvious limitations. For example, the effect of the ratio of the Young's modulus of the fiber to that of the matrix for a composite can not be accounted for in the rigid-inclusion model (this ratio is equal to infinity in the rigid model for any matrix material). Although there are a large amount of experimental data and numerous analytical results based on different theories for estimating the effective properties of fiber-reinforced composites, direct comparison of the BEM results with these data was not attempted in this study (except with that in Ref. [18]), because of the wide variations in those data. More realistic models of the fiber-reinforced composites using the rigid or elastic inclusion approaches need to be studied using the developed BEM in future applications.

The boundary integral equation developed for this study, Eq. (6), is essentially an integral equation of the first kind, which, used in its original form, may raise the question of stability and convergence of its solutions when using iterative solvers as in the FMM. Our experience has shown that even for integral equations of the first kind, the FMM BEM, which uses iterative solvers such as GMRES, can still deliver fast converging and stable results with good preconditioners. Our selection of using the right preconditioner in Eq. (22) turns out to be very effective.

The RVE used in this study is of finite size as shown in Fig. 8, that is embedded in an infinite space filled with the matrix material and loaded remotely (cf., again, 2D models in infinite space used in Refs. [9–14,16,17]). This is chosen so that an infinite domain problem can be solved, which is easier to handle concerning the boundary conditions and, in general, converges faster than an interior problem using the FMM. In this infinite domain problem, the displacement and stress fields on the surfaces of the RVE (data-collection surfaces) need to be calculated after the boundary solutions on all the inclusions are obtained with the fast multipole BEM. This calculation of the fields inside the domain takes extra CPU time, which can be substantial for large models, although it can be computed by using the FMM also [30]. An interior problem defined on the finite sized RVE directly can certainly be implemented with some modifications of Eq. (20) and may provide some improvements to the current RVE model. For example, the boundary solutions (displacements and tractions) on the RVE surfaces, which are available after the solution of an interior problem, can be used directly to evaluate the effective properties. A more reliable, and perhaps more elegant, approach for computing the effective modulus is to use FMM for periodic boundary conditions [25]. Our preliminary analysis with the two dimensional Laplace problems [17] shows that the periodic FMM BEM can be implemented easily, and the increase of the CPU time over the ordinary FMM is less than 20%. The effective property obtained with an equivalent formula of (26) and with the periodic FMM did not differ very much. The elastic counterpart of the periodic FMM is now underway.

The rigid-inclusion model for fiber-reinforced composites may have the potential in some very urgent applications, such as modeling of the emerging carbon nanotube (CNT)-based composites (see, e.g., Refs. [42–45]). The Young's moduli of carbon nanotubes are in general greater than 1 TPa along the tube direction, about two orders higher than those of many matrix materials [43,44]. To model the CNT-based composites, continuum mechanics approaches using the FEM or BEM [46–49] may still be applied if the overall behaviors and properties of the CNT-based composites are to be investigated. However, CNTs are usually produced in different shapes and sizes (for example, being curved, twisted, or bundled), and are difficult to align in a composite. Thus the computational models for such composites may need to contain a much larger number of fibers in a RVE, as compared to those for traditional composites for which the fibers can be aligned easily and distributed uniformly, mainly because of their larger scales. The BEM can model multimaterial problems easily since it uses elements only on boundaries and interfaces of the problem domain. With the fast multipole BEM, the solution time has also been reduced dramatically for large-scale problems. The rigid-inclusion model further simplifies the BEM approach and increases its efficiency in the analysis of some special composite materials, as demonstrated by the examples in the previous section. All these features and new development make the BEM very appealing in large scale analysis of CNT-based composites for estimating their overall mechanical properties. Studies are underway along this line in modeling CNT-based composites by using the developed fast multipole BEM with new interface conditions based on molecular dynamics simulations of CNT-fiber pullout tests.

The work reported in this paper, on using the rigid-inclusion models for analyzing fiber-reinforced composites, is only the first step in the development of a more general FMM BEM for studying such materials and many others. The developed BIE formulation and the FMM BEM can be extended readily for other problems. A FMM BEM solver for general inclusion problems can be developed, where the inclusions can be elastic or rigid, or simply a void. Other RVE models, for example, with periodic boundary conditions, can be implemented as stated above. Interfacing the developed BEM with other methods (such as molecular dynamics) for multiscale analyses of CNT-based composites can also be considered and may present unique advantages over other domain-based methods. Higher-order boundary elements can be applied to further increase the efficiency and accuracy of the BEM. A practical and important development for the BEM code is to develop an improved preprocessor that can generate the boundary element mesh for a RVE containing a large number of truly randomly distributed and oriented fibers, including curved ones, so that more realistic models of composites can be analyzed based on real experimental or fabrication parameters. Finally, full parallelization of the BEM code can be implemented to further increase the robustness of the developed fast multipole BEM for even larger models based, eventually, directly on scanned 3D models of composite material samples.

7 Conclusion

A new boundary integral equation formulation for the analysis of an elastic medium containing rigid inclusions is derived in this paper. This new BIE contains only the weakly-singular displacement kernel from the fundamental solution and thus is much more efficient to solve than the traditional singular BIE. The fast multipole boundary element method is employed to solve this new BIE. The developed BIE formulation and FMM BEM code are found to be very stable and the results converge in about 10 iterations for a tolerance of 10^{-5} with the preconditioned GMRES. The numerical results for a spherical rigid inclusion in an elastic domain match very closely with the analytical solution. Short- and moderately long-fiber-reinforced composites are investigated using the developed BEM and their effective Young's moduli are estimated using the BEM displacement and stress results for the representative volume elements. The largest model studied contains more than 5800 fibers and has the total degrees of freedom over 10 millions. These preliminary results clearly demonstrate the effectiveness, efficiency and promises of the developed fast multipole BEM for studying fiber-reinforced composites, when the fibers are much stiffer than the matrix material.

Acknowledgments

Y.J.L. would like to acknowledge the support by the Academic Center for Computing and Media Studies of the Kyoto University and the fellowship of the Japan Society for the Promotion of Science (JSPS). The authors thank the three reviewers for their valuable comments about this paper.

References

[1] Mackerle, J., 1994, “Finite Element and Boundary Element Library for Composites—A Bibliography (1991–1993),” Finite Elem. Anal. Design, **17**, pp. 155–165.

[2] Achenbach, J. D., and Zhu, H., 1989, “Effect of Interfacial Zone on Mechanical Behavior and Failure of Fiber-Reinforced Composites,” J. Mech. Phys. Solids, **37**, pp. 381–393.

[3] Zhu, H., and Achenbach, J. D., 1991, “Effect of Fiber-Matrix Interphase Defects on Microlevel Stress States at Neighboring Fibers,” J. Compos. Mater., **25**, pp. 224–238.

[4] Gulrajani, S. N., and Mukherjee, S., 1993, “Sensitivities and Optimal Design of Hexagonal Array Fiber Composites With Respect to Interphase Properties,” Int. J. Solids Struct., **30**, pp. 2009–2026.

[5] Pan, L., Adams, D. O., and Rizzo, F. J., 1998, “Boundary Element Analysis for Composite Materials and a Library of Green’s Functions,” Comput. Struct., **66**, pp. 685–693.

[6] Liu, Y. J., Xu, N., and Luo, J. F., 2000, “Modeling of Interphases in Fiber-Reinforced Composites Under Transverse Loading Using the Boundary Element Method,” J. Appl. Mech., **67**, pp. 41–49.

[7] Liu, Y. J., and Xu, N., 2000, “Modeling of Interface Cracks in Fiber-Reinforced Composites With the Presence of Interphases Using the Boundary Element Method,” Mech. Mater., **32**, pp. 769–783.

[8] Chen, X. L., and Liu, Y. J., 2001, “Multiple-Cell Modeling of Fiber-Reinforced Composites With the Presence of Interphases Using the Boundary Element Method,” Comput. Mater. Sci., **21**, pp. 86–94.

[9] Dundurs, J., and Markenscoff, X., 1989, “A Green’s Function Formulation of Anticracks and Their Interaction With Load-Induced Singularities,” J. Appl. Mech., **56**, pp. 550–555.

[10] Hu, K. X., and Chandra, A., 1993, “Interactions Among General Systems of Cracks and Anticracks—An Integral-Equation Approach,” J. Appl. Mech., **60**, pp. 920–928.

[11] Hu, K. X., and Huang, Y., 1993, “A Microcracked Solid Reinforced by Rigid-Line Fibers,” Compos. Sci. Technol., **49**, pp. 145–151.

[12] Hu, K. X., Chandra, A., and Huang, Y., 1994, “On Crack, Rigid-Line Fiber, and Interface Interactions,” Mech. Mater., **19**, pp. 15–28.

[13] Chandra, A., Huang, Y., Wei, X., and Hu, K. X., 1995, “A Hybrid Micro-Macro BEM Formulation for Micro-Crack Clusters in Elastic Components,” Int. J. Numer. Methods Eng., **38**, pp. 1215–1236.

[14] Huang, Y., Hu, K. X., and Chandra, A., 1995, “Stiffness Evaluation for Solids Containing Dilute Distributions of Inclusions and Microcracks,” J. Appl. Mech., **62**, pp. 71–77.

[15] Leite, L. G. S., Coda, H. B., and Venturini, W. S., 2003, “Two-Dimensional Solids Reinforced by Thin Bars Using the Boundary Element Method,” Eng. Anal. Boundary Elem., **27**, pp. 193–201.

[16] Dong, C. Y., Lo, S. H., and Cheung, Y. K., 2003, “Interaction Between Cracks and Rigid-Line Inclusions by an Integral Equation Approach,” Comput. Mech., **31**, pp. 238–252.

[17] Nishimura, N., and Liu, Y. J., 2004, “Thermal Analysis of Carbon-Nanotube Composites Using a Rigid-Line Inclusion Model by the Boundary Integral Equation Method,” Comput. Mech., (in press).

[18] Ingber, M. S., and Papathanasiou, T. D., 1997, “A Parallel-Supercomputing Investigation of the Stiffness of Aligned, Short-Fiber-Reinforced Composites Using the Boundary Element Method,” Int. J. Numer. Methods Eng., **40**, pp. 3477–3491.

[19] Primo, A. R. M., Wrobel, L. C., and Power, H., 2000, “Boundary Integral Formulation for Slow Viscous Flow in a Deforming Region Containing a Solid Inclusion,” Eng. Anal. Boundary Elem., **24**, pp. 53–63.

[20] Kit, H. S., Mykhas’skiv, V. V., and Khaj, O. M., 2002, “Analysis of the Steady Oscillations of a Plane Absolutely Rigid Inclusion in a Three-Dimensional Elastic Body by the Boundary Element Method,” J. Appl. Math. Mech., **66**, pp. 817–824.

[21] Nishimura, N., 2002, “Fast Multipole Accelerated Boundary Integral Equation Methods,” Appl. Mech. Rev., **55**, pp. 299–324.

[22] Greengard, L., and Helsing, J., 1998, “On the Numerical Evaluation of Elastostatic Fields in Locally Isotropic Two-Dimensional Composites,” J. Mech. Phys. Solids, **46**, pp. 1441–1462.

[23] Greengard, L., Kropinski, M. C., and Mayo, A., 1996, “Integral Equation Methods for Stokes Flow and Isotropic Elasticity in the Plane,” J. Comput. Phys., **125**, pp. 403–414.

[24] Helsing, J., 1995, “An Integral Equation Method for Elastostatics of Periodic Composites,” J. Mech. Phys. Solids, **43**, pp. 815–828.

[25] Greengard, L., and Rokhlin, V., 1987, “A Fast Algorithm for Particle Simulations,” J. Comput. Phys., **73**, pp. 325–348.

[26] Fu, Y., Klimkowski, K. J., Rodin, G. J., Berger, E., Browne, J. C., Singer, J. K., Geijn, R. A. V. D., and Vemaganti, K. S., 1998, “A Fast Solution Method for Three-Dimensional Many-Particle Problems of Linear Elasticity,” Int. J. Numer. Methods Eng., **42**, pp. 1215–1229.

[27] Peirce, A. P., and Napier, J. A. L., 1995, “A Spectral Multipole Method for Efficient Solution of Large-Scale Boundary Element Models in Elastostatics,” Int. J. Numer. Methods Eng., **38**, pp. 4009–4034.

[28] Popov, V., and Power, H., 2001, “An $O(N)$ Taylor Series Multipole Boundary Element Method for Three-Dimensional Elasticity Problems,” Eng. Anal. Boundary Elem., **25**, pp. 7–18.

[29] Nishimura, N., Yoshida, K., and Kobayashi, S., 1999, “A Fast Multipole Boundary Integral Equation Method for Crack Problems in 3D,” Eng. Anal. Boundary Elem., **23**, pp. 97–105.

[30] Yoshida, K., Nishimura, N., and Kobayashi, S., 2001, “Application of Fast Multipole Galerkin Boundary Integral Equation Method to Crack Problems in 3D,” Int. J. Numer. Methods Eng., **50**, pp. 525–547.

[31] Lai, Y.-S., and Rodin, G. J., 2003, “Fast Boundary Element Method for Three-Dimensional Solids Containing Many Cracks,” Eng. Anal. Boundary Elem., **27**, pp. 845–852.

[32] Rizzo, F. J., 1967, “An Integral Equation Approach to Boundary Value Problems of Classical Elastostatics,” Q. Appl. Math., **25**, pp. 83–95.

[33] Rizzo, F. J., Shippy, D. J., and Rezayat, M., 1985, “A Boundary Integral Equation Method for Radiation and Scattering of Elastic Waves in Three Dimensions,” Int. J. Numer. Methods Eng., **21**, pp. 115–129.

[34] Mukherjee, S., 1982, *Boundary Element Methods in Creep and Fracture*, Applied Science Publishers, NY.

[35] Banerjee, P. K., 1994, *The Boundary Element Methods in Engineering*, 2nd ed., McGraw–Hill, NY.

[36] Brebbia, C. A., and Dominguez, J., 1989, *Boundary Elements—An Introductory Course*, McGraw–Hill, NY.

[37] Kane, J. H., 1994, *Boundary Element Analysis in Engineering Continuum Mechanics*, Prentice–Hall, Englewood Cliffs, NJ.

[38] Takahashi, T., Kobayashi, S., and Nishimura, N., 1999, “Fast Multipole BEM Simulation of Overcoring in an Improved Conical-End Borehole Strain Measurement Method,” in *Mechanics and Engineering—In Honor of Professor Qinghua Du’s 80th Anniversary*, edited by Yao, Z. H., Tsinghua University Press, Beijing, pp. 120–127.

[39] Yoshida, K., 2001, “Applications of Fast Multipole Method to Boundary Integral Equation Method,” Ph.D. dissertation, Department of Global Environment Engineering, Kyoto University.

[40] Timoshenko, S. P., and Goodier, J. N., 1987, *Theory of Elasticity*, 3rd ed., McGraw–Hill, NY.

[41] Mura, T., 1987, *Micromechanics of Defects in Solids*, 2nd revised ed., Kluwer Academic, Dordrecht.

[42] Thostenson, E. T., Ren, Z. F., and Chou, T.-W., 2001, “Advances in the Science and Technology of Carbon Nanotubes and Their Composites: A Review,” Compos. Sci. Technol., **61**, pp. 1899–1912.

[43] Ruoff, R. S., and Lorents, D. C., 1995, “Mechanical and Thermal Properties of Carbon Nanotubes,” Carbon, **33**, pp. 925–930.

[44] Lu, J. P., 1997, “Elastic Properties of Single and Multilayered Nanotubes,” J. Phys. Chem. Solids, **58**, pp. 1649–1652.

[45] Qian, D., Dickey, E. C., Andrews, R., and Rantell, T., 2000, “Load Transfer and Deformation Mechanisms in Carbon Nanotube-Polystyrene Composites,” Appl. Phys. Lett., **76**, pp. 2868–2870.

[46] Fisher, F. T., Bradshaw, R. D., and Brinson, L. C., 2002, “Effects of Nanotube Waviness on the Modulus of Nanotube-Reinforced Polymers,” Appl. Phys. Lett., **80**, pp. 4647–4649.

[47] Fisher, F. T., Bradshaw, R. D., and Brinson, L. C., 2003, “Fiber Waviness in Nanotube-Reinforced Polymer Composites—I: Modulus Predictions Using Effective Nanotube Properties,” Compos. Sci. Technol., **63**, pp. 1689–1703.

[48] Liu, Y. J., and Chen, X. L., 2003, “Evaluations of the Effective Materials Properties of Carbon Nanotube-Based Composites Using a Nanoscale Representative Volume Element,” Mech. Mater., **35**, pp. 69–81.

[49] Chen, X. L., and Liu, Y. J., 2004, “Square Representative Volume Elements for Evaluating the Effective Material Properties of Carbon Nanotube-Based Composites,” Comput. Mater. Sci., **29**, pp. 1–11.

Rayleigh Waves Generated by a Thermal Source: A Three-Dimensional Transient Thermoelasticity Solution

H. G. Georgiadis[1]
Mechanics Division,
National Technical University of Athens,
Zographou GR-15773, Greece
Member ASME
e-mail: georgiad@central.ntua.gr

G. Lykotrafitis
Graduate Aeronautical Laboratories,
California Institute of Technology,
Mail Stop 105-50,
Pasadena, CA 91125

A three-dimensional transient thermoelastic solution is obtained for Rayleigh-type disturbances propagating on the surface of a half-space. These surface waves are generated by either a buried or surface thermal source, which has the form of a concentrated heat flux applied impulsively. In an effort to model this problem as realistically as possible, the half-space material is taken to respond according to Biot's fully coupled thermoelasticity. The problem has relevance to situations involving heat generation due to: (i) laser action (impulsive electromagnetic radiation) on a surface target, (ii) underground nuclear activity, and (iii) friction developed during underground fault motions related to seismic activity. The problem was attacked with unilateral and double bilateral Laplace transforms, which suppress, respectively, the time variable and two of the space variables. The Rayleigh wave contribution is obtained as a closed-form expression by utilizing asymptotics, complex-variable theory and certain results for Bessel functions. The dependence of the normal displacement associated with the Rayleigh wave upon the distance from the source epicenter and the distance from the wavefront is also determined.
[DOI: 10.1115/1.1825438]

1 Introduction

A class of interesting problems of thermomechanical wave motions arises from the action of a thermal source in a conducting and deformable body. The source can be situated either on the surface or inside the medium (buried source). Typical problems of this class involve: (i) laser action (impulsive electromagnetic radiation) on a surface target (see e.g. Morland [1], Sve and Miklowitz [2], Bechtel [3], Hetnarski and Ignaczak [4], and Royer and Chenu [5]), (ii) underground nuclear activity (see e.g., Bullen and Bolt [6]), and (iii) friction developed during underground fault motions related to seismic activity (see e.g., Kanamori et al. [7]). In many cases, these problems can be viewed as a three-dimensional (3D) situation involving a thermoelastic half-space under either a surface or buried heat source. This situation is studied here by employing the coupled inertial thermoelasticity theory of Biot [8] (see also Achenbach [9]). In particular, we focus attention on the surface disturbance of the Rayleigh-type and provide a closed-form expression for the associated displacement field. Indeed, past experience with pure mechanical (i.e., without any thermal effects) versions of the present problem indicates that the Rayleigh-wave disturbance is the *dominant* one over the surface after a certain time (see e.g., the 2D analysis of Garvin [10] involving a buried dilatational source in a half-plane and the 3D analysis of Pekeris and Lifson [11] involving a buried concentrated vertical force in a half-space).

We should mention that a recent study by the present authors and Brock (Lykotrafitis, Georgiadis, and Brock [12]) dealt with the same problem studied here and provided an evaluation of the complete field at the surface. This field comprises thermoelastic dilatational and Rayleigh waves, and elastic shear waves. However, the latter study relies much upon numerical analysis (involving numerical wavenumber integrations and numerical Laplace-transform inversions) and does not furnish an analytical expression for the evaluation of the surface displacements. Instead, our aim here is to provide a simple *closed-form* expression for the Rayleigh-wave disturbance without using any special numerical technique. This was made possible by using asymptotics and certain results of complex-variable theory and Bessel functions in addition to the basic integral-transform analysis of Ref. [12]. The key idea used is making explicit the appearance of Rayleigh-wave poles by obtaining an approximate form of the Rayleigh function that exhibits no dispersion but still depends upon the thermoelastic constants. Notably, this approximate form is numerically very close to the exact one giving therefore very accurate results.

It should be mentioned that most of the studies published before on wave propagation induced by sudden heating model the problems as *one-dimensional* (see e.g., Boley and Tolins [13], and Hetnarski and Ignaczak [14]), employ *uncoupled* thermoelasticity (see e.g., Sve and Miklowitz [2]) or treat only *infinite* domains, i.e., full spaces (see e.g., Predeleanu [15], Fleurier and Predeleanu [16], Sharp and Crouch [17], and Manolis and Beskos [18,19]). Also, some of the aforementioned works consider the special case of a *time-harmonic* response. On the contrary, the present study aims at a more realistic formulation of these problems and is therefore based on the transient coupled inertial thermoelasticity, while it treats a three-dimensional problem in a half-space domain. Notice that the relevance of the constitutive theory used here to *thermal-shock* problems—particularly the importance of inertial and thermal-coupling effects—was shown in the studies of Hetnarski [20], Boley and Tolins [13], Sternberg and Chakravorty [21,22], and Francis [23]. More recent work employing this theory in transient problems of wave propagation and fracture was

---

[1] To whom correspondence should be addressed.

Contributed by the Applied Mechanics Division of THE AMERICAN SOCIETY OF MECHANICAL ENGINEERS for publication in the ASME JOURNAL OF APPLIED MECHANICS. Manuscript received by the Applied Mechanics Division, March 2, 2004; final revision, May 24, 2004. Associate Editor: H. Gao. Discussion on the paper should be addressed to the Editor, Professor Robert M. McMeeking, Journal of Applied Mechanics, Department of Mechanical and Environmental Engineering, University of California-Santa Barbara, Santa Barbara, CA 93106-5070, and will be accepted until four months after final publication in the paper itself in the ASME JOURNAL OF APPLIED MECHANICS.

done by, among others, Atkinson and Craster [24], Brock [25], Brock, Rodgers and Georgiadis [26], Brock and Georgiadis [27], Georgiadis, Brock, and Rigatos [28], and Georgiadis, Rigatos, and Brock [29]. Finally, within the context of a different theory, namely inertialess and uncoupled thermoelasticity, solutions for thermally activated surface displacements in a half-space were obtained by Barber [30] and Barber and Martin-Moran [31].

2 Problem Statement

Consider a 3D body in the form of a half-space $z>-H$ (see Fig. 1) which is both thermally conducting and deformable. The body is initially at rest and at uniform temperature $\tilde{T}_0$. At time $t=0$, a thermal source acts at a point situated at a depth H below the surface. This point of the half-space is taken as the origin of the Cartesian coordinate system (x,y,z). A concentrated thermal source having an impulsive time variation is assumed, with the understanding that the solution of this problem (Green's function or fundamental solution) can be integrated in space and time to give then the solution for any general thermal loading. Also, the source has an intensity KQ, where K is the thermal conductivity with dimensions of (power)(length)$^{-1}$(°C)$^{-1}$, °C means degrees of temperature and Q is a multiplier expressed in (°C)(length)(time).

Then, according to the linear, isotropic, inertial coupled thermoelasticity theory (Biot [8], Achenbach [9], Chadwick [32], and Carlson [33]), the governing equations for this problem are written as

$$\boldsymbol{\sigma}=\mu(\nabla\mathbf{u}+\mathbf{u}\nabla)+\lambda(\nabla\cdot\mathbf{u})\mathbf{1}-\kappa_0(3\lambda+2\mu)\theta\mathbf{1}, \tag{1}$$

$$\mathbf{q}=-K\nabla\theta, \tag{2}$$

$$\mu\nabla^2\mathbf{u}+(\lambda+\mu)\nabla(\nabla\cdot\mathbf{u})-\kappa_0(3\lambda+2\mu)\nabla\theta=\rho\frac{\partial^2\mathbf{u}}{\partial t^2}, \tag{3}$$

$$K\nabla^2\theta-\rho c_v\frac{\partial\theta}{\partial t}-\kappa_0(3\lambda+2\mu)\tilde{T}_0\frac{\partial(\nabla\cdot\mathbf{u})}{\partial t} + KQ\cdot\delta(t)\cdot\delta(x)\cdot\delta(y)\cdot\delta(z)=0, \tag{4}$$

where (1) is the Neumann-Duhamel law, (2) is the heat-conduction Fourier law, (3) is the displacement-temperature equation of motion, and (4) is the coupled heat equation. Also, in the above equations, $\boldsymbol{\sigma}$ is the stress tensor, $\mathbf{u}$ is the displacement vector, $\theta=\tilde{T}-\tilde{T}_0$ is the change in temperature, $\tilde{T}$ is the current temperature, $\tilde{T}_0$ is the initial temperature, $\mathbf{q}$ is the heat-flux vector, (λ,μ) are the Lame constants, κ_0 is the coefficient of linear expansion, ρ is the mass density, c_v is the specific heat at constant deformation, $\delta(\ )$ is the Dirac delta distribution, $\mathbf{1}$ is the identity tensor, ∇ is the gradient operator, and $\nabla^2=(\partial^2/\partial x^2)+(\partial^2/\partial y^2)+(\partial^2/\partial z^2)$ is the Laplace operator. All field quantities above are functions of (x,y,z,t).

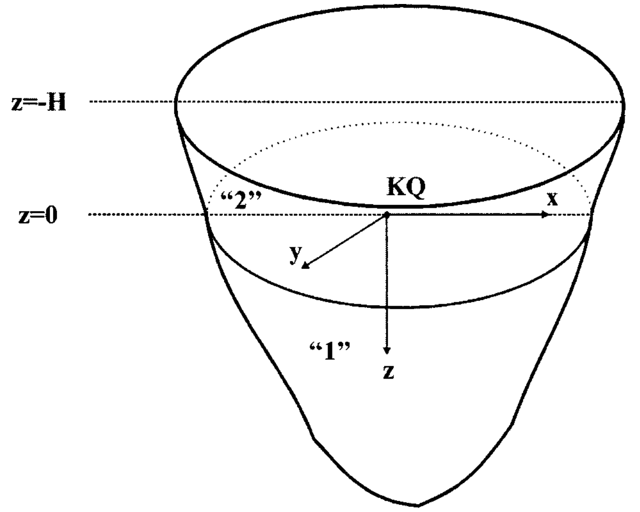

Fig. 1 A thermally conducting and deformable body in the form of 3D half-space under the action of a buried $(H\neq 0)$ or surface $(H=0)$ heat source

In addition, zero initial conditions are taken, i.e.

$$\mathbf{u}=\partial\mathbf{u}/\partial t=\theta=0 \quad \text{for } t\leq 0 \ \text{ in } (-\infty<x<\infty, -\infty<y<\infty, -H<z<\infty), \tag{5}$$

and we also assume that the half-space surface $z=-H$ is traction free and insulated (i.e., no heat is conducted through the half-space surface and air). Finally, the pertinent *finiteness* conditions at remote regions (Ignaczak and Nowacki [34]) state that the field at infinity remains bounded although temperature signals travel—according to Biot's theory—at an infinite speed.

The objective of the present work is to determine the vertical displacement at the surface for the problem described by Eqs. (1)–(5). The solution of this problem is greatly facilitated by removing the source term in (4) and considering this term as a discontinuity along an *imagined plane* at $z=0$. This strategy was introduced first by Pekeris [35] (see also Miklowitz [36]) in treating the pure mechanical problem of a half-space under a buried vertical force. Considering thus an imaginary plane along $z=0$ that separates the original half-space into the half-space $0<z<\infty$ (region 1 in Fig. 1) and the strip $-H<z<0$ (region 2 in Fig. 1), we write the pertinent continuity and discontinuity conditions at $z=0$ along with the standard boundary conditions at $z=-H$

$$\mathbf{u}^{(1)}(x,y,0,t)=\mathbf{u}^{(2)}(x,y,0,t), \tag{6a}$$

$$\theta^{(1)}(x,y,0,t)=\theta^{(2)}(x,y,0,t), \tag{6b}$$

$$\sigma_{zj}^{(1)}(x,y,0,t)=\sigma_{zj}^{(2)}(x,y,0,t), \tag{6c}$$

$$\frac{\partial\theta^{(1)}(x,y,0,t)}{\partial z}-\frac{\partial\theta^{(2)}(x,y,0,t)}{\partial z}=Q\cdot\delta(t)\cdot\delta(x)\cdot\delta(y), \tag{6d}$$

$$\sigma_{zj}(x,y,-H,t)=0, \tag{7a}$$

$$\frac{\partial\theta(x,y,-H,t)}{\partial z}=0, \tag{7b}$$

where $-\infty<x<\infty$, $-\infty<y<\infty$, $(j=x,y,z)$, and the superscript in parentheses 1 or 2 attached to a field quantity means that the plane $z=0$ is approached as $z\to 0^+$ or $z\to 0^-$, respectively.

In this way, the original problem (1)–(5) and (7) is equivalent to the problem described by (1)–(3) and (5)–(7) and with the equation $K\nabla^2\theta-\rho c_v(\partial\theta/\partial t)-\kappa_0(3\lambda+2\mu)\tilde{T}_0(\partial(\nabla\cdot\mathbf{u})/\partial t)=0$ replacing now Eq. (4). Further, a convenient normalization is performed allowing the two field equations of the problem [i.e., Eqs. (3) and (4) with no source terms] to take the form

$$\nabla^2\mathbf{u}+(m^2-1)\nabla\Delta+\kappa\nabla\theta-m^2\frac{\partial^2\mathbf{u}}{\partial s^2}=0, \tag{8}$$

$$\frac{\kappa}{m^2}\nabla^2\theta-\frac{\kappa}{hm^2}\frac{\partial\theta}{\partial s}+\frac{\varepsilon}{h}\frac{\partial\Delta}{\partial s}=0, \tag{9}$$

where $s=V_1 t$ is the normalized time (with dimension of length),-

$V_1=[(\lambda+2\mu)/\rho]^{1/2}$ is the dilatational-wave velocity in the *absence* of thermal effects (i.e., within the "pure" mechanical theory), $\kappa=-\kappa_0(3\lambda+2\mu)/\mu=\kappa_0(4-3m^2)<0$ is the normalized coefficient of linear expansion, $\varepsilon=(\tilde{T}_0/c_v)(\kappa V_2/m)^2$ is the dimensionless coupling coefficient, $h=(KV_2/\mu m c_v)$ is the thermoelastic characteristic length, $V_2=(\mu/\rho)^{1/2}$ is the shear-wave velocity, $m=V_1/V_2>1$, and $\Delta=\nabla\cdot\mathbf{u}$ is the dilatation. As regards the range of numerical values that ε and h take on, for most materials the characteristic length is very small [typically $h=O(10^{-10}\,\text{m})$, see, e.g., Chadwick [32]] but the coupling coefficient can be as high as $\varepsilon=O(10^{-1})$ (e.g., $\varepsilon=0.36$ for Polycarbonate at $\tilde{T}_0=40°\text{C}$). The fact that h is very small with respect to s for a rather wide time-range will be conveniently utilized in the ensuing analysis.

3 Basic Integral-Transform Analysis

This section essentially reproduces relevant material from our recent related work (Lykotrafitis, Georgiadis, and Brock [12]). This material is briefly presented here for the sake of completeness and because of the need to introduce certain definitions. It is also emphasized that although the form of conditions (6) and (7) suggest existence of an axisymmetric field, the basic integral-transform analysis presented here is appropriate for more general *nonaxisymmetric* situations. This is why we do not use the Hankel transform below. Certainly, the fact that we deal with an axisymmetric field in our specific problem will emerge in the course of solving the problem.

The dependence of the problem on the variables (x,y,s) is suppressed through the use of multiple Laplace transforms (see e.g., van der Pol and Bremmer [37], and Carrier et al. [38]). The unilateral transform pair (direct and inverse transform) is defined as

$$\Phi(x,y,z,p)=\int_0^\infty \varphi(x,y,z,s)\cdot e^{-ps}ds, \tag{10a}$$

$$\varphi(x,y,z,s)=(1/2\pi\mathrm{i})\int_{\Gamma_1}\Phi(x,y,z,p)\cdot e^{ps}dp, \tag{10b}$$

and the direct transform suppresses the timelike variable s. The double bilateral transform pair is defined as

$$\Phi^*(q,w,z,p)=\int_{-\infty}^{\infty}\int_{-\infty}^{\infty}\Phi(x,y,z,p)\cdot e^{-p(qx+wy)}dxdy, \tag{11a}$$

$$\Phi(x,y,z,p)=(p/2\pi\mathrm{i})^2\int_{\Gamma_2}\int_{\Gamma_3}\Phi^*(q,w,z,p)\cdot e^{p(qx+wy)}dqdw, \tag{11b}$$

and the direct transform suppresses the space variables (x,y). In what follows, we save a capital letter for the unilateral direct transform, whereas the double bilateral direct transform is denoted by an asterisk. It is also noticed that (van der Pol and Bremmer [37]): (1) Because of Lerch's theorem for the uniqueness of unilateral Laplace transforms and because of the existence of Widder's inversion formula for real p, it is sufficient to view $\Phi(x,y,z,p)$ as a function of a *real* variable p over some segment of the real axis in the half-plane of analyticity. Once $\Phi(x,y,z,p)$ is determined as an explicit function of p in the course of solving the transformed differential equations, its definition can be extended to the whole complex p-plane, except for isolated singular points, through analytic continuation. (2) The variables q and w should be treated as *complex*. (3) The integration path Γ_j, with $(j=1,2,3)$, is a line parallel to the imaginary axis in the associated transform plane and lies *within* the region of analyticity.

Applying now (10a) and (11a) to the governing equations (1), (8), and (9), and considering (5) yields the following general expressions for the transformed temperature change, displacements and stresses (details of this procedure are given in Appendix A of Ref. [12]). These expressions are, of course, different in the regions 1 and 2 of the original half-space.

(a) Region 1 $(0<z<\infty)$:

$$\begin{bmatrix} \dfrac{\kappa}{m^2}\Theta^* \\ pU_x^* \\ pU_y^* \\ pU_z^* \\ \dfrac{1}{\mu}\Sigma_{xy}^* \\ \dfrac{1}{\mu}\Sigma_{xz}^* \\ \dfrac{1}{\mu}\Sigma_{yz}^* \\ \dfrac{1}{\mu}\Sigma_{xx}^* \\ \dfrac{1}{\mu}\Sigma_{yy}^* \\ \dfrac{1}{\mu}\Sigma_{zz}^* \end{bmatrix} = \begin{bmatrix} M_+ & M_- & 0 & 0 & 0 & 0 & 0 & 0 \\ -q & -q & 1 & 0 & 0 & 0 & 0 & 0 \\ -w & -w & 0 & 1 & 0 & 0 & 0 & 0 \\ a_+ & a_- & \dfrac{q}{\beta} & \dfrac{w}{\beta} & 0 & 0 & 0 & 0 \\ -2qw & -2qw & w & q & 0 & 0 & 0 & 0 \\ 2qa_+ & 2qa_- & -\dfrac{T_w}{\beta} & \dfrac{wq}{\beta} & 0 & 0 & 0 & 0 \\ 2wa_+ & 2wa_- & \dfrac{wq}{\beta} & -\dfrac{T_q}{\beta} & 0 & 0 & 0 & 0 \\ T_{w+} & T_{w-} & 2q & 0 & 0 & 0 & 0 & 0 \\ T_{q+} & T_{q-} & 0 & 2w & 0 & 0 & 0 & 0 \\ -T & -T & -2q & -2w & 0 & 0 & 0 & 0 \end{bmatrix} \begin{bmatrix} X_1e^{-pa_+z} \\ X_2e^{-pa_-z} \\ X_3e^{-p\beta z} \\ X_4e^{-p\beta z} \\ 0 \\ 0 \\ 0 \\ 0 \end{bmatrix}. \tag{12}$$

(b) Region 2 $(-H<z<0)$:

$$\begin{bmatrix} \frac{\kappa}{m^2}\Theta^* \\ pU_x^* \\ pU_y^* \\ pU_z^* \\ \frac{1}{\mu}\Sigma_{xy}^* \\ \frac{1}{\mu}\Sigma_{xz}^* \\ \frac{1}{\mu}\Sigma_{yz}^* \\ \frac{1}{\mu}\Sigma_{xx}^* \\ \frac{1}{\mu}\Sigma_{yy}^* \\ \frac{1}{\mu}\Sigma_{zz}^* \end{bmatrix} = \begin{bmatrix} M_+ & M_+ & M_- & M_- & 0 & 0 & 0 & 0 \\ -q & -q & -q & -q & 1 & 0 & 1 & 0 \\ -w & -w & -w & -w & 0 & 1 & 0 & 1 \\ -a_+ & a_+ & -a_- & a_- & \frac{-q}{\beta} & \frac{-w}{\beta} & \frac{q}{\beta} & \frac{w}{\beta} \\ -2qw & -2qw & -2qw & -2qw & w & q & w & q \\ -2qa_+ & 2qa_+ & -2qa_- & 2qa_- & \frac{T_w}{\beta} & \frac{-wq}{\beta} & \frac{-T_w}{\beta} & \frac{wq}{\beta} \\ -2wa_+ & 2wa_+ & -2wa_- & 2wa_- & \frac{-wq}{\beta} & \frac{T_q}{\beta} & \frac{wq}{\beta} & \frac{-T_q}{\beta} \\ T_{w+} & T_{w+} & T_{w-} & T_{w-} & 2q & 0 & 2q & 0 \\ T_{q+} & T_{q+} & T_{q-} & T_{q-} & 0 & 2w & 0 & 2w \\ -T & -T & -T & -T & -2q & -2w & -2q & -2w \end{bmatrix} \begin{bmatrix} X_5 e^{pa_+z} \\ X_6 e^{-pa_+z} \\ X_7 e^{pa_-z} \\ X_8 e^{-pa_-z} \\ X_9 e^{p\beta z} \\ X_{10} e^{p\beta z} \\ X_{11} e^{-p\beta z} \\ X_{12} e^{-p\beta z} \end{bmatrix} \tag{13}$$

where Θ^* is the multiply-transformed change in temperature, and (U_x^*, U_y^*, U_z^*) and $(\Sigma_{xy}^*, \Sigma_{xz}^*, \ldots, \Sigma_{zz}^*)$ are the multiply-transformed components of, respectively, the displacement vector and the stress tensor. We should also notice that solution (12) is bounded at $z\rightarrow\infty$ appropriately satisfying thus the finiteness conditions, whereas such constraints need not be imposed on solution (13). In the above equations, the yet unknown $X_1, X_2, \ldots, X_{12}$ are arbitrary functions of (q,w,p) which have to be determined from the boundary conditions in each specific problem. Also, the following definitions are employed in (12) and (13):

$$a_\pm = (m_\pm^2 - q^2 - w^2)^{1/2}, \tag{14a}$$

$$\beta = (m^2 - q^2 - w^2)^{1/2} \tag{14b}$$

$$m_\pm = \frac{1}{2}\left[\left(1+\frac{1}{(hp)^{1/2}}\right)^2 + \frac{\varepsilon}{hp}\right]^{1/2} \pm \frac{1}{2}\left[\left(1-\frac{1}{(hp)^{1/2}}\right)^2 + \frac{\varepsilon}{hp}\right]^{1/2}, \tag{15}$$

$$M_\pm = m_\pm^2 - 1, \tag{16}$$

$$T = 2\beta^2 - m^2 = m^2 - 2(q^2 + w^2), \tag{17a}$$

$$T_\pm = 2a_\pm^2 - m^2 \tag{17b}$$

$$T_{q\pm} = T_\pm + 2q^2, \tag{18a}$$

$$T_{w\pm} = T_\pm + 2w^2 \tag{18b}$$

$$T_q = T + q^2, \tag{19a}$$

$$T_w = T + w^2. \tag{19b}$$

Further, a new complex variable ζ is defined through $\zeta^2 = q^2 + w^2$ allowing the placement of necessary *branch cuts* for the functions $a_\pm \equiv a_\pm(\zeta,p) = (m_\pm^2 - \zeta^2)^{1/2}$ and $\beta \equiv \beta(\zeta) = (m^2 - \zeta^2)^{1/2}$. These restrictions in the ζ-plane are in accord with the chosen solution forms in (12) and (13). For the representative case of $\beta(\zeta)$, Fig. 2 depicts these branch cuts (the cuts are situated outwards with respect to the origin $\zeta=0$—a similar situation exists for the functions $a_\pm(\zeta,p)$). In this way, it is $\operatorname{Re} a_+ \geqslant 0$, $\operatorname{Re} a_- \geqslant 0$, and $\operatorname{Re}\beta \geqslant 0$ in the cut plane. Also, we record here the two possible arrangements of m_+, m_-, and m with respect to their magnitude. This information in conjunction with the placement of branch cuts will enable the proper definition of the regions of analyticity of various functions appearing in the analysis.

The quantities m_+ and m_- are p-dependent (recall that p is real and non-negative), whereas m is constant. From their definitions, the following inequalities follow:

$$m_- < m_+ < m \quad \text{for } hp > \frac{m^2(1+\varepsilon)-1}{m^2(m^2-1)}, \tag{20a}$$

$$m_- < m < m_+ \quad \text{for } hp < \frac{m^2(1+\varepsilon)-1}{m^2(m^2-1)}. \tag{20b}$$

In addition, useful approximations for the quantities m_+ and m_- can be obtained from (15) by taking $s\rightarrow(1/p)$, when s is very small or very large, and by performing series expansion and keeping the dominant terms (see e.g., Carrier et al. [38] for similar procedures). The following approximate forms considerably simplify unilateral Laplace transform inversions

$$m_+ \cong 1 \quad \text{and} \quad m_- \cong \frac{1}{(hp)^{1/2}} \quad \text{for } \frac{s}{h} \ll 1, \tag{21a}$$

$$m_+ \cong \left(\frac{1+\varepsilon}{hp}\right)^{1/2} \quad \text{and} \quad m_- \cong \frac{1}{(1+\varepsilon)^{1/2}} \quad \text{for } \frac{s}{h} \gg 1. \tag{21b}$$

Notice that validity of (20*a*) or (20*b*) is necessary but not sufficient for, respectively, the validity of (21*a*) or (21*b*).

Finally, it turns out that the case in (20*a*) is rather impractical since it corresponds to an *extremely small* initial time interval of the process, which for most conducting materials is $t < O(10^{-13}\,\text{s})$. This is found by taking $s\rightarrow(1/p)$ for very small s (i.e., for very small time). In the present study, information is needed generally for longer times so we shall focus interest only on the case (20*b*) and employ (21*b*) appropriately. Any case with, say, $(s/h)\geqslant 100$ leads to a reasonable approximation for $m_\pm$. The results in (21*b*) are indeed robust because the normalized time is scaled by an extremely small length (the thermoelastic characteristic length).

Now, transforming via (10*a*) and (11*a*) the continuity/discontinuity conditions (6) and the boundary conditions (7), in view also of the general transformed solutions (12) and (13), leads to a linear algebraic system of 12 equations in the 12 unknown

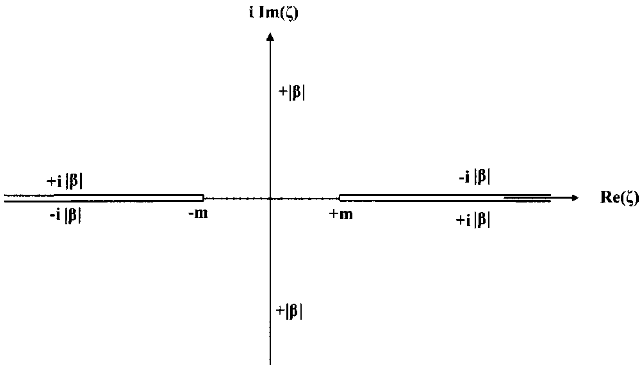

Fig. 2 Branch cuts for the function $\beta(\zeta)\equiv(m^2-\zeta^2)^{1/2}$ in the complex ζ-plane. Similar branch cuts, emanating from the points $m_{\pm}(p)$, are also introduced for the functions $a_{\pm}(\zeta)\equiv(m_{\pm}^2-\zeta^2)^{1/2}$.

$X_1, X_2, \ldots, X_{12}$. Obviously, an exact (i.e., *symbolical* and not numerical) solution to the system is sought here and this was made possible by using MATHEMATICA™. The expressions for $X_1, X_2, \ldots, X_{12}$ are given in Appendix A.

Having available the solution $(X_1, X_2, \ldots, X_{12})$ and therefore, by (12) and (13), the general expressions for the double transformed temperature, displacements and stresses allows determining the field quantities at any point of the original space and at any time instant through successive *inversions* of the type (11*b*) and (10*b*). However, we emphasize at this point that a treatment employing the Cagniard–deHoop technique [9,36,39] to accomplish the transform inversions in an exact manner seems to be impossible due to the very complicated multiple transformed solution in the present problem. In the simpler buried-source problems of non-thermal type such a difficulty was not met and the Cagniard–deHoop technique had successfully been applied (see e.g., Pekeris [35], Garvin [40], and Payton [41]). Indeed, we note that, after the appropriate contour integration involved in the Cagniard–deHoop technique, the integrand in the semi-infinite branch-line integration is still *p*-dependent and, therefore, the unilateral transform inversion is impossible to be carried out exactly through the standard inspection procedure. For more details on this difficulty, we refer to the work by Georgiadis et al. [29], who treated the counterpart 2D problem and employed an *approximation* at a similar point of the analysis. Their asymptotic approach is, however, different than that employed here (see Sec. 4 below).

We close the presentation of the basic integral-transform analysis by noticing that if, instead of $\delta(t)$, a general dependence from time of the thermal loading in (4) is to be considered (denoted by an arbitrary function $g(t)$), then the quantity Q in the equations of Appendix A has to be replaced by $(Q/V_1)\cdot G(p)$, where $G(p)$ denotes the unilateral Laplace transform of the function $g((s/V_1)\equiv t)$.

4 Transformed Solution and Asymptotic Considerations

In what follows, we focus attention on the evaluation of the vertical displacement at the surface $u_z(x,y,z=-H,t)$. In view of the previous results, the multiply transformed displacement $U_z^*(q,w,z=-H,p)\equiv U_z^*(\zeta,z=-H,p)$ is given by

$$U_z^*(\zeta,z=-H,p)=\kappa Q V_1\frac{T}{p^2}\,\frac{a_+e^{-a_-pH}-a_-e^{-a_+pH}}{D(\zeta,p)},\tag{22}$$

where the functions $a_+(\zeta,p)$ and $a_-(\zeta,p)$, and the complex variable ζ have been defined before. Also, from (17*a*) and the definition of ζ, it is $T=m^2-2\zeta^2$. One may notice that the very definition of the variable ζ and the form of U_z^* in (22) exhibit the *axisymmetric* nature of the problem, a fact that will become evident in the ensuing procedure. Finally, of central importance to the solution for the *surface* disturbances is the function *D*, which is associated with waves of Rayleigh type. This is given as

$$D\equiv D(\zeta,p)=a_-M_-R_+-a_+M_+R_-,\tag{23}$$

where the functions

$$R_+\equiv R_+(\zeta,p)=4\zeta^2a_+\beta+T^2,\tag{24a}$$

$$R_-\equiv R_-(\zeta,p)=4\zeta^2a_-\beta+T^2,\tag{24b}$$

can be identified as the *thermoelastic* counterparts of the nonthermal pure-elastic Rayleigh function (transformed function), which is given as $R^{\text{elastic}}=4\zeta^2a\beta+T^2$, with $a\equiv a(\zeta)=(1-\zeta^2)^{1/2}$ and $\beta\equiv\beta(\zeta)$ given as before (see e.g., Achenbach [9], Miklowitz [36]). Contrary to the latter case, R_+ and R_- exhibit a *p*-dependence showing therefore that the thermoelastic Rayleigh waves in the physical space/time domain are dispersive. However, it was shown in the study of Georgiadis, Brock, and Rigatos [28] that generally the thermoelastic Rayleigh-wave velocity varies only slightly with time, a result explained in view of the fact that while there is a strong shear contribution (which remains unaffected by thermal effects) to the Rayleigh waves, the dilatational part of them is very weak (see e.g., Viktorov [42]). We will take advantage of this result immediately initiating the asymptotic considerations to obtain $u_z(x,y,z=-H,t)$.

It will be shown, indeed, that the function *D* can be expressed in terms of an *approximate* Rayleigh function that exhibits *no dispersion* (i.e., this Rayleigh function does not contain the time transform variable *p*) but still depends on the coupling constant ε. The approximate form of the function *D* itself will exhibit dependence upon the thermoelastic constants (ε,h) and the transform variables (ζ,p). First, one may write from (23) and (24) the following expression for the function (D/a_+):

$$\frac{D}{a_+}=4\zeta^2a_-\beta M_+\left(\frac{M_-}{M_+}-1\right)+T^2M_+\left(\frac{a_-M_-}{a_+M_+}-1\right).\tag{25}$$

Now, the terms (M_-/M_+) and $[(a_-M_-)/(a_+M_+)]$ in the above expression, in view of (14*a*) and (16), are written as

$$\frac{M_-}{M_+}=\frac{m_-^2-1}{m_+^2-1}\tag{26a}$$

and

$$\frac{a_-M_-}{a_+M_+}=\frac{(m_-^2-\zeta^2)^{1/2}}{(m_+^2-\zeta^2)^{1/2}}\,\frac{m_-^2-1}{m_+^2-1}.\tag{26b}$$

Further, when $(s/h)\gg1$, use of the expressions for m_+ and m_- in either (15) or (21*b*) lead to the results

$$\left|\frac{M_-}{M_+}\right|\ll1\tag{27a}$$

and

$$\left|\frac{a_-M_-}{a_+M_+}\right|\ll1.\tag{27b}$$

To give a numerical estimate, we obtain values of the ratio $[(a_-M_-)/(a_+M_+)]$ for different *p*'s (recall that *p* is the time Laplace-transform variable). The constants of a model material utilized in the present study to derive numerical results (see Sec. 6 below) are employed. These constants are $\varepsilon=0.011$, $h=1.864\times10^{-9}$ m, and Poisson's ratio $\nu=0.3$ [which gives a ratio of wave velocities $m\equiv(V_1/V_2)=1.8708$]. Also, we take $\zeta=\zeta_R$, which is the value corresponding to the arrival of the Rayleigh wavefront—see Eq. (36) below and which for the model material is calculated to be $\zeta_R=2.0162$. Then, the following values of the ratio in question are obtained:

$$[(a_-M_-)/(a_+M_+)] = -1.73840\times 10^{-11} \quad \text{for } p=10^2,$$

$$[(a_-M_-)/(a_+M_+)] = -1.51502\times 10^{-15} \quad \text{for } p=10^0,$$

$$[(a_-M_-)/(a_+M_+)] = -4.79091\times 10^{-23} \quad \text{for } p=10^{-5},$$

which clearly show that for increasing time (i.e., decreasing p) the ratio rapidly diminishes and can practically be taken equal to zero. The same applies to the ratio (M_-/M_+) as well.

Then, (27) allow writing (25) under the following approximate form:

$$\frac{D}{a_+} = -M_+(4\zeta^2 a_-\beta + T^2), \tag{28}$$

and, since $m_+ \gg 1$ for $(s/h)\gg 1$, one may further obtain in view of (16)

$$\frac{D}{a_+} = -m_+^2(4\zeta^2 a_-\beta + T^2), \tag{29}$$

where in the last two expressions and, also, in what follows the quantities m_+ and m_- assume the forms [taken from (21*b*)]

$$m_+ = \left(\frac{1+\varepsilon}{hp}\right)^{1/2}, \tag{30a}$$

$$m_- = \frac{1}{(1+\varepsilon)^{1/2}}. \tag{30b}$$

Finally, in view of the above, Eq. (29) becomes

$$\frac{D}{a_+} = -\frac{1+\varepsilon}{hp}\left[(m^2-2\zeta^2)^2 + 4\zeta^2\left(\frac{1}{1+\varepsilon}-\zeta^2\right)^{1/2}(m^2-\zeta^2)^{1/2}\right]$$
$$\equiv -\frac{1+\varepsilon}{hp}R^{\text{therm}}, \tag{31}$$

where the symbol $\equiv$ means equality by definition.

In the above result, the approximate Rayleigh function R^{therm} exhibits no dispersion (i.e., it does not depend upon p) but depends upon the coupling constant ε. All the above approximations will properly be utilized below.

The next step is to determine the zeros of the function (D/a_+), which is given in (31). This information will be utilized later in the inversion procedure. By invoking the principle of the argument (see e.g., Carrier et al. [38], and Ablowitz and Fokas [43]), it can be shown that the two real zeros $\zeta=\pm\zeta_R$ of the function (D/a_+) are the only zeros of this function in the entire ζ-plane. These correspond to axisymmetric thermoelastic Rayleigh wavefronts propagating with a velocity $V_R = V_1/\zeta_R$ along the traction-free half-space surface. Working with real p such that $p>0$ [which, of course, is necessary for the convergence of the integral defining the unilateral Laplace transform in Eq. (10*a*)] in the case of interest $m_- < m < m_+$ [cf. Eq. (20*b*)], we can obtain a closed-form expression for the root ζ_R by utilizing factorization operations of the kind encountered in solving Wiener–Hopf equations (see e.g., Achenbach [9], Carrier et al. [38], and Ablowitz and Fokas [43]). The function (D/a_+) is analytic in the ζ-plane cut along the interval $(m_- < |\text{Re}(\zeta)| < m,\ \text{Im}(\zeta)=0)$ and behaves like $2m_+^2(m^2-m_-^2)\zeta^2$ $\{$with $m_+=[(1+\varepsilon)/hp]^{1/2}$ and $m_-=(1+\varepsilon)^{-1/2}\}$ as $|\zeta|\to\infty$. Consequently, an auxiliary function $S(\zeta)$ is introduced through the definition

$$S \equiv \frac{(D/a_+)}{2m_+^2(m^2-m_-^2)(\zeta^2-\zeta_R^2)}, \tag{32}$$

which possesses the desired asymptotic property $S(\zeta)\to 1$ as $|\zeta|\to\infty$ and, additionally, has neither zeros nor poles in the ζ-plane. The only singularities of S are the branch points $\zeta=\pm m_-$ and $\zeta=\pm m$ [which are shared with the original function (D/a_+)], so it is single-valued in the ζ-plane cut along the interval $(m_- < |\text{Re}(\zeta)| < m,\ \text{Im}(\zeta)=0)$. Then, the standard technique of factorization through the use of Cauchy's integral theorem (see e.g., Achenbach [9], Carrier et al. [38], and Ablowitz and Fokas [43]) allows writing

$$S = S^+\cdot S^-, \tag{33}$$

where S^+ and S^- are analytic functions in the overlapping half-planes $\text{Re}(\zeta) > -m_-$ and $\text{Re}(\zeta) < m_-$, respectively. These are given by

$$S^{\pm}(\zeta) = \exp\left[-\frac{1}{\pi}\int_{m_-}^{m}\arctan\left(\frac{4\omega^2|a_-||\beta|}{T^2}\right)\frac{d\omega}{\omega\pm\zeta}\right], \tag{34}$$

where

$$a_- \equiv a_-(\omega) = (m_-^2-\omega^2)^{1/2}, \tag{35a}$$

$$\beta \equiv \beta(\omega) = (m^2-\omega^2)^{1/2}. \tag{35b}$$

Further, one may observe from (34) that $S^+(\zeta=0)=S^-(\zeta=0)$ and, therefore, $S(\zeta=0)=[S^+(\zeta=0)]^2$. Now, we exploit the latter observation by taking $\zeta=0$ and also take into account (32)–(34) to obtain the following *explicit* formula for the root of the function (D/a_+). This root defines the speed of thermoelastic Rayleigh waves

$$\zeta_R = \frac{m^2}{[2(m^2-m_-^2)]^{1/2}\cdot S^+(\zeta=0)}. \tag{36}$$

It is noticed, finally, that the inequality $m<\zeta_R$ always holds.

5 Inversion Procedure and Solution in the Physical Space/Time

In view of the definition (11*b*), one can write the unilateral Laplace transformed vertical displacement in the form

$$U_z(x,y,z=-H,p) = \left(\frac{p}{2\pi i}\right)^2\int_{-i\infty}^{+i\infty}\int_{-i\infty}^{+i\infty}U_z^*(q,w,z=-H,p)$$
$$\cdot e^{pqx}e^{pwy}\,dq\,dw, \tag{37}$$

where U_z^* is given in (22). Next, axisymmetry (circular symmetry) of the problem will become clear and be exploited. To this end, we set $q=i\sigma$ and $w=i\tau$ so that $\zeta^2\equiv q^2+w^2=-(\sigma^2+\tau^2)=-\rho^2$, and further consider the polar coordinates (r,ϑ) and (ρ,ϕ) defined through the relations $x+iy=re^{i\vartheta}$ and $\sigma+i\tau=\rho e^{i\phi}$. The first set of polar coordinates refers to the physical plane (x,y), whereas the second set to the transform plane (σ,τ). Considering also the case $x\geq 0$ and $y\geq 0$ (which, as will become clear soon, does not impose any restriction to the solution), it should be $\text{Im}(\sigma)\geq 0$ and $\text{Im}(\tau)\geq 0$, whereas $\rho\equiv(\sigma^2+\tau^2)^{1/2}\geq 0$.

Now, in view of (22), (31) and the newly introduced polar coordinates, we obtain

$$U_z(r,\theta,z=-H,p)$$
$$=\frac{\kappa QV_1}{4\pi^2}\int_0^{\infty}\left(\int_0^{2\pi}\frac{a_+Te^{-a_-Hp}-a_-Te^{-a_+Hp}}{D(\rho,p)}\right.$$
$$\left.\times\exp(-ipr\rho\cdot\cos(\phi-\vartheta))\,d\phi\right)\rho\,d\rho, \tag{38}$$

and further, by observing that the inner integral in (38) is actually independent on the starting limit of the integration interval, we eliminate the variable ϑ from the problem and get

$$U_z(r,\theta,z=-H,p) = \frac{\kappa Q V_1}{4\pi^2}\int_0^{\infty}\left(\frac{a_+ T e^{-a_- Hp} - a_- T e^{-a_+ Hp}}{D(\rho,p)} \times \int_0^{2\pi}\exp(-ipr\rho\cdot\cos\phi)d\phi\right)\rho d\rho = \frac{\kappa Q V_1}{2\pi}\int_0^{\infty}\frac{a_+ T e^{-a_- Hp} - a_- T e^{-a_+ Hp}}{D(\rho,p)} J_0(pr\rho)\cdot\rho d\rho. \tag{39}$$

In the above relation, we have $a_{\pm}=(m_{\pm}^2+\rho^2)^{1/2}$, $\beta=(m^2+\rho^2)^{1/2}$, $T=m^2+2\rho^2$, and

$$D(\rho,p)=-\frac{1+\varepsilon}{hp}\left(\frac{1+\varepsilon}{hp}+\rho^2\right)^{1/2}\left[(m^2+2\rho^2)^2-4\rho^2\left(\frac{1}{1+\varepsilon}+\rho^2\right)^{1/2}(m^2+\rho^2)^{1/2}\right]=-\frac{1+\varepsilon}{hp}\left(\frac{1+\varepsilon}{hp}+\rho^2\right)^{1/2}R^{\text{therm}}, \tag{40}$$

while the following standard result for the Bessel function $J_0(\,)$ was used (see e.g., Watson [44])

$$\frac{1}{2\pi}\int_0^{2\pi}\exp(-ipr\rho\cdot\cos\phi)d\phi=J_0(pr\rho). \tag{41}$$

One may observe that the last integral in (39) is but an *inverse* Hankel transform (see e.g., Bracewell [45]). This confirms the circular symmetry of the problem.

Next, another change of variable defined by setting $\omega=pr\rho$ leads to the following expression for a normalized expression of the unilateral Laplace-transformed vertical displacement at the surface

$$U_z^{\text{norm}}(r,z=-H,p)=-\frac{1}{2(m^2-m_-^2)r^2}\times\int_0^{\infty}\frac{\left(e^{-a_- Hp}-\dfrac{a_-}{a_+}e^{-a_+ Hp}\right)T}{m_+^2\left(\dfrac{\omega^2}{p^2r^2}+\zeta_R^2\right)\cdot S\left(i\dfrac{\omega}{pr}\right)}\times\frac{\omega}{p^2}J_0(\omega)d\omega, \tag{42}$$

where $U_z^{\text{norm}}=(2\pi U_z)/(\kappa Q V_1)$, and the symbols a_+, a_-, and T take the following forms [which, of course, follow from the definitions in (14*a*) and (17*a*) and the several changes of variable in the previous analysis]

$$a_{\pm}=\left(m_{\pm}^2+\frac{\omega^2}{p^2r^2}\right)^{1/2}, \quad T=m^2+2\frac{\omega^2}{p^2r^2}. \tag{43a,b}$$

Finally, we consider the inverse unilateral Laplace transform in (10*b*) and, further, interchange the latter integration and the integration in (42). This is permissible since the integral in (10*b*) converges *uniformly* within its region of convergence in the complex *p*-plane [37]. Cf. Miklowitz [36] and Markenscoff and Ni [46], e.g., for similar interchanges of the integration order in multiple transform inversions. In this way, we obtain the normalized vertical displacement at the surface, $u_z^{\text{norm}}=(2\pi u_z)/(\kappa Q V_1)$, in the physical space/time

$$u_z^{\text{norm}}(r,z=-H,s) = -\frac{1}{4\pi i}\frac{1}{(m^2-m_-^2)\zeta_R^2 r^2}\cdot\int_0^{\infty}\left(\int_{c-i\infty}^{c+i\infty}\frac{\left(e^{-a_- Hp}-\dfrac{a_-}{a_+}e^{-a_+ Hp}\right)T}{m_+^2(p-ip_R)(p+ip_R)\cdot S\left(i\dfrac{\omega}{pr}\right)}e^{ps}dp\right)\times\omega J_0(\omega)d\omega, \tag{44}$$

where

$$a_+=\left(\frac{1+\varepsilon}{h}\right)^{1/2}\frac{1}{p}\gamma_+, \tag{45a}$$

$$a_-=\frac{1}{(1+\varepsilon)^{1/2}p}\gamma_-, \tag{45b}$$

$$\gamma_+\equiv\gamma_+(p,\omega)=\left(p+\frac{h}{(1+\varepsilon)r^2}\omega^2\right)^{1/2}, \tag{46a}$$

$$\gamma_-\equiv\gamma_-(p,\omega)=\left(p^2+\frac{(1+\varepsilon)}{r^2}\omega^2\right)^{1/2}, \tag{46b}$$

and

$$p_R=\frac{\omega}{\zeta_R r}. \tag{47}$$

Notice that the branch cuts depicted in Fig. 3 should be introduced to render the functions γ_+ and γ_- single-valued. Also, the constant c in the inner integral of (44) is taken slightly greater than zero since all *singularities* (poles and branch points) of the corresponding integrand are situated in the plane Re(p)⩽0. Specifically, these singularities include the poles at $\pm ip_R$, the branch point $-h\omega^2((1+\varepsilon)r^2)^{-1}$ for the function γ_+, and the branch points $\pm i\omega(m_- r)^{-1}$ for the function γ_- (see Fig. 3).

With the above results available, we now focus interest on the thermoelastic Rayleigh waves. As is well-known (see e.g., Chao et al. [47], Achenbach [9], and Miklowitz [36]), analytically the Rayleigh-wave effects correspond to the contributions from certain poles in the integrands of the inversion integrals. Indeed, in our previous analysis we were able to make explicit the appearance of Rayleigh-wave poles [cf. Eq. (44)].

We proceed now to evaluate the pole contribution in (44) obtaining therefore an approximate solution for the thermoelastic Rayleigh-wave signals along the half-space surface. Care should be exercised, however, in evaluating the functions $a_+(p,\omega)$ and $a_-(p,\omega)$ at the points $\pm ip_R$, which lie along the Bromwich path $(c-i\infty,c+i\infty)$ (see Fig. 3). The following results are obtained:

$$a_+=\mp i\zeta_R\ell_R^{1/2}\exp(\pm i\theta/2), \tag{48a}$$

$$a_-=\mp i|a_{R-}| \quad \text{at} \quad p=\pm ip_R, \tag{48b}$$

where

$$a_{R-}=(m_-^2-\zeta_R^2)^{1/2}, \tag{49a}$$

$$\ell_R=(1+\tan^2\theta)^{1/2}, \tag{49b}$$

$$\tan\theta=\frac{(1+\varepsilon)r}{h\zeta_R\omega}. \tag{49c}$$

The symbol θ in the above relations (denoting an angle in Fig. 3) should not be confused with the symbol used earlier to denote the change in temperature. Then, (44) provides the following expression for the disturbance due to the thermoelastic Rayleigh waves

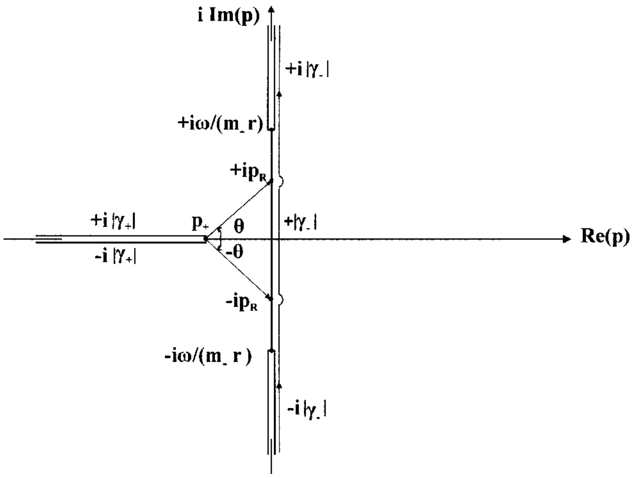

Fig. 3 Branch cuts for the functions $\gamma_+(p,\omega)$ and $\gamma_-(p,\omega)$, and the Bromwich path in the complex p-plane

$$u_z^{\text{norm}}(r,z=-H,s)=-\frac{\Lambda}{r^2}\int_0^\infty f(r,H,\omega,s)\cdot\omega\cdot J_0(\omega)d\omega, \tag{50}$$

where

$$f(r,H,\omega,s)=\exp\left(-\frac{\omega|a_{R-}|H}{\zeta_R r}\right)\cos\left(\frac{\omega s}{\zeta_R r}\right)-\frac{|a_{R-}|\exp\left(-\frac{\omega}{r}\ell_R^{1/2}H\cos(\theta/2)\right)}{\zeta_R\ell_R^{1/2}}\times\cos\left[\frac{\omega s}{\zeta_R r}-\frac{\theta}{2}-\left(\frac{\omega}{r}\ell_R^{1/2}H\sin(\theta/2)\right)\right], \tag{51}$$

$$\Lambda=\frac{m^2-2\zeta_R^2}{4\left(\frac{1+\varepsilon}{h}\right)\cdot S(\zeta_R)\cdot(m^2-m_-^2)\zeta_R^2}. \tag{52}$$

Further, as the analysis in Appendix B shows, the second term of $f(r,H,\omega,s)$ in (51) is negligible with respect to the first term. Omitting the small term, the normalized vertical displacement becomes

$$u_z^{\text{norm}}(r,z=-H,s)=-\frac{\Lambda}{r^2}\int_0^\infty \exp\left(-\frac{\omega|a_{R-}|H}{\zeta_R r}\right)\times\cos\left(\frac{\omega s}{\zeta_R r}\right)J_0(\omega)\omega d\omega. \tag{53}$$

Finally, evaluation of the integral in (53) (Watson [44]) yields the following *closed-form* expression for the normalized vertical displacement at the surface due to Rayleigh waves generated by a buried thermal source in a half-space

$$u_z^{\text{norm}}(r,z=-H,s)=-\frac{\Lambda}{r^2}\text{Re}\left[\frac{\frac{|a_{R-}|H}{\zeta_R r}-i\frac{s}{\zeta_R r}}{\left[1+\left(\frac{|a_{R-}|H}{\zeta_R r}-i\frac{s}{\zeta_R r}\right)^2\right]^{3/2}}\right], \tag{54}$$

where r is the radial distance from the epicenter, Re[ ] denotes the real part of a complex function, and the quantities Λ, a_{R-} and ζ_R depend on the material constants. It is also of notice that u_z^{norm} depends on the ratio (H/r).

6 Numerical Results, Further Asymptotic Results, and Concluding Remarks

Numerical results from the previous expression are obtained easily through the use of MATHEMATICA™ for both numerical integrations and symbolic manipulations involved. A model material was considered to derive the results shown in the graphs of Figs. 4 and 5. It is characterized by the following constants: coupling constant $\varepsilon=0.011$, thermoelastic characteristic length $h=1.864\times10^{-9}$ m, and Poisson's ratio $\nu=0.3$ [this value gives a ratio of wave velocities $m\equiv(V_1/V_2)=1.8708$]. The graphs present the variation of the normalized vertical displacement $u_z^{\text{norm}}\equiv2\pi u_z(\kappa QV_1)^{-1}$ with the normalized time $V_1(r^2+H^2)^{-1/2}t$. In Fig. 4, the case $r=10H$ is considered, whereas in Fig. 5, both cases $r=40H$ and $r=160H$ are presented. In all cases, $H=100$ m is taken but a numerical inspection showed that the shape of pulse does not change appreciably if normalization is utilized (the displacement itself becomes larger for smaller depths).

The graphs show the generation of the thermoelastic Rayleigh wave at the half-space surface. We notice that as the distance of the observation station from the epicenter increases, the shape of the Rayleigh disturbance appears to become sharper because of the contraction of the real time scale with the increase of the length $(r^2+H^2)^{1/2}$. Also, as the observation station moves away from the epicenter, *decay* in amplitude occurs after a certain point. This attenuation is due to the 3D geometry of the problem (see for analogous nonthermal situations in Pekeris and Lifson [11], and Achenbach [9]). On the contrary, the latter result is not encountered in the respective 2D problem of a nonthermal buried dilatational source treated by Garvin [10], where once the Rayleigh pulse takes its shape, it is not decaying.

In the sequel, we further investigate the behavior of $u_z^{\text{norm}}(r,z=-H,s)$ at *large* distances from the epicenter, i.e., for $r\gg H$. In this case, it is $(r^2+H^2)^{1/2}\cong r$ and the normalized vertical displacement takes the form

$$u_z^{\text{norm}}(r\gg H,z=-H,s)\cong-\Lambda\ \text{Re}\left[\frac{X-iYr}{(r^2+X^2-Y^2r^2-i2XYr)^{3/2}}\right], \tag{55}$$

where $X=|a_{R-}|\cdot H/\zeta_R$ and $Y=V_Rt/r$. Taking $r\gg H$ leads to the conclusion that $r\gg X$ and then (55) takes the even simpler form

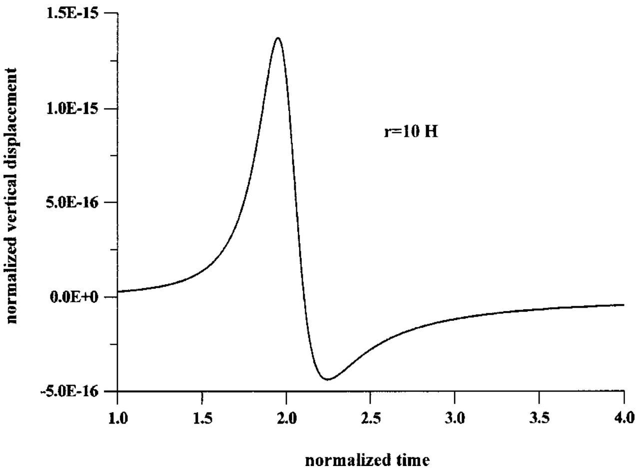

Fig. 4 The variation of the normalized vertical displacement $u_z^{\text{norm}}\equiv2\pi u_z(\kappa QV_1)^{-1}$ with the normalized time $s(r^2+H^2)^{-1/2}$ indicating the arrival of a thermoelastic Rayleigh wave at the station $r=10H$. The constants have the values $\varepsilon=0.011$, $h=1.864\times10^{-9}$ m, $\nu=0.3$, and $H=100$ m.

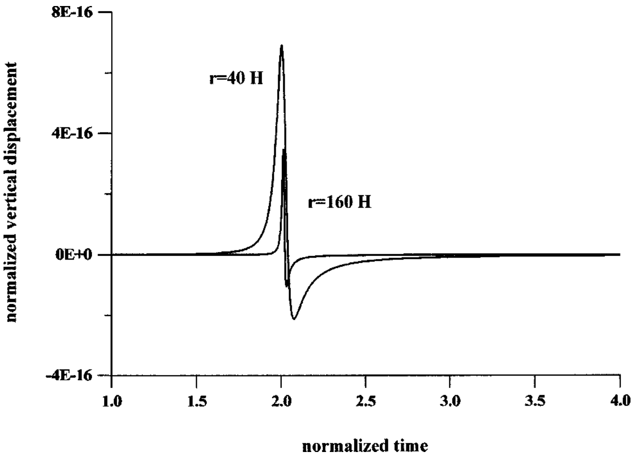

Fig. 5 The variation of the normalized vertical displacement $u_z^{\mathrm{norm}} \equiv 2\pi u_z(\kappa Q V_1)^{-1}$ with the normalized time $s(r^2+H^2)^{-1/2}$ indicating the arrival of a thermoelastic Rayleigh wave at the stations $r=40\,H$ and $r=160\,H$. The constants have the values $\varepsilon=0.011$, $h=1.864\times 10^{-9}$ m, $\nu=0.3$, and $H=100$ m.

$$u_z^{\mathrm{norm}}(r \gg H, z=-H, s) \cong -\Lambda\ \mathrm{Re}\left[\frac{X-iYr}{(r^2-Y^2r^2-i2XYr)^{3/2}}\right]. \tag{56}$$

In addition, we can investigate the field *near* the Rayleigh wavefront. To this end, the transformation $x_R=V_R t-r$ is used in (56), where x_R denotes the distance from the Rayleigh wavefront, providing

$$\begin{aligned} &u_z^{\mathrm{norm}}(r \gg H, z=-H, s) \\ &\quad \cong -\frac{\Lambda}{r^{1/2}}\mathrm{Re}\left[\frac{\dfrac{X}{r}-i\left(\dfrac{x_R}{r}+1\right)}{\left[-x_R\left(\dfrac{x_R}{r}+2\right)-i2X\left(\dfrac{x_R}{r}+1\right)\right]^{3/2}}\right]. \end{aligned} \tag{57}$$

Now, by taking $r \gg X$ and $r \gg x_R$, we get the following expression for the vertical displacement far from the epicenter and, at the same time, very close to the Rayleigh wavefront

$$u_z^{\mathrm{norm}}(r \gg H, r \gg x_R, z=-H, s) \cong -\frac{\Lambda}{(8r)^{1/2}}\mathrm{Re}\left[\frac{-i}{(-x_R-iX)^{3/2}}\right]. \tag{58}$$

The above relation reveals that the displacement varies with the distance from the epicenter as $u_z^{\mathrm{norm}}(r \gg H, r \gg x_R, z=-H, s) \approx r^{-1/2}$, while in the case of a source that is situated very close to the surface (i.e., when $x_R \gg X$) the displacement varies with the distance from the Rayleigh wavefront as $u_z^{\mathrm{norm}}(r \gg H, r \gg x_R, z=-H, s) \approx x_R^{-3/2}$. The first of the aforementioned results shows that the surface effects attenuate with distance as $r^{-1/2}$, the physical explanation of which is that the surface waves in our 3D problem are essentially cylindrical waves (see Ref. [9] for analogous situations in classical elastodynamics).

In conclusion, the 3D transient dynamic problem of a thermoelastic half-space under thermal buried or surface loading is treated in this paper. The loading has the form of a concentrated heat flux applied impulsively and Biot's fully coupled thermoelasticity is utilized. The problem has relevance to situations involving heat generation due to, e.g., laser action (impulsive electromagnetic radiation) on a surface target, underground nuclear activity, and friction developed during underground fault motions. Here, we were particularly interested in determining in *closed form* the disturbance associated with the propagation of the thermoelastic Rayleigh waves. This was made possible by using multiple Laplace transforms, asymptotics, complex-variable theory and certain results for Bessel functions. The dependence of the normal displacement associated with the Rayleigh wave upon the distance from the source epicenter and the distance from the wavefront was also determined.

Appendix A

The solution of the 12×12 algebraic system of Sec. 3 reads

$$\begin{aligned} X_1 = -\kappa Q V_1 e^{-2a_- Hp}\Bigg(&-(e^{2a_- Hp}-e^{-2(a_+-a_-)Hp})a_- M_- TE \\ &+\left(e^{2a_- Hp}+e^{-2(a_+-a_-)Hp}-2\frac{M_-}{M_+}e^{-(a_+-a_-)Hp}\right)a_+ M_+ TE \\ &+(e^{2a_- Hp}+e^{-2(a_+-a_-)Hp})D\Bigg)\Big/(BA), \end{aligned} \tag{A1}$$

$$\begin{aligned} X_2 = \kappa Q V_1\Bigg(&-a_- e^{-(a_++3a_-)Hp}\Bigg[-2e^{2a_- Hp}+(e^{(a_++a_-)Hp} \\ &+e^{(a_++3a_-)Hp})\frac{M_-}{M_+}\Bigg]\cdot M_+ TE+e^{-2a_- Hp}((-1 \\ &+e^{2a_- Hp})M_+ a_+ TE+(1+e^{2a_- Hp})D)\Bigg)\Big/(CA), \end{aligned} \tag{A2}$$

$$\begin{aligned} X_3 = &-2\kappa Q V_1 \beta q T e^{-(a_++a_-+\beta)Hp}(a_+ e^{a_+ Hp}-a_- e^{a_- Hp})(T_q \\ &+w^2)/(FA), \end{aligned} \tag{A3}$$

$$\begin{aligned} X_4 = &\,2\kappa Q V_1 \beta w T e^{-(a_++a_-+\beta)Hp}(a_+ e^{a_+ Hp}-a_- e^{a_- Hp})(T_w \\ &+q^2)/(FA), \end{aligned} \tag{A4}$$

$$X_5 = -\frac{\kappa Q V_1}{2a_+ m^2 p(M_+-M_-)} = -\frac{\kappa Q V_1}{B}, \tag{A5}$$

$$\begin{aligned} X_6 = &-\kappa Q V_1 e^{-(2a_++a_-)Hp}\{a_- e^{a_- Hp}M_- TE+a_+((e^{a_- Hp}M_+ \\ &-2e^{a_+ Hp}M_-)TE)+e^{a_- Hp}D/(BA)\}, \end{aligned} \tag{A6}$$

$$X_7 = \frac{\kappa Q V_1}{C}, \tag{A7}$$

$$\begin{aligned} X_8 = &\,\kappa Q V_1 e^{-(a_++2a_-)Hp}(a_-(2e^{a_- Hp}M_+-e^{a_+ Hp}M_-)TE \\ &+a_+ e^{a_+ Hp}(M_+ T(-E))+e^{a_+ Hp}D)/(CA), \end{aligned} \tag{A8}$$

$$X_9 = X_{10} = 0, \tag{A9}$$

$$\begin{aligned} X_{11} = &-2\kappa Q V_1 \beta q T e^{-(a_++\beta)Hp}(-a_-+a_+ e^{(a_+-a_-)Hp})(T_q \\ &+w^2)/(FA), \end{aligned} \tag{A10}$$

$$\begin{aligned} X_{12} = &\,2\kappa Q V_1 \beta w T e^{-(a_++a_-+\beta)Hp}(-a_+ e^{a_+ Hp}+a_- e^{a_- Hp})(T_w \\ &+q^2)/(FA), \end{aligned} \tag{A11}$$

where

$$\begin{aligned} A = &\,(a_+ M_+-a_- M_-)T(T_q T_w-q^2w^2)+4a_+ a_- \beta(M_+-M_-) \\ &\times(q^2T_q+2q^2w^2+w^2T_w), \end{aligned} \tag{A12}$$

$$B = 2a_+ m^2(M_+-M_-)p, \tag{A13}$$

$$C = 2a_- m^2(M_+-M_-)p, \tag{A14}$$

$$D = 4a_+ a_- \beta(M_+-M_-)(q^2T_q+2q^2w^2+w^2T_w), \tag{A15}$$

$$E = T_q T_w-q^2w^2, \tag{A16}$$

$$F = m^2 p. \tag{A17}$$

Appendix B

Considering the ratio $\mathfrak{R}$ of the fluctuation amplitudes of the first and second terms in (51), we obtain

$$\mathfrak{R}=\frac{\zeta_R l_R^{1/2}}{|a_{R-}|}\exp\left(\frac{\omega}{r}H\left[l_R^{1/2}\cos(\theta/2)-\frac{|a_{R-}|}{\zeta_R}\right]\right). \qquad (B1)$$

We will examine this ratio and conclude that $\mathfrak{R}$ takes on very large values in the entire range of ω provided that the distance from the epicenter r is much greater than the thermoelastic characteristic length h. The length h is *very small* for most materials $[h=O(10^{-10}\,\mathrm{m})$ as mentioned in the main text of the paper$]$ and, therefore, the requirement $(r/h)\gg 1$ does not pose any serious limitation. Similarly to the case of Eq. (21*b*), any choice with, say, $(r/h)\geqslant 100$ leads to a reasonable approximation. To cover the entire range of ω-values, we discern the following possibilities:

(1) Considering $(\omega/r)\to 0$, Eqs. (49*c*) and (49*b*) provide the results $\lim_{(\omega/r)\to 0}\tan\theta=\infty$, $\lim_{(\omega/r)\to 0}\ell_R^{1/2}=\infty$ and $\lim_{(\omega/r)\to 0}\cos(\theta/2)=2^{-1/2}$. Then, we find that $\lim_{(\omega/r)\to 0}((\omega/r)H[l_R^{1/2}\cos(\theta/2)-(|a_{R-}|/\zeta_R)])=0$ and $\lim_{(\omega/r)\to 0}\mathfrak{R}=\infty$.

(2) Considering $(\omega/r)\to\infty$, Eqs. (49*c*) and (49*b*) provide the results $\lim_{(\omega/r)\to\infty}\tan\theta=0$, $\lim_{(\omega/r)\to\infty}\ell_R^{1/2}=1$ and $\lim_{(\omega/r)\to\infty}\cos(\theta/2)=1$. Also, from (36) and (49*a*) we may infer that $(|a_{R-}|/\zeta_R)<1$. Then, working as in the above case, we find that $\lim_{(\omega/r)\to\infty}\mathfrak{R}=\infty$.

(3) Considering $\omega=O(r)$, Eqs. (49*c*) and (49*b*) lead us to conclude that $\tan\theta$ and $\ell_R^{1/2}$ takes on very large values. Consequently, it is $\cos(\theta/2)\cong 2^{-1/2}$ and by (B1) it is seen that $\mathfrak{R}$ takes on very large values in this case too.

Finally, we note that a numerical evaluation of the two terms in (51) showed that the amplitude of the first term is, at minimum, about 20 orders of magnitude greater than the amplitude of the second term.

References

[1] Morland, L. W., 1968, ''Generation of Thermoelastic Stress Waves by Impulsive Electromagnetic Radiation,'' AIAA J., **6**, pp. 1063–1070.
[2] Sve, C., and Miklowitz, J., 1973, ''Thermally Induced Stress Waves in an Elastic Layer,'' ASME J. Appl. Mech., **40**, pp. 161–168.
[3] Bechtel, J. H., 1975, ''Heating of Solid Targets With Laser Pulses,'' J. Appl. Phys., **46**, pp. 1585–1593.
[4] Hetnarski, R. B., and Ignaczak, J., 1994, ''Generalized Thermoelasticity: Response of Semi-Space to a Short Laser Pulse,'' J. Therm. Stresses, **17**, pp. 377–396.
[5] Royer, D., and Chenu, C., 2000, ''Experimental and Theoretical Waveforms of Rayleigh Waves Generated by a Thermoelastic Laser Line Source,'' Ultrasonics, **38**, pp. 891–895.
[6] Bullen, K. E., and Bolt, B. A., 1987, *An Introduction to the Theory of Seismology*, Cambridge University Press, Cambridge.
[7] Kanamori, H., Anderson, D. L., and Heaton, T. H., 1995, ''Frictional Melting During the Rupture of the 1994 Bolivian Earthquake,'' Science, **279**, pp. 839–841.
[8] Biot, M. A., 1956, ''Thermoelasticity and Irreversible Thermodynamics,'' J. Appl. Phys., **27**, pp. 240–253.
[9] Achenbach, J. D., 1973, *Wave Propagation in Elastic Solids*, North–Holland, NY.
[10] Garvin, W. W., 1956, ''Exact Transient Solution of the Buried Line Source Problem,'' Proc. R. Soc. London, Ser. A, **234**, pp. 528–541.
[11] Pekeris, C. L., and Lifson, H., 1957, ''Motion of the Surface of a Uniform Elastic Half-Space Produced by a Buried Pulse,'' J. Acoust. Soc. Am., **29**, pp. 1233–1238.
[12] Lykotrafitis, G., Georgiadis, H. G., and Brock, L. M., 2001, ''Three-Dimensional Thermoelastic Wave Motions in a Half-Space Under the Action of a Buried Source,'' Int. J. Solids Struct., **38**, pp. 4857–4878.
[13] Boley, B. A., and Tolins, I. S., 1962, ''Transient Coupled Thermoelastic Boundary Value Problems in the Half-Space,'' ASME J. Appl. Mech., **29**, pp. 637–646.
[14] Hetnarski, R. B., and Ignaczak, J., 1993, ''Generalized Thermoelasticity: Closed-Form Solutions,'' J. Therm. Stresses, **16**, pp. 473–498.
[15] Predeleanu, M., 1987, ''Analysis of Thermomechanical Coupling by Boundary Element Method,'' in *Thermomechanical Couplings in Solids*, edited by Bui, H. D. and Nguyen, Q. S., Elsevier, Amsterdam, pp. 305–318.
[16] Fleurier, J., and Predeleanu, M., 1987, ''On the Use of Coupled Fundamental Solutions in B.E.M. for Thermoelastic Problems,'' Eng. Anal. Boundary Elem., **4**, pp. 70–74.
[17] Sharp, S., and Crouch, S. L., 1987, ''Heat Conduction, Thermoelasticity and Consolidation,'' in *Boundary Element Methods in Mechanics*, edited by Beskos, D. E., Elsevier, Amsterdam, pp. 440–498.
[18] Manolis, G. D., and Beskos, D. E., 1989, ''Integral Formulation and Fundamental Solutions of Dynamic Poroelasticity and Thermoelasticity,'' Acta Mech., **76**, pp. 89–104.
[19] Manolis, G. D., and Beskos, D. E., 1990, ''Integral Formulation and Fundamental Solutions of Dynamic Poroelasticity and Thermoelasticity,'' Acta Mech., **83**, pp. 223–226.
[20] Hetnarski, R. B., 1961, ''Coupled One-Dimensional Thermal Shock Problem for Small Times,'' Arch. Mech. Stosow., **13**, pp. 295–306.
[21] Sternberg, E., and Chakravorty, J. G., 1959, ''On Inertia Effects in a Transient Thermoelastic Problem,'' ASME J. Appl. Mech., **26**, pp. 503–509.
[22] Sternberg, E., and Chakravorty, J. G., 1959, ''Thermal Shock in an Elastic Body With a Spherical Cavity,'' Q. Appl. Math., **17**, pp. 205–218.
[23] Francis, P. H., 1972, ''Thermo-Mechanical Effects in Elastic Wave Propagation: A Survey,'' J. Sound Vib., **21**, pp. 181–192.
[24] Atkinson, C., and Craster, R. V., 1992, ''Fracture in Fully Coupled Dynamic Thermoelasticity,'' J. Mech. Phys. Solids, **40**, pp. 1415–1432.
[25] Brock, L. M., 1995, ''Slip/Diffusion Zone Formation at Rapidly-Loaded Cracks in Thermoelastic Solids,'' J. Elast., **40**, pp. 183–206.
[26] Brock, L. M., Rodgers, M., and Georgiadis, H. G., 1996, ''Dynamic Thermoelastic Effects for Half-Planes and Half-Spaces With Nearly-Planar Surfaces,'' J. Elast., **44**, pp. 229–254.
[27] Brock, L. M., Georgiadis, H. G., and Tsamasphyros, G., 1997, ''The Coupled Thermoelasticity Problem of the Transient Motion of a Line Heat/Mechanical Source Over a Half-Space,'' J. Therm. Stresses, **20**, pp. 773–795.
[28] Georgiadis, H. G., Brock, L. M., and Rigatos, A. P., 1998, ''Transient Concentrated Thermal/Mechanical Loading of the Faces of a Crack in a Coupled-Thermoelastic Solid,'' Int. J. Solids Struct., **35**, pp. 1075–1097.
[29] Georgiadis, H. G., Rigatos, A. P., and Brock, L. M., 1999, ''Thermoelastodynamic Disturbances in a Half-Space Under the Action of a Buried Thermal/Mechanical Line Source,'' Int. J. Solids Struct., **36**, pp. 3639–3660.
[30] Barber, J. R., 1972, ''Distortion of the Semi-Infinite Solid Due to Transient Surface Heating,'' Int. J. Mech. Sci., **14**, pp. 377–393.
[31] Barber, J. R., and Martin-Moran, C. J., 1982, ''Green's Functions for Transient Thermoelastic Contact Problems for the Half-Plane,'' Wear, **79**, pp. 11–19.
[32] Chadwick, P., 1960, ''Thermoelasticity: The Dynamical Theory,'' in *Progress in Solid Mechanics*, edited by Sneddon, I. N. and Hill, R., North–Holland, Amsterdam, Vol. 1, pp. 263–328.
[33] Carlson, D. E., 1972, ''Linear Thermoelasticity,'' in *Handbuch der Physik*, edited by Flugge, S., Springer-Verlag, Berlin, **VIa/2**, pp. 297–345.
[34] Ignaczak, J., and Nowacki, W., 1962, ''The Sommerfeld Radiation Conditions for Coupled Problems of Thermoelasticity,'' Arch. Mech. Stosow., **1**, pp. 3–13.
[35] Pekeris, C. L., 1955, ''The Seismic Buried Pulse,'' Proc. Natl. Acad. Sci. U.S.A., **41**, pp. 629–638.
[36] Miklowitz, J., 1978, *The Theory of Elastic Waves and Waveguides*, North–Holland, Amsterdam.
[37] van der Pol, B., and Bremmer, H., 1950, *Operational Calculus Based on the Two-Sided Laplace Integral*, Cambridge University Press, Cambridge.
[38] Carrier, G. F., Krook, M., and Pearson, C. E., 1966, *Functions of a Complex Variable*, McGraw–Hill, New York.
[39] deHoop, A. T., 1960, ''The Surface Line Source Problem,'' Appl. Sci. Res., Sect. B, **8**, pp. 349–356.
[40] Garvin, W. W., 1965, ''Exact Transient Solution of the Buried Line Source Problem,'' Proc. R. Soc. London, Ser. A, **234**, pp. 528–541.
[41] Payton, R. G., 1968, ''Epicenter Motion of an Elastic Half-Space Due to Buried Stationary and Moving Line Sources,'' Int. J. Solids Struct., **4**, pp. 287–300.
[42] Viktorov, I. A., 1967, *Rayleigh and Lamb Waves*, Plenum Press, NY.
[43] Ablowitz, M. J., and Fokas, A. S., 1997, *Complex Variables*, Cambridge University Press, Cambridge.
[44] Watson, G. N., 1966, *Theory of Bessel Functions*, Cambridge University Press, Cambridge.
[45] Bracewell, R., 1965, *The Fourier Transform and Its Applications*, McGraw–Hill, New York.
[46] Markenscoff, X., and Ni, L., 2001, ''The Transient Motion of a Dislocation With a Ramp-Like Core,'' J. Mech. Phys. Solids, **49**, pp. 1603–1619.
[47] Chao, C. C., Bleich, H. H., and Sackman, J., 1961, ''Surface Waves in an Elastic Half Space,'' ASME J. Appl. Mech., **28**, pp. 300–301.

Coupled Plastic Wave Propagation and Column Buckling

Denzil G. Vaughn

James M. Canning

John W. Hutchinson

Division of Engineering and Applied Sciences,
Harvard University,
Cambridge, MA 02138

The plastic buckling of columns is explored in a regime where plastic wave propagation and lateral buckling are nonlinearly coupled. Underlying the work is the motivation to understand and quantify the dynamic crushing resistance of truss cores of all-metal sandwich plates where each truss member is a clamped column. Members are typically fairly stocky such that they buckle plastically and their load carrying capacity decreases gradually as they buckle, even at slow loading rates. In the range of elevated loading rates of interest here, the columns are significantly stabilized by lateral inertia, resisting lateral motion and delaying buckling and loss of load carrying capacity to relatively large overall plastic strains. The time scale associated with dynamic axial behavior, wherein deformation spreads along the column as a plastic wave, is comparable to the time scale associated with lateral buckling such that the two phenomena are coupled. Several relevant problems are analyzed using a combination of analytical and numerical procedures. Material strain-rate dependence is also taken into account. Detailed finite element analyses are performed for axially loaded columns with initial imperfections, as well as for inclined columns in a truss core of a sandwich plate, with the aim of determining the resistance of the column to deformation as dependent on the loading rate and the relevant material and geometric parameters. In the range of loading rates of interest, dynamic effects result in substantial increases in the reaction forces exerted by core members on the faces of the sandwich plate with significant elevation in energy absorption.

[DOI: 10.1115/1.1825437]

1 Introduction

Pursued extensively for over 50 years, the dynamic axial loading of columns is still an important subject because of its relevance to a wide range of engineering applications. Much interesting mechanics underlies qualitative and quantitative understanding of dynamic column buckling, and the subject has not been without controversy. Here, columnar truss members of all metal truss core sandwich plates motivate the study as these sandwich plates have the potential for replacing solid plate construction for a range of applications including ship hulls, armored vehicles, and chemical plants [1] where impulsive loads are of concern. For applications involving high intensity dynamic crushing loads, cores can experience nominal strain rates greater than $10^3\ \mathrm{s}^{-1}$. Column members in truss cores are usually sufficiently stocky such that buckling occurs well into the plastic range, especially when the columns are stabilized by lateral inertia at elevated loading rates. The basic cellular unit of a tetragonal truss core is shown in Fig. 1. Although the columns in the core are inclined with respect to the crushing direction, they nevertheless behave in a manner similar to an axially compressed column due to the fact that their end displacements are constrained by the face sheets in the direction parallel to the sheets. Of primary interest is the resistance of the columns to deformation, the forces they exert on the face sheets during dynamic crushing, and the energy they absorb. Most of the emphasis in this paper will be on axially compressed columns, but the direct relevance of results for axially compressed columns to inclined columns will be demonstrated in the second half of the paper.

There is a large literature on dynamic plastic buckling of columns [2–5] and perhaps a rationale for further study is warranted. In the applications motivating this study, a representative column would be relatively stocky, typically 0.1 m in length, and subject to a suddenly imposed velocity on the order of $100\ \mathrm{ms}^{-1}$ at one end corresponding to an overall strain rate of $10^3\ \mathrm{s}^{-1}$. The loading rates of interest are such that the initial stages of the deformation are dominated by the propagation of a plastic axial wave down the column. Buckling is resisted by lateral inertia. Overall compressive strains of 20% or more can be achieved before appreciable buckling deflections occur. Buckling deflections, which depend on initial imperfection amplitudes, develop in the later stages of the crushing. Thus, during the initial stage of deformation, the forces exerted on the face sheets are similar to those exerted by a straight rod undergoing dynamic axial deformation. As buckling deformations develop, the forces depend in a complicated way on coupled plastic wave propagation and lateral buckling.

The early study of Abrahamson and Goodier [3] on column impact has aspects in common with the problem and loading rates of interest here. Specifically, their experiments involved impact velocities in the range of interest here, and overall compressive strains on the order of 20% due primarily to axial straining were observed. However, the primary motivation underlying the work in [3] was buckling and not the forces exerted during the impact. In addition, the theoretical approach of these authors was to decouple the axial deformation from the buckling deformation by assuming the axial stress state was established prior to the growth of buckling deformations. Calladine and English [5] also decoupled axial deformations from bucking deformations in their study of the various influences of inertia on dynamic buckling. As will be seen in the body of the paper, this decoupling is justified since their work focused on a range of relatively low impact velocities; the maximum impact velocity in their experiments did not exceed $10\ \mathrm{ms}^{-1}$. These authors make the important observation that inertial stabilization effects scale differently with column size than material strain-rate effects, a point that will be discussed in the present paper as well.

The problem that couples plastic wave propagation and lateral buckling has only recently received attention [6–8], with analyti-

---

Contributed by the Applied Mechanics Division of THE AMERICAN SOCIETY OF MECHANICAL ENGINEERS for publication in the ASME JOURNAL OF APPLIED MECHANICS. Manuscript received by the Applied Mechanics Division, April 21, 2004; final revision, May 3, 2004. Editor: R. M. McMeeking. Discussion on the paper should be addressed to the Editor, Professor Robert M. McMeeking, Journal of Applied Mechanics, Department of Mechanical and Environmental Engineering, University of California-Santa Barbara, Santa Barbara, CA 93106-5070, and will be accepted until four months after final publication in the paper itself in the ASME JOURNAL OF APPLIED MECHANICS.

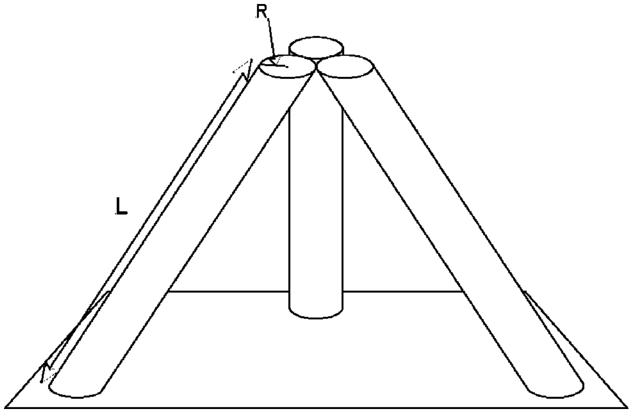

Fig. 1 Tetragonal Truss Core

cal and numerical approaches with primary emphasis on the buckle shape. Here, the coupled nonlinear problem is analyzed using a numerical approach, accounting for both imperfections and material strain rate dependence, with emphasis on the forces required to deform the column and the energy dissipated by the column. However, to shed light on the initial stages of the deformation history, the next section of the paper presents results for the propagation of plastic axial waves down a rod following the classic treatments of von Karman and Duwez [9] and Taylor [10]. An important dimensionless loading rate parameter tied to the dynamic effects emerges from this analysis. The fully coupled problem is analyzed for a wide range of loading rates utilizing the commercially available codes ABAQUS/Standard and ABAQUS/Explicit. Reaction forces and energy dissipation are determined as a function of geometric, material and loading parameters. With the aid of numerical analysis, it is also demonstrated that the forces exerted on the face sheets by inclined columns in a truss core can be well approximated using results for the axially compressed column.

2 Uniaxial Waves in a Rod

2.1 Wave Equation for Rate-Independent Material. Taylor [10] and von Karman and Duwez [9] considered a one-dimensional plastic wave propagating down a rod. Taylor's approach was conducted within a finite strain setting, and a similar approach will be followed here, but with a different choice of variables. (Several authors have remarked to the effect that von Karman and Duwez also use a finite strain approach in their analysis, but their treatment of finite strain aspects is not nearly as transparent as that of Taylor.) Consider a semi-infinite bar extending from $x=0$ to $x=\infty$ at $t=0$, with a material point at x at $t=0$ located at $X=x+u(x,t)$ at t. The logarithmic (true) strain is related to the displacement gradient by $\varepsilon=\ln(1+\partial u/\partial x)$. Analytical solutions are restricted to rods made of rate-independent materials such that the true stress (force per current area) can be regarded as a function of true strain, $\sigma(\varepsilon)$. Material rate-dependence is taken into account in Sec. 2.3. In this subsection and the next, attention is limited to problems with monotonic straining such as a compression wave with no elastic unloading. Following the earlier work of Taylor and von Karman and Duwez, the rod is assumed to be incompressible and the effect of radial inertia is neglected. With A as the cross-sectional area of the rod in the deformed state and $F=\sigma A$ as the force carried by the rod, equilibrium requires $\partial F/\partial X=\rho A\partial^2 u/\partial t^2$, where ρ is the density of the material. Incompressibility implies $dA/d\varepsilon=-A$. When expressed in terms of $u(x,t)$, the equilibrium equation can be written as

$$\frac{\partial^2 u}{\partial x^2}=\frac{1}{c(\varepsilon)^2}\frac{\partial^2 u}{\partial t^2} \tag{1}$$

where the strain-dependent wave speed is

$$c(\varepsilon)=\sqrt{\frac{E_t-\sigma}{\rho}}\,e^{-\varepsilon} \tag{2}$$

and $E_t=d\sigma/d\varepsilon$ is the tangent modulus of the true stress-log strain curve. The wave speed, E_t, σ, and ε all depend on u through the expressions listed above.

Three limiting cases of (1) and (2) are worth identifying. When yielding occurs with small strains and $E_t \gg |\sigma|$, $c=\sqrt{E_t/\rho}$, which is often referred to as the plastic wave speed. The finite strain formulation gives $c=\sqrt{\sigma_Y/\rho}$ for a plastic compression wave propagating along an elastic-perfectly plastic rod ($E_t=0$) where σ_Y is the yield stress. The wave speed of a tensile wave approaches zero when $\sigma=E_t$, corresponding to the Considere condition for necking localization.

2.2 Compression Wave in an Infinitely Long Bar Subject to Constant Velocity at Its End. The solution produced independently during World War II by von Karman and Duwez [9] and Taylor [10] for uniaxial impact loading of a long rod provides insight to the column problems of interest in this paper. Specifically, at the higher rates of loading of interest, the column remains nearly straight in the early stage of deformation and behavior is dominated by an axial plastic compression wave.

For the case of a semi-infinitely long bar ($0\leqslant x<\infty$) at rest at $t=0$ and subject to a uniform velocity, $\dot{u}(0,t)=V>0$, at its left end, a similarity solution to (2) exists [9,10] with dependence on a single dimensionless variable $\xi=x/(c_0 t)$ where $c_0=c(0)=\sqrt{E/\rho}$ is the elastic wave speed with E as Young's modulus. The solution is simple but highly nonlinear and implicit. Only the details of interest will be presented here. The solution depends on the relation between ε and ξ defined by $c(\varepsilon)/c_0=\xi$ and the inverse of this relation denoted by $\varepsilon=g(\xi)$. The regime $\xi>1$ lies ahead of the disturbance; the regime $\xi_U<\xi<1$ has the strain dependence $\varepsilon=g(\xi)$; and the regime $0<\xi<\xi_U$ has uniform strain with $\varepsilon\equiv\varepsilon_U=g(\xi_U)$ and uniform velocity $\dot{u}=V$. The front of the section of the rod having uniform strain ε_U and velocity V propagates down the rod with speed $c(\varepsilon_U)$. The transition value ξ_U depends on the imposed velocity V according to the highly implicit equation

$$(1-e^{g(\xi_U)})\xi_U+\int_{\xi_U}^{1}(1-e^{g(\xi)})d\xi=\frac{V}{c_0} \tag{3}$$

The solution is illustrated for a Ramberg–Osgood stress–strain relation

$$\frac{\varepsilon}{\varepsilon_Y}=\frac{\sigma}{\sigma_Y}+\left(\frac{\sigma}{\sigma_Y}\right)^n \tag{4}$$

with yield stress σ_Y, yield strain $\varepsilon_Y=\sigma_Y/E$, strain hardening exponent $N=1/n$ ($0<N<1$) and tangent modulus

$$\frac{E}{E_t}=1+n\left(\frac{\sigma}{\sigma_Y}\right)^{n-1} \tag{5}$$

Details of the solution, which must be obtained numerically using (3), are plotted in Fig. 2. Both the strain and the nominal compressive stress (compressive force per original area, $\sigma_N=-\sigma e^{-\varepsilon}$) in the uniformly strained region are displayed.

An analytical approximation is obtained by assuming the strains are small and neglecting σ compared to E_t in (2) such that $c(\varepsilon)=\sqrt{E_t/\rho}$. Then, neglecting the linear stress contribution to the strain in (4), it is readily shown that $g(\xi)=-\varepsilon_Y(\xi/\sqrt{N})^{-2/(1-N)}$ with

$$\frac{\varepsilon_U}{\varepsilon_Y}=-\left[\frac{1+N}{2\sqrt{N}}\left(\frac{V}{c_0\varepsilon_Y}\right)\right]^{2/(N+1)} \tag{6}$$

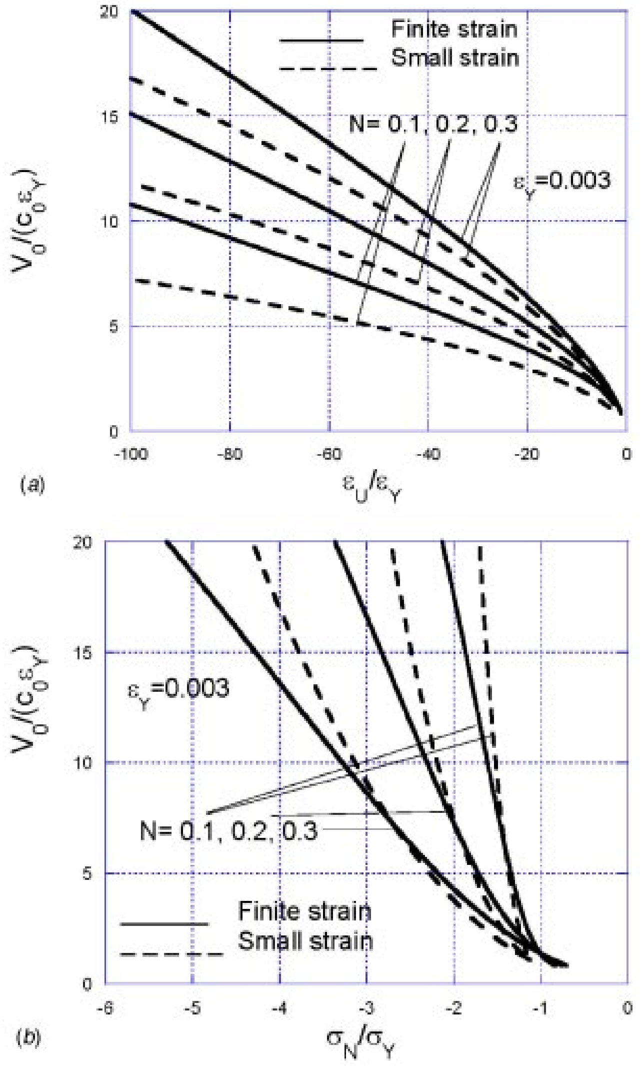

Fig. 2 Plastic compression wave propagating along a rod for both the small strain approximation and the finite strain solution. (*a*) Strain ε_U in the region of uniform deformation behind the propagating front. (*b*) Nominal compressive stress at the left end of the rod and in the adjacent region of uniform strain. The normalizations for the small strain approximation are valid for all yield strains; the results for the finite strain solution are computed with $\varepsilon_Y = 0.003$.

$$\frac{\sigma_N}{\sigma_Y}=\left[\frac{1+N}{2\sqrt{N}}\left(\frac{V}{c_0\varepsilon_Y}\right)\right]^{2N/(N+1)} \tag{7}$$

$$\frac{c(\varepsilon_U)}{c_0}=\sqrt{N}\left[\frac{1+N}{2\sqrt{N}}\left(\frac{V}{c_0\varepsilon_Y}\right)\right]^{-(1-N)/(1+N)} \tag{8}$$

The small strain solution depends on the imposed velocity, V, and initial yield strain through the single parameter, $V/c_0\varepsilon_Y$, which will be seen to be the most important dimensionless parameter governing dynamic effects in the present study. The small strain approximation is also plotted in Fig. 2, where it is seen that it indeed captures the essential trends for $V/c_0\varepsilon_Y$ as large as about 20. The front of the uniformly strained section of the rod propagates at a small fraction of the elastic wave speed when $V/c_0\varepsilon_Y \approx 10$, corresponding to imposed velocities V that are typically several percent of the elastic wave speed. Since an initial yield strain usually lies within the range from 0.001 to 0.01, it follows that for structural metals plastic wave propagation effects become dominantly important for impact velocities V typically in the range from 10 to 100 ms^{-1}.

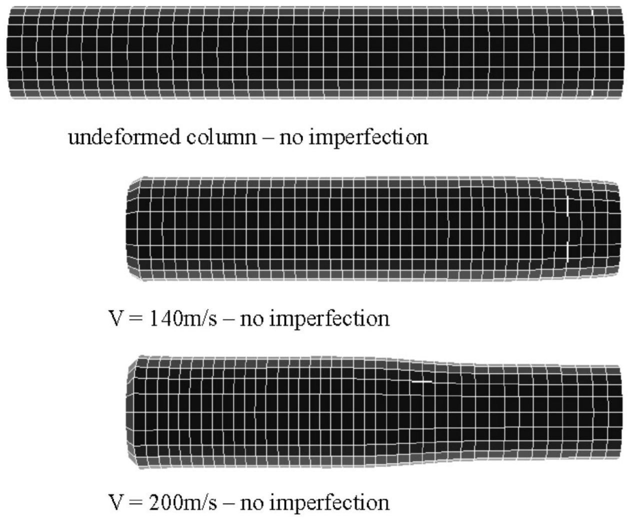

Fig. 3 Undeformed and deformed meshes for a straight rod subject to velocities $V = 140\ \text{ms}^{-1}$ and $V = 200\ \text{ms}^{-1}$ [$V/(c_0\varepsilon_Y) = 13.3$ and 19] at its left end and fixed at its right end. The deformed rods have been deformed to an overall strain of 20%. No material rate dependence.

2.3 Dynamic Compression of Finite Length Rods. In this section the study of dynamic compressive behavior of the straight column, or rod, is continued accounting the effect of finite length. As in the previous section, the rod is initially at rest. At $t = 0$, a uniform velocity, $V > 0$, is imposed at its left end while the right end at $x = L$ is fixed. In the study in this subsection the material is taken to be the rate-independent limit of a structural stainless steel, Al6XN, currently being considered as a possible candidate for truss cores. This material has substantial strain hardening that is nearly linear and moderate strain-rate sensitivity. The full rate-dependent specification of the material is given below in anticipation of its use in subsequent sections. In tension, the relation between true stress and true strain is taken to be strictly bilinear for each value of plastic strain-rate:

$$\sigma=\begin{cases} E\varepsilon, & \varepsilon \le \varepsilon_Y(1+(\dot\varepsilon_p/\dot\varepsilon_0)^m) \\ \sigma_Y(1+(\dot\varepsilon_p/\dot\varepsilon_0)^m)+E_t\varepsilon_p, & \varepsilon > \varepsilon_Y(1+(\dot\varepsilon_p/\dot\varepsilon_0)^m) \end{cases} \tag{9}$$

with $E = 190$ GPa, $\sigma_Y = 400$ MPa, $E_t = 2.4$ GPa, $\dot\varepsilon_0 = 4920\ \text{s}^{-1}$, $m = 0.154$, $\rho = 7920\ \text{kg m}^{-3}$, and Poisson's ratio $\nu = 0.3$. The strain-rate dependence results in a 57% elevation of the stress for $\dot\varepsilon = 1000\ \text{s}^{-1}$ versus the stress at $\dot\varepsilon = 0.01\ \text{s}^{-1}$ at the same ε_p. The rate-independent limit used in this section is obtained by setting $m = 0$. Comparisons will be made between predictions with and without rate-sensitivity in the following sections.

The finite strain version of ABAQUS Explicit [11] has been used to compute the responses. The right face of the column is attached to a fixed rigid plate and left face of the column is attached to a rigid plate with prescribed uniform velocity V for $t \ge 0$. The column model is comprised of eight-noded linear hexahedral elements. The model accounts for radial inertia. In the computations, the initial length of the rod is $L = 0.122$ m and its radius R is taken to be $L/13$. An undeformed mesh and a representative deformed mesh at an overall compressive strain of 20% are shown in Fig. 3 for two values of V. Further mesh refinement does not appreciably alter the results discussed below. The range of imposed velocities of relevance to the applications described in the Introduction is $V/(c_0\varepsilon_Y) \le 20$.

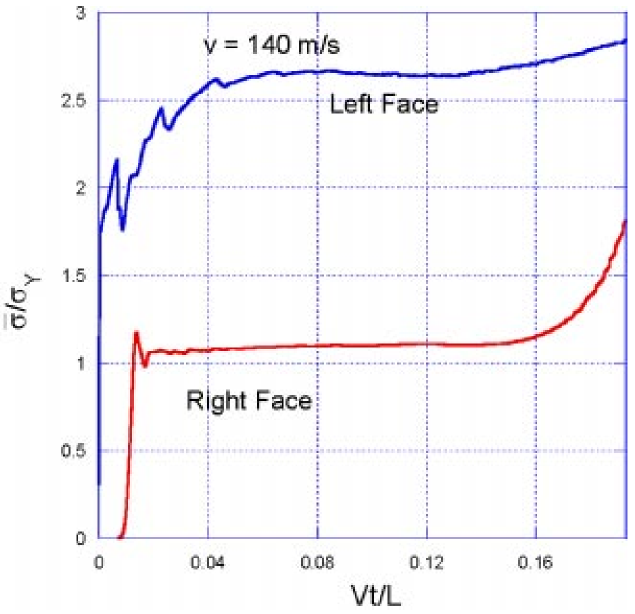

Fig. 4 Nominal stress exerted by a rod on the plates at its two ends, where the left plate impacts the rod at $V=140\ \mathrm{ms}^{-1}$ $[V/(c_0\varepsilon_Y)=13.3]$ and the right plate is fixed.

The response of the column to a constant velocity $V=140$ m/s $[V/(c_0\varepsilon_Y)=13.3]$ is shown in Fig. 4. The forces on the left and right plates are shown. Oscillations in the force on the left plate at early times in the history are due to numerical effects associated with the abrupt increase of the applied velocity. To reduce these oscillations, the applied velocity on the left plate is increased from zero to V in a more gradual manner according to $V(1-e^{-t/t_0})$. The oscillations are largely smoothed out and behavior for $Vt/L>0.05$ is virtually unaffected by the choice of t_0 as long as $V_0t_0/L<0.02$. Oscillatory effects are much smaller on the right face since there is no response until the arrival of the elastic compression wave.

Aside from oscillations at early times, the force on the left plate is fairly constant throughout the deformation and well above with the yield stress, consistent with the results for the infinitely long rod discussed in the previous section. The force on the left face remains level to a nominal overall strain of 20% $(Vt/L=0.2)$, at which point the computation was terminated. Thus, due to inertial effects there is a significant difference between the force a core element will exert on the face sheet towards a blast loading and on the face sheet away from the blast. The deformed mesh in Fig. 3 shows the rod at 20% strain $(Vt/L=0.2)$ where the thicker, uniformly compressed region has just reached the far end in the case $V=140$ m/s, while for the rod subject to the higher end velocity $V=200$ m/s the compressed region has only spread over two-thirds the length of the rod at the same overall strain.

Results such as those shown in Fig. 4 have been computed for 20 m/s$\leqslant V \leqslant$200 m/s. For $V<20$ m/s $[V/(c_0\varepsilon_Y)<1.9]$, dynamic effects are not nearly so pronounced with plastic deformation occurring more uniformly along the rod and end forces that are nearly equal.

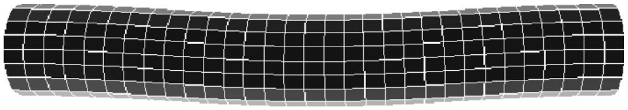

undeformed column – with imperfection

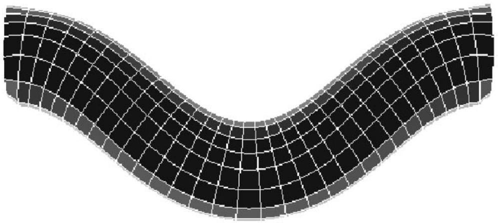

static – with imperfection

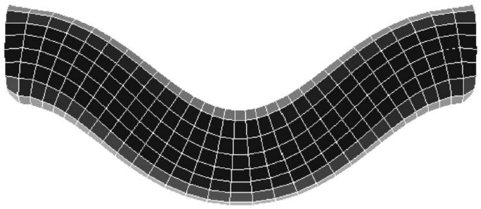

v = 20m/s – with imperfection

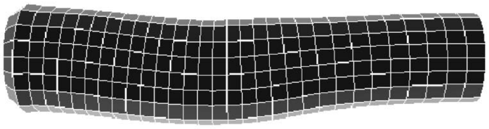

v=200m/s – with imperfection

Fig. 5 Undeformed and deformed meshes of column with initial imperfection for quasistatic, $V=20$ m/s, and $V=200$ m/s $[V/(c_0\varepsilon_Y)=1.9]$ and high $[V/(c_0\varepsilon_Y)=19]$. No material rate dependence.

3 Coupled Plastic Wave Propagation and Lateral Buckling for Axially Compressed Columns

In this section, results for the straight, finite length column analyzed in the previous section are determined under circumstances where the column is permitted to buckle. The material comprising the column is described by (9) which includes rate-dependence, however, results will be presented to highlight the roles of both strain hardening and strain-rate dependence. As in the study of the previous section, the ends of the column are "welded" to rigid plates and thus effectively clamped against rotation at each end. The left plate experiences an imposed uniform velocity V starting at $t=0$, while the right end is fixed. The dynamic calculations are carried out using a three-dimensional meshing using hexahedral elements with ABAQUS Explicit; quasi-static calculations use the Standard version. A geometric imperfection is introduced to promote lateral buckling motion in the form of an initial transverse deflection

$$w(x)=\frac{\zeta R}{2}\left[1-\cos\left(\frac{2\pi x}{L}\right)\right] \tag{10}$$

where ζ is the normalized imperfection amplitude. As will be shown later, an axially compressed column with imperfection amplitude $\zeta=1/4$ provides a reasonable approximation to the response of the tetragonal truss core construction where the members are inclined but have no initial imperfection. Under dynamic conditions, a perfectly straight column that is not inclined does not buckle, assuming no other imperfections due either to loading or material asymmetry. The nature of the governing equations is such that solution bifurcations do not occur. Dynamic buckling requires an initial asymmetric imperfection of some type, and, moreover, the development of the lateral buckling motion depends on the imperfection amplitude. For relatively stocky columns of interest here, an imperfection with $\zeta=1/4$ can be regarded as realistic, and later it will be shown that the buckling response is not a strong function of ζ in this range.

The role of inertia in altering the column response is illustrated in Fig. 5 where deformed columns at a nominal strain of 20% are

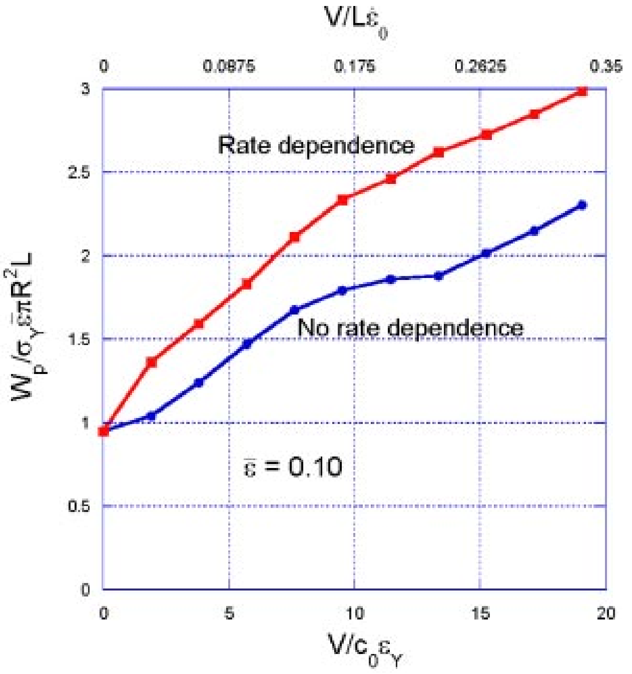

Fig. 6 Plastic energy dissipation as a function of $V/(c_0\varepsilon_Y)$ [and $V/(L\dot{\varepsilon}_0)$], with and without strain-rate dependence at an overall strain $\bar{\varepsilon}=0.1$ for the material specified by (9) and $c_0\varepsilon_Y/(L\dot{\varepsilon}_0)=0.0175$.

shown for very slow (quasistatic loading) and two other imposed velocities, $V=20$ m/s and 200 m/s. The buckled shapes of the quasistatically loaded column and that with $V=20$ m/s are similar and representative of the classical mode of a clamped beam. By contrast, the column loaded with $V=200$ m/s ($V/\varepsilon_Y c_0=19.4$) has undergone relatively little lateral displacement even at an overall strain of 20% and it is evident from the deformed shape that the majority of compression has occurred within the left half of the column. The plastic wave traveling from the left end has not yet spread over the entire column at the instant of the deformation in Fig. 5, and lateral buckling is just beginning to develop.

There are important consequences of the dynamic stabilization of the columns against lateral buckling seen in Fig. 5. In applications of all-metal sandwich construction for blast resistant plate structures, energy absorption in the core is an important component of superior performance. Any delay of buckling of a truss core member due to inertial stabilization translates into greater plastic energy dissipation. The column in Fig. 5 loaded at $V=200$ m/s has absorbed the energy equivalent of the material strained to 20% under uniaxial compression, albeit nonuniformly along its length. The energy absorbed by the column loaded quasistatically to 20% overall strain is considerably less since it undergoes significant lateral buckling and loss of load carrying capacity. Under uniaxial compression, energy absorption scales with $\sigma_Y\bar{\varepsilon}\pi R^2L$, where $\bar{\varepsilon}=Vt/L$ is the overall strain, and Fig. 6 displays the plastic energy dissipation in the column at $\bar{\varepsilon}=0.1$ normalized by this factor as a function of $V/(\varepsilon_Y c_0)$, with and without material strain-rate dependence. This plot brings out the exceptionally strong influence of dynamic loading on plastic dissipation as measured by the parameter $V/(\varepsilon_Y c_0)$; energy absorption can be enhanced by a factor of 2 or more in the range $V/(\varepsilon_Y c_0)>10$.

AL6XN has moderately high strain hardening. To separate out the influence of strain hardening on inertial stabilization and its related effects, columns of elastic-perfectly plastic material are investigated with the same initial yield stress as AL6XN in (9). The overall load-end shortening responses under quasistatic loading with and without strain hardening (both materials have $m=0$) are plotted in Fig. 7, where each of the two columns have an initial imperfection with $\zeta=1/4$. High strain hardening leads to significantly more postbuckling load carrying capacity. The substantial quasistatic postbuckling capacity for both columns is a consequence of their relative stockiness ($L/R=13$) and the fact that they are clamped on both ends.

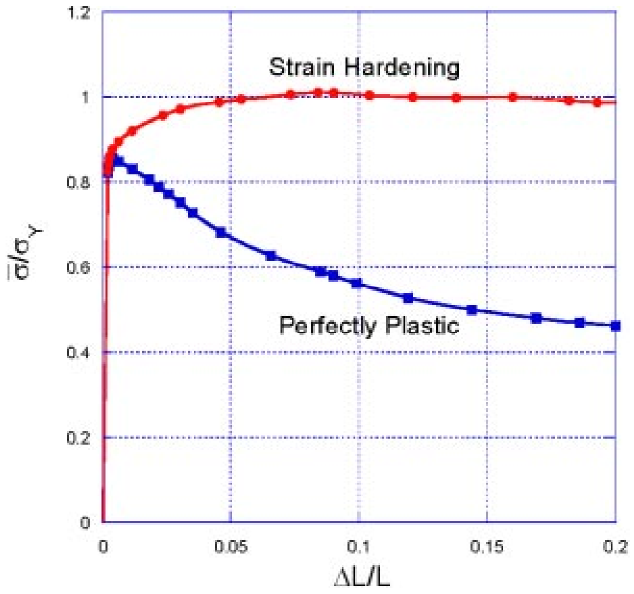

Fig. 7 Quasistatic nominal stress-end shortening behavior with and without strain hardening. The material is specified by (9) with $E_t=0$ and $m=0$ for the elastic-perfectly plastic case and $E_t=2.4$ GPa and $m=0$ for the hardening material. The stockiness ratio is $R/L=0.077$ and the imperfection amplitude is $\zeta=1/4$.

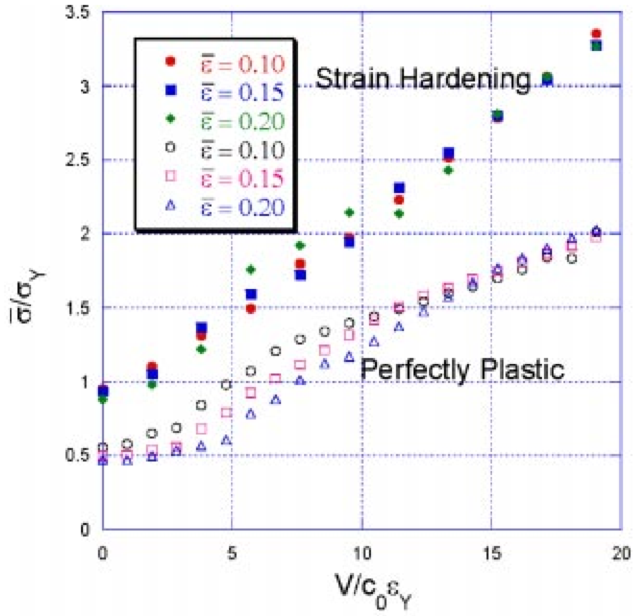

Fig. 8 Nominal stress acting by the column on the left plate as a function of the normalized imposed velocity V at three levels of overall strain for both an elastic-perfectly plastic material [(9) with $E_t=0$ and $m=0$] and a material with high strain hardening [(9) with $E_t=2.4$ GPa, $m=0$]. The imperfection amplitude is $\zeta=1/4$.

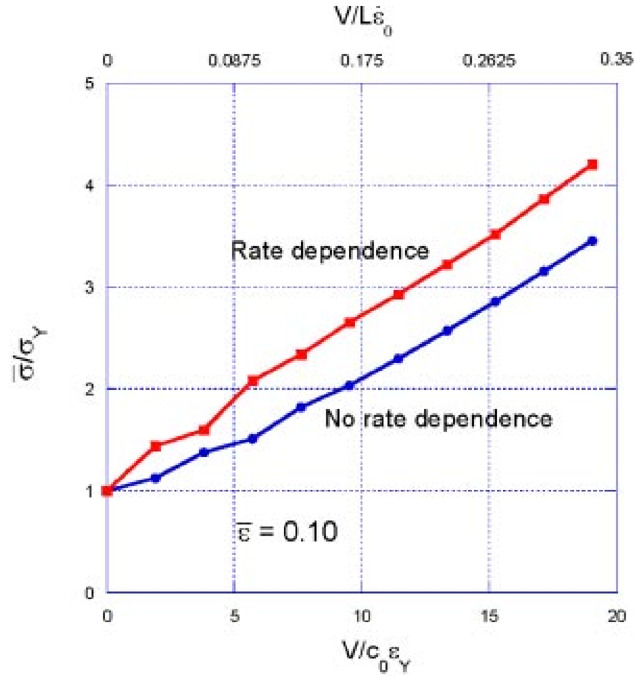

Fig. 9 Nominal stress acting by the column on the left plate as a function of the normalized imposed velocity V for a strain hardening material (9) with $(m=0.154)$ and without $(m=0)$ strain-rate dependence at an overall strain of 10%. The imperfection amplitude is $\zeta=1/4$ and $c_0\varepsilon_Y/(L\dot{\varepsilon}_0)=0.0175$.

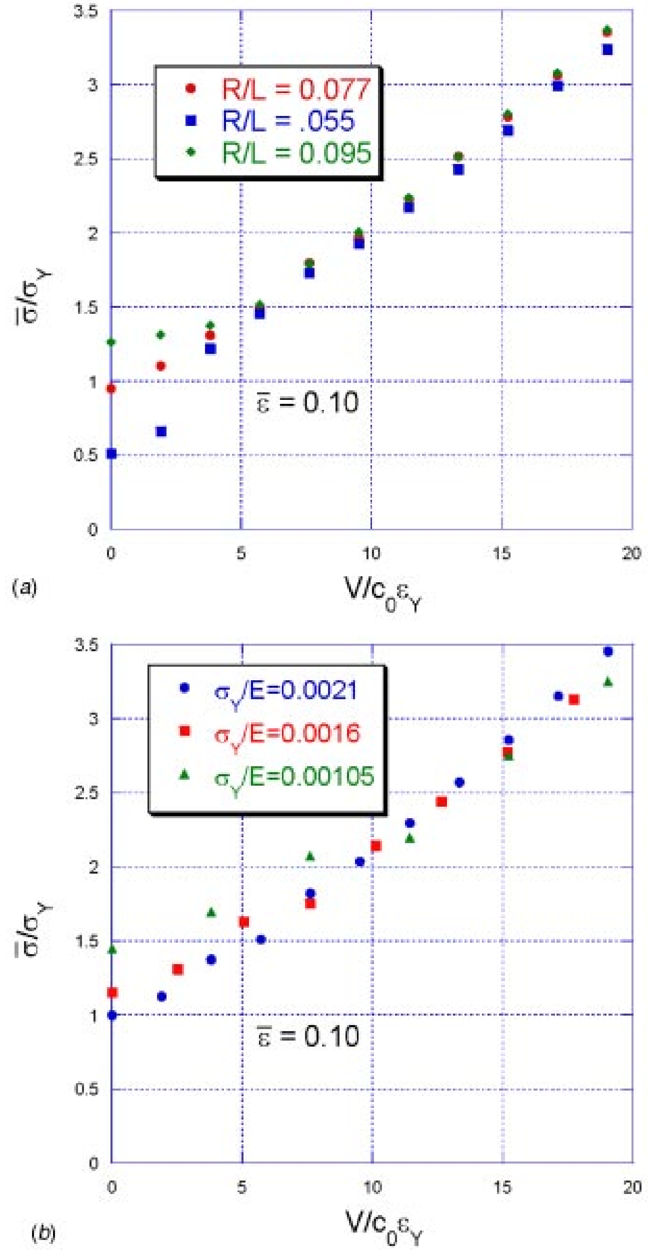

Fig. 10 (*a*) Effect of the stockiness, *R*/*L*, on the nominal stress acting by the column on the left plate as a function of the normalized imposed velocity *V* for a strain hardening material with no strain-rate dependence [(9) with $E_t=2.4$ GPa, $m=0$]. The imperfection amplitude is $\zeta=1/4$. (*b*) Effect of the yield strain, $\varepsilon_Y=\sigma_Y/E$, on the nominal stress acting by the column on the left plate as a function of the normalized imposed velocity *V* for a strain hardening material with no strain-rate dependence [(9) with $E_t=2.4$ GPa, $m=0$]. The imperfection amplitude is $\zeta=1/4$.

Computed values of the normalized force exerted by the column on the plate on the left end as a function of imposed velocity are given in Fig. 8 for a column of elastic-perfectly plastic material and of strain hardening typical of AL6XN in (9), both with no rate-dependence $(m=0)$. With F as the force, the normalization is $\bar{\sigma}/\sigma_Y$, where $\bar{\sigma}=F/A_0$ is the nominal stress and A_0 is the initial cross-sectional area of the column. It can be seen that the force is nearly independent of strain, consistent with the responses discussed earlier in Fig. 4, except for the elastic-perfectly plastic column at low levels of imposed velocity. The most striking feature of the results in Fig. 8 is the large amplification of the force exerted by the column on the left plate as V is increased. Force amplification arises from two sources: (1) inertial stabilization of the column against buckling and (2) the momentum imparted to the column by the left plate. The component associated with inertial stabilization gives rise to the increased plastic dissipation of Fig. 6.

The effect of material strain-rate dependence on the reaction force on the left plate is shown in Fig. 9. The lower curve is that discussed for AL6XN with strain-rate dependence suppressed [$m=0$ in (9)] while the upper curve incorporates the strain-rate dependence of this material. When material rate-dependence is taken into account, additional dimensionless parameters arise: m and $V/(L\dot{\varepsilon}_0)$. The results in Fig. 9 include the values of $V/(L\dot{\varepsilon}_0)$ on the abscissa. The elevation of the reaction force due to material strain-rate dependence over the corresponding force for the rate-independent material is what would be expected for the overall strain rate of $10^3\ \mathrm{s}^{-1}$ [corresponding to the impact velocity with $V/(\varepsilon_Y c_0)=11.6$ in Fig. 9]; the influence is similar to that seen in Fig. 6 on the energy dissipation.

Based on dimensional considerations, the normalized reaction force depends on a relatively large dimensionless parameter set according to

$$\frac{\bar{\sigma}}{\sigma_Y}=f\left(\frac{V}{\varepsilon_Y c_0},N,\frac{\sigma_Y}{E},\frac{R}{L},\frac{Vt}{L},\frac{V}{L\dot{\varepsilon}_0},m\right) \tag{11}$$

with $c_0=\sqrt{E/\rho}$. Equation (11) brings out the point emphasized by Calladine and English [5] that inertial effects and material rate-dependence effects scale differently with respect to column length. In the range of behavior in which inertial effects are dominated by axial deformation, the controlling parameter is $V/(\varepsilon_Y c_0)$. The dimensionless parameter controlling the influence of material rate-dependence is $V/L\dot{\varepsilon}_0$. The results presented above suggest that the dependence of end forces and energy dissipation on material strain-rate dependence through m and $V/L\dot{\varepsilon}_0$ is more-or-less what would be expected at the overall strain-rate, given its effect in elevating the flow stress in (9). In the range of overall strain Vt/L from 0.05 to more than 0.2, the normalized reaction force is essentially independent of strain for relatively stocky columns, except for small strain hardening at low imposed velocities.

The effect of the slenderness ratio, R/L, and the initial yield strain, $\varepsilon_Y=\sigma_Y/E$, on the normalized reaction force at an overall strain of 10% are shown in Figs. 10(*a*), 10(*b*). The slenderness ratio has a significant effect at small $V/(\varepsilon_Y c_0)$ but almost no effect at higher values of this parameter, consistent with the fact that the buckling deflections remain small until overall strains are in excess of 20%. Similarly, for the normalizations used in Fig. 10(*b*), there is little dependence on the initial yield strain.

In summary, for a specific material in the range of imposed velocities satisfying $V/(\varepsilon_Y c_0)>5$ and for overall strains from roughly 5% to 20%, the single most important dimensionless parameter in (11) is $V/(\varepsilon_Y c_0)$, with $V/L\dot{\varepsilon}_0$ playing a secondary role, such that the nominal reaction stress resisting the motion of the plate imposing its velocity on the column has the form

$$\frac{\bar{\sigma}}{\sigma_y}=f\left(\frac{V}{\varepsilon_Y c_0},\frac{V}{L\dot{\varepsilon}_0}\right). \tag{12}$$

4 The Dynamic Response of Tetragonal Truss Core

Finite element calculations have been performed on the tetragonal truss core unit of Fig. 1 under conditions where the rigid bottom plate is held fixed and the rigid top plate to which the core faces are welded is suddenly accelerated towards the bottom plate with velocity V. The emphasis here is on the reaction force exerted by the core element on the top plate, and it will be shown that this resistance can be successfully modeled using the results for the axially loaded columns of the previous section. Each member of the unit of the regular tetrahedron in Fig. 1 is a column of length L and solid circular cross-section of radius R with $R/L=0.077$. The precise geometry is shown in Fig. 1. The height, H of the core is specified by $H/L=\sqrt{2/3}$. The material is that specified in (9) with no strain rate dependence $(m=0)$. Results are computed for various imposed velocities for overall strains up to 20% $(\bar{\varepsilon}=Vt/H=0.2)$. The average reaction stress, $\bar{\sigma}$, acting on the top plate and plotted in Fig. 11 is the net vertical force divided by the area of the tetragonal unit. The results of the simulations for the tetragonal core are plotted as solid points. As in the case of the axially loaded columns, there is relatively weak dependence on overall strain for strains in the range from 5% to 20%.

The insert in Fig. 11 compares the deformed shape of a member of the tetragonal unit for a case with quasistatic loading with one subject to high velocity loading, both at an overall strain of about 20%. The deformation of the dynamically loaded member is primarily confined to its upper third while the lower portion of the member remains almost straight. By contrast, the member deformed quasistatically undergoes bending deformations due to buckling over its entire length.

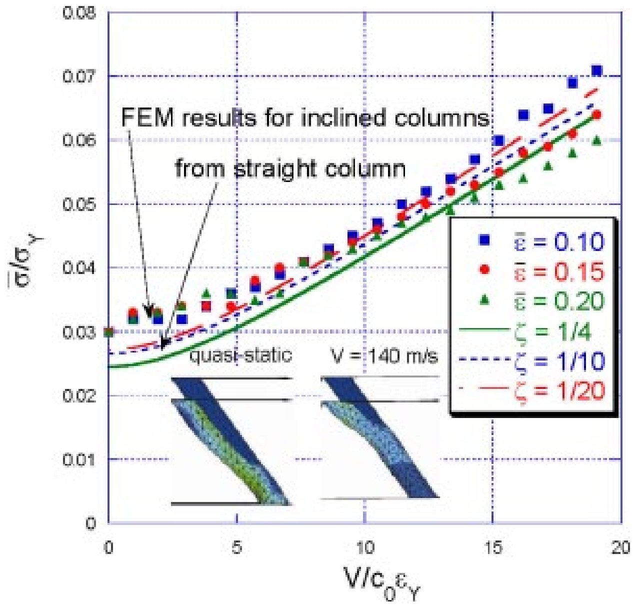

Fig. 11 Normal component of reaction force exerted by an inclined column member of a tetragonal truss core on left plate as a function of normalized imposed velocity V at three levels of overall strain and the result derived from an axially loaded column with three levels of initial imperfection. The insert on the right shows the dynamically loaded column (with $V/c_0\varepsilon_Y=15$) while the insert on the left shows the quasistatically deformed column.

Included in Fig. 11 are predictions of the average reaction stress based on the results obtained in the previous section for the axially loaded clamped column with three levels of initial imperfection. To plot the results based on the axially loaded column, the length and aspect ratio of the column are identified with those of the inclined member. Furthermore, the axial velocity applied to the upper end of the column is the component of the approach velocity of the two plates resolved in the direction parallel to the column, i.e. $\sqrt{2/3}V$, and, as before, the lower end is fixed. Similarly, the vertical component of the reaction force acting on the upper plate is taken to be $3\sqrt{2/3}$ times the axial force in the column and converted to the stress averaged over the unit cell in Fig. 11. Since the results for the axial column are almost independent of the overall strain in the range from 5% to 20% (cf. Fig. 8), only the average over the strain range is plotted in Fig. 11 for the column approximation. The effect of the initial imperfection level is not large for the three levels shown and $\zeta=1/4$ seems to be a realistic choice. Finally, it is noted that the results based on those for the axially compressed column provide a reasonable approximation to the reaction force exerted by the tetragonal core.

5 Summary

The dimensionless parameter $V/(\varepsilon_Y c_0)$ can be used to gauge whether coupled plastic wave propagation and lateral buckling occurs in columns whose ends experience a relative velocity V, and relatively strong dynamics occur when $V/(\varepsilon_Y c_0)>5$. For relatively stocky columns, overall end-shortening corresponding to compressive strains of 20% or more can be achieved before appreciable bucking deformation occurs. The reaction force at the end of the column resisting the imposed motion is amplified by a factor of 2 or more above that for a quasistatically loaded column. Similarly, the energy dissipated in plastic deformation by the column at a given overall imposed strain is significantly increased due to the inertial stabilization of the column. The roles of the various geometric and material parameters are detailed in the paper for the case of constant velocity loading. These results provide insight into how columns can be expected to behave under other types of dynamic axial loading. The present paper reveals the importance of dynamic effects in the performance of truss cores of all-metal sandwich plates under high intensity dynamic loads.

Acknowledgments

This work has been supported in part by the ONR under Grant No. N00014-02-1-0700 and in part by the Division of Engineering and Applied Sciences, Harvard University. The authors acknowledge helpful discussions with N.A. Fleck and V. Deshpande.

References

[1] Xue, Z., and Hutchinson, J. W., 2004, "Preliminary assessment of sandwich plates subject to blast loads," Int. J. Mech. Sci., **45**, pp. 687–705.
[2] Johnson, W., and Reid, S. R., 1978, "Metallic energy dissipating systems," Appl. Mech. Rev., **31**, pp. 277–288.
[3] Abrahamson, G. R., and Goodier, J. N., 1966, "Dynamic flexural buckling of

rods within an axial plastic compression wave,'' J. Appl. Mech., **33**, pp. 241–247.

[4] Karagiozova, D., and Jones, N., 1996, ''Dynamic elastic-plastic buckling phenomena in a rod due to axial impact,'' Int. J. Impact Eng., **18**, pp. 919–947.

[5] Calladine, C. R., and English, R. W., 1984, ''Strain rate and inertia effects in the collapse of two types of energy-absorbing structures,'' Int. J. Mech. Sci., **26**, pp. 689–701.

[6] Anwen, W., and Wenying, T., 2003, ''Characteristic-value analysis for plastic dynamic buckling of columns under elastoplastic compression waves,'' Int. J. Non-Linear Mech., **38**, pp. 615–628.

[7] Lepik, Ulo, 2001, ''Dynamic buckling of elastic-plastic beams including effects of axial stress waves,'' Int. J. Impact Eng., **25**, pp. 537–552.

[8] Kenny, S., Pegg, N., and Taheri, F., 2002, ''Finite element investigations on the dynamic plastic buckling of a slender beam subject to axial impact,'' Int. J. Impact Eng., **27**, pp. 179–195.

[9] von Karman, T., and Duwez, P., 1950, ''The propagation of plastic deformation in solids,'' J. Appl. Phys., **21**, pp. 987–994.

[10] Taylor, G. I., 1958, *The Scientific Papers of G. I. Taylor*, Cambridge University Press, London, Vol. 1.

[11] ABAQUS/Explicit User's Manual, Version 6.2, Hibbit, Karlsson and Sorensen Inc., 2001.

Journal of
Applied
Mechanics

Brief Notes

A Brief Note is a short paper that presents a specific solution of technical interest in mechanics but which does not necessarily contain new general methods or results. A Brief Note should not exceed 2500 words *or equivalent* (a typical one-column figure or table is equivalent to 250 words; a one line equation to 30 words). Brief Notes will be subject to the usual review procedures prior to publication. After approval such Notes will be published as soon as possible. The Notes should be submitted to the Editor of the JOURNAL OF APPLIED MECHANICS. Discussions on the Brief Notes should be addressed to the Editorial Department, ASME International, Three Park Avenue, New York, NY 10016-5990, or to the Editor of the JOURNAL OF APPLIED MECHANICS. Discussions on Brief Notes appearing in this issue will be accepted until two months after publication. Readers who need more time to prepare a Discussion should request an extension of the deadline from the Editorial Department.

Exact Critical Loads for a Pinned Half-Sine Arch Under End Couples

Jen-San Chen
Professor
e-mail: jschen@ntu.edu.tw

Jian-San Lin
Graduate Student

Department of Mechanical Engineering,
National Taiwan University, Taipei, Taiwan 10617

In this note we show that for a pinned half-sine arch under end couples snap-through buckling will occur unsymmetrically if the initial height of the shallow arch is greater than 6.5466r, where r is the radius of gyration of the cross section. The closed-form expression for the critical couple can be obtained analytically. [DOI: 10.1115/1.1827244]

1 Introduction

The prediction of snap-through buckling of a shallow arch is a classical problem in applied mechanics. Fung and Kaplan [1] derived the exact critical loads for a pinned half-sine arch under sinusoidal loading. For other load distributions such as uniform pressure and a concentrated force at the midpoint, the critical loads can be obtained by summing a few terms of a rapidly converging Fourier series. For a complete review of the previous works of arch stability, the readers are referred to the two books by Simitses [2,3]. In all these previous works, the external loads causing snap-through buckling are lateral forces. In this note we consider the case when the sinusoidal arch is under couples at both ends.

2 Equilibrium Equation

We consider a pinned shallow arch with equal and opposite moments M^* applied to the two ends. This model finds application in an electromechanical switching device with a curved beam coated with piezoelectric films on the top and bottom surfaces. The end moment is proportional to the actuating voltage. The equilibrium equation of the loaded arch can be written as

$$EI(y-y_0)_{,xxxx}-p^*y_{,xx}+M^*[-\delta'(x)+\delta'(x-L)]=0 \tag{1}$$

p^* is the axial force

$$p^*=\frac{AE}{2L}\int_0^L(y_{,x}^2-y_{0,x}^2)dx \tag{2}$$

E, A, and I are Young's modulus, area, and moment of inertia of the cross section. L is the distance between the two pinned ends. δ' is the derivative of the Dirac delta function with respect to x. $y_0(x)$ is the initial shape of the arch. Equations (1) and (2) can be nondimensionalized to the forms

$$(u-u_0)_{,\xi\xi\xi\xi}-pu_{,\xi\xi}+\frac{\pi}{4}M[-\delta'(\xi)+\delta'(\xi-\pi)]=0 \tag{3}$$

$$p=\frac{1}{2\pi}\int_0^\pi(u_{,\xi}^2-u_{0,\xi}^2)d\xi \tag{4}$$

where

$$u=\frac{y}{r},\quad u_0=\frac{y_0}{r},\quad \xi=\frac{\pi x}{L},\quad p=\frac{p^*L^2}{\pi^2EI},\quad M=\frac{4M^*L^2}{\pi^5EIr} \tag{5}$$

r is the radius of gyration of the cross section. The initial shape of the arch is assumed to be in the form

$$u_0(\xi)=h\sin\xi \tag{6}$$

It is assumed that the shape of the deformed arch can be expanded as

$$u(\xi)=\sum_{n=1}^{\infty}\alpha_n\sin n\xi \tag{7}$$

After expanding the derivative of the Dirac delta function δ' as a Fourier sine series and substituting Eqs. (6) and (7) into Eqs. (3) and (4) we obtain the equations for α_n

$$n^4\alpha_n+n^2p\alpha_n+q_n=0,\quad n=1,2,3,\ldots \tag{8}$$

where

$$p=\frac{1}{4}\sum_{k=1}^{\infty}k^2\alpha_k^2-\frac{h^2}{4}, \tag{9}$$

$$q_1=M-h, \tag{10}$$

Contributed by the Applied Mechanics Division of THE AMERICAN SOCIETY OF MECHANICAL ENGINEERS for publication in the ASME JOURNAL OF APPLIED MECHANICS. Manuscript received by the ASME Applied Mechanics Division, January 28, 2004; final revision, May 19, 2004. Associate Editor: R. C. Benson.

$$q_n=0, \quad n=2,4,6,\ldots, \tag{11}$$

$$q_n=nM, \quad n=3,5,7,\ldots \tag{12}$$

3 Equilibrium Configurations

Equation (8) represents a set of an infinite number of coupled nonlinear equations for an infinite number of coordinates α_n. There are two types of solutions.

3.1 Symmetrical Solution. $\alpha_{2i}=0$, where $i=1,2,3,\ldots$ The equations in Eq. (8) with even number of n are satisfied automatically because of condition (11). The remaining coordinates α_{2i+1} can be related to α_1 by a simple deduction procedure from Eq. (8) as

$$\alpha_{2i+1}=\frac{-\alpha_1 q_{2i+1}}{(2i+1)^2[4i(i+1)\alpha_1-q_1]}, \quad i=1,2,3,\ldots \tag{13}$$

After substituting Eq. (13) into Eq. (9), and substituting the resulting p into Eq. (8) for $n=1$, we obtain the following equation for α_1

$$f_1(\alpha_1)+\sum_{i=1}^{\infty}\left\{\frac{q_{2i+1}^2\alpha_1^3}{4(2i+1)^2[4i(i+1)\alpha_1-q_1]^2}\right\}=0 \tag{14}$$

where

$$f_1(\alpha_1)=\alpha_1+\frac{\alpha_1}{4}(\alpha_1^2-h^2)+q_1 \tag{15}$$

In the special case when $M=0$, the three solutions of Eq. (14) are denoted by P_0, P_1^+, and P_1^- [4], respectively. P_0 represents the original shape, Eq. (6). P_1^- is another stable configuration on the other side. P_1^+ is an unstable position between P_0 and P_1^-.

3.2 Unsymmetrical Solution. $\alpha_{2j}\neq 0$ for some j, and all other $\alpha_{2i}=0$, $i=1,2,3,\ldots, i\neq j$. This type of solution involves odd number of n in Eq. (7), plus one additional harmonic with $n=2j$. For this type of solution we can solve for p from the $2j$th equation of Eq. (8) as

$$p=-4j^2 \tag{16}$$

After substituting Eq. (16) into the $(2i+1)$-th equation in Eq. (8) we can solve for α_{2i+1} exactly as

$$\alpha_{2i+1}=\frac{q_{2i+1}}{(2i+1)^2[4j^2-(2i+1)^2]} \quad i=0,1,2,\ldots \tag{17}$$

After substituting Eqs. (16) and (17) into Eq. (9) we can solve for α_{2j} as

$$\alpha_{2j}=\pm\frac{1}{2j}\sqrt{h^2-16j^2-\frac{q_1^2}{(4j^2-1)^2}-\sum_{i=1}^{\infty}\frac{q_{2i+1}^2}{(2i+1)^2[4j^2-(2i+1)^2]^2}} \tag{18}$$

This pair of solutions are denoted as $P_{1(2j)}^{\pm}$.

4 Snap-Through Buckling

By inspecting Eq. (14) for the root locus of α_1 we can show that for smaller h the root α_1 corresponding to P_0 will merge with $\alpha_1(P_1^+)$ as M increases from zero. For larger h, on the other hand, $\alpha_1(P_0)$ will merge with $\alpha_1(P_{12}^{\pm})$ instead, which is known explicitly from Eq. (17) as

$$\alpha_1(P_{12}^{\pm})=\frac{q_1}{3} \tag{19}$$

There then exists a special h, denoted by $\bar{h}$, at which $\alpha_1(P_0)$ will merge with both $\alpha_1(P_1^+)$ and $\alpha_1(P_{12}^{\pm})$ simultaneously. This situation occurs when Eq. (14) admits a double root, which requires the derivative of Eq. (14) with respect to α_1 to vanish

$$4\frac{df_1}{d\alpha_1}+\sum_{i=1}^{\infty}\left\{\frac{q_n^2\alpha_1^2}{(2i+1)^2[4i(i+1)\alpha_1-q_1]^2}\left[3-\frac{8i(i+1)\alpha_1}{4i(i+1)\alpha_1-q_1}\right]\right\}=0 \tag{20}$$

Therefore, if h is smaller than $\bar{h}$, the arch will snap symmetrically. On the other hand, if h is greater than $\bar{h}$, the arch will snap unsymmetrically. This note intends to present the exact critical moment for the latter case. After replacing α_1 in Eqs. (14) and (20) by $q_1/3$, both equations can be rearranged further into the forms

$$(1+9\kappa_1)M^2-2hM+144-8h^2=0 \tag{21}$$

$$(1+3\kappa_2)M^2-2hM+12-2h^2=0 \tag{22}$$

where

$$\kappa_1=\sum_{i=1}^{\infty}\frac{1}{(2i-1)^2(2i+3)^2}=\frac{9\pi^2-64}{576} \tag{23}$$

$$\kappa_2=\sum_{i=1}^{\infty}\frac{1}{(2i-1)^3(2i+3)^3}=\frac{51\pi^2-512}{1536} \tag{24}$$

After eliminating M from Eqs. (21) and (22) we can solve for this special h as $\bar{h}=6.5466$.

For the easy use in practical design procedure, we may summarize the conclusion in terms of physical parameters as follows. If the initial height h^* at the midpoint of the sinusoidal arch under end couples is greater than $6.5466r$, the shallow arch will snap unsymmetrically, and the critical couples can be found exactly as

$$M_{\mathrm{cr}}^{*\pm}=\frac{\pi^3 EI}{9L^2}\left[16h^*\pm 2\sqrt{(64+72\pi^2)h^{*2}-1296r^2\pi^2}\right] \tag{25}$$

M_{cr}^{*+} corresponds to the critical couple which will snap the arch from position P_0 to P_1^-. On the other hand, M_{cr}^{*-}, which is always negative, corresponds to the critical couple which will allow the arch to snap back from position P_1^- to P_0.

References

[1] Fung, Y. C., and Kaplan, A., 1952, "Buckling of Low Arches or Curved Beams of Small Curvature," NACA Technical Note 2840.

[2] Simitses, G. J., 1986, *Elastic Stability of Structures*, R. E. Krieger, Malabar, FL, Chap. 7.

[3] Simitses, G. J., 1990, *Dynamic Stability of Suddenly Loaded Structures*, Springer, New York, Chap. 7.

[4] Hsu, C. S., 1967, "The Effects of Various Parameters on the Dynamic Stability of a Shallow Arch," ASME J. Appl. Mech., **34**, pp. 349–358.

Analysis of the Bridgman Procedure to Characterize the Mechanical Behavior of Materials in the Tensile Test: Experiments and Simulation

Diego J. Celentano
e-mail: dcelenta@lauca.usach.cl

Eduardo E. Cabezas and Claudio M. García
Departamento de Ingeniería Mecánica,
Universidad de Santiago de Chile,
Av. Bdo. O'Higgins 3363, Santiago, Chile

This note presents an experimental analysis and a numerical simulation of the mechanical behavior experienced by cylindrical specimens of pure copper during the tensile test. A set of experiments has been carried out in order to derive the hardening parameters that characterize the material response. The simulation of the deformation process during the whole test is performed with a finite element large strain elastoplasticity-based formulation. The results of the simulation show that the mechanical characterization involving the classical Bridgman correction factor, defined in terms of logarithmic strains and aimed at predicting the stress distribution at the necking zone, cannot properly describe the hardening response for this material. Therefore, the use of a different correction factor, which consequently leads to another set of hardening parameters, is proposed. Finally, an adequate experimental validation of the numerical results is obtained for this last case. [DOI: 10.1115/1.1827243]

1 Introduction

The diffuse necking process of cylindrical samples used in the tensile test has been extensively studied (see, e.g., Refs. [1–3]). In particular, Bridgman [1] derived, based on some geometric considerations of the deformation pattern, analytical expressions for the stress distribution at the neck written in terms of the true (logarithmic) strain in this zone. Thus, this procedure allowed an adequate experimental derivation of the parameters involved in the hardening response. However, such relationships are only valid for certain materials (e.g., low carbon steels, some aluminum alloys, etc.) for which the maximum deformation ε_p^* related to a uniform strain and stress distributions along the specimen (i.e., just before the necking development) is around 0.10. Therefore, the applicability of this methodology to any material is rather limited.

On the other hand, several finite element large strain formulations usually defined within the plasticity framework have been developed and applied to the analysis of this test (see, e.g., Refs. [4–10], and references therein). Furthermore, some of such formulations have been validated with given experimental data considering cylindrical specimens of different materials. Nevertheless, Bridgman's assumptions have been only confirmed for materials presenting $\varepsilon_p^* \approx 0.10$.

The aim of this note is to analyze the Bridgman procedure to characterize the mechanical behavior, specifically the hardening response, of materials in the tensile test. To this end, an experimental analysis and a numerical simulation of the deformation process experienced by cylindrical specimens of pure copper is presented. This material has been intentionally chosen since the straightforward application of the earlier mentioned analytical expressions [1] to predict the stress distribution at the neck is not adequate because, as shown below, ε_p^* (which is a material characteristic parameter) is approximately 0.05 for this case. The experimental procedure undertaken to characterize some specific features of the material response is briefly described in Sec. 2 where details on the derivation of the parameters involved in the assumed potential plastic hardening law are also given. The numerical simulation of the tensile test is performed in Sec. 3. A full description of the large strain isotropic elastoplasticity-based formulation together with the corresponding finite element model used in the analysis can be found in Refs. [9,10]. First, the simulation is carried out with the hardening parameters derived from the experiments by applying the classical Bridgman stress correction factor. The respective numerical results show an inaccurate description of the hardening response for this material. Therefore, the use of an alternative correction factor, which consequently leads to another set of hardening parameters, is proposed. Then, the results obtained with these last parameters are found to adequately agree with the experimental measurements. Aside from the engineering stress-strain curve, different results at the section undergoing extreme necking are specifically analyzed: ratio of current to initial diameter in terms of the elongation and both load and mean true axial stress versus logarithmic strain.

2 Experimental Characterization

The experimental procedure adopted in this work to characterize the mechanical behavior of a material consisted of the following steps [9,10].

(1) Selection of the material and the specimen to be tested according to the American Society for Testing and Materials (ASTM) standards [11]. Cylindrical specimens of pure copper with a nominal diameter of 9 mm have been chosen considering an initial extensometer length of 50 mm.

(2) Chemical characterization to check an adequate composition according to the selected material. This routine task is carried out by means of an optical spectrometer.

(3) Mechanical tensile test. Engineering stress-strain curves have been obtained with five specimens considering a load cell speed of 2.5 mm/min (value within the range specified by the ASTM standards [11]). Only average experimental values will be shown below due to the good repeatability achieved in the measurements. As usual, the engineering stress is defined as P/A_0, where P is the axial load and A_0 is the initial transversal area while the engineering strain or elongation is computed as $(L-L_0)/L_0$, with L and L_0 being the current and initial extensometer lengths, respectively.

(4) Characterization of the plastic behavior. At high levels of elongation, the stress and strain distributions are no longer uniform along the specimen due to the necking formation that takes place in the samples. Therefore, the engineering stress-strain curve cannot provide a proper description of the physical phenomena involved in the test. Following the procedure proposed by Bridgman [1], the mechanical response can be adequately described by a different stress-strain curve defined in terms of the mean equivalent stress $\overline{\sigma}_{\mathrm{eq}}$ versus an equivalent deformation $\varepsilon_{\mathrm{eq}}$ (composed of an elastic and plastic contributions) respectively given by $\overline{\sigma}_{\mathrm{eq}}=f_B P/A$ and $\varepsilon_{\mathrm{eq}}=\overline{\sigma}_{\mathrm{eq}}/E+\varepsilon_p$, where $f_B(\varepsilon_p)\leqslant 1$ is an assumed known correction factor applied to the mean true axial stress P/A, A is the current transversal area at the necking zone, E is the Young's modulus, $\varepsilon_p=\ln(A_0/A)=-2\ln(D/D_0)$ is the true (logarithmic) deformation and D is the current diameter (as can be seen, D is the additional variable to be measured). Taking into account the correction factors shown in Fig. 1(a), two different experimental $\overline{\sigma}_{\mathrm{eq}}-\varepsilon_{\mathrm{eq}}$ relationships, respectively, plotted in Figs. 1(b) and 1(c), have been obtained from four specimens. It should

---

Contributed by the Applied Mechanics Division of THE AMERICAN SOCIETY OF MECHANICAL ENGINEERS for publication in the ASME JOURNAL OF APPLIED MECHANICS. Manuscript received by the ASME Applied Mechanics Division, May 18, 2004, final revision, June 17, 2004. Editor: R. M. McMeeking.

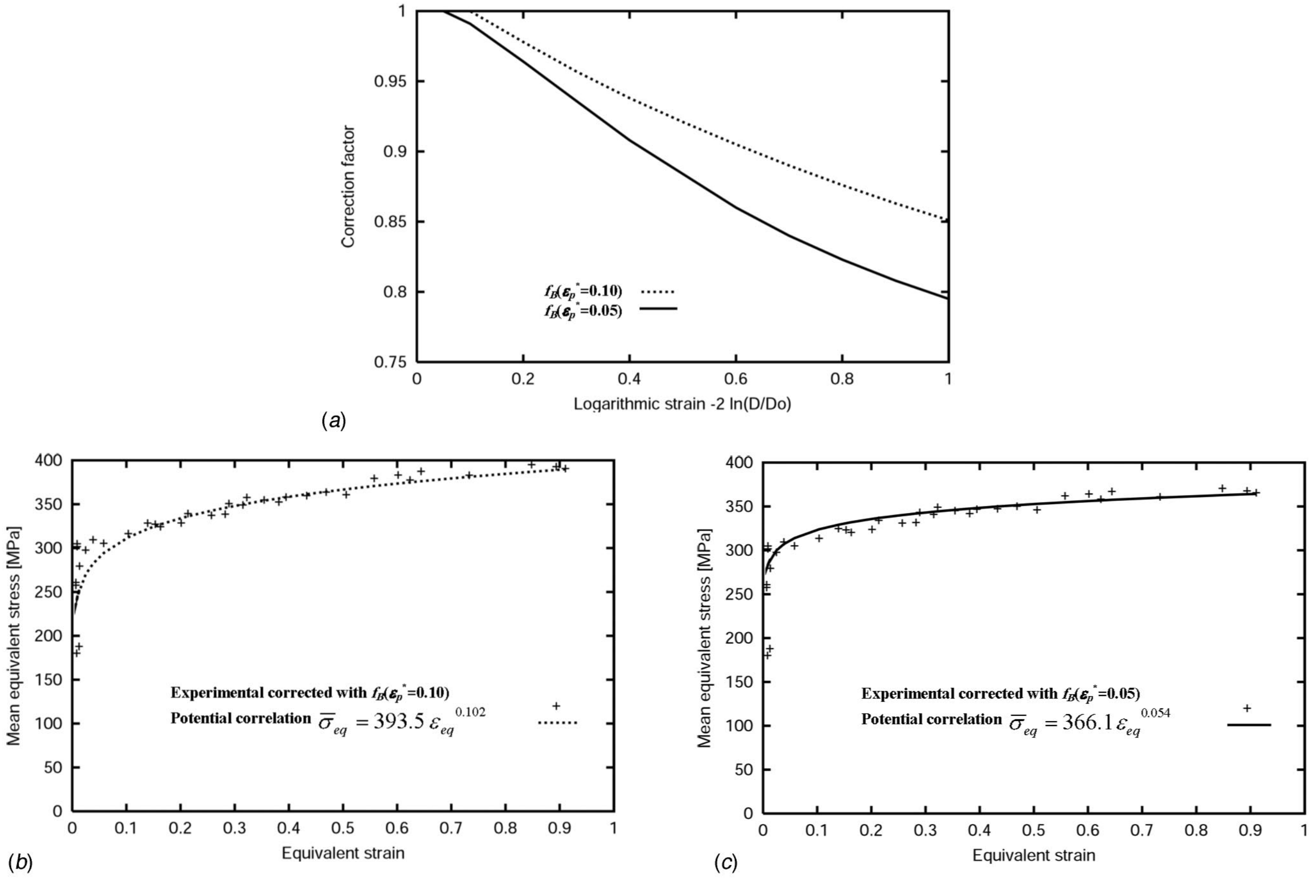

Fig. 1 Analysis of a copper cylindrical tension specimen. (*a*) Correction factor versus true deformation. Mean equivalent stress versus equivalent deformation obtained with (*b*) $f_B(\varepsilon_p^*=0.10)$ and (*c*) $f_B(\varepsilon_p^*=0.05)$.

be noted that $f_B(\varepsilon_p^*=0.10)$ is the classical Bridgman expression while $f_B(\varepsilon_p^*=0.05)$ is a proposed function specifically derived for pure copper through the experimental-numerical methodology detailed in Ref. [10] (in both cases, $f_B=1$ for $0 \leqslant \varepsilon_p \leqslant \varepsilon_p^*$ and $f_B < 1$ for $\varepsilon_p > \varepsilon_p^*$). Accordingly, two potential correlations of the type $\overline{\sigma}_{\mathrm{eq}} = A^p \varepsilon_{\mathrm{eq}}^{n^p}$ (as usual [1–10], this potential expression is assumed to govern the plastic isotropic hardening behavior of the material with A^p and n^p being hardening material parameters) have been derived from these data via a standard least-squares technique. They are, respectively, presented in Figs. 1(*b*) and 1(*c*) where, as can be seen, two different sets of hardening parameters have been obtained [$A^p=393.5$ MPa; $n^p=0.102$ for $f_B(\varepsilon_p^*=0.10)$ and $A^p=366.1$ MPa; $n^p=0.054$ for $f_B(\varepsilon_p^*=0.05)$]. The numerical responses computed with these properties are compared and discussed in Sec. 3.

3 Numerical Simulation and Experimental Validation

The main objective of the present analysis is to assess the numerical predictions corresponding to the two sets of hardening properties derived in the mechanical characterization described earlier for pure copper tensile cylindrical specimens and, additionally, to compare these responses with the respective experimental measurements. The other material properties considered in the computations are: Young's modulus 115,000 MPa, Poisson's ratio 0.34 and yield strength 188 MPa. Moreover, details about the spatial discretization used can be found in Refs. [9,10].

Figure 2 shows the engineering stress-strain relationship and some results at the section undergoing extreme necking: the diameter relation versus the elongation in the necking zone and, in addition, the load and mean true axial stress both against the logarithmic deformation. Experimental values as well as numerical results corresponding to the hardening parameters derived with $f_B(\varepsilon_p^*=0.10)$ and $f_B(\varepsilon_p^*=0.05)$ are all plotted together for comparison. In what follows, these two numerical solutions will be simply identified with the symbols $f_B(\varepsilon_p^*=0.10)$ and $f_B(\varepsilon_p^*=0.05)$, respectively.

In sharp contrast with the numerical predictions of $f_B(\varepsilon_p^*=0.10)$, an overall good agreement between the simulation obtained with $f_B(\varepsilon_p^*=0.05)$ and the experimental values can be observed. This is particularly apparent at high levels of elongation. Specifically, the engineering stress [Fig. 2(*a*)] and the diameter ratio [Fig. 2(*b*)] predicted by $f_B(\varepsilon_p^*=0.10)$ are both unrealistically overestimated in the engineering strain range where the neck formation occurs. Although both simulations have been computed up to the same final (fracture) elongation of 13.2%, note that the corresponding logarithmic strains at this stage are completely different [see Figs. 2(*c*) and 2(*d*)]: 0.67 for $f_B(\varepsilon_p^*=0.10)$ and 0.92 for $f_B(\varepsilon_p^*=0.05)$.

The experimentally measured load decreases from an elongation of 1.23% or, equivalently, from a logarithmic deformation ε_p of 0.045 onwards. The corresponding deformations provided by the two simulations are 5.12% and 0.058 for $f_B(\varepsilon_p^*=0.10)$ and 4.16% and 0.048 for $f_B(\varepsilon_p^*=0.05)$. However, the mean true axial stress continues increasing until the fracture stage where a large amount of plastic hardening can be appreciated. This indicates that a geometrical instability occurs (instead of a constitutive instability) since, as it is well known, the effect on the stress caused by the reduction of the transversal area at the necking zone pre-

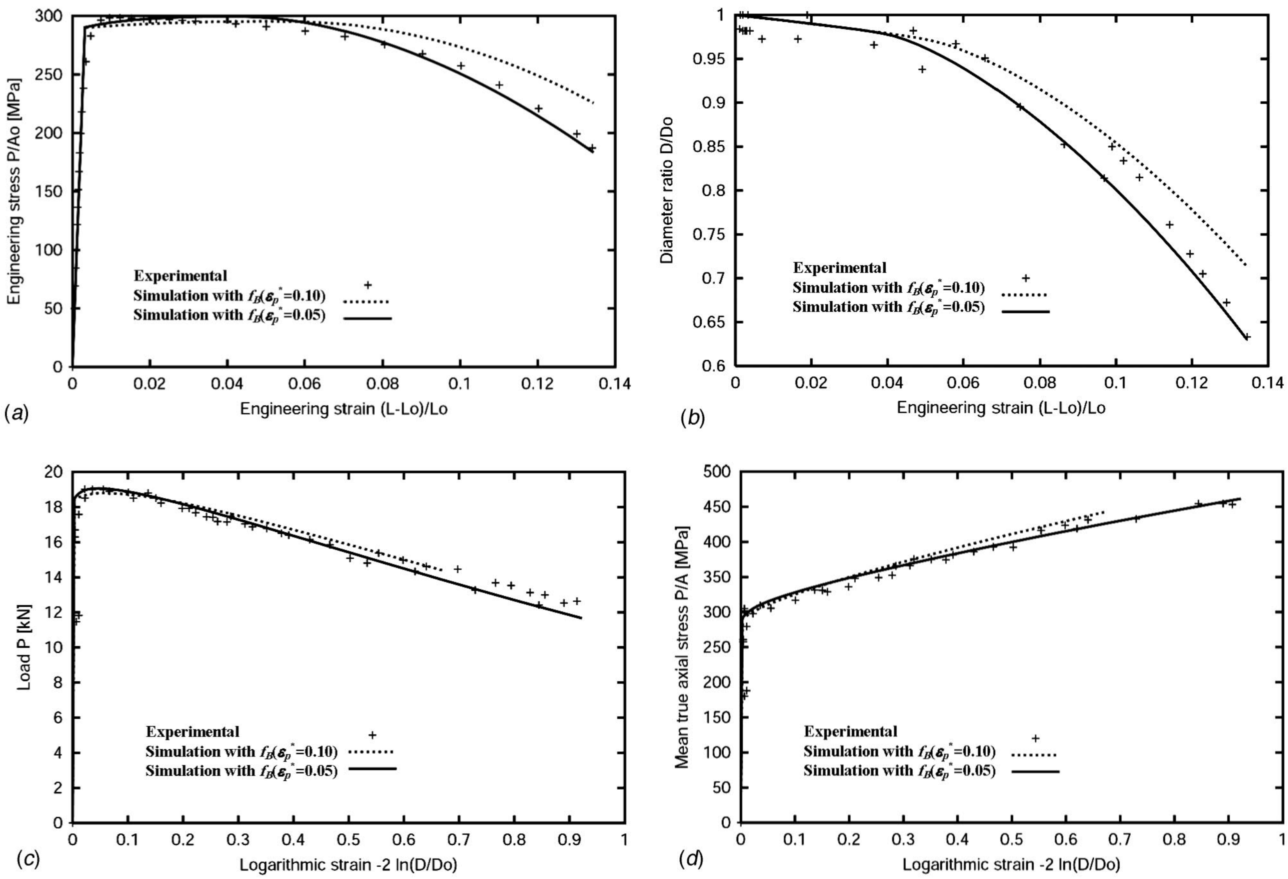

Fig. 2 Analysis of a copper cylindrical tension specimen. (*a*) Engineering stress-strain relationship. Results at the section undergoing extreme necking: (*b*) ratio of current to initial diameter versus axial elongation, (*c*) load versus true deformation, and (*d*) mean true axial stress vs true deformation.

dominates over the material hardening. Once the maximum load is reached, the regions of the specimen outside the necking zone begin to elastically unload.

The numerical predictions for the ratio of current to initial diameter in terms of the elongation start with a linear relationship, reflecting uniform distributions of stresses and strains, which presents an approximate slope of 0.5 due to the incompressibility nature of the plastic flow. This situation is kept up to elongations of 5.0% for $f_B(\varepsilon_p^*=0.10)$ and 4 % for $f_B(\varepsilon_p^*=0.05)$ that correspond, as mentioned earlier, to the respective points of maximum load. Afterwards, a sudden reduction of the diameter takes place causing the necking formation and, hence, nonhomogeneous stress and strain distributions along the specimen. As can be seen, the numerical results obtained with $f_B(\varepsilon_p^*=0.05)$ fit the experimental ones reasonably well during the whole test even with the inherent difficulty associated with the measurement of the diameter at the neck.

The experimental value of the logarithmic deformation corresponding to the maximum load is very close to the exponent n^p for the correlation obtained with $f_B(\varepsilon_p^*=0.05)$. Moreover, note that the well-known condition stated by the simplified relationship $n^p=\varepsilon_p^*$ [2,3] is nearly fulfilled in this case. This fact explains the satisfactory experimental validation of the numerical results corresponding to the hardening parameters experimentally derived through the application of the correction factor $f_B(\varepsilon_p^*=0.05)$. Larger values of n^p, like that obtained via $f_B(\varepsilon_p^*=0.10)$, lead to a unrealistic response for this specific material.

4 Conclusions

An experimental characterization and a numerical simulation of the mechanical behavior occurring in pure copper cylindrical specimens during the standard tensile test have been presented. The study has focused on the analysis of the Bridgman procedure aimed at deriving the material hardening parameters via the application of a stress correction factor that accounts for the nonhomogeneous stress and strain distributions along the specimen once the neck forms. It has been shown that the classical correction factor has led to a unrealistic material response. Therefore, the use of an alternative correction factor, obtained through a previously reported experimental-numerical methodology, has been proposed in order to derive another set of hardening parameters. The results provided by the simulation for this last case are consistent with the experimental data. However, it remains to be seen in further research if this alternative correction factor is applicable to other materials exhibiting $\varepsilon_p^*\approx 0.05$ in the tensile test.

Acknowledgments

The support provided by the Chilean Council of Research and Technology CONICYT (FONDECYT Project No. 1020026) and the Department of Technological and Scientific Research at the University of Santiago de Chile (DICYT-USACH) is gratefully acknowledged. The authors wish to express their appreciation to the Aeronautical Technical Academy at Santiago de Chile for the provision of experimental facilities.

References

[1] Bridgman, P., 1952, *Studies in Large Plastic and Fracture*, McGraw-Hill, London.

[2] Dieter, G., 1988, *Mechanical Metallurgy - SI Metric Edition*, McGraw-Hill, London.

[3] Nádai, A., 1950, *Theory of Flow and Fracture of Solids*, McGraw-Hill, London.

[4] Needleman, A., 1972, ‘‘A Numerical Study of Necking in Circular Cylindrical Bar,’’ J. Mech. Phys. Solids, **20**, pp. 111–127.

[5] Tvergaard, V., and Needleman, A., 1984, ‘‘Analysis of the Cup-Cone Fracture in a Round Tensile Bar,’’ Acta Metall., **32**, pp. 157–169.

[6] Simo, J., and Armero, F., 1992, ‘‘Geometrically Non-Linear Enhanced Strain Mixed Methods and the Method of Incompatible Modes,’’ Int. J. Numer. Methods Eng., **33**, pp. 1413–1449.

[7] Tvergaard, V., 1993, ‘‘Necking in Tensile Bars with Rectangular Cross-Section,’’ Comput. Methods Appl. Mech. Eng., **103**, pp. 273–290.

[8] Goicolea, J., Gabaldón, F., and García Garino, C., 1996, ‘‘Analysis of the Tensile Test Using Hypo and Hyperlastic Models,’’ (in Spanish) *Proceedings of the III Congress on Numerical Methods in Engineering*, pp. 875–885.

[9] Celentano, D., 2002, ‘‘Thermomechanical Analysis of the Tensile Test: Simulation and Experimental Validation,’’ Structural Engineering and Mechanics, **13**(6), pp. 591–614.

[10] Cabezas, E., and Celentano, D., 2004, ‘‘Experimental and Numerical Analysis of the Tensile Test Using Sheet Specimens,’’ Finite Elem. Anal. Design, **40(5-6)**, pp. 555–575.

[11] Annual Book of ASTM Standards, 1988, Section 3: Metals Test Methods and Analytical Procedures.